




# UNITED STATES DEPARTMENT OF TRANSPORTATION

## GLOBAL POSITIONING SYSTEM (GPS)

### ADJACENT BAND COMPATIBILITY ASSESSMENT

1432.0	FIXED	MOBILE** (** EXCEPT AERONAUTICAL MOBILE)		
1435.0		MOBILE (aeronautical telemetry)		
1525.0	SHARED USG/NON-USG	MOBILE SATELLITE (space-to-Earth)		
1559.0		RADIO-NAVIGATION SATELLITE (space-to-Earth) (space-to-space)		AERONAUTICAL RADIONAVIGATION
1610.0		RADIODETERMINATION-SATELLITE SATELLITE (Earth-to-space)	AERONAUTICAL RADIONAVIGATION	MOBILE SATELLITE (Earth-to-space)
1610.6	RADIO ASTRONOMY	RADIODETERMINATION-SATELLITE SATELLITE (Earth-to-space)	AERONAUTICAL RADIONAVIGATION	MOBILE SATELLITE (Earth-to-space)
1613.8				



## FINAL REPORT

APRIL 2018

## **EXECUTIVE SUMMARY**

The goal of the U.S. Department of Transportation (DOT) Global Positioning System (GPS) Adjacent Band Compatibility Assessment is to evaluate the maximum transmitted power levels of adjacent band radiofrequency (RF) systems that can be tolerated by GPS and Global Navigation Satellite System (GNSS) receivers. The results of this effort advance the Department's understanding of the extent to which such adjacent band transmitters impact GPS/GNSS devices used for transportation safety purposes, among numerous other civil applications. The assessment described in this report addresses transmitters in bands adjacent to the 1559-1610 MHz radionavigation satellite service (RNSS) band used for GPS Link 1 (L1) signals that are centered at 1575.42 MHz.

The assessment includes two primary components:

- One component, led by the DOT Office of the Assistant Secretary for Research and Technology (OST-R), focused on all civilian GPS devices and their applications, apart from certified aviation. Through this component of the Study, categories of receivers were evaluated that included aviation (non-certified), cellular, general location/navigation, high precision, timing, and space-based receivers. An element of this effort was to determine equipment susceptibility to adjacent band interference to support analyses for deriving compatible power levels.
- The other component, led by the Federal Aviation Administration (FAA), focused on certified GPS avionics, and was conducted by analysis to determine the adjacent band power levels that conform to existing certified GPS aviation equipment standards.

The DOT GPS Adjacent Band Study is the product of an extensive process to gather stakeholder views and input. OST-R and FAA benefited significantly from feedback received via governmental and public outreach on equipment use cases, interaction scenarios, propagation models, and transmitter characteristics.

Certified GPS avionics meet their performance requirements when operating within the RF interference (RFI) environment defined in appropriate FAA Technical Standard Orders (TSOs). For civil GPS/GNSS receivers other than certified avionics, receiver testing needed to be conducted to determine the Interference Tolerance Masks (ITMs) for various categories of receivers. ITM defines, for a particular receiver, the maximum received aggregate interference power that can be tolerated by the corresponding tested GPS/GNSS receiver.

To accomplish this testing, OST-R sought to include a broad range of devices used in rail, aviation, motor vehicle, maritime, and space applications, among a number of other civil uses of GPS/GNSS including timing, surveying, precision agriculture, weather forecasting, earthquake monitoring, and emergency response. The GPS/GNSS receivers for this test effort were provided by U.S. Government and industry partners and represented the diverse nature of GPS/GNSS applications and services.

GPS/GNSS receiver testing, led by the OST-R/Volpe Center, was conducted at the U.S. Army Research Laboratory (ARL) at the White Sands Missile Range (WSMR) facility in New Mexico in April of 2016 with 80 civil GPS and GNSS receivers tested, as shown in Figure ES-1. The Air Force GPS Directorate conducted testing of military GPS receivers the week prior to the civil receivers being tested.

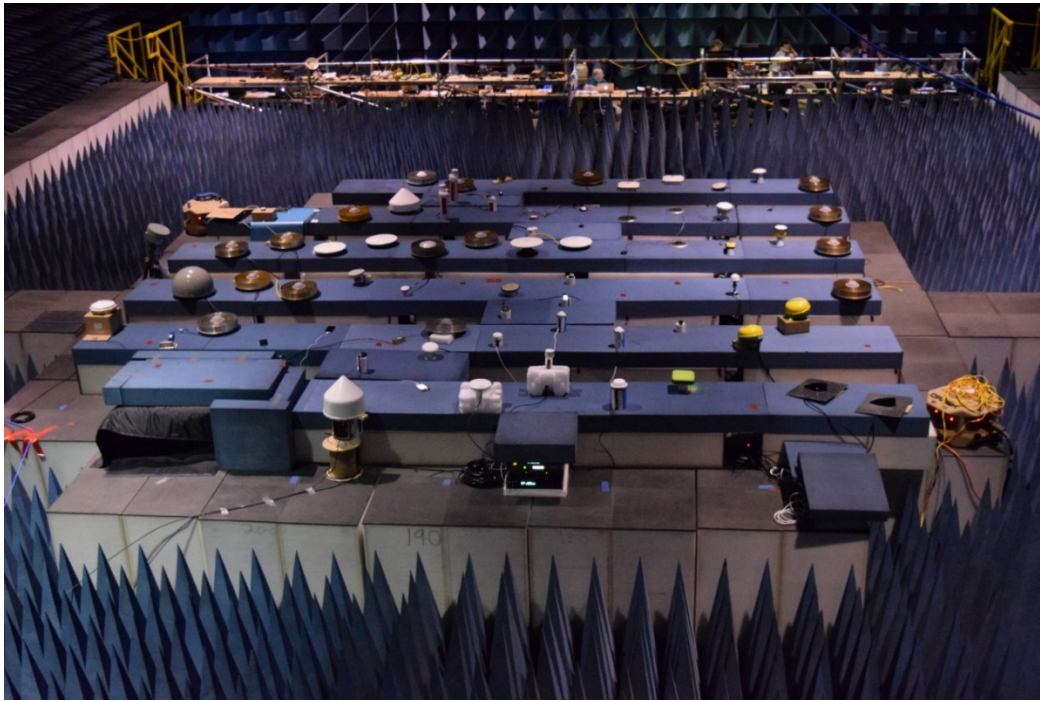


**Figure ES-1: GPS/GNSS Receivers in WSMR Anechoic Chamber**

In determining the transmit power level analysis, it is important to understand real-world scenarios and the proximity those applications of GPS/GNSS may come to adjacent band transmitters. A graphic of various emergency response uses is shown in Figure ES-2. First responders are increasingly using GPS/GNSS to locate patients both during emergencies and as a normal course of duty. As shown in the figure, there are multiple uses of GPS/GNSS for navigation of emergency service response vehicles, as well as asset tracking, including increased situational awareness of where response personnel and vehicles are located. An unmanned aircraft system (UAS) or drone, which also has a GPS/GNSS receiver incorporated also plays a role in this scenario, supporting the response effort. Drones are becoming of increasing importance in collecting imagery and sensor data in response to natural disasters and other incidents.

This scenario illustrates that use of a GPS/GNSS receiver can be quite close in distance -- within tens of meters of a base station transmitter and potentially very close to a handset as well transmitting in the adjacent band. The GPS/GNSS receiver also could be located vertically above the base station.



**Figure ES-2: Emergency Response Use Case**

Results for the high precision receiver category for an emitter at 1530 MHz based on results of analysis and testing are presented in Figure ES-3. These results are for a typical cellular base station power level of 29 dBW (794 watts) with the base station antenna 25 m above the ground. In this figure, the horizontal axis is the lateral distance between the GPS/GNSS receiver and the base station. The vertical axis is the height of the GPS/GNSS receiver above the ground. Note the high precision category of receiver exceeds a 1 dB signal-to-noise density ( $C/N_0$ ) interference protection criteria at a distance beyond 14 km from the transmitter. When this occurs, the behavior of the GPS/GNSS receiver can become unpredictable in its ability to meet the accuracy, availability, and integrity requirements of its intended application and a receiver in a mobile application may not be able to reacquire GPS positioning as the mobile application encounters multiple, closely-spaced emitters in an urban scenario. Furthermore, this category of receiver experiences loss of lock for low elevation GPS/GNSS satellites at distances up to 3 km with loss of lock on all satellites at approximately 1 km from the transmitter.

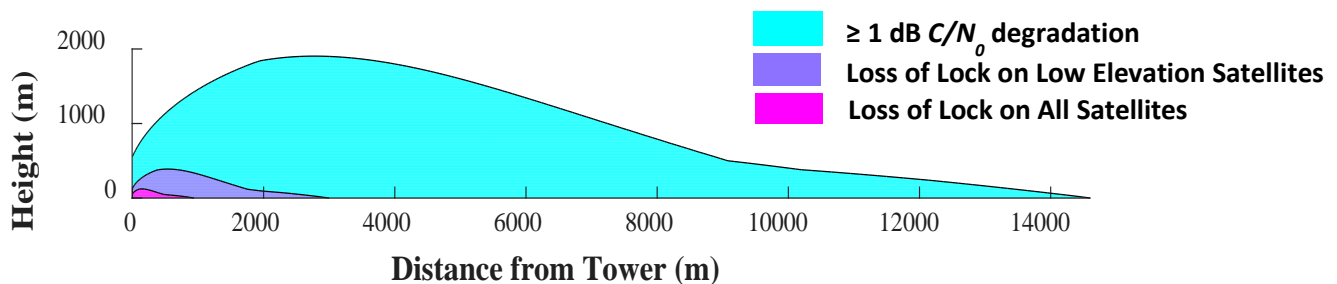


**Figure ES-3: Impact of a 29 dBW Cellular Base Station Transmitting at 1530 MHz on a High Precision GPS/GNSS Receiver**

Further analysis was performed to determine the maximum tolerable power levels for various categories of civil GPS/GNSS receivers for deployments of a macro urban and micro urban cellular network at frequencies within 100 MHz of GPS L1 (1475 – 1675 MHz). As an example, the results for 1530 MHz are shown in Table ES-1 for general location and navigation (GLN), high precision (HPR), Timing (TIM), and cellular (CEL) receivers. The transmit power level as quantified by the effective isotropic radiated power (EIRP) that can be tolerated is a function of distance from the transmitter. Two distances were chosen for evaluation (10 m and 100 m). The results demonstrate that other than the cellular devices, the other categories of GPS/GNSS receivers are sensitive to adjacent band power and can tolerate levels in the milliwatts or microwatts range as described below, depending on the separation distance to the transmitter.

**Table ES-1: Maximum Tolerable Power Level  
for GPS/GNSS Receivers at 1530 MHz**

Deployment	Stand off distance (m)	Max Tolerable EIRP (dBW)			
		GLN	HPR	TIM	CEL
Macro Urban	10	-31.0	-41.9	-20.6	10.9
	100	-11.0	-21.9	-0.6	31
Micro Urban	10	-29.8	-41.2	-20.1	10.7
	100	-9.8	-21.1	-0.1	30.8

Deployment	Stand off distance (m)	Max Tolerable EIRP			
		GLN	HPR	TIM	CEL
Macro Urban	10	0.8 mW	64 $\mu$ W	8.7 mW	12.3 W
	100	79.4 mW	6.5 mW	0.9 W	1.26 kW
Micro Urban	10	1 mW	76 $\mu$ W	9.8 mW	11.7 W
	100	104 mW	7.8 mW	1 W	1.2 kW

Table ES-2 depicts the maximum tolerable power levels of space-based receivers used for performing scientific measurements. A future NASA mission, COSMIC-2, fitted with a TriG receiver built by NASA/Jet Propulsion Laboratory, was modeled, simulated, and analyzed using various cellular network deployment scenarios. The COSMIC-2 mission will be operating at an orbit of 800 km.

**Table ES-2: Maximum Tolerable Power Level  
for Space-Based Receivers at 1530 MHz**

Deployment Scenario	Number of Base Stations	Max Tolerable Power	
		dBW	EIRP
Macro Cell	184,500	11	12.6 W
Macro Cell	67,240	16	39.8 W
Macro Cell	44,850	17	50.1 W
Macro Cell	24,140	21	125.9 W
Macro + Micro Cell	282,186	8	6.3 W
Macro + Micro Cell	102,841	12	15.8 W
Macro + Micro Cell	69,477	14	25.1 W
Macro + Micro Cell	39,695	16	39.8 W

For certified GPS avionics, the FAA analyzed a number of scenarios including:

- 1) Inflight Aircraft with a Ground-based Handset
- 2) Inflight Aircraft with a Ground Base Station
- 3) Inflight Aircraft with an Onboard Handset
- 4) Aircraft on the ground with an Onboard Handset
- 5) Aircraft at Gate / Single Handset Source on or near Boarding Stairs or Jetway
- 6) Aircraft at Gate/Users Inside Airport
- 7) Terrain Awareness Warning System (TAWS) / Helicopter TAWS (HTAWS) Scenarios with Ground-based Mobile Broadband Handsets
- 8) TAWS and HTAWS Scenarios with Broadband Base Station

The analysis for certified avionics is based on the concept of an “assessment zone” (see Figure ES-4) inside of which GPS performance may be compromised or unavailable and GPS-based safety systems will be impacted accordingly due to the elevated levels of RFI. Under the described engineering and operational assumptions, helicopter operations are the limiting factor in the analysis. These analyses indicate that protection of certified avionics, operating under the assumption of the described 250 foot (76.2 m) radius assessment zone, requires that the ground station transmission not exceed 9.8 dBW (10W) (cross-polarized) at 1531 MHz. This limit is obtained from the HTAWS scenario which was found to be the most restrictive of the certified aviation scenarios examined.

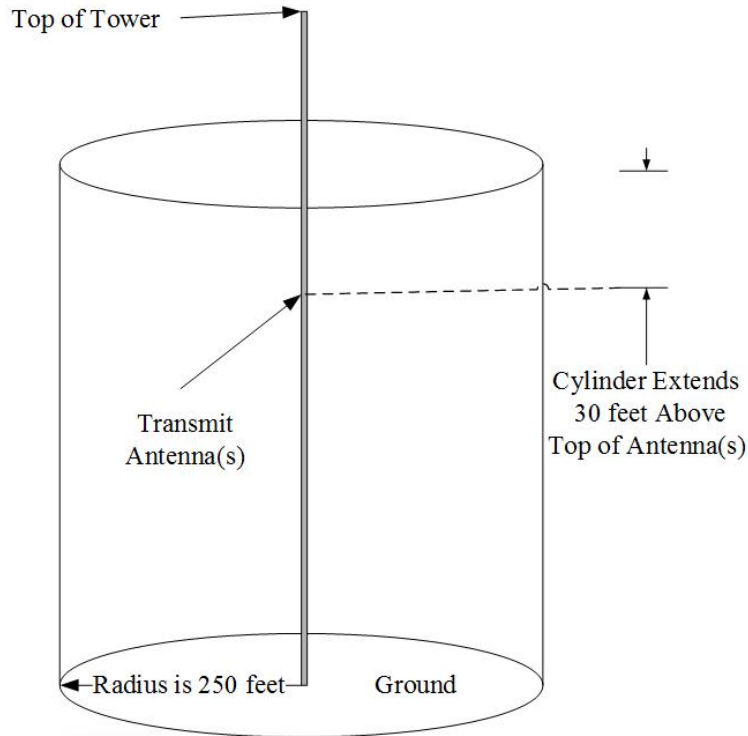


**Figure ES-4: Candidate Assessment Zone (Not to Scale)**

This concept generated a number of comments and questions from the aviation community when vetted through RTCA, Inc. One rotorcraft operator stated that its pilots use visual reference within the assessment zone and the assessment zone would have no negative impact on their operation. However, there were unresolved concerns expressed by several, though not all, operators about the assessment zone and its impacts to aviation operations and safety.

These concerns include: technical and human factors issues associated with re-initialization of GPS after loss of the signal or when the signal reception is intermittent; workload and human factors impacts on pilots to monitor and track assessment zone locations; the possibility that pilot workload, confusion, or error could lead to aircraft inadvertently entering an assessment zone and losing needed GPS functionality; and impacts to onboard and ground systems that are dependent upon GPS, such as Automatic Dependent Surveillance (ADS) Broadcast/Contract (B/C), or fixed-wing and helicopter terrain awareness warning system including obstacle alerting.

The FAA has not completed an exhaustive evaluation of the operational scenarios in developing this assessment zone. Further, the current analyses do not include an operational assessment of the impact of the assessment zone in densely populated areas, which may present additional variables, including the risk posed to people and property for operations such as UAS using certified avionics which may be required to operate within the assessment zone.

However, based on the results of the OST-R testing and analysis of the other categories of receivers, the transmitter power level that can be tolerated by certified aviation may cause interference with, or degradation to, most other categories of GPS/GNSS receivers including those used for General Aviation and drones, as detailed in the results set forth in this report.

The U.S. Department of Transportation would like to thank all of the Federal departments and agencies for their participation in this effort, including the National Telecommunications and Information Administration (NTIA) and Federal Communications Commission (FCC), as well the GPS/GNSS receiver manufacturers who participated in the testing, and all of the stakeholders who attended the public workshops and RTCA meetings and provided valuable feedback during this effort.



# TABLE OF CONTENTS

EXECUTIVE SUMMARY .....	II
TABLE OF CONTENTS.....	IX
LIST OF FIGURES .....	XIII
LIST OF TABLES .....	XVI
1. INTRODUCTION.....	17
2. BACKGROUND.....	20
3. Civil Receiver Testing.....	22
3.1 Anechoic/Radiated Testing .....	22
3.1.1 Devices Under Test (DUTs).....	22
3.1.1.1 GPS/GNSS Receivers Tested.....	23
3.1.1.2 Antennas Tested .....	25
3.1.2 Anechoic Chamber .....	26
3.1.3 Location in Chamber .....	26
3.1.3.1 GNSS Signal Generation.....	28
3.1.3.2 Interference Signal Generation .....	32
3.1.3.2.1 Type 1 Signals .....	34
3.1.3.2.2 Type 2 Signals .....	35
3.1.3.2.1 Intermodulation .....	36
3.1.4 System Calibration and Chamber Mapping .....	37
3.1.4.1 GNSS System.....	37
3.1.4.2 SPIGAT.....	40
3.1.5 Test Sequence.....	40
3.1.5.1 Linearity Test .....	41
3.1.5.2 Interference Test.....	41
3.1.6 Data Processing/ITM formation .....	42
3.1.6.1 Data Conversion and Format .....	43
3.1.6.2 1 dB CNR Degradation .....	44
3.1.6.3 ITM Data Processing.....	45
3.1.7 ITM Aggregation and Test Results .....	50
3.1.8 Loss of Lock Data Processing .....	55

3.2	Conducted (Wired) Testing.....	58
3.2.1	Devices Test .....	58
3.2.2	Signal Generation .....	59
3.2.2.1	Signal Acquisition.....	60
3.2.2.2	Out-of-Band Emissions.....	60
3.2.3	System Calibration .....	62
3.2.4	Test Sequence.....	63
3.2.5	Data Processing .....	63
3.2.5.1	Comparison Tests.....	63
3.2.5.2	OOBE Results .....	64
3.2.5.3	Acquisition Results .....	65
3.3	Antenna Characterization.....	67
3.3.1	Selected Antennas .....	68
3.3.2	Chamber Measurements .....	68
3.3.3	Live-Sky Measurements.....	71
3.3.4	Bench Test Measurements (Active Sub-assembly Measurements).....	73
4.	Transmit Power Level Analysis (Excluding Certified Aviation) .....	75
4.1.1	Approach .....	75
4.1.2	Network Transmitter Parameters.....	75
4.1.2.1	Base Stations .....	75
4.1.2.2	Handsets .....	78
4.1.3	Use Case Development.....	78
4.1.3.1	Receiver Antenna Patterns .....	81
4.1.4	Propagation Models.....	85
4.1.5	Forward Modeling Results and Sensitivity .....	89
4.1.6	Inverse Transmit Power Calculation Results and Sensitivity Analysis.....	91
4.1.6.1	Inverse Transmit Power Calculation Results .....	91
4.1.6.2	Sensitivity Analysis.....	96
4.1.6.2.1	Aggregation Effects.....	96
4.1.6.2.2	Effects of Propagation Models .....	99
4.1.6.2.3	EIRP masks for Median ITMs.....	102
4.1.7	Summary of Transmit Power Level Calculation .....	103

4.2	Spaceborne and Science Applications.....	106
4.2.1	Radio Occultation (GNSS-RO) .....	107
4.2.2	NASA/JPL TriG Receiver Overview .....	108
4.2.3	Spaceborne Receiver Assessment for Science-Based Applications.....	108
4.2.3.1	Summary of TriG Receiver System Characteristics Used for Analysis.....	109
4.2.3.2	Terrestrial LTE Deployment Scenarios .....	110
4.2.3.3	Summary of BS Transmitter System Characteristics Used for Analysis .....	113
4.2.3.4	TriG Receiver Analysis.....	113
4.2.3.5	Results .....	115
5.	Certified Aviation Receiver .....	118
5.1	Determination of Tolerable Interference Levels .....	118
5.1.1	Area of Aviation Operation .....	119
5.1.2	Tracking and Acquisition Thresholds .....	121
5.1.2.1	Receiver Tracking Limit Criteria for Adjacent-Band RFI.....	121
5.1.2.2	Receiver Acquisition Limit Criteria for Adjacent-Band RFI.....	122
5.1.2.3	Receiver Tracking Limit Criteria for Broadband Handset RFI In-band to GPS.....	123
5.1.3	Transmitter and Receiver Component Assumptions .....	123
5.1.3.1	GPS Receive Antenna Gain .....	123
5.1.3.2	Broadband Wireless Base Station and Mobile Handset Characteristics .....	125
5.1.3.2.1	Broadband Wireless Base Station Characteristics .....	125
5.1.3.2.2	Broadband Wireless Mobile Handset Characteristics .....	126
5.2	Transmit Power Level Calculations .....	126
5.2.1	Use Case/Interaction Scenario Development .....	127
5.2.1.1	Inflight Aircraft/Ground-Based Source Scenario Set .....	127
5.2.1.1.1	Inflight Aircraft/Ground-Based Handset Cases.....	127
5.2.1.1.2	Inflight Aircraft/Ground-Based Base Station Cases.....	128
5.2.1.1.3	Inflight Aircraft / Discretely-located Ground Base Station Cases .....	128
5.2.1.1.4	Inflight Aircraft / Randomly-located Ground Base Station Cases .....	128
5.2.1.2	TAWS/HTAWS and Low Altitude Positioning and Navigation Scenarios.....	128
5.2.1.2.1	TAWS / HTAWS and Pos/Nav Scenarios with Ground-based Mobile Broadband Handsets.....	129
5.2.1.2.2	TAWS and HTAWS Scenarios with Broadband Base Stations .....	129
5.2.1.3	Handset Sources on Board Aircraft.....	129

5.2.1.3.1	Onboard Handset Operation for Aircraft Inflight.....	129
5.2.1.3.2	Onboard Handset Operation for Aircraft on Ground.....	130
5.2.1.4	Aircraft at Gate Scenarios .....	130
5.2.1.4.1	Aircraft at Gate / Single Handset Source on or near Boarding Stairs or Jetway.....	130
5.2.1.4.2	Aircraft at Gate/30 Users Inside Airport .....	130
5.2.2	Propagation Models.....	131
5.2.2.1	Single Path Propagation Model.....	131
5.2.2.2	Aggregate Effects Model .....	132
5.2.3	Tolerable Transmit Power Calculation Results and Sensitivity Analysis .....	133
5.2.3.1	Tolerable Transmit Power Calculation Method Overview .....	133
5.2.3.1.1	Tolerable Transmit Power Calculation Method – Base Station Cases .....	133
5.2.3.1.2	Tolerable Transmit Power Calculation Method – Handset Cases .....	134
5.2.3.2	Results for Inflight Aircraft/Ground-based Handset Cases.....	134
5.2.3.3	Results for Inflight Aircraft / Ground Based Base Station Cases .....	135
5.2.3.4	Results for Onboard Handset Operation for Aircraft on Ground.....	139
5.2.3.5	Results for Aircraft at Gate/30 Users Inside Airport .....	140
5.2.3.6	Results for Inflight Aircraft TAWS/HTAWS and Low Altitude Pos/Nav .....	142
5.2.3.7	Frequency Dependencies .....	147
5.2.3.8	Sensitivity Analysis Results .....	148
5.2.3.9	Certified Aviation Receiver Analysis Results Summary .....	152
6.	SUMMARY.....	155
	ACRONYM LIST.....	159
	REFERENCES .....	163
	ACKNOWLEDGEMENTS .....	164

## LIST OF FIGURES

Figure 3-1: Chamber Dimensions and Layout (Top View) .....	26
Figure 3-2: DUT and Calibration Grid Locations.....	27
Figure 3-3: Photo of the DUTs on the test grid .....	28
Figure 3-4: GNSS Signal Generation and Recording .....	29
Figure 3-5: GNSS Signal Playback and Transmission .....	30
Figure 3-6: Interference Frequencies and Signal Levels Tested.....	33
Figure 3-7: Interference System Configuration for Radiated Test .....	33
Figure 3-8: Measured gain response: (a) bandpass RF filter with tighter rejection requirements, (b) bandpass RF filter with more relaxed rejection requirements.....	34
Figure 3-9: Type 1 Signal Captured during WSMR Testing @ 1530 MHz.....	35
Figure 3-10: Type 2 Signal Captured during WSMR Testing @ 1530 MHz.....	36
Figure 3-11: Intermodulation Signal Captured during WSMR Testing .....	37
Figure 3-12: Measured Gain of Two MiniCircuits ZRL-2400-LN Amplifiers .....	38
Figure 3-13: GNSS Signal Received Power Variation across the Test Grid (1227 MHz).....	39
Figure 3-14: GNSS Signal Received Power Variation across the Test Grid (1561 MHz).....	39
Figure 3-15: Power Correction Representations for Three Frequencies .....	40
Figure 3-16: ITM Processing Block Diagram .....	45
Figure 3-17: Sample plot for calibrated interference power overlaid with time aligned CNR data for a given DUT at a particular interference frequency.....	46
Figure 3-18: Determining the tolerable interference level from the CNR versus interference power for a one PRN after time alignment and calibration of interference power.....	47
Figure 3-19: Overlaid L1 C/A ITMs from two radiated LTE test events for a single DUT. Test-2 and Test-3 refer to the first and second LTE tests respectively.....	47
Figure 3-20: CDF of measurement uncertainty calculate from per DUT differences across PRNs (black) and test to test difference (red) for the 10 MHz LTE interference signal .....	49
Figure 3-21: CDF of measurement uncertainty calculate from per DUT differences across PRNs (black) and test to test difference (red) for the 1 MHz AWGN interference signal .....	49
Figure 3-22: GPS L1 C/A bounding ITM for each category of receivers .....	50
Figure 3-23: HPR bounding ITMs for each of the emulated GNSS signals.....	51
Figure 3-24: HPR Bounding ITMs for each of the emulated GNSS signals. ITM bounding masks for the 1 MHz AWGN and 10 MHz LTE interference signals are shown .....	52
Figure 3-25: 10 MHz Statistical Mask Results for High Precision receivers: (a) GPS L1 C/A (b) All Emulated GNSS Signals .....	53
Figure 3-26: Determination of Loss of Lock Interference Level from CNR Data .....	54
Figure 3-27: Interference Power resulting in Loss of Lock for GPS L1 C/A-code (High Elevation Angle). .....	56
Figure 3-28: Interference Power resulting in Loss of Lock.....	57
Figure 3-29: Interference System Configuration for Wired Tests .....	59
Figure 3-30: OOB Levels Associated with LTE Signal Power used in Testing .....	60

Figure 3-31: Comparison of IP causing 1 dB degradation for the LTE Interference Signal from Radiated and Wired Testing. (a) Shows a High Precision receiver and (b) shows a Cellular device. ....	62
Figure 3-32: Interference power causing 1 dB CNR degradation for baseline and OOBE tests. (a) Shows a High Precision receiver and (b) shows a Cellular device. ....	63
Figure 3-33: Summary acquisition performance for 1525 MHz. (a) Number of DUTs (b) average acquisition time for ICD minimum and low elevation satellites. ....	64
Figure 3-34: Summary acquisition performance for 1550 MHz. (a) Number of DUTs (b) average acquisition time for ICD minimum and low elevation satellites. ....	64
Figure 3-35: Summary acquisition performance for 1620 MHz. (a) Number of DUTs (b) average acquisition time for ICD minimum and low elevation satellites. ....	65
Figure 3-36: Summary acquisition performance for 1645 MHz. (a) Number of DUTs (b) average acquisition time for ICD minimum and low elevation satellites. ....	65
Figure 3-37: Frequency Selectivity of the 14 External Antennas. ....	68
Figure 3-38: Relative RHCP Gain Patterns of the 14 Antennas at 1575 MHz (red vertical lines correspond to 5 deg elevation angle) ....	68
Figure 3-39: Relative L1 RHCP Antenna Gain Estimated from Live-sky $C/N_0$ Measurements for Three GLN Integrated Antennas and Quadratic Fit. ....	69
Figure 3-40: Relative L1 RHCP Antenna Gain Estimated from Live-sky $C/N_0$ Measurements for an Integrated HPR Antenna and Quadratic Fit ....	70
Figure 3-41: Live-sky $C/N_0$ Measurements for a CEL Device ....	70
Figure 3-42: Filter/LNA Responses measured with Bench Testing ....	71
Figure 4-1: Macrocell Radius and Intersite Distance are $A$ and $B$ , respectively. Each hexagon is referred to as either a sector or cell. ....	74
Figure 4-2: Macro Base Station Antenna Gain Patterns (top – elevation; bottom – azimuth) ....	75
Figure 4-3: Small cell Base Station Antenna Gain Patterns (elevation patterns shown; both patterns are omnidirectional in azimuth) ....	75
Figure 4-4: Emergency Response Use Case ....	78
Figure 4-5: Relative VPOL Antenna Gain Patterns for 1530 MHz. ....	81
Figure 4-6: Gain Patterns Illustrating Generation of GLN Coefficients for 1530 MHz. ....	82
Figure 4-7: Illustration of use case analysis region ....	86
Figure 4-8: Macro Urban Base Station (EIRP = 59 dBm), Bounding GAV, 1540 MHz ....	87
Figure 4-9: Maximum Impacted Lateral Distance for Bounding GAV, Macro Urban Base Station (EIRP = 59 dBm) ....	88
Figure 4-10: Macro Urban Base Station (EIRP = 59 dBm), Bounding HPR, 1530 MHz. ....	88
Figure 4-11: (a) Tolerable $EIRP(r, f)$ map in the vertical computation domain, (b) Tolerable $EIRP(X, f)$ as a function of standoff distance $X$ . ....	90
Figure 4-12: Tolerable $EIRP(X, f)$ as a function of standoff distance $X$ up to $X=500$ m ....	91
Figure 4-13: EIRP( $f, ds=10m$ ) for the HPR category: L1 C/A, micro urban deployment, bounding EIRP Mask, and FSPL propagation ....	92
Figure 4-14: EIRP( $f, ds=10m$ ) for five receiver categories of receivers: L1 C/A, micro urban deployment, bounding EIRP Mask, and FSPL propagation ....	93

Figure 4-15: Comparison of EIRP( $f, d_s=10\text{m}$ ) L1 C/A and All GNSS masks for the HPR category of receivers: Micro urban deployment, bounding EIRP Mask, and FSPL propagation .....	93
Figure 4-16: EIRP( $f, d_s=10\text{m}$ ) for five categories of receivers: All GNSS, micro urban deployment, bounding EIRP Mask, and FSPL propagation .....	94
Figure 4-17: micro deployment used for the aggregation sensitivity analysis. A small cell of radius $r_{cell}$ , and transmitters' interspacing distance ISD. ....	95
Figure 4-18: (a) Overlay of EIRP( $X, f$ ) as a function of standoff distance $X$ for the case of single and multiple base stations (b) Difference between EIRP( $X, f$ ) for the two cases .....	96
Figure 4-19: Overlay of $EIRP(X, f)$ tolerance masks for the case of a single base station and that of multiple transmitter case.....	97
Figure 4-20: Tolerable EIRP levels for the case of two ray path loss propagation model (a) Tolerable $EIRP(r, f)$ map in the vertical computation domain, (b) Tolerable $EIRP(X, f)$ as a function of standoff distance $X$ .....	98
Figure 4-21: (a) Overlay of $EIRP(X, f)$ as a function of standoff distance $X$ for the case of FSPL and two ray path loss propagation (b) Difference in tolerable EIRP( $X, f$ ) due to propagation models .....	99
Figure 4-22: Comparison between two ray and FSPL EIRP tolerance masks $EIRP(X, f)$ for $X=100\text{m}$ standoff distance .....	100
Figure 4-23: EIRP levels corresponding to L1 C/A median ITMs.....	100
Figure 4-24: Time Difference of Arrival of GNSS Signal .....	106
Figure 4-25: Example Satellite View of the U.S. Cities.....	107
Figure 4-26: Earth Station Deployment Zone Model (Report ITU-R SA. 2325-0).....	110
Figure 5-1: Candidate Assessment Zone .....	119
Figure 5-2: CW Interference Susceptibility vs. Frequency, Tracking Mode.....	120
Figure 5-3: Lower Hemisphere Installed V-pol and H-pol Receive Antenna Patterns Max. Gain vs. Elevation Angle.....	122
Figure 5-4: Upper Hemisphere Installed V-pol. And H-pol. Receive Antenna Patterns Max. Gain vs. Elevation Angle.....	123
Figure 5-5: Handset Scenario Probabilities .....	133
Figure 5-6: WIRSO Banking Scenario 1 – $P(z)$ values Using Two Methods .....	136
Figure 5-7: Aggregate Handset Signal Loss .....	138
Figure 5-8: Aircraft at Gate with Thirty Uniformly Distributed Handsets in Terminal .....	138
Figure 5-9: (1-CDF) Aggregate Power Factor.....	139
Figure 5-10: HTAWS Dual Polarization 20 m Emitter Antenna-Mean Limits.....	146
Figure 5-11: (1-CDF) for Most Restrictive Mean Limit Condition of Figure 5-10.....	147
Figure 5-12: HTAWS Dual Polarization 10 m Emitter Antenna-Mean Limits.....	147
Figure 5-13: (1-CDF) for Most Restrictive Mean Limit Condition of Figure 5-12.....	148
Figure 5-14: HTAWS Vertical Polarization 25 m Emitter Antenna-Mean Limits.....	148
Figure 5-15: (1-CDF) for-Most Restrictive Mean Limit Condition of Figure 5-14 .....	149

## LIST OF TABLES

Table 3-1: GPS/GNSS Receiver Categories .....	23
Table 3-2: GNSS Signal Generation Equipment .....	30
Table 3-3: GNSS Signals Generated for Test .....	31
Table 3-4: Minimum Received GNSS Signal Power Levels for Interference Test Events .....	31
Table 3-5: Test Schedule .....	41
Table 3-6: Interference Signal Parameters.....	42
Table 3-7: CSV Data Format .....	44
Table 3-8: Receivers Tested.....	58
Table 3-9: Ratio of OOBE limit density to.....	60
Table 3-10: Wired Test and Data Summary .....	61
Table 3-11: Characterized GNSS Antennas .....	66
Table 3-12: LNA Performance Characteristics measured with Bench Testing.....	72
Table 4-1: Base Station Characteristics from ITU-R M.2292 .....	74
Table 4-2: Summary of Compiled Use Case Information .....	77
Table 4-3: Summary of Geometric Parameters .....	79
Table 4-4: Coefficients for GLN, GAV, TIM, and HPR Receivers for Modeling Relative VPOL Antenna Gain at 22 Frequencies .....	80
Table 4-5: Coefficients for GLN, GAV, TIM, and HPR Receivers for Modeling Relative HPOL Antenna Gain at 22 Frequencies .....	83
Table 4-6: Tolerable Base Station $EIRP(ds, f)$ for L1 C/A bounding masks for Type-2 Interference signal using FSPL propagation model.....	102
Table 4-7: Tolerable Base Station $EIRP(ds, f)$ for All GNSS bounding masks for Type-2 Interference signal using FSPL propagation model.....	103
Table 4-8: Summary Table of Satellite TriG Receiver Characteristics Used for M&S .....	109
Table 4-9: Zone Model - ES Zone-specific Radial Distance from City Center.....	110
Table 4-10: Typical Cell Radius (CR) - ITU-R M.2292 .....	111
Table 4-11: Total # of ES (Macrocell Deployment Only .....	111
Table 4-12: Assumed Transmitter Levels per Sector (Typical per ITU-R M.2292) .....	112
Table 4-13: Summary of Simulation Runs .....	113
Table 4-14: COSMIC-2 Interference Results (Macro ES Only, All ES Tx Power 32 dBW).....	115
Table 4-15: Sentinel-6 Interference Results .....	115
Table 5-1: Analysis Scenarios and Conditions .....	124
Table 5-2: WIRSO Scenario Based Limits from Two Methods.....	135
Table 5-3: WIRSO Scenario Based Limits from Random Method .....	136
Table 5-4: Comparison of Two Methods for WIRSO Scenario Based Limits.....	137
Table 5-5: Hexagonal Grid Power Limits Computed Using Two Methods .....	141
Table 5-6: Hexagonal Grid Power Limits Computed Using 433m ISD Flat Earth Scenario .....	142
Table 5-7: Power Limits for Landed Helicopter at Various Separation Radii from Central Tower.....	143
Table 5-8: Hexagonal Grid Scenario Based Limits .....	144
Table 5-9: Summary of Scenarios & Findings .....	151



## 1. INTRODUCTION

The goal of the U.S. Department of Transportation (DOT) Global Positioning System (GPS) Adjacent Band Compatibility Assessment is to evaluate the maximum transmitted power levels of adjacent band radiofrequency (RF) systems that can be tolerated by GPS and Global Navigation Satellite System (GNSS) receivers. The results of this effort advance the Department's understanding of the extent to which such adjacent band transmitters impact GPS/GNSS devices used for transportation safety purposes, among numerous other civil applications. The assessment described in this report addresses transmitters in bands adjacent to the 1559-1610 MHz radionavigation satellite service (RNSS) band used for GPS Link 1 (L1) signals that are centered at 1575.42 MHz.

The assessment had two primary components:

- One component, led by the DOT Office of the Assistant Secretary for Research and Technology (OST-R), focused on all civilian GPS devices and their applications, apart from certified aviation. Through this component of the Study, categories of receivers were evaluated that included aviation (non-certified), cellular, general location/navigation, high precision, timing, and space-based receivers. An element of this effort was to determine equipment susceptibility to adjacent band interference to support analyses for deriving compatible power levels.
- The other component, led by the Federal Aviation Administration (FAA), focused on certified GPS avionics, and was conducted by analysis to determine the adjacent band power levels that conform to existing certified GPS aviation equipment standards.

The DOT GPS Adjacent Band Study is the product of an extensive process to gather stakeholder views and input. OST-R and FAA benefited significantly from feedback received via governmental and public outreach. This feedback was important to ensure broad agreement and understanding of equipment use cases, interaction scenarios, propagation models, and transmitter characteristics.

For the OST-R component of the effort, the first public workshop was held in September 2014 at DOT's Volpe Center in Cambridge, MA. Five subsequent workshops were held at locations on both coasts of the United States (Los Angeles, CA and Washington, DC) to obtain broad stakeholder participation. These workshops presented the elements of the OST-R assessment: equipment susceptibility testing, development of use cases and interaction scenarios, transmitter characteristics, and propagation modeling assumptions, and finally, the analysis and assessment results. Initial planning of the DOT GPS Adjacent Band Compatibility Assessment focused on testing receivers that only process GPS signals. However, based upon feedback from public outreach, the assessment was expanded to include widely available equipment that also processes GNSS signals from other satellite navigation constellations in the 1559-1610 MHz band.

While the compatibility assessment is intended to be generally applicable in terms of the type of adjacent band system, the main focus for this L1 band assessment was on Long Term Evolution (LTE) signals. The OST-R effort included extensive equipment testing to derive interference tolerance masks (ITMs). The ITM defines, for a given frequency, the maximum power allowed to ensure the tested GPS/GNSS receiver did not experience more than a 1 dB reduction in carrier-to-noise density ratio (CNR) for various categories of GPS/GNSS receivers. The receiver ITMs were derived from radiofrequency equipment testing, both radiated and conducted, for frequencies ranging from 1475 MHz to 1675 MHz (GPS L1 +/- 100 MHz). These ITMs were then used with appropriate use cases and interaction scenarios to determine maximum transmitter EIRP levels that could be tolerated from adjacent band transmitters.

The equipment susceptibility testing involved 80 GPS/GNSS receivers tested in an anechoic chamber in April 2016. The GPS/GNSS receivers for this test effort were provided by U.S. Government (USG) partners and industry and represented the diverse nature of GPS/GNSS applications and services. In addition to this primary test effort, more focused testing on a subset of equipment was conducted with wired testing in a laboratory setting and antenna characterizations in a different anechoic chamber. The receiver test data from the primary test effort was analyzed to develop ITMs, based on a 1 dB CNR degradation, which provided bounding performance for each GPS/GNSS receiver category.

These bounding ITMs and GPS/GNSS antenna characteristics were the primary inputs to use case scenario assessments to determine the maximum Effective Isotropic Radiated Power (EIRP) that could be tolerated in the adjacent radiofrequency bands for each GPS/GNSS receiver category. Space-based applications are different from other GPS/GNSS applications considered, primarily due to the need to account for aggregation effects of multiple transmitters visible in orbit. Although OST-R derived ITMs for space-based receivers, along with other GPS/GNSS receiver types, OST-R deferred to the National Aeronautics and Space Administration (NASA) for assessing adjacent-band transmitter power levels that can be tolerated for this receiver category.

The FAA's public outreach for their component of the GPS Adjacent Band Compatibility Assessment was initiated in early 2014 with RTCA Inc., an aviation advisory body. This outreach was followed in October 2014 with a document detailing the FAA's approach to the assessment for certified aviation and the request to RTCA to vet assumptions and respond to specific questions. These questions ranged from receiver/antenna characteristics and their applicability to fixed- and rotary-winged aircraft to specific propagation modes to be used and interaction scenarios.

RTCA also was requested to comment on use of an exclusion zone concept and its implications for operations and flight safety. RTCA completed the review and provided comments to FAA in 2015. The FAA was approached starting in 2016 by one entrant with an analysis approach for certified aviation that included a specific transmitter network and exclusion zone. This proposal

was reviewed by RTCA and was considered with the material originally vetted by them in FAA's assessment of maximum tolerable EIRP for certified aviation.

The FAA effort did not require receiver and antenna equipment testing because certified aviation receiver standards specify the maximum tolerable interference environment to ensure all receiver functions are protected. The FAA effort also considered use cases based upon one specific, proposed adjacent-band LTE network.

This report is organized as follows. Section 2 provides background information to the study. Section 3 discusses the radiated and wired tests performed and provides results for all civil receiver categories with the exception of the certified aviation receiver category. Section 4 presents the analysis to determine the tolerable transmit power levels, including use cases for applications other than certified aviation. Analysis of aggregate effects for on-orbit space applications is provided by the National Aeronautics and Space Administration (NASA). Section 5 discusses the analysis approach and presents the results for the certified aviation receiver category. Section 6 provides an overall summary of the report. Additional information on test results and analyses are included in the appendices.

## 2. BACKGROUND

Over the past three decades, GPS has grown into a global utility providing multi-use service integral to U.S. national security, economic growth, transportation safety, and homeland security, and as an essential element of the worldwide economic infrastructure. GPS affects the lives of the American public every day, ranging from its use in all modes of transportation to incorporation of GPS timing into the electric grid, communications networks, point of sale transactions, banking and finance, as well as applications of GPS for surveying, precision agriculture, weather forecasting, earthquake monitoring, and emergency response. The range of commercial and civil applications of GPS continues to expand and the importance of many GPS and GNSS applications has significantly increased.

Private sector innovations in the use of GPS greatly exceed any originally envisioned or imagined applications. However, unlike communication systems where performance improvements are enabled by coordinated changes to both the transmitting and receiving systems, GPS has shown that user processing innovations can significantly improve performance without changing the transmitted GPS signals. These innovations have enabled the civil community to develop and implement new GPS antenna/receiver technologies and applications, with minimal dependency on government actions. As the economic and security importance of positioning, navigation, and timing (PNT) gained international recognition, other countries have initiated or renewed their commitments to provide satellite navigation systems, fueling further development of new user-based GPS/GNSS technologies.

The framework for GPS policy is defined by Presidential Policy. Title 10 United States Code, Section 2281 (b) states that the GPS Standard Positioning Service shall be provided for peaceful civil, commercial and scientific uses on a continuous worldwide basis. The 2010 National Space Policy sustains the overall radiofrequency environment in which critical U.S. space systems such as GPS operate and calls for continued U.S. leadership in the service, provision, and use of GNSS.

This policy reaffirms existing U.S. commitments under National Security Presidential Directive (NSPD)-39, U.S. Space-Based Positioning, Navigation, and Timing Policy (15 December 2004) to provide continuous, worldwide access to civil GPS, free of direct user fees; pursue international GNSS cooperation including use of foreign PNT to augment and strengthen the resiliency of GPS; operate and maintain GPS to meet published standards; and take steps to detect and mitigate GPS interference. Per NSPD-39, DOT serves as the civil lead for GPS.

At the direction of the DOT Deputy Secretary, FAA and OST-R developed the GPS Adjacent Band Compatibility Assessment Plan to provide a means to advance the Department's understanding of the adjacent radiofrequency band power levels that would be compatible for GPS civil applications. The plan identifies the processes to: (a) derive adjacent-band transmitter power limit criteria for assumed new applications necessary to ensure continued operation of GPS services, and (b) determine similar levels for future GPS receivers utilizing modernized GPS and interoperable GNSS signals [1]. This document provided the framework for the

processes and assumptions that resulted in the testing and analysis conducted during the effort and presented in this report.

### **3. CIVIL RECEIVER TESTING**

#### **3.1 Anechoic/Radiated Testing**

In planning and preparation for receiver testing, OST-R held multiple public workshops to discuss plans for the Study and to foster the exchange of information among interested parties. These workshops took place on September 18, 2014 (see 79 Fed. Reg. 47171), December 4, 2014 (see 79 Fed. Reg. 68345), March 12, 2015 (see 80 Fed. Reg. 8125), and October 2, 2015 (see 80 Fed. Reg. 57915). Representatives from NTIA, FCC, and NIST, and other Space-Based PNT EXCOM departments and agencies participated in the public workshops.

A draft test plan was issued for public comment on September 9, 2015 (see 80 Fed. Reg. 54368). There were six organizations and individuals who provided written comments on the draft of the test plan: Ligado, GPS Innovation Alliance, Greenwood Telecom, Alliance for Telecommunications Industry Solutions (ATIS), General Motors, and Logan Scott. The Department carefully reviewed and considered the comments that were submitted in devising a final test plan, as well as other information that was offered in the course of the public workshops. In addition, DOT made public its Nondisclosure Agreement (NDA) for the protection of certain confidential or proprietary information that may be offered by companies that participated in the Study (see 81 Fed. Reg. 12564). DOT executed five NDAs with Deere & Company, GM Global Technology Operations LLC, Novatel Inc., Trimble Navigation Limited, and u-Blox AG.

After the Test Plan was finalized and published (see 81 Fed. Reg. 12564), GPS/GNSS receiver testing, led by the OST-R/Volpe Center, was conducted at the U.S. Army Research Laboratory (ARL) at the White Sands Missile Range (WSMR) facility in New Mexico in April of 2016. Results from the testing described in this section were presented at public workshops held on October 14, 2016 (see 81 Fed. Reg. 68105) and on March 30, 2017 (see 82 Fed. Reg. 13924). Information from all of the public workshops that were held can be found at a website hosted by the National Space-Based PNT Coordination Office (NCO) at <http://www.gps.gov/spectrum/ABC/>.

##### **3.1.1 Devices Under Test (DUTs)**

DOT sought to include a broad range of devices used in rail, aviation, motor vehicle, maritime, and space applications, among a number of other civil uses of GPS/GNSS including timing, surveying, precision agriculture, weather forecasting, earthquake monitoring, and emergency response. The GPS/GNSS receivers for this test effort were provided by USG partners and industry.

Six categories of GPS/GNSS receivers were considered for the OST-R portion of the effort, which are identified in Table 3-1. High precision (HPR) and the differential Network (NET) receivers are grouped together into one category since HPR receivers are commonly used in differential networks. General aviation receivers include non-certified receivers and are separate from certified aviation receivers which did not require testing since existing certified aviation

receiver standards specify the maximum tolerable interference environment to ensure all receiver functions are protected. Space-based receivers were included with assistance from NASA.

**Table 3-1: GPS/GNSS Receiver Categories**

Number	Category	Abbreviation
1	General Aviation (Non-Certified)	GAV
2	General Location/Navigation	GLN
3	High Precision/Networks	HPR/NET
4	Timing	TIM
5	Cellular	CEL
6	Space Based	SPB

**3.1.1.1 GPS/GNSS Receivers Tested**

During the WSMR anechoic radiated chamber testing in April 2016, DOT and other participants tested 80 GPS/GNSS receivers listed along with the associated antennas in Table 3-2.

Duplicated entries in Table 3-2 indicate that two identical receiver/antenna model pairings were tested, which occurred in three instances. In addition, 14 (out of the 80) were subsequently subjected to additional conducted/wired testing at Zeta Associates as indicated by an asterisk next to the receiver name in Table 3-2. The Air Force GPS Directorate conducted testing of military GPS receivers the week prior to the civil receivers being tested.

**Table 3-2: List of GPS/GNSS Receivers Tested at WSMR**

Receiver	Antenna
Android S5*	Integrated
Android S6	Integrated
Android S7	Integrated
Arbiter Systems 1088B-Satellite Control Clock	Arbiter AS0087800
Arbiter Systems 1094B-GPS Substation Clock	Arbiter AS0087800
Ashtech uZ-CGRS	Choke Ring
Ashtech Z-12	Choke Ring
Dual Electronics - SkyPro XGPS 150	Integrated
Dynon 2020	Integrated
Dynon 250	Integrated
EVA-7M    EVK-7EVA-0	AeroAntenna Technology Inc AT2775-41-TNCF

EVA-M8M EVK-M8EVA-0	AeroAntenna Technology Inc AT2775-41-TNCF
EVK-6n	Passive patch
EVK-7P	Passive patch
EVK-M8N*	Passive patch
EVK-M8T	Passive patch
Furuno GP-33	GPA017/19
Garmin - Area 560	AeroAntenna Technology Inc AT2775-41-TNCF
Garmin - GLOGPS (GPS & GLONASS)	Integrated
Garmin - GPSMap 696*	AeroAntenna Technology Inc AT2775-41-TNCF
Garmin EDGE 1000	Integrated
Garmin ETREX 20x	Integrated
Garmin GPSMap 295	AeroAntenna Technology Inc AT2775-41-TNCF
Garmin GPSMAP 64	Integrated
Garmin GPSMAP 741	Garmin GA 38 GPS/GLONASS antenna
Hemisphere R330	Hemisphere A42
Javad Delta II*	JAVAD JAVRINGANT_DM
Javad Delta-3	Choke Ring
Javad EGGDT-160	Choke Ring
JAVAD Triumph-1	Integrated
LEA-M8F EVK-M8F-0	AeroAntenna Technology Inc AT2775-41-TNCF
LEA-M8S EVK-M8N-0	AeroAntenna Technology Inc AT2775-41-TNCF
Leica GR10	TRM59800.00
Leica GRX1200GGPRO	Leica AX1202GG
Leica GRX1200GGPRO*	LEIAT504
MAX-7C EVK-7C-0	AeroAntenna Technology Inc AT2775-41-TNCF
MAX-7Q EVK-7N-0	AeroAntenna Technology Inc AT2775-41-TNCF
MAX-M8Q	Passive patch
MAX-M8Q EVK-M8N-0	AeroAntenna Technology Inc AT2775-41-TNCF
NAVCOM SF3050*	NAVCOM ANT-3001R
NovAtel 628 Card w/ Flex pack	703GG
Novatel OEM628V-G1S-B0G-TTN-H installed in Development board	Patch
Schweitzer Eng. Labs SEL-2401-Satellite Synchronized Clock	SEL 235-0209
Septentrio PolaRx4Pro*	AERO AERAT1675_120
Septentrio PolaRx4TR Pro	Choke Ring



Septentrio PolaRx5TR Pro*	TRM59800.00
Septentrio PolaRx5TR Pro*	TRM59800.00
SF3000	Integrated
SF3000	Integrated
SiRF III	AeroAntenna Technology Inc AT2775-41-TNCF
Supercruise "VCP"	Shark Fin
Supercruise "VCP"	Shark Fin
Symmetricom SyncServer S350	AeroAntenna AT575-142
Symmetricom Xli	Symmetricom Antenna 1
Symmetricom Xli	AeroAntenna AT575-142
Symmetricom-GPS	Symmetricom Antenna 2
Topcon Net-G3A Sigma	Topcon CR-G3
TriG	Choke Ring
TriG V2	Choke Ring
Trimble 5700*	Trimble TRM41249.00
Trimble Acutime 360	Integrated
Trimble Ag-382	Integrated
Trimble Ag-382	Integrated
Trimble Bison III	Trimble 70229-52
Trimble Geo 7X	Integrated
Trimble NETR5	Trimble TRM55971.00
Trimble NETR5	Trimble Zephyr Geodetic Model 2
Trimble NETR5*	Trimble Zephyr 59800-00
Trimble NETR9	TRM59800.00
Trimble NETR9*	Trimble TRM29659.00
Trimble NETRS	Ant com Active L1/L2
Trimble NETRS	Trimble Zephyr Geodetic
Trimble NetRS	TRM59800.00
Trimble NETRS*	Ashtech ASH701945B_M
Trimble R8	Integrated
Trimble SMT360 GPS receiver*	Trimble SMT-360 Antenna
Trimble SPS461	GA530 Ruggedized
Trimble SPS855	Trimble Zephyr 2
Trimble SPS985	Integrated
uBlox EVU-6P-0-001	AeroAntenna Technology Inc AT2775-41-TNCF

\*Subsequently subjected to additional conducted/wired testing at Zeta Associates

### 3.1.1.2 Antennas Tested

In addition to the antennas listed in Table 3-11, that were subjected to radiated testing at WSMR while connected to the corresponding receivers listed in this table, a subset of these antennas and some additional antennas were subsequently characterized in a smaller anechoic chamber at MITRE in Bedford, MA. See Section 3.3.1.

### 3.1.2 Anechoic Chamber

The radiated adjacent band testing was performed at the Army Research Laboratory (ARL) Anechoic Chamber located at WSMR. The test configuration and approximate dimensions for the Electromagnetic Vulnerability Assessment Facility (EMVAF) are shown in Figure 3-1.

The GNSS equipment test area was approximately 24' × 24' and was radiated from above using two separate antennas. One antenna radiated the interference signals while the other radiated GNSS signals with both approximately 25' above the center of the test area. The signal generation equipment was located on the mezzanine platform while participant collection and support equipment was located at the opposite end of the chamber. To emulate standard field operation of each particular receiver as closely as possible, some receivers were located in the participant area and RF cables were run to their respective antennas. Receivers with integrated antennas were placed directly in the test area with data collection/control cables typically routed to the participant area.

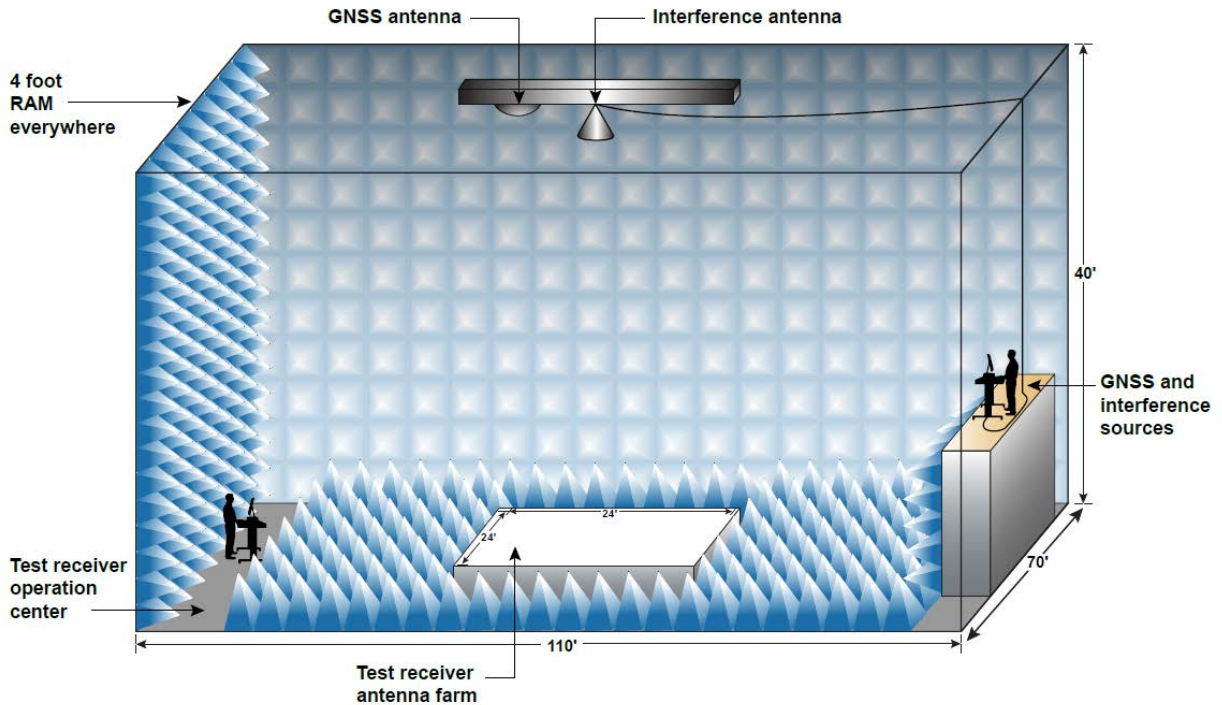
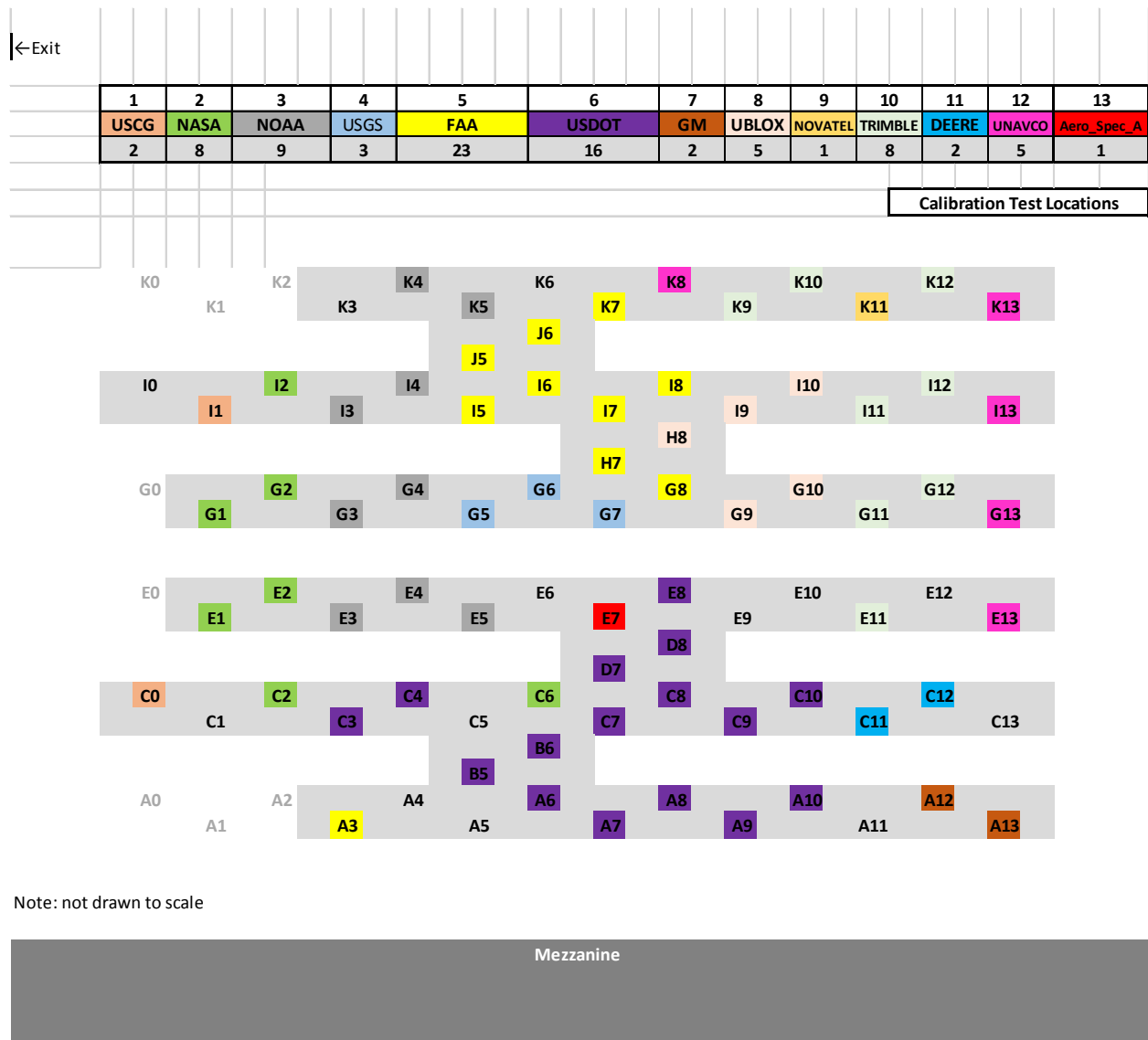


Figure 3-1: Chamber Dimensions and Layout

### 3.1.3 Location in Chamber

During the radiated testing, there were 12 participating organizations including DOT's Federal partners and agencies, and GPS/GNSS receiver manufacturers. The organizations included: 1) United States Coast Guard (USCG), 2) NASA, 3) National Oceanic and Atmospheric Administration (NOAA), 4) United States Geological Survey (USGS), 5) FAA, 6) U.S. DOT, 7) General Motors (GM), 8) u-blox, 9) NovAtel, 10) Trimble, 11) John Deere, and 12) UNAVCO, a

non-profit university-governed consortium that facilitates geoscience research and education using geodesy sponsored by NASA and the National Science Foundation. The participating organizations, number of receivers and location on the test grid can be found in Figure 3-2. A cavity backed spiral antenna used for signal calibration and chamber mapping was placed at the edge of the test grid between locations E0 and G0. This antenna was connected to a spectrum analyzer and used for continuous signal and interference monitoring. In addition, a horn antenna connected to a spectrum analyzer was setup in the middle of the test grid (E7) for signal and interference monitoring and situational awareness for participants.



**Figure 3-2: DUT and Calibration Grid Locations**

Figure 3-3 is a photo of the DUTs during the anechoic chamber testing.

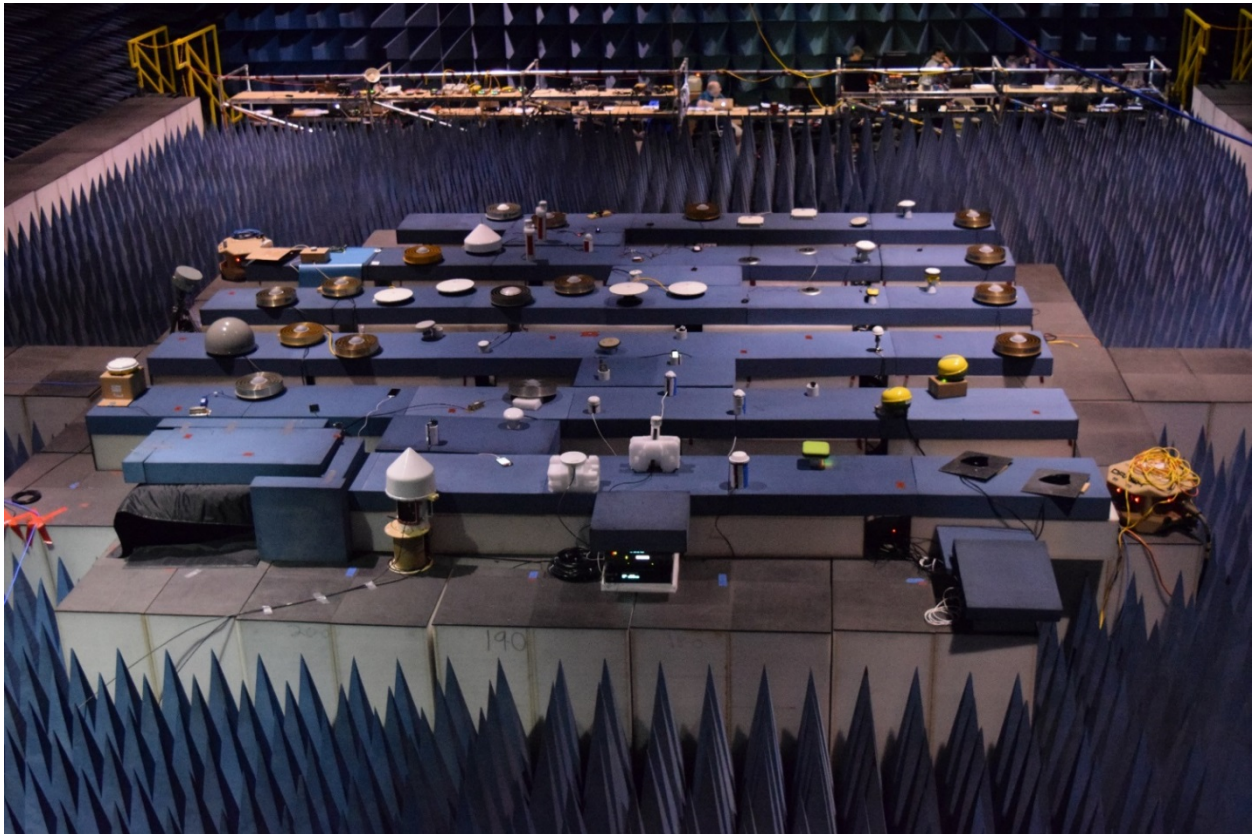


**Figure 3-3: Photo of the DUTs on the test grid**

### **3.1.3.1 GNSS Signal Generation**

The GNSS signal generation and recording process is shown in Figure 3-4. The recording was conducted at MITRE prior to the test period. Simulated satellite signals were generated using a set of four Spirent GSS8000 GNSS signal simulators. These are commercial research and test devices that produce high-fidelity RF signals as they would appear at the output of a GNSS receive antenna. The GSS8000 simulators allow specification of received signals, received signal power level, satellite orbital parameters, user location, etc. The simulators were programmed to synchronously generate signals for GPS+ Wide Area Augmentation System (WAAS), Beidou, GLONASS, and Galileo. The L1+L2 radio frequency outputs of the simulators generating the GPS+WAAS, Beidou, and Galileo signals were passively combined using a single channel of a Spirent GSS8368 Signal Combiner. The GLONASS L1 signals were passed through the second channel of the GSS8368 signal combiner.

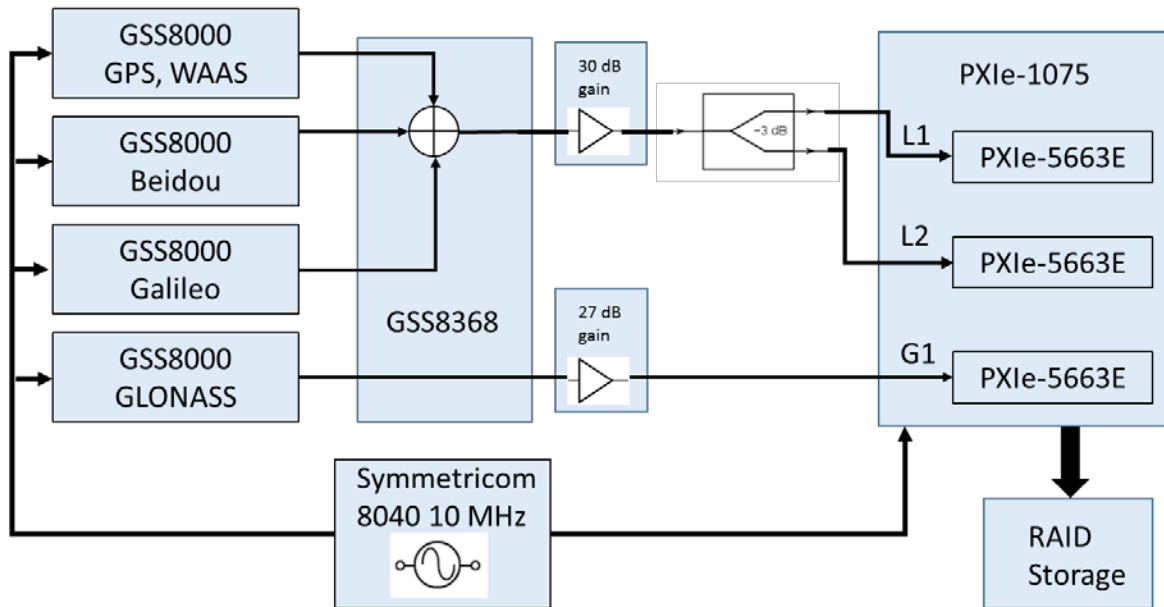


**Figure 3-4: GNSS Signal Generation and Recording**

The resultant RF data was recorded using a set of three National Instruments (NI) PXIe-5663E Vector Signal Analyzers housed in a National Instruments PXIe-1075 chassis. The three channels were recorded into 26.4 MHz wide bands centered at 1227.6 MHz, 1572.2 MHz, and 1602 MHz at 33 MS/s using 16 bit complex samples. The sampled data was then recorded on an NI HDD-8265 12 Terabyte Redundant Array of Independent Disks (RAID) (see Figure 3-4). The total recording time for the interference test events is approximately seven hours in length.

The GNSS signal playback and transmission process is illustrated in Figure 3-5. During the test period, the recorded GNSS signals were converted back to RF using a set of three National Instruments PXIe-5673E Vector Signal Generators (VSG) using the same sample rate as was used to record the data. The outputs of the three signal generators were combined using a Narda model 4372A-3 passive 3-port combiner. The output of this combiner was passed through a Vaunix Technology LDA-602 variable attenuator.

The attenuation level was established during chamber mapping and calibration (see Section 3.1.4) such that the received signal strength was at or above the power levels specified below. The output of the attenuator was followed by a splitter (that was connected to a spectrum analyzer during the test) and then an RF isolator with approximately 60 dB of isolation to prevent RF power from entering the system through the antenna. The isolator was connected to a custom passive L1/G1/L2 GNSS patch antenna that was suspended from the ceiling of the test chamber (see Figure 3-1). Prior to the WSMR deployment, the GNSS signal playback system was tested in a chamber at MITRE to ensure that the playback accurately reproduced the desired scenarios.

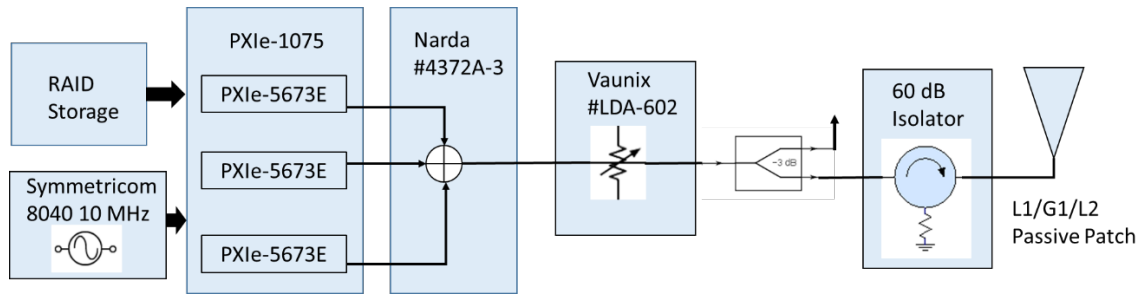


**Figure 3-5: GNSS Signal Playback and Transmission**

The equipment that was transported to and set up in the chamber is listed in Table 3-2.

**Table 3-2: GNSS Signal Generation Equipment**

Equipment	Make/Model	Notes
RAID storage	National Instruments HDD-8265	12 TB
3-channel VSG chassis	National Instruments PXIe-1075	Includes computer controller (PXIe-8133) with LabView software.
VSGs (3 each)	National Instruments PXIe-5673E	Each VSG consists of NI PXIe-5450 (400 MS/s I/Q Signal Generator), PXIe-5611 (I/Q Vector Modulator), and PXIe-5652 (RF Signal Generator).
Combiner	Narda 4372A-3	Passive 3-port
Digitally-controlled variable attenuator	Vaunix LDA-602	Provides up to 50 dB attenuation; controlled by VSG chassis computer.
Isolator	Addington Laboratories 222-0170A	Provides approximately 60 dB isolation.
Passive GNSS antenna	MITRE custom	RHCP antenna covers 1559 – 1610 MHz and 1212 – 1242 MHz
Rb Frequency Source	Symmetricom 8040	10 MHz
Amplifiers	MiniCircuits ZRL-2400-LN	23-30 dB gain. Used for chamber calibration (see Section 4.3.4.2).
Cables	Various	As needed and with appropriate connectors.

The GNSS signals that were generated and recorded at MITRE and then broadcast in the chamber at WSMR are indicated in Table 3-3.

**Table 3-3: GNSS Signals Generated for Test**

Signal
GPS L1 C/A-code
GPS L1 P-code
GPS L1C
GPS L1 M-code
GPS L2 P-code
SBAS L1
GLONASS L1 C
GLONASS L1 P
BeiDou B1I
Galileo E1 B/C

For the interference test events, the transmitted GNSS signal powers were calibrated to yield the minimum signal levels specified in Table 3-4 at the location in the test grid with the lowest received power (see Section 3.1.4). The signal powers were held constant over the duration of the event, except for the linearity test.

**Table 3-4: Minimum Received GNSS Signal Power Levels for Interference Test Events**

Signal	Minimum Received Power out of 0 dBic antenna (dBW)
GPS C/A-code	-158.5 for 8 SVs, -168.5 for 1 SV, -178.5 for 1 SV
GPS L1 P(Y)-code	-161.5 for 8 SVs, -171.5 for 1 SV, -181.5 dBW for 1 SV
GPS L1C	-157 for 8 SVs, -167 for 1 SV, -177 for 1 SV
GPS L1 M-code	-158 for 8 SVs, -168 dBW for 1 SV, -178 dBW for 1 SV
GPS L2 P(Y)-code	-164.5 for 8 SVs, -174.5 for 1 SV, -184.5 for 1 SV
GPS L2 M-code	-161 dBW for 8 SVs, -171 dBW for 1 SV, -181 dBW for 1 SV
SBAS L1	-158.5 for 2 SVs
GLONASS L1 C	-161 for 10 SVs, -171 for 1 SV, -181 for 1 SV
GLONASS L1 P	-161 for 10 SVs, -171 for 1 SV, -181 for 1 SV
BeiDou B1I	-163 for 10 SVs, -173 for 1 SV, -183 for 1 SV
Galileo E1 B/C	-157 for 10 SVs, -167 for 1 SV, -177 for 1 SV

The user was located at 32N, 106W, 0 m height relative to the WGS-84 ellipsoid and was stationary over the simulated time span. The simulated start time was April 18, 2016 08:00

MDT. Yuma-style almanacs for the GPS, GLONASS, BeiDou, and Galileo constellations are provided in Appendix A.

Errors that the GNSS simulators were capable of emulating were set to zero except for ionospheric delay and tropospheric delay errors, which are described in Appendix A. The objective of the simulator configuration was to minimize pseudorange and carrier phase errors from all sources (e.g., satellite clock errors, satellite ephemeris errors, residual ionosphere, residual troposphere) for the devices under test to enable measurement of the introduced interference source effects without the influence of other errors that are not attributable to the interference source. Since GNSS receivers typically apply tropospheric and ionospheric correction models, these error sources were emulated to minimize residual receiver measurement errors.

### **3.1.3.2 Interference Signal Generation**

The Software Programmable Interference Generator for ABC Testing (SPIGAT) was assembled to generate additive white Gaussian noise (AWGN) and simulated LTE signals as interference at controlled power levels at specified frequencies. This system was automated to execute these tests for a suite of 22 discrete interference frequencies at appropriate signal levels with minimal operator intervention. The frequencies and signal levels tested are shown in Figure 3-6 and the interference system configuration for the radiated test is depicted in Figure 3-7. The VSG generated either 1 MHz AWGN (Type 1) or LTE (Type 2) signals at a fixed level at the appropriate carrier frequency and the adjustable attenuator controlled the signal level input from the VSG to the high power amplifier (HPA).

Using the attenuator in this fashion ensured Adjacent Channel Leakage Ratio (ACLR) from the VSG was maintained through different test levels. The HPA output was provided to an RF switch that directed the interference signal through one of 22 RF cavity filters. Lastly, the amplified and filtered interference signal was directed to a linearly polarized standard gain horn transmit antenna that irradiated the GNSS receivers under test. Directional couplers were included in the signal generation path to provide monitor points and a circulator was added to provide overload protection.



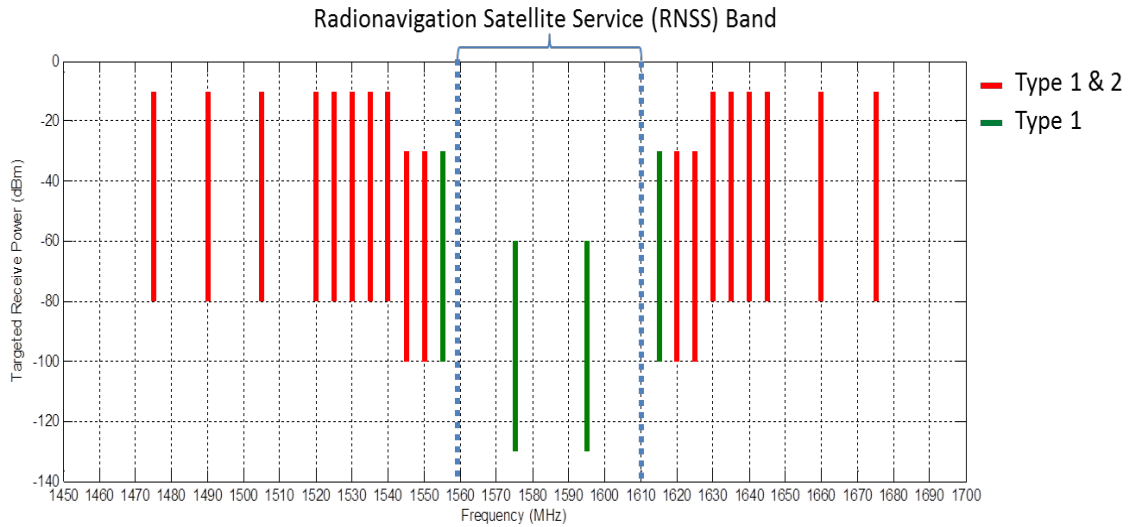


**Figure 3-6: Interference Frequencies and Signal Levels Tested**

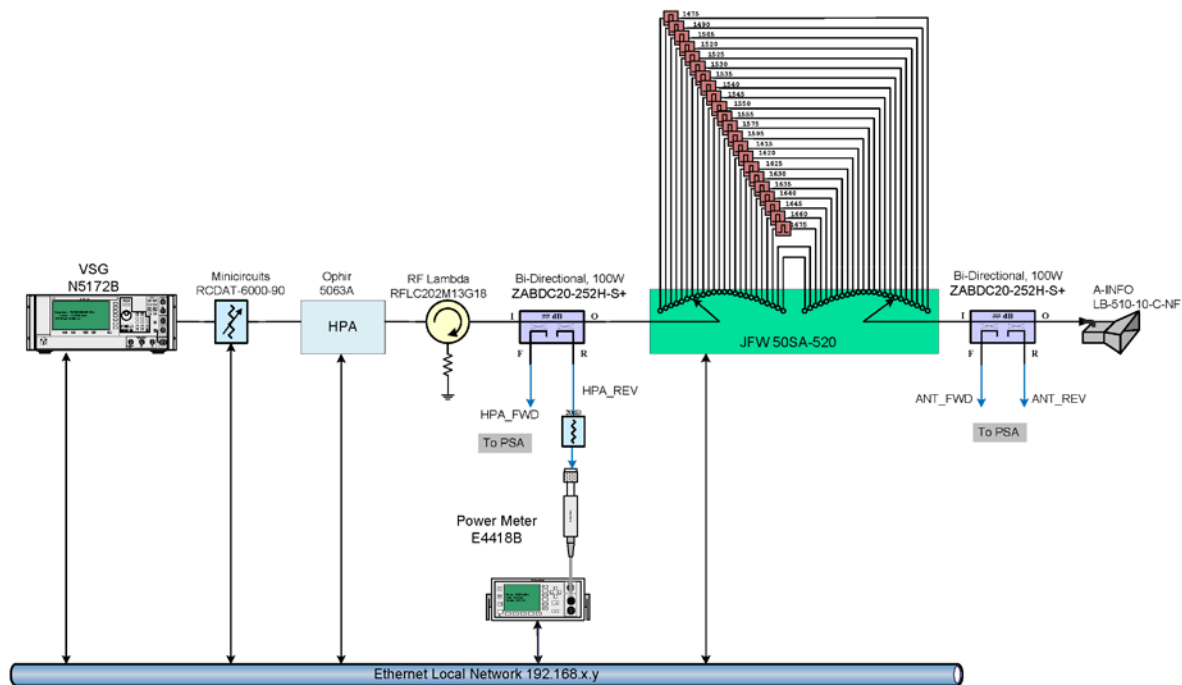


**Figure 3-7: Interference System Configuration for Radiated Test**

Test execution for each interference test signal was controlled by a pre-defined configuration file. The configuration file contained the frequencies to be tested, power levels, signal type, and test durations. The control computer was “GPS time aware” by obtaining receiver time from a GPS receiver tracking signals directly from the GNSS signal generator. This allowed time alignment with receiver data during processing. The interference control software recorded GPS time and instrument settings once per second into SPIGAT summary files for each test event.

One of the more important considerations for SPIGAT was the RF filters and ensuring they were sufficient to attenuate out-of-band emissions (OOBE) so that degradation measured was due almost entirely to the fundamental signal only. (The impacts of OOBE with the fundamental signal were investigated in the wired testing.) The RF passband cavity filters used to condition the interference were grouped into two categories based on roll-off specification. Filters centered at test frequencies nearer (but outside of) the RNSS band, namely 1540, 1545, 1550, 1555, 1615, 1620, and 1625 MHz were designed to meet tighter roll-off requirements with the primary feature being 65 dB rejection at 9 MHz from center. The remaining filters were designed to meet a more relaxed set of requirements with 65 dB rejection at 20 MHz from center. The measured frequency dependent gain for these two filter types are shown in Figure 3-8. Further details on SPIGAT and WSMR test conditions are provided in Appendix A.

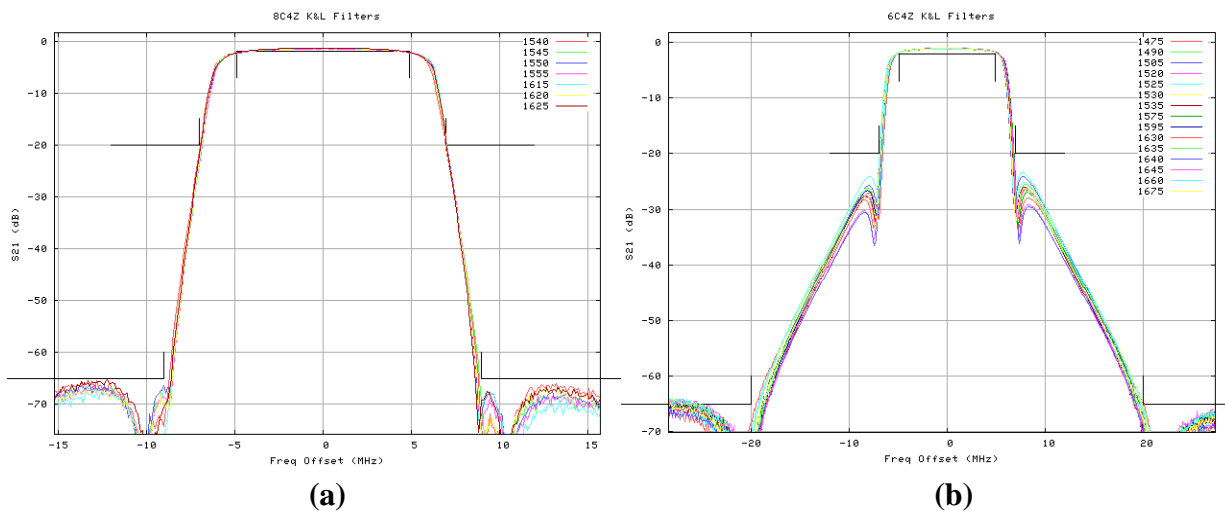


**Figure 3-8: Measured gain response for (a) bandpass RF filter with tighter rejection requirements, (b) bandpass RF filter with more relaxed rejection requirements.**

### 3.1.3.2.1 Type 1 Signals

The Type 1 signal was selected for testing at all 22 frequencies to provide a narrowband signal for assessment of a general receiver mask not specifically tied to LTE. The signal tested was bandpass AWGN with bandwidth  $B=1$  MHz. Some early consideration was given to using continuous wave (CW) interference but this 1 MHz signal was adopted based primarily on concerns some receivers might employ techniques specifically designed to mitigate CW signals. The AWGN signal was generated offline and had a duration of approximately 0.021 seconds. This signal file was loaded into the VSG, up-converted to the appropriate frequency, and played out continuously end to end from VSG memory. Figure 3-9 is a spectrum analyzer capture of the Type 1 signal as received in the EMVAF test area during testing.



**Figure 3-9: Type 1 Signal Captured during WSMR Testing @ 1530 MHz**

### 3.1.3.2.2 Type 2 Signals

The Type 2 signal emulated LTE characteristics representing both a downlink and an uplink. The downlink was emulated as a fully loaded base-station with Orthogonal Frequency Division Multiplexing (OFDM), and the uplink with Sub-Carrier OFDM (SC-OFDM). The LTE digital waveforms were generated using the MATLAB LTE package. As with the Type 1 signal, these LTE representations were loaded on the VSG, up-converted to the appropriate carrier frequency, and played out end to end from VSG memory. The durations of the downlink and uplink files were two seconds each. The specific settings and commands used in MATLAB are provided with Appendix A. Figure 3-10 is a spectrum analyzer capture of the Type 2 signal as received in the EMVAF test area during testing.

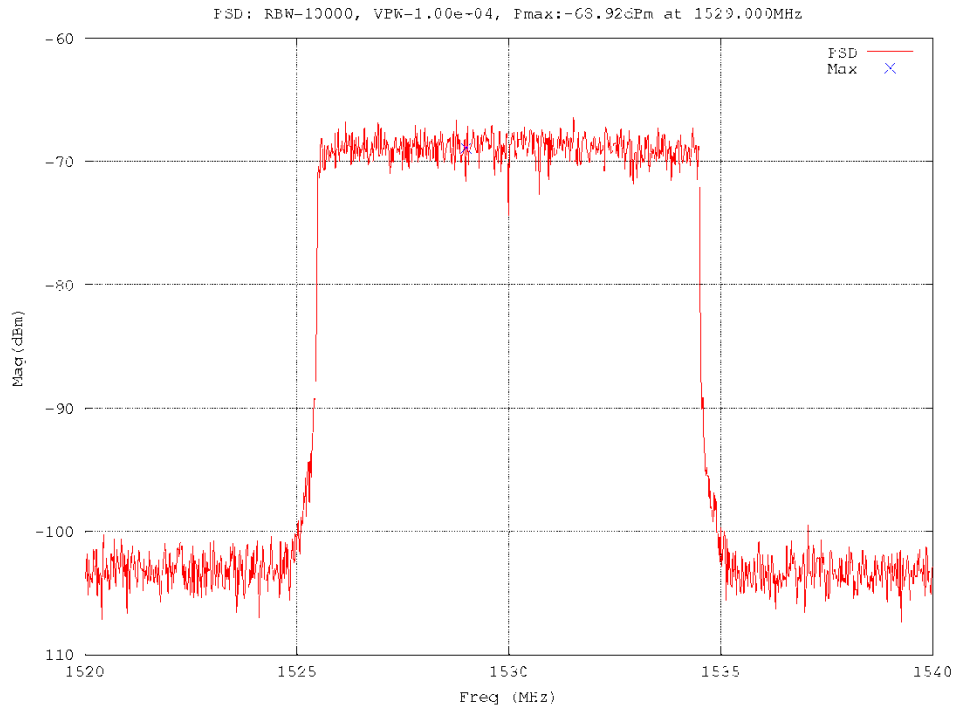


**Figure 3-10: Type 2 Signal Captured during WSMR Testing @ 1530 MHz**

### 3.1.3.2.1 Intermodulation

The Type 1 and 2 interference signals provide a measure of the effect of an interfering signal on a particular GPS/GNSS receiver but do not capture impacts of spurious emissions due to two or more signals operating simultaneously at different center frequencies. The intermodulation signal test was included to demonstrate this potential impact by simultaneously transmitting Type 2 downlink signals at center frequencies of 1530 MHz and 1550 MHz. The 3<sup>rd</sup> order intermodulation product of these center frequencies falls near the center of the L1 band. For this specific test, the 1550 MHz signal was generated so that it was approximately 10 dB lower than the 1530 MHz signal. The downlink LTE representation discussed earlier was up-converted to 1530 and 1550 MHz and played out end to end from VSG memory. The duration of the intermodulation file was 0.5 seconds. Figure 3-11 is a spectrum analyzer capture of the intermodulation signal as received in the EMVAF test area during testing.

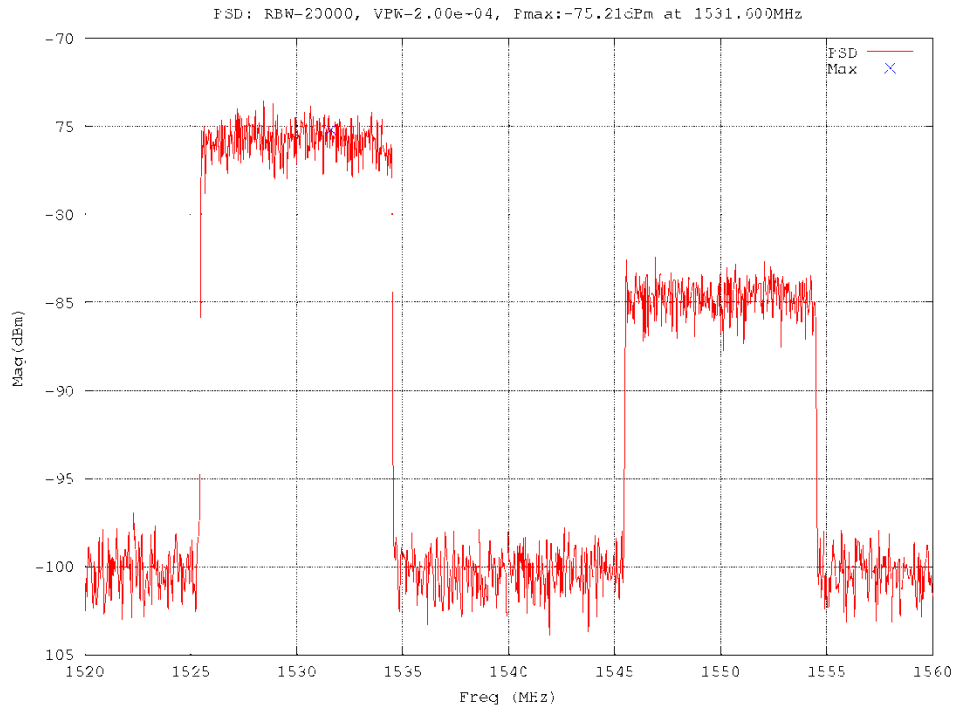


**Figure 3-11: Intermodulation Signal Captured during WSMR Testing**

### 3.1.4 System Calibration and Chamber Mapping

System calibration and chamber mapping included several efforts at WSMR; 1) GNSS calibration, 2) SPIGAT calibration, 3) and, chamber mapping. GNSS calibration is described in Section 3.1.4.1 and the remaining topics are discussed in Section 3.1.4.2 and Appendix A.

#### 3.1.4.1 GNSS System

To calibrate the GNSS signal power levels, the playback system was modified slightly from the configuration shown in Figure 3-5. Two LNAs were inserted after the variable attenuator to increase the output power level. This power increase allowed the received GNSS signal levels to be accurately measured by a spectrum analyzer connected to a RHCP cavity-backed spiral antenna that was moved across 45 points in the test grid. The gains of the two LNAs were determined from measurement (see Figure 3-12).

The calibration proceeded in two steps. First, the VSGs in the playback system were utilized to produce tones at two frequencies (1227 MHz and 1561 MHz) to determine the variation in received power across the test grid at these frequencies. These variations, as measured using a RHCP cavity-backed spiral antenna at 45 locations spanning the test grid, are shown in Figure 3-13 and Figure 3-14. The numerical values on each of these plots are in dBm.

Second, to establish the output power of the three VSGs in the playback system, a GNSS signal from a single satellite was emulated (GPS P-code for 1227 MHz, GPS P-code at 1575 MHz, and

GLONASS C for 1602 MHz) and the received power measured at the location at the edge of the test grid where the received power was a minimum. The measured power, adjusted by the known LNA and cavity-backed spiral antennas gains, was compared to the target received power levels in Table 3-4. The resultant differences were used to establish power settings for each of the three VSGs in the playback system for the test events. The VSG output powers were adjustable both relatively and absolutely (through power commands sent digitally by computer interface to each VSG to change relative gains, and through removal of the two LNAs as well as commands to the digital variable attenuator that followed the combined VSG outputs). The objective of this calibration process was to ensure that the power levels specified in Table 3-4 were achieved or exceeded out of a 0 dBic receive antenna at any location in the test grid. As evident from Figure 3-13 and Figure 3-14, when the target minimum received GNSS signal levels were achieved at the worst-case location in the grid (grid corners), they were exceeded by up to 3.7 dB at the center of the grid.

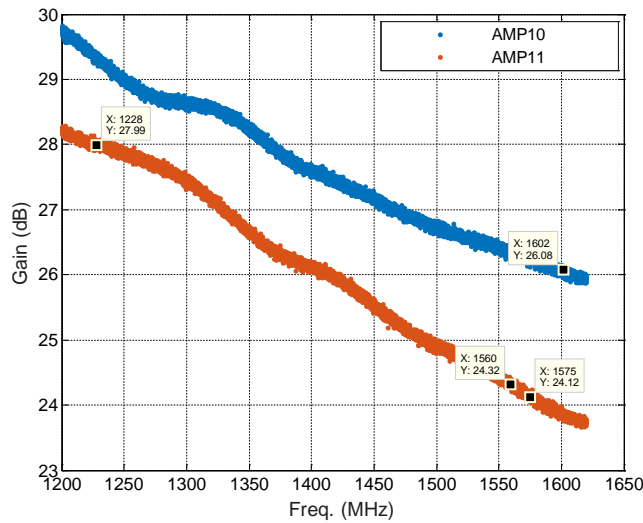


**Figure 3-12: Measured Gain of Two MiniCircuits ZRL-2400-LN Amplifiers**

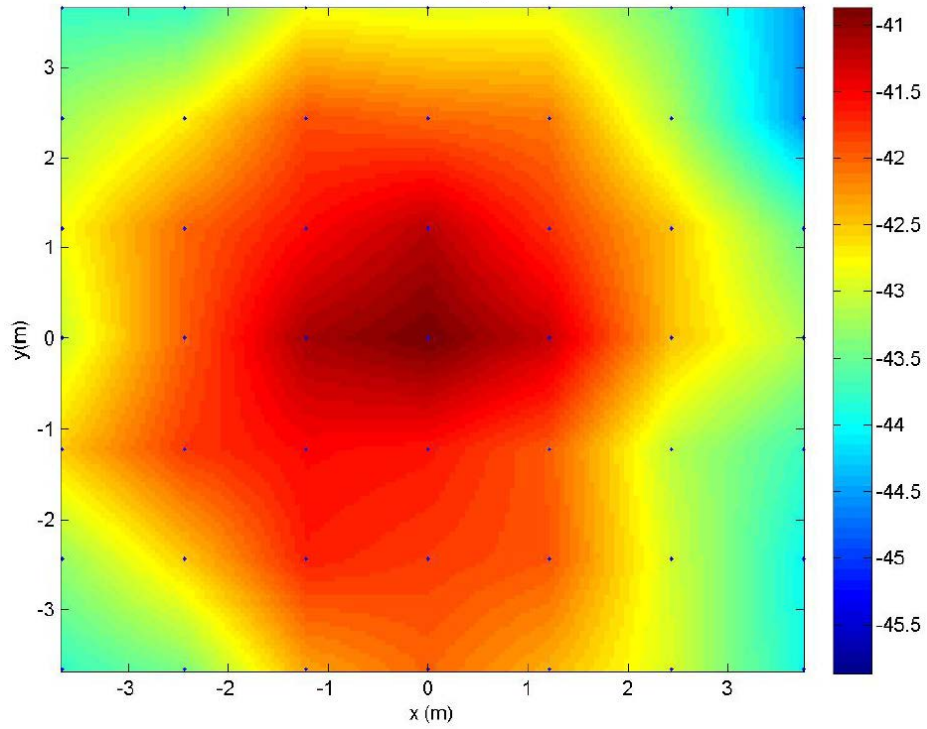


**Figure 3-13: GNSS Signal Received Power Variation across the Test Grid (1227 MHz)**

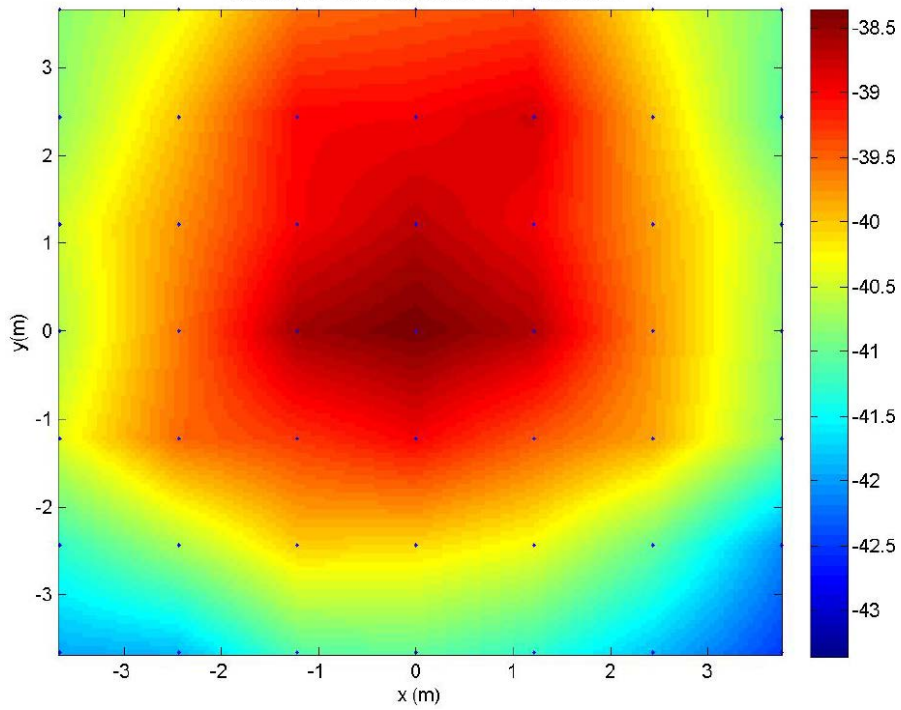


**Figure 3-14: GNSS Signal Received Power Variation across the Test Grid (1561 MHz)**

### 3.1.4.2 SPIGAT

The interference system was calibrated to determine the system biases for each interference frequency and to ensure the intended power levels were achieved in the test area. This calibration was accomplished by selecting a reference location at the edge of test area at approximately the 3 dB beamwidth of the interference transmit antenna and measuring CW tones generated by SPIGAT at all 22 discrete frequencies. The CW tones were measured using a cavity backed spiral antenna (AST-1507AA) mounted on a tripod, calibrated RF cable, and a spectrum analyzer (Agilent E4445A). This procedure resulted in a correction table per frequency utilized by SPIGAT. The interference linearity was also measured from this reference location to demonstrate received power over the test range at each frequency matched the intended levels.

### 3.1.4.3 Chamber Mapping

Chamber mapping was conducted after calibration was complete to determine RF power variation across the test area. Mapping used a grid of 45 measurement points separated by approximately four feet which encompassed the test area. Chamber mapping was completed at the beginning and end of DOT testing with all equipment installed in the test area. These two mappings were very consistent and final mapping values used with receiver processing represented their average. Examples of the final power mapping at 1475, 1575 and 1675 MHz are provided in Figure 3-15. This figure shows the expected performance of the interference antenna beamwidth becoming narrower at higher frequencies. The location of each receiver tested was known relative to the mapping grid and this mapping data was used to modify SPIGAT test event summary files and generate unique interference power profiles per frequency for each receiver location.

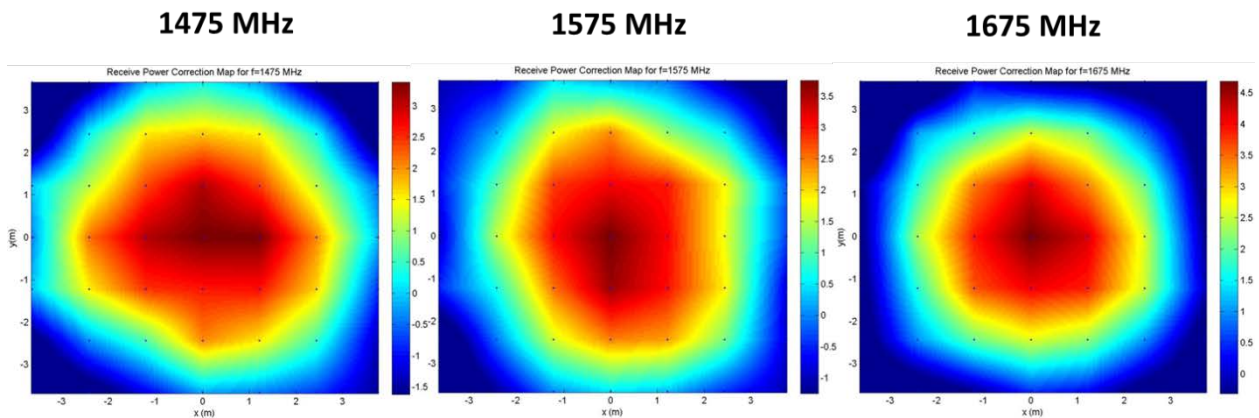


Figure 3-15: Power Correction Representations for Three Frequencies

### 3.1.5 Test Sequence

The test schedule executed at WSMR is shown in Table 3-5. In addition to Type 1, Type 2, and intermodulation signals described previously there was also a CNR linearity test. Table 3-5 shows the day each test was executed and test number. Type 1 and Type 2 signal tests were



given priority so these were tested on separate days to increase the likelihood of obtaining a more robust data set. The in-band test mentioned in this table was the result of removing Type 1 signals directly in the RNSS band from this test sequence and testing separately. A discussion of the rationale for this change is provided later in this section. Lastly, each test event listed in the table was preceded by a stabilization period of at least fifteen minutes with the GNSS system turned ON to allow participants to reset equipment, verify GNSS signal tracking, and ensure data collection was started.

**Table 3-5: Test Schedule**

<b>Day of Week (24-28 April 2016)</b>	<b>Test and Number</b>
Monday	CNR linearity - Test01
Tuesday	Type 1 signal - Test02 Type 2 signal – Test03
Wednesday	Type 2 Signal – Test04 Type 1 Signal – Test05
Thursday	In-Band – Test56 CNR linearity - Test07 Intermodulation – Test89

### 3.1.5.1 Linearity Test

The GPS/GNSS receivers’ CNR estimators need to operate in their linear region. A linearity test was conducted on the CNR estimators varying GNSS signal power. SPIGAT was not used for this test event. For this test, GNSS signals of each type were generated to match their intended levels during interference testing (i.e. majority of GPS L1 C/A were generated at -158.5 dBW and two SVs were at the lower specified power levels of -10 and -20 dB). After five minutes at these nominal levels, the test sequence had each signal power increased by two dB every 15 seconds until they reached +10 dB relative to the nominal level. Each signal power was then decreased by two dB every 15 seconds until they reached -20 dB relative to the nominal level. Finally, each signal power was increased by two dB every 15 seconds until power was returned to nominal levels. The receivers were allowed to track for a brief period following the last signal power step before concluding this test event.

### 3.1.5.2 Interference Test

Each of the individual interference tests used the exact same sequence. The interference test sequence for each frequency started with a quiescent period of five minutes with no interference to establish baseline CNR followed by stepping through the full power range at two dB steps with 15 second dwells at each level. This sequence was repeated for all desired frequencies for each interference signal. Table 3-6 shows the specific frequencies, power levels, and LTE signal types used in this testing. The power range for the intermodulation test event was -90 to -20 dBm for the signal generated at 1530 MHz and -100 to -30 dBm for 1550 MHz.

As mentioned above, the Type 1 test event had the two in-band frequencies (1575 MHz and 1595 MHz) extracted from the full set of 22 test frequencies and made into a separate test event. During the set-up period at the chamber, some system verification testing revealed that for these two in-band frequencies noise from the high-power amplifier (VSG power turned OFF) would affect receiver performance. The system reconfiguration required to circumvent this issue was to place a 20-dB attenuator at the output of the interference generation system which effectively lowered the output noise floor. The interference power was increased for the addition of this 20-dB attenuator to meet the desired interference test range. For in-band and intermodulation test events, SPIGAT was commanded to run two interference test cycles back to back (hence, Test56 and Test89 designations).

**Table 3-6: Interference Signal Parameters**

Center Frequency (MHz)	$[p_{min}, p_{max}]$ (dBm)	LTE Interference Signal		Bandpass Noise Interference Signal
		Signal Bandwidth	LTE Type	
1475	[-80,-10]	10 MHz, LTE	Downlink	1 MHz
1490	[-80,-10]	10 MHz, LTE	Downlink	1 MHz
1505	[-80,-10]	10 MHz, LTE	Downlink	1 MHz
1520	[-80,-10]	10 MHz, LTE	Downlink	1 MHz
1525	[-80,-10]	10 MHz, LTE	Downlink	1 MHz
1530	[-80,-10]	10 MHz, LTE	Downlink	1 MHz
1535	[-80,-10]	10 MHz, LTE	Downlink	1 MHz
1540	[-80,-10]	10 MHz, LTE	Downlink	1 MHz
1545	[-100,-30]	10 MHz, LTE	Downlink	1 MHz
1550	[-100,-30]	10 MHz, LTE	Downlink	1 MHz
1555	[-100,-30]	-	-	1 MHz
1575	[-130,-60]	-	-	1 MHz
1595	[-130,-60]	-	-	1 MHz
1615	[-100,-30]	-	-	1 MHz
1620	[-100,-30]	10 MHz, LTE	Uplink	1 MHz
1625	[-100,-30]	10 MHz, LTE	Uplink	1 MHz
1630	[-80,-10]	10 MHz, LTE	Uplink	1 MHz
1635	[-80,-10]	10 MHz, LTE	Uplink	1 MHz
1640	[-80,-10]	10 MHz, LTE	Uplink	1 MHz
1645	[-80,-10]	10 MHz, LTE	Uplink	1 MHz
1660	[-80,-10]	10 MHz, LTE	Uplink	1 MHz
1675	[-80,-10]	10 MHz, LTE	Downlink	1 MHz

### 3.1.6 Data Processing/ITM formation

During testing, organizations used their own programs/software for data collection. This delegation of data collection responsibility was necessary since many of the 80 receivers had proprietary interfaces. At the end of each test day, data collected from each receiver was transferred to DOT's master data repository. The participants were requested to provide a data acquisition system (e.g. laptop) with DVD/CD recording capability or asked to use USB hard drives to transfer data. All data was archived prior to the receivers and participants leaving the test area.

### 3.1.6.1 Data Conversion and Format

The master data repository was setup inside the chamber to allow participants to transfer data from each receiver to this repository. The master repository consisted of a desktop with a local storage array which accommodated all the data. Each participant was given a blank external hard drive, which stayed with them throughout the test, was dedicated to transfer data to the repository at the end of each test. Blank DVD/CDs were also made available for those who wanted to copy the data to DVDs, then the data were copied to the repository (through the repository desktop).

Data was provided from each participant in National Maritime Electronics Association (NMEA) 0183, Receiver Independent Exchange (RINEX versions 2.11, 3.00, 3.01 and 3.03), or commonly defined comma separated variable format (CSV). The preference was to have data provided in CSV format when possible. Table 3-7 identifies the desired data from each GNSS receiver tested. It was understood that all data types may not be available and for these instances fields should be denoted not available, “NaN”. The CSV format accommodates twelve fields to indicate GPS time, position estimate and satellites tracked for each GNSS constellation and signal type. This data is followed with satellite specific data needed for the analysis. Each constellation signal type is allocated 32 satellites and SBAS is allocated two satellites with the data grouped by data block as described in Table 3-7.

Each receiver has a separate data file for each test run. The nomenclature of the file name is as follows: ParticipantLC\_ParticipantID\_Test#\_Date.extension, where ParticipantLC is a unique indicator for the antenna location (and receiver if integrated), ParticipantID maps to the receiver/antenna tested and origination, Test# indicates the test run number for that day, Date is the day of the actual test, and an extension is used to indicate the type file (ex. NMEA, RINEX or CSV). The ParticipantLC and ID were provided during test set-up. After the test week all the data files were converted to a commonly defined CSV as well as MAT format, as shown in Table 3-7 using MATLAB. To facilitate post-data processing, MATLAB Datenum and GPS Week columns were added at the beginning of the table, and the file’s naming convention was changed to add device under test number (DUT#), participant’s acronym, receiver’s name, and the category for receiver category.

**Table 3-7: CSV Data Format**

Field #	Parameter	Units	Comment
1	GPS Seconds of Week	Seconds	
2	Latitude	Degrees	relative to WGS84
3	Longitude	Degrees	relative to WGS84
4	Height	Meters	relative to WGS84 (orthometric)
5	GPS L1 C/A-code Tracked		
6	GPS L1 P-code Tracked		
7	GPS L1C Tracked		
8	GPS L2 P-code Tracked		
9	GLONASS L1 C Tracked		
10	GLONASS L1 P Tracked		
11	BeiDou B1I Tracked		
12	Galileo E1 B/C Tracked		
13	SBAS L1 C/A-code Tracked		
<p>Next are 32 satellite slots per signal type for GPS, GLONASS, BeiDou and Galileo. Each slot contains four data parameters. Satellite order is 1 through 32. SBAS has two satellite slots with four data parameters each. SBAS pseudo random noise (PRN) codes are 135 and 138.</p>			
14	Carrier Phase <sub>(PRN-1,GPS C/A)</sub>	meters	
15	Loss of Lock Flag <sub>(PRN-1,GPS C/A)</sub>	binary (0 or 1)	Cycle slip or loss of carrier phase lock indicator. 0 indicates no loss of lock, 1 means lost lock.
16	Carrier to Noise Ratio <sub>(PRN-1,GPS C/A)</sub>	dB-Hz	
17	Pseudorange <sub>(PRN-1,GPS C/A)</sub>	meters	
18 – 141	GPS L1 C/A-code measurements for satellite signals 2-32		
142 – 269	GPS L1 P-code measurements for satellite signals 1-32		
270 – 397	GPS L1C measurements for satellite signals 1-32		
398 – 525	GPS L2 P-code measurements for satellite signals 1-32		
526 – 653	GLONASS L1 C satellite signals 1-32		
654 – 781	GLONASS L1 P satellite signals 1-32		
782 – 909	BeiDou B1I satellite signals 1-32		
910 – 1037	Galileo E1 B/C measurements for satellite signals 1-32		
1038 - 1045	SBAS L1 C/A-code measurements for satellites signals from PRNs 135 and 138		

### 3.1.6.2 1 dB CNR Degradation

The 1 dB carrier-to-noise ratio (CNR) interference protection criterion (IPC) has been used in responding to FCC rulemaking proceedings that assessed the potential impact to GPS services, [2] and was the subject of much discussion and stakeholder feedback at the OST-R workshops.

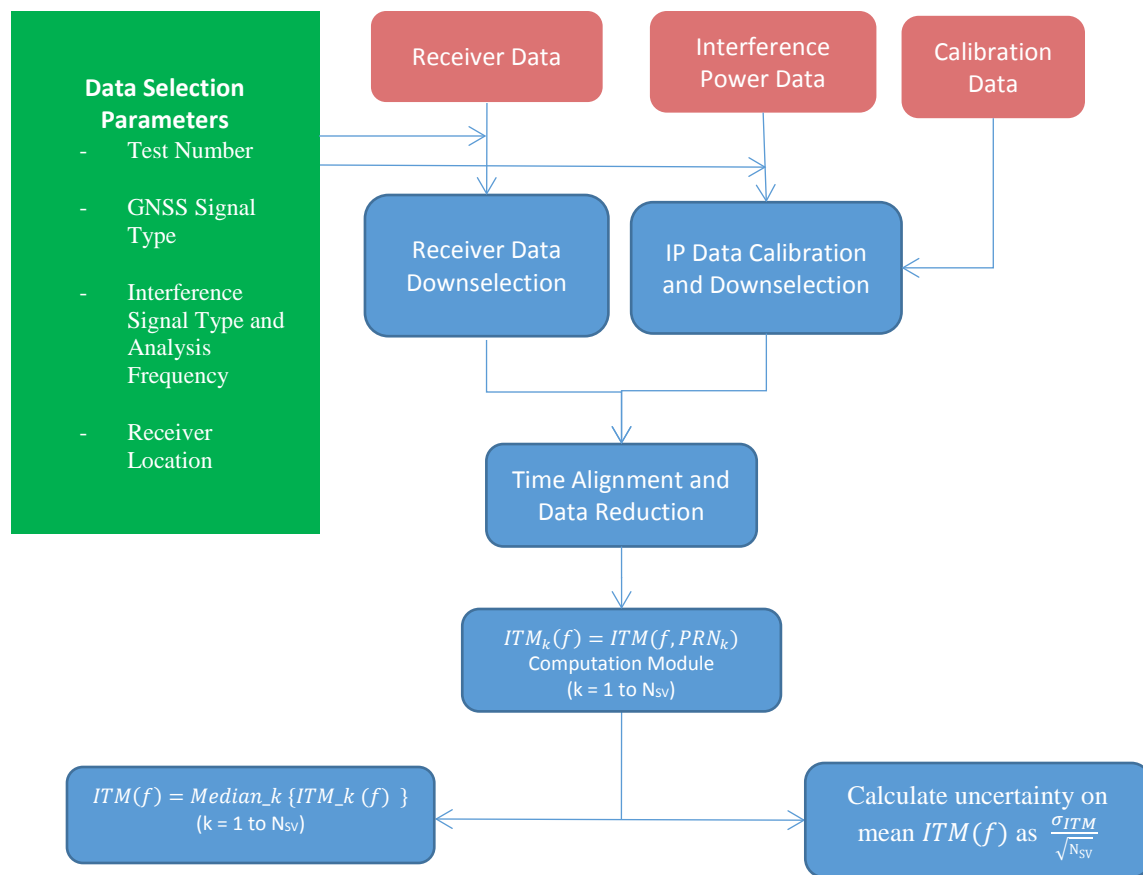
A 1 dB  $C/N_0$  degradation (-1 dB  $C/N_0$ ) due to a new interference source is equivalent to an  $I_0/N_0$  ratio of -6 dB, where  $C$  is the level of the observable desired information signal, while  $N_0$  is the competing unwanted noise and  $I_0$  is the interference level. This  $I_0/N_0$  ratio of -6 dB means that a new interference level is actually one fourth the level of the existing noise level and the total unwanted  $N_0 + I_0$  level is now 25% higher which is highly significant to system designers.

There are multiple interference mechanisms that can degrade  $C/N_0$  of a GPS receiver. However, it is difficult to isolate the specific interference mechanism for each GPS receiver without sufficient technical information, such as receiver design, radio frequency filter selectivity, low noise amplifier gain, noise figure, 1 dB gain compression point and third-order intercept point from the GPS receiver manufacturers. Participation by GPS/GNSS receiver manufacturers in the DOT GPS Adjacent Band effort was on a voluntary basis and there was no obligation to provide this information.

Given the myriad of GPS/GNSS applications requiring accuracy to support their mission applications ranging from tens of meters to millimeters, there is not a single "accuracy degradation limit" that could be applied and trying to do so would be an intractable effort.

### **3.1.6.3 ITM Data Processing**

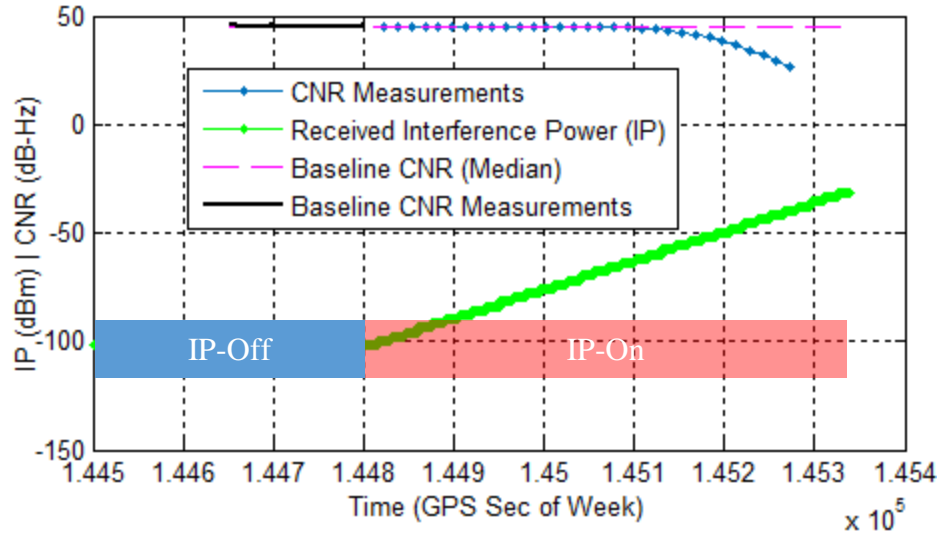
The Interference Tolerance Mask (ITM) defines, for a given frequency, the maximum aggregate power allowed to ensure the tested GPS/GNSS receiver did not experience more than a 1 dB reduction in CNR for various categories of GPS/GNSS receivers. For a given DUT, the interference power (IP) data was calibrated using the mapping measurements interpolated to the DUT location. The CNR data corresponding to the GNSS signal being analyzed is time aligned with the calibrated interference data.



**Figure 3-16: ITM Processing Block Diagram**

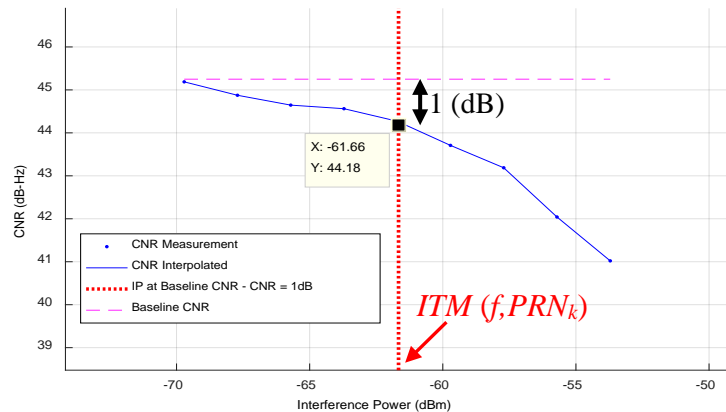
The IP level which causes 1-dB CNR degradation is then determined on a per PRN basis. The median of results across PRNs is the value of the interference tolerance mask  $ITM(f)$  at frequency  $f$  for that DUT. The use of mean and median produced similar results but the median operation was chosen because it is less sensitive to outliers. Only the PRNs at minimum ICD powers were used in the ITM analysis (not lower power to emulate low elevation satellites). A description of the overall processing is outlined in Figure 3-16.

Figure 3-17 shows the time aligned IP and reduced CNR data. The baseline CNR ( $CNR_{BL}$ , magenta dashed line) is calculated by averaging over the last 2.5 minutes of the IP-off interval (black line). During the IP-on interval, data reduction was performed by averaging CNR over the last 12 seconds of each 15 seconds IP step in order to allow for three seconds settling time. The blue trace in this figure is the resulting reduced CNR time series.



**Figure 3-17: Sample plot for calibrated interference power overlaid with time aligned CNR data for a given DUT at a particular interference frequency**

The time aligned and reduced CNR data can be plotted directly as a function of IP for each  $PRN$  and  $ITM(f, PRN_k)$  can be found using linear interpolation as shown in Figure 3-18.



**Figure 3-18: Determining the tolerable interference level from the CNR versus interference power for a single satellite after time alignment and calibration of interference power**

The test for each interference signal type was performed twice as described in Section 3.1.5. The average of the resulting two interference tolerance values was taken as the final  $ITM(f)$  for each interference signal type and GNSS signal supported by a DUT. Figure 3-19 depicts the ITMs for L1 C/A signal for a single DUT and shows repeatability between both LTE tests.

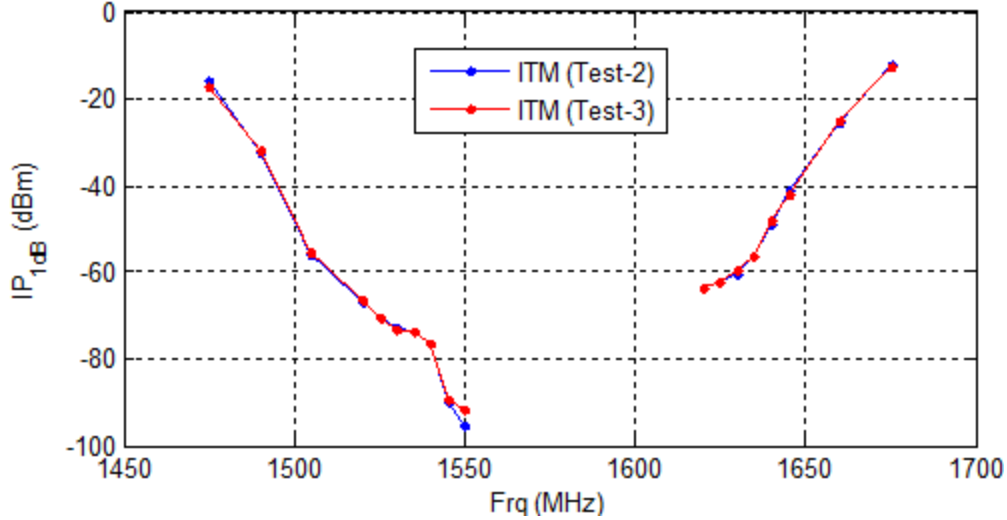


**Figure 3-19: Overlaid L1 C/A ITMs from two radiated LTE test events for a single DUT. Test-2 and Test-3 refer to the first and second LTE tests respectively.**

It is important to note that the algorithm does not calculate a 1-dB CNR degradation value if the CNR dynamic range defined as the difference between  $CNR_{BL}$  and the smallest 12 second average CNR value within each IP progression ( $CNR_{Min}$ ) is less than 1.5 dB. In addition, the algorithm also checks that this dynamic range is statistically significant. This is done by ensuring that the standard deviation of the difference is small relative to its mean value. This criterion used by the algorithm is shown in the following expression (in dB).

$$CNR_{BL} - CNR_{Min} > 3 \times \sqrt{\text{var}(CNR_{BL}) + \text{var}(CNR_{Min})} \quad (3-1)$$

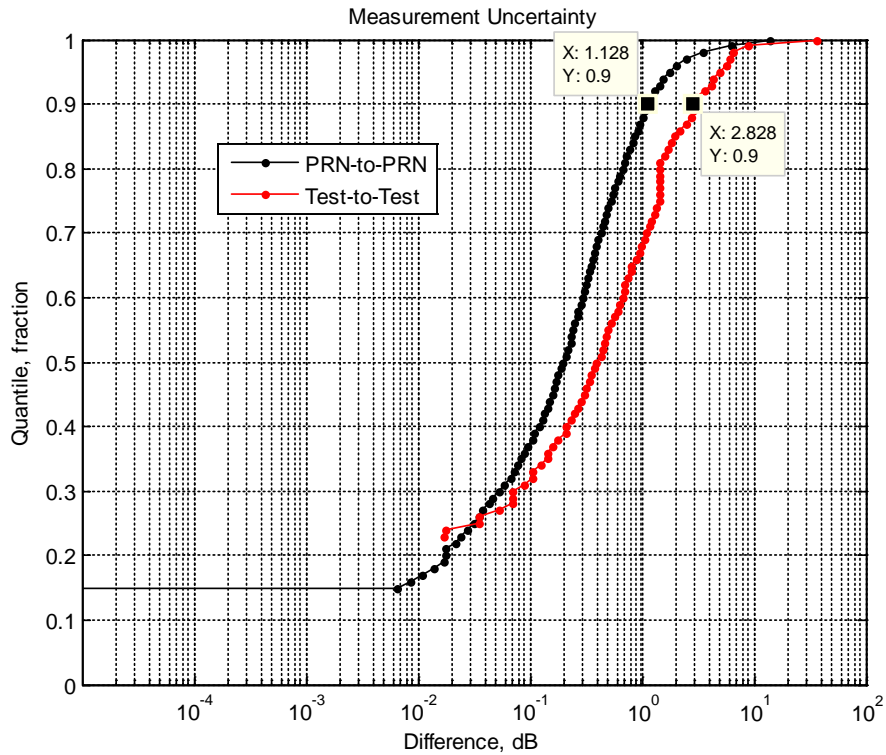
Where  $\text{var}(\cdot)$  represents the measurement variance divided by the number of measurements for each of the two quantities. Additional quality checks are performed for each IP step. For example, the algorithm requires that at least three measurements be reported within the last 12 seconds interval of each step and that the standard deviation of the mean within each step be less than  $\frac{1}{2}$  dB.

The averaging across repeated tests was subject to additional quality control checks. For each DUT, GNSS signal, interference type, and center frequency combination, this average was performed only when the difference between the results produced by the two tests is less than 10 dB. For the cases when the difference exceeded this threshold, the test producing a value closer to the interpolated value between adjacent frequencies is kept, and the result of the other test was disregarded as an outlier.

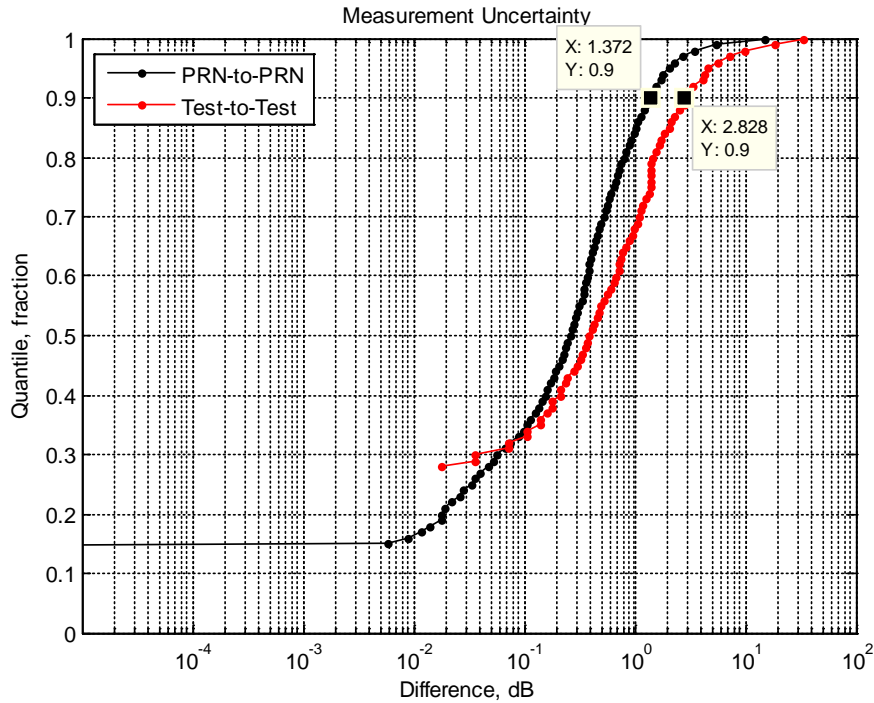
The differences in results between repeated tests were analyzed as a measure of uncertainty due to environmental and equipment variability and is a real measure of test repeatability. Another uncertainty measure was calculated by considering the variability of  $ITM(f, PRN_k)$  across PRNs for each DUT as shown. The empirical cumulative distribution function (CDF) for both error



quantities just described are shown in Figure 3-20 for the 10 MHz LTE and Figure 3-21 for the 1 MHz AWGN interference signals. These plots show that 90 percentile of the uncertainty is less than 1.5 dB based on PRN variability analysis and less than 3 dB in terms of test repeatability. This is a near upper bound estimate on the measurement error. The median of both uncertainty measures are less than 0.5 dB.



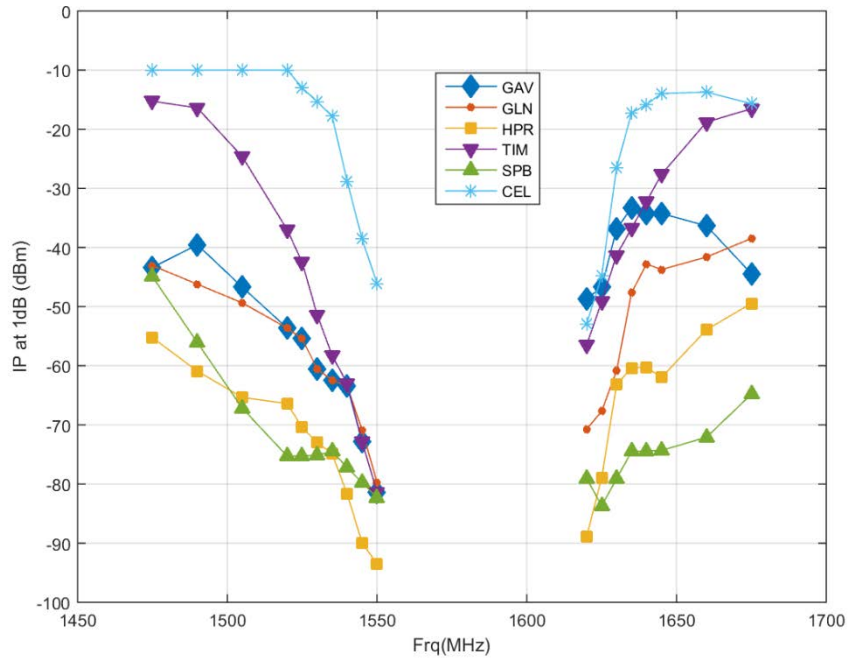
**Figure 3-20: CDF of measurement uncertainty calculate from per DUT differences across PRNs (black) and test to test difference (red) for the 10 MHz LTE interference signal**



**Figure 3-21: CDF of measurement uncertainty calculate from per DUT differences across PRNs (black) and test to test difference (red) for the 1 MHz AWGN interference signal**

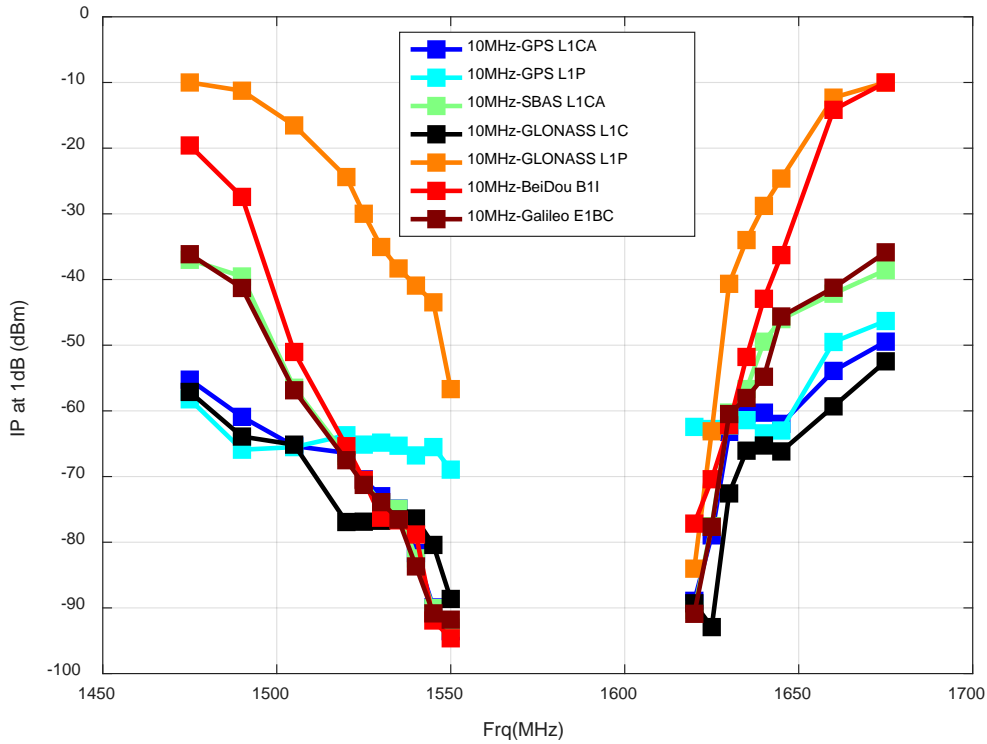
### 3.1.7 ITM Aggregation and Test Results

The bounding ITM mask is the one that protects all receivers within a category. The value of the bounding ITM at each frequency is found by taking the minimum of ITM(f) across all receivers in the category (i.e. at a particular frequency, this is the smallest interference power that causes 1-dB degradation for any receiver in the category). Multiple bounding ITMs are generated based by determining one for each interference signal type and GNSS signal combination. The bounding masks for each category corresponding to the 10 MHz LTE interference signal and L1 C/A GPS signal are shown in Figure 3-22. This plot shows the HPR and SPB categories to be the most susceptible in terms of received interference power levels with the cellular category generally being the most tolerant of LTE interference.



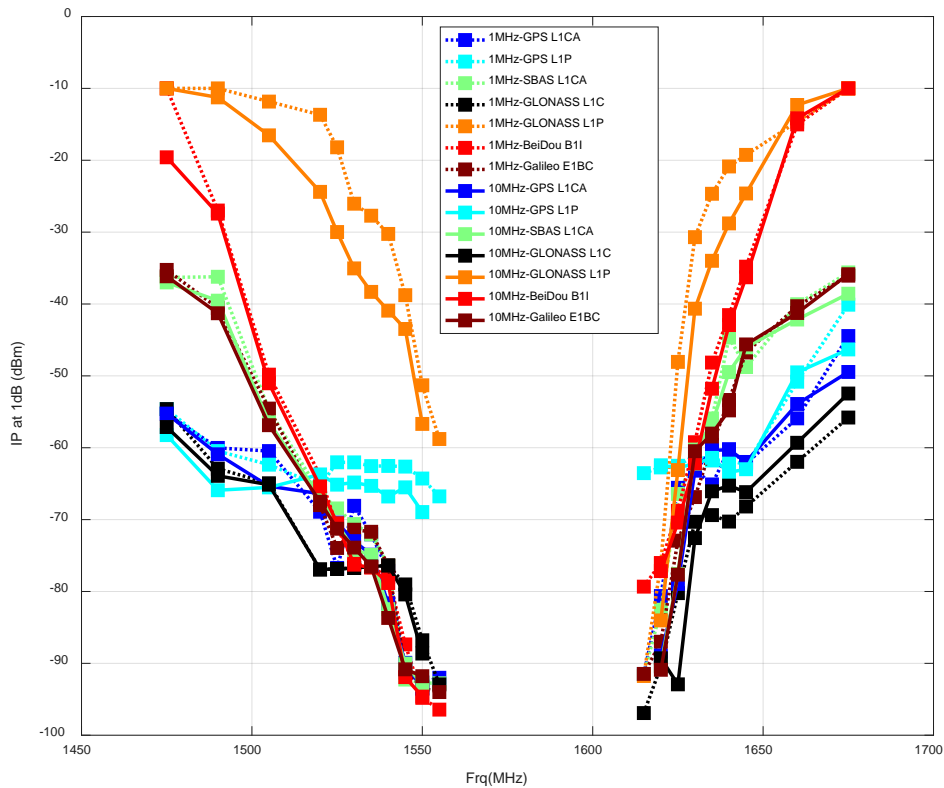
**Figure 3-22: GPS L1 C/A bounding ITM for each category of receivers**

These ITMs are also calculated for all other emulated GNSS signals. This is shown in Figure 3-23 for the HPR receiver category. Interference power levels from a 10 MHz LTE type signal should not exceed any of the masks depicted in this figure if all GNSS signals are to be protected for the HPR category.



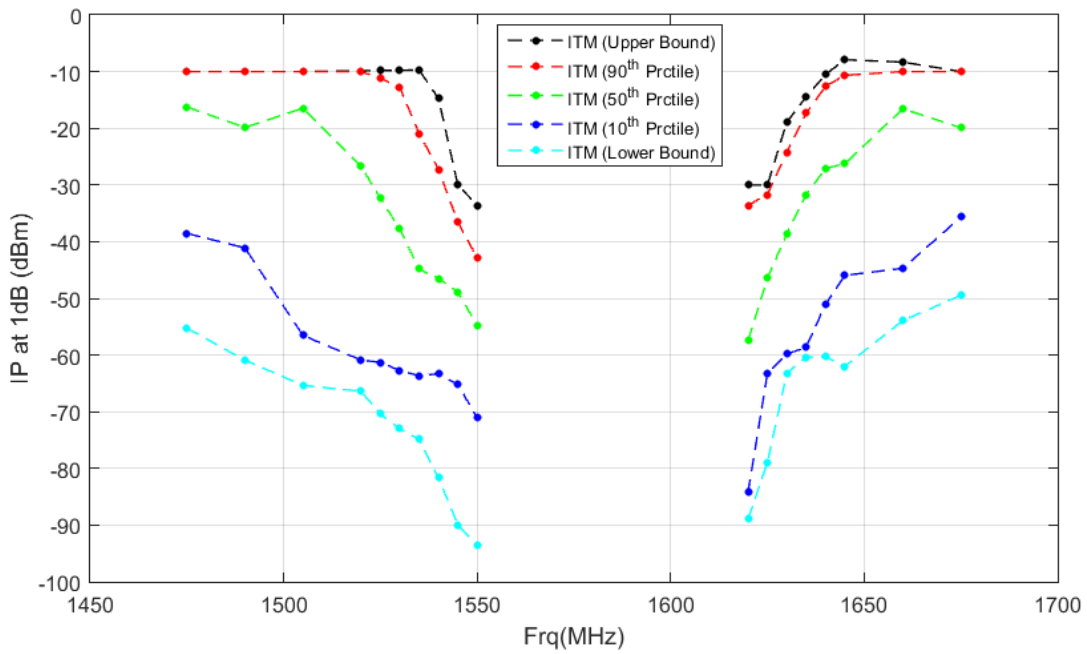
**Figure 3-23: HPR bounding ITMs for each of the emulated GNSS signals**

Figure 3-24 overlays the HPR bounding ITMs corresponding to both the 10 MHz LTE interference signal (solid lines) and the 1MHz AWGN interference signal (dotted lines). In general, the results show a weak dependence for the bounding ITMs on interference signal type helping to further generalize the results beyond the LTE type signal if needed. An exception to that is the GLONASS L1 P bounding ITM that shows up to 10 dB more sensitivity to the 10 MHz LTE signal. This is likely due to one or more receivers processing GLONASS L1 P signal that did not collect valid data during the 1 MHz interference signal test.

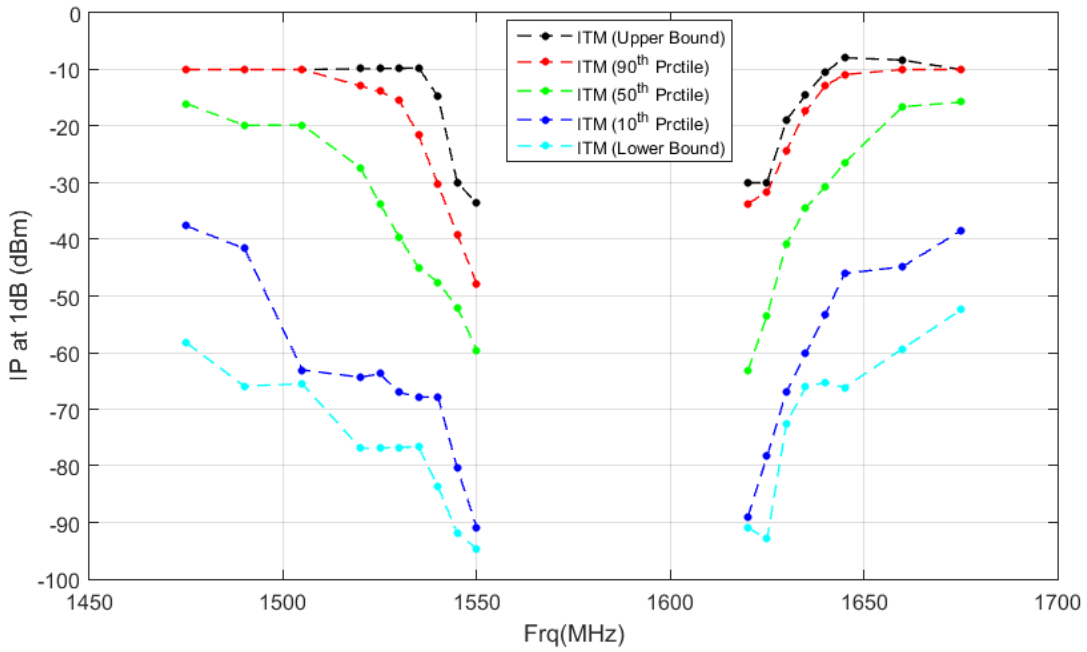


**Figure 3-24: HPR Bounding ITMs for each of the emulated GNSS signals. ITM bounding masks for the 1 MHz AWGN and 10 MHz LTE interference signals are shown**

Figure 3-25 (a) shows the aggregate result for the HPR category and L1 C/A GPS signal type. The lower and upper bounds, as well as the various percentile levels are presented to give an indication of the data distribution. The lower the percentile level the more protection it offers. For example, the 10th percentile indicates the received interference power level that leaves 10% of the tested receivers unprotected while the 90th percentile is the value that leaves 90% of the receivers unprotected. In order to ensure tolerable level of interference to all tested receivers only the lower bound (or minimum value) is considered. Figure 3-25 (b) shows the same percentile results but for ITMs that protect all emulated GNSS signals processed by the tested HPR receivers. This is done by first calculating the minimum ITM across the supported GNSS signals for each DUT and then calculating the various percentiles across DUTs. These two plots indicate that the interference power levels needed to protect all GNSS signals are generally lower but comparable the L1 C/A ITM levels for the tested receivers.



(a)



(b)

**Figure 3-25: 10 MHz Statistical Mask Results for High Precision receivers for (a) GPS L1 C/A (b) All Emulated GNSS Signals.**

A comprehensive set of bounding and statistical ITMs have been produced for all receiver categories and GNSS signal type combinations, and are shown grouped by interference signal type in Appendix B.

These bounding masks can then be used in an inverse modeling analysis to compute the tolerable transmitter EIRP levels corresponding to a given transmit application and use-case parameters. In particular, the bounding masks for the L1 C/A GPS signals are used later in this report to calculate tolerable EIRP levels by receiver application.

### 3.1.8 Loss of Lock Data Processing

As discussed in Section 3.1.5.2, the ITMs are the interference levels that resulted in a 1 dB degradation in CNR. As illustrated in Figure 3-26, most receivers continued to report CNR measurements after the interference level exceeded the ITM. Within this report, “loss of lock” is defined to be situation in which the interference increased to the point where the receiver ceased reporting CNR for a particular signal and a particular satellite. The “loss of lock” point is interpreted herein to mean that the DUT is no longer able to track that signal type (i.e. L1 C/A).

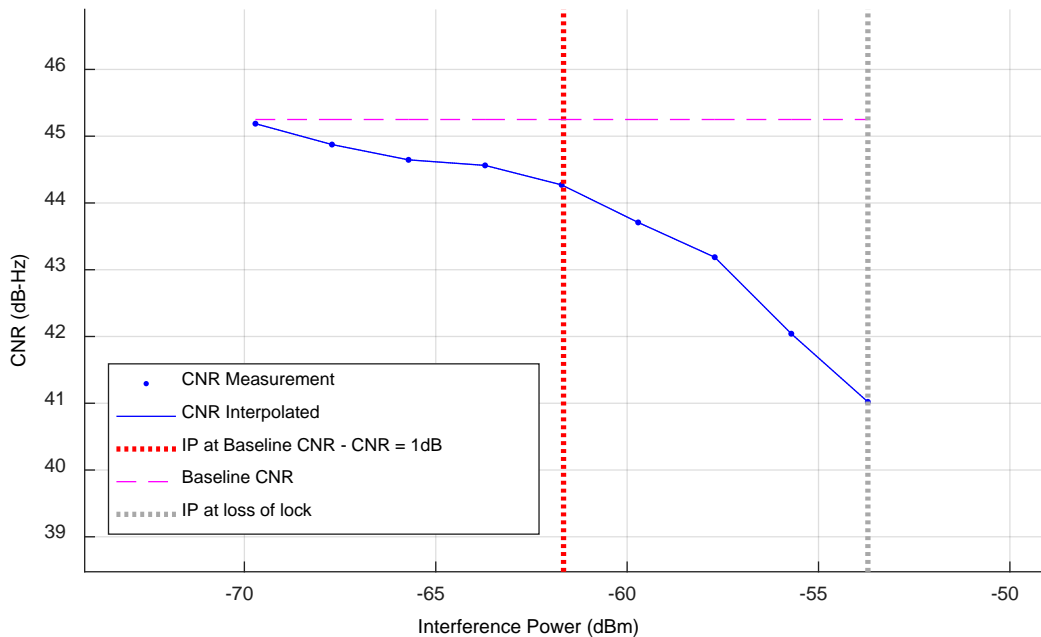


**Figure 3-26: Determination of Loss of Lock Interference Level from CNR Data**

The processing of CNR to yield interference levels corresponding to loss-of-lock was consistent with the processing used to determine ITMs, with the exception illustrated in Figure 3-26. Namely, that the loss-of-lock interference level was determined based upon the highest level of interference for each signal/satellite for which the DUT reported a CNR value. Although, as

discussed in Section 3.1.6.1, collected data for each DUT included a “loss-of-lock indicator” this data was found to be unreliable, not available, or inconsistent amongst DUTs. Therefore, the approach outlined above was adopted to determine the loss-of-lock interference levels.

Two loss-of-lock levels were determined for each DUT, for each interference type, and for each interference frequency:

1. High-elevation satellite – this interference level corresponded to loss-of-lock for the nominally powered GNSS signals (See Table 3-4), i.e., the ones that were not attenuated by 10 dB or 20 dB with respect to the specified minimums in applicable Interface Control Documents or Interface Specifications. This interference level was averaged across all applicable (up to 10) satellites.
2. Low-elevation satellite – this interference level corresponded to loss-of-lock for the GNSS signals that were 10 dB below nominal (see Table 3-4). Only one such signal was broadcast for each GNSS constellation (GPS, GLONASS, Galileo, BeiDou). The “low-elevation” designation is appropriate, since as discussed in Section 3.3 typical DUT antennas provide approximately 10 dB less gain towards low-elevation angle satellites than they do towards zenith. In the chamber testing, the GNSS transmit antenna was at zenith so all GNSS signals arrived from zenith in the testing. This situation is different from the real-world, in which GNSS signals can arrive from all elevation angles in the upper hemisphere.

The loss-of-lock levels computed using the above method should be viewed as the received interference power levels for which there is very high confidence that high- or low-elevation angle satellites are completely unusable by a GPS/GNSS receiver. These estimated loss-of-lock levels may be significant overbounds for several reasons including:

- As noted in Section 3.1.4.1, DUTs in the center of the test grid experienced received GNSS signal levels that were more than 3 dB greater than the minimum specified levels for each GNSS signal type. If they were presented with minimum specified GNSS signal levels, it is likely that these DUTs would lose lock on GNSS signals in the presence of lower levels of interference.
- It is likely that many DUTs continued to track and output  $C/N_0$  for satellites that would no longer be useful for navigation due to poor tracking quality. For instance, many DUTs reported GPS C/A-code  $C/N_0$ 's below 20 dB-Hz. The GPS C/A-code signal includes 50 bps navigation data that is unencoded (i.e., no forward error correction is utilized). At 20 dB-Hz, the bit-energy to noise density  $E_b/N_0$  is 3 dB and it is not theoretically possible to read the navigation data as necessary for positioning without external assistance. With an  $E_b/N_0$  of 3 dB, it is unlikely that the DUT could track carrier phase to provide a coherent phase reference, but even if it could the probability of correctly decoding a 300-bit GPS navigation data subframe without error is less than 0.0001.

Figure 3-27 and Figure 3-28 show interference powers resulting in loss-of-lock for high-elevation and low-elevation angle satellite GPS C/A-code signals, respectively. The interference powers resulting in loss-of-lock for high elevation angle satellites were typically 15 – 25 dB



higher than 1 dB ITMs. The interference powers resulting in loss-of-lock for low elevation angle satellites were typically 5 – 15 dB higher than 1 dB ITMs.

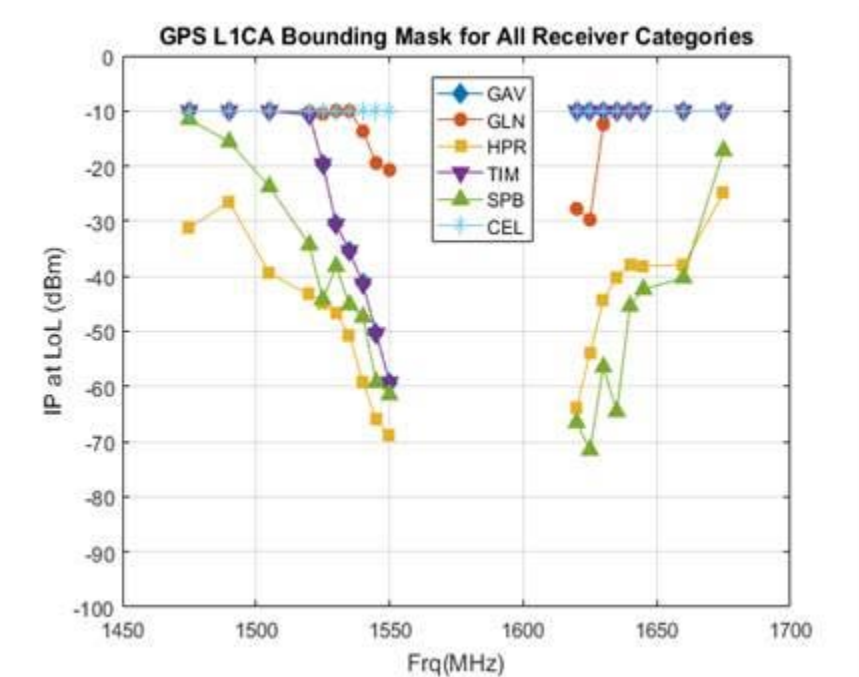


**Figure 3-27: Interference Power resulting in Loss of Lock for GPS L1 C/A-code (High Elevation Angle).**

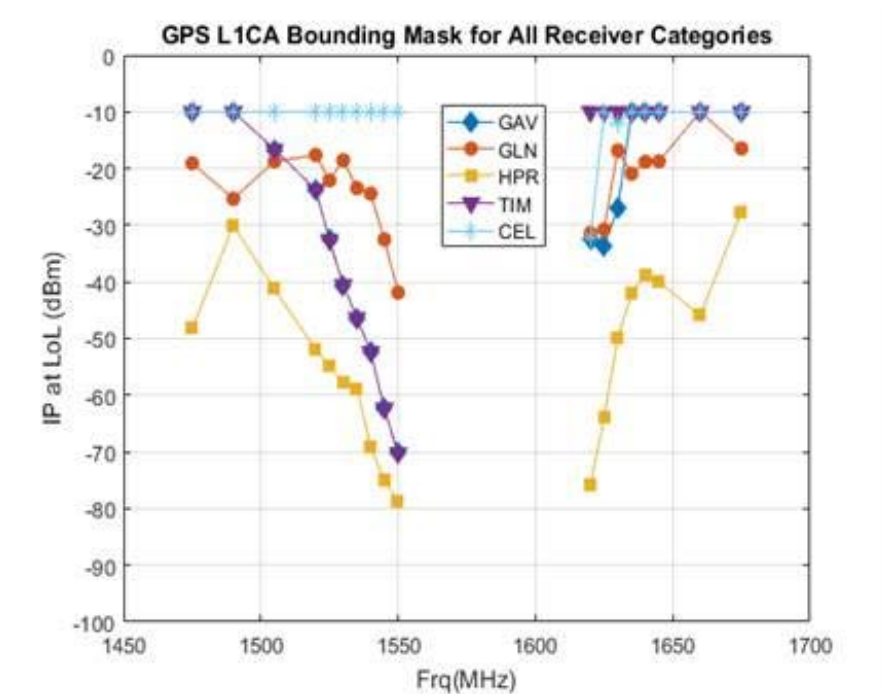


**Figure 3-28: Interference Power resulting in Loss of Lock for GPS L1 C/A-code (Low Elevation Angle).**

Additional loss of lock results are provided in Appendix C.

### 3.2 Conducted (Wired) Testing

Wired tests were executed subsequent to WSMR radiated tests for specialized scenarios suited to a laboratory environment. This testing was conducted during July 2016 at Zeta Associates Inc. in Fairfax, VA. The specific objectives for wired testing included: (1) evaluation of the impact of adjacent-band interference on signal acquisition, (2) comparison between wired and radiated receiver susceptibility to adjacent band interference with 1 MHz bandpass noise and 10 MHz LTE (same signals as used in the anechoic chamber), and (3) assessment of the impact of an adjacent band transmitter noise floor (out-of-band to the interference source, in-band to GPS/GNSS) in addition to the fundamental emission.

#### 3.2.1 Devices Test

For this testing, fourteen of the 80 receivers tested at WSMR were selected and provided by USG partners. These receivers covered all GPS/GNSS categories from WSMR except Space Based. The receiver categorization, and specific port location are given in Table 3-8. Notice the majority of receivers tested were from the high precision category.

**Table 3-8: Receivers Tested**

<b>8-Way Splitter w/Individual Amps. After</b>	<b>8-Way Splitter w/Single Amp. in Front</b>
1. Monitor (spectrum analyzer)	1. TIM
2. HPR	2. GAV
3. HPR	3. HPR
4. CEL	4. HPR
5. GLN	5. HPR
6. HPR	6. HPR
7. HPR	7. HPR
8. Monitor (spiral enclosure)	8. HPR

### **3.2.2 Signal Generation**

Wired testing utilized the same core signal generation equipment as used for radiated testing at WSMR. The conducted circuit is shown in Figure 3-29. In addition to the GNSS playback and SPIGAT systems used at WSMR, a circuit was added for simulating out-of-band emissions (OOBE--lower left in figure where this is added in-band noise to GNSS but out-of-band for fundamental interference signal). The interference, GNSS and OOBE signals are added by a power combiner and conducted to the devices under test via multi-port power splitters with an isolator at each port to prevent port interaction. After the isolator, a broadband LNA provides necessary gain as a substitute for the active antenna in the radiated environment, with test power referenced to the LNA input. To allow static configuration throughout testing, adjustable attenuators were included on the GNSS and OOBE signal paths not only to set proper levels but also to serve as switches (when at high attenuation) for complete removal of these signals as necessary. Other modifications to the interference system included the substitution of a lower power HPA (more than adequate for the reduced attenuation of the conducted path) and a notch filter targeting the RNSS band.

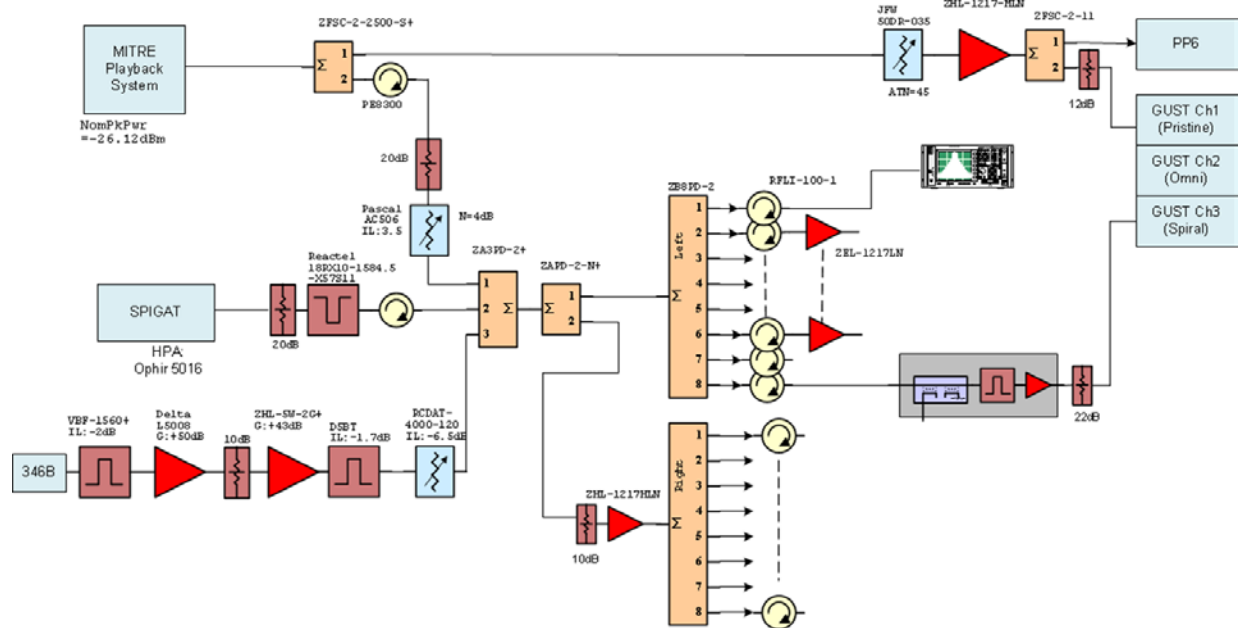


**Figure 3-29: Interference System Configuration for Wired Tests**

### 3.2.2.1 Signal Acquisition

Signal acquisition tests were executed at four adjacent-band frequencies using LTE signals at 1525, 1550, 1620 and 1645 MHz. The test sequences removed the GNSS signals for 30 seconds and then allowed at least 90 seconds after they were reintroduced for the receiver to reacquire and track. (The original test plan used 120 seconds to allow GNSS signals to be reacquired, but after analyzing pre-test data it was determined this time could be shortened to 90 seconds to expedite the test.) These tests are therefore more indicative of Warm or Hot Start versus the potentially more challenging acquisition condition of Cold Start. This sequence of removing and reintroducing signals was repeated in sets of five iterations starting with a set where interference was turned OFF. After this quiescent period, the interference was turned ON and after each successive completion of five iterations its power was incremented by 2 dB. Interference power ranged from -60 to -10 dBm for the outer two frequencies (1525 and 1645 MHz) and -80 to -30 dBm for the inner two frequencies (1550 and 1620 MHz). The maximum power tested in each range matched the maximum power used in the baseline LTE tests for these frequencies.

### 3.2.2.2 Out-of-Band Emissions

Out-Of-Band Emissions (OOBE) refer to the emissions from adjacent frequency band terrestrial deployments into the 1559-1610 MHz band. For OOBE tests, the OOBE circuit generated a flat wideband noise pedestal centered on the RNSS band with spectral density controlled by the programmable attenuator. OOBE density levels used for testing were defined by associating the LTE power levels at the specified maximums of 62 dBm (32 dBW) for base stations and 23 dBm (-7 dBW) for handsets with each wideband OOBE limit as summarized in Table 3-9. The LTE/OOBE ratio is defined at these limits and applied (added) to the target LTE signal power at each point in the test to determine the corresponding OOBE level that should be received. Figure 3-30 depicts the relationship between the OOBE (in dBW/Hz) and LTE power levels (in dBm) at the receiver's RF input port. This relationship is linear with a slope of one since OOBE

and LTE signal powers undergo the same path loss (neglecting the slight dependence of path loss on frequency). This figure also shows the approximate OOB level (horizontal dashed line) for a receiver noise floor of -201.5 dBW/Hz and associated LTE receive power levels (intersection of the dashed horizontal line and LTE receive power vs. received OOB lines) which would cause a 1 dB CNR degradation for the various handset and base station limits outlined in Table 3-9. Additional details on the conducted testing OOB levels are provided in Appendix D.

**Table 3-9: Ratio of OOB limit density to LTE power for setting OOB testing levels**

	OOBE density [dBW/MHz]	LTE power [dBW]	ratio OOB/LTE [dB/MHz]
FCC base station*	-70	32	-102
FCC handset*	-70	-7	-63
Proposed base station**	-100	32	-132
Proposed handset**	-105	-7	-98

\* Based upon FCC Mobile Satellite Service Ancillary Terrestrial Component (ATC) rules, contained within Title 47 of the Code of Federal Regulations, Part 25.

\*\* Based upon characteristics of a proposed adjacent-band LTE network.

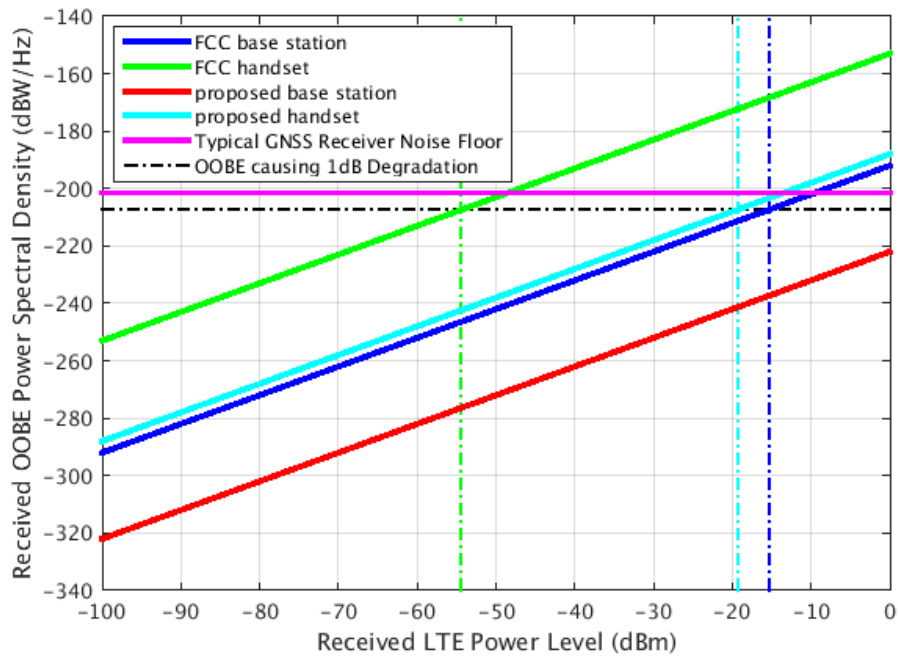


**Figure 3-30: OOB Levels Associated with LTE Signal Power used in Testing**

### 3.2.3 System Calibration

Calibration of SPIGAT was accomplished in the same fashion as described for WSMR with 22 CW tones at each frequency and measuring with a spectrum analyzer to generate a bias table. The spectrum analyzer in this instance was connected to the power splitter versus the cavity backed spiral in the chamber. The GNSS playback signal levels were verified by showing CNR estimates from the GPS receiver used for monitoring at WSMR matched the levels observed in this laboratory setting.

### 3.2.4 Test Sequence

Wired tests were executed for baseline 1 MHz bandpass noise and 10 MHz LTE signals, FCC and proposed OOB levels, and signal acquisition. Tests were numbered 10 through 18 with Table 3-10 summarizing the test schedule.

**Table 3-10: Wired Test and Data Summary**

Day of Week (25-29 July 2016)	Test and Number
Monday	Type 2 – Test10 Type 1 – Test11
Tuesday	Type 2 w/OOB FCC – Test12 Acq. @ 1525 MHz – Test13 (120 sec. dwell)
Wednesday	Test14 stopped early/network issue Acq. @ 1620 MHz – Test15
Thursday	Acq. @ 1645 MHz – Test16 Acq. @ 1550 MHz – Test17
Friday	Type 2 w/Proposed OOB – Test18

### 3.2.5 Data Processing

The following sections detail results from the wired testing for GPS L1 C/A processing only. Processing for wired results followed the approach discussed above for determining 1 dB CNR degradations as a function of interference power. Signal acquisition processing required its own considerations and is discussed in that section.

#### 3.2.5.1 Comparison Tests

The comparison tests were intended to demonstrate equivalence between the radiated and wired test environments. Two example results of interference power causing 1 dB CNR degradation are shown in Figure 3-31 for the LTE interference signal. Example (a) in this figure compares results for a high precision receiver. Here performance matches very well for frequencies closest to the RNSS band while for frequencies further away the radiated performance is superior. This divergence is an expected result since at WSMR the receiver used its native antenna which included some filtering (along with a low noise amplifier) which served to suppress peripheral interference. The difference, therefore, is directly related to not having this filter/LNA module available in the wired testing. Example (b) of that same figure is a case where the antenna was integrated with the enclosure. For wired testing the signal could be inserted directly after the passive element. In this instance, the radiated and wired results match very closely because both include all components influencing mitigation of adjacent interference. In general, comparisons of radiated and wired tests showed expected agreement with differences attributable to bypassing of active antennas in the wired test.

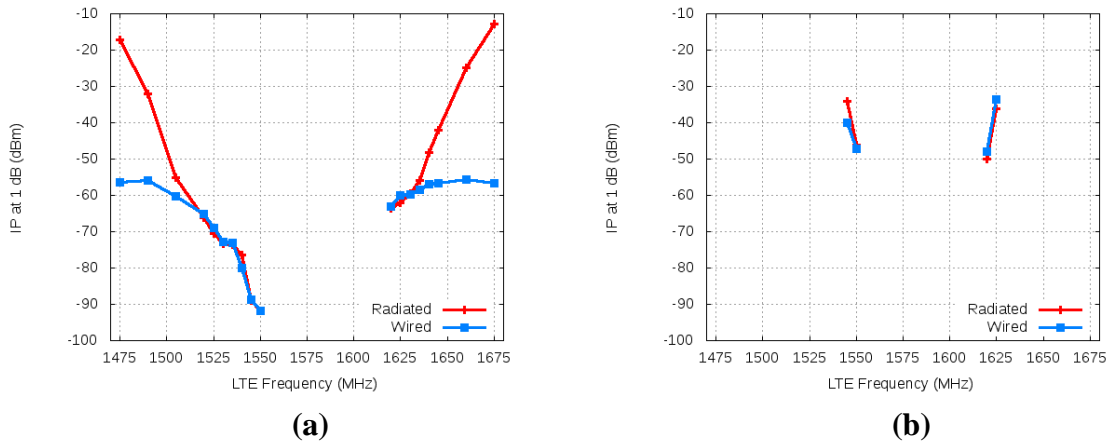


**Figure 3-31: Comparison of IP causing 1 dB degradation for the LTE Interference Signal from Radiated and Wired Testing for: (a) High Precision receiver and (b) Cellular device.**

### 3.2.5.2 OOBE Results

Tests conducted with OOBE were executed by adding noise in the RNSS band as shown in the wired test description. Figure 3-32 provides examples of two receivers with significantly different rejection performance for adjacent band interference. These examples show baseline (wired) performance of interference power causing a 1 dB degradation contrasted with OOBE performance for FCC prescribed and proposed levels for one applicant. As Figure 3-30 predicted, receiver performance can be impacted by inclusion of OOBE at FCC base station and FCC handset levels. This result is clearly demonstrated in (b) since this receiver provides good rejection of adjacent interference and therefore inclusion of noise in the RNSS band results in 1 dB CNR degradation not observed with the baseline test. The most distinct difference in performance is evident for handset frequencies, where adding OOBE at the FCC limits result in 1 dB CNR degradation at approximately -50 dBm compared with much more robust performance when OOBE is not included. The proposed base station OOBE limits did not result in 1 dB CNR degradation with the LTE power levels tested and for proposed handset limits the 1 dB CNR degradation level was observed at approximately -15 dBm : In context of distance and presuming complete rejection of adjacent band interference, the proposed OOBE limits for base station and handsets suggest 1 dB CNR degradation could be expected within approximately 4 meters (3.5 m) and 2 meters, respectively. These numbers were obtained for a receiver noise level of -201.5 dBW/Hz and assuming free space path loss and an omnidirectional transmitter antenna gain pattern.



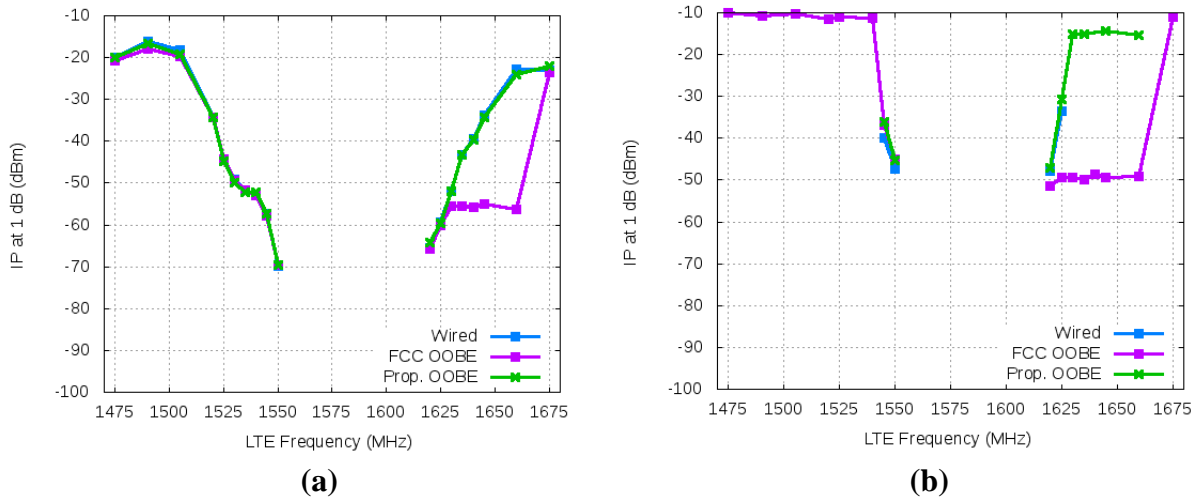


**Figure 3-32: Interference power causing 1 dB CNR degradation for baseline and OOB tests for (a) High Precision receiver and (b) Cellular device.**

### 3.2.5.3 Acquisition Results

Receiver acquisition tests were processed to show both average acquisition time, and the interference power level when receivers could no longer acquire. Acquisition time was computed for L1 C/A signals at the specified minimum power level (-128.5 dBm for L1 C/A) and also for one satellite that was set 10 dB lower to represent low elevation or challenged environments. For the specified minimum signals, the acquisition time was defined as the receiver acquiring and tracking four or more of these satellites. Since more than four satellites are generally in view at the specified minimum levels this is considered a modest criterion for establishing acquisition. For the low elevation satellite, the acquisition time was simply when this satellite was first acquired and tracked. At each interference power level, acquisition time from the five iterations was averaged to provide a single value. Note that at each power step an acquisition time was computed only if the receiver met the acquisition criterion for all five iterations.

The results from all receivers tested were compiled for each test frequency and are shown in Figure 3-33 through Figure 3-36. Figure “(a)” provide the number of receivers satisfying the acquisition criteria for specified minimum (“ICD Min. Power”) and low elevation (“Low Elevation”) signals. Additionally, the figure shows the number of receivers at each interference power step where the CNR degradation is less than 1 dB (“IP @ 1 dB”). For example in Figure 3-33 (a), there were two receiver where the interference power associated with their 1 dB CNR degradation was less than the starting power level of -60 dBm and therefore this count starts at ten. This figure shows further that this count of “IP at 1 dB” appears closely associated with the number of receivers capable of acquiring the signal emulating low elevation conditions.

For the GPS receivers tested, the 1 dB C/N0 degradation point can be an indicator of negative impact to signal acquisition time in low elevation satellite conditions.. Figure “(b)” show average acquisition time for specified minimum and low elevation signals and generally demonstrate acquisition degradation with increasing interference power.

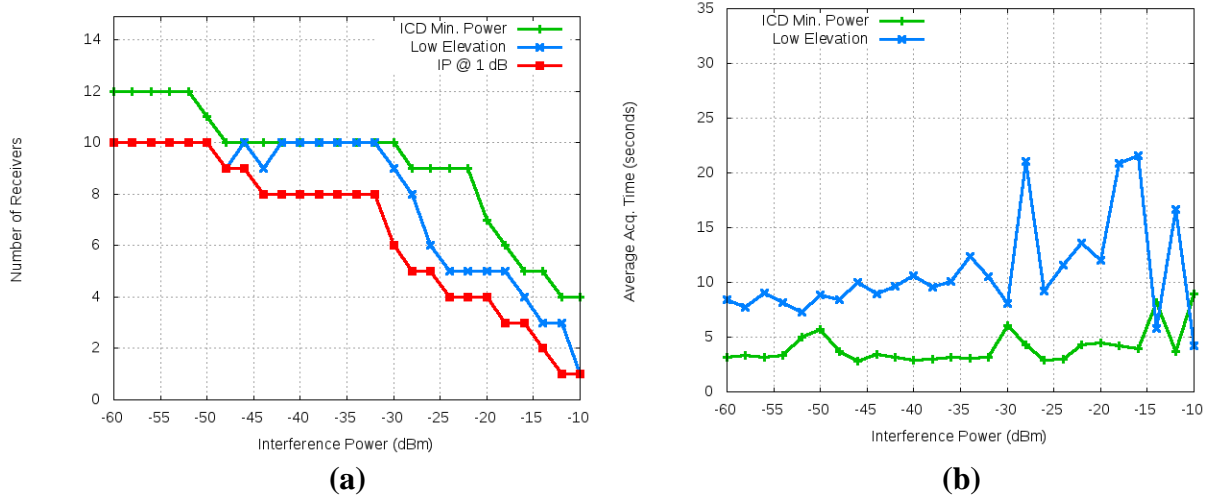


**Figure 3-33: Summary acquisition performance for 1525 MHz for ICD minimum and low-elevation satellites. (a) Number of DUTs, and (b) average acquisition time.**

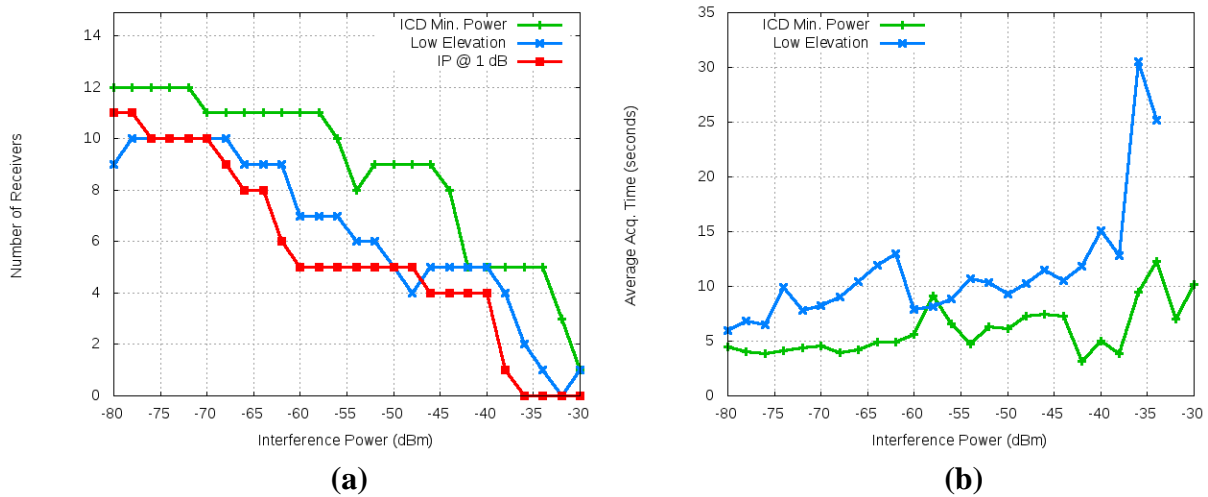


**Figure 3-34: Summary acquisition performance for 1550 MHz for ICD minimum and low-elevation satellites. (a) Number of DUTs and (b) average acquisition time.**

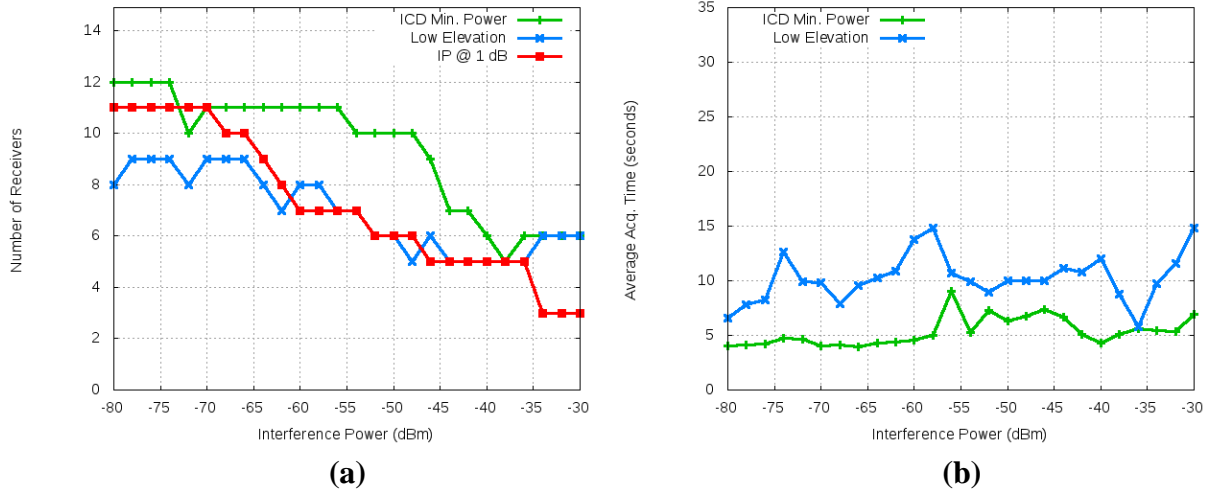


**Figure 3-35: Summary acquisition performance for 1620 MHz for ICD minimum and low-elevation satellites. (a) Number of DUTs, and (b) average acquisition time.**

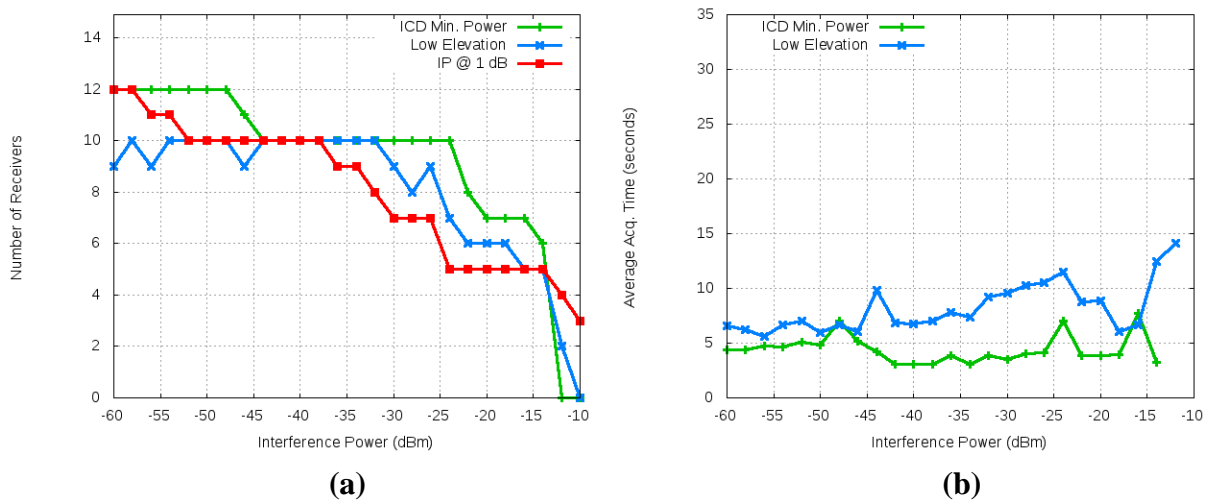


**Figure 3-36: Summary acquisition performance for 1645 MHz for ICD minimum and low-elevation satellites. (a) Number of DUTs, and (b) average acquisition time.**

### 3.3 Antenna Characterization

Twenty GNSS antennas, most of which were involved in the WSMR testing, were characterized with respect to frequency selectivity, elevation pattern, and RF gain/compression characteristics through anechoic chamber/live-sky/RF measurements in order to help interpret the WSMR test results and facilitate the calculation of tolerable transmit power.

A representative set of antennas was characterized through a set of activities including:

- 1) Anechoic chamber measurements - From June through August 2016, the gain patterns for 14 external antennas were measured in an anechoic chamber at MITRE in Bedford, MA.

- 2) Live-sky  $C/N_0$  measurements – In August 2016 and February 2017, the relative gain patterns of five antennas that were integrated with GNSS receivers were estimated using live-sky GPS C/A-code  $C/N_0$  measurements.
- 3) Active sub-assembly measurements - From August through October 2016, the gain and compression characteristics of the active subassemblies of four external antennas were measured at Zeta Associates in Fairfax, VA.

The following subsections describes these antenna characterization activities and the resultant measurements.

### 3.3.1 Selected Antennas

Table 3-11 lists the antennas that were characterized.

**Table 3-11: Characterized GNSS Antennas**

Manufacturer	Model	Characterization Approach
AeroAntenna	AT575-142-614-50	Anechoic chamber
AeroAntenna	AT2775-42SYW	Anechoic chamber
Arbiter	AS0087800	Anechoic chamber
Garmin	EDGE 1000	Live-sky $C/N_0$ measurement
Garmin	eTrex 20x	Live-sky $C/N_0$ measurement
Garmin	GA-25	Anechoic chamber
Garmin	GA-38	Anechoic chamber
Garmin	GPSMAP 64	Live-sky $C/N_0$ measurement
Hemisphere	804-3059-0	Anechoic chamber
Javad	Triumph-1	Live-sky $C/N_0$ measurement
Leica	AX1202GG	Anechoic chamber and active sub-assembly measurements
Navcom	82-001020-3001LF	Anechoic chamber
PCTel	3977D	Anechoic chamber
Samsung	S5	Live-sky $C/N_0$ measurement
Trimble	Bullet 360 Antenna 101155-10	Anechoic chamber
Trimble	Choke Ring 29659-00	Anechoic chamber and active sub-assembly measurements
Trimble	Zephyr 41249-00	Anechoic chamber
Trimble	Zephyr Geodetic 2 55971-00	Anechoic chamber and active sub-assembly measurements
Trimble	TRM59800 module	Active sub-assembly measurements
u-blox	ANN-MS-0-005	Anechoic chamber

### 3.3.2 Chamber Measurements

Two-dimensional (elevation and azimuth) gain patterns for incident signals of four polarization types, right hand circularly polarized (RHCP), left hand circularly polarized (LHCP), vertically polarized (V), and horizontally polarized (H) were measured at 22 frequencies: 1475, 1490, 1495, 1505, 1520, 1530, 1535, 1540, 1545, 1550, 1555, 1575, 1595, 1615, 1620, 1625, 1630, 1635, 1640, 1645, 1660, and 1675 MHz. The measurements were made in a 30 ft × 21 ft × 15 ft

anechoic chamber at MITRE in Bedford, MA. A calibrated, automated antenna measurement system developed by Nearfield Systems was utilized.

All 14 antennas were active, and the gains measured were thus a combination of passive element gain and amplifier gain. Absolute gain of the passive elements of each active antenna was not directly observable without breaking into the antennas. Antenna directivity, however, was calculated from the patterns using Nearfield Systems' NSI2000 software.

Figure 3-37 and Figure 3-38 provide some example results. Figure 3-37 shows the frequency selectivity of the 14 antennas for incident RHCP signals as seen at antenna boresight. Note the wide variation in selectivity to adjacent-band signals. Figure 3-38 shows the relative RHCP antenna gain vs off-boresight angle at 1575.42 MHz for the 14 antennas. Each curve is normalized to 0 dBic gain at boresight. In this figure, each point in the plotted results represents an average across 180 deg of azimuth. The red vertical lines correspond to 5 deg elevation angle on either side of the antenna. Additional measurements are provided in Appendix E.

The boresight directivities of the 14 measured antennas for RHCP signals at 1575.42 MHz varied from 3.2 dBic to 8.0 dBic with a mean directivity of 5.4 dBic. Assuming 90% efficiency for all of the antennas yields a rough estimate for passive element gains ranging from 2.7 dBic to 7.5 dBic with a mean of 4.7 dBic. In the WSMR radiated chamber testing, all of the tested receivers' antennas were boresighted at the transmitting GNSS signal and interference generator antennas.

The measured relative antenna gain patterns can be utilized to model what gains would be seen towards GNSS satellites and interference sources at other elevation angles in the "real world". For instance, the results in Figure 3-38 justify the interpretation of the GNSS signal levels that were generated at -10 dB power relative to specified minimum levels in the WSMR radiated testing as corresponding to what would be seen in the real world towards low elevation angle satellites for many of the tested antennas (note that the data in Figure 3-38 indicates relative gains ranging from -3 dB to -15 dB for gain towards a satellite at 5 deg elevation above the horizon vs gain towards a satellite at zenith).

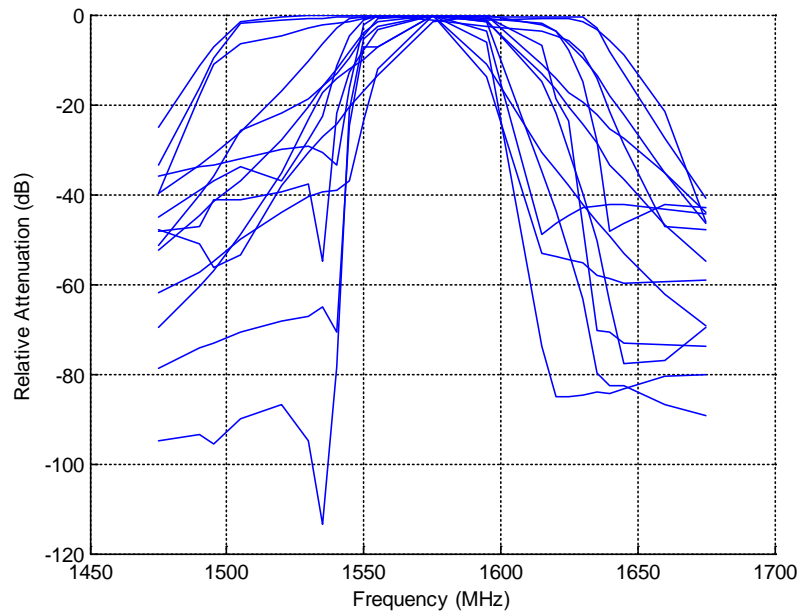


**Figure 3-37: Frequency Selectivity of the 14 External Antennas**

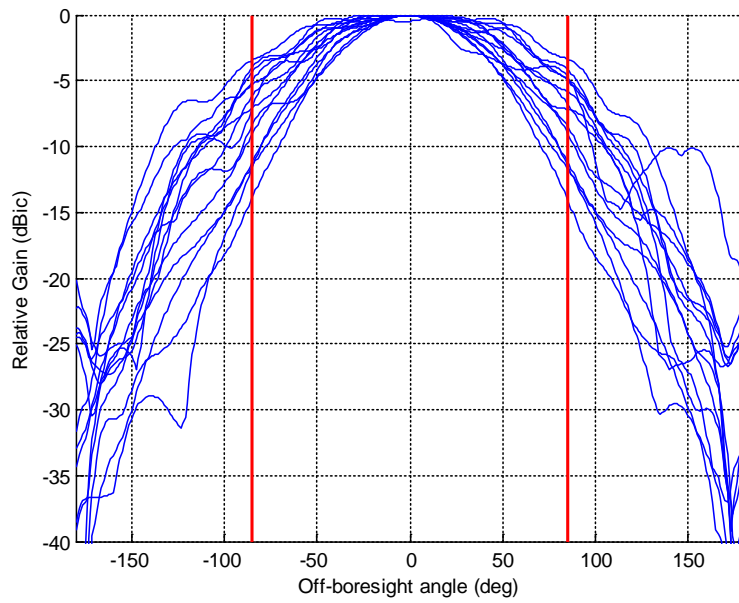


**Figure 3-38: Relative RHCP Gain Patterns of the 14 Antennas at 1575 MHz (red vertical lines correspond to 5 deg elevation angle)**

### 3.3.3 Live-Sky Measurements

Some of the GNSS receivers tested at WSMR utilize integrated antennas. Estimates of their relative antenna gain patterns at 1575 MHz were obtained through measurements of GPS C/A-code  $C/N_0$  over short time intervals in an outdoor environment in two locations (rooftop of a building at MITRE's Bedford, MA complex and at Zeta's Fairfax, VA location) with clear sky views. Estimated relative gain pattern results using this method for four integrated GLN antennas are shown in Figure 3-39 and for an integrated HPR antenna in Figure 3-40. Measured GPS C/A  $C/N_0$  from a cellular device is shown in Figure 3-41 as a function of azimuth and elevation. Based on analysis of this data and cellular GPS antenna design, placement and performance, the use case analysis that follows simply assumed 0 dBi for antenna gain in all directions.

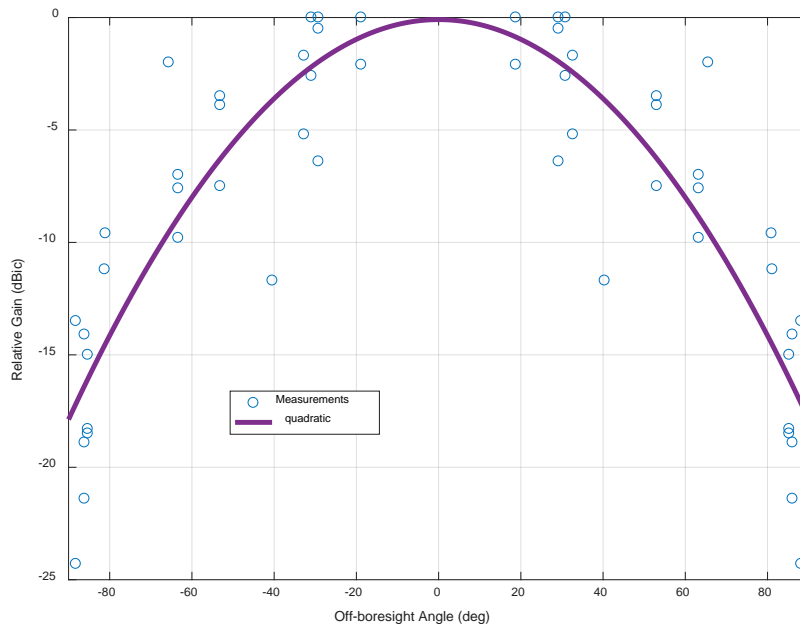


**Figure 3-39: Relative L1 RHCP Antenna Gain Estimated from Live-sky  $C/N_0$  Measurements for Three GLN Integrated Antennas and Quadratic Fit**

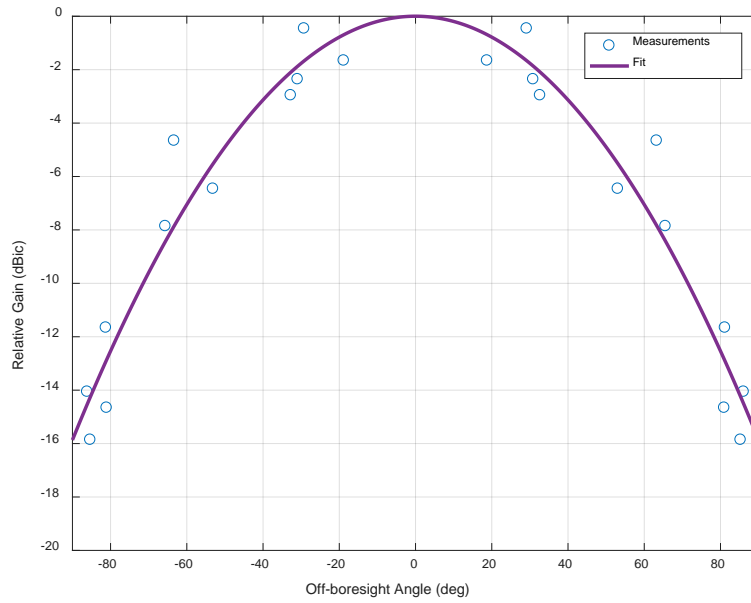


**Figure 3-40: Relative L1 RHCP Antenna Gain Estimated from Live-sky  $C/N_0$  Measurements for an Integrated HPR Antenna and Quadratic Fit**

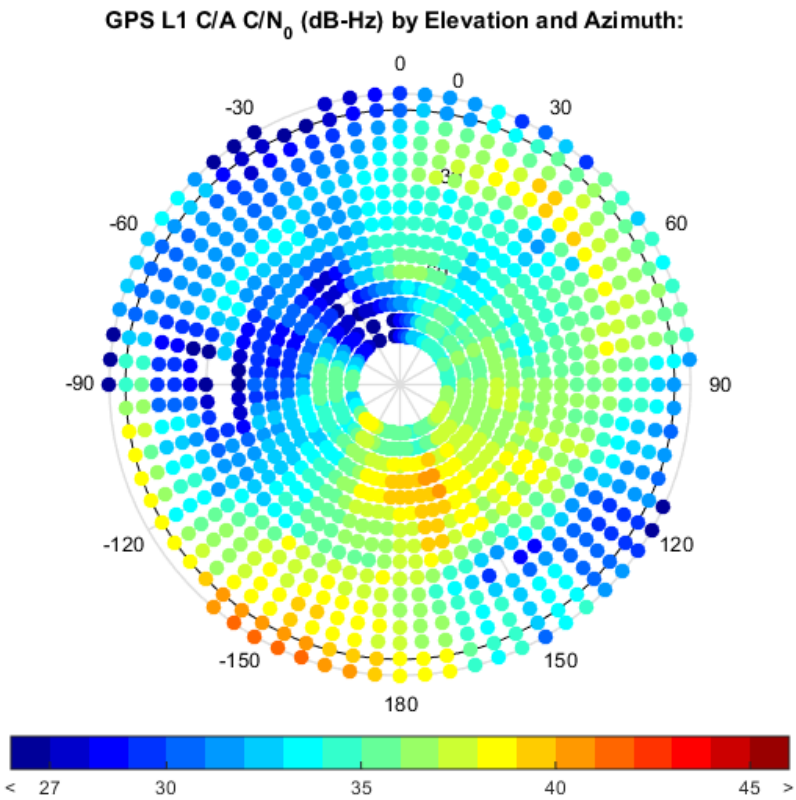


**Figure 3-41: Live-sky  $C/N_0$  Measurements for a CEL Device**



### 3.3.4 Bench Test Measurements (Active Sub-assembly Measurements)

Bench test measurements were conducted on a further reduced set of antennas at Zeta to characterize key filter/LNA performance parameters. The antennas were disassembled to access the passive element connection to the filter/LNA assembly and then the response measured with a network analyzer from approximately 1 GHz to 2 GHz. The LNA was powered for this testing by inserting a bias-T on the RF output path and applying the required DC power. Results from three antennas tested are shown in Figure 3-42 where each has been normalized for the measured gain at GPS L1. These three antennas types were utilized at WSMR and as MITRE testing demonstrated have vastly different characteristics presumably to meet their respective functions. One of the filter/LNA devices was relatively narrowband and only passes GPS L1, another was wider and clearly intended to pass both GPS and GLONASS L1, and lastly, the third device was much wider and intended to pass MSS signals, GPS and GLONASS L1.

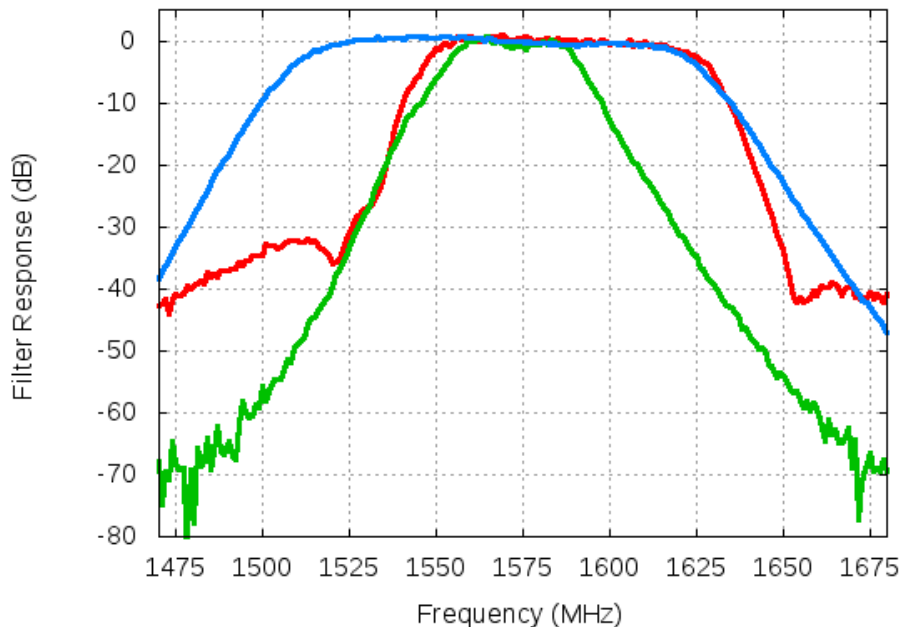


**Figure 3-42: Normalized Filter/LNA Responses measured with Bench Testing**

In addition to characterizing each assemblies response versus frequency, the devices were also tested with a spectrum analyzer using “Intermod (TOI)” instrument software at the GPS L1 frequency to understand typical LNA characteristics of gain, 1dB compression (P1dB), input and output third-order intercept points (IIP3 and OIP3) (in-band only). These results are shown in Table 3-12 and again demonstrate the significant diversity observed with fielded GNSS antennas.

**Table 3-12: LNA Performance Characteristics measured with Bench Testing**

Measurement at L1	Assembly #1	Assembly #2	Assembly #3
Gain (dB)	28	40	49
IIP3 (dBm)	-12.7	-39.6	-29.3
OIP3 (dBm)	14.4	-1.4	17.7
Input P1dB (dBm)	-25	-50	-42

The results of the antenna characterization indicate there is a very wide range of up to 80 dB in selectivity farther away from the GPS band (1500/1650 MHz), which can explain the observed 50-dB range in IP for 1 dB CNR degradation. This variation in selectivity is most pronounced for HPR devices, due to the fact that many HPR devices are designed to receive both GNSS signals in the 1559 – 1610 MHz band as well as augmentation data over MSS satellites in the 1525 – 1559 MHz band. HPR devices that are not designed to process MSS signals also tend to utilize wider bandwidths relative to other DUT categories to provide increased measurement precision in the presence of multipath. There is a much narrower range up to 20 dB in selectivity close to the GPS band (1550/1600 MHz) which is lower than the IP for 1 dB CNR degradation observed for these frequencies.

Although changing antennas was not the focus of this effort, cost, viability, etc. should be considered to determine the feasibility of such a solution. Antenna filtering can cause deleterious effects on receiver performance, such as group delay and other distortions. Also, many HPR DUTs are designed to receive augmentation data via MSS and to retain this functionality the receiver passband needs to continue to extend into the applicable portion of the 1525 – 1559 MHz band.

## **4. TRANSMIT POWER LEVEL ANALYSIS (EXCLUDING CERTIFIED AVIATION)**

### **4.1.1 Approach**

This section derives the transmit EIRP levels that can be tolerated by each category of GPS/GNSS receivers except for certified aviation. Two complementary analyses are performed. The first is a forward modeling approach that calculates the receive power map for a given EIRP level and network deployment type. The receive power map is compared with the ITM( $f$ ), where  $f$  is the frequency of interest, to identify the region where the corresponding category of receivers is not protected from adjacent band interference. The second is an inverse modeling analysis that calculates the tolerable EIRP for any given separation distance between the transmitter and user's receiver over a range of receiver heights.

For the transmit power level analysis, it is necessary to characterize the proposed transmitter network deployment and the GPS/GNSS receiver use case scenarios. To ensure compatibility with all receivers within a category, the bounding ITMs from Section 3 are used. The use of the bounding ITMs ensures that the resultant EIRP values will protect 100% of the receivers tested.

### **4.1.2 Network Transmitter Parameters**

Representative parameters for adjacent-band LTE networks were identified primarily from three sources:

- 1) International Telecommunication Union Radiocommunication Sector (ITU-R) reports and recommendations.
- 2) Federal Communication Commission (FCC) Mobile Satellite Service Ancillary Terrestrial Component (ATC) rules, contained within Title 47 of the Code of Federal Regulations, Part 25 (47 CFR 25).
- 3) Proposals for adjacent-band networks contained within FCC filings.

#### **4.1.2.1 Base Stations**

Report ITU-R M.2292 (henceforth "M.2292") provides "Characteristics of terrestrial IMT-Advanced systems for frequency sharing/interference analyses." [3] For the 1-2 GHz band, these include the characteristics listed in Table 4-1 for five deployment types.

**Table 4-1: Base Station Characteristics from M.2292**

	Macro rural	Macro suburban	Macro urban	Small cell outdoor/Micro urban	Small cell indoor/Indoor urban
Cell radius/ Deployment density	> 3 km (5 km typical)	0.5 – 3 km (1 km typical)	0.25 – 1 km (0.5 km typical)	1 – 3 per urban macro cell, <1 per suburban macro site	Depending on indoor coverage/capacity demand
Antenna height	30 m	30 m	25 m	6 m	3 m
Sectorization	3 sectors	3 sectors	3 sectors	Single sector	Single sector
Downtilt	3 deg	6 deg	10 deg	not applicable	not applicable
Antenna polarization	+/-45 deg	+/-45 deg	+/-45 deg	Linear	Linear
Maximum antenna gain	18 dBi	16 dBi	16 dBi	5 dBi	0 dBi
Maximum EIRP/sector*	61 dBm	59 dBm	59 dBm	40 dBm	24 dBm

\*Values shown for this parameter are for 10-MHz LTE signals.

For macrocells, the cell radius and intersite distance are defined in Figure 4-1. Note that for macrocells, the parameters  $A$  and  $B$  in the figure have the relationship  $B = 3A/2$ . For small cells, each base station is located at the center of a cell resulting in an intersite distance  $B = \sqrt{3}A$ .

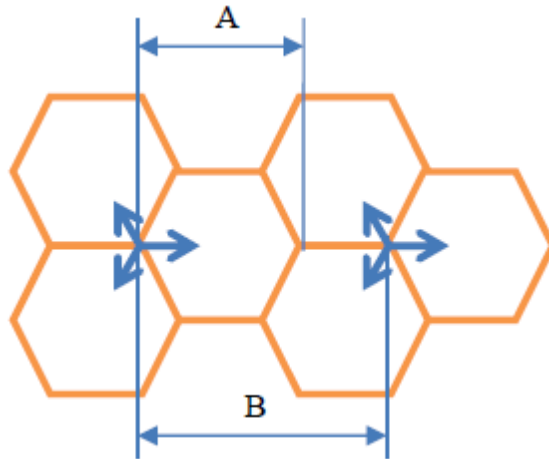


**Figure 4-1: Macrocell Radius and Intersite Distance are  $A$  and  $B$ , respectively. Each hexagon is referred to as either a sector or cell.**

M.2292 references Recommendation ITU-R F.1336 (henceforth “F.1336”) for recommended antenna gain patterns for each deployment type and provides input parameters. The normalized gain patterns for the macro deployments are shown in Figure 4-2 and for the small cell deployments in Figure 4-3.

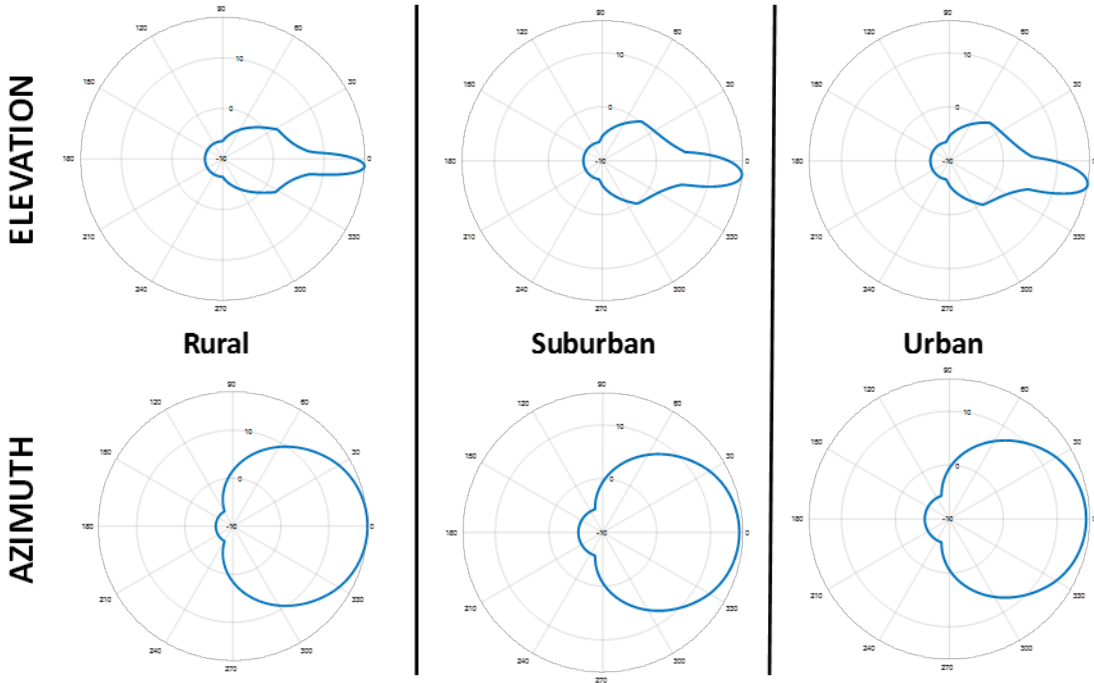


**Figure 4-2: Macro Base Station Antenna Gain Patterns (top – elevation; bottom – azimuth)**

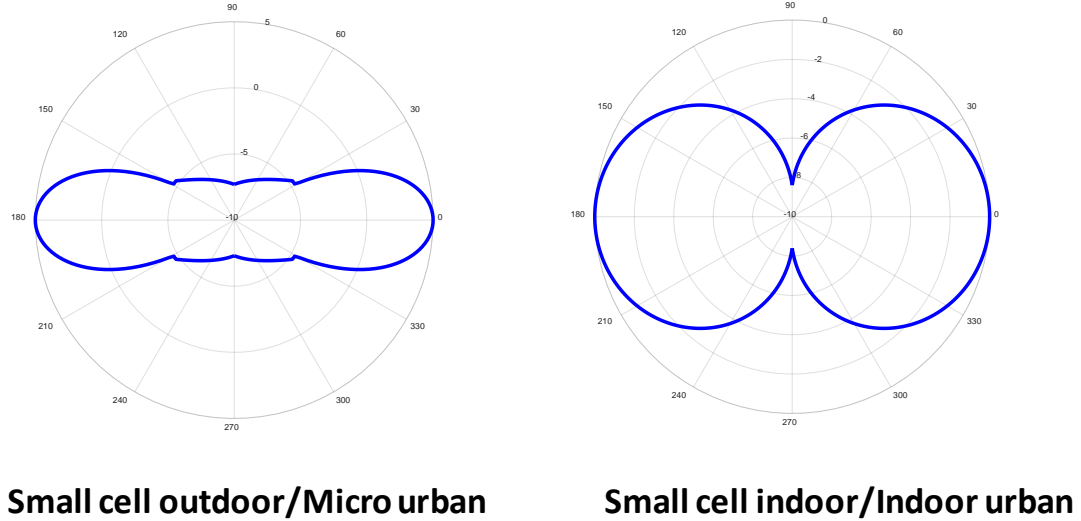


**Figure 4-3: Small cell Base Station Antenna Gain Patterns (elevation patterns shown; both patterns are omnidirectional in azimuth)**

M.2292 indicates that base stations are only active 50% of the time, resulting in a time-average EIRP that is half of the maximum value shown in Table 4-1. This EIRP reduction was not utilized to be conservative, noting that a base station could be operating with 100% loading for

long enough periods to cause disruptions to GNSS receivers. Also for conservatism, the “peak” side-lobe gain patterns from F.1336 were used, as opposed to the “average” side-lobe gain patterns. As suggested in F.1336, the average side-lobe patterns may be more appropriate for studies involving an aggregation of base stations.

For the certified aviation analysis conducted by the FAA, a base station antenna gain pattern based upon a specific LTE network proposal was utilized. See Appendix G.

#### **4.1.2.2 Handsets**

For handsets, M.2292 recommends modeling the antenna gain pattern as -3 dBi in all directions with a maximum power supplied to the antenna of 23 dBm. This results in a handset model that uses an isotropic antenna gain pattern with maximum EIRP of 20 dBm. Within this report, two other EIRPs (still paired with an isotropic antenna assumption) are examined: 23 dBm and 30 dBm.

M.2292 indicates that handsets are active 50, 70, or 100% of the time depending on deployment type. As with the base station models in this report, 100% handset activity was assumed for conservatism since this level of activity can occur for short periods for any deployment type. Further, M.2292 notes other factors that can diminish interference effects from handsets including: power control that diminishes typical EIRPs by 21 – 32 dB, building shielding (up to 20 dB), and body shielding (4 dB). These three loss factors are also not considered within this report for conservatism, since there are situations where none of the three losses may apply. For instance, a handset can be outdoors at the edge of cell coverage transmitting maximum EIRP towards a GPS/GNSS receiver without any intervening obstructions.

#### **4.1.3 Use Case Development**

Understanding GPS/GNSS receiver use cases scenarios are important so that the geometric parameters, specifically a receiver height and lateral offset from a transmitter can be determined. Also, it is important that use cases representative each receiver category and can provide a worst-case scenario so most, if not all, receivers in that category are protected. In addition, use cases are needed in conjunction with ITMs, propagation models, and transmitter scenarios to determine what power levels can be tolerated adjacent to GPS/GNSS signals.

Use cases were compiled with input from DOT federal partners and agencies. Members of the working group were provided a template that contained questions related to how their organizations use GPS/GNSS receivers to support their mission. In particular, questions included identifying height, speed, terrain, antenna orientation and integration, and urbanization areas.

Also, outreach was conducted with GPS/GNSS receiver manufacturers. Manufacturers were provided the same template as DOT’s federal partners. Additionally, manufacturers provided presentations during several of the workshops that summarized use cases by category for the receivers they manufacture.

A summary of the compiled results can be found in Table 4-2. The results generally indicate that each category has a large range of geometric parameters.

**Table 4-2: Summary of Compiled Use Case Information**

Category	Height (feet AGL)		Speed (mph)	Urbanization	Terrain	Antenna Integration	Antenna Orientation
	Min	Max					
GAV	0	40k	920	Urban/Suburban/Rural	Flat/Sloped/Canyon Open/Impeded Land/Water	Yes/No	Variable
GLN	0	1,000	600	Urban/Suburban/Rural	Flat/Sloped/Canyon Open/Impeded Land/Water	Yes/No	Variable
HPR	0	20,000	180	Urban/Suburban/Rural	Flat/Sloped/Canyon Open/Impeded Land/Water	Yes/No	Variable
TIM	0	1000s	100	Urban/Suburban/rural	Flat Open Land	No	Fixed
CEL	0	100s	100s	Urban/Suburban/rural	Flat/Sloped/Canyon Open/Impeded Land/Water	Yes	Variable
SPB	1,700k	4,300k	16k	n/a	n/a	No	Variable

In an effort to further down-select representative use cases, priorities identified by the space-Based PNT EXCOM and PNT Advisory Board were compiled as a method to prioritize the use case development. These priorities include:

- Existing use cases
- Vital to economic, public safety, scientific, and national security
- Focus on HPR and TIM
- Focus analysis on most sensitive cases
- Apply the 1 dB degradation criteria
- Include Multi-GNSS

When factoring in these priorities, three use case scenarios were identified for further in-depth investigation:

- 1) Agriculture/Farming
- 2) Construction/infrastructure
- 3) Emergency response

A graphic of the emergency response uses case is shown in Figure 4-4. First responders are increasingly using GPS to locate patients both during emergencies and as a normal course of duty. As shown in the figure, there are multiple use of GPS in this scenario applying GLN receivers for navigation of the emergency service response vehicles, as well as asset tracking, including increased awareness of where response personnel and vehicles are located. A GAV receiver on a drone also plays a role in this scenario, supporting the response effort. Drones are becoming of increasing importance in collecting imagery and sensor data in response to natural disasters and other incidents.

This scenario illustrates that use of a GPS/GNSS receiver can be quite close in distance (10's of meters) to a base station transmitter and potentially very close to a handset as well transmitting in the adjacent band. The GPS/GNSS receiver also potentially could be vertically above the base station height.



**Figure 4-4: Emergency Response Use Case**



A presentation given at workshop VI can be found in Appendix H, which provides a breakdown of the three use case scenarios. Table 4-3 summarizes the geometric parameters of the three priority scenarios. These applications/use cases happen routinely and bound the impact of base station transmitters.

**Table 4-3: Summary of Geometric Parameters**

Use Case Scenarios	Use case	Category	Vital Needs	Lateral Distance(s)	Vertical height(s)
<b>Agriculture/ Farming</b>	Precision Farming	HPR	Economic	10 ft and greater from base station	0-20 ft above ground
	Crop Health Monitoring	GLN/GAV	Economic	10 ft and greater from base station	Up to and above base station
<b>Construction/ Infrastructure</b>	Surveying	HPR	Economic	1 city block and greater from the base station	Up to and above base station
<b>Emergency Response</b>	UAS/UAV	GLN/GAV	Public Safety/ National Security	10 ft and greater from base station	Up to and above base station
	Emergency Services	GLN/CEL			
	Emergency Response				

#### 4.1.3.1 Receiver Antenna Patterns

Models for GLN, GAV, TIM, HPR, and CEL receivers relative antenna gain patterns as a function of frequency were developed based upon the antenna characterization activities described in Section 3.3.

The following simple model was found to be representative for relative VPOL and HPOL antenna gain patterns for GLN, GAV, TIM, and HPR receivers:

$$G(\theta) = -\alpha\theta^2$$

where  $G$  is the relative antenna gain (dBi),  $\theta$  is the off-boresight angle (deg), and  $\alpha$  is a unitless coefficient.

Based upon curve fits using the 14 external, active antennas that were measured in an anechoic chamber as discussed in Section 3.3, the coefficients in Table 4-4 were determined. The curve fitting approach used was a standard unweighted linear least squares fit of the single parameter equation above.

**Table 4-4: Coefficients for GLN, GAV, TIM, and HPR Receivers for Modeling Relative VPOL Antenna Gain at 22 Frequencies\***

Frequency (MHz)	$\alpha$ , GLN&GAV	$\alpha$ , TIM	$\alpha$ , HPR
1475	3.6511e-04	6.6446e-04	8.2449e-04
1490	4.0306e-04	7.4609e-04	8.4546e-04
1495	4.5153e-04	7.4928e-04	8.4870e-04
1505	4.6656e-04	7.4815e-04	7.6944e-04
1520	4.9953e-04	7.6698e-04	7.6808e-04
1530	4.9687e-04	7.4564e-04	7.7055e-04
1535	4.4305e-04	7.4764e-04	7.5991e-04
1540	7.0113e-04	7.7206e-04	7.5869e-04
1545	6.5594e-04	7.5573e-04	7.7657e-04
1550	5.0195e-04	6.8500e-04	8.1978e-04
1555	5.4545e-04	6.3767e-04	8.5491e-04
1575	5.7732e-04	5.5176e-04	8.5922e-04
1595	5.3406e-04	6.0901e-04	8.6792e-04
1615	3.9454e-04	5.0824e-04	8.2166e-04
1620	4.2042e-04	5.4509e-04	8.2117e-04
1625	4.5397e-04	5.4762e-04	8.1460e-04
1630	4.7544e-04	6.6388e-04	8.2114e-04
1635	4.2583e-04	6.3971e-04	8.3291e-04
1640	3.5254e-04	5.5736e-04	8.3908e-04
1645	3.4695e-04	5.4974e-04	8.4719e-04
1660	4.4364e-04	5.8069e-04	7.8310e-04
1675	4.7622e-04	5.9775e-04	8.4784e-04

\*In the table entries, “e-04” denotes an exponent to the minus 4 power, i.e., “ $\times 10^{-4}$ ”.

As an example of the relative gain patterns, Figure 4-5 shows the modeled relative VPOL antenna gain patterns at 1530 MHz.

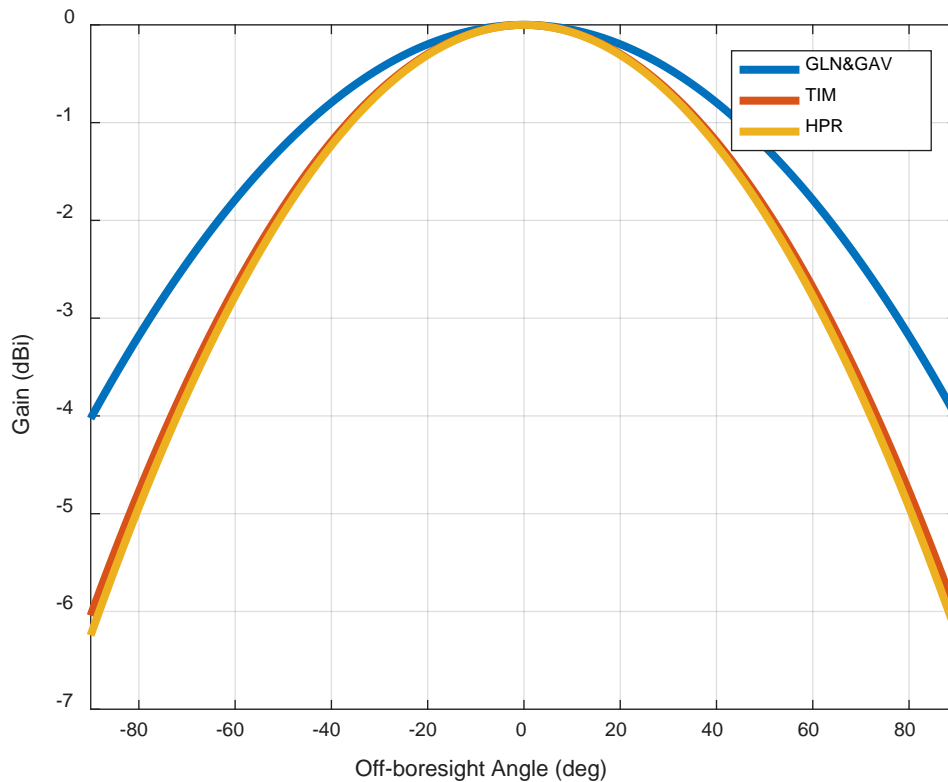


**Figure 4-5: Relative VPOL Antenna Gain Patterns for 1530 MHz**

The coefficients were generated using the following procedure:

- The 14 measured antennas were grouped by category (GLN/GAV, TIM, or HPR).
- Within each category, and for each frequency, the VPOL antenna patterns were:
  - Adjusted by estimated active subassembly gain at L1 so that they nominally included only passive element gain and filtering.
  - Converted from dBi to linear units, averaged, and then converted back to dBi.
- The mean VPOL antenna pattern for each category and each frequency was then:
  - Forced to be symmetric with off-boresight angle from -180 to 180 deg
  - Fitted with a quadratic polynomial. Since only the relative pattern is of interest, the bias term is not important. The forced symmetry results in the linear term being equal to zero. The quadratic term became the  $\alpha$  value within Table 4-4.

This procedure addresses the following considerations:

- Given that only a small set of measured patterns were available for each category, the raw data averaged across units within a category includes variations that would not be expected from a larger sample size.
- When averaging patterns, the pattern for the antenna with the least amount of attenuation at each frequency was deemed to be most important (because an antenna with a tremendous amount of filtering would be associated with a receiver with a high ITM that

is not greatly impacted by adjacent band interference at that frequency). This prompted the averaging of gains in linear units (not dB).

- Asymmetries in gain patterns with positive vs negative off-boresight angle is unimportant since the antenna could be oriented arbitrarily in azimuth relative to an adjacent-band interference source in the real world.

Figure 4-6 provides an example of the data processing. Three GLN VPOL antenna gain patterns at 1530 MHz are shown in the figure. These patterns already have the active subassembly gain at L1 removed from them (15.0 – 19.9 dB for these units). The three patterns are averaged together in linear units, converted back to dBi, and forced to be symmetric with respect to off-boresight angle to form the “Mean” gain shown in the figure. The final curve shown in the figure is the quadratic polynomial fit (obtained with MATLAB polyfit), with the  $\alpha$  value shown in Table 4-4 of  $4.9687\text{e-}04$ . Using the equation above, this model yields a relative gain value of zero at boresight (by definition) and a relative gain value of  $-(4.9687 \times 10^{-4})(90)^2 = -4.0$  dBi at 90 deg off-boresight angle.

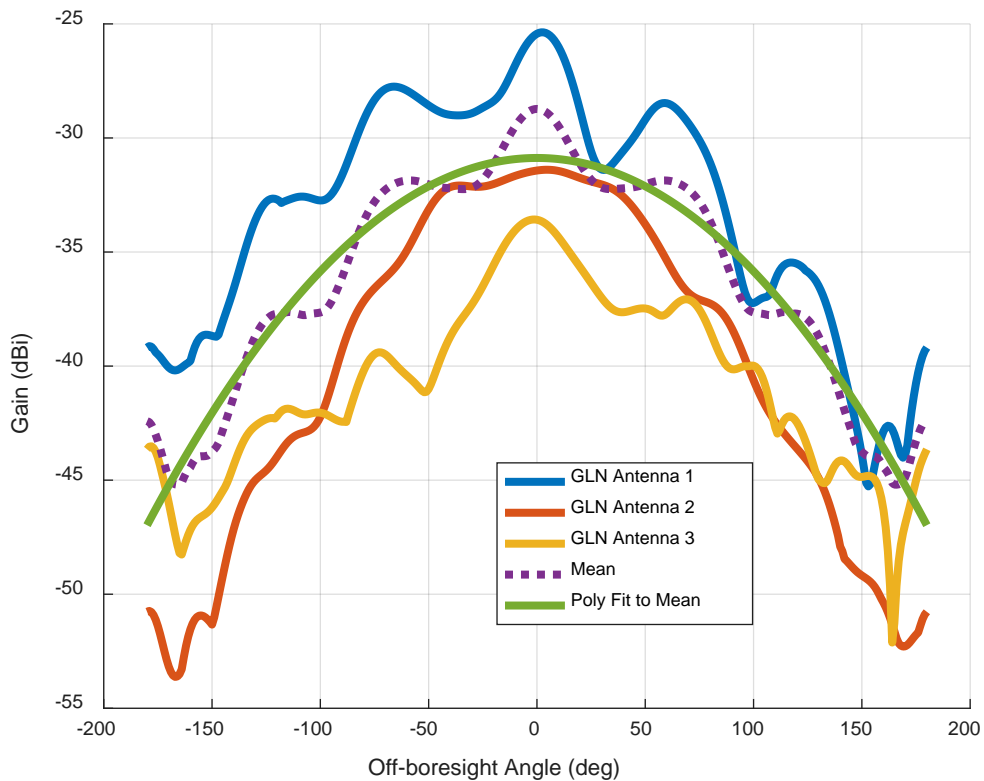


**Figure 4-6: Gain Patterns Illustrating Generation of GLN Coefficients for 1530 MHz**

The results for HPOL are shown in Table 4-5. For base stations using +/-45 deg cross-polarization, the VPOL and HPOL gain patterns were averaged.

**Table 4-5: Coefficients for GLN, GAV, TIM, and HPR Receivers for Modeling Relative HPOL Antenna Gain at 22 Frequencies\***

Frequency (MHz)	$\alpha$ , GLN&GAV	$\alpha$ , TIM	$\alpha$ , HPR
1475	4.8398e-04	5.5084e-04	8.4574e-04
1490	4.7233e-04	6.2100e-04	8.3577e-04
1495	4.8102e-04	6.2399e-04	8.3705e-04
1505	5.1078e-04	6.4098e-04	7.6026e-04
1520	5.8403e-04	6.7548e-04	7.4805e-04
1530	6.5353e-04	6.6919e-04	7.4907e-04
1535	7.1505e-04	6.7349e-04	7.3921e-04
1540	6.4548e-04	6.8364e-04	7.4000e-04
1545	5.4709e-04	6.7359e-04	7.6239e-04
1550	5.6432e-04	5.0510e-04	8.1090e-04
1555	5.5046e-04	4.4691e-04	8.4732e-04
1575	4.5639e-04	4.6423e-04	8.5749e-04
1595	5.0855e-04	5.5868e-04	8.5147e-04
1615	6.5552e-04	5.4371e-04	7.9655e-04
1620	6.4930e-04	5.4973e-04	7.9416e-04
1625	6.6186e-04	5.3681e-04	7.8823e-04
1630	6.9139e-04	5.9523e-04	7.9844e-04
1635	7.6854e-04	4.6848e-04	8.0766e-04
1640	7.7504e-04	1.3496e-04	8.0420e-04
1645	7.4623e-04	3.9051e-05	8.0746e-04
1660	7.1712e-04	9.1810e-05	7.5459e-04
1675	5.9731e-04	1.0261e-04	8.5621e-04

\*In the table entries, “e-04” denotes an exponent to the minus 4 power, i.e., “ $\times 10^{-4}$ ”.

For CEL antennas, a relative gain value of 0 dBi is recommended for all directions for two reasons:

- Cell-phone antennas are typically low-gain, but with erratic patterns depending on the shielding of the cell-phone case, other components, and interaction with the human body holding it (see, e.g., measurements in Section 3.3.3).
- The cell-phone antenna could be oriented in any direction.

#### 4.1.4 Propagation Models

Three propagation models were considered within this report for all receivers except for certified aviation and spaceborne. These models are free-space, two-ray, and the Irregular Terrain Model. The free-space and two-ray models were introduced in Section 4.1.1. The Irregular Terrain Model is an implementation (with improvements) of the Longley-Rice propagation model by the NTIA<sup>1</sup>. Propagation losses yielded by this model (on a median level) differ by less than 2 dB from free-space propagation loss (FSPL) for the relevant distances and frequency range (i.e. distances up to half the interspacing distance between transmitters and frequencies between 1475 and 1675 MHz). However, NTIA additionally recommends using a blended model that is FSPL for small distances and transitions to Irregular Terrain Model starting at a 100 m distance.

<sup>1</sup>See <https://www.its.bldrdoc.gov/resources/radio-propagation-software/itm/itm.aspx>.

Therefore when the tolerable EIRP levels are considered for distances of 100 m or less, as is the case for civil receivers use cases (excluding use cases for space-based and certified aviation receivers), both the blended and FSPL models yield the same results.

The equations used to perform forward and inverse modeling analysis are first developed for the case of free space path loss propagation. The modified equations for the case of a two-ray path loss are subsequently presented. All of the forward and inverse modeling results presented in this report do not consider OOBE and thus the impact is dictated by the fundamental emissions of the interference source. If an adjacent band system were deployed for which this assumption is invalid, lower EIRP values may be necessary to protect GNSS and would need to be determined for the applicable OOBE limits. See Section 3.2.5.2 for a discussion of OOBE levels.

For receiver power calculations, an LTE signal with dual  $\pm 45^\circ$  polarization is equivalent to a signal radiating with twice the power and  $+45^\circ$  polarization when signals in the two polarizations are uncorrelated. This signal can then be decomposed into vertically and horizontally polarized signals. Considering this along with propagation loss, and receiver and transmitter antenna gains, the corresponding voltage complex amplitude received by an RHCP antenna is shown below

$$A_v(\vec{r}_T, \vec{r}, f) = \sqrt{2 \cdot \frac{P(f)}{2} \cdot \frac{1}{L_p(\vec{r}_T, \vec{r})} \cdot G_{Td}(\vec{r}_T, \vec{r}) \cdot G_{Rdv}(\vec{r}_T, \vec{r}, f) \cdot e^{j\frac{2\pi}{\lambda}R_d}} \quad (4-1)$$

$$A_h(\vec{r}_T, \vec{r}, f) = j \cdot \sqrt{2 \cdot \frac{P(f)}{2} \cdot \frac{1}{L_p(\vec{r}_T, \vec{r})} \cdot G_{Td}(\vec{r}_T, \vec{r}) \cdot G_{Rdh}(\vec{r}_T, \vec{r}, f) \cdot e^{j\frac{2\pi}{\lambda}R_d}} \quad (4-2)$$

$$\begin{aligned} A(\vec{r}_T, \vec{r}, f) &= A_v + A_h \\ &= \sqrt{\frac{P(f)}{L_p(\vec{r}_T, \vec{r})} \cdot G_{Td}(\vec{r}_T, \vec{r}) \cdot e^{j\frac{2\pi}{\lambda}R_d} \cdot \left( \sqrt{G_{Rdv}(\vec{r}_T, \vec{r}, f)} + j \cdot \sqrt{G_{Rdh}(\vec{r}_T, \vec{r}, f)} \right)} \\ &= (G_{R,max})^{\frac{1}{2}} \cdot \sqrt{\frac{EIRP(f)}{L_p(\vec{r}_T, \vec{r})} \cdot g_{Td}(\vec{r}_T, \vec{r}) \cdot e^{j\frac{2\pi}{\lambda}R_d} \cdot \left( \sqrt{g_{Rdv}(\vec{r}_T, \vec{r})} + j \cdot \sqrt{g_{Rdh}(\vec{r}_T, \vec{r})} \right)} \end{aligned} \quad (4-3)$$

where:

$R_d = |\vec{r} - \vec{r}_T|$  is the distance between the transmitter and receiver antennas,

$G_{R,max}$  is the antenna gain at boresight assumed equal for both polarizations,

$g_{Td}(\vec{r}_T, \vec{r})$  is the normalized transmitter gain in the direction of the receiver antenna,

$g_{Rdv}(\vec{r}_T, \vec{r})$  and  $g_{Rdh}(\vec{r}_T, \vec{r})$  are the normalized receiver antenna gains in the direction of the transmitter antenna for the case of horizontal and vertical polarizations respectively.

The term  $L_p(\vec{r}_T, \vec{r})$  is the free space path loss factor defined in the following equation:

$$L_p(\vec{r}_T, \vec{r}) = \left( \frac{4\pi R_d}{\lambda} \right)^2 \quad (4-4)$$

The power coupled into the receiver from its antenna output is found by taking  $\frac{1}{2}$  the amplitude squared as follows

$$P(\vec{r}_T, \vec{r}, f) = \frac{1}{2} G_{R,max} \cdot \frac{EIRP(f)}{L_p(\vec{r}_T, \vec{r})} \cdot g_{Td}(\vec{r}_T, \vec{r}) \cdot \left| \left( \sqrt{g_{Rdv}(\vec{r}_T, \vec{r}, f)} + j \cdot \sqrt{g_{Rdh}(\vec{r}_T, \vec{r}, f)} \right) \right|^2 =$$

$$\frac{1}{2} G_{R,max} \cdot \frac{EIRP(f)}{L_p(\vec{r}_T, \vec{r})} \cdot g_{Td}(\vec{r}_T, \vec{r}) \cdot (g_{Rdv}(\vec{r}_T, \vec{r}, f) + g_{Rdh}(\vec{r}_T, \vec{r}, f)) \quad (4-5)$$

This power is outside the receiver tolerance when it exceeds the tolerance level  $ITM(f) \cdot G_{R,max}$ . This inequality is shown in the equation below.

$$\frac{P(\vec{r}_T, \vec{r}, f)}{G_{R,max}} = \frac{1}{2} \cdot \frac{EIRP(f)}{L_p(\vec{r}_T, \vec{r})} \cdot g_{Td}(\vec{r}_T, \vec{r}) \cdot (g_{Rdv}(\vec{r}_T, \vec{r}, f) + g_{Rdh}(\vec{r}_T, \vec{r}, f)) > ITM(f) \quad (4-6)$$

The forward modeling uses this inequality to determine the impacted region for a predetermined EIRP(f) level.

On the other hand, the inverse modeling solves for the value EIRP( $\vec{r}$ ,  $f$ ) that ensures compatibility for a given transmitter and receiver location. An EIRP map for all receiver locations in a vertical plane relative to a fixed transmitter is created using the following equation

$$EIRP(\vec{r}, f) = \frac{L_p(\vec{r}_T, \vec{r}) \cdot ITM(f)}{\frac{1}{2} g_{Td}(\vec{r}_T, \vec{r}) \cdot (g_{Rdv}(\vec{r}_T, \vec{r}, f) + g_{Rdh}(\vec{r}_T, \vec{r}, f))} \quad (4-7)$$

This map is performed in the vertical y-z plane containing the phase center of the transmit antenna and in the direction of maximum gain of a sector antenna and in any direction in the case of an omnidirectional antenna.

For given use cases associated with one category of receivers, the range of GNSS application operational heights and a standoff distance  $d_s$  will determine the an EIRP mask  $EIRP(d_s, f)$  according to the following equation

$$EIRP(d_s, f) = \text{Min}_{\vec{r} \in R_{uc}} \{ EIRP(\vec{r}_T, \vec{r}, f) \} \quad (4-8)$$

Where  $R_{uc}$  is the use cases analysis region as shown in Figure 4-7.

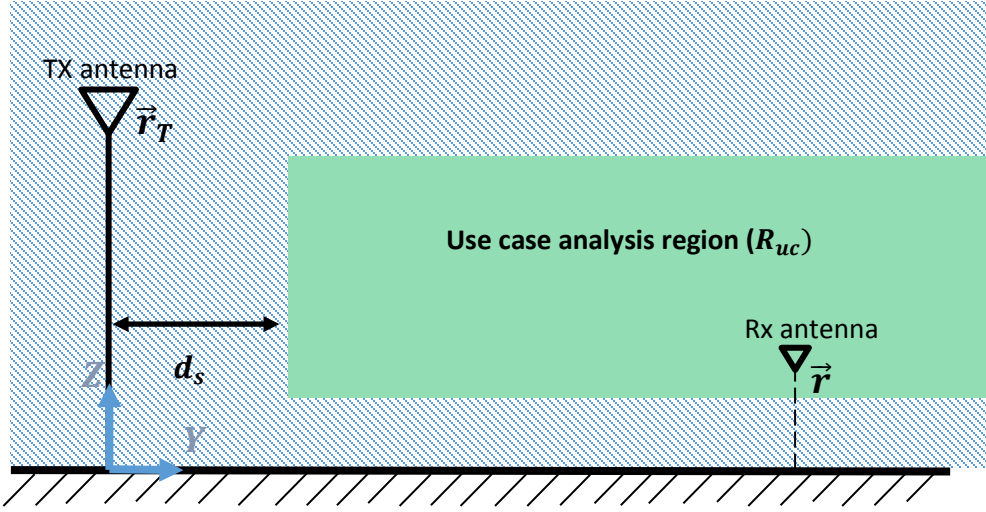


Figure 4-7: Illustration of use case analysis region

In order to ensure compatibility with all receivers within a category the bounding ITMs are used. This will result in EIRP values that protect 100% of the receivers tested. Results for the median ITM within each category are also presented resulting in power levels that would leave 50% of the receivers unprotected.

The inverse modeling modified equation for the case of two ray path loss is shown below.

$$EIRP(\vec{r}, f) = \frac{ITM(f)}{\frac{1}{2} \cdot g_{Td}(\vec{r}_T, \vec{r}) \cdot (g_{Rdv}(\vec{r}_T, \vec{r}, f) \cdot PF_{2Ray,v}(\vec{r}, f) + g_{Rdh}(\vec{r}_T, \vec{r}, f) \cdot PF_{2Ray,h}(\vec{r}, f))} \quad (4-9)$$

Where  $PF_{2Ray,v}(r, f)$  and  $PF_{2Ray,h}(r, f)$  represent respectively the vertical and horizontal polarization path factors (also sometimes referred to as *path gains* in the literature) derived in Appendix F.

The inverse modeling equation can be easily rearranged to get the inequality expression for the forward modeling

$$\frac{1}{2} EIRP(f) \cdot g_{Td}(\vec{r}_T, \vec{r}) \cdot (g_{Rdv}(\vec{r}_T, \vec{r}, f) \cdot PF_{2Ray,v}(r, f) + g_{Rdh}(\vec{r}_T, \vec{r}, f) \cdot PF_{2Ray,h}(r, f)) > ITM(f) \quad (4-10)$$

When solving for tolerable EIRP for the case of multiple transmitters, the inverse modeling equations stay the same with a summation in the denominator over all transmitters. For example the FSPL inverse modeling equation takes the following form when aggregate effects are considered.



$$EIRP(\vec{r}, f) = \frac{ITM(f)}{\sum_T \alpha_T \cdot \left( \frac{1}{2} \cdot \frac{1}{L_p(\vec{r}_T, \vec{r})} \cdot g_{Td}(\vec{r}_T, \vec{r}) \cdot (g_{Rdv}(\vec{r}_T, \vec{r}, f) + g_{Rdh}(\vec{r}_T, \vec{r}, f)) \right)} \quad (4-11)$$

$\alpha_T$  is a power control term for the general case when EIRP is not same for all transmitters. The analysis in this report will use  $\alpha_T = 1$  for all transmitters whenever aggregation is considered.

#### 4.1.5 Forward Modeling Results and Sensitivity

Appendix I provides a comprehensive set of forwarding modeling results for two adjacent-band LTE base station deployment types (macro urban and small cell outdoor/micro urban; see Table 4-1) and also for LTE mobile devices. Type 2 (10 MHz LTE) signals were assumed. Base station results were produced for each of the 11 potential adjacent-band LTE downlink frequencies listed in Table 3-6 (1475, 1490, 1505, 1520, 1525, 1530, 1535, 1540, 1545, 1550, 1675 MHz) and handset results for each of the 7 potential adjacent-band LTE uplink frequencies (1620, 1625, 1630, 1635, 1640, 1645, 1660 MHz).

An example of the base station forward modeling results is shown in Figure 4-8. The results shown on the plot assumes a macro urban base station (EIRP = 59 dBm/sector, height = 25 m, other characteristics as described in Section 3.4.2.1) operating at 1530 MHz, free space propagation, and the most sensitive (bounding) GAV GPS/GNSS device category processing GPS C/A-code signals. The three contours in the plot depict the two-dimensional areas where the received interference level from a macro urban base station exceeds three thresholds: (1) the ITM (i.e., where the bounding GAV device category experienced a 1 dB CNR degradation), (2)  $LOL_L$ , the loss-of-lock threshold for low-elevation angle satellites, and (3)  $LOL_H$ , the loss-of-lock threshold for high-elevation angle satellites.

The base station is situated near the bottom left of the plot with its antennas located at the point (0, 25 m) in  $x, y$  where  $x$  is the lateral distance from the base station and  $y$  is the height above ground. The GAV DUT was assumed to have an antenna with the relative gain pattern modeled as discussed in Section 3.4.3.1.

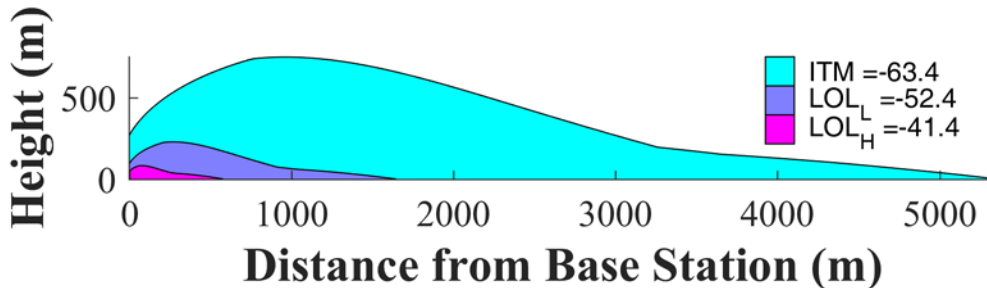
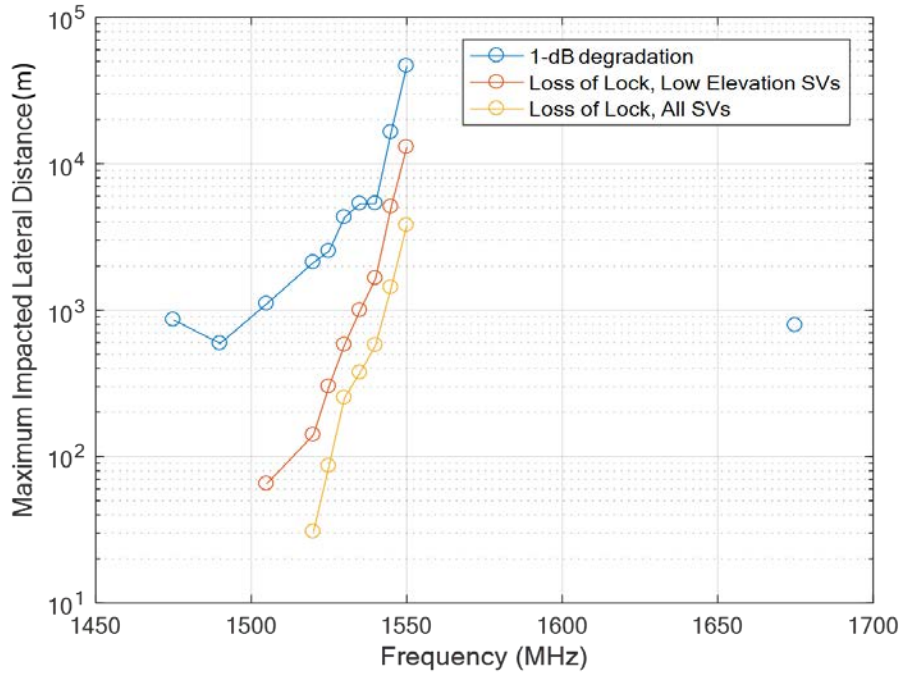


Figure 4-8: Macro Urban Base Station (EIRP = 59 dBm), Bounding GAV, 1540 MHz

Appendix I also includes summary charts such as shown in Figure 4-8. Each summary chart shows, for each applicable frequency, the maximum impacted lateral distance for each DUT type and each LTE transmitter type (e.g. macro urban base station, small cell outdoor base station, handset). For instance, at 1540 MHz Figure 4-9 has three data points that correspond to the maximum horizontal extent of the impacted region contours from Figure 4-8.



**Figure 4-9: Maximum Impacted Lateral Distance for Bounding GAV, Macro Urban Base Station (EIRP = 59 dBm)**

Results for the HPR receiver category at 1530 MHz are presented in Figure 4-5. Note the HPR category experienced a 1 dB (or greater) CNR degradation beyond 14 km from the transmitter and loss of lock occurred on low elevation satellites out to 3 km with loss of lock on all satellites out to approximately 1 km.

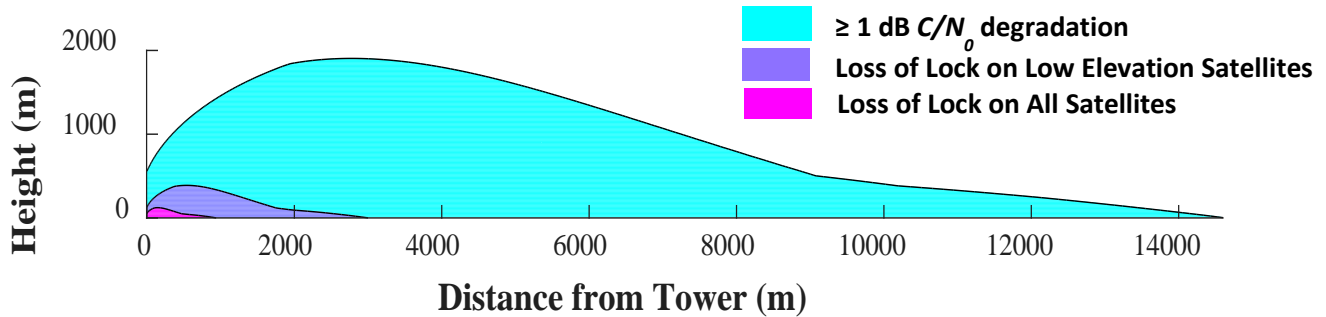


**Figure 4-60: Macro Urban Base Station (EIRP = 59 dBm), Bounding HPR, 1530 MHz**

Appendix I is organized as follows. For GPS C/A-code and assuming free-space propagation, Section I.1, I.2, and I.3 present forward modeling results for macro base stations, small cell outdoor/micro urban base stations, and handsets, respectively. Section I.4 examines the sensitivity of the results to:

- Less sensitive DUTs – results for the median-performing vs the most-sensitive DUTs.
- GNSS signals – results for other GNSS signal types vs. GPS C/A-code.
- Propagation models – the variability of the results with propagation model.

#### 4.1.6 Inverse Transmit Power Calculation Results and Sensitivity Analysis

##### 4.1.6.1 Inverse Transmit Power Calculation Results

Inverse modeling is used to determine EIRP tolerance masks  $EIRP(d_s, f)$  for a category of GNSS receivers and for a given standoff distance  $d_s$ . The details of this analysis including the relevant equations and parameters are described in section 4.1.4. This inverse modeling is only applied to the 10 MHz LTE downlink frequencies. The treatment of uplink frequencies is only considered in the forward analysis since at the time of the writing of this report the authors were not aware of any proposals to limit the maximum EIRP for handsets to a value below what is specified in the M.2292 document.

For the HPR category, the EIRP map for the bounding L1 C/A ITM is shown in Figure 4-11 (a) for the single micro urban base station at a center frequency of 1530 Hz. The use case analysis has shown that receiver heights extends to at and above the height of a base station in all categories and therefore the tolerable EIRP as a function of standoff distance can be found by taking the minimum along heights up to and above base station heights as shown in Figure 4-11 (b). The extent of the impact region is >10 km from the transmitter for an EIRP of 29 dBW and 1.8 km for EIRP of 10 dBW.

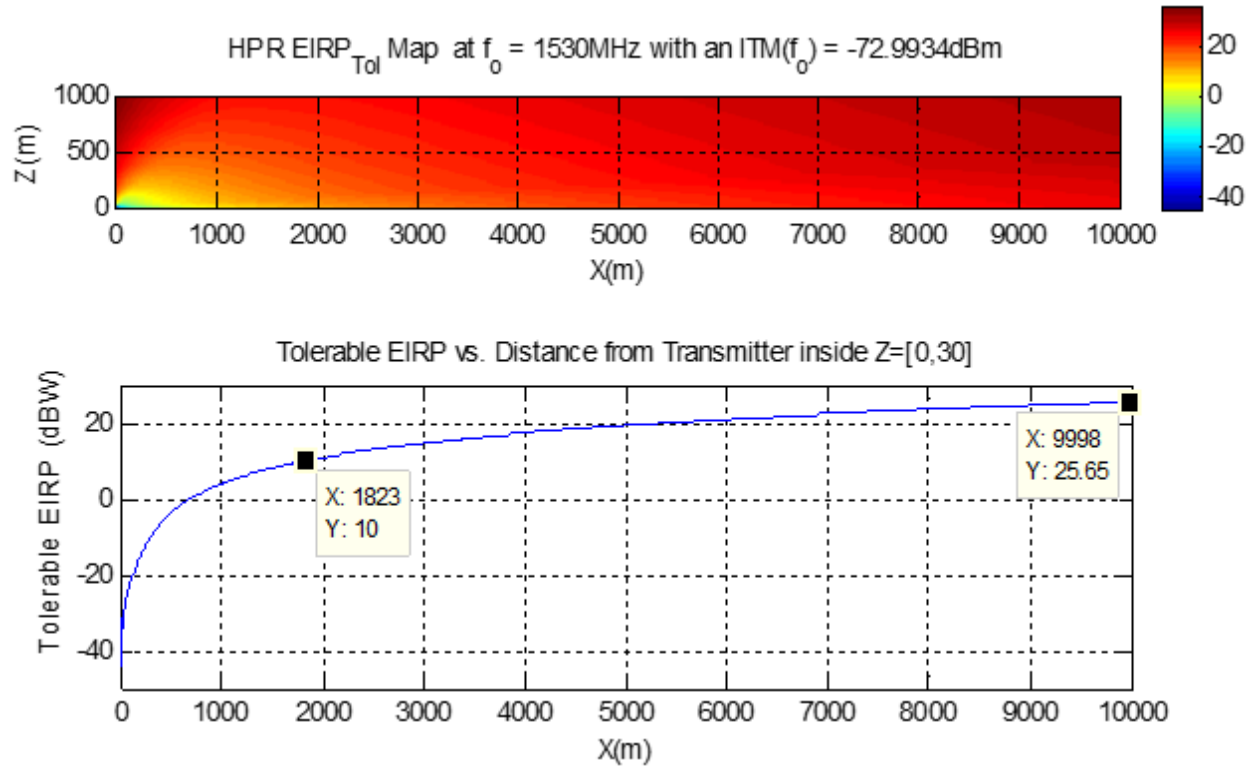


**Figure 4-71: Tolerable EIRP results. (top) Tolerable  $EIRP(\vec{r}, f)$  map in the vertical computation domain, (bottom) Tolerable  $EIRP(X, f)$  as a function of standoff distance  $X$ .**

However, the computation domain only needs to extend up to half the distance between the nearest two base stations in a uniform network deployment. For the case of micro urban deployment a computation domain up to 500 meters is sufficient. Below is the zoomed in version of the Figure 4-12 to illustrate the EIRP levels that protect HPR receivers processing L1 C/A signals at short distances from the transmitter.

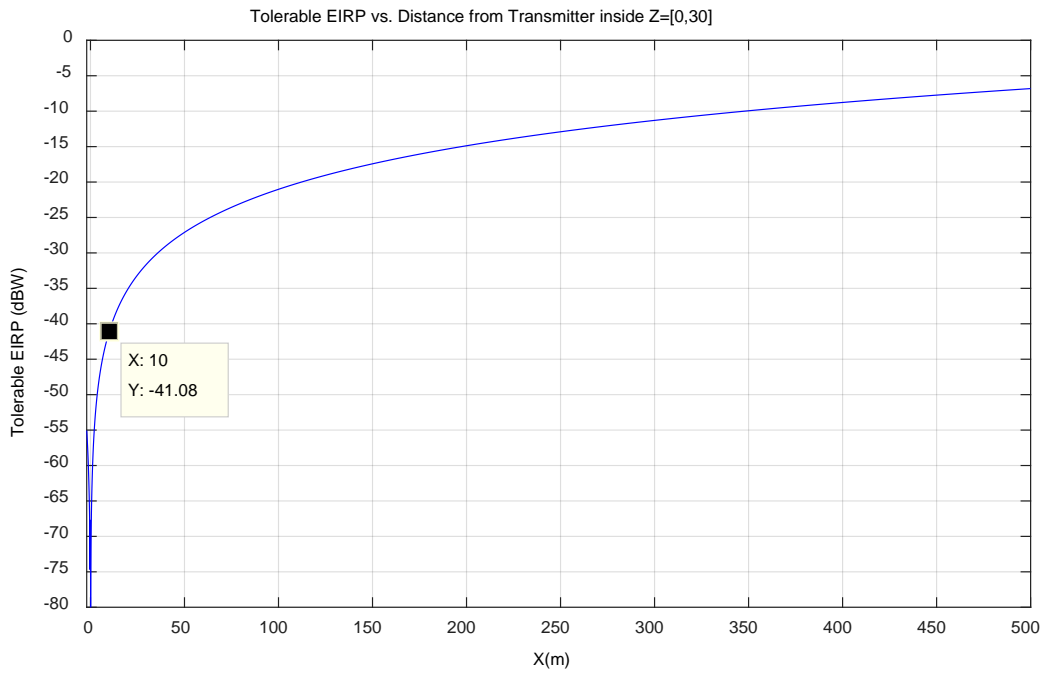


**Figure 4-82: Tolerable  $EIRP(X, f)$  as a function of standoff distance  $X$  up to  $X=500$  m**

The marker in this figure indicates the maximum tolerable EIRP,  $EIRP(d_s, f)$ , with  $d_s=10$  m and  $f=1530$  MHz. If this is repeated across all base station frequencies, a maximum tolerable EIRP mask can be generated as shown in Figure 4-13 below.

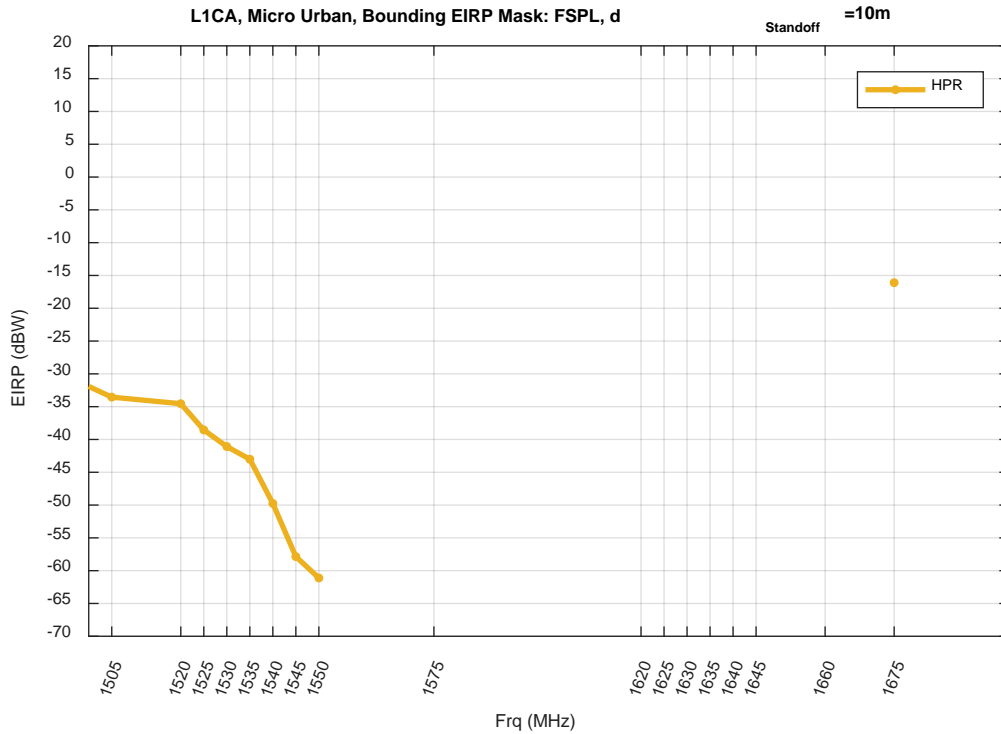


**Figure 4-9: EIRP(f,ds=10m) for the HPR category: L1 C/A, micro urban deployment, bounding EIRP Mask, and FSPL propagation**

It is worth noting that use cases indicated that receivers can be as close as 10 ft (3.0 m) to the base station. It was not clear that they can approach that distances at heights comparable to that of the base station. If receivers approach the base station height at the 10 ft standoff distance the tolerable EIRP levels will be lower by approximately 5 dB. This analysis can be repeated to generate EIRP masks for all categories of receivers at different standoff distances. Figure 4-14 depicts the L1 C/A EIRP masks for all five categories for the 10 m standoff distance. A more comprehensive set of results for 10, 100 and 500 m standoff distances that protects L1 C/A along with all other emulated GNSS signals are shown in Appendix J.

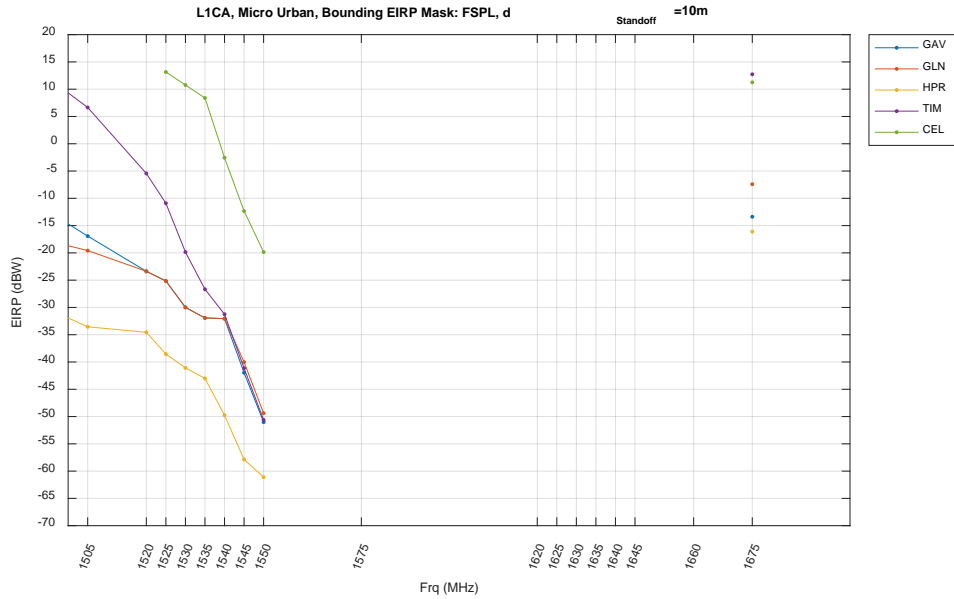


**Figure 4-10: EIRP(f,ds=10m) for five receiver categories of receivers: L1 C/A, micro urban deployment, bounding EIRP Mask, and FSPL propagation**

The HPR tolerable EIRP levels that protects L1 C/A and all GNSS signals for the same 10 m standoff distance are compared in Figure 4-15.

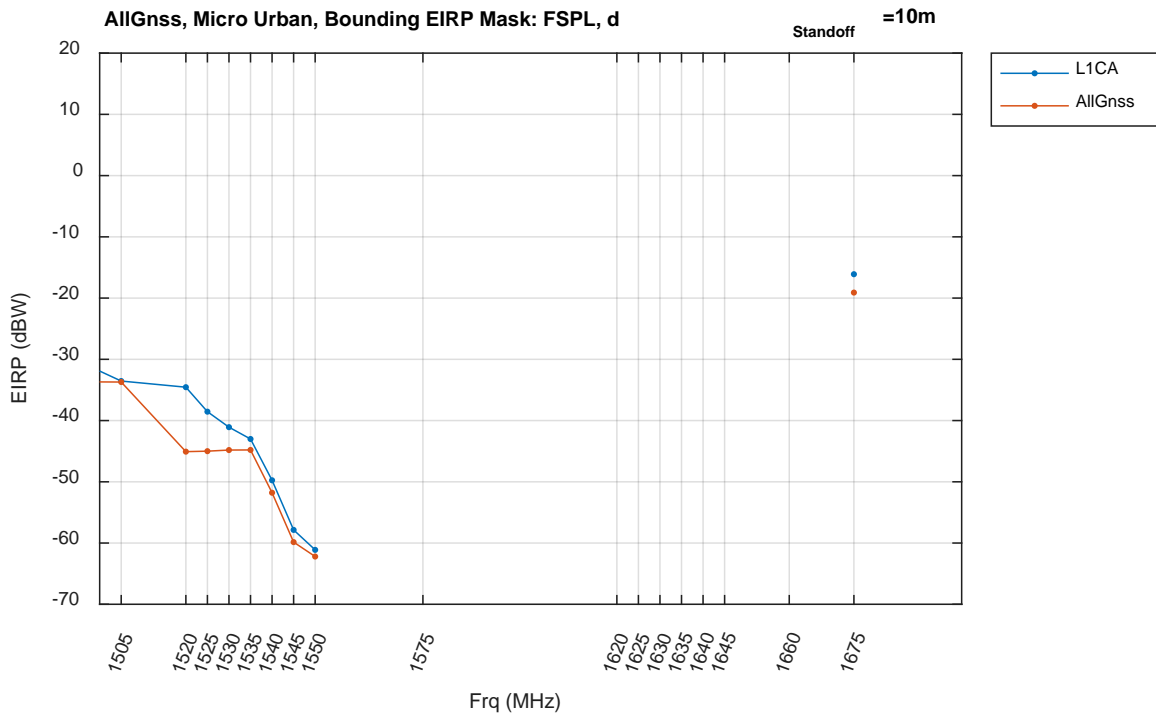


**Figure 4-11: Comparison of EIRP(f,ds=10m) L1 C/A and All GNSS masks for the HPR category of receivers: Micro urban deployment, bounding EIRP Mask, and FSPL propagation**

As expected, the levels that protect all GNSS signals are lower than the ones that protect L1 C/A signals since they are calculated based on the minimum of all bounds across emulated services. Figure 4-16 presents the resulting all GNSS EIRP masks for five categories of receivers at a standoff distance of 10 m.

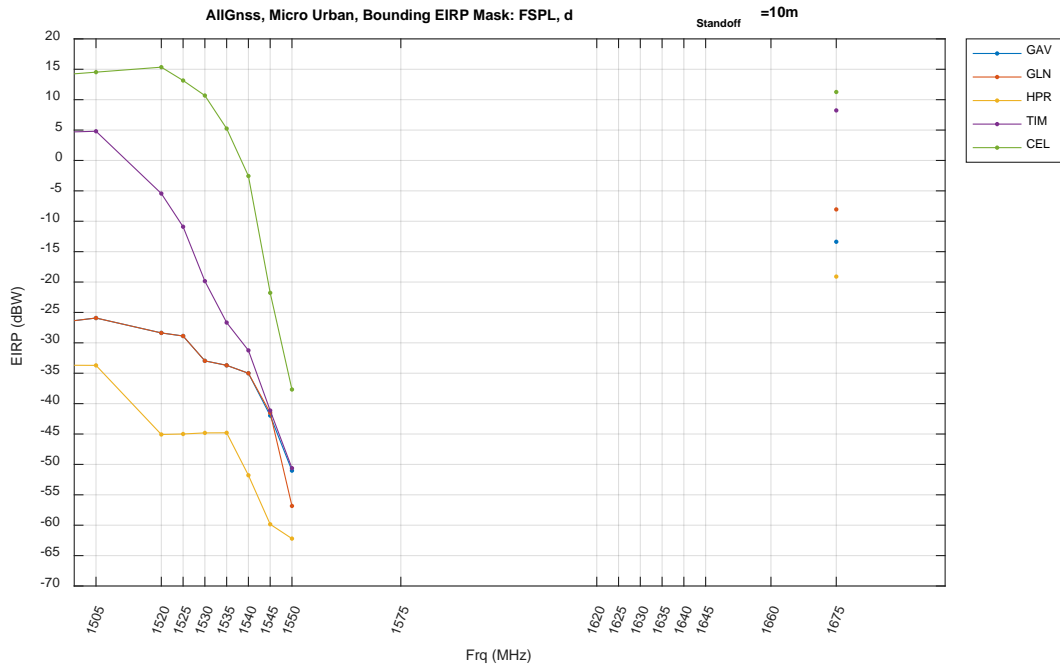


**Figure 4-12: EIRP( $f, d_s=10m$ ) for five categories of receivers: All GNSS, micro urban deployment, bounding EIRP Mask, and FSPL propagation**

An exhaustive list of plots that include results for the macro deployments are shown in Appendix J.

#### 4.1.6.2 Sensitivity Analysis

The transmit power level results presented in Section 4.1.6.1 considers only a single transmitter and FSPL propagation model. This subsection examines how these results vary when aggregation effects of multiple transmitters are considered. The sensitivity of these results to the propagation model used is also considered. Finally, the transmit power levels corresponding to the median ITMs are also discussed as part of this sensitivity analysis.

##### 4.1.6.2.1 Aggregation Effects

When multiple transmitters are radiating at equal EIRP, the single base station is expected to dominate for small standoff distances. As this distance increases, the aggregate effects become significant and limit the tolerable EIRP levels below that of a single transmitter. The aggregation analysis is here performed using a micro urban deployment of two full rings of adjacent cells around the center cell. In Figure 4-17, the center cell is in white, the inner ring of adjacent cells is



in yellow, and the outer ring of adjacent cells is in green. For urban and suburban regions, signals emitted from additional transmitters outside what is simulated here will have diminished effect on aggregate results. Additionally, they are expected to encounter blockage from buildings and terrain that will further diminish their contribution to the final results.

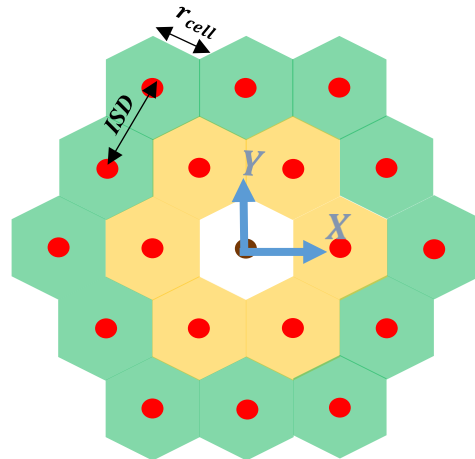


**Figure 4-13: micro deployment used for the aggregation sensitivity analysis.  
A small cell of radius  $r_{cell}$ , and transmitters' interspacing distance ISD.**

This analysis was performed in the vertical plane for the center transmitter (i.e.  $y=0$  plane) for the HPR L1 C/A Bounding ITM. These results are overlaid with that of a single base station in Figure 4-18.

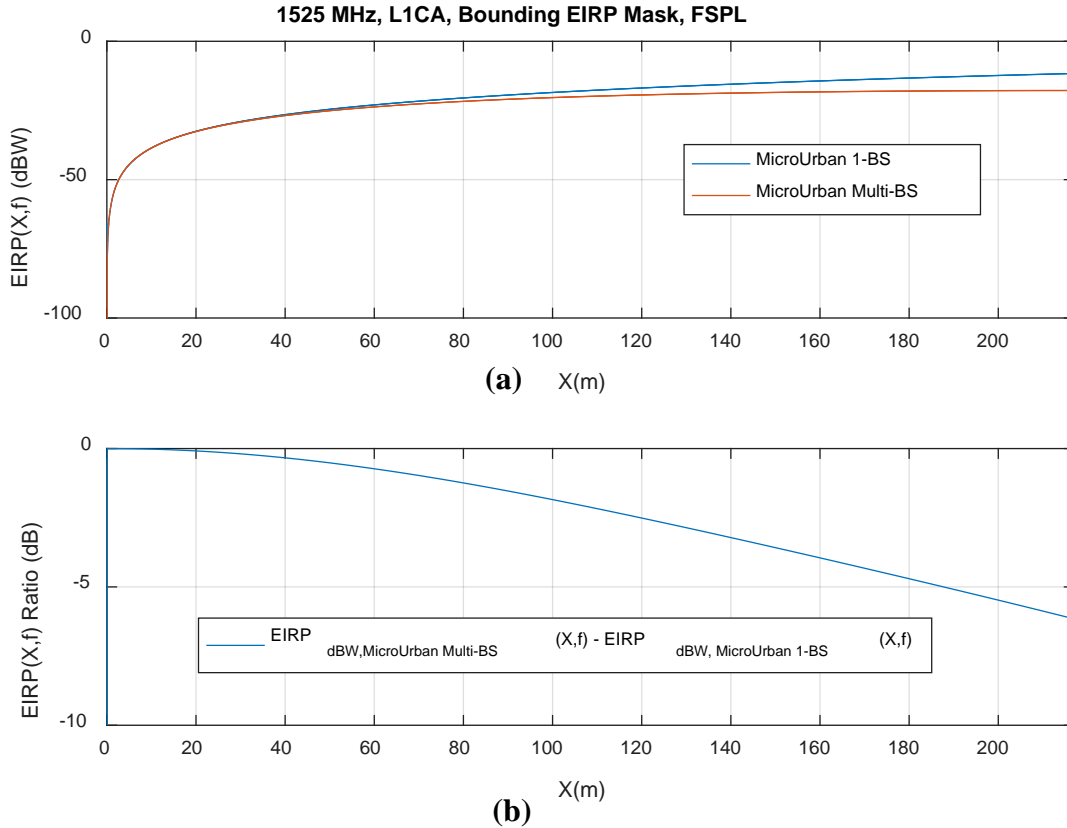


**Figure 4-18: (a) Overlay of  $EIRP(X, f)$  as a function of standoff distance  $X$  for the case of single and multiple base stations, (b)  $EIRP(X, f)$  ratio in dB for the two cases**

As previously discussed, the computation domain was limited to half the distance between transmitters beyond which the tolerable EIRP will start dropping again due to the proximity to the next transmitter. Figure 4-18 (a) shows the aggregation effects to be noticeable for standoff distances greater than 20 m. For example, a standoff distance 100 m the aggregation effect reduces the tolerable EIRP by approximately 1.8 dB relative to the case of a single transmitter. This reduction grows to about 5.5 dB at 200 m standoff distance.

In Figure 4-19 the tolerable  $EIRP(f, d_s)$  masks for the single and multiple transmitters cases are compared at a standoff distance of  $d_s=100$  m. It shows similar reduction in EIRP on the order of 2 dB for all frequencies.

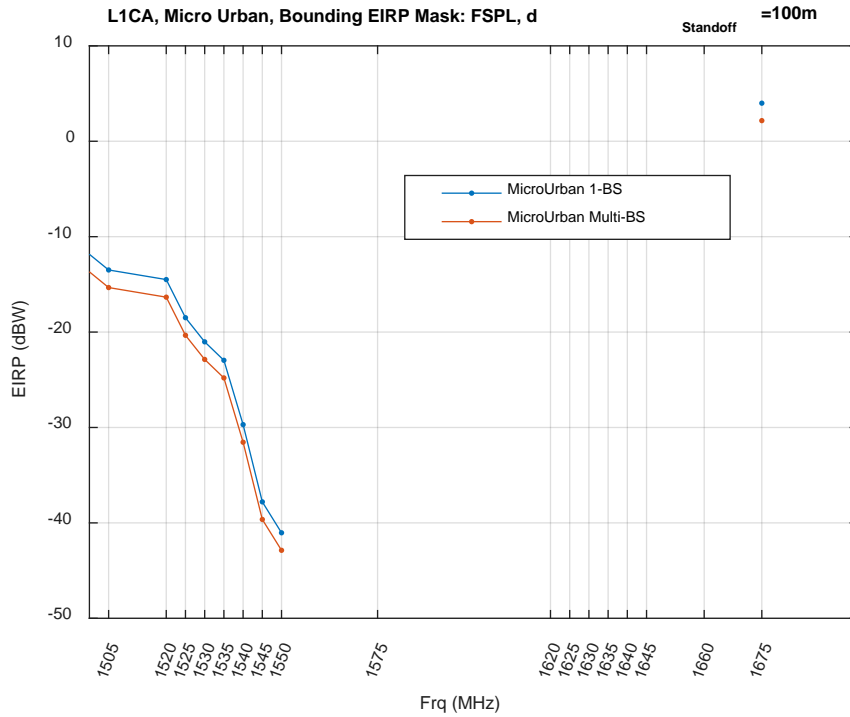


**Figure 4-19: Overlay of  $EIRP(X, f)$  tolerance masks for the case of a single base station and that of multiple transmitter case**

#### 4.1.6.2.2 Effects of Propagation Models

The results shown so far are based on FSPL propagation. The sensitivity of HPR results to the use of two ray path loss as opposed to FSPL model is considered in this section for the case of micro urban single transmitter. The Irregular Terrain Model is the same as the FSPL model for standoff distances up to 100 m and is therefore indirectly accounted for in this analysis. The two ray path loss tolerable EIRP map and the EIRP function of standoff distance are Figure 4-20.

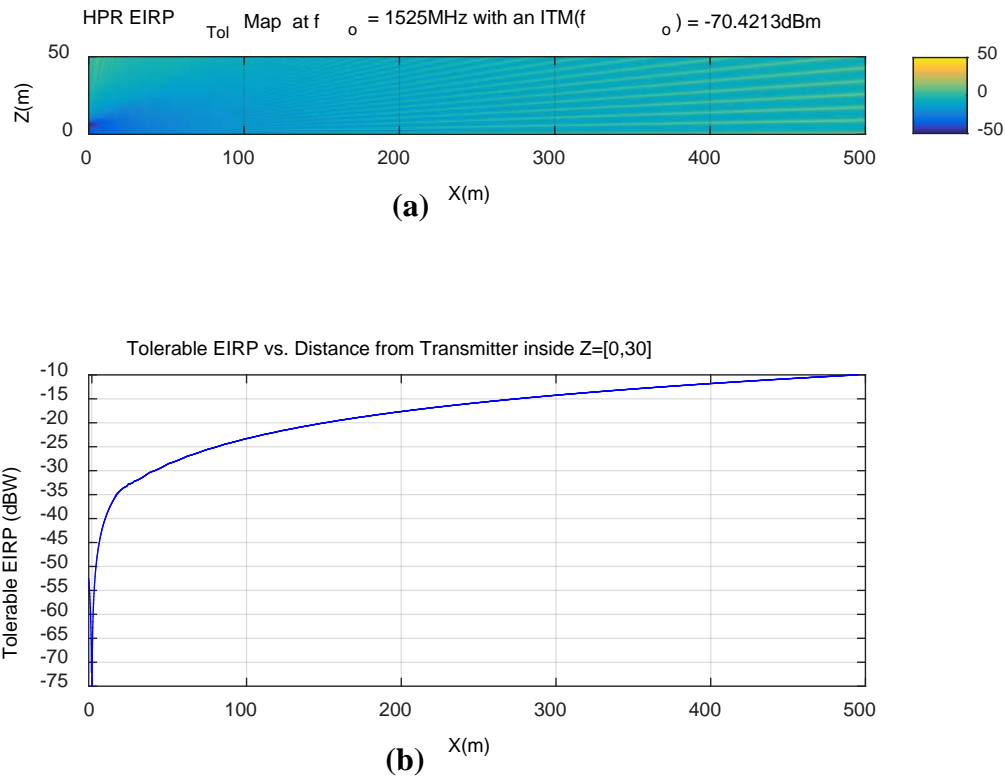


**Figure 4-14: Tolerable EIRP levels for the case of two ray path loss propagation model.**

- (a) Tolerable  $EIRP(\vec{r}, f)$  map in the vertical plane,**
- (b) tolerable  $EIRP(X, f)$  as a function of standoff distance X.**

The two ray  $EIRP(X, f)$  is overlaid with the FSPL in Figure 4-21 (a), and their difference is shown in Figure 4-21 (b). These figures show that tolerable EIRP levels are similar for both models up to a distance of about 20 m after which the two ray path loss results in lower tolerable levels. For a standoff distance of 100 m, the two ray path loss results in 4.8dB lower tolerable level than that of FSPL.

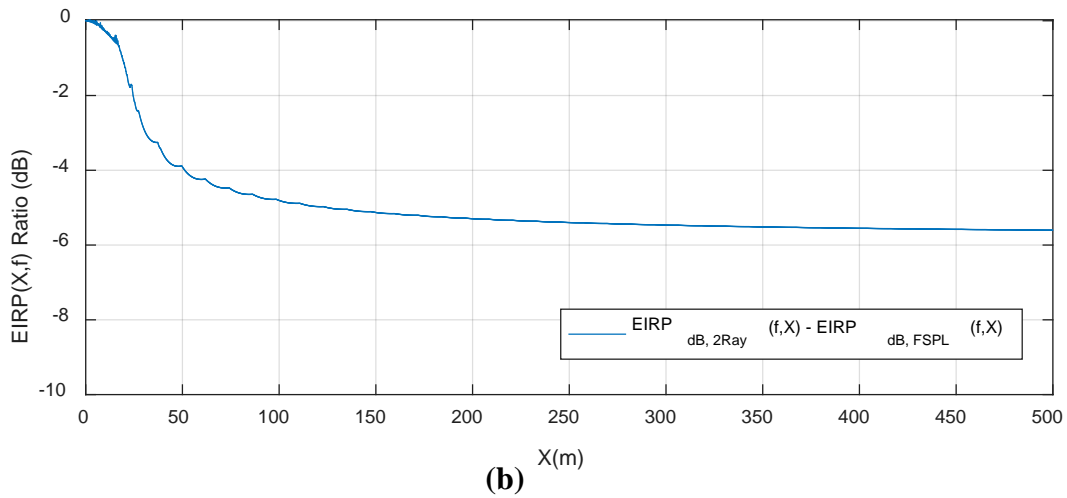
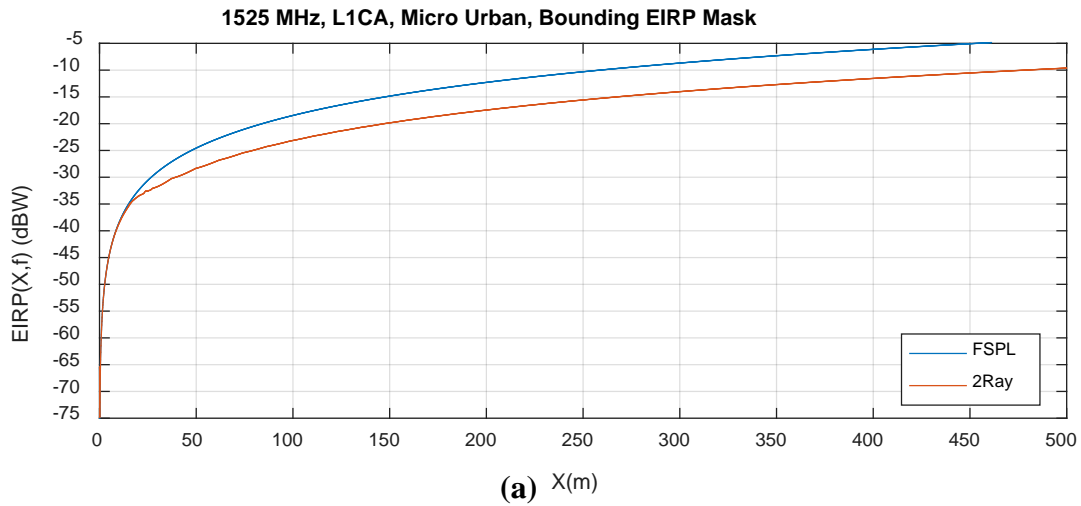


**Figure 4-15: (a) Overlay of  $EIRP(X, f)$  as a function of standoff distance  $X$  for the case of FSPL and two ray path loss propagation, (b) ratio of  $EIRP(X, f)$  in the above plot in dB**

This analysis is applied to the remaining downlink frequencies and an EIRP tolerance mask for the two ray path loss is produced. This mask is overlaid with that of FSPL in Figure 4-22. A more comprehensive set of results is presented in Appendix J.

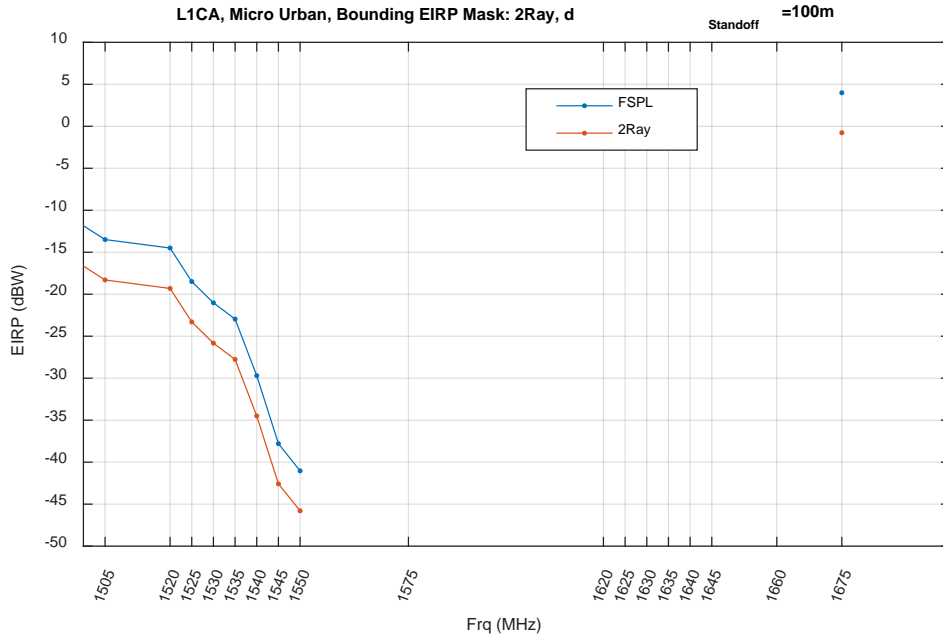


**Figure 4-16: Comparison between two ray and FSPL EIRP tolerance masks  $EIRP(X, f)$  for  $X=100m$  standoff distance**

#### 4.1.6.2.3 EIRP masks for Median ITMs

EIRP levels based on median ITMs protect 50% of the tested receivers and leave the rest unprotected. The resulting EIRP levels corresponding to the median masks are shown in Figure 4-23 for a micro urban cell transmitter and L1 C/A signals.

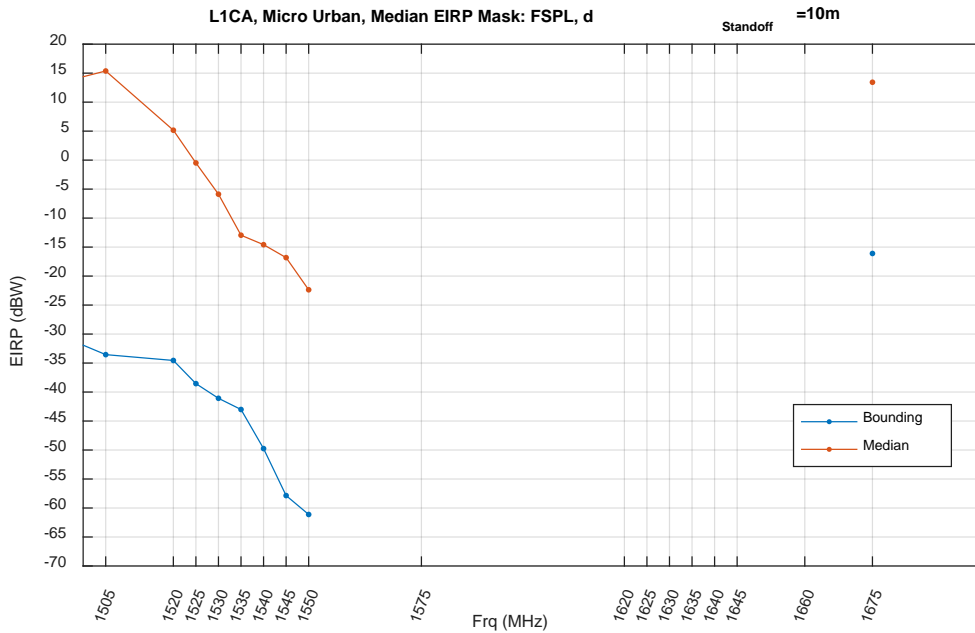


**Figure 4-17: EIRP levels corresponding to L1 C/A median ITMs**

Because of the linearity of the inverse modeling equation, at a particular frequency, the difference in the tolerable EIRP levels equals the difference between the bounding and the median ITMs for that same frequency in dB.

#### **4.1.7 Summary of Transmit Power Level Calculation**

The approach to determine tolerable EIRP levels for a given standoff distance (inverse modeling), as well as the one to determine minimum standoff distance for a given EIRP value (forward modeling) were described in section 4.1.4. Interference source (transmitter) characteristics were primarily obtained from M.2292 (Characteristics of Terrestrial IMT-Advanced Systems for Frequency Sharing/Interference Analyses) and proposals to FCC for adjacent band network applications. Base station characteristics are summarized in Table 4-1 and handset characteristics are summarized in Section 4.1.2.2. Base station antenna patterns are shown in Figure 4-2 and Figure 4-3.

GNSS receiver antenna measurements for each one of the 22 frequencies used in the WSMR tests were done to determine the appropriate antenna pattern to use for each category of receivers. Parabolic fits to these measurements were ultimately used as inputs to the forward and inverse modeling calculations. The results of these fits are shown in Table 3-16 and Table 4-5 for vertical and horizontal polarization respectively. The propagation loss was estimated through the FSPL model and the Two-ray model. Since the Irregular Terrain Model is expected to have the same properties as FSPL for distances up to 100 meters it is indirectly considered as part of the FSPL analysis.

Tolerable EIRP levels for base stations that protect all tested receivers processing the L1 C/A signal are shown in Table 4-6 at standoff distances of 10 and 100 meters for two different deployments. The base station results for receivers that process the other tested GNSS signals are shown in Table 4-7.

**Table 4-6: Tolerable Base Station  $EIRP(d_s, f)$  for L1 C/A bounding masks for Type-2 Interference signal using FSPL propagation model**

			Tolerable EIRP (dBW) by Interference Frequency (MHz)										
Deployment Type	$d_s$ (m)	Cat	1475	1490	1505	1520	1525	1530	1535	1540	1545	1550	1675
Micro Urban	10	GAV	-14.25	-10.21	-16.92	-23.37	-25.15	-29.99	-31.93	-32.06	-41.96	-51.03	-13.38
		GLN	-13.94	-16.9	-19.58	-23.37	-25.15	-29.99	-31.93	-32.06	-40.02	-49.38	-7.41
		HPR	-23.11	-28.65	-33.55	-34.55	-38.55	-41.08	-43.01	-49.75	-57.86	-61.12	-16.1
		TIM	15.22	14.71	6.65	-5.44	-10.9	-19.85	-26.67	-31.24	-41.14	-50.61	12.73
		CEL	n/a*	n/a*	n/a*	n/a*	13.15	10.77	8.39	-2.56	-12.33	-19.85	11.26
	100	GAV	5.75	9.78	3.08	-3.37	-5.15	-9.98	-11.92	-12.03	-21.95	-31.02	6.63
		GLN	6.06	3.1	0.42	-3.37	-5.15	-9.98	-11.92	-12.03	-20.01	-29.38	12.59
		HPR	-3.03	-8.56	-13.49	-14.5	-18.49	-21.02	-22.96	-29.7	-37.8	-41.04	3.99
		TIM	35.23	34.74	26.69	14.6	9.14	0.19	-6.63	-11.2	-21.1	-30.6	32.73
		CEL	n/a	n/a	n/a	n/a	33.15	30.77	28.39	17.44	7.67	0.15	31.26
Macro Urban	10	GAV	-14.77	-10.75	-17.52	-24.02	-25.8	-30.66	-32.59	-32.82	-42.67	-51.67	-14.02
		GLN	-14.46	-17.44	-20.17	-24.02	-25.8	-30.66	-32.59	-32.82	-40.72	-50.02	-8.05
		HPR	-24	-29.54	-34.39	-35.39	-39.38	-41.92	-43.84	-50.58	-58.7	-61.99	-17
		TIM	14.51	13.93	5.87	-6.25	-11.71	-20.65	-27.47	-32.05	-41.94	-51.3	12.42
		CEL	n/a	n/a	n/a	n/a	13.22	10.84	8.46	-2.49	-12.26	-19.78	11.33
	100	GAV	5.22	9.24	2.47	-4.03	-5.81	-10.68	-12.6	-12.85	-22.68	-31.68	5.97
		GLN	5.53	2.56	-0.18	-4.03	-5.81	-10.68	-12.6	-12.85	-20.74	-30.03	11.93
		HPR	-4.04	-9.58	-14.42	-15.42	-19.41	-21.95	-23.87	-30.61	-38.73	-42.03	2.96
		TIM	34.5	33.91	25.85	13.73	8.27	-0.67	-7.49	-12.08	-21.96	-31.32	32.41
		CEL	n/a*	n/a*	n/a*	n/a*	33.22	30.84	28.46	17.51	7.74	0.22	31.33

\*n/a signifies no CNR degradation of 1-dB was detected within the tested range of interference power



**Table 4-7: Tolerable Base Station  $EIRP(d_s, f)$  for All GNSS bounding masks for Type-2 Interference signal using FSPL propagation model**

			Tolerable EIRP (dBW) by Interference Frequency (MHz)										
Deployment Type	$d_s$ (m)	Cat	1475	1490	1505	1520	1525	1530	1535	1540	1545	1550	1675
Micro Urban	10	GAV	-14.25	-27.21	-25.92	-28.37	-28.88	-32.97	-33.7	-35.01	-41.96	-51.03	-13.38
		GLN	-19.94	-27.21	-25.92	-28.37	-28.88	-32.97	-33.7	-35.01	-41.52	-56.83	-8.05
		HPR	-26.11	-33.65	-33.71	-45.08	-45	-44.82	-44.8	-51.79	-59.85	-62.2	-19.1
		TIM	15.22	4.5	4.8	-5.44	-10.9	-19.85	-26.67	-31.24	-41.14	-50.61	8.23
		CEL	10.68	13.7	14.52	15.35	13.15	10.68	5.25	-2.56	-21.78	-37.68	11.26
	100	GAV	5.75	-7.22	-5.92	-8.37	-8.87	-12.96	-13.7	-14.98	-21.95	-31.02	6.63
		GLN	0.06	-7.22	-5.92	-8.37	-8.87	-12.96	-13.7	-14.98	-21.51	-36.83	11.95
		HPR	-6.03	-13.56	-13.65	-25.02	-24.94	-24.76	-24.75	-31.74	-39.79	-42.13	0.99
		TIM	35.23	24.53	24.84	14.6	9.14	0.19	-6.63	-11.2	-21.1	-30.6	28.23
		CEL	30.68	33.7	34.52	35.35	33.15	30.68	25.25	17.44	-1.78	-17.68	31.26
Macro Urban	10	GAV	-14.77	-27.75	-26.51	-29.02	-29.53	-33.64	-34.36	-35.77	-42.67	-51.67	-14.02
		GLN	-20.46	-27.75	-26.51	-29.02	-29.53	-33.64	-34.36	-35.77	-42.22	-57.47	-8.69
		HPR	-27	-34.54	-34.55	-45.91	-45.83	-45.65	-45.63	-52.62	-60.69	-63.08	-20
		TIM	14.51	3.73	4.02	-6.25	-11.71	-20.65	-27.47	-32.05	-41.94	-51.3	7.92
		CEL	10.75	13.77	14.59	15.41	13.22	10.75	5.32	-2.49	-21.71	-37.61	11.33
	100	GAV	5.22	-7.76	-6.53	-9.03	-9.54	-13.65	-14.37	-15.8	-22.68	-31.68	5.97
		GLN	-0.47	-7.76	-6.53	-9.03	-9.54	-13.65	-14.37	-15.8	-22.24	-37.49	11.3
		HPR	-7.04	-14.58	-14.58	-25.94	-25.86	-25.68	-25.66	-32.64	-40.72	-43.11	-0.04
		TIM	34.5	23.71	24	13.73	8.27	-0.67	-7.49	-12.08	-21.96	-31.32	27.91
		CEL	30.75	33.77	34.59	35.41	33.22	30.75	25.32	17.51	-1.71	-17.61	31.33

As expected from the WSMR tests on receiver susceptibility, the smallest base station EIRP is imposed by the HPR receivers. For L1 C/A signals and macro-urban networks, the tolerable EIRP decreases monotonically from about -24 dBW (4 mW) at 1475 MHz, to -42 dBW (< 0.1 mW) at 1530 MHz, to -62 dBW (< 1  $\mu$ W) at 1550 MHz; for micro-urban networks the results increase by a fraction of a dB. For all GNSS signals, the above values decrease by a few dB.

The tabulated results also show that the results are not sensitive to the deployment type when a single base station is considered. The differences between the two deployments are  $\leq 1$  dB for any frequency, category, and standoff distance combination. The average difference is 0.6 dB. However, the levels that protect all GNSS signals can be as much as 15 dB lower than those needed to protect L1 C/A signals from base station emissions with an average difference of 3.5 dB across all frequencies and five categories considered in Table 4-6 and Table 4-7. It is worthy to note that the difference in results between 10 and 100m standoff distances is a constant of 20 dB with a tolerance of less than 0.1 dB despite accounting for the antenna pattern. This is because for FSPL propagation the tolerable EIRP at a particular standoff distance is found when the phase center of the receiver antenna is approximately aligned with the centerline direction of the transmit antenna's main beam. This will result in a very small difference in angles of incidence and therefore similar receiver gain value at the 10 and 100 meters standoff distances. Therefore, the difference in results between these two standoff distances is primarily controlled by the difference in FSPL which is the ratio of the distances squared in dB.

These values become even smaller if two-ray path loss and aggregation effects are considered. Also, these results did not show significant sensitivity to the transmitter antenna types (omni or sectoral antennas associated with the deployment type).

Tolerable EIRP levels for handsets that protect all tested receivers processing the L1 C/A signal are shown in Table 4-8 at a standoff distance of 10 m. The results in Table 4-8 assume free space propagation and only a single handset. As for the base station results, the EIRP values would become even smaller if two-ray path loss and aggregation effects are considered.

**Table 4-8. Tolerable Handset  $EIRP(d_s, f)$  for GPS L1 C/A-code bounding masks for Type-2 Interference signal using FSPL propagation model at a standoff distance of 10 m**

Tolerable EIRP (dBW) by Interference Frequency (MHz)							
Cat	1620	1625	1630	1635	1640	1645	1660
GAV	-19.2	-17.1	-7.1	-3.7	-5.2	-5.2	-6.6
GLN	-41.3	-38.1	-31.0	-18.1	-13.7	-14.7	-11.9
HPR	-57.0	-47.1	-31.3	-28.3	-28.2	-29.8	-22.1
TIM	-26.3	-19.0	-10.3	-5.9	-1.8	2.7	11.8
CEL	-26.3	-18.1	0.2	9.4	10.9	12.8	13.1

## 4.2 Spaceborne and Science Applications

This section of the report describes the analysis and evaluation of a proposed LTE base station network operating on adjacent radio frequency bands to space-based receivers. The emphasis of this section is on the assessment to GNSS receivers used as a science application. Additional information can be found in Appendix K.

The following evaluation assesses the impact to one of these GNSS-based science applications, radio occultations (RO), where space-based GNSS receivers are used to perform measurements of the troposphere, stratosphere, and up through the layers of the atmosphere until reaching the ionosphere. This is not to say that the other GNSS-based science applications are not affected by a proposed LTE base station network, but RO science is an application that is particularly susceptible and, thus, the focus of this assessment. RO measurements of the atmosphere, coupled with traditional methodologies for Earth observation, have significantly improved accuracy and predictability of weather forecasts. RO measurements of the ionosphere have also improved our ability to monitor ‘space weather’ (the distribution of charged particles in the uppermost part of the atmosphere), which is essential to ensure the successful operation of satellites.

Specifically, NASA’s assessment focuses on the RO receiver, called the TriG (formerly also known as TriGNSS), which was developed by the NASA/Jet Propulsion Laboratory (JPL). The TriG is the newest RO receiver of the BlackJack class of GNSS receivers and can perform substantially more (up to three (3) times more) measurements than previous versions. The increase in performance is partially due to the TriG’s ability to receive signals from all GNSS constellations including the GPS, GLONASS, Galileo, BeiDou, regional space-based navigation constellations such as QZSS and NavIC, and SBAS, such as Wide Area Augmentation System (WAAS) and European Geostationary Navigation Overlay Service (EGNOS).

Radio Frequency Interference (RFI) is a particular problem when GNSS signals are being used for science applications. During RO measurements, the GNSS signal is defocused by tens of dB at low ray heights, where the signal-to-noise ratio (SNR) is already in a marginal zone. In fact, in this already marginal zone, tracking loops cannot be closed and the captured data is running open loop. Additional noise from RFI contaminates these marginal-SNR data over specific areas. The spatially correlated noise can bias the captured data and greatly affect the recent climate record, while providing incorrect weather predictions over the affected areas.

#### **4.2.1 Radio Occultation (GNSS-RO)**

RO/GNSS-RO is the disruption/interruption of GNSS signals from a spacecraft by the intervention of a celestial body. RO is a relatively new method for the indirect measurement of temperature, pressure and water vapor in the stratosphere and the troposphere. These measurements are made from specifically designed GNSS receivers on-board a Low-Earth-Orbit (LEO) satellite. The techniques utilize the unique radio signals continuously transmitted by the GNSS satellites (GPS, GLONASS, Galileo, etc.) orbiting the Earth at an approximate altitude of 20,000 km above the surface. The GNSS radio signals are influenced both by the electron density in the ionosphere and by the variations of temperature, pressure and water vapor in the atmosphere which are used in meteorology. RO measurements are also used to derive various ionospheric parameters (Total Electron Content (TEC), Electron Density Profiles (EDP), L-band scintillation, etc.) for understanding earth and space weather dynamics.

From the point of view of a LEO satellite (at an altitude of 700-800 km), the GNSS satellites continually rise above, or set behind, the horizon of the Earth. During these so-called "radio occultation", where the GNSS and the LEO satellite are just able to "see" each other through the atmosphere, the GNSS signals will be slightly delayed and their ray path slightly bent (refracted) on the way through the layers of the atmosphere (see Figure 4-24). The excess range increases as the ray propagates through denser media at lower altitudes (and highly-refractive water vapor in the atmosphere). This delay is a function of density ( $n/V$ ), which is related to temperature by the ideal gas law:  $P \cdot V = n \cdot R \cdot T$ .

A typical occultation sounding will last one (1) to two (2) minutes, and during this time the LEO satellite will receive signals where the ray paths have different minimum distances to the surface of the Earth, from zero up to approximately 100 km. The GNSS satellites transmit on multiple frequencies, and with a receiver rate of 50 Hz this will yield around 6000 rays, making up two profiles of phase residuals up/down through the lowest 100 km of the atmosphere and the ionosphere up to, or down from, the ~700 km height of the LEO satellite.

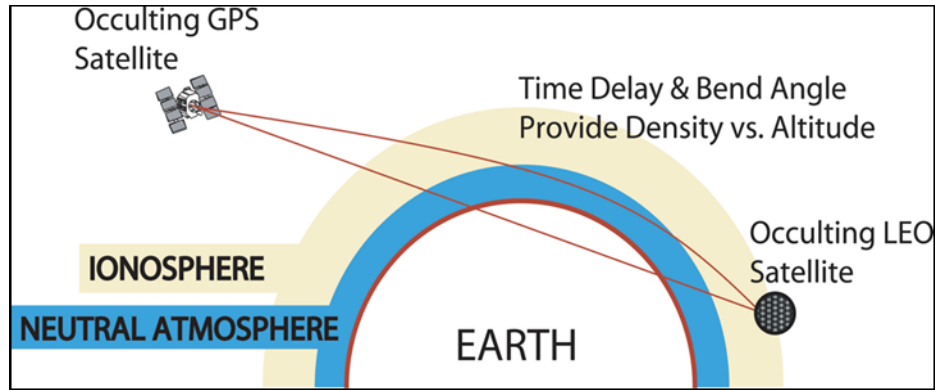


**Figure 4-24: Straight Line versus Actual Path of GNSS Signal**

The residual positioning error and determination of time delays, derived from the measurements taken during a RO event, are key parameters in the obtaining the temperature, pressure, and water vapor characteristics of the atmosphere at different heights. Given sub-mm measurement precision, RO can determine atmospheric temperature profiles to 0.1 – 0.5 Kelvin (K) accuracy from 8 - 25 km height levels.

NASA has several radio occultation receivers in its portfolio, including the Integrated GPS Occultation Receiver (IGOR), the IGOR+, and the more recently developed receiver called the TriG receiver.

#### **4.2.2 NASA/JPL TriG Receiver Overview**

The NASA/JPL developed TriG receiver functions as a multi-function GNSS receiver. This single receiver has multiple antenna inputs and can be configured to operate in a navigation capacity, as well as, simultaneously, in a scientific measurement role. In its traditional function, coupled with a choke ring antenna, the TriG serves as a device for space vehicle navigation and precise orbit determination (POD). The receiver provides accurate information to space vehicle operators on position, velocity, and time.

Configured in a scientific measurement mode, the TriG, coupled with a series of specially designed antenna arrays, performs RO measurements of GNSS signals. TriG receivers are able to receive all GNSS signals: GPS, Galileo, GLONASS, Compass, as well as other navigation signals (QZSS, DORIS, etc.). This capability increases the number of RO measurements that can be made during any given orbit.

#### **4.2.3 Spaceborne Receiver Assessment for Science-Based Applications**

NASA has performed an assessment of the potential impacts caused by a proposed terrestrial LTE network operating in the adjacent band to GPS L1. Two (2) future science missions, COSMIC-2 and Sentinel-6 (formerly, Jason Continuity of Service (Jason-CS)), were used as the

basis for these assessments. NASA's assessment is to the TriG receiver performing a science application using the RO technique.

To determine the impact to the TriG receiver, the aggregate interference power at the output of the TriG receiver antenna was calculated using MATLAB to model the interference scenario, as well as the TriG receiver system, and simulate the interference effects to the satellites in orbit. Satellites operating in LEO gain a much broader view of the earth (dependent upon antenna characterizations and operating parameters), which must be accounted for in performing the analysis.



**Figure 4-18: Example Satellite View of the U.S. Cities**

Unlike the assessments performed in Section 3, in-orbit satellites will see a greater number of potential interference sources (e.g. – increased number of terrestrial Base stations (ES)) and the aggregate of those interference sources will be the major contributing factor in the assessment, see Figure 4-25.

#### **4.2.3.1 Summary of TriG Receiver System Characteristics Used for Analysis**

Table 4-9 summarizes the satellite TriG receiver system characteristics for the analyses performed on COSMIC-2 and Sentinel-6. The interference threshold in this table is the RFI power at the output of the flight RO antenna which causes a -1 dB C/No degradation in the TriG receiver as used in the COSMIC2-A mission. It was derived from the power density observed by the 0 dBiL standard gain horn used in during the DOT ABC test at a RFI power level causing a 1 dB C/No degradation. Since the TriG choke ring antenna was located at a different spot, it actually received about 3.2 dB more RFI power per meter squared ( $m^2$ ). In addition, the choke ring antenna had about +3.7 dBi linear gain toward the RFI source, adding 3.7 dB to the threshold power. After these corrections, the LTE power at 1530 MHz that causes a 1 dB C/No degradation is  $-78.2 \text{ dBm} + 3.2 \text{ dB} + 3.7 \text{ dB} = -71.3 \text{ dBm}$ , defined at the output of the receive antenna.

Another adjustment that was made to estimate the effect on the flight receiver is the difference in noise floors due to the extra antenna temperature from black body radiation coming from the ceiling and walls of the WSMR anechoic chamber. During the test, the noise floor is estimated

to be 349 Kelvin (K). This is based on preamplifier (Preamp) noise of 51 K, antenna temp of 300 K, and filter loss of 0.8 dB. The noise floor in flight is estimated to be 224 K based on Preamp noise of 51 K, antenna temp of 150 K, and filter loss of 0.8 dB. This difference shows an adjustment to lower the 1 dB threshold by 1.9 dB. Therefore, the normalized in-flight RFI power of is calculated to be approximately -73 dBm (-71.3 dBm – 1.9 dB = -73.2 dBm) from the antenna corresponding to a -1 dB degradation of C/No.

**Table 4-9: Summary Table of Satellite TriG Receiver Characteristics Used for Modeling and Simulation**

Receiver Characteristic	COSMIC-2	Sentinel-6
Satellite Orbit Altitude	800 km	1330 km
Satellite Orbit Inclination Angle	72°	66°
TriG Forward Receive Antenna Type	12-Element Array	6-Element Array
TriG Forward Receive Antenna Downtilt (relative to satellite velocity vector)	26.2°	34.2°
TriG Forward Receiver Antenna Main-Beam Gain @ 1530 MHz (single subarray)	+ 13.4 dBic	+ 10.5 dBic
TriG Aft Receive Antenna Type	Not modeled	12-Element Array
TriG Aft Receive Antenna Downtilt (relative to satellite velocity vector)	Not modeled	34.0°
TriG Aft Receiver Antenna Main-Beam Gain @ 1530 MHz (single array)	Not modeled	+ 12.5 dBic
Interference Threshold (-1 dB C/No)	- 73 dBm	- 73 dBm

#### 4.2.3.2 Terrestrial LTE Deployment Scenarios

The aggregate interference is dependent upon several factors. A few factors are satellite related, including orbital parameters and receiver system characteristics. The other determining factor comes from the interference sources. The most important factor is the transmitter characteristics and the total number of sources (e.g., LTE base stations (BS)). Since TriG receiver systems (performing the RO technique) operate in LEO, they have a direct line-of-sight to a broad area of the U.S., and the aggregate interference is dependent upon the long-term deployment scenario of the LTE operator.

NASA used three parameters, the City Zone model, the City Population and the BS Cell radius to determine the total number of BS that could be deployed in the LTE network. The assumptions used for each of the parameters are described below.

The City Zone model was used to determine the physical area around a city center location that the simulated LTE network would be deployed over. The baseline City Zone model was chosen to conform to the only available accepted model given in ITU Report ITU-R SA.2325-0 [4] (International Mobile Telecommunication (IMT) sharing at 2GHz) for an BS deployment based on three (3) zones (e.g. – urban, suburban, and rural) with given radial distances from a city center latitude/longitude location. An example City Zone model with the typical macro cellular will have a hexagonal grid layout deployed about a city center. Because the LTE services to be provided by the proposed and analyzed network may not be as widespread in terms of city area as the conventional LTE deployment described in SA.2325-0 a second City Zone model with a smaller Suburban and Rural zone size was analyzed. Parameters for both the City Zone models are listed in Table 4-10.

**Table 4-10: Zone Model - ES Zone-specific Radial Distance from City Center**

<b>Zone Model</b>	<b>Urban Zone (km)</b>	<b>Suburban Zone (km)</b>	<b>Rural Zone (km)</b>
1	0 – 3	3 – 20	20 – 50
2	0 – 3	3 – 10	10 – 30

In addition to a City Zone model it was necessary to define the BS cell radius (CR) parameter in order to determine the BS grid layout within each City Zone. The typical M.2292 zone values listed in Table 4-11 were used as the baseline cell radius (CR) in the simulation.

In consideration to the where the proposed LTE network is to be deployed, the size of the city population was an additional parameter that was included in the simulations. If a U.S. city had a population of greater than 125,000, but less than 250,000, it was included in the analyses for half of the simulations. Cities with populations of over 250,000 were included in all simulations.

Accordingly, the number of assumed cities included in each simulation was chosen from:

- City Population > 125K: 225 cities or
- City Population > 250K: 82 cities

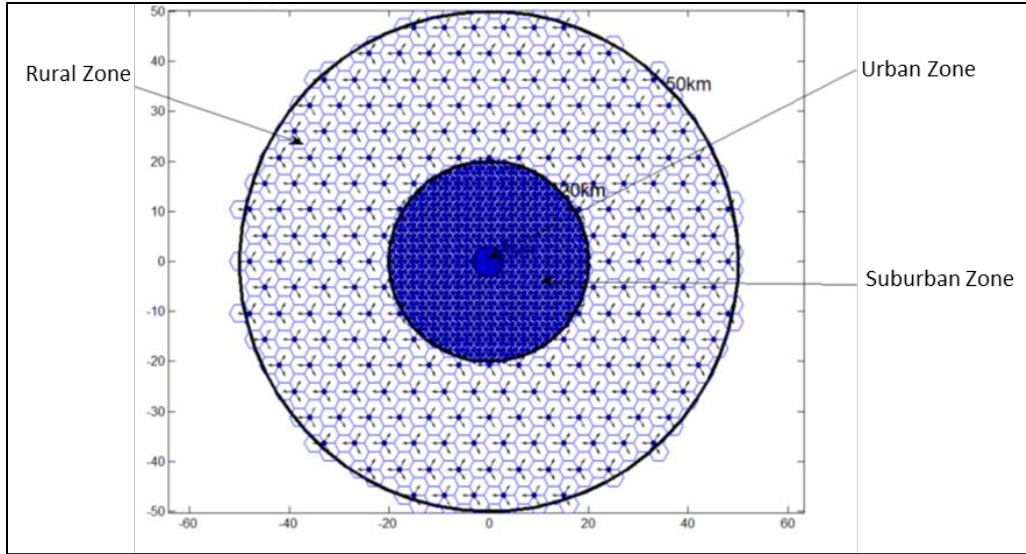


**Figure 4-196: Base station Deployment Zone Model (Report ITU-R SA. 2325-0)**

**Table 4-11: Typical Cell Radius (CR) - M.2292**

Zone Type	City Population	CR (km)
Urban	All	0.5
Suburban	All	1.0
Rural	All	5.0

In addition to the above ‘typical’ model for the cell radius, half of the 16 simulation groups use a variation of the cell model, referred to as ‘scaled’ model. In the ‘scaled’ model, the cell radius increases up to double its typical value, as the city population decreases. This decreases the effective number of cell stations, as well as the resulting interference.

Using the set of Zone Model, City Population and Cell Radius parameters, NASA calculated the total number of BS required for deployment for each simulation run. Table 4-12 depicts the number of Base stations for the set of three parameters for a LTE network deployment consisting of only macrocells.

**Table 4-12: Total # of BS (Macrocell Deployment Only)**

Zone Model	City Population (in 1000s)	Cell Radius	Number of BS			
			Urban	Suburban	Rural	Total
1	> 125	Table 4-10	11,700	143,100	29,700	184,500
1	> 250	Table 4-10	4,264	52,152	10,824	67,240
2	> 125	Table 4-10	11,700	33,750	12,150	57,600
2	> 250	Table 4-10	4,264	12,300	4,428	20,992



### 4.2.3.3 Summary of BS Transmitter System Characteristics Used for Analysis

In addition to the parameters described above, the following simulation parameters were considered and chosen by NASA for the analysis performed.

- BS antenna side-lobe pattern:
  - F.1336-4 Recommends 3.1. (Macro)
  - F.1336-4 Recommends 3.2. (Micro)

Elevation Mask: Two (2) BS mask angles are utilized for the analysis:

- A 0° elevation mask on the BS so that all BS that see the satellite above 0° elevation angle are included in the aggregate interference calculation, and
- A 5° mask angle so that only BS that see the satellite above 5° elevation angle contribute to the aggregate interference.

BS Activity Factor (AF):

An AF of 3 dB, corresponding to 50% of the Base stations transmitting simultaneously, is used throughout the analysis.

*Note:* If 100% of the Base stations are transmitting simultaneously, the peak interference levels in the results will be 3 dB higher. In this case the other resulting interference statistics would be increased in time duration or frequency of occurrence as well.

BS Transmitter Power (EIRP):

Table 4-13 depicts the nominal transmit power used for some of the simulations (as per M.2292). Considerations were also given to the maximum transmit powers of 10 dBW and 32 dBW EIRP per channel per sector.

**Table 4-13: Assumed Transmitter Levels per Sector (Typical per M.2292)**

BS Type	Typical Max. Transmit Power/Channel/Sector (EIRP)
Macrocell - Urban	26 dBW
Macrocell - Suburban	26 dBW
Macrocell - Rural	28 dBW
Microcell (any zone)	7 dBW

### 4.2.3.4 TriG Receiver Analysis

Two (2) NASA missions (COSMIC-2 and Sentinel-6) that include the TriG receiver, as a science-based function (e.g. - RO technique) were utilized for analysis. A MATLAB simulation program was developed to model the receiver on-board a satellite, using mission-specific parameters, and interference statistics were calculated for an LTE network deployment of BS distributed in U.S. cities.

For the spaceborne receiver analysis the aggregate interference power at the output of the GPS receiver antenna is calculated at ten (10) second time steps in the satellite orbit from BS distributed among U.S. cities. The MATLAB program was set up to model a 10-day orbit of the satellite.

The analysis calculates the interference value and is not dependent upon the carrier signal. The aggregate interference to the receiver antenna output is calculated using a summation of the interference from each source. A simple link budget formula is used to calculate the interference received from a single source, LTE BS. The total aggregate interference is determined through the summation of interference from the individual sources:

$$\mathbf{Rx\ Int\ Pwr}_{\mathbf{agg}} = \sum_{(\mathbf{Int\ sources})} \mathbf{Tx\ Pwr\ (EIRP)}_{\mathbf{off-boresight}} - \mathbf{FSPL} - \mathbf{Pol\ Loss} + \mathbf{Rx\ Ant\ Gain}_{\mathbf{off-boresight}}$$

where,

**Rx Int Pwr<sub>agg</sub>** = Aggregate interference power level (dBm)

**Tx Pwr (EIRP)<sub>off-boresight</sub>** = Tx power output including antenna off-boresight calculations (dBm) (See below)

**FSPL** = Free Space Loss (dB)

**Pol Loss** = Loss of dissimilar polarizations (Linear to RCHP Polarization = - 3 dB)

**Rx Ant Gain<sub>off-boresight</sub>** = Rx antenna gain including off-boresight calculations (dBic)

The macro and micro cell sector antenna gain value towards the satellite for each time step was calculated by determining the off-boresight azimuth (AZ) and elevation (EL) look angle gain value from the appropriate F.1336 model gain pattern equations<sup>2</sup>.

A total of 96 simulation runs were performed for COSMIC-2, while a lesser, but still representative, number of runs (16 runs) were performed for Sentinel-6. Each of the simulation runs varied one or more LTE BS deployment parameters.

While it is unknown how the LTE operator will be performing their network deployment, the variations in simulation runs should be demonstrative. Further, the variations in runs may be representative of an LTE network through its various phases of deployment (initial deployment through full deployment).

Table 4-14 shows how the various parameters of the terrestrial network and the space receiver are modeled in the different runs of simulation-1 group.

---

<sup>2</sup> As defined in M.2292 and F.1336-4.

**Table 4-14: Summary of Simulation Runs**

Run	Sim No.	Run Designator	COSMIC-2	Sentinel-6	BS Tx EIRP	Zone Model	City Population	Cell Radius	Elevation Mask	Macrocell Only	Total # of Earth Stations
1	1	a	X		M.2292 levels	1	> 125K	Typical	0°	X	184,500
2	1	b	X	X	M.2292 levels	1	> 125K	Typical	5°	X	184,500
3	1	c	X		32 dBW	1	> 125K	Typical	0°	X	184,500
4	1	d	X		32 dBW	1	> 125K	Typical	5°	X	184,500
5	1	e	X		10 dBW	1	> 125K	Typical	0°	X	184,500
6	1	f	X	X	10 dBW	1	> 125K	Typical	5°	X	184,500

#### 4.2.3.5 Results

The aggregate interference results for the TriG receiver, functioning as a science measurement instrument, are presented in the following.

The received aggregate interference levels calculated during the simulations range from -90 dBm to -40 dBm.

The following tables use an aggregate interference threshold of -73 dBm (1526 – 1536 MHz) which corresponds to a -1 dB degradation of receiver C/No.

It should be noted that the loss-of-lock threshold for the TriG receiver occurs between -59 to -35 dBm aggregate interference power in the 1526-1536 MHz band. Loss-of-Lock at -59 dBm was seen in Test 04 with RFI at 1525 MHz and LOL at -35 dBm was seen in Test 04 at 1530 MHz.

The entries in the results tables are interpreted as follows:

- **Column 3: Max Int. Level (dBm)**  
Indicates the maximum aggregate interference level calculated at the receiver antenna output.
- **Column 4: % Time > Threshold**  
Indicates the percent time, over the 10-day simulation period, where the aggregate interference at the TriG receiver antenna output exceeds the threshold level (-73 dBm). As an example, if the value is about 10% of the time, the TriG receiver will have C/No degraded by at least 1 dB for a cumulative of 24 hours.
- **Column 5: # of Int Events**  
Indicates that over the 10-day period, the total number of interference events which exceed the -73 dBm threshold.
- **Column 6: Avg Dur Int Event (min)**  
Indicates the mean average duration (in minutes) of an interference event for the entire 10-day period. As discussed before, the duration of an atmospheric occultation (as the signal path moves from skimming the Earth's surface to an altitude of about 100 km) is only one to two minutes.

- **Column 7: Max Int Event (min)**  
Indicates the maximum duration (in minutes) that was recorded for a single interference event over the 10-day period.
- **Column 8: Max Allow EIRP Level (dBW/10 MHz)**  
Indicates a reverse-engineered maximum BS transmitter power level (in dBW) distributed across a 10 MHz bandwidth per channel per sector. The reverse-engineered value calculated in this column would bring the interference level to the -73 dBm threshold value for 1 dB C/N<sub>0</sub> degradation. The calculated level is based on the maximum interference level received during the 10-day period.

Table 4-15 shows the COSMIC-2 results for the simple scenario of macro cell BS at 32 dBW EIRP. As the number of stations decreases from simulation 1 to 2 for the zone-1 model, and from simulation 5 to 6 for the zone-2 model, there is about 5 dB less interference in zone-2 compared to zone-1, which is expected because the zone-2 model uses about 3 times less stations. There is about 4 dB less interference in models using transmitter elevation mask of 5° (run d) compared to the 0° mask (run c), indicating that less than half of the available stations affect the satellite in the 5° mask case. For the most challenging model (1c), using 184,500 macro cell stations, the tolerable EIRP is 11 dBW.

**Table 4-15: COSMIC-2 Interference Results (Macro BS Only, All BS Tx Power 32 dBW)**

Sim No.	Run Designator	Max Int. Level (dBm)	% Time > Thresh	# of Int Events	Avg Dur Int. Event (min)	Max Int Event (min)	Max Allow EIRP Level (dBW/10 MHz)
1	c	-52	6.9	141	6.9	14.5	11
1	d	-56	4.7	101	6.5	11.8	15
2	c	-57	5.0	132	5.3	12.0	16
2	d	-61	3.4	96	4.9	10.2	20
5	c	-57	4.5	109	5.7	12.8	16
5	d	-61	3.0	74	5.8	10.2	20
6	c	-62	2.9	99	4.1	10.3	21
6	d	-66	1.9	55	4.8	8.2	25

Table 4-16 shows the Sentinel-6 results for the simple scenario of macro cell ES at 32 dBW EIRP, and as the number of stations decreases from simulation 3 to 4 for the zone-1 model. There is about 2 dB less interference in models using transmitter elevation mask of 5° (run d) compared to the 0° mask (run c), indicating that more than half of the available stations affect the satellite in the 5° mask case. For the most challenging model (3c), using 74,612 macro cell stations, the tolerable EIRP is 23 dBW.

Please note that simulations 3 and 4 use the above mentioned variation of the cell model, referred to as ‘scaled’ model, in which the cell radius increases up to double its typical value, as the city population decreases; this results in fewer stations, and less interference, compared to the simulations 1 and 2.

**Table 4-16: Sentinel-6 Interference Results  
(Macro BS Only, All BS Tx Power +32 dBW/10 MHz)**

Sim No.	Run Designator	Max Int. Level (dBm)	% Time > Thresh	Max Allow EIRP Level (dBW/10 MHz)
3	c	-64	7.3	23
3	d	-66	5.2	25
4	c	-68	4.9	27
4	d	-70	3.4	29

## 5. CERTIFIED AVIATION RECEIVER

### 5.1 Determination of Tolerable Interference Levels

Certified GPS, GPS/SBAS and GPS/ground-based augmentation system (GBAS) airborne equipment will meet their performance requirements when operating within the radio frequency (RF) interference (RFI) environment defined in appropriate Federal Aviation Administration (FAA) Technical Standard Orders (TSOs). These technical standard orders invoke industry Minimum Operational Performance Standards (MOPS) developed through RTCA (RTCA/DO-229, RTCA/DO-253 and RTCA/DO-316). Sections 3.7.2 and 3.7.3 of the International Civil Aviation Organization (ICAO) GNSS Standards and Recommended Practices (SARPs) [5] also contain Continuous Wave (CW) and band limited noise interference levels, respectively, for which these receivers satisfy their performance specifications and operational objectives.

This analysis addresses all receivers compliant with the requirements<sup>3</sup> of:

- Technical Standard Order (TSO)-C145()<sup>4</sup>, *Airborne Navigation Sensors Using The Global Positioning System Augmented By The Satellite Based Augmentation System*. This standard invokes RTCA/DO-229, *Minimum Operational Performance Standards for GPS/Wide Area Augmentation System Airborne Equipment*.
- TSO-C146(), *Stand-Alone Airborne Navigation Equipment Using The Global Positioning System Augmented By The Satellite Based Augmentation System*. This standard invokes RTCA/DO-229, *Minimum Operational Performance Standards for GPS/Wide Area Augmentation System Airborne Equipment*.
- TSO-C161(), *Ground Based Augmentation System Positioning and Navigation Equipment*. This standard invokes RTCA/DO-253, *Minimum Operational Performance Standards for GPS/Local Area Augmentation System Airborne Equipment*.
- TSO-C196(), *Airborne Supplemental Navigation Sensor for Global Positioning System Equipment Using Aircraft-Based Augmentation*. This standard invokes RTCA/DO-316, *Minimum Operational Performance Standards for GPS/Aircraft-Based Augmentation System Airborne Equipment*.
- TSO-C204(), *Circuit Card Assembly Functional Sensors using Satellite-Based Augmentation System (SBAS) for Navigation and Non-Navigation Position/Velocity/Time Output*. This standard invokes RTCA/DO-229, *Minimum Operational Performance Standards for GPS/Wide Area Augmentation System Airborne Equipment*.
- TSO-C205(), *Circuit Card Assembly Functional Class Delta Equipment Using The Satellite-Based Augmentation System For Navigation Applications*. This standard invokes RTCA/DO-229, *Minimum Operational Performance Standards for GPS/Wide Area Augmentation System Airborne Equipment*.
- TSO-C206(), *Circuit Card Assembly Functional Sensors using Aircraft-Based Augmentation for Navigation and Non-Navigation Position/Velocity/Time Output*. This

---

<sup>3</sup> Where specifications are referenced, the latest version is assumed.

<sup>4</sup> “()” encompasses all versions.

standard invokes RTCA/DO-316, *Minimum Operational Performance Standards for Global Positioning System/Aircraft Based Augmentation System Airborne Equipment*.

Note that many receivers were designed to comply with the RFI environments defined within these standards even though they were certified to an earlier standard (TSO-C129a<sup>5</sup>). This analysis does not specifically address receivers that comply only with TSO-C129a. However, that category of receivers<sup>6</sup> was designed to be lower-performance and narrowband. If the receivers assessed under this analysis are shown to be compatible with signals from a network, the FAA then accepts any residual risk that some early-generation GPS receivers not tested to RTCA/DO-229, RTCA/DO-253, and RTCA/DO-316 may experience harmful interference.

### **5.1.1 Area of Aviation Operation**

As the National Airspace System (NAS) continues the transition to Performance Based Navigation (PBN), GNSS and its aircraft-, satellite-, and ground-based augmentation systems (ABAS, SBAS and GBAS) will serve as the key enablers of satellite-based navigation and of surveillance through Automatic Dependent Surveillance-Broadcast (ADS-B).

The Wide Area Augmentation System (WAAS), FAA's SBAS, providing service in North America, was commissioned for initial operational capability in 2003. Users equipped with certified WAAS equipment now have access to precision vertical approach at thousands of airports given the development of Localizer Performance with Vertical Guidance (LPV) procedures across the NAS. WAAS also provides these users with the ability to fly area navigation (RNAV) procedures in the en route and terminal areas. Further, the FAA has approved the use of WAAS for en route and terminal operation in the NAS without requiring any other equipment onboard general aviation aircraft. WAAS is also an essential positioning source for most ADS-B compliant aircraft.

GPS, with aircraft-based augmentations such as Receiver Autonomous Integrity Monitoring (RAIM), serves a large number of users in the NAS. Air carriers and high end business users integrate GPS/RAIM with their Flight Management System (FMS) to conduct RNAV procedures within en route and terminal areas.

Currently, there are two public-use GBAS ground systems in the NAS providing Category (CAT) I procedures serving airports at Newark and Houston. The FAA anticipates increased adoption of GBAS in the near-future as aircraft OEMs continue to equip aircraft with GBAS and a number of airports install GBAS following the successful implementation in Houston and Newark. CAT II and III procedures are also anticipated with new or updated ground systems.

---

<sup>5</sup> TSO-C129, Airborne Supplemental Navigation Equipment Using the Global Positioning System (GPS).

<sup>6</sup> These receivers should not be confused with the “non-certified aviation receivers” addressed elsewhere in this Report.

The analysis in this Report is based on the concept of an “assessment zone” (Figure 5-1) inside of which GPS performance may be compromised or unavailable and GPS-based safety systems will be impacted accordingly due to the elevated levels of RFI.

The derivation of the assessment zone concept was based on engineering and operational assumptions where helicopter operations are the limiting factor. As expected, this concept generated a number of comments and questions from the community. It is worth noting that one rotorcraft operator stated that its pilots use visual reference within the assessment zone and the assessment zone would have no negative impact on their operation. However, from [6], there were unresolved concerns expressed by several, though not all, operators about the assessment zone and its impacts to aviation operations and safety.

These concerns include: technical and human factors issues associated with re-initialization of GPS after loss of the signal or when the signal reception is intermittent; workload and human factors impacts on pilots to monitor and track assessment zone locations; the possibility that pilot workload, confusion, or error could lead to aircraft inadvertently entering an assessment zone and losing needed GPS functionality; and impacts to onboard and ground systems that are dependent upon GPS, such as ADS B/C, or fixed-wing and helicopter terrain awareness warning system (TAWS/HTAWS) including obstacle alerting [6].

The FAA has not completed an exhaustive evaluation of the operational scenarios in developing this assessment zone. Further, the current analyses do not include an operational assessment of the impact of the assessment zone in densely populated areas. For example, the risk posed to people and property for operations such as unmanned aircraft systems (UAS) using certified avionics may be significant as such aircraft may be required to operate within the assessment zone.



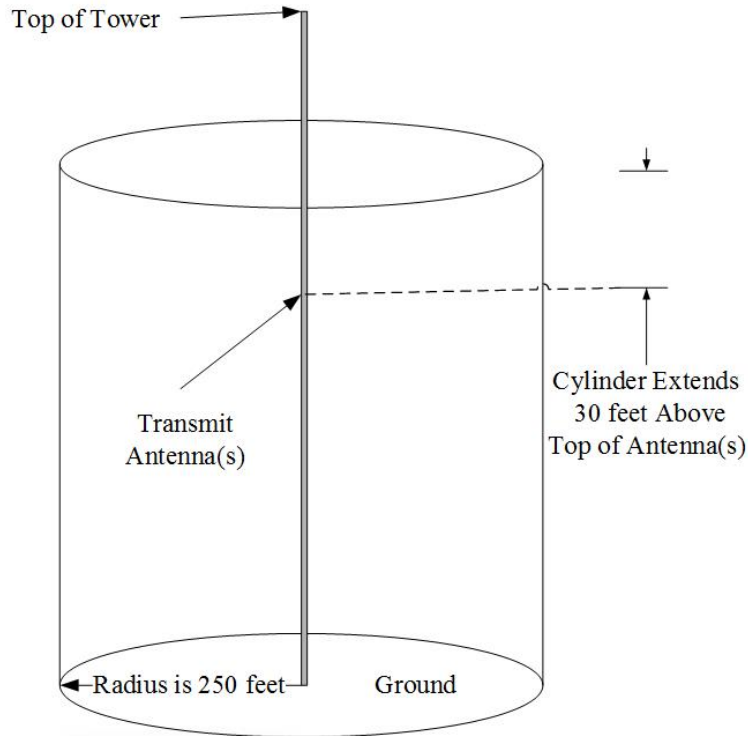


**Figure 5-1: Candidate Assessment Zone (Not to Scale)**

### 5.1.2 Tracking and Acquisition Thresholds

The tracking and acquisition performance requirements for GPS airborne receivers are defined in FAA TSO-C145, TSO-C146, TSO-C161, TSO-C196, TSO-C204, TSO-C205 and TSO-C206. The RFI aspects of these standards are identical. The relevant characteristics were first published in 1996 and invoked by the FAA in May of 1998. The same requirements have been harmonized internationally [ [5], paragraph 3.7.4] since 2001. The passband for this equipment is from 1565.42 MHz to 1585.42 MHz.

#### 5.1.2.1 Receiver Tracking Limit Criteria for Adjacent-Band RFI

MOPS adjacent- and in-band RFI rejection requirements are specified for continuous wave (CW, narrowband) radio frequency interference for the GPS band. All TSO (and European TSO [ETSO]) approved equipment is designed and tested to ensure that these requirements are satisfied. For convenience, the CW susceptibility limit curve for receiver tracking mode is shown in Figure 5-2. The adjacent-band susceptibility limits will be applied in the RFI impact analysis of the broadband wireless handset and base station emissions. Adjacent band base station broadband emission RFI effects are modelled as if the entire fundamental emission power is concentrated at the emission center frequency.<sup>7</sup>

<sup>7</sup> This assumption was validated during previous activities performed in 2011.

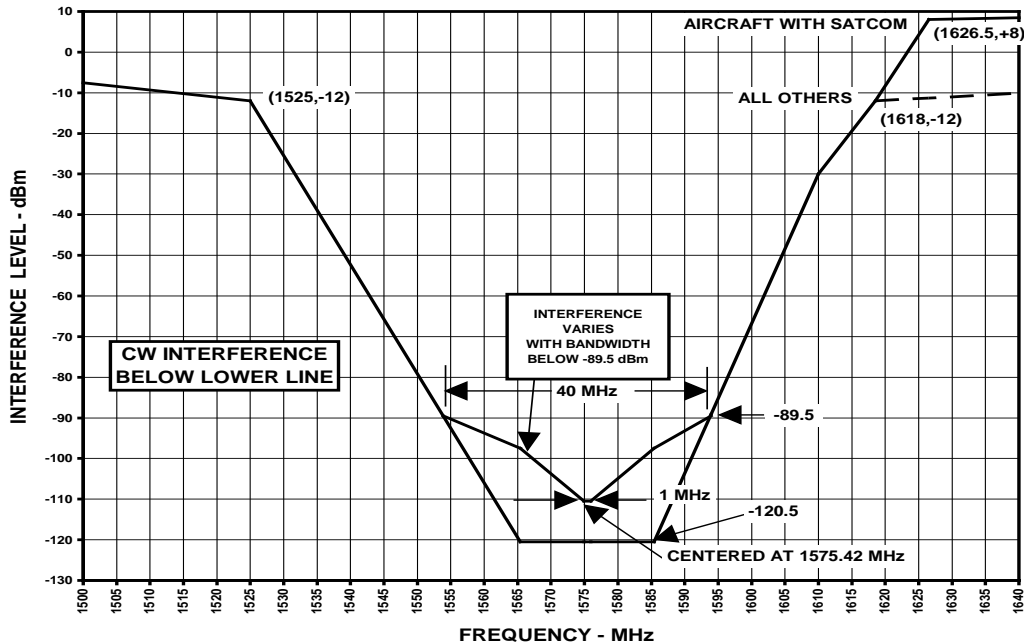


**Figure 5-2: CW Interference Susceptibility vs. Frequency, Tracking Mode**

To preserve the aeronautical safety margin, the maximum mean aggregate RFI power must be kept at least 6 dB below the curves at any center frequency point<sup>8</sup>. An additional constraint on the aggregate RFI is that the probability the received RFI exceeds a value 2 dB below the limit curve is less than  $10^{-6}$ /hour. The  $10^{-6}$ /hour probability represents a 1/10 portion of the overall continuity requirement for aircraft operations from en route to non-precision approach<sup>9</sup>. This  $10^{-6}$ /hour limit is understood as the probability of a single disruptive RFI event. As with previous analyses, the frequency point for limit determination is the emission center frequency. For any aircraft attitude under study, the aggregate mean and rare ( $10^{-6}$ ) limits apply simultaneously. A limit computed at one center frequency can be converted to the corresponding limit at a different center frequency by using Figure 5-2 and the appropriate mask slope. For example, the slope between 1525 MHz and 1565.42 MHz is -2.6843 dB/MHz.

### 5.1.2.2 Receiver Acquisition Limit Criteria for Adjacent-Band RFI

Another consideration is the ability for the aviation receiver to acquire GPS satellite signals. Acquisition is normally accomplished prior to takeoff and, under ideal circumstances, GPS acquisition is not necessary during flight. However, power interruptions on the aircraft or loss of GPS due to aggregate RF interference require that the aircraft be capable of GPS acquisition while airborne. Since acquisition is more demanding than tracking, the receiver standards

<sup>8</sup> This safety margin applies for aircraft airborne and ground operations.

<sup>9</sup> The reliability of the positioning service is specified in terms of continuity (see Section 2.3.3 of the WAAS Performance Standard [13]) The more stringent requirement is for en route through non-precision approach where the service is defined from the surface of the earth to 100,000 feet. The associated continuity requirement is  $10^{-5}$  per hour.

specifications require operation with a 6 dB lower interference test condition than in the tracking case. As a result, the acquisition test threshold is -34.1 dBm (-64.1 dBW) and applying a safety margin would then result in an interference threshold at -70.1 dBW.

Rather than apply this limit directly, the FAA previously determined in the 2012 Interim FAA Study Report [7] that the analysis should account for a maximum probability of  $10^{-3}$  that the interference exceeds -64.1 dBW. While this approach discounts the additional risk to acquisition that occurs during banking or other real-world effects, it does recognize that acquisition would likely become possible at some point as the aircraft continues to fly out of the area of peak interference. For the assessment in this Report this particular threshold was not the limiting condition, so for all the certified aviation use cases/interaction scenarios in this analysis only the tracking mode was considered.

### **5.1.2.3 Receiver Tracking Limit Criteria for Broadband Handset RFI In-band to GPS**

In this Report, all the scenarios associated with new broadband handset unwanted RFI to certified GPS aviation receivers assume operation in the presence of a baseline non-aeronautical noise-like RFI environment within the receiver passband (i.e., in-band RFI to the receiver). As stated in [8], the in-band susceptibility for broad bandwidth non-aeronautical RFI is specified (e.g., in RTCA DO-229 Appendix C, Table C-2 [9]) as -110.5 dBm/MHz (-140.5 dBW/MHz) in a  $\pm 10$  MHz band centered on 1575.42 MHz. As with the adjacent band susceptibility, this limit represents an airborne receiver test condition limit and, for aviation safety considerations, the mean environment aggregate RFI power spectral density (PSD) must be kept at least 6 dB below the test limit. Recent studies (e.g. [8]) have shown that an existing baseline environment results in an aggregate received RFI whose probability distribution tail essentially reaches the operational probability limit for precision approach. As such, any additional aggregate impact from new broadband wireless source unwanted emission will need to be well below that of the baseline environment. The limit used for these analyses is that the aggregate effect from additional in-band RFI does not increase the exceedance probability by more than 6% [10].

### **5.1.3 Transmitter and Receiver Component Assumptions**

The transmitter portion is intended to be a single description for the full DOT ABC study. Regarding the receiver, the primary assumptions are the interference threshold (above) and the receiver antenna gain model. However, the “transmitter” material in this section describes important assumptions used in the FAA certified aviation receiver analyses; some of which may be different than in the other DOT analyses.

#### **5.1.3.1 GPS Receive Antenna Gain**

An FAA Federal Advisory Committee, RTCA Special Committee (SC-159), has developed a representative lower hemisphere antenna gain pattern model for the GPS receive antenna mounted on the top of the aircraft fuselage. The vertical and horizontal polarization pattern models are assumed to be azimuthally symmetric and dependent solely on the elevation angle from the aircraft horizon and represent the maximum gain for the particular RFI signal

polarization. The gain pattern model is dependent on the approach category for which the aircraft is certified.

The lower hemisphere aircraft receive antenna pattern model in terms of gain versus elevation angle (angle between the aircraft horizon and the line joining aircraft and RFI source) is illustrated in Figure 5-3. This pattern is used for the broadband handsets and base stations unwanted emission analyses when those source antenna heights are below the aircraft antenna height.

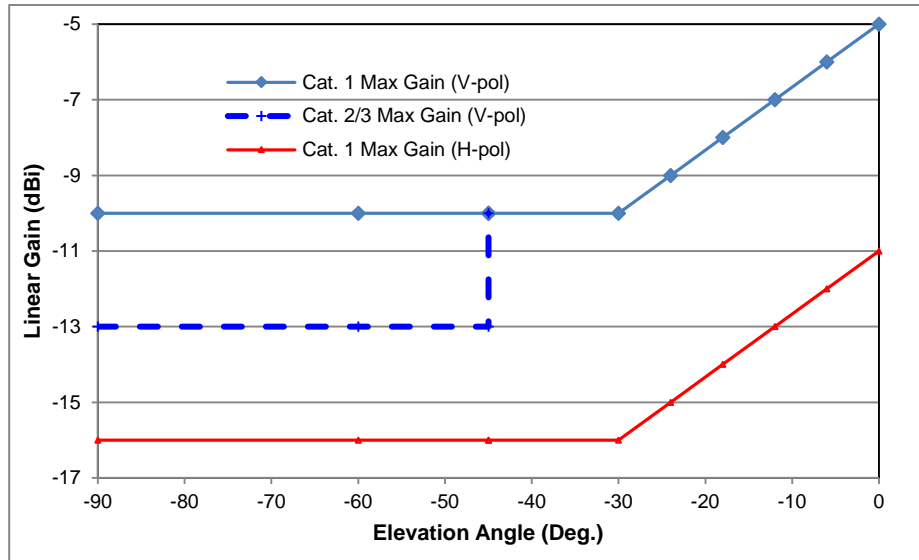


**Figure 5-3: Lower Hemisphere Installed V-pol and H-pol Receive Antenna Patterns Max. Gain vs. Elevation Angle**

(Cat. I GVPOL = -10 dBi for  $-90^\circ \leq el < -30^\circ$ ; =  $-10 + (5 + el/6)$  for  $-30^\circ \leq el \leq 0^\circ$ )  
 (Cat. II/III GVPOL = -13 dBi for  $-90^\circ \leq el < -45^\circ$ ; = Cat. I GVPOL for  $-45^\circ \leq el \leq 0^\circ$ )  
 (GHPOL = -16 dBi for  $-90^\circ \leq el < -30^\circ$ ; =  $-16 + (5 + el/6)$  for  $-30^\circ \leq el \leq 0^\circ$ )

The upper hemisphere aircraft installed receive antenna maximum gain pattern model for linear vertical polarization is shown in Figure 5-4. This pattern is used in cases where the source antennas are at, or above, the height of the aircraft antenna.

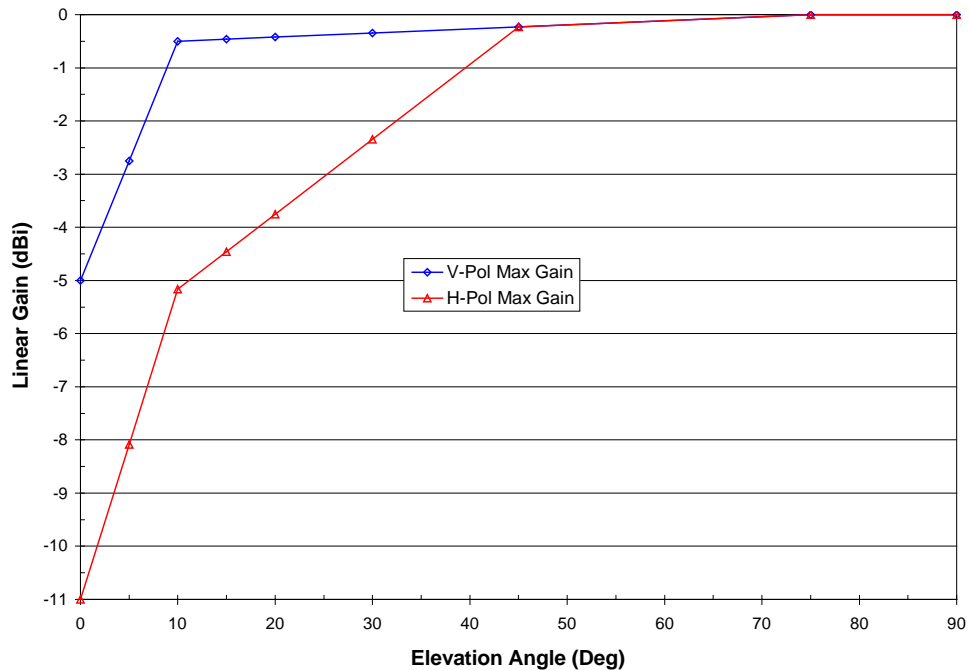


**Figure 5-4: Upper Hemisphere Installed V-pol. And H-pol. Receive Antenna Patterns Max. Gain vs. Elevation Angle**

$$(GVPOL = 0 \text{ dBi}, 75^\circ \leq el; = -0.5 + 0.0077(el - 10), 10^\circ \leq el \leq 75^\circ; = -5 + 0.45 \cdot el, 0 \leq el < 10^\circ)$$

$$(GHPOL = GVPOL, 45^\circ \leq el \leq 90^\circ; = GVPOL - (6 \cdot (45 - el) / 45), 0^\circ \leq el \leq 45^\circ)$$

In the analyses that follow, the aircraft antenna is either assumed to be boresighted at zenith (for an aircraft in level flight) or banked (for a banking aircraft) at a particular angle towards a particular azimuth bearing.

### 5.1.3.2 Broadband Wireless Base Station and Mobile Handset Characteristics

#### 5.1.3.2.1 Broadband Wireless Base Station Characteristics

The broadband wireless base stations used in this analysis are assumed to utilize a 3-lobed transmit antenna pattern with a narrow beam elevation plane shape and a broader beam azimuth plane shape. The three lobes are assumed to be centered nominally  $120^\circ$  apart and down-tilted slightly in elevation (see Appendix G for antenna pattern details). The base station signal radiation is assumed to be either vertically polarized or  $\pm 45$  degree cross-polarized. This cross-polarized signal is equivalently modeled for GPS RFI analyses as a dual, equal amplitude vertically and horizontally polarized signal. The antenna lobes are each assumed to transmit an equal effective isotropic radiated power (EIRP) relative to beam-center. Determination of that EIRP value for compatibility with aviation GPS operation is the goal of the study. The necessary emission bandwidth is assumed to be 10 MHz at a 1531 MHz center frequency though other possible center frequencies were considered.

The analyses used two different strategies for the key base station parameter of antenna height above terrain: one, a fixed height for all antennas; or two, a set of heights specified by a representative deployment over a wide area. The antenna towers were either at specific deployment locations (e.g., a hexagonal grid of locations with fixed grid spacing) or a random distribution of locations with a given average surface concentration.

### 5.1.3.2.2 Broadband Wireless Mobile Handset Characteristics

In order to perform the certified avionics assessment versus broadband wireless mobile handsets operating above 1610 MHz, a worst-case approach was used. Broadband wireless handsets in these analyses are assumed to have a similar necessary emission bandwidth as the base station but with a center frequency at or above 1616 MHz. Maximum fundamental power was assumed to be less than 1 Watt (0 dBW). The assumed handset antenna height above terrain is 1.8 meters unless otherwise noted and has an omnidirectional antenna pattern. The handset is assumed to have a specified unwanted effective isotropic radiated power spectral density limit (less than -95 dBW/MHz) within the GPS receiver band (1565.42 – 1585.42. MHz). For one scenario, ground-based handsets were assumed to be randomly distributed with an average surface concentration of up to 180 per square kilometer. Other scenarios utilized a different distribution.

## 5.2 Transmit Power Level Calculations

The following material discusses various scenarios and conditions used for the analyses in this Report. Table 5-1 summarizes these activities.

**Table 5-1: Analysis Scenarios and Conditions**

Scenario	Conditions
Inflight Aircraft / Ground-based Handset	Final Approach Fix (FAF) Waypoint (WP) Cat. I Decision Height (DH) Cat. II DH
Inflight Aircraft / Ground Base Station	Random and discrete tower locations, Specified aircraft locations and altitudes, flight attitudes: -25°, 0° banking
Inflight Aircraft / Onboard Handset	10K ft altitude
Aircraft on Ground / Onboard Handset	Aircraft antenna at 4 m
Aircraft at Gate / Single Handset Source on or near Boarding Stairs or Jetway	0 dBW @ 1616 MHz

Aircraft at Gate/Users Inside Airport	Random distribution of thirty handsets
TAWS / HTAWS Scenarios with Ground-based Mobile Broadband Handsets	Three handset surface concentrations(30, 75, 180 per sq. km), with -95 dBW/MHz in the GPS L1 receiver passband,  Two aircraft antenna heights (25.9 & 53.3 m)
TAWS and HTAWS Scenarios with Broadband Base Station	Base stations located on a grid with 433m or 693m inter-station distance. Base station heights of 6, 10, 15 and 25 m were considered, with 2, 4, 6, and 8 degree antenna down tilt. Aircraft was assumed at the worst- case location on the assessment zone, both level flight and 25 degree bank toward the base station <sup>10</sup> . Additional parameters including sloping ground were utilized as part of a sensitivity analysis as described in 5.3.3.8.

## 5.2.1 Use Case/Interaction Scenario Development

The certified aviation assessment considered five use cases or interaction scenarios. In all scenarios, the key parameters of interest were aircraft and source antenna heights and orientation, number and relative location of the sources with respect to the aircraft, and the aircraft GPS receiver operation under assessment. The results for these scenarios are summarized below and additional information can be found in the FAA GPS Adjacent-Band Compatibility Study Methodology and Assumptions with RTCA SC-159 [10].

### 5.2.1.1 Inflight Aircraft/Ground-Based Source Scenario Set

As noted above, for all the interaction scenarios the GPS receivers are assumed to operate in the signal tracking mode. Four sub-cases were considered within this set: Handsets, discretely-located base stations, randomly-located base stations and TAWS/HTAWS/low-altitude scenarios.

#### 5.2.1.1.1 Inflight Aircraft/Ground-Based Handset Cases

The geometric parameters for this group of cases (Final Approach Fix waypoint (FAF WP), Category I decision height and Category II decision height) were developed from previous studies. The FAF WP case was also used to represent airborne terminal area operations, while the other 2 cases represent limiting cases on aircraft precision approaches. The mobile broadband

---

<sup>10</sup> These parameters focus on a “small cell” topology for the broadband wireless base stations.

ground-based handsets in these cases were assumed to have a 1.8 meter antenna height and randomly located in a uniform distribution at one of three different surface concentrations (30, 75, 180 per sq. km) extending to the radio horizon (except where excluded from annular sector zones). The assumed unwanted EIRP level for these handsets was -95 dBW/MHz in the GPS L1 receiver passband.

#### **5.2.1.1.2 Inflight Aircraft/Ground-Based Base Station Cases**

The interference analysis methodology for the ground base station cases used a representative scenario encompassing three different aircraft waypoint locations (JTSON, WIRSO, FIROP) on the RNAV (RNP 0.11) approach to DCA Runway 19. Corresponding antenna heights (548.6 m, 125.64 m, 67.52 m) were used to represent points on a typical aircraft approach to a landing. The aircraft was either in level flight or in a 25° bank toward the worst-case direction. These cases were assessed under discrete and random base station location scenarios.

#### **5.2.1.1.3 Inflight Aircraft / Discretely-located Ground Base Station Cases**

For the discretely located case, base stations are at different radii and typically have a varying height distribution. In the discrete propagation model the effective antenna height of a given tower was generally the tower height above the ground at its base (taken from representative deployment data) added to a correction term that accounts for the average height of the tower base above mean sea level (MSL). The local ground height at the tower base was determined from The National Map of the United States Geological Survey (USGS). This data is available at "<https://nationalmap.gov/elevation.html>". The aircraft antenna height was adjusted for the same average base ground height. This correction feature accounted for the first order effect the terrain variation on the path loss and also provided accurate antenna pattern angles needed for a "flat earth" analysis. Additional correction was used for situations where the terrain exhibits a significant slope in the direction toward the aircraft in addition to undulation.

#### **5.2.1.1.4 Inflight Aircraft / Randomly-located Ground Base Station Cases**

The randomly located base station case is included in the analysis only for comparison with results from the discrete scenario. Based on prior analysis [10], and even though this case may under-bound the resultant power emission limit computation, these results serve as a check on the discrete case result. Randomly located analysis was also used to address the relative impact for higher concentrations of base stations with correspondingly smaller radius cells.

#### **5.2.1.2 TAWS/HTAWS and Low Altitude Positioning and Navigation Scenarios**

The encounter scenarios for TAWS and HTAWS are premised on aircraft operations at low altitude relative to the terrain while using the installed GPS receiver to determine position/velocity data for comparison with a terrain and obstacle data base. The aircraft may be in level flight or banking up to a given angle (aircraft- and operation-dependent).

The same TAWS/HTAWS encounter geometries were also assumed to hold for low altitude aircraft Positioning/Navigation (Pos/Nav) operations. The principal difference in Pos/Nav



operations is that the GPS receiver position/velocity output is used to determine aircraft flight control signals (e.g., a helicopter on a point-in-space approach) or attitude determination (e.g., UAS attitude and heading reference system [AHRS] applications).

#### **5.2.1.2.1 TAWS / HTAWS and Pos/Nav Scenarios with Ground-based Mobile Broadband Handsets**

In a previous analysis [7], the mobile broadband handset aggregate unwanted emissions were determined to be most significant for the Cat II DH scenario where the aircraft antenna was 25.9 m above the ground. In that analysis, assessment zones were assumed where mobile handsets could NOT be operated (e.g., within the airport runway object-free area, obstacle clearance zone, etc.).

For this analysis the mobile broadband handsets were assumed to be randomly distributed at one of 3 different surface concentrations (30, 75, 180 per sq. km). Their assumed unwanted emission level was -95 dBW/MHz in the GPS L1 receiver passband. At these surface concentration values, the fundamental emission effects were insignificant. The two different aircraft antenna height cases analyzed were 25.9 m and 53.3 m.

#### **5.2.1.2.2 TAWS and HTAWS Scenarios with Broadband Base Stations**

The hexagonal cellular system for this scenario consists of a central tower plus 19 concentric hexagonal rings of towers, all at a particular inter-site distance (ISD) (i.e., distance between towers) for a total of 1,141 towers with a grid maximum radius of 8.2 km. The aircraft (in this case a helicopter) is assumed to 250 feet (76.2 m) from the central tower at an azimuth bearing of 30 degrees. This is the same azimuth as that of the main lobe of one of the three antennas on the central tower, the three being equally spaced 120 degrees apart. Transmissions are assumed to be equal power vertically and horizontally polarized so both the vertical and horizontal polarization attenuation curves of the aircraft GPS antenna were used. Both flat ground and sloping ground scenarios were examined. The nominal emitter antenna down tilt was 6 degrees.

### **5.2.1.3 Handset Sources on Board Aircraft**

#### **5.2.1.3.1 Onboard Handset Operation for Aircraft Inflight**

In this scenario, the broadband wireless handsets were assumed to be operating with an on-board WiFi access point when the aircraft is above 10,000 feet (AGL) altitude. The handsets were expected to exhibit similar unwanted emissions in the GPS L1 band as in their wideband communication mode on the ground. Emissions in the WiFi transmit band (2.45 GHz) were expected to be similar to a standard mobile WiFi transceiver. If that assertion is correct, then these handsets would not present a special RFI compatibility issue on the aircraft where WiFi device operation is already permitted.

#### **5.2.1.3.2 Onboard Handset Operation for Aircraft on Ground**

In contrast to the inflight scenario, when the aircraft is taxiing toward the gate the onboard broadband handsets were assumed to communicate through a standard ground base station outside the aircraft. Because of the partial shielding provided by the aircraft fuselage, the handsets were assumed to operate at full transmit power for their necessary emission. The aircraft antenna height was assumed to be 4 m above ground and at a representative location at the start of the taxiway and the aircraft GPS receiver was assumed to be in the signal tracking mode. Propagation of handset emissions to the aircraft GPS antenna were characterized by the model in RTCA/DO-235 [5.3-3] Appendix E.6.2.

For the unwanted emission analyses, the GPS receiver was assumed to operate in the presence of a baseline level of RFI emanating from other randomly-distributed sources outside the aircraft. The analysis uses a 3x3 cabin configuration (i.e., three seats per window) meaning that there are three seats per window location on each side of the aircraft, resulting in a total of 189 seats. The handsets were distributed in a random assortment of discrete locations throughout the passenger cabin for a few representative values of total handset count. Path loss values at possible locations were taken from [5.3-3] Appendix E, Table E-10.

#### **5.2.1.4 Aircraft at Gate Scenarios**

##### **5.2.1.4.1 Aircraft at Gate / Single Handset Source on or near Boarding Stairs or Jetway**

This scenario used a single broadband wireless handset operating at full emission power and the signal propagation was assumed to be far field free-space. Handset location relative to the GPS aircraft antenna was assumed such that the receive antenna gain was -5 dBi. Given the propagation conditions and a single source, the result is deterministic. In this case for a single handset with 0 dBW EIRP operating at 1616 MHz, the minimum handset antenna separation distance for compatibility is 3.5 m. This separation might be assured by aircraft fuselage size and geometry. The unwanted handset RFI analysis was also included in the baseline RFI effect as well as the effect of unwanted RFI from a concentration of general sources inside the airport terminal.

##### **5.2.1.4.2 Aircraft at Gate/30 Users Inside Airport**

This scenario was comprised of 30 wireless broadband handsets operating in an airport terminal gate area that generate RFI to a GPS receiver on an aircraft located outside the terminal in front of the gate area. The scenario is well documented in [10]. The key factors for this analysis were as follows.

- 1) The aircraft GPS antenna height is assumed to be 4 meters above ground and 34 meters from front edge of terminal area.
- 2) The handset antenna heights are all 3 m above the aircraft antenna level (2 m above terminal floor).

- 3) The terminal area is assumed to be symmetrically spaced in front of the aircraft with a 20 meters average depth and 50 meters width.
- 4) 30 handsets are assumed to be uniformly distributed throughout the 1000 sq. m. area.
- 5) Handsets are assumed to be operating in the 1610-1656.5 MHz band with -95 dBW/MHz unwanted EIRP in the GPS L1 band.
- 6) The median path loss model was two-ray free-space at these distances but with additional building loss incorporated as follows: 20% of handsets incur an additional 20 dB loss, 60% an additional 15 dB loss, and 20% an additional 10 dB loss (excess loss assigned relative to decreasing distance from front terminal wall).

## 5.2.2 Propagation Models

The RFI propagation path loss models used for the certified aviation assessment are based on the flat-earth approximation. In other words, the ground under the aircraft is assumed to be essentially smooth and flat out to a radio horizon from the point on the ground directly under the aircraft. In line-of-sight propagation conditions at radio frequencies near that of the GPS carrier, this radio horizon value generally depends on the aircraft GNSS and RFI source antenna heights and the amount of atmospheric refraction along the propagation path. A 4/3 Earth radius approximation for the refractive effect on the radio horizon is used in all propagation models.

The propagation models used in this analysis can be categorized as two different types: (1) those scenarios where diffuse scattering, diffraction, and blockage were factors analyzed using probabilistic path loss; and (2) clear line-of-sight scenarios which were analyzed using deterministic free space path loss. For this assessment, the point above which free space path loss is used generally occurs at an aircraft antenna height above ground of 550 meters. Above 550 meters, various parameter limits associated with the probabilistic models are exceeded thus making their use problematic. Also at these aircraft heights, line-of-sight conditions generally prevail which means that use of free space path loss was most appropriate.

### 5.2.2.1 Single Path Propagation Model

For free space propagation, the signal power loss over a single path is given by the well-known inverse square law propagation model. For probabilistic propagation, the models developed by the cellular radio community are generally applicable. These models have one feature in common; the probabilistic nature of the path loss is very well approximated by the product of a slow fading process and a fast fading process (as a consequence, this is also true for the single path received interference power/power density). The slow fading process is approximated by a log-normal distribution while the fast fading process is described by a non-central chi-squared distribution. The log-normal component is completely determined by two parameters,  $\mu$  and  $\sigma$  and the chi-squared process by the parameters,  $L$ ,  $\psi_0$  and  $\rho_0$ . The range-dependent median path loss between the GPS antenna and the interference source determines the primary component in the parameter  $\mu$  while the remaining parameters vary with range depending on the scenario.

A principal component in the slow-fade parameter,  $\mu$ , is the single path-median isotropic path loss. For this analysis, the median isotropic path loss was modelled using a continuous set of three basic deterministic range-dependent segments. For short ranges, a two-ray path loss model was used for distances less than the first breakpoint distance “ $r_1$ .” For long ranges, a Hata-Okumura path loss model was used for distances greater than the second breakpoint distance “ $r_2$ .” At intermediate ranges, at distances greater than  $r_1$  but less than  $r_2$ , the path loss model depended on antenna heights contained in a given scenario. A modified Erceg/Greenstein model was used as the intermediate range model for most handset scenarios (aircraft antenna height  $\leq 80$  m, source antenna  $\leq 2$  m). In all other scenarios the intermediate range path loss model used an exponential fit between the short and long range models (log-linear interpolation (on path loss) versus range between the  $r_1$  and  $r_2$  values). In some scenarios a moderate amount of effort was required to determine the appropriate breakpoint distances. Additional details on path loss models and the calculation of breakpoint values and other model parameters are provided in Appendix F.

### 5.2.2.2 Aggregate Effects Model

For uniformly distributed, randomly-located interference sources, once the single path interference characteristics have been determined, it is possible to determine analytically the mean, standard deviation, and cumulative probability distribution associated with aggregate received interference power. In this case, the received power from a randomly located interfering emitter was modeled as the product of a slow fading process (log-normally distributed) and a fast fading process having a non-central chi-squared distribution with the parameters described above.

For sources having a known discrete distribution (i.e. the location and height parameters associated with each source are known), two possible approaches may be used to determine the aggregate interference power, the mean value and the cumulative distribution function. The single source received interference power in this case is also a random variable and is described by the product of a slow fading process and a fast fading process. Thus the aggregate interference power, its mean value and cumulative distribution can be determined using an analytic approach. Alternatively, it is possible to use a Monte Carlo simulation to determine both the mean aggregate interference power and cumulative probability distribution for the discrete source distribution case. Appendix F contains details of the aggregate statistics computation. The analysis of received aggregate interference from handset sources assumes that handsets are uniformly distributed over some area at an unknown random distance from the aircraft GPS receiver. Exceptions to this assumption include scenarios where the aircraft is located at the gate with handsets located within the terminal or on a stairway about to enter the aircraft. In these exception cases, a discrete distribution of handsets was assumed. For interference from base station sources, both a discrete and a random distribution of base stations were assumed.

### 5.2.3 Tolerable Transmit Power Calculation Results and Sensitivity Analysis

The spectrum engineering assumptions and path loss models described above were used to perform inverse transmit power calculations. Generally, this type of calculation first aggregated at one location the RFI from all emitters contained in the given scenario then calculated the single common EIRP transmission limit that satisfied the tolerable RFI constraint. Both mean based and rare event based type constraints are applicable though variations on this general method are possible and are described below.

#### 5.2.3.1 Tolerable Transmit Power Calculation Method Overview

Two major basic types of tolerable transmit power calculations are used in this certified aviation receiver assessment. In the broadband base station calculation method, the station fundamental (adjacent band) EIRP is not known a priori and is the goal of the analysis. The tolerance criteria are simple receiver-based limits (see Sec. 5.1.2.1). In contrast for the associated broadband wireless handsets, the unwanted handset EIRP (in-band to the GPS receiver) is assumed to be at a specified limit and baseline in-band RFI is also present. Additionally, the tolerance criterion is different (see Sect. 5.1.2.3) in that the growth in exceedance probability of the composite RFI is limited to a percentage above the baseline case.

##### 5.2.3.1.1 Tolerable Transmit Power Calculation Method – Base Station Cases

The transmit power calculation method for the base station cases assumed that each of the three antenna beams on a base station tower transmit with a normalized (unity) EIRP. A mean aggregate power factor (AF) is then computed at a desired aircraft location such as a waypoint by combining the RFI from all base station sources using the probabilistic path loss and probabilistic models described above (Sec. 5.2.2). In linear units, the AF is the received power divided by the EIRP. The analytic transmit power calculation method for the base station cases has two major steps<sup>11</sup>. The mean AF is computed first and then the CDF of the AF is computed. The random variable Z is the normalized AF, defined as AF/(mean AF). The CDF P(z) is defined as the probability that Z is less than or equal to z.

The corresponding mean based and rare event EIRP limits for an antenna are computed using equations (5-1) and (5-2), respectively. These equations were derived from the information provided in paragraph 5.1.2 and the spectrum mask information of Figure 5-2. The parameter “Zcrit” in equation (5-2) is the argument of the AF CDF that corresponds to a threshold exceedance probability of 10<sup>-6</sup>.

$$\text{Mean\_Based\_EIRP\_Limit} = -64.11 \text{ dBW} - 10 * \log_{10}(\text{Mean AF}) \quad (5-1)$$

$$\text{Rare\_Event\_EIRP\_Limit} = -60.11 \text{ dBW} - 10 * \log_{10}(Z_{\text{crit}}) \quad (5-2)$$

The more stringent of the two results from

---

<sup>11</sup> In the alternative Monte Carlo method, the mean AF and the AF CDF are determined together in a single computation.

equations (5-1) and (5-2) is then the applicable limit for the particular case under study.

All the RFI calculations for the base station cases assumed the emitter has a center frequency of 1531 MHz with a 10 MHz emission bandwidth. Equations (5-1) and (5-2) are specific for a center frequency of 1531 MHz. Examples of how to convert from the 1531 MHz based EIRP limit calculated in this analysis to the corresponding limit at a different frequency are shown in section 5.2.3.7.

#### **5.2.3.1.2 Tolerable Transmit Power Calculation Method – Handset Cases**

The method for evaluating the impact of ground based broadband wireless handsets is different and more indirect than that of evaluating the RFI impact of base station emitters. Analysis has shown that the fundamental emission of the broadband wireless mobile handsets, at least up to the assumed 0 dBW maximum power and operation above 1616 MHz, are not of concern for certified avionics. As a result, rather than determining an unknown fundamental power level of the base stations as described above, the broadband wireless handsets are assumed to operate with a specified unwanted emission limit (-95 dBW/MHz) within the aviation GPS receiver passband. For certain scenarios, various values for the average number of handsets per unit area (randomly distributed) are also assumed up to a maximum. The tolerability criterion for the handset cases (5.1.2.3) is a limit on the percentage growth in RFI impact for the addition of new handset sources to the baseline RFI condition. For handset cases the RFI impact is quantified by the probability of the aggregate RFI power density exceeding the certified aviation receiver MOPS test threshold (-140.5 dBW/MHz). Appendix F has details on computing the aggregate RFI cumulative probability distribution.

#### **5.2.3.2 Results for Inflight Aircraft/Ground-based Handset Cases**

Details of the baseline RFI impact computation are given in [8]. In summary the baseline condition is developed by a random distribution of sources (1.8 m antenna height) out to the radio horizon at an average concentration of 100 per square kilometer with an individual unwanted emission of -81.1 dBW/MHz. The limiting case baseline scenario geometry in [8] is the Category II DH waypoint (25.94 m aircraft antenna height). Table 5 of [8] shows the aggregate received RFI power density exceeds the MOPS test threshold (-140.5 dBW/MHz) at a probability of  $3.0144 \times 10^{-4}$  as predicted by the generalized model.

The RFI impact of the composite of broadband wireless handsets with the baseline RFI is analyzed in two steps. First a random distribution of only the broadband wireless handsets is analyzed with the same scenario geometric constraints as in the baseline RFI case. The handsets (1.8 m antenna height, 180 per sq. km. average) are assumed to emit -95 dBW/MHz unwanted power density in the GPS receiver passband ( $1575.42 \pm 10$  MHz). The desired analysis results are the handset-only statistics (mean and CDF). Then these statistics are combined with those of the baseline to form the composite statistics (computation details in Appendix F).

The handset scenario baseline and composite statistical results are shown in two CDF (1-P(z)) curves (Figure 5-5). The dashed (baseline) curve is based on an average concentration of 100 baseline emitters per square kilometer. The solid (composite) curve is based on 280 total emitters per square kilometer. In Figure 5-5, the Z value (x-axis point)<sup>12</sup> at which the baseline curve exceeds the MOPS test limit is 16.4722. The associated y-axis (1-P(z)) value is 3.0144x10<sup>-4</sup>. Since the composite case (baseline + handsets) mean value is somewhat higher, the composite curve Z value is 15.34512 at the MOPS threshold and the associated probability on the red solid curve is 3.06224x10<sup>-4</sup>. This 1.59% probability increase from the baseline probability is below the maximum tolerable increase of 6%. Thus, this scenario is assessed as not a critical or limiting scenario based on the assumed handset-related parameters.

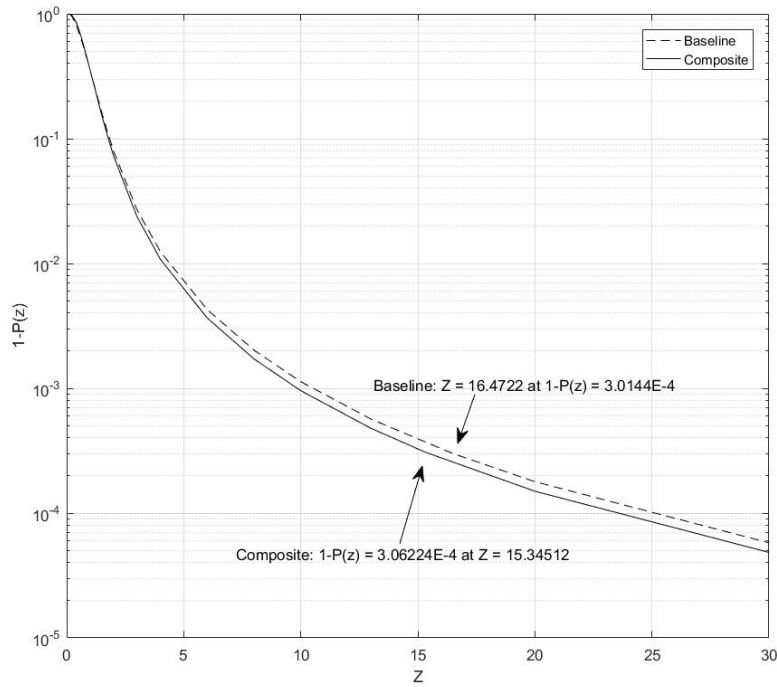


**Figure 5-5: Handset Scenario Probabilities**

### 5.2.3.3 Results for Inflight Aircraft / Ground Based Base Station Cases

Results presented here were obtained for the WIRSO case discussed in Section 5.2.1.1.2. This specific waypoint places the aircraft nadir axis at 38.8816° North latitude and 77.046° West longitude with the GPS antenna at an altitude of 125.64 meters above Mean Sea Level (MSL). The aircraft was located over the Potomac River near the Tidal Basin in Washington DC.

<sup>12</sup> As defined earlier, the x-axis parameter Z is the algebraic ratio of the aggregate power density to the mean aggregate power density. Thus the point Z=1 corresponds the mean aggregate power density.

The analysis was performed assuming each interfering base station operates in the adjacent band just below the GPS L1 band with an emission bandwidth of 10 MHz. While analyses for three different base station center frequencies was initially intended, the results herein were completed only for the frequency 1531 MHz. Extension to other frequencies can be performed as described in Section 5.1.2 of this Report. The base station key operational parameters are described in Section 5.1.3.2.

The propagation model used in the analysis was that described above in Section 5.2.2.1. As discussed, this model incorporated a median path loss component between the GPS antenna and the interference source which, along with the normalized base station and GPS antenna gains, determined the log normal distribution parameter,  $\mu$ . The single path median isotropic path loss,  $PL(r)$ , is composed of three range dependent segments. The WIRSO median isotropic path loss model used a two-ray model for short ranges ( $r < r_1$ ), an exponential fit model for intermediate ranges ( $r_1 \leq r \leq r_2$ ), and the Hata-Okumura model for longer ranges ( $r > r_2$ ). The detailed definition of these models is contained in Appendix F.

As a further refinement, the WIRSO interference scenario analysis also included a terrain dependent slope correction factor which was incorporated into the Hata-Okumura long range median path loss model [10]. To accurately model the scenario terrain slope, the area surrounding the aircraft location was divided into 12 azimuth sectors of nominally 30° angular width. (See Appendix F for additional details.)

Table 5-2 lists transmission power limits computed using the WIRSO scenario. The results of this table were obtained using both the Analytic Statistical method and the Monte Carlo method and there is good agreement between the results of the two methods. The Mean Power Based EIRP Limit value in the table is based on the mean limit of -64.1 dBW at 1531 MHz while the Rare Event Based EIRP Limit value is based on the -60.1 dBW limit. These results apply for both flight attitudes.



**Table 5-2: WIRSO Scenario Based Limits from Two Methods**

<b>Method</b>	<b>Flight Attitude</b>	<b>Mean Agg. Power Factor (dB)</b>	<b>Mean Power Based EIRP Limit (dBW)</b>	<b>Zcrit</b>	<b>Rare Event Based EIRP Limit (dBW)</b>
Analytic Statistical	Level Flight	-97.85	33.75	3.0974	32.84
Monte Carlo	Level Flight	-97.89	33.79	3.0205	32.99
Analytic Statistical	Banking, -25 deg.	-94.41	30.31	3.3547	29.06
Monte Carlo	Banking, -25 deg.	-94.47	30.37	3.5300	28.89

The results listed in Table 5-2 include values for “Zcrit”, the Z value (as defined earlier Z is the aggregate interference factor (AF)/mean AF) for which the probability of the corresponding CDF curve is  $1 \times 10^{-6}$ . Figure 5-6 consists of two curves for the WIRSO banking scenario which overlap for low values of Z but diverge at Z values of about 3.35 and higher. This figure provides an indication of the solution sensitivity to the solution method. The ordinate of each curve is plotted as “1 - CDF” (i.e., “1 – P(z)”) instead of as a traditional CDF for the sake of convenience. The curves shown correspond to the bottom two rows of Table 5-2. While the precision of the Monte Carlo results for higher Z values could be improved if more time-consuming calculations were made, that exercise is unnecessary given Z values for 1-P(z) values below  $1 \times 10^{-6}$  are not needed.

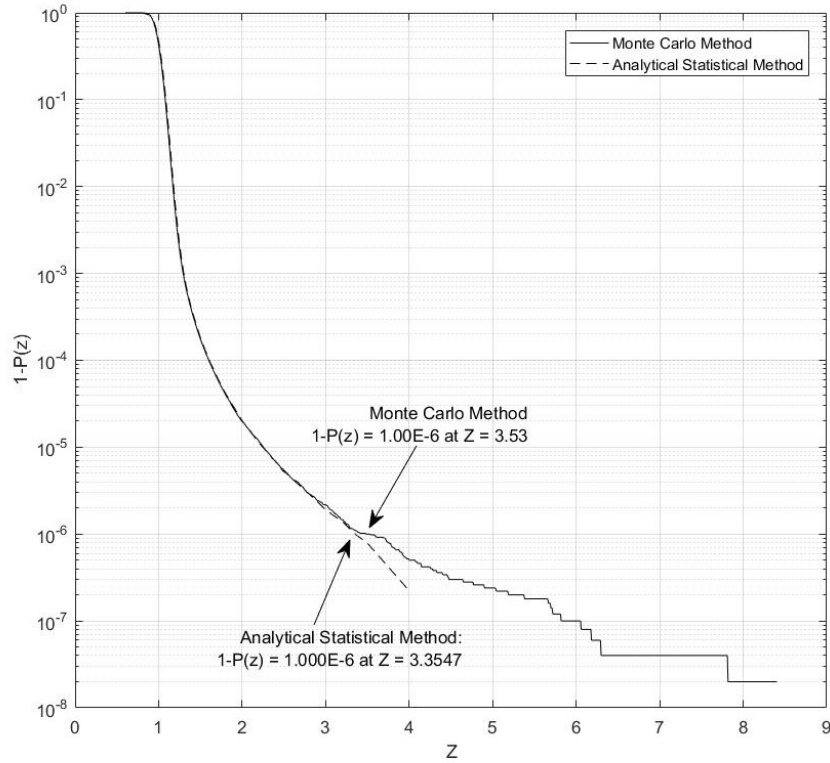


**Figure 5-6: WIRSO Banking Scenario 1 – P(z) values Using Two Methods**

The WIRSO scenario results were also computed using a third method. The WIRSO limits computed using the random location method are shown in Table 5-3. A random location model scenario result was computed for each limit type because the underlying assumptions used to model the tower locations were adjusted.

**Table 5-3: WIRSO Scenario Based Limits from Random Method**

Random Model Scenario	Flight Attitude	Mean Agg. Power Factor (dB)	Mean Power Based EIRP Limit (dBW)	Zcrit	Rare Event Based EIRP Limit (dBW)
1	Level Flight	-97.45	33.35	2.497	33.37
2	Banking at -25deg	-95.48	31.38	2.497	31.41

A comparison of the EIRP limits computed using the Analytical Statistical discrete and random location methods (random-discrete result) is shown in Table 5-4. The comparison shows relatively good agreement for the level flight scenario mean power based limit but there are larger differences for the banking scenario and for the rare event based limits. These differences arise from the same fundamental issue, i.e., the highly asymmetrical distribution of the towers

with respect to azimuth and distance. The analytical statistical method uses actual tower locations while the random method used random assignment based on an approximation of the tower locational distribution. Of more significance, the analytical statistical method computes a cumulative distribution function directly from a characteristic function which was computed using actual tower locations. In theory the analytical statistical method will more accurately capture the probabilistic impact of the asymmetric tower distribution. The primary purpose of the random method in this instance was to serve as a reasonableness check for the analytical statistical method solution. As a result, the analytical statistical method based limits of Table 5-2 are cited as the WIRSO results.

**Table 5-4: Comparison of Two Methods for WIRSO Scenario Based Limits**

<b>Flight Attitude</b>	<b>Method Delta - Mean Power Based EIRP Limit (dBW)</b>	<b>Method Delta - Rare Event Based EIRP Limit (dBW)</b>
Level Flight	0.40	-0.53
Banking at -25deg	-1.07	-2.35

#### **5.2.3.4 Results for Onboard Handset Operation for Aircraft on Ground**

The locations of the handsets are the random variables selected in each realization within the Monte Carlo simulation. This effort distributed handset locations uniform randomly throughout the cabin and computed the normalized aggregate personal electronic device (PED) power factor ( $F_{AGG,PED}/IPL_{MIN}$ ) which is independent of PED EIRP. Although biasing handset locations toward the front of the aircraft (lower path losses) where potentially more first-class passengers would operate a handset was considered, the Monte Carlo results in Figure 5-7 suggest such a constraint is unnecessary. The difference between the maximum and mean aggregate power factor indicates that the handset locations need not be biased toward the front. With more than approximately 20 handsets, the difference between the maximum and mean power factor is less than 3 dB.

Assuming 100 of the 189 possible handsets<sup>13</sup> are operating simultaneously indicates mean aggregate signal loss of approximately 52 dB. Using this loss with a fundamental handset power of 0 dBW gives a power at the aircraft antenna of -22 dBm. This fundamental power is essentially at the aviation mask with 6 dB safety margin for the 1616 MHz frequency. Considering the emissions level of -95 dBW/MHz, this level leads to unwanted emissions in the GPS L1 band of -147 dBW/MHz. At the limit of all 189 handsets operating, the

---

<sup>13</sup> During the scenario development, the number of users were chosen to provide an overbound/stress case to support the stated conclusion that no interference to certified avionics is expected from handsets with the postulated technical characteristics.

aggregate signal loss is 48 dB which results in slight exceedance of the aviation mask with safety margin included. The scenario of all 189 devices operating simultaneously at exactly their maximum levels for both fundamental and unwanted emissions is considered very conservative so this is not deemed a limiting case. These results indicate that no further assessment was required. If a further assessment were to be performed, it should also include computation of a baseline RFI condition without broadband wireless handsets as stated in Section 5.2.1.3.2.

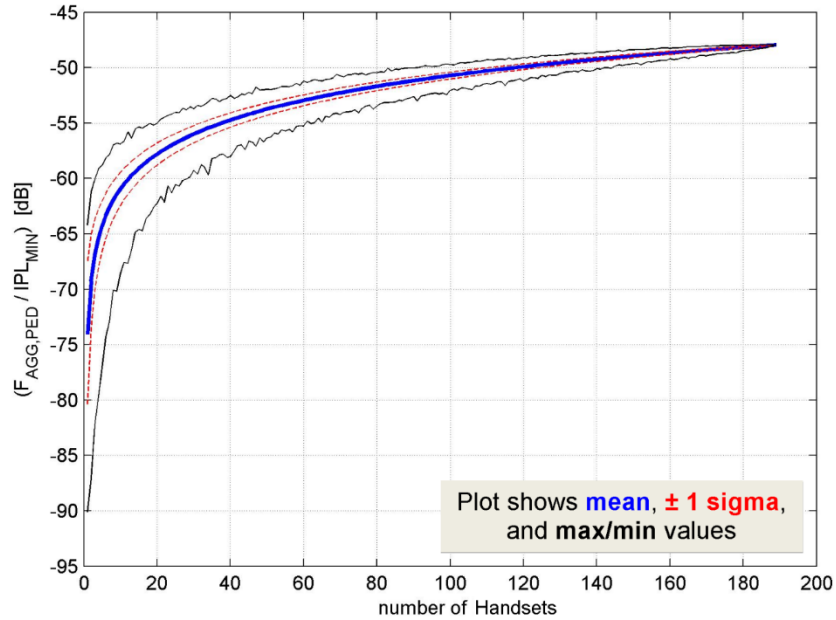


**Figure 5-7: Aggregate Handset Signal Loss**

### 5.2.3.5 Results for Aircraft at Gate/30 Users Inside Airport

Computations from RTCA DO-235B Appendix E, Equations E-1 and E-2 were again applied to compute the aggregate power factor and normalization factor. The scenario can be visualized as shown in Figure 5-8.

Scenario: Plane at Gate with 30 Uniformly Distributed Handsets in Terminal

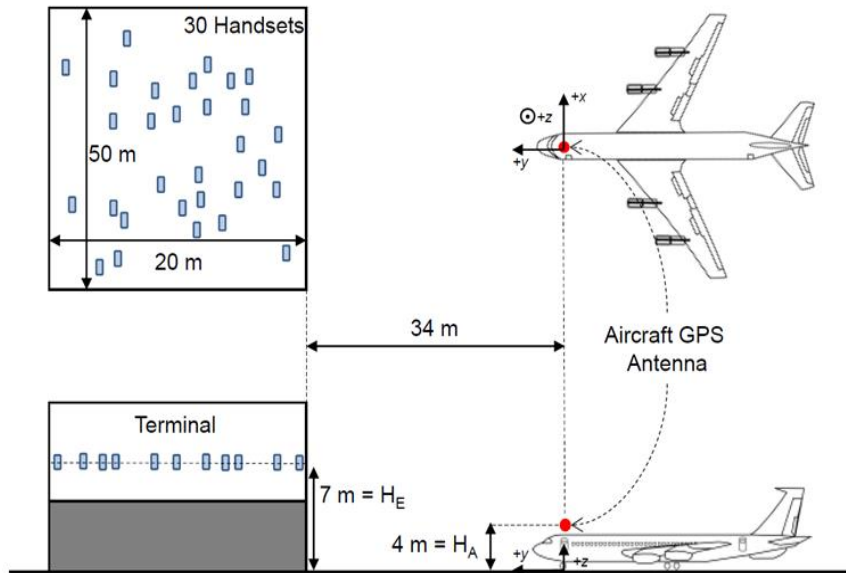
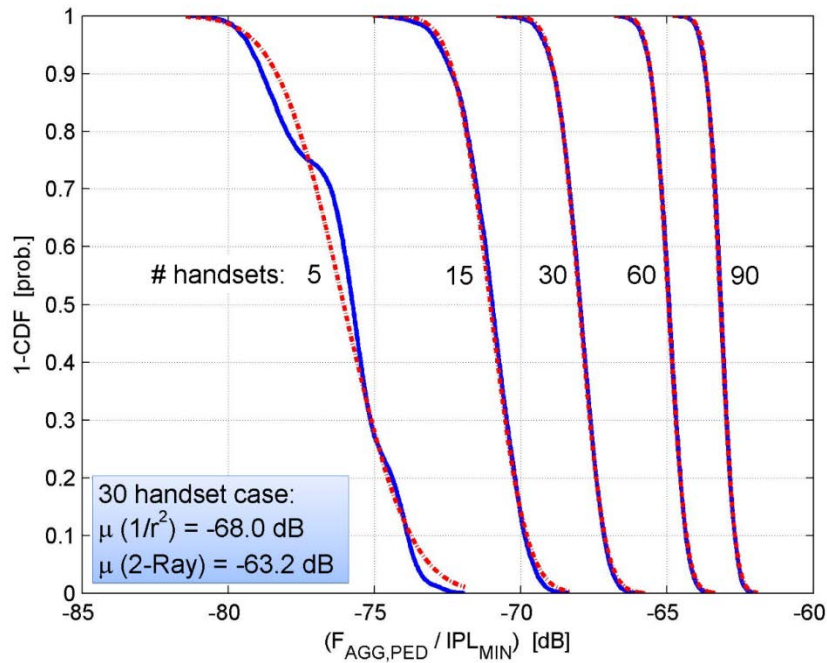


Figure 5-8: Aircraft at Gate with Thirty Uniformly Distributed Handsets in Terminal

Figure 5-9 shows the normalized factor as function of the number of handsets. (To compute the aggregate RFI power, add the handset EIRP to the abscissa. For example, 30 handsets with unwanted emissions at -95 dBW/MHz and 60 handsets<sup>14</sup> with unwanted emissions at -81 dBW/MHz result in a mean received aggregate interference power of -145.9 dBW/MHz.) These results indicate that no further assessment was required. If a further assessment were to be performed, it should also include computation of a baseline RFI condition (general sources inside and outside the terminal) without broadband wireless handsets as stated in Section 5.2.1.4.1.

<sup>14</sup> During the scenario development, the number of users were chosen to provide an overbound/stress case to support the stated conclusion that no interference to certified avionics is expected from handsets with the postulated technical characteristics.



**Figure 5-9: (1-CDF) Aggregate Power Factor**

### 5.2.3.6 Results for Inflight Aircraft TAWS/HTAWS and Low Altitude Pos/Nav

The limiting EIRP for the emitters used in this scenario was evaluated using a different distribution of towers and a different relative aircraft location than the evaluation at the WIRSO waypoint described above. The hexagonal cellular system of this scenario consists of a central tower plus 19 concentric hexagonal rings of towers, all at a particular inter-site distance (ISD) for a total of 1,141 towers with a grid maximum radius of 8.2 km. The helicopter is assumed to 250 feet (76.2 m) from the central tower at an azimuth bearing of 30 degrees. This is the same azimuth as that of the main lobe of one of the three antennas on the central tower, the three being equally spaced 120 degrees apart. Transmissions were assumed to be equal power vertically and horizontally polarized so both the vertical and horizontal polarization attenuation curves of the aircraft GPS antenna were used. Both flat ground and sloping ground scenarios were examined.

The nominal emitter antenna down tilt was 6 degrees. Sensitivity analysis for this scenario included varying the degree of down tilt and the aircraft distance from the central tower keeping in mind the importance of having the helicopter located in the center of a main lobe of a central tower antenna. Other parameter sensitivity variations included using vertical polarization-only type transmissions, varying the ISD and “rounding out” the perimeter of the hexagonal grid system into a circle (thereby increasing the number of towers to 1,345).

In this scenario, the dual polarization nature of the RF signal makes the calculation of the  $r_1$  breakpoint more complex. This breakpoint was set to be the closest radius at which the vertical and horizontal polarization path losses are equal just beyond the point at which the vertical

polarized ray is at its critical grazing angle (at approximately 112.5 m). Also different in this study is that the Hata  $r_2$  breakpoint was set to be 1,000 m in all scenarios.

A consistent result of all the parameter variations studied is that more than 90% of all RFI comes from the central tower. While this is not surprising due to the distances involved, a consequence is that the two-ray model becomes the primary path loss model, whereas in the WIRSO scenario all towers were beyond the  $r_1$  breakpoint. The scenario primacy of the two-ray model in combination with the sensitivity of the aircraft antenna to polarization type and elevation angle meant that an additional level of detail to the RFI calculation procedure was needed. The two-ray path loss calculations were modified to account for the direct and reflected rays entering the helicopter antenna at different elevations and hence attenuated differently. The two-ray path loss model also computes different reflection coefficients (magnitude and phase) for vertically and horizontally polarized waves.

This scenario used a different antenna pattern than the WIRSO scenario. The transmit antenna models for both scenarios are functions of azimuth and elevation but in this scenario the central tower antenna oriented at an azimuth of 30 degrees had a minimum gain of -15 dB imposed for elevations lower than -22 degrees in order to account for a lack of symmetry. Details for the base station antennas are contained in Appendix G.

The EIRP limits computed using both the Monte Carlo and Analytic Statistical methods are shown in Table 5-5. The results show good agreement between the two methods. Some parameter combinations were Not Computed (NC) because they obviously would not constitute a limiting condition and are thus rendered moot. The assumptions used to calculate the results of Table 5-5 include a helicopter located 76.20 m (250 ft.) from the central tower with all tower heights of 25 m for flat ground scenarios. The sloping ground scenarios assume a funnel shaped terrain with an upward slope of 10 milliradians with the central tower at the bottom of the funnel. In the sloping ground scenario the height above local ground for all towers remains 25 m but the effective tower height with respect to the aircraft increases with the rising ground.

**Table 5-5: Hexagonal Grid Power Limits Computed Using Two Methods**

Scenario Number	Inter Site Distance (m)	Aircraft Bank Angle (deg)	Terrain Slope (milli-radians)	Tower Antenna Down Tilt (deg)	Aircraft Height (m)	Mean Based Limit (dBW)		Rare Event Based Limit (dBW)	
						Monte Carlo	Analytic Statistical	Monte Carlo	Analytic Statistical
#1	693	0	0	6	16.99	13.35	13.34	13.37	NC
#2	433	0	0	6	16.99	13.31	13.3	13.36	NC
#3	693	0	10	6	16.99	13.30	13.26	13.32	NC
#4	433	0	10	6	16.99	13.21	13.11	13.29	13.06
#5	433	25	10	6	16.99	10.28	10.27	10.34	10.18
#6	433	25	10	8	14.29	10.16	10.36	10.19	NC

Results were computed for other hexagonal grid scenarios using the Monte Carlo method. These results are shown in Table 5-6. The results were computed using the same general assumptions listed for Table 5-5. None of the results contained in Table 5-6 indicate a more stringent limit than that indicated by Table 5-5.



**Table 5-6: Hexagonal Grid Power Limits Computed Using 433m ISD Flat Earth Scenario**

GPS Rx antenna height at Max EIRP (m)	Max Tx EIRP (Multiple Towers) (dBW)					
	No Banking				25° Banking	
	6m Base Station Tower with 2° Down Tilt	10m Base Station Tower with 4° Down Tilt	15m Base Station Tower with 6° Down Tilt	25m Base Station Tower with 8° Down Tilt	15m Base Station Tower with 6° Down Tilt	25m Base Station Tower with 8° Down Tilt
4	24.90	20.45	16.19	13.26	14.13	11.80
6	23.84	19.83	15.60	12.96	12.92	11.72
8	22.95	19.62	15.28	12.17	11.97	10.71
10	22.51	19.61	15.37	11.79	11.44	10.40
12	22.18	19.24	15.89	11.78	11.34	10.38
14	22.41	19.59	16.75	12.36	11.60	10.37
16	*	19.91	17.81	13.06	12.45	10.45
18	*	20.31	18.46	13.90	12.63	10.68
20	*	*	19.78	14.86	13.90	11.05
22	*	*	21.02	15.98	15.09	11.50
24	*	*	22.53	17.31	16.36	12.10
26	*	*	*	18.45	*	13.09
28	*	*	*	19.62	*	13.96
30	*	*	*	20.73	*	15.25
32	*	*	*	22.17	*	16.58
34	*	*	*	23.63	*	18.03

\*Not assessed

EIRP limits were also computed for a helicopter on the ground. These results are shown in Table 5-7 and none of the results contained in this Table indicate a limit more stringent than that indicated by Table 5-5.

**Table 5-7: Power Limits for Landed Helicopter at Various Separation Radii from Central Tower**

<b>Separation Radius from GPS Rx to Central Tower (ft)</b>	<b>Base Station Antenna height (m)</b>	<b>Base Station Antenna down tilt (deg)</b>	<b>GPS Rx antenna height at Max EIRP (m)</b>	<b>Max Tx EIRP (Multiple Towers) (dBW)</b>
50	25	8	4	14.59
100	25	8	4	18.31
200	25	8	4	13.82
250	25	8	4	13.26

Power limits obtained from a wide range of additional scenarios were computed using the randomly distributed base station method. The results are shown in Table 5-8. Note that some of the limits in this table are much lower than the 10 dBW limit recommended in this section. All limits below 10 dBW were computed using an aircraft to tower distance of only 100 ft. instead of the cylinder radius of 250 ft. used in Table 5-5. Further, the values in this table were read from the minimum points along a series of curves, so the aircraft height and EIRP values do not have the same high precision as the results reported in the other tables.

**Table 5-8: Hexagonal Grid Scenario Based Limits  
from Randomly Located Base Station Method**

<b>Aircraft Lateral Separation Distance to Center Tower (ft.)</b>	<b>Flight Attitude</b>	<b>Center Tower Height (m)</b>	<b>Aircraft Antenna Height (m)</b>	<b>Mean Power Based EIRP Limit (dBW)</b>	<b>Tower Antenna Downtilt (deg)</b>
250	Level	10	7.5	17.6	2
250	Level	15	12	14.8	2
250	Level	20	10	12.6	8
250	Level	25	12.25	14	8
100	Level	10	6	5	8
100	Level	15	14	6	2
100	Level	20	16	4	8
100	Level	25	20	4	8
250	Banking	10	8	14	2
250	Banking	15	12 to 16	12	2
250	Banking	20	14 to 16	11.5	4
250	Banking	25	20	10.4	4
100	Banking	10	8	2.8	4
100	Banking	15	14	2.5	2
100	Banking	20	16	2.6	8
100	Banking	25	24	2	2

**5.2.3.7 Frequency Dependencies**

Using the slope of the spectrum mask of Figure 5-2 allows an EIRP transmit power limit computed at one frequency to be converted to an equivalent limit at a different frequency. For example, the spectrum mask shows the permissible interference level decreasing from -12.0 dBm at 1525.0 MHz to -103.267 dBm at 1559.0 MHz, a slope of -2.68432 dB/MHz. It then follows that a transmit limit such as 10 dBW at 1531 MHz corresponds to a limit of -16.84 dBW at 1541 (i.e., 10 dBW + (-2.68432 x (1541 – 1531) dB)) and a limit of -43.69 dBW at 1551 MHz (i.e., 10

dBW + (-2.68432 x (1551 – 1531) dB)). These examples apply for frequencies between 1525 MHz and 1565 MHz where the slope of the spectrum mask is the same.

### 5.2.3.8 Sensitivity Analysis Results

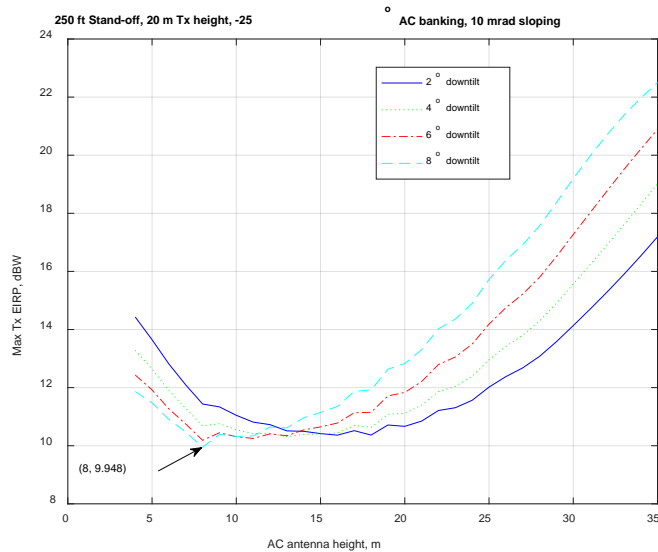
The HTAWS case presents the most restrictive limits so solution sensitivities to various parameters are best demonstrated using examples from this case. An important interplay between the parameters focuses on placing the aircraft in the center of the main lobe of the RFI emitter antenna beam. The relationship of the aircraft and the emitter main lobe varies with both antenna heights, the degree of the emitter antenna down tilt and the distance between the antennas. Banking (vs. level flight) also has a significant impact because the aircraft antenna gains vary with elevation angle and banking changes the effective elevation angle. Sloping (vs. flat) ground has a noticeable impact because the Hata path loss model contains a slope dependent parameter and the total height of all towers, except the central one, increases with radius. The computed limit is also sensitive to the emitter polarization because, at some elevations, the aircraft antenna gains are larger for vertically than for horizontally polarized signals. All analyses in this Report assume either vertically polarized radio waves or an equal power combination of vertically and horizontally polarized waves (i.e., dual polarization). The parameters varied during the HTAWS case study are listed below and after each parameter type the range of values explored are listed in parentheses. The computed maximum limit is sensitive to the following parameters and the interplay between these parameters:

- The heights of the emitter (10, 15, 20, 25 meters) and aircraft antennas (4 to 35 meters)
- The down tilt angle of the emitter antenna (2, 4, 6, 8 degrees)
- The ground distance between the two antennas (100 feet vs. 250 feet and vicinity)
- Flat ground vs. Sloping ground (upward with a 10 milliradian slope)
- Level flight vs. banking (at 25 degrees)
- Vertical vs. dual polarization (equal power vertical and horizontal polarization)

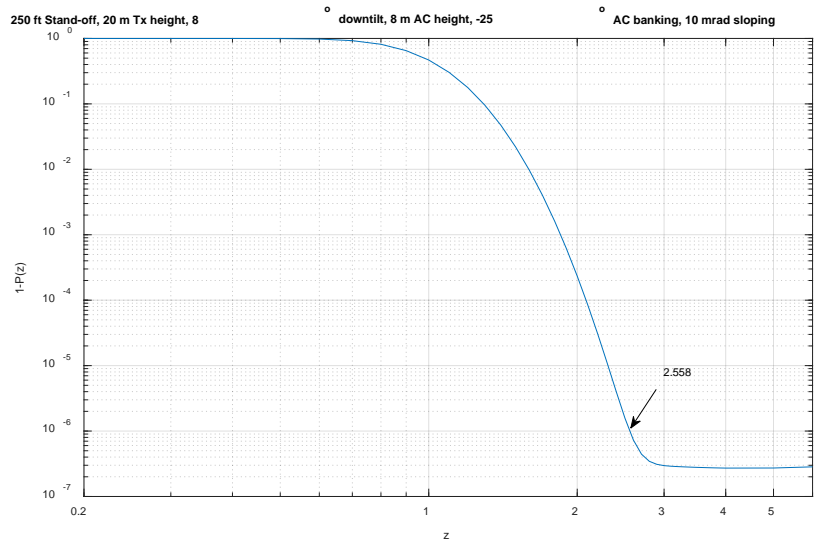
Figure 5-10, Figure 5-12, and Figure 5-14 depict how a computed mean based limit is sensitive to various parameter changes. Figure 5-11, Figure 5-13, and Figure 5-15 show the corresponding “1-CDF” (i.e., “1-P(z)”) curve based on parameter set of the most restrictive mean based limit of the preceding figure. Each of these three mean based limit figures contains four curves with different amounts of antenna down tilt. Each abscissa varies the aircraft (AC) antenna height and the ordinate displays the resultant limit values. Figure 5-10, Figure 5-12, and Figure 5-14 show an ordered pair of numbers for the abscissa and ordinate values that correspond to the most restrictive mean based limit. All these figures used an assessment zone radius of 250 feet. Calculations were also performed for a standoff radius of 100 feet, which results in lower limits (not shown). Figure 5-10 and Figure 5-12, are for dual polarization while Figure 5-14 is for vertical polarization. Figure 5-10 uses a 20 m height emitter while Figure 5-12 uses a 10 m height emitter and Figure 5-14 uses a 25 m height. Figure 5-10 shows a limit of 9.948 dBW, the lowest mean based limit computed with dual polarization. The corresponding rare event based limit is 9.869 dBW, as computed with Equation 5.3-2 using the Zcrit value of 2.558 taken from Figure 5-11.

Figure 5-14 presents an even lower mean based limit of 7.945 dBW with vertical polarization only. The corresponding rare event based limit computed with Equation 5.3-2 using the  $Z_{crit}$  value of 2.530 from Figure 5-15 is slightly lower at 7.9138 dBW. Thus Figure 5-14 and Figure 5-15 demonstrate the importance of wave polarization type on the computed limit.

The rare event limit of 9.869 dBW for dual polarization is lowest limit computed at the 250 ft. (76.2 m) assessment zone radius. The one single limit value of 9.8 dBW cited in this Report is derived from rounding down the computed result. This rounding allows for the additional effect of a random distribution of base station emitters, as in [10] Section.3.5.2, that extends beyond the central hexagonal grid sources out to the radio horizon at a decreasing surface concentration. It is very important to note that this result assumes (equal power split) dual polarization and highlights that a requirement for cross-polarization emissions from the base stations must be captured in any license application or issuance. A vertical polarization (only) based limit must be significantly lower than 9.8 dBW.



**Figure 5-10: HTAWS Dual Polarization 20 m Emitter Antenna-Mean Limits**



**Figure 5-11: (1-CDF) for Most Restrictive Mean Limit Condition of Figure 5-10**

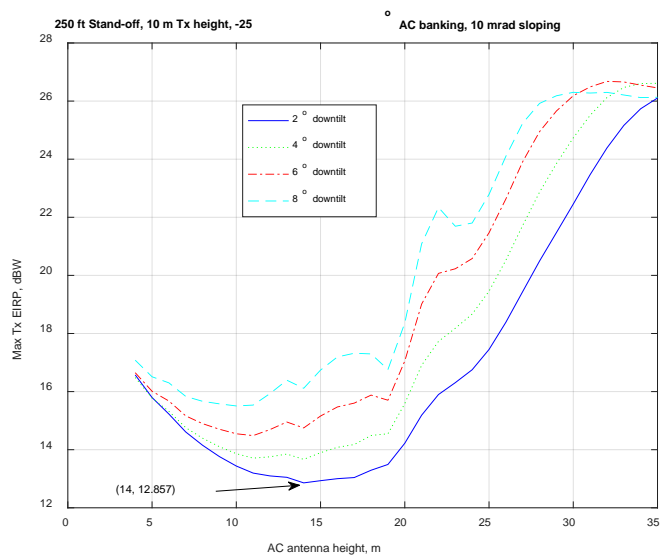


**Figure 5-12: HTAWS Dual Polarization 10 m Emitter Antenna-Mean Limits**

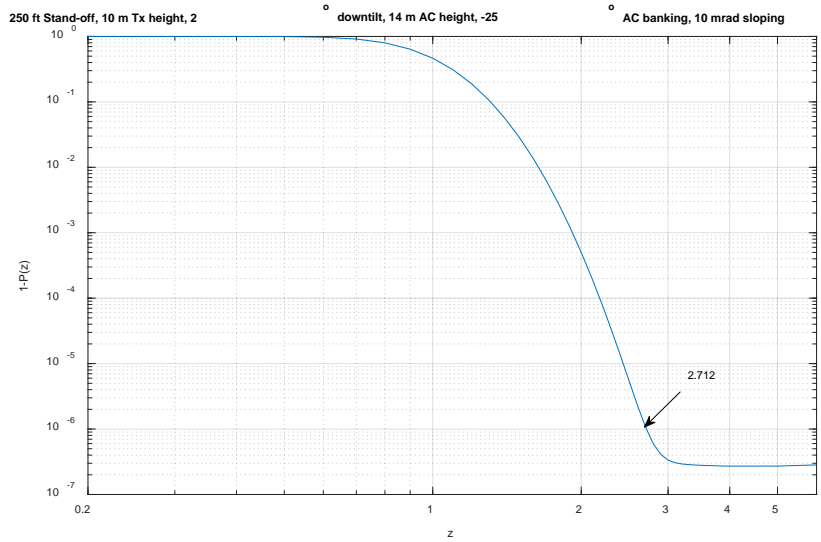


**Figure 5-13: (1-CDF) for Most Restrictive Mean Limit Condition of Figure 5-12**

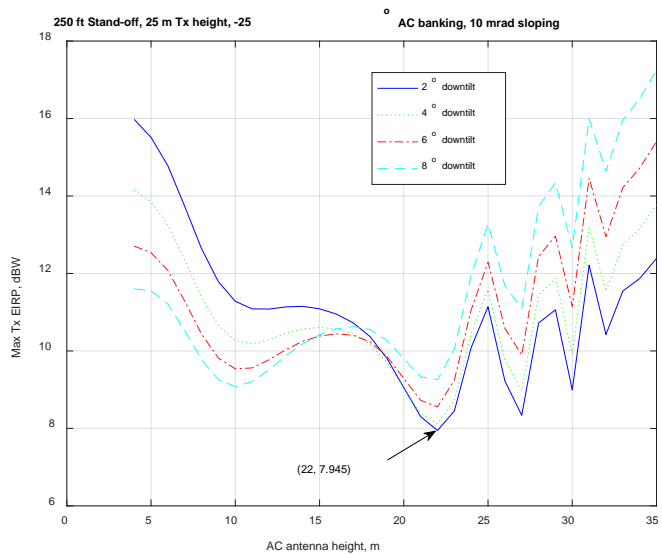


**Figure 5-14: HTAWS Vertical Polarization 25 m Emitter Antenna-Mean Limits**

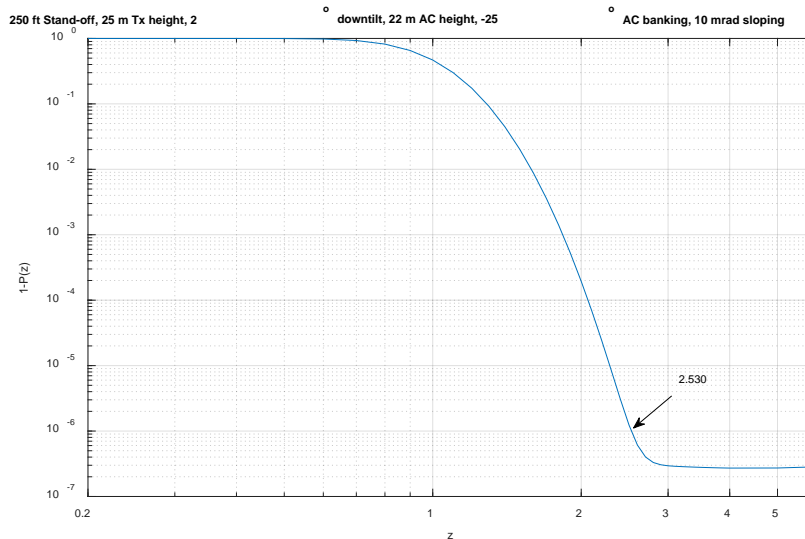


**Figure 5-15: (1-CDF) for-Most Restrictive Mean Limit Condition of Figure 5-14**

### 5.2.3.9 Certified Aviation Receiver Analysis Results Summary

RFI degradation calculations for a variety of scenarios have been performed by the FAA in order to determine a maximum tolerable power transmission level for usage of frequencies near the GPS L1 band. All analyses were conducted in accordance with the procedures recommended in the applicable RTCA [10] and FAA Technical Center [8] reports with the procedures refined when necessary. A summary of these results from the performed analyses is provided in Table 5-9.

The “Handset” cases assessed showed these do not present a limiting case or scenario for certified aviation receivers. The “Ground Station” analyses computed aggregate RFI power assuming an aircraft was located at the WIRSO waypoint in Washington, DC (i.e., near Reagan National airport over the Potomac River). This analysis used a realistic set of 1,068 towers as well as extensive modeling of the surrounding terrain so that the impact of slope on the Hata-Okumura path loss model could be ascertained. The “HTAWS” analyses assumed towers are deployed in a symmetrical hexagonal grid pattern with the aircraft located 76.2 meters (i.e., 250 feet) from the central tower. Terrain modelling for this analysis assumed either flat ground or an idealized symmetrical funnel shaped terrain with a slope of 10 milliradians in all directions.

Different transmit antenna patterns were used by the Ground Station and HTAWS analyses. In addition to tower deployment, terrain modeling and transmit antenna patterns, another major difference between these two analyses is signal polarization. As recommended in [10], the Ground Station analysis set assumed all radio transmissions were vertically polarized only.



However, to evaluate the HTAWS case, the FAA RFI analysis methodology evaluated vertical polarization only, as well as dual polarization consisting of equal power vertical and horizontal polarized transmissions. The issue of radio polarization type is significant because the aircraft GPS antenna gain varies according to signal elevation and polarization. The Ground Stations analysis simulated the RFI encountered by an aircraft at an altitude of 125.64 m at an actual waypoint over the Potomac River found an EIRP limit of 28.9 dBW. The HTAWS analysis simulated a helicopter flying within 76.2 meters of a cellular system tower of a hexagonal grid system dictates a significantly lower limit of 9.8 dBW.

The two cases yielded such different limits due to differences in the lateral separation distance from the aircraft to the closest tower. The distance from aircraft nadir to the closest tower base for the WIRSO scenario is a relatively large 1,396 m while the minimum separation distance in the hexagonal grid scenario is 76.2 m. Assuming for a moment a simple free space path loss model, this difference in separation distance would result in a 25 dB difference in path loss to the closest tower. The actual delta path loss to the closest tower between the two analyses is larger because 76.2 m is within the zone of a two-ray path loss model but no tower in the WIRSO scenario was within the two-ray zone. In all the hexagonal grid scenarios examined the central tower provided at least 90% of the scenario total aggregate RFI power (in some scenarios much more). Further, the hexagonal grid scenario with an Inter-Station Distance (ISD) of 433 m had 37 towers within 1,396 m, and even a grid with an ISD of 633 m has 14 towers inside the radius of the closest WIRSO tower. Though the evaluation of the RFI at other waypoints was suggested by the RTCA document [10], it is unlikely that these would include an aircraft flying within 76.2 meters of a tower.

These analyses indicate that protection of certified avionics, operating under the assumption of the described 250 foot (76.2 m) radius assessment zone, requires that the Ground Station transmission EIRP not exceed 9.8 dBW (cross-polarized) at 1531 MHz. This limit is obtained from the HTAWS scenario which was found to be the most restrictive of the scenarios examined. The limit from the Discrete Tower scenario at the WIRSO waypoint was found to be 28.9 dBW with considerably larger Ground Station ISD. Limit values at other frequencies can be computed as described in section 5.2.3.7 using the spectral mask slope of Figure 5-2.

**Table 5-9: Summary of Scenarios and Findings**

Scenario	Conditions	Comments
Inflight Aircraft / Ground-based Handset	Final Approach Fix & Waypoint, Cat. I & Cat. II Decision Height	Cat. II determined as most stringent case; Assessed, <6% threshold increase, not deemed a critical or limiting scenario (see 5.2.3.2)
Inflight Aircraft / Ground Base Station	Random and discrete tower locations, Aircraft level & banking	Assessed 1531 MHz at WIRSO location 125.64 m altitude. Differences between 0° , 25° attitude as well as rare event attributed to tower distributions (see 5.2.3.3)
Inflight Aircraft / Onboard Handset	Aircraft at 10K ft. altitude	Assessment premised on handset exhibiting characteristics of WiFi at 2.45 GHz, no further assessment required (see 5.2.1.3.1)
Aircraft on Ground / Onboard Handset	Aircraft antenna at 4 m	Assessed, not deemed a critical or limiting scenario (see 5.2.3.4)
Aircraft at Gate / Single Handset Source on or near Boarding Stairs or Jetway	0 dBW @ 1616 MHz	Assessed, 3.5 m minimum separation distance (see 5.2.1.4.1)
Aircraft at Gate/Users Inside Airport	Random distribution of thirty handsets	Assessed, not deemed critical or limiting scenario (see 5.2.3.5)
TAWS / HTAWS Scenarios with Ground-based Mobile Broadband Handsets	Three handset surface concentrations with -95 dBW/MHz in the GPS L1 receiver passband, Two aircraft antenna heights	Assessed, found fundamental emission effects insignificant, no further assessment required (see 5.2.1.2.1)
TAWS and HTAWS Scenarios with Broadband Base Station	Base stations located on a grid with 433 m or 693 m inter-station distance. Base station heights of 6, 10, 15 and 25 m were considered, with 2, 4, 6, and 8 degree antenna down tilt. Aircraft was assumed at the worst-case location on the assessment zone, both level flight and 25 degree bank toward the base station. Additional parameters including sloping ground were utilized as part of a sensitivity analysis as described in 5.2.3.8.	Fixed location base stations in hexagonal grid with 433 m and 693 m ISDs, flat earth and funnel terrain, aircraft lateral distances of 15.2-76.2 m, 25° and 0° banking. Both Monte Carlo and Analytic Statistical methods used for assessment (see 5.2.3.6) Assessment found HTAWS the most restrictive scenario (see 5.2.3.8)

## 6. SUMMARY

This report describes DOT's efforts to evaluate the adjacent band radiofrequency band power levels that can be tolerated by GPS and GNSS receivers. The assessment described in this report addresses transmitters in bands adjacent to the 1559-1610 MHz radionavigation satellite service (RNSS) band used for GPS L1 signals that are centered at 1575.42 MHz.

Results from GNSS receiver testing conducted in the ARL anechoic chamber facility at WSMR to assess their sensitivity to adjacent band interference in the range 1475 to 1675 MHz are presented in this report for the six categories of receivers tested. The radiated GNSS signals included GPS, SBAS, GLONASS, BeiDou, and Galileo signals. The radiated interference waveforms included 1 MHz AWGN and 10 MHz LTE signals (referred to as Type-1 and Type-2). The GNSS and interference signals were radiated through separate and collocated antennas as shown in the chamber layout diagram.

The collected test data capture the performance degradation of each device through the CNR which decreases as the interference power increases and the signal power stays fixed. In this report, the main analysis of GNSS receiver susceptibility to adjacent band interference refers to the interference power level at which the average CNR for a device drops by 1-dB from its baseline (interference-free) value. The resulting interference power level vs. interference frequency is referred to as the Interference Tolerance Mask for that device. The test data were also used for a secondary analysis of receiver susceptibility to determine the interference power level at which a receiver assembly loses signal tracking (referred to as Loss of Lock).

These bounding ITMs per receiver category and the GPS/GNSS antenna characteristics were the primary inputs to use case scenario assessments to determine the maximum Effective Isotropic Radiated Power that could be tolerated in the adjacent radiofrequency bands for each GPS/GNSS receiver category. Space-based applications are different from other GPS/GNSS applications considered, primarily due to the need to account for aggregation effects of multiple transmitters visible in orbit. Although OST-R derived ITMs for space-based receivers, along with other GPS/GNSS receiver types, OST-R deferred to NASA for assessing adjacent-band transmitter power levels that can be tolerated for this receiver category.

The L1 C/A bounding ITM is the lowest interference power at a given frequency that resulted in a 1 dB CNR reduction for at least one receiver in the category (for each receiver category). Most sensitive categories are the high precision and space-based receivers. The least sensitive category is the cellular category.

The Loss of Lock power levels for high elevation angle satellites (nominal signal power -128.5 dBm) were typically 15 – 25 dB higher than the ITM levels. The loss of Lock Interference power levels for low elevation angle satellites (signal power -138.5 dBm) were typically 5 – 15 dB higher than ITM levels as would be expected since the low elevation were emulated by a 10 dB reduced power levels from the nominal signal power to account for change of receiver antenna gain at low elevations.

During July 2016, 14 GNSS receivers were tested for further ABC assessment in a laboratory setting at Zeta Associates Inc. in Fairfax, VA. The test objectives were: (1) evaluation of the impact of adjacent-band interference on signal acquisition, (2) comparison between wired and radiated receiver susceptibility to adjacent band interference with 1 MHz bandpass noise and 10 MHz LTE, and (3) assessment of adjacent band transmitter OOB impacts.

The ITMs from the wired test exhibited good agreement with the radiated results when the same active antenna was used or when the bypassed active antenna components were properly considered in the comparison. The wired test also showed that the FCC OOB limits (base station and handset limits) have the potential to impact ITMs as does one entrants' proposed OOB limits for handsets at separation distances less than 2 meters.

The results of these tests indicate that the 1-dB CNR degradation level is a good indicator of the region where acquisition starts to be impacted for some receivers. This is especially noticeable for the lower power GNSS signals emulating low elevation satellites or attenuated GNSS signal due to foliage or other environmental factor.

The approach to determine tolerable EIRP levels for a given standoff distance (inverse modeling), as well as the one to determine minimum standoff distance for a given EIRP value (forward modeling) were described in the approach section. Interference source (transmitter) characteristics were primarily obtained from M.2292 and proposals to FCC for adjacent band network applications.

Antenna Measurements for each one of the 22 frequencies used in the WSMR tests were done to determine the appropriate antenna pattern to use for each category of receivers. Parabolic fits to these measurements were ultimately used as inputs to the forward and inverse modeling calculations. The propagation loss was estimated through the Free-Space Path Loss model and the Two-ray model. Since the Irregular Terrain Model is expected to have the same properties as FSPL for distances up to 100 meters it is indirectly considered as part of the FSPL analysis.

Understanding GPS/GNSS receiver use cases scenarios are important so that the geometric parameters, specifically a receiver height and lateral offset from a transmitter can be determined. Also, it is important that use cases representative each receiver category and can provide a worst-case scenario so most, if not all, receivers in that category are protected. In addition, use cases are needed in conjunction with ITMs, propagations models, and transmitter scenarios to determine what power levels can be tolerated adjacent to GPS/GNSS signals.

Use cases were compiled through substantial outreach with DOT federal partners and agencies. Members of the working group were provided a template that contained questions related to how their organizations use GPS/GNSS receivers to support their mission. In particular, questions included identifying height, speed, terrain, antenna orientation and integration, and urbanization areas.

The use case analysis has shown that receiver heights extends to at and above the height of a base station in all categories and therefore the tolerable EIRP as a function of standoff distance can be found by taking the minimum along heights up to and above base station heights. The extent of the impact region for a high precision receiver is >10 km from the transmitter for an EIRP of 29 dBW and 1.8 km for EIRP of 10 dBW.

In the area of impact, the behavior of the GPS/GNSS receiver can become unreliable in its ability to meet the accuracy, availability, and integrity requirements of its intended function, impacting safety-critical applications such as transportation, the earthquake early warning system, and space-based missions using GPS/GNSS receivers, as well as high precision users such as precision agriculture, machine control, and surveying.

Tolerable EIRP levels to protect all tested receivers processing the L1 C/A signal are shown in at standoff distances of 10 and 100 meters for two different deployments. For L1 C/A signals and macro-urban networks, the tolerable EIRP decreases monotonically from about -24 dBW (4 mW) at 1475 MHz, to -42 dBW (< 0.1mW) at 1530 MHz, to -62 dBW (<1  $\mu$ W) at 1550 MHz; for micro-urban networks the results increase by a fraction of a dB. For all GNSS signals, the above values decrease by a few dB.

For certified GPS avionics, the FAA analyzed a number of scenarios including:

- 1) Inflight Aircraft with a Ground-based Handset
- 2) Inflight Aircraft with a Ground Base Station
- 3) Inflight Aircraft with an Onboard Handset
- 4) Aircraft on the ground with an Onboard Handset
- 5) Aircraft at Gate / Single Handset Source on or near Boarding Stairs or Jetway
- 6) Aircraft at Gate/Users Inside Airport
- 7) Terrain Awareness Warning System (TAWS) / Helicopter TAWS (HTAWS) Scenarios with Ground-based Mobile Broadband Handsets
- 8) TAWS and HTAWS Scenarios with Broadband Base Station

The analysis is based on the concept of an “assessment zone” inside of which GPS performance may be compromised or unavailable. In this region GPS based instrument flight rules (IFR) operations will be restricted due to the elevated levels of RFI. Different transmit antenna patterns were used by the Ground Station and HTAWS analyses. In addition to tower deployment, terrain modeling and transmit antenna patterns, another major difference between these two analyses is signal polarization. The Ground Station analysis set assumed all radio transmissions were vertically polarized only. However, to evaluate the HTAWS case, the FAA RFI analysis methodology evaluated vertical polarization only, as well as dual polarization consisting of equal power vertical and horizontal polarized transmissions.

The issue of radio polarization type is significant because the aircraft GPS antenna gain varies according to signal elevation and polarization. The Ground Stations analysis simulated the RFI encountered by an aircraft at an altitude of 125.64 m at an actual waypoint over the Potomac River found an EIRP limit of 28.9 dBW. The Helicopter Terrain Awareness Warning System (HTAWS) analysis simulated a helicopter flying within 76.2 meters of a cellular system tower of

a hexagonal grid system dictates a significantly lower limit of 9.8 dBW. A very important difference between the two case analyses is simply the lateral separation distance from the aircraft to the closest tower. The distance from aircraft nadir to the closest tower base for the WIRSO scenario is a relatively large 1,396 m while the minimum separation distance in the hexagonal grid scenario is 76.2 m.

This limit is obtained from the HTAWS scenario which was found to be the most restrictive of the certified aviation scenarios examined. The FAA analysis of certified aviation indicate that protection of certified avionics, operating under the assumption of the described 250 foot (76.2 m) radius assessment zone, requires that the ground station transmission not exceed 9.8 dBW (10W) (cross-polarized) at 1531 MHz. Based on the results of the OST-R testing and analysis of the other categories of receivers, the transmitter power level that can be tolerated by certified aviation may cause interference with, or degradation to, most other categories of GPS/GNSS receivers including those used for General Aviation and drones.

## ACRONYM LIST

ABAS	Aircraft-Based Augmentation System
ABC	Adjacent Band Compatibility
AC	Aircraft
ACLR	Adjacent Channel Leakage Ratio
ADS-B	Automatic Dependent Surveillance-Broadcast
AF	Aggregate Factor
AFSS	Autonomous Flight Safety System
AFTS	Automated Flight Termination System
AFTU	Automated Flight Termination Unit
AGL	Above Ground Level
AHRS	Attitude and Heading Reference System
ARL	Army Research Laboratory
ATC	Ancillary Terrestrial Component
ATIS	Alliance for Telecommunications Industry Solutions
AWGN	Additive White Gaussian Noise
AZ	Azimuth
CAR	Certified Aviation Receiver
CAT	Category
CDF	Cumulative Distribution Function
CEL	Cellular
CNR	Carrier-to-Noise density Ratio
COSMIC	Constellation Observing System for Meteorology, Ionosphere and Climate
CR	Cell Radius
CSV	Comma Separated Variable
CW	Continuous Wave
CYGNSS	Cyclone Global Navigation Satellite System
dB	decibel
dB <sub>i</sub>	decibel isotropic
dB <sub>c</sub>	decibel isotropic circular
dB <sub>m</sub>	decibel-milliwatt
dB <sub>W</sub>	decibel-watt
DORIS	Doppler Orbitography by Radiopositioning Integrated on Satellite
DOT	U.S. Department of Transportation
DUT	Device Under Test
DSAC	Deep Space Atomic Clock
EDP	Electron Density Profile
EIRP	Effective Isotropic Radiated Power
EL	Elevation
BS	Base station
ETSO	European Technical Standard Order
EMVAF	Electromagnetic Vulnerability Assessment Facility
FAA	Federal Aviation Administration

FAF	Final Approach Fix
FCC	Federal Communications Commission
FMS	Flight Management System
FSPL	Free-Space Path Loss
GAV	General Aviation
GBAS	Ground-Based Augmentation System
GEO	Geostationary
GHz	gigahertz
GLN	General Location and Navigation
GM	General Motors
GNSS	Global Navigation Satellite System
GNSS-R	GNSS Reflectometry
GPS	Global Positioning System
GRACE	Gravity Recovery and Climate Experiment
GUST	Geostationary Uplink System Type-1
HITL	Human-in-the-Loop
HPA	High Power amplifier
HPOL	Horizontal Polarization
HPR	High-Precision Receiver
HTAWS	Helicopter Terrain Awareness Warning System
Hz	hertz
ICAO	International Civil Aviation Organization
ICD	Interface Control Document
IFR	Instrument Flight Rules
IGOR	Integrated GPS Occultation Receiver
IMT	International Mobile Telecommunication
IP	Interference Power
IPC	Interference Protection Criteria
ISD	Inter-Site Distance
ISS	International Space Station
ITM	Interference Tolerance Mask
ITU-R	International Telecommunications Union Radiocommunication Sector
JPL	Jet Propulsion Laboratory
K	kelvin
kHz	kilohertz
km	kilometer
KPI	Key Performance Indicator
L1 C/A	GPS L1 Course Acquisition
LEO	Low Earth Orbit
LNA	Low Noise Amplifier
LOL	Loss of Lock
LPV	Localizer Performance with Vertical Guidance
LTE	Long Term Evolution
m	meter
M&S	Modeling and Simulation
MATLAB	Matrix Laboratory



MHz	megahertz
MOPS	Minimum Operational Performance Standard
MSL	Mean Sea Level
MSS	Mobile Satellite Service
mW	milliwatt
NaN	Not a Number
NAS	National Airspace System
NASA	National Aeronautics and Space Administration
NC	Not Computed
NCO	National Space-Based PNT Coordination Office
NDA	Non-Disclosure Agreement
NET	Networks
NI	National Instruments
NISAR	NASA-ISRO Synthetic Aperture Radar
NMEA	National Maritime Electronics Association
NOAA	National Oceanic and Atmospheric Administration
NTIA	National Telecommunications and Information Administration
OFDM	Orthogonal Frequency Division Multiplexing
OOBE	Out of Band Emissions
OST-R	DOT Office of the Assistant Secretary for Research and Technology
PBN	Performance-Based Navigation
PF	Power Factor
POD	Precise Orbit Determination
Pos/Nav	Positioning/Navigation
PRN	Pseudorandom Noise
PSD	Power Spectral Density
QZSS	Quazi-Zenith Satellite Service System
RAID	Redundant Array of Independent Disks
RAIM	Receiver Autonomous Integrity Monitoring
RAM	Radiant Absorbent Material
RF	Radiofrequency
RFI	Radiofrequency Interference
RHCP	Right-Hand Circular Polarization
RINEX	Receiver Independent Exchange
RNAV	Area Navigation
RNSS	Radionavigation Satellite Service
RO	Radio Occultation
RTCA	Formerly Radio Technical Commission for Aeronautics (now RTCA, Inc)
Rx	Receiver
SARPS	Standards and Recommended Practices
SBAS	Satellite-Based Augmentation System
SC-OFDM	Sub-Carrier Orthogonal Frequency Division Multiplexing
SNR	Signal-to-Noise Ratio
SPB	Space-Based
SPIGAT	Software Programmable Interference Generator for ABC Testing
SWO	Space Weather Observation

SWOT	Surface Water and Ocean Topography
TAWS	Terrain Awareness Warning System
TEC	Total Electron Content
TIM	Timing
TSO	Technical Standard Order
Tx	Transmitter
$\mu\text{W}$	microwatt
UAS	Unmanned Aircraft System
USCG	U.S. Coast Guard
USG	U.S. Government
USGS	U.S. Geological Survey
VPOL	Vertical Polarization
VSG	Vector Signal Generator
WAAS	Wide Area Augmentation System
WGS	World Geodetic System
WP	Waypoint
WSMR	White Sands Missile Range

## REFERENCES

- [1] DOT GPS Adjacent Band Compatibility Assessment Plan December 2012.
- [2] U.S. Air Force Background Paper on Use of 1-dB Decrease in C/No As GPS Interference Protection Criterion June 2017.
- [3] ITU-R Report M.2292: Characteristics of Terrestrial IMT-Advanced systems for frequency sharing/interference Analyses.
- [4] ITU Report ITU-R SA.2325-0: Sharing between space-to-space links in space research, space orientation and Earth exploration-satellite services and IMT systems in the frequency bands 2025-2110 MHz and 2200-2290 MHz.
- [5] ICAO SARPs Annex 10 Volume I Appendix B.
- [6] Report of the Tactical Operations Committee in Response to Tasking from the Federal Aviation Administration, December 2016.
- [7] Status Report: Assessment of Compatibility of Planned LightSquared Ancillary Terrestrial Component Transmissions in the 1526-1536 MHz Band with Certified Aviation GPS Receivers, FAA Report PR 25, January 25, 2012.
- [8] Final Report: A Generalized Statistical Model for Aggregate Radio Frequency Interference to Airborne GPS Receivers from Ground Based Emitters (DOT/FAA/TC-14/30, Rev. 1), August 7, 2017.
- [9] Minimum Operational Performance Standards for GPS/Wide Area Augmentation System Airborne Equipment, RTCA/DO-229.
- [10] FAA GPS Adjacent-Band Compatibility Study Methodology and Assumptions with RTCA SC-159 mark-ups, RTCA Paper No. 095-15/SC159-1040.
- [11] Final Report: A Generalized Statistical Model for Aggregate Radio Frequency Interference to Airborne GPS Receivers from Ground Based Emitters (DOT/FAA/TC-14/30), September. 30, 2014.
- [12] FAA GPS Adjacent-Band Compatibility Study Methodology and Assumptions with RTCA SC-159 mark-ups, RTCA Paper No. 095-15/SC159-1040.
- [13] Global Positioning System Wide Area Augmentation System (WAAS) Performance Standard, October 31, 2008.

## **ACKNOWLEDGEMENTS**

The authors would like to thank the following organizations for their contribution to the success of the testing and data collection efforts:

Aerospace Corporation

Army Research Laboratory (ARL), Electromagnetic Vulnerability Assessment Facility (EMVAF)

Federal Aviation Administration (FAA)

Federal Communication Commission (FCC)

General Motors (GM)

John Deere

MIT Lincoln Laboratory (MITLL)

MITRE Corporation

National Aeronautics and Space Administration (NASA)

National Oceanic and Atmospheric Administration (NOAA)

National Telecommunications and Information Administration (NTIA)

NovAtel

Trimble

U-Blox

UNAVCO

United States Air Force (USAF)

United States Coast Guard (USCG)

United States Geological Survey (USGS)

Zeta Associates

# **APPENDIX A**

## **WSMR TEST DETAILS**

# TABLE OF CONTENTS

TABLE OF CONTENTS.....	2
LIST OF FIGURES .....	3
LIST OF TABLES .....	4
REFERENCES .....	5
APPENDIX.....	6
Appendix A. WSMR Test Details.....	6
A.1 Interference System Development Considerations.....	6
A.2 Chamber Mapping .....	8
A.3 Chamber Mapping Comparison and Stability.....	10
A.4 System Calibration.....	18
A.5 Interference System Linearity.....	19
A.6 Comparison of Measured vs. Predicted Power .....	21
A.7 SPIGAT Antenna Characterizations .....	23
A.7.1 AST-1507AA .....	23
A.7.2 LB-510-10-C-NF.....	27
A.8 WSMR Activity Summary.....	29
A.9 Chamber OOBE.....	30
A.10 GNSS Signal Generation .....	38
A.10.1.1 Transmit antenna characterization .....	38
A.10.2 Almanacs.....	39
A.10.2.1 GPS Almanac.....	39
A.10.2.2 GLONASS Almanac.....	56
A.10.2.3 Galileo Almanac .....	69
A.10.2.4 BeiDou Almanac.....	83
A.10.2.5 SBAS Satellites .....	96
A.10.3 Emulated errors .....	96

## LIST OF FIGURES

Figure A-1: Chamber Mapping Grid .....	10
Figure A-2: Mapping Point differences between April 25th and April 28th.....	12
Figure A-3: Histogram of Differences between April 25th and April 28th Mappings.....	13
Figure A-4: Power Differences across the Test Grid between April 25th and April 28th Mappings (freqs. run from 1475 to 1675 at each point from left to right) .....	14
Figure A-5: Mapping Point differences between April 22nd and April 25th.....	15
Figure A-6: Histogram of Differences between April 22nd and April 25th Mappings.....	16
Figure A-7: Power Differences across the Test Grid between April 22nd and April 28th Mappings (freqs. run from 1475 to 1675 at each point from left to right) .....	17
Figure A-8: Comparison of Mapping Corrections from DOT Test Week.....	18
Figure A-9: Comparison of Targeted Power (Recorded in Control File) and Measured Power corrected for Spiral Antenna Gain and Cable Loss .....	20
Figure A-10: Comparison of Targeted Power (Recorded in Control File) Differenced.....	21
Figure A-11: Diagram of Special Test where Transmit and Receive.....	22
Figure A-12: Measured Power at P33 (corrected for spiral gain and calibration cable) compared with Predicted Power (interference system output power, horn antenna gain, horn cable loss, and Free Space Loss).....	23
Figure A-13: AST-1507AA Positioning; Back View.....	25
Figure A-14: AST-1507AA Boresight Measurements .....	26
Figure A-15: (a) A-Info Horizontal Position Side View, (b) A-Info Vertical Position Side Vie	27
Figure A-16: LB-510-10-C-NF Vertical Gain @ Boresight vs. Frequency .....	28
Figure A-17: LB-510-10-C-NF Vertical Pattern @ 1475, 1575 and 1675 MHz.....	29
Figure A-18: Spectra Showing Expanding Regrowth for Increasing HPA Input Power .....	31
Figure A-19: Example Gain Response of Narrow and Relaxed Filters.....	35
Figure A-20: Composite PSDs for Innermost LTE Signals at -30 dBm.....	36
Figure A-21: Composite PSDs for Innermost LTE Signals at -10 dBm.....	37
Figure A-22: Composite PSDs for the Innermost Relaxed-filter LTE Signals at -10 dBm .....	38
Figure A-23: GNSS Signal Generator Transmit Antenna Gain Patterns.....	39

## LIST OF TABLES

Table A-1: Interference Transmitter Specifications .....	6
Table A-2: LTE Parameters definition for the downlink and uplink signals.....	7
Table A-3: Example of Instrument settings for 1675 MHz .....	10
Table A-4: Calibration Values inserted into measlabtable.cfg: .....	19
Table A-5: AST-1507AA, Serial #174 .....	26
Table A-6: Summary of WSMR Activities for April ABC Testing (4/4-4/28).....	29
Table A-7: Attenuation for Regrowth Spectra to Correspond to Radiated Tests .....	32



## **REFERENCES**

**There are no sources in the current document.**

## APPENDIX

### Appendix A. WSMR Test Details

This Appendix provides a review of important aspects related to SPIGAT, the GNSS signal generation, and activities performed during the DOT test week at WSMR. Included are descriptions for generating the LTE signals, adjusting the mapping data to provide power measurements across the equipment test area, analysis demonstrating measured vs. expected power on the antenna floor, stability of power measurements over the test week, linearity of power over test limits, system calibration, antenna and cable measurements used in these analyses, and lastly, a summary of activities for the entire month at WSMR.

#### A.1 Interference System Development Considerations

The high level specifications for development of the SPIGAT capability are shown in Table A-1. These specifications and the test configuration at the EMVAF drove several critical decisions in development of SPIGAT. Three key issues were ensuring the maximum interference power could be achieved across the entire test area, automating the interference tests as well as system calibration and mapping, and lastly, ensuring interference signals were conditioned properly so GNSS equipment degradation could be attributed to the fundamental signal being generated and not unwanted emissions. Achieving the maximum power required a HPA that ultimately was provided by the support engineers at WSMR. Additionally, satisfying maximum power also required careful consideration of component insertion losses and ultimately sourcing a standard gain horn designed for the interference frequency range to be tested. The desire to complete the test effort in a single week dictated automation and sourcing an RF switch capable of handling these power levels and frequencies to be tested. And lastly, the filters required performance characteristics to sufficiently attenuate OOB when generating LTE signals and led to development of 22 RF passband cavity filters specifically for this test effort. Each of these areas is touched on in later sections of this Appendix.

**Table A-1: Interference Transmitter Specifications**

Name	Value	Unit
Range of selectable center frequencies	[1475, 1490, 1505, 1520, 1525, 1530, 1535, 1540, 1545, 1550, 1555, 1575, 1595, 1615, 1620, 1625, 1630, 1635, 1640, 1645, 1660, 1675]	MHz
Automation capability	Software controlled selection of center frequency, signal type, and transmit power	N/A
Interference signal generation capability	White noise or LTE	N/A

Number of selectable bandwidths	2	N/A
3 dB bandwidth (Signal Type-1 )	1	MHz
3 dB bandwidth (Signal Type-2 )	Consistent with LTE	N/A
Maximum power the setup is capable of delivering at any receiver location	$\geq -10$	dBm

Another consideration for this testing was the LTE waveforms to be used for the downlink and uplink signals. The LTE package offered by Keysight for its VSG products was considered originally but ultimately it was determined the MATLAB emulation, which also adheres to the LTE standard, had sufficient fidelity for this test effort. MATLAB generated time series representation of the downlink and uplink signals and these were converted so they could be loaded into the VSG for continuous replay. The actual MATLAB commands used to generate the downlink and uplink waveforms are shown below in respective order.

```
[rmcwaveform_DL,rmcgrid_DL,rmccfgout_DL] =
lteRMCDLTool(rmcconfig_DL,rand([1,10000]));
[rmcwaveform_UL,rmcgrid_UL,rmccfgout_UL] =
lteRMCULTool(rmcconfig_UL,rand([1,10000]));
```

The associated configuration MATLAB structures used in the commands above are shown in Table A-2. The duration of the uplink and downlink files was two seconds each and these were played out continuously end to end from VSG memory.

**Table A-2: LTE Parameters definition for the downlink and uplink signals**

<b>Downlink Parameters Definition</b>	<b>Uplink Parameters Definition</b>
Rmcconfig_DL.RC='R.2'	Rmcconfig_UL.RC = 'A3-5'
Rmcconfig_DL.NDLRB=50	Rmcconfig_UL.NULRB = 50
Rmcconfig_DL.CellRefP=1	
Rmcconfig_DL.NCellID=0	Rmcconfig_UL.NCellID = 0
Rmcconfig_DL.CyclicPrefix='Normal'	Rmcconfig_UL.CyclicPrefixUL = 'Normal'
Rmcconfig_DL.CFI=2	
Rmcconfig_DL.Ng='Sixth'	
Rmcconfig_DL.PHICHDuration='Normal'	
Rmcconfig_DL.NFrame=0	Rmcconfig_UL.NFrame = 0
Rmcconfig_DL.NSubframe=0	Rmcconfig_UL.NSubframe = 0
Rmcconfig_DL.TotSubframes=2000	Rmcconfig_UL.TotSubframes = 2000
	Rmcconfig_UL.CyclicShift = 0
	Rmcconfig_UL.Shortened = 0
	Rmcconfig_UL.Hopping = 'Off'
Rmcconfig_DL.OCNG = 'On'	Rmcconfig_UL.SeqGroup = 0

Rmcconfig_DL.Windowing = 16	Rmcconfig_UL.Windowing = 16
Rmcconfig_DL.DuplexMode = 'FDD'	Rmcconfig_UL.DuplexMode = 'FDD'
	Rmcconfig_UL.NTxAnts = 1
Rmcconfig_DL.SerialCat = 1	
Rmcconfig_DL.SamplingRate = 15360000	Rmcconfig_UL.SamplingRate = 15360000
Rmcconfig_DL.Nfft = 1024	Rmcconfig_UL.Nfft = 1024
Rmcconfig_DL.PDSCH.TxScheme = 'Port0'	
Rmcconfig_DL.PDSCH.Modulation = {'QPSK'}	Rmcconfig_UL.PUSCH.Modulation = 'QPSK'
Rmcconfig_DL.PDSCH.NLayers = 1	Rmcconfig_UL.PUSCH.NLayers = 1
Rmcconfig_DL.PDSCH.Rho = 0	
Rmcconfig_DL.PDSCH.RNTI = 1	Rmcconfig_UL.RNTI = 1
Rmcconfig_DL.PDSCH.RVSeq = [0 1 2 3]	Rmcconfig_UL.PUSCH.RVSeq = [0 2 3 1]
Rmcconfig_DL.PDSCH.RV = 0	Rmcconfig_UL.PUSCH.RV = 0
Rmcconfig_DL.PDSCH.NHARQProcesses = 8	Rmcconfig_UL.PUSCH.NHARQProcesses = 8
Rmcconfig_DL.PDSCH.NTurboDecIts = 5	Rmcconfig_UL.PUSCH.NTurboDecIts = 5
	Rmcconfig_UL.PUSCH.DynCyclicShift = 0
	Rmcconfig_UL.PUSCH.NBundled = 0
	Rmcconfig_UL.PUSCH.BetaACK = 2
Rmcconfig_DL.PDSCH.CSIMode = 'PUCCH 1-1'	Rmcconfig_UL.PUSCH.BetaCQI = 2
Rmcconfig_DL.PDSCH.PMIMode = 'Wideband'	Rmcconfig_UL.PUSCH.BetaRI = 2
Rmcconfig_DL.PDSCH.PRBSset = [0:49]	Rmcconfig_UL.PUSCH.PRBSset = [0:49]
Rmcconfig_DL.PDSCH.TrBlkSizes = [4392 4392 4392 4392 0 4392 4392 4392 4392]	Rmcconfig_UL.PUSCH.TrBlkSizes = [5160 5160 5160 5160 5160 5160 5160 5160 5160]
Rmcconfig_DL.PDSCH.CodedTrBlkSizes = [12960 13800 13800 13800 13800 0 13800 13800 13800]	Rmcconfig_UL.PUSCH.CodedTrBlkSizes = [14400 14400 14400 14400 14400 14400 14400 14400 14400]
	Rmcconfig_UL.PUSCH.PMI = 0
	Rmcconfig_UL.PUSCH.OrthCover = 'On'

## A.2 Chamber Mapping

Chamber mapping determined RF power across the chamber floor and was ultimately used to adjust SPIGAT test event summary files to establish power incident at each device tested. Mapping was also accomplished with the GNSS signal generation system to demonstrate power uniformity over the test area. The approach for mapping was to first establish a grid that encompassed equipment placed in the test area. Figure A-1 shows the grid utilized in this effort with 45 measurement points (blue diamonds) spaced approximately four feet apart. The mapping grid origin for purposes of labeling points is at the bottom left corner of this figure (point X=0 and Y=0). Each axis spanned values from 0 to 6. For reference, the mapping point at the center of the grid was identified as P33 and was directly below the interference transmit and GNSS antennas and P03 as will be described in a later section was the reference point used for system calibrations. The red rectangles represent the area used for equipment under test.

The mapping and calibration procedure used a cavity backed spiral antenna mounted on a tripod, calibrated RF cable, and a spectrum analyzer. The characteristics of the cavity backed spiral are provided in a later section along with cable and transmit antenna characterizations. Power measurements were made by positioning the tripod over a designated mapping point, boresighting the cavity backed spiral on the transmit antenna using a laser pointer attached to the antenna, having the interference generation and GNSS systems generate tones at each required frequency, and lastly, having the spectrum analyzer step through each frequency and measure the power of these tones. The interference signal generation system used the system calibration file (described in a later section) to target a power level of -40 dBm as measured at the spiral antenna. Measurements were taken with analyzer settings; auto-calibration disabled, preamplifier ON with internal attenuation fixed at 6 dB (lowest available), span of 1 MHz using 1001 points centered at the measurement frequency with resolution and video bandwidths of 5 kHz, averaging ON and set to four frames, and using the RMS detector (see Table A-3).

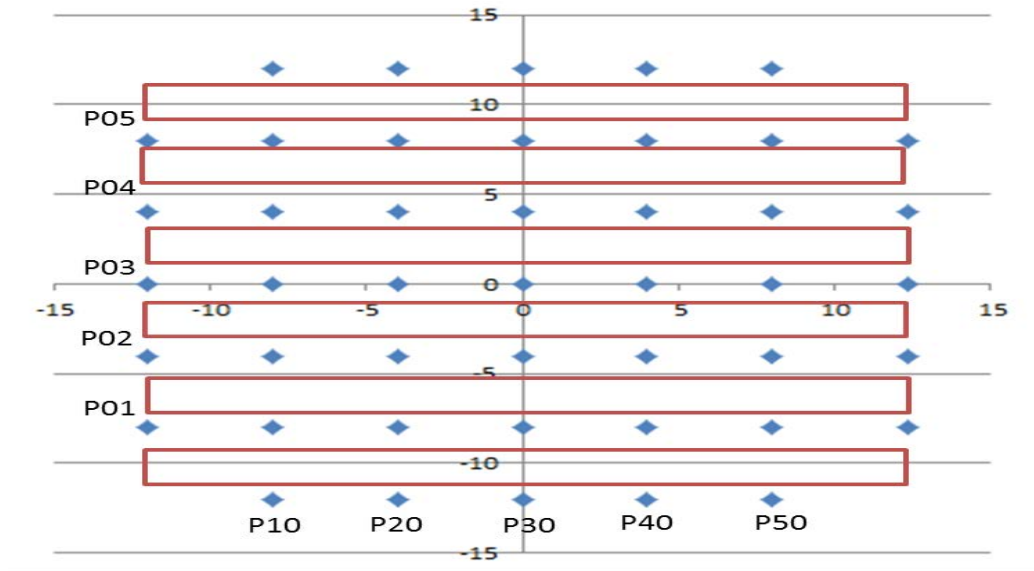


**Figure A-1: Chamber Mapping Grid**

**Table A-3: Example of Instrument settings for 1675 MHz**

att:	+6.00E+00	mkx:	+1.6750000000000000E+009
autoatt:	0	mky:	-5.38870E+01
autocal:	OFF	pdiv:	+1.000E+01
avgstate:	1	peaky:	0
cont:	0	points:	+1001
det:	AVER	preamp:	1
fcent:	+1.6750000000000000E+009	rbw:	+5.10000000E+003
fref:	EXT	reflev:	-3.400E+01
fspan:	+1.0000000000000000E+006	sweep:	+1.46600000E-001
fstart:	+1.6745000000000000E+009	trace:	WRIT
fstop:	+1.6755000000000000E+009	vavg:	+4
		vbw:	+5.10000000E+003

### A.3 Chamber Mapping Comparison and Stability

Chamber mapping at all 45 points was accomplished at the beginning (4/25) and end (4/28) of DOT testing with all equipment installed in the test area. Mapping was also accomplished with all equipment removed during the prior week (4/22) to establish variation introduced with GNSS equipment in the test area. (Section A.8 provides a high level review of activities conducted for the entire month of April at WSMR). For processing the mapping data, the power at each frequency was adjusted for the target power of -40 dBm, spiral antenna gain at boresight and calibration cable loss. Additionally, the calibration antenna was approximately 1.5 feet above the blue absorbing material where GNSS equipment was placed for test. To account for this difference, an additional 0.5 dB was included for this height differential to reflect the additional free space loss. (Note the face of the transmit horn antenna was 25 feet above the blue absorbing material so at these frequencies the difference of 1.5 feet equates to approximately 0.5 dB less power received for equipment on the absorber compared with cavity backed spiral measured power.) Ultimately, the corrected mapping measurements are interpolated to each equipment test location and added to the interference system control file to determine the unique power received at each of these locations.

The mappings performed on 4/25 and 4/28 were compared and found to be very consistent. Figure A-2 shows a scatter plot of mapping location differences per frequency and demonstrates the variation across these dates was within plus or minus approximately 0.5 dB. When the differences are histogrammed by magnitude however (see Figure A-3), it can be observed that over 98% of the mapping points agreed to within plus or minus 0.25 dB. Figure A-4 further compares the power differences spatially and shows the lower left and upper right corners had the largest variations. The final corrected mapping values provided for DOT receiver processing represented the average of mapping from 4/25 and 4/28.

A mapping comparison was also made between 4/22 when no equipment was installed in the test area and 4/25 to get a sense for how much the equipment affected received power. This can be seen in Figure A-5 with a scatter plot of these differences. Notice the scale is double in this figure compared with the previous scatter plot and differences were as large as plus or minus 1 dB. Figure A-6 shows the histogram of the differences and in this comparison approximately 75% of the mapping points agreed to within plus or minus 0.25 dB. The spatial comparison is shown in Figure A-7. The largest differences are generally in the upper left corner which could be due to concentration of equipment towards this end of the chamber. It should be noted that increased variation between a clean chamber test area and one populated with over 80 pieces of equipment under test is not surprising. This level of variation is actually considered very good and was confirmed by the WSMR test engineers based on their experience with this chamber.

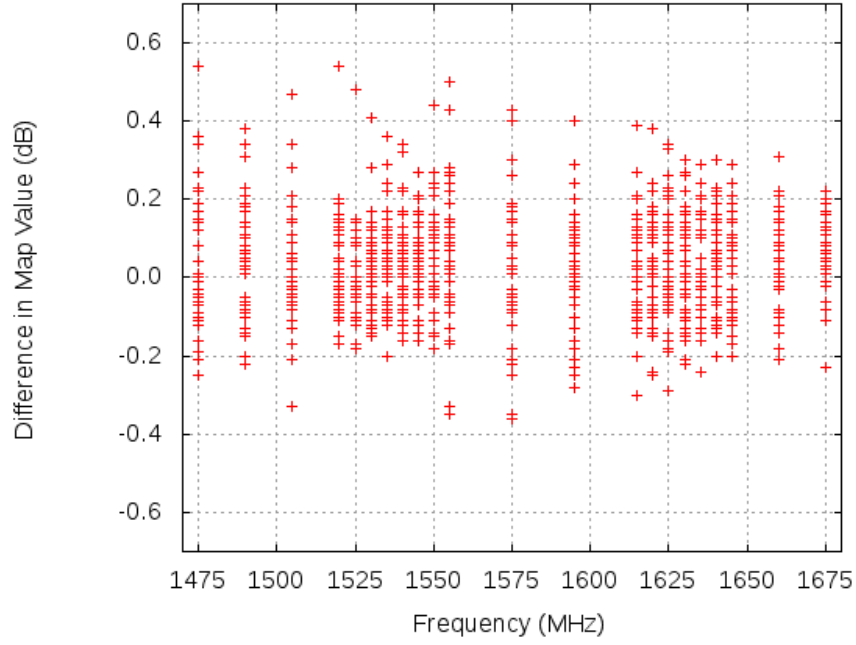


**Figure A-2: Mapping Point differences between April 25th and April 28th**



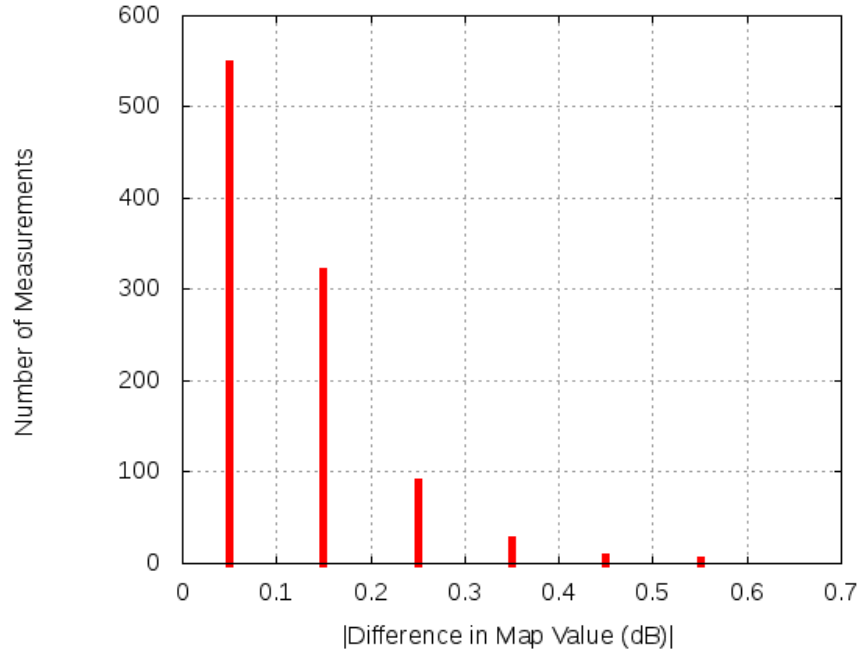


**Figure A-3: Histogram of Differences between April 25th and April 28th Mappings**

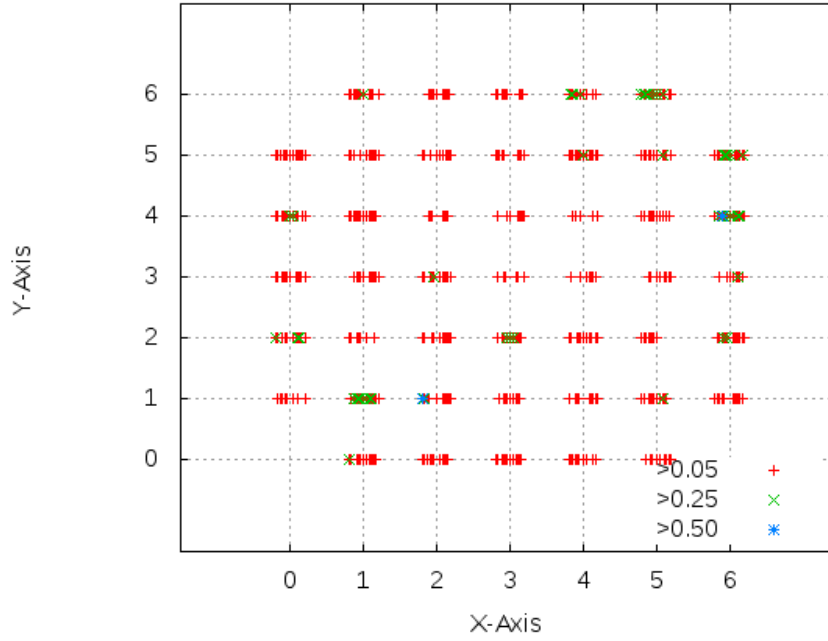


**Figure A-4: Power Differences across the Test Grid between April 25th and April 28th Mappings (freqs. run from 1475 to 1675 at each point from left to right)**

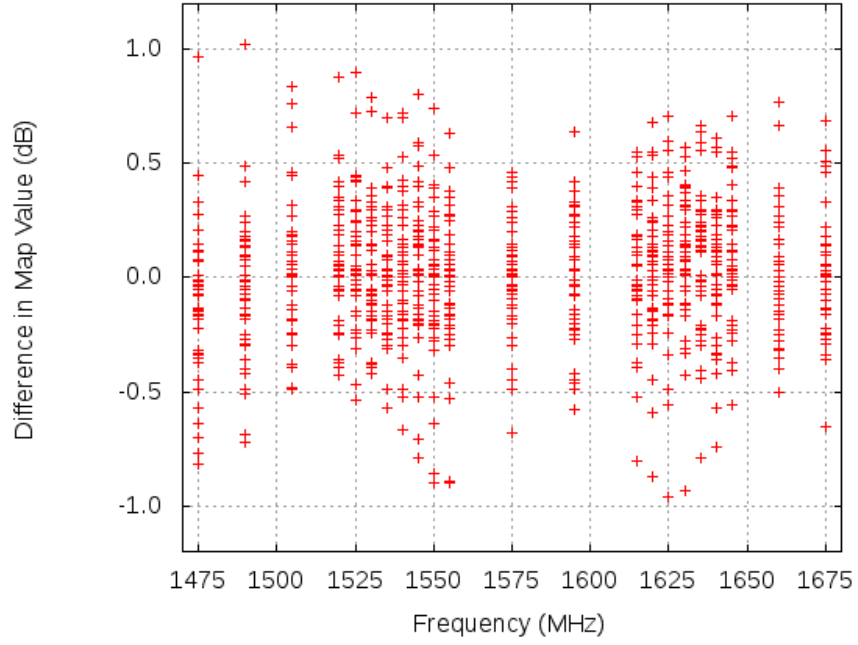


**Figure A-5: Mapping Point differences between April 22nd and April 25th**

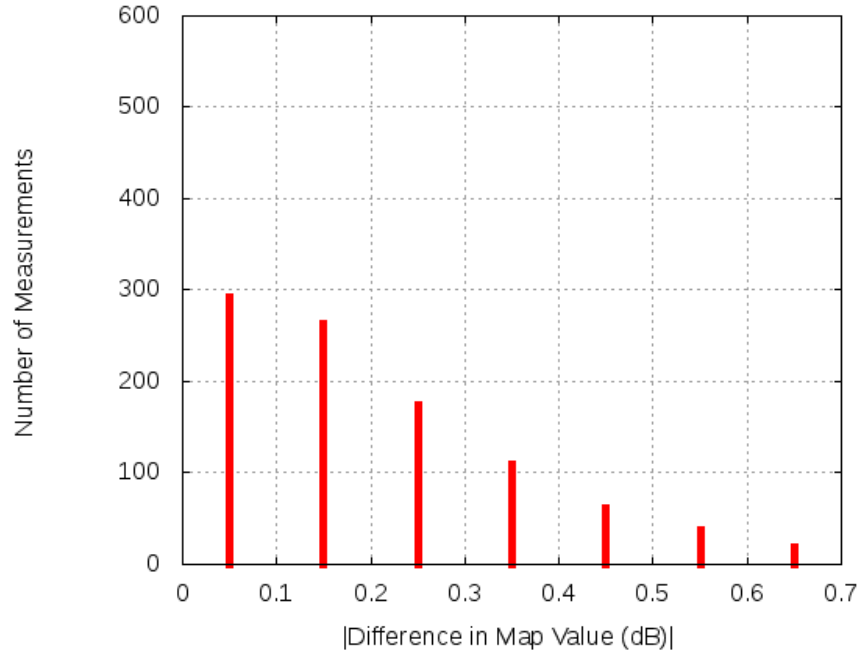


**Figure A-6: Histogram of Differences between April 22nd and April 25th Mappings**

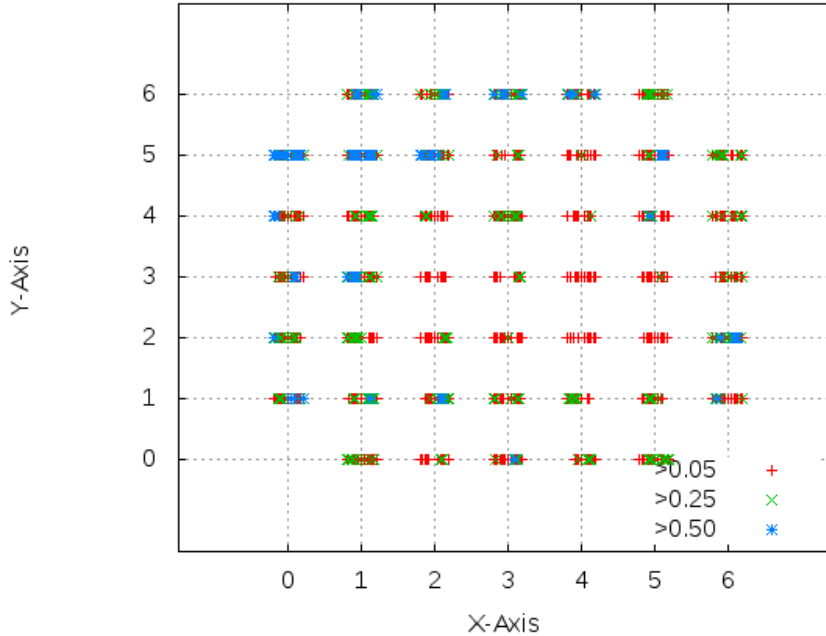


**Figure A-7: Power Differences across the Test Grid between April 22nd and April 28th Mappings (freqs. run from 1475 to 1675 at each point from left to right)**

One additional comparison noteworthy from mapping is how interference power varied over the course of the DOT test week. The previous analysis demonstrated the variation for all 45 mapping locations at the start and end of testing. During the test week, a mapping procedure was generally executed at reference location P03 in the AM and PM of each day as a confidence check on test stability. Figure A-8 shows all P03 mappings during DOT week after being corrected for target power, cavity backed spiral gain, calibration cable and the same 0.5 dB mentioned above for height differential of the calibration antenna. The variation from morning to evening and day to day was extremely well behaved with all measurements agreeing within 0.4 dB. For comparison purposes, the mapping at the reference location was also provided for 4/22 when no equipment was present in the test area. It is important to note that the calibration antenna was moved numerous times over each day either for full mapping or to allow participants access to the test area. Temperature was also recorded over the course of the one month test effort and observed to vary by as much as 6 degrees C. This temperature variation would be another source influencing daily power measurement variation.

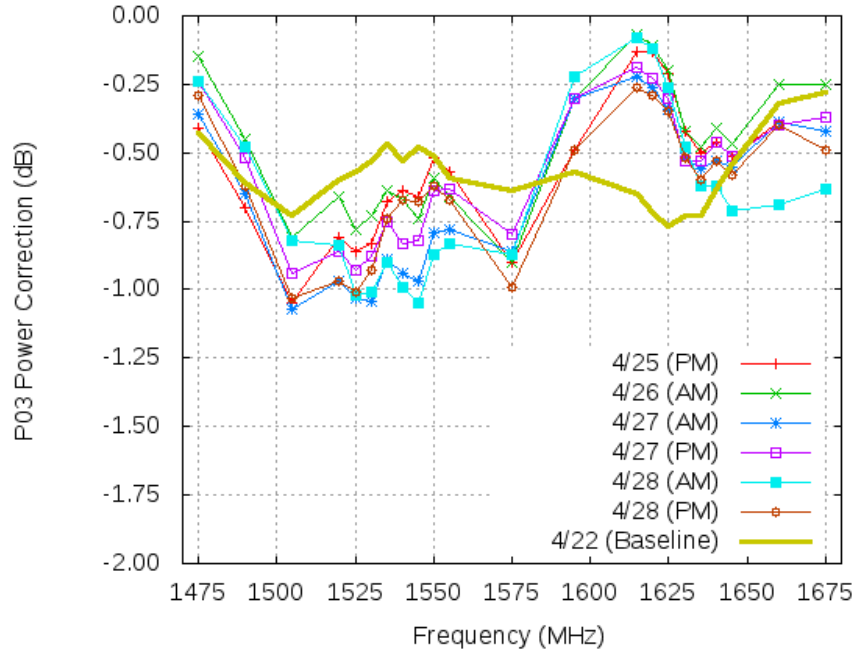


**Figure A-8: Comparison of Mapping Corrections from DOT Test Week**

#### A.4 System Calibration

Calibration of the interference and GNSS systems were handled differently. This section describes the interference system calibration only. The calibration procedure determined the reference point on the grid as well as VSG settings to achieve desired power for each of the 22 interference test frequencies. The reference point for system calibration was determined by finding the location receiving the least power from among grid points P03, P30, P36, and P63. These peripheral points represent roughly the 3 dB beamwidth of the transmit antenna and therefore selecting the location with the least received power ensures the majority of the test area will receive the desired interference power or higher. Location P03 was determined as this point and was used as the reference throughout all chamber testing. The calibration procedure was very similar to mapping except it used a notional VSG setting as a starting point and then computed power corrections per frequency to achieve -40 dBm at P03. This calculation used the notional VSG setting, cavity backed spiral antenna gain, and calibration cable loss. During the two week check out period prior to the formal test numerous system calibrations were executed. Based on consistency of these measurements it was decided to take the linear average of these

values to fix the calibration table. The dates used in this average are provided below. Table A-4 provides the average calibration values.

cal\_p03\_20160408\_144622, cal\_p03\_20160411\_144033, cal\_p03\_20160412\_142537,  
cal\_p03\_20160413\_131930, cal\_p03\_20160415\_180323

**Table A-4: Calibration Values inserted into measlabtable.cfg:**

Frequency (MHz)	Cal. Value (dB)	Cal. Value (dB)	Frequency (MHz)
1475	-3.30	1575	-4.90
1490	-3.21	1595	-5.29
1505	-3.34	1615	-6.08
1520	-3.69	1620	-6.03
1525	-3.50	1625	-6.27
1530	-3.61	1630	-6.11
1535	-3.59	1635	-6.01
1540	-3.70	1640	-6.22
1545	-3.78	1645	-6.52
1550	-4.09	1660	-6.53
1555	-4.28	1675	-6.71

One additional consideration for compensation of calibration values was use of a CW tone at center frequency versus the LTE signal. The concern was the LTE signal would have additional signal attenuation at filter edges due to roll-off vice the CW tone at center frequency. The signal power loss for the LTE signal versus the single-tone was analyzed for each of the filters (6 and 8 section filters) and the maximum difference was 0.17 dB. Given this small value it was decided adding a compensation term for LTE signal attenuation was not warranted.

## **A.5 Interference System Linearity**

The interference linearity procedure measured interference power over the entire range for each test frequency. This procedure was executed from P03 and stepped through the full range of power in 2 dB steps with a CW tone. For the interference frequencies furthest from the RNSS band the range was -80 to -10 dBm, for the three frequencies closet to and just above and below the RNSS band the range was -100 to -30 dBm, and lastly, for the two frequencies in the RNSS band the range was -130 to -60 dBm. As with calibration and mapping, the spiral antenna, calibration cable and spectrum analyzer were used to measure and record each power measurement. Figure A-9 shows measured power corrected for spiral antenna gain and cable loss

versus target power commanded by the interference system. This figure shows all frequency and power measurements together and demonstrates the expected linear relationship from approximately -100 dBm and higher. Below -100 dBm, the spectrum analyzer was not able to accurately resolve the tone being received due to the measurement system noise floor. To further demonstrate interference system performance, Figure A-10 shows the difference between targeted and measured power for select frequencies. These figures show that over the power range tested the interference system faithfully delivered intended power to within approximately 0.5 dB.

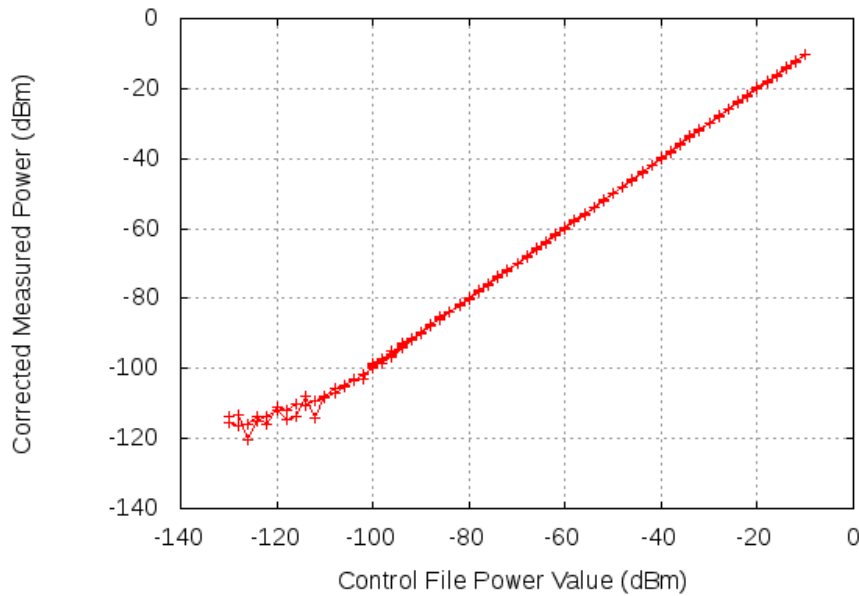


**Figure A-9: Comparison of Targeted Power (Recorded in Control File) and Measured Power corrected for Spiral Antenna Gain and Cable Loss**



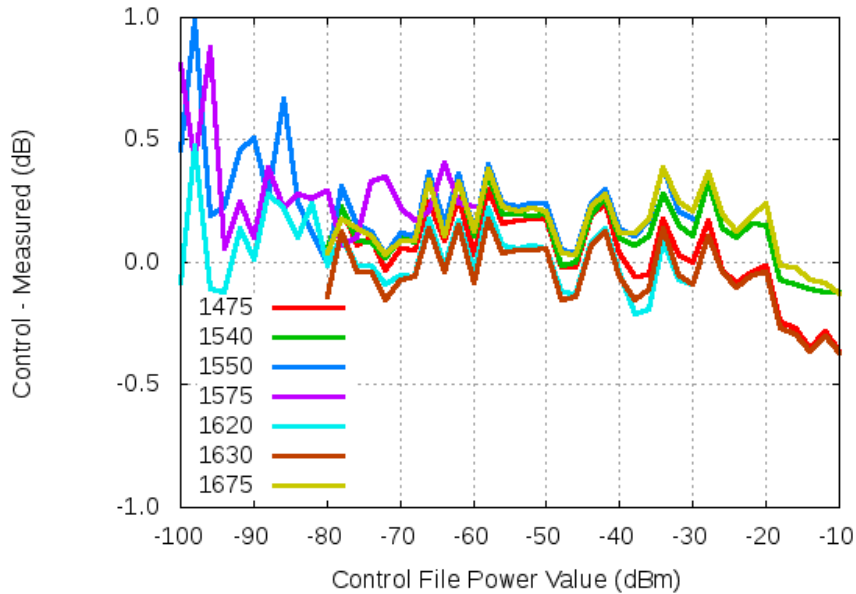


**Figure A-10: Comparison of Targeted Power (Recorded in Control File) Differenced from Measured Power for Select Frequencies**

### A.6 Comparison of Measured vs. Predicted Power

The measured power versus predicted power was estimated by making a special calibration of the SPIGAT system. In this instance, interference system output was routed through a 60 dB attenuator and into the spectrum analyzer used with the cavity backed spiral for making measurements on the chamber floor. Therefore, cable/antenna to the transmit antenna and cable/antenna from the receive antenna were bypassed (see Figure A-11) to obtain a direct power measurement at the output of the interference system. The mapping procedure was executed as if the calibration antenna was being utilized in the test area. The predicted power was then computed using measured power from the spectrum analyzer corrected for the 60 dB attenuator and associated cables, cable loss to the transmit antenna, transmit antenna gain, and free space loss to the calibration antenna. This predicted power was then compared with measurements made with the calibration antenna located at P33 which is directly below the transmit antenna (peak beam).

$$FSL = -27.55 + 20 \text{ Log } (f_{\text{MHz}}) + 20 \text{ Log } (R_{\text{meter}})$$

$R_{\text{meter}} = 7.16\text{m}$  (WSMR indicated face of horn to top of blue absorbing material directly below is 25'. Calibration antenna is 1.5' above absorbing material.)

Figure A-12 shows the result of the comparison using mapping data from 4/22 when the chamber was clear of any test equipment. The figure demonstrates very good agreement between predicted and measured power within approximately 0.5dB.

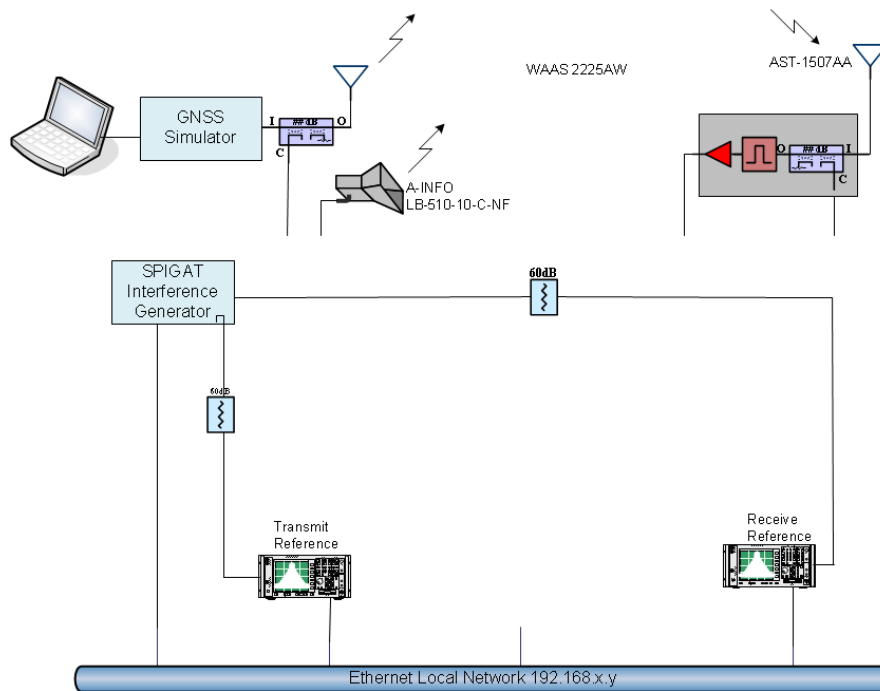


**Figure A-11: Diagram of Special Test where Transmit and Receive Antenna Paths were Bypassed**

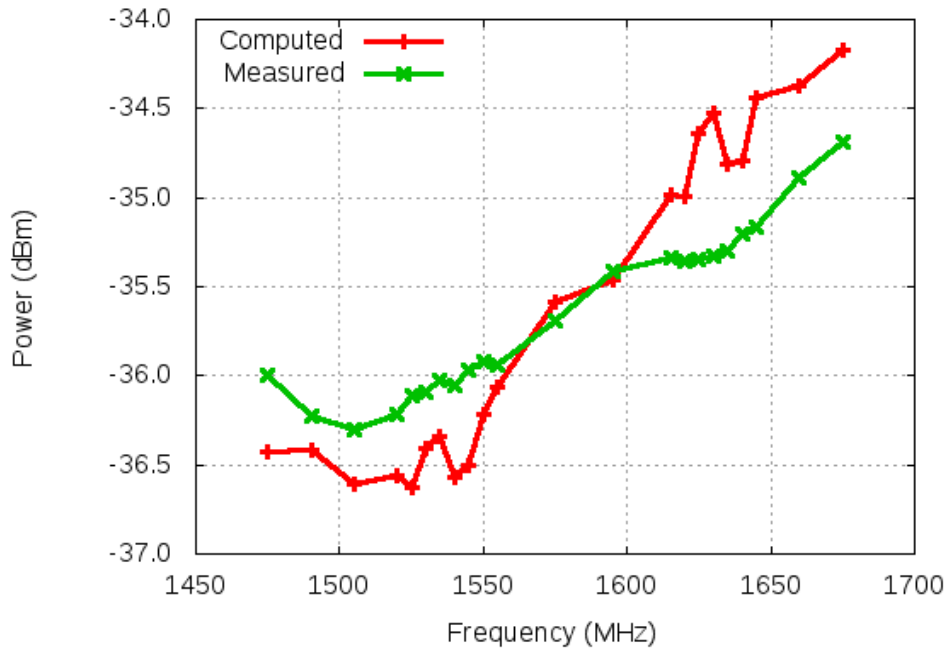


**Figure A-12: Measured Power at P33 (corrected for spiral gain and calibration cable) compared with Predicted Power (interference system output power, horn antenna gain, horn cable loss, and Free Space Loss)**

## A.7 SPIGAT Antenna Characterizations

The Cavity Backed Spiral (Cobham AST-1507AA) and Standard Gain Horn (A-Info LB-510-10-C-NF) antennas used in the test effort were provided to Leading Systems Technologies (LST) of Fairfax, VA in March 2016 for gain and pattern characterizations. Characterization of the spiral is key since it is required to calibrate received power of interference and GNSS signals across the chamber test area while characterization of the horn is also desired to validate A-info’s product data sheet and assist with link budget computations.

### A.7.1 AST-1507AA

The critical estimates from the LST characterization in support of the ABC test effort are measurements when the spiral is boresighted on the source. The orientation of the Cobham spiral for testing at LST is provided in Figure A-13. The Figure represents the view from the back of the antenna in the LST anechoic chamber and in this illustration the green dashed line and the green arrow represent the axis of rotation for beam pattern observations. The beam pattern measurements off boresight are not provided in this note but the 3 dB beamwidth was determined to be approximately 80 degrees. For boresight characterization, the spiral antenna was rotated sequentially from 0, 30, 45, 60, 90, 120, 135 and 150 degrees about the axis directed toward the source. The orange rectangle represents the TNC female connector, which was positioned facing up with respect to the ground as shown for the 0 degree orientation. The source antenna was vertically polarized for these measurements due to better performance in this chamber for the frequencies of interest. The frequency response of the spiral was measured from 800 to 2000 MHz inclusive of the frequencies of interest for ABC testing from 1227 to 1675 MHz.

Figure A-14 provides spiral antenna gain characteristics when boresighted at the source. The similar response for each orientation of this antenna demonstrates its excellent axial ratio properties. It is also interesting to note that variation with respect to antenna orientation above 1450 MHz is on the order of 0.25 dB which is reportedly approaching the accuracy limits for the LST chamber. Table A-5 provides average gain and axial ratio versus frequencies required in the ABC test effort. There are 22 frequencies utilized for interference generation and three specified for GNSS antenna mapping. For purposes of completeness, the insertion loss of the RF cable used at WSMR between the cavity backed spiral and the spectrum analyzer for mapping and calibration activities has been included in this same table.

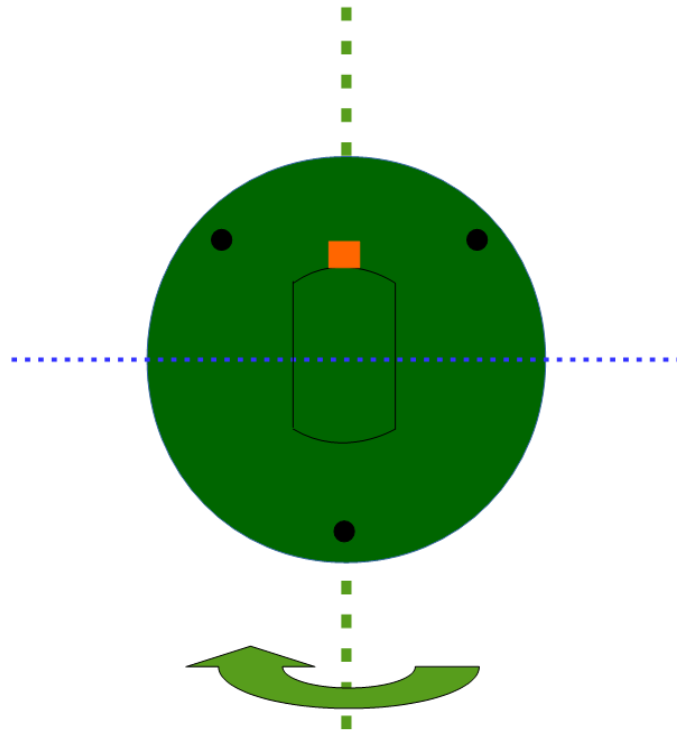


**Figure A-13: AST-1507AA Positioning; Back View**

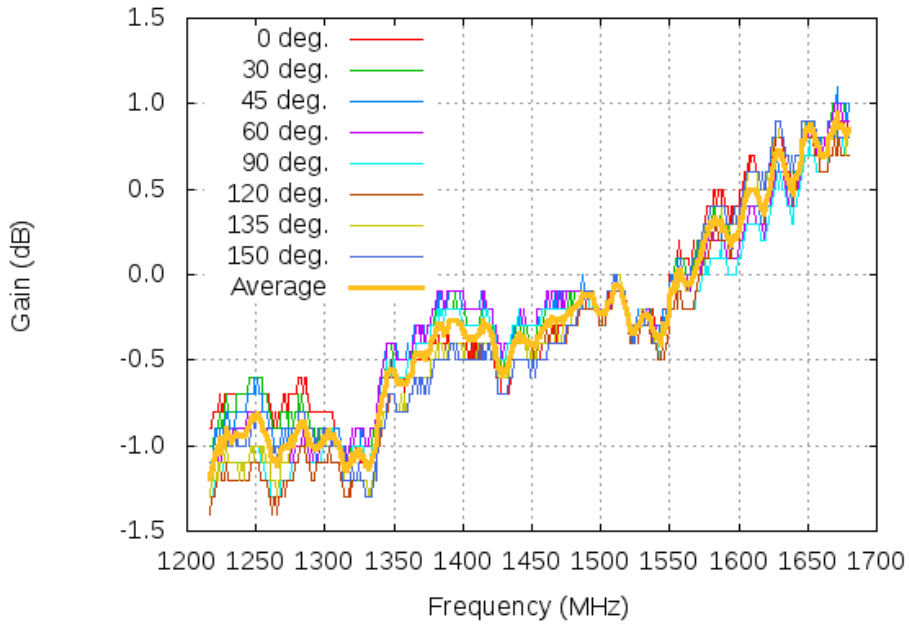


**Figure A-14: AST-1507AA Boresight Measurements**

**Table A-5: AST-1507AA, Serial #174**

Frequency (MHz)	Gain @ Boresight (dBil)	Axial Ratio (dB)	Cable Loss (dB)
1227*	-0.98	0.50	7.76
1475.	-0.24	0.20	8.44
1490.	-0.11	0.10	8.42
1505.	-0.18	0.10	8.45
1520.	-0.28	0.10	8.52
1525.	-0.34	0.10	8.54
1530.	-0.24	0.10	8.57
1535.	-0.25	0.10	8.60
1540.	-0.35	0.10	8.63
1545.	-0.29	0.20	8.64
1550.	-0.16	0.20	8.66
1555.	-0.07	0.30	8.72
1561*	-0.06	0.30	8.74
1575.	0.21	0.30	8.76

1595.	0.17	0.30	8.78
1605*	0.45	0.40	8.76
1615.	0.44	0.30	8.75
1620.	0.41	0.30	8.75
1625.	0.65	0.30	8.77
1630.	0.73	0.30	8.79
1635.	0.56	0.30	8.83
1640.	0.54	0.20	8.87
1645.	0.69	0.20	8.88
1660.	0.70	0.20	9.00
1675.	0.86	0.30	9.08

\*GNSS Antenna Mapping Frequencies for ABC Test

### A.7.2 LB-510-10-C-NF

The A-Info horn antenna gain and pattern performance were characterized at two source antenna orientations. For this testing, the source antenna and A-info polarizations were matched and the horn was rotated to measure pattern response. Figure A-15(a) shows the A-Info position for horizontal polarization measurements and (b) shows the position for vertical polarization measurements. The frequency response of the horn was measured from 800 to 2000 MHz but the frequencies of interest are primarily 1475 to 1675 MHz. Figure A-16 shows the horn gain at boresight for vertical polarization and Figure A-17 shows beam pattern response for the same polarization. Comparing these measurements with the A-Info product specification show a reasonably good match.

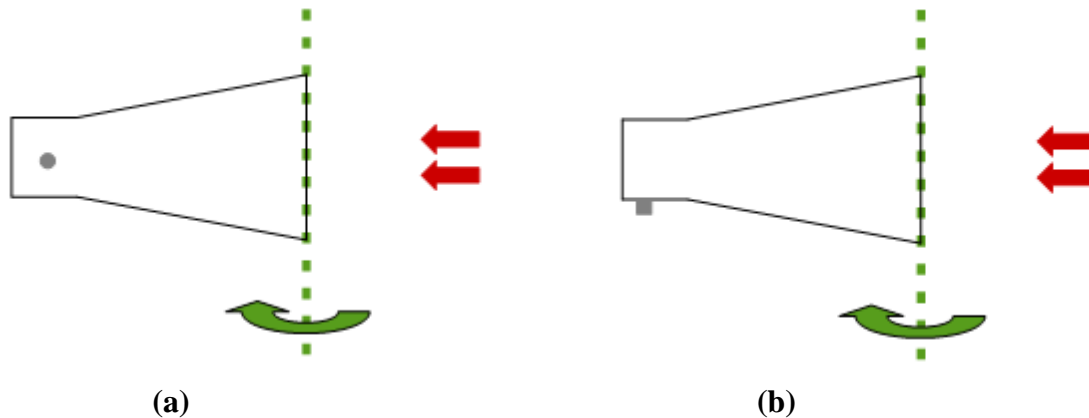
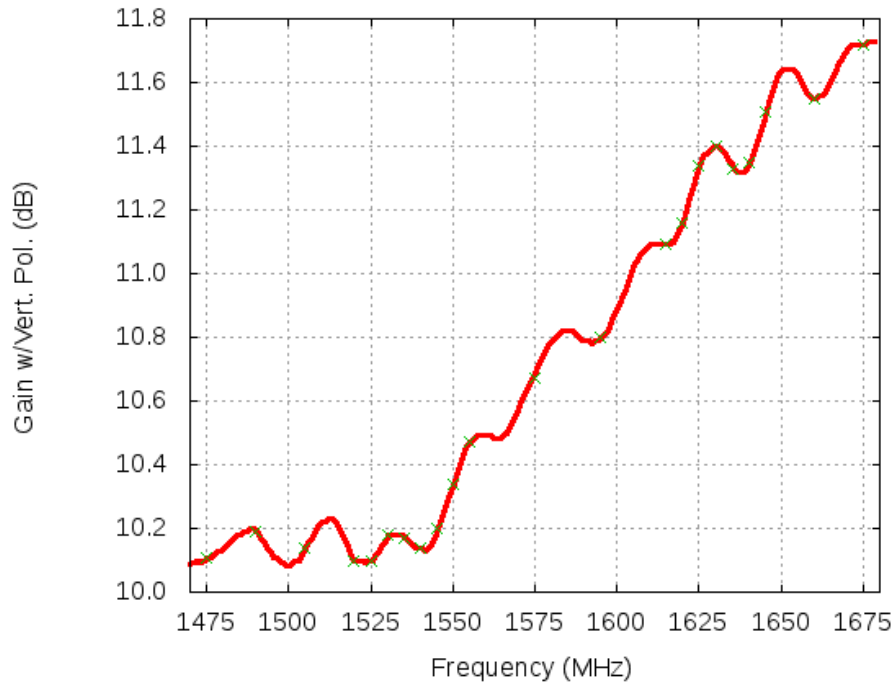
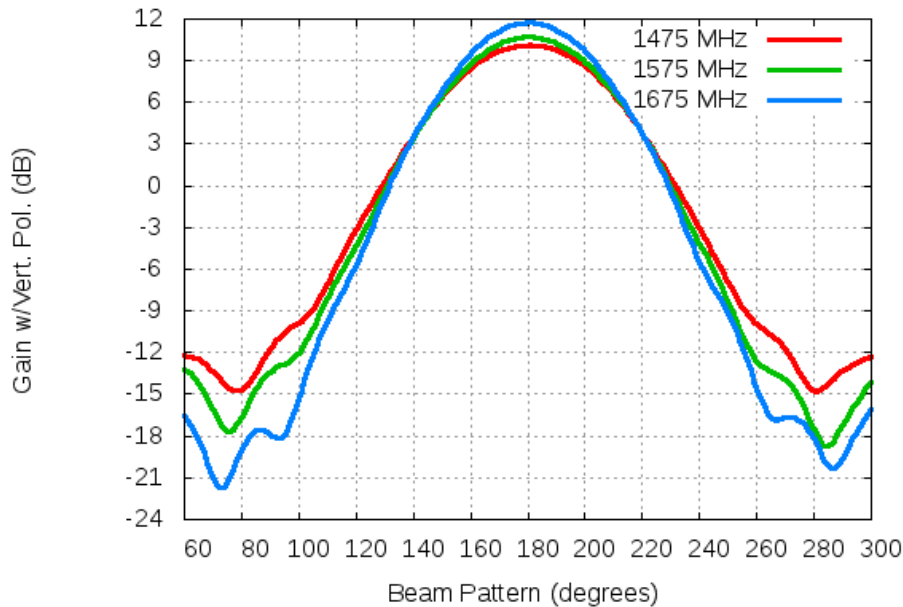


Figure A-15: (a) A-Info Horizontal Position Side View,  
(b) A-Info Vertical Position Side View



**Figure A-16: LB-510-10-C-NF Vertical Gain @ Boresight vs. Frequency**





**Figure A-17: LB-510-10-C-NF Vertical Pattern @ 1475, 1575 and 1675 MHz**

**A.8 WSMR Activity Summary**

Table A-6 summarizes the activities for the entire month spent at WSMR. “F-Map” was a complete 45 point mapping used in the final corrections of SPIGAT event summary files.

**Table A-6: Summary of WSMR Activities for April ABC Testing (4/4-4/28)**

Day	AWGN	LTE	In-band	IMD	C/No	5-Map	A-Map	F-Map	P03 Cal/Map	Set-up/Remove
M T W Th	Arrived, unpacked equipment, installed transmit antennas, established grid, characterized HPA and cables, dry-ran calibration and mapping, calibrated GNSS signals. Determined 1575 and 1595 MHz AWGN tests needed separate runs due to inherent noise of HPA in-band. Adjusted GNSS antenna lower at end of the 7 <sup>th</sup> to address reflections off horn (final location).									
F M <sup>2</sup>		4/08 <sup>1</sup>	4/11	4/11	4/08		4/08 4/11		4/08 4/11	

T		4/12		4/12	4/12	4/12	4/12		4/12	
W	4/13							4/13	4/13(2)	
Th										Set-up
F								4/15	4/15 <sup>4</sup>	
M	4/18		4/18		4/18				4/18(2)	
T	4/19	4/19							4/19(2)	
W		4/20		4/20	4/20	4/20			4/20	
Th		4/21 <sup>3</sup>		4/21	4/21	4/21			4/21	
F								4/22	4/22	Remove
M					4/25			4/25	4/25	Set-up
T	4/26	4/26							4/26	
W	4/27	4/27							4/27	
Th			4/28	4/28	4/28			4/28	4/28	Remove

1-“Eared” version of Type 2 LTE signal. All other Type-2 runs were with no “Ears”.

2-Characterization (system linearity) test run on 4/11.

3-No L2 signals.

4-Final calibration table established for all follow-on testing. Full mapping on 4/15 used this table.

Checkout
DOD
Civil

## A.9 Chamber OOB

The fundamental components of the SPIGAT include a VSG to generate interference signals and an HPA to provide sufficient amplification to achieve desired test levels. Given the limited ACLR of a typical VSG and the potential for spectral regrowth due to HPA nonlinearity at high input power, bandpass cavity filters were specified for SPIGAT with sufficient out of band rejection to ensure that receiver CNR measurements would reflect degradation caused by the fundamental of the interference, exclusive of any OOB produced. The following test data and analysis demonstrate that the OOB suppression provided by SPIGAT during LTE radiated tests performed at WSMR was sufficient to prevent receiver CNR degradation due to OOB in the RNSS band.

In SPIGAT the interference signal passes from the VSG through a programmable attenuator and into the HPA. The amplified signal then passes through a bandpass cavity filter (specific to the signal frequency and selected by RF switch) before being directed to devices under test. At

WSMR the signal was routed through a long cable to the transmit antenna where it was radiated toward antennas on the chamber floor.

To assess the adequacy of OOB suppression, spectra at the output of the HPA were recorded via spectrum analyzer (connected through a 60 dB pad). Spectra were recorded for a range of input power levels by fixing the signal power at the VSG while adjusting the programmable attenuator in 2 dB increments over the desired range. These measurements were taken while generating the downlink signal at 1550 MHz as this is the LTE test signal closest to the RNSS band and, therefore, most relevant to the OOB question. The expansion of spectral regrowth as signal power increases is apparent from a suite of such measurements shown in Figure A-18.

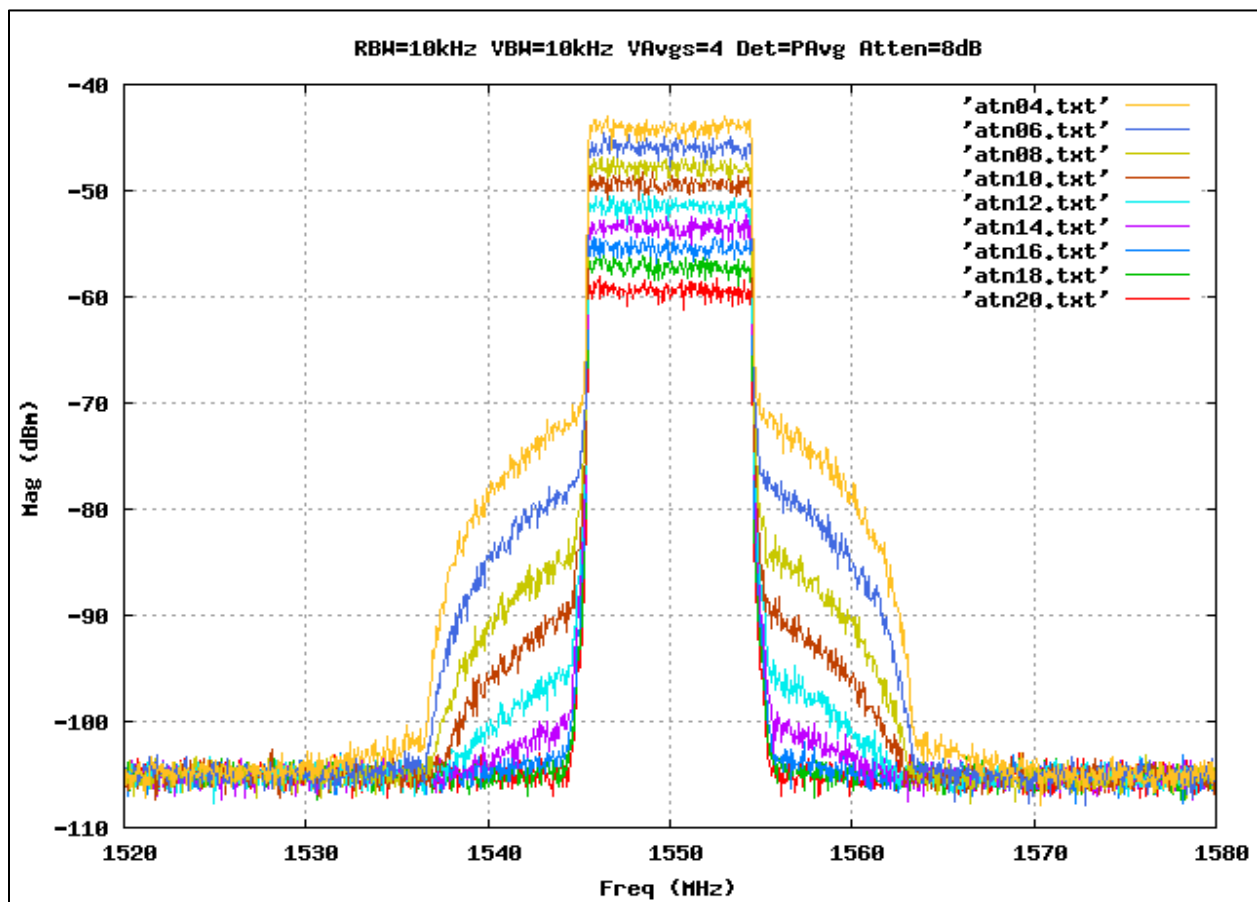


**Figure A-18: Spectra Showing Expanding Regrowth for Increasing HPA Input Power**

The spectra thus recorded with the 60 dB pad are mapped to test levels by comparing VSG and attenuator settings with those set during radiated tests. Table A-7 shows the correspondence. Given VSG power fixed at 0 dBm (for regrowth spectra), the spectrum that corresponds to a

radiated test level is the one with attenuation nominally equal to the test attenuation less the test VSG power. As an example, radiated tests of the 1550 MHz signal at -30 dBm are achieved with VSG power of -5.91 dBm and 20 dB attenuation. Given VSG power fixed to 0 dBm, the corresponding regrowth measurement has nominal attenuation of 26 dB.

**Table A-7: Attenuation for Regrowth Spectra to Correspond to Radiated Tests**

	radiated tests				regrowth measurements		
	A	B	C=A-B	D	E=D-C=B-A	~E	
frequency [MHz]	test level [dBm]	VSG power [dBm]	Attenuation [dB]	attenuated power [dBm]	VSG power [dBm]	required attenuation [dB]	nominal attenuation [dB]
1550	-30	-5.91	20	-25.91	0	25.91	26
1620	-30	-3.97	20	-23.97	0	23.97	24
1550	-10	-5.91	0	-5.91	0	5.91	6
1620	-10	-3.97	0	-3.97	0	3.97	4
1535	-10	-6.41	0	-6.41	0	6.41	6
1630	-10	-3.89	0	-3.89	0	3.89	4

As noted above, regrowth spectra were recorded only for interference at 1550 MHz. In the following, results presented for 1620 MHz (and other frequencies) were achieved by shifting data taken at 1550 MHz. This seems appropriate because even though 1550 and 1620 MHz interference signals were distinctly generated during radiated tests using the LTE downlink and uplink signals, respectively, both signals produce a flat 9 MHz wide pedestal with steep roll off. Given this similar energy distribution, the spectral regrowth for 1620 MHz interference is expected to have similar shape. On the other hand, the HPA gain at 1620 MHz is about 0.5 dB lower than at 1550 MHz. Therefore, regrowth at 1550 MHz may be slightly more severe than at 1620 MHz for a given input power since the higher gain at 1550 MHz moves the HPA farther into compression. In summary, the 1550 MHz spectra applied to 1620 MHz may be slightly pessimistic there (i.e. regrowth overstated).

For reference in the remaining discussion, the measured filter gain response of the 1550 and 1630 MHz filters are shown in Figure A-19 in the same scale as the figures that follow. The 1550 MHz filter is representative of the set of filters (including 1620 MHz) having narrow rolloff constraints while the 1630 MHz filter is representative of the set having more relaxed parameters.

Figure A-20 and Figure A-21 represent the 1550 and 1620 MHz LTE interference signals (blue curves) as seen at the chamber floor for the -30 dBm test level (Figure A-20) and the -10 dBm test level (Figure A-21). These two signals are selected because they are at the tested LTE

frequencies closest to and on either side of the RNSS band of interest. The curves were obtained as follows. Spectra were selected with appropriate nominal attenuation for correspondence with the target test level (see Table A-7). The measured filter response (1550 or 1620 MHz) was added to the spectra to produce the composite post-filter signal shape. This approach of measuring the HPA output and applying the filter response allows inspection of OOB that may otherwise be lost to the instrument noise floor if measured directly at the filter output, due to steep rolloff of the cavity filters and limited dynamic range of the measuring device. Each composite curve was then adjusted to the test level by subtracting the average of all points within the 9 MHz pedestal and adding back the value of the test level (-30 or -10 dBm). Finally, the curve was converted from units of dBm/9MHz to dBW/Hz by adding factors of -69.54 (to convert /9 MHz to /Hz) and -30 (to convert dBm to dBW).

Regarding other figure elements, the vertical black lines mark the edges of the RNSS band. The horizontal orange line is the ambient noise floor density, defined as  $N_0 = kT$ , for  $T = 290 K$ , which is approximately -204 dBW/Hz. The size of additive OOB relative to the ambient noise floor determines the magnitude of  $C/N_0$  degradation experienced by a receiver. For example, the horizontal yellow line, which is 16.3 dB lower than the orange line, is the level for additive noise of constant density across the full receiver bandwidth which would produce 0.1 dB degradation in the receiver. This is so merely because it is the noise density that when added to the ambient noise density, raises the floor by 0.1 dB. OOB is not likely to be of constant density, but the line is included to serve as a useful reference. Receiver degradation is negligible (i.e. less than 0.1 dB) for OOB with density below the yellow line. Thus OOB suppression can be assessed by comparing the magnitude of OOB with this reference.

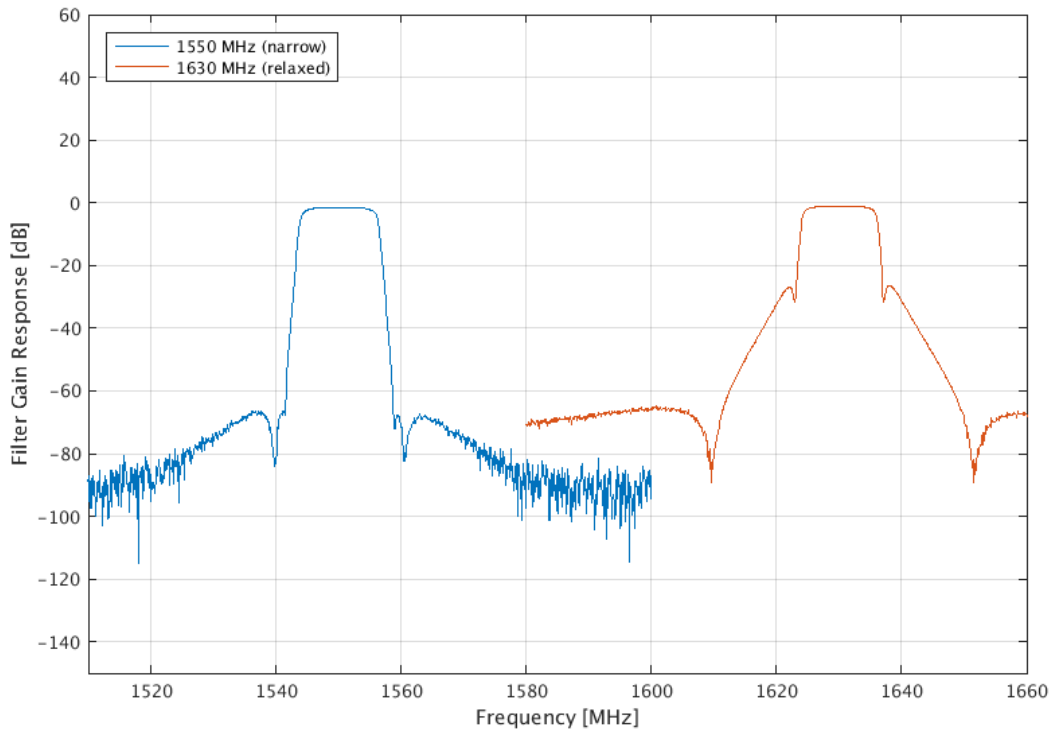
Figure A-20 represents the interference signals at the -30 dBm test level using the 26 dB regrowth spectra for 1550 MHz and the 24 dB spectra for 1620 MHz. This is the highest level reached in radiated tests for these inner frequencies. By inspection of the plot the OOB in the RNSS band is below the yellow reference line, thereby causing negligible degradation. The darker blue curve shows the portion of the regrowth spectra that was dominated by the noise floor of the measuring instrument. From other measurements taken with better instrument settings at higher HPA input power (less signal attenuation), it is known that the instrument noise floor can be reduced by at least 12 dB without exposing any spectral regrowth at this power level. For this reason a shadow noise floor (light grey) has been represented on the plot to demonstrate that for the -30 dBm test level there is exceptional margin. This result also applies to the other signals that are tested only to this level but farther from the RNSS band, namely the signals at 1545 and 1625 MHz. In summary, OOB suppression is more than adequate to prevent receiver CNR degradation due to OOB from the four LTE signals closest to the RNSS band at their levels of test.

Figure A-21 represents the interference signals at the -10 dBm test level using the 6 dB regrowth spectra for 1550 MHz and the 4 dB spectra for 1620 MHz. This level is above the test range for

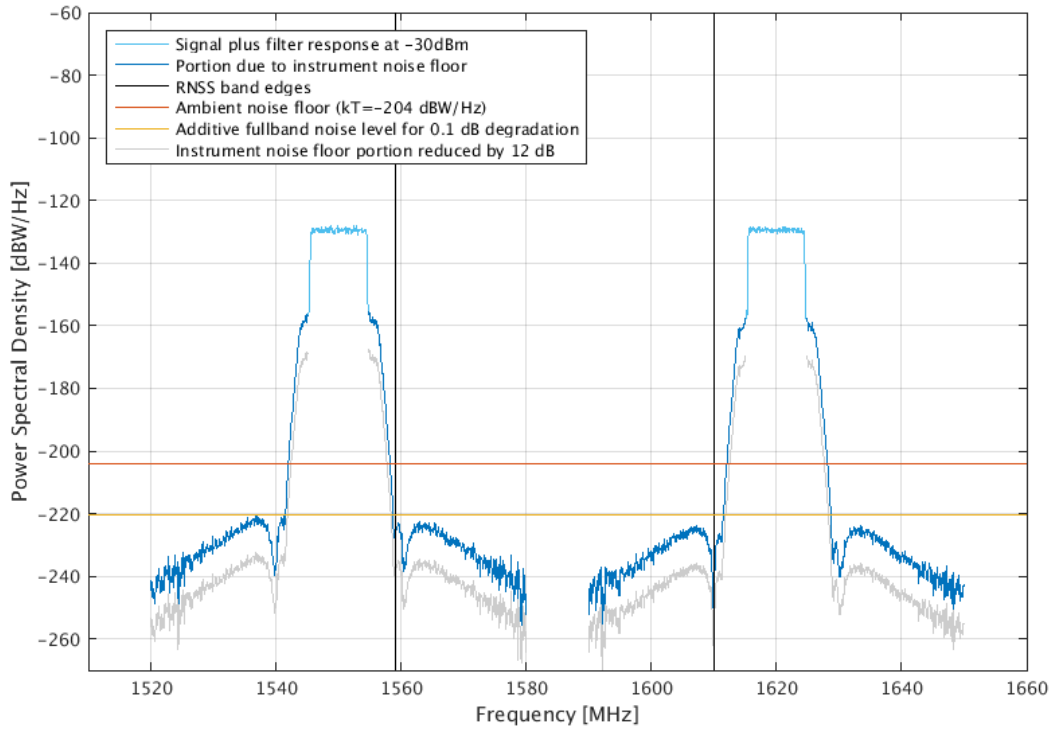
these inner signals but was the original level used to specify filter attenuation and rolloff performance to satisfy OOB requirements. In this case, some OOB within the RNSS band rises above the yellow reference line, but it is in the extreme frequencies of the band, narrower than 2 MHz between 1559 and 1561 MHz and narrower than 3 MHz between 1607 and 1610 MHz. The innermost signals tested at the -10 dBm level are at 1540 and 1630 MHz, each of which is a full 10 MHz farther from the RNSS band. This additional separation is more than enough for the 1540 MHz signal to shift the 2 MHz of OOB to be outside the RNSS band, since this signal uses a filter having the same narrow rolloff constraints as the 1550 and 1620 MHz filters. However, application to the 1630 MHz signal is less apparent since this filter has more relaxed parameters.

Figure A-22 represents the 1535 and 1630 MHz interference signals at the -10 dBm test level using the 6 dB regrowth spectra for 1535 MHz and the 4 dB spectra for 1630 MHz. These two frequencies are the innermost signals using filters having the more relaxed parameters. As depicted, OOB is well below the yellow 0.1 dB reference line, indicating receiver degradation is negligible. This result also applies to the other signals that use filters having the relaxed parameters, all of which are tested to this level but are farther from the RNSS band, namely 1475 through 1530 and 1635 through 1675 MHz.

In summary, the analysis demonstrates that OOB suppression at WSMR was sufficient for all levels of test at each LTE frequency. Figure A-20 demonstrates that OOB is sufficiently suppressed for all narrow-filter signals up through the -30 dBm test level (i.e. the full test range for 1545, 1550, 1620 and 1625, but only up to -30 dBm for 1540); Figure A-21 demonstrates this at the -10 dBm test level for all narrow-filter signals that run to this level (i.e. 1540; but also 1545 and 1625 although these are not actually tested at this level); and Figure A-22 demonstrates this for all relaxed-filter signals up to the -10 dBm test level (i.e. the full test range for 1475 through 1535 and 1630 through 1675).



**Figure A-19: Example Gain Response of Narrow and Relaxed Filters**



**Figure A-20: Composite PSDs for Innermost LTE Signals at -30 dBm**



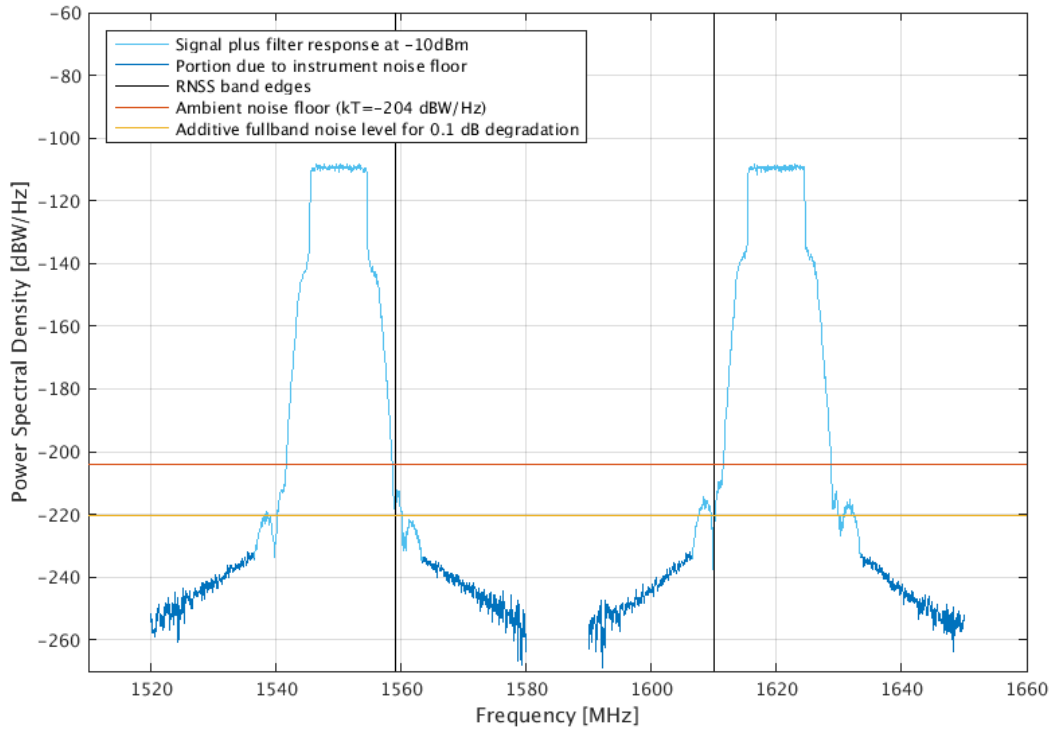


**Figure A-21: Composite PSDs for Innermost LTE Signals at -10 dBm**

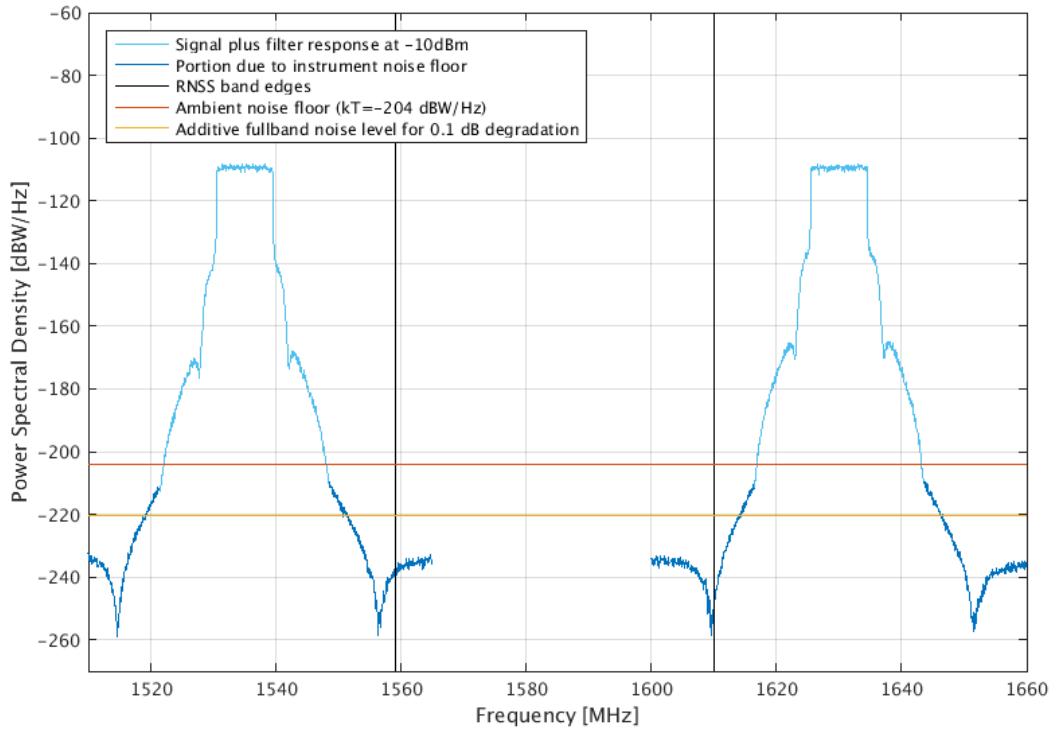


**Figure A-22: Composite PSDs for the Innermost Relaxed-filter LTE Signals at -10 dBm**

## A.10 GNSS Signal Generation

This section provides some details of the GNSS signal generation system.

### A.10.1.1 Transmit antenna characterization

The gain patterns of the GNSS transmitting antenna at various center frequencies are shown in Figure A-23. At boresight, this antenna provides RHCP gains of  $\sim 0.1$  dBic (1227 MHz), 4.4 dBic (1572 MHz), and 4.0 dBic (1602 MHz).

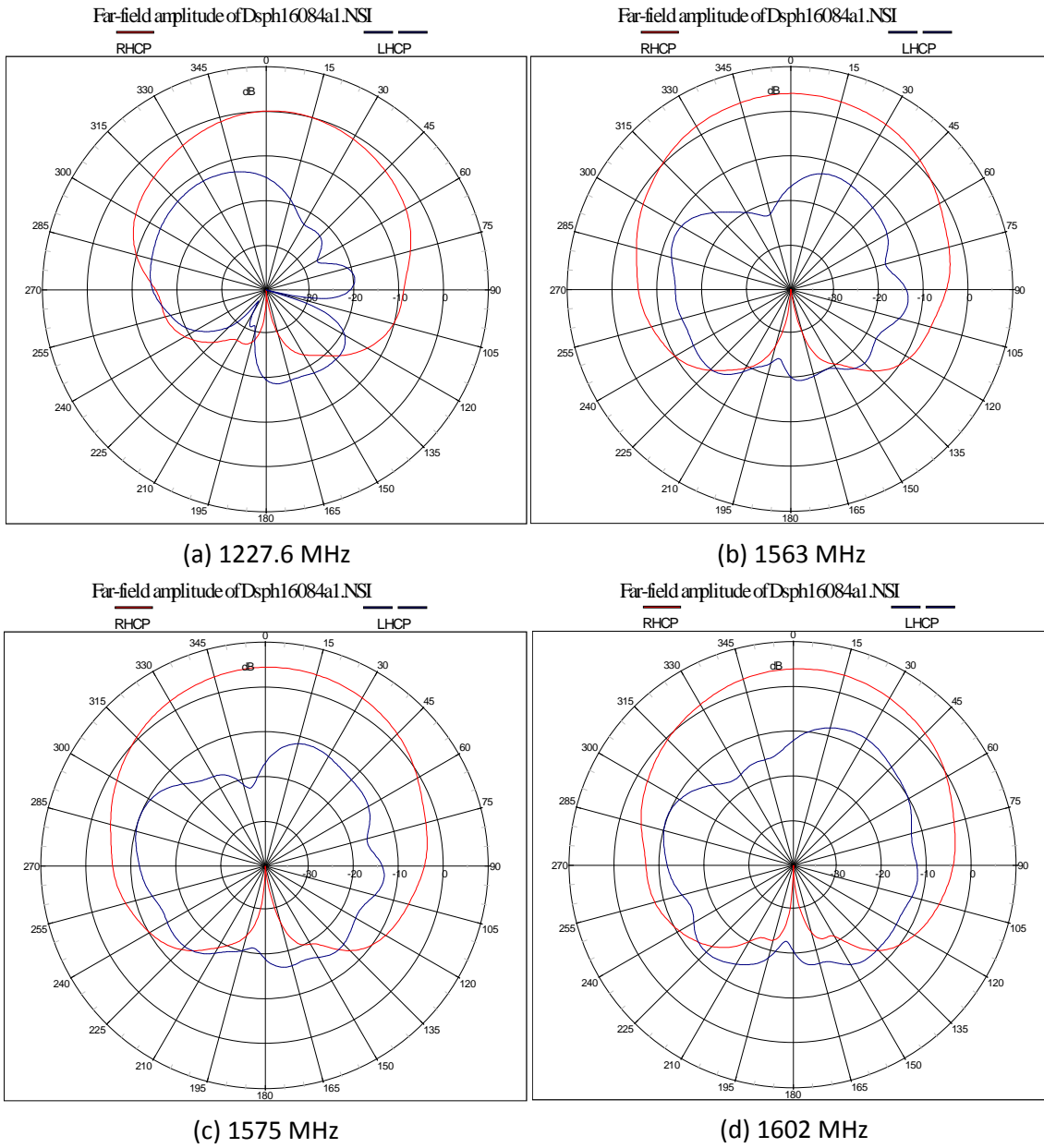


**Figure A-23: GNSS Signal Generator Transmit Antenna Gain Patterns**

## A.10.2 Almanacs

### A.10.2.1 GPS Almanac

PRN-24 was generated at -10 dB and PRN-29 at -20 dB relative to the nominal received power levels (see Table 7). Both of these satellites are visible throughout the entire 6 hour simulation time. Using the GNSS generation equipment (see Section 4.3.3.1), due to a limitation on the number of available channels the Spirent signal generator limits the number of emulated GPS satellites to no more than ten based upon dilution of precision (DOP) (with PRN-24 and PRN-29 forced to always be present).

```

***** Week 869 almanac for PRN-01 *****
ID:                01
Health:            0
Eccentricity:      0.000000000000000e+000
Time of Applicability(s): 144000
Orbital Inclination(rad): 9.59931088700065e-001
Rate of Right Ascen(r/s): 0.000000000000000e+000
SQRT(A) (m 1/2):  5.15370081099980e+003
Right Ascen at Week(rad): 2.74046301800000e+000
Argument of Perigee(rad): -1.20197773000000e+000
Mean Anom(rad):    -2.25293839000000e+000
Af0(s):            0.000000000000000e+000
Af1(s/s):          0.000000000000000e+000
week:              869

```

```

***** Week 869 almanac for PRN-02 *****
ID:                02
Health:            0
Eccentricity:      0.000000000000000e+000
Time of Applicability(s): 144000
Orbital Inclination(rad): 9.59931088700065e-001
Rate of Right Ascen(r/s): 0.000000000000000e+000
SQRT(A) (m 1/2):  5.15370081099980e+003

```

Right Ascen at Week(rad): 1.59598827400000e+000  
 Argument of Perigee(rad): 2.71410071800000e+000  
 Mean Anom(rad): -1.21557569500000e+000  
 Af0(s): 0.00000000000000e+000  
 Af1(s/s): 0.00000000000000e+000  
 week: 869

\*\*\*\*\* Week 869 almanac for PRN-03 \*\*\*\*\*

ID: 03  
 Health: 0  
 Eccentricity: 0.00000000000000e+000  
 Time of Applicability(s): 144000  
 Orbital Inclination(rad): 9.59931088700065e-001  
 Rate of Right Ascen(r/s): 0.00000000000000e+000  
 SQRT(A) (m 1/2): 5.15370081099980e+003  
 Right Ascen at Week(rad): 4.49386715899998e-001  
 Argument of Perigee(rad): 8.89944077000001e-001  
 Mean Anom(rad): -1.57409238800000e+000  
 Af0(s): 0.00000000000000e+000  
 Af1(s/s): 0.00000000000000e+000  
 week: 869

\*\*\*\*\* Week 869 almanac for PRN-04 \*\*\*\*\*

ID: 04  
 Health: 0  
 Eccentricity: 0.00000000000000e+000  
 Time of Applicability(s): 144000  
 Orbital Inclination(rad): 9.59931088700065e-001  
 Rate of Right Ascen(r/s): 0.00000000000000e+000  
 SQRT(A) (m 1/2): 5.15370081099980e+003

Right Ascen at Week(rad): 1.61451172800000e+000  
Argument of Perigee(rad): 4.73291158999999e-001  
Mean Anom(rad): 1.62043118500000e+000  
Af0(s): 0.00000000000000e+000  
Af1(s/s): 0.00000000000000e+000  
week: 869

\*\*\*\*\* Week 869 almanac for PRN-05 \*\*\*\*\*

ID: 05  
Health: 0  
Eccentricity: 0.00000000000000e+000  
Time of Applicability(s): 144000  
Orbital Inclination(rad): 9.59931088700065e-001  
Rate of Right Ascen(r/s): 0.00000000000000e+000  
SQRT(A) (m 1/2): 5.15370081099980e+003  
Right Ascen at Week(rad): -5.81213951099999e-001  
Argument of Perigee(rad): 1.29498612900000e+000  
Mean Anom(rad): 1.22770595600000e+000  
Af0(s): 0.00000000000000e+000  
Af1(s/s): 0.00000000000000e+000  
week: 869

\*\*\*\*\* Week 869 almanac for PRN-06 \*\*\*\*\*

ID: 06  
Health: 0  
Eccentricity: 0.00000000000000e+000  
Time of Applicability(s): 144000  
Orbital Inclination(rad): 9.59931088700065e-001  
Rate of Right Ascen(r/s): 0.00000000000000e+000  
SQRT(A) (m 1/2): 5.15370081099980e+003

Right Ascen at Week(rad): 5.16054987899998e-001  
Argument of Perigee(rad): -1.46300911900000e+000  
Mean Anom(rad): 9.50933694800001e-001  
Af0(s): 0.00000000000000e+000  
Af1(s/s): 0.00000000000000e+000  
week: 869

\*\*\*\*\* Week 869 almanac for PRN-07 \*\*\*\*\*

ID: 07  
Health: 0  
Eccentricity: 0.00000000000000e+000  
Time of Applicability(s): 144000  
Orbital Inclination(rad): 9.59931088700065e-001  
Rate of Right Ascen(r/s): 0.00000000000000e+000  
SQRT(A) (m 1/2): 5.15370081099980e+003  
Right Ascen at Week(rad): -1.53364002700000e+000  
Argument of Perigee(rad): 2.92355132100000e+000  
Mean Anom(rad): -3.03474617000000e+000  
Af0(s): 0.00000000000000e+000  
Af1(s/s): 0.00000000000000e+000  
week: 869

\*\*\*\*\* Week 869 almanac for PRN-08 \*\*\*\*\*

ID: 08  
Health: 0  
Eccentricity: 0.00000000000000e+000  
Time of Applicability(s): 144000  
Orbital Inclination(rad): 9.59931088700065e-001  
Rate of Right Ascen(r/s): 0.00000000000000e+000  
SQRT(A) (m 1/2): 5.15370081099980e+003

Right Ascen at Week(rad): -1.47555172400000e+000  
 Argument of Perigee(rad): 2.97652006100000e+000  
 Mean Anom(rad): 2.57835054400000e+000  
 Af0(s): 0.00000000000000e+000  
 Af1(s/s): 0.00000000000000e+000  
 week: 869

\*\*\*\*\* Week 869 almanac for PRN-09 \*\*\*\*\*

ID: 09  
 Health: 0  
 Eccentricity: 0.00000000000000e+000  
 Time of Applicability(s): 144000  
 Orbital Inclination(rad): 9.59931088700065e-001  
 Rate of Right Ascen(r/s): 0.00000000000000e+000  
 SQRT(A) (m 1/2): 5.15370081099980e+003  
 Right Ascen at Week(rad): -1.56848144500000e+000  
 Argument of Perigee(rad): 1.45941114400000e+000  
 Mean Anom(rad): 2.32180273500000e+000  
 Af0(s): 0.00000000000000e+000  
 Af1(s/s): 0.00000000000000e+000  
 week: 869

\*\*\*\*\* Week 869 almanac for PRN-10 \*\*\*\*\*

ID: 10  
 Health: 0  
 Eccentricity: 0.00000000000000e+000  
 Time of Applicability(s): 144000  
 Orbital Inclination(rad): 9.59931088700065e-001  
 Rate of Right Ascen(r/s): 0.00000000000000e+000  
 SQRT(A) (m 1/2): 5.15370081099980e+003



Right Ascen at Week(rad): 2.67993223700000e+000  
Argument of Perigee(rad): 5.90835452000001e-001  
Mean Anom(rad): -3.54773163799999e-001  
Af0(s): 0.00000000000000e+000  
Af1(s/s): 0.00000000000000e+000  
week: 869

\*\*\*\*\* Week 869 almanac for PRN-11 \*\*\*\*\*

ID: 11  
Health: 0  
Eccentricity: 0.00000000000000e+000  
Time of Applicability(s): 144000  
Orbital Inclination(rad): 9.59931088700065e-001  
Rate of Right Ascen(r/s): 0.00000000000000e+000  
SQRT(A) (m 1/2): 5.15370081099980e+003  
Right Ascen at Week(rad): 1.40136146500000e+000  
Argument of Perigee(rad): 6.84068560999999e-001  
Mean Anom(rad): 3.11031377300000e+000  
Af0(s): 0.00000000000000e+000  
Af1(s/s): 0.00000000000000e+000  
week: 869

\*\*\*\*\* Week 869 almanac for PRN-12 \*\*\*\*\*

ID: 12  
Health: 0  
Eccentricity: 0.00000000000000e+000  
Time of Applicability(s): 144000  
Orbital Inclination(rad): 9.59931088700065e-001  
Rate of Right Ascen(r/s): 0.00000000000000e+000  
SQRT(A) (m 1/2): 5.15370081099980e+003

Right Ascen at Week(rad): -4.82020854899998e-001  
Argument of Perigee(rad): -8.12766790000000e-001  
Mean Anom(rad): -2.84381163100000e+000  
Af0(s): 0.00000000000000e+000  
Af1(s/s): 0.00000000000000e+000  
week: 869

\*\*\*\*\* Week 869 almanac for PRN-13 \*\*\*\*\*

ID: 13  
Health: 0  
Eccentricity: 0.00000000000000e+000  
Time of Applicability(s): 144000  
Orbital Inclination(rad): 9.59931088700065e-001  
Rate of Right Ascen(r/s): 0.00000000000000e+000  
SQRT(A) (m 1/2): 5.15370081099980e+003  
Right Ascen at Week(rad): -2.52682590500000e+000  
Argument of Perigee(rad): 1.50618374300000e+000  
Mean Anom(rad): -5.35064935699999e-001  
Af0(s): 0.00000000000000e+000  
Af1(s/s): 0.00000000000000e+000  
week: 869

\*\*\*\*\* Week 869 almanac for PRN-14 \*\*\*\*\*

ID: 14  
Health: 0  
Eccentricity: 0.00000000000000e+000  
Time of Applicability(s): 144000  
Orbital Inclination(rad): 9.59931088700065e-001  
Rate of Right Ascen(r/s): 0.00000000000000e+000  
SQRT(A) (m 1/2): 5.15370081099980e+003

Right Ascen at Week(rad): -2.54563283900000e+000  
Argument of Perigee(rad): -2.09949839100000e+000  
Mean Anom(rad): -9.34581875800001e-001  
Af0(s): 0.00000000000000e+000  
Af1(s/s): 0.00000000000000e+000  
week: 869

\*\*\*\*\* Week 869 almanac for PRN-15 \*\*\*\*\*

ID: 15  
Health: 0  
Eccentricity: 0.00000000000000e+000  
Time of Applicability(s): 144000  
Orbital Inclination(rad): 9.59931088700065e-001  
Rate of Right Ascen(r/s): 0.00000000000000e+000  
SQRT(A) (m 1/2): 5.15370081099980e+003  
Right Ascen at Week(rad): -2.59459817400000e+000  
Argument of Perigee(rad): -7.41997718999999e-001  
Mean Anom(rad): -4.29327011100000e-001  
Af0(s): 0.00000000000000e+000  
Af1(s/s): 0.00000000000000e+000  
week: 869

\*\*\*\*\* Week 869 almanac for PRN-16 \*\*\*\*\*

ID: 16  
Health: 0  
Eccentricity: 0.00000000000000e+000  
Time of Applicability(s): 144000  
Orbital Inclination(rad): 9.59931088700065e-001  
Rate of Right Ascen(r/s): 0.00000000000000e+000  
SQRT(A) (m 1/2): 5.15370081099980e+003

Right Ascen at Week(rad): -4.65248584700001e-001  
Argument of Perigee(rad): -3.85978222000000e-001  
Mean Anom(rad): 9.20198559800000e-001  
Af0(s): 0.00000000000000e+000  
Af1(s/s): 0.00000000000000e+000  
week: 869

\*\*\*\*\* Week 869 almanac for PRN-17 \*\*\*\*\*

ID: 17  
Health: 0  
Eccentricity: 0.00000000000000e+000  
Time of Applicability(s): 144000  
Orbital Inclination(rad): 9.59931088700065e-001  
Rate of Right Ascen(r/s): 0.00000000000000e+000  
SQRT(A) (m 1/2): 5.15370081099980e+003  
Right Ascen at Week(rad): 5.76244592700001e-001  
Argument of Perigee(rad): -2.75002646400000e+000  
Mean Anom(rad): -1.65793895700000e-001  
Af0(s): 0.00000000000000e+000  
Af1(s/s): 0.00000000000000e+000  
week: 869

\*\*\*\*\* Week 869 almanac for PRN-18 \*\*\*\*\*

ID: 18  
Health: 0  
Eccentricity: 0.00000000000000e+000  
Time of Applicability(s): 144000  
Orbital Inclination(rad): 9.59931088700065e-001  
Rate of Right Ascen(r/s): 0.00000000000000e+000  
SQRT(A) (m 1/2): 5.15370081099980e+003

Right Ascen at Week(rad): 2.68705499200000e+000  
 Argument of Perigee(rad): -2.43825757500000e+000  
 Mean Anom(rad): 1.04815793000000e+000  
 Af0(s): 0.00000000000000e+000  
 Af1(s/s): 0.00000000000000e+000  
 week: 869

\*\*\*\*\* Week 869 almanac for PRN-19 \*\*\*\*\*

ID: 19  
 Health: 0  
 Eccentricity: 0.00000000000000e+000  
 Time of Applicability(s): 144000  
 Orbital Inclination(rad): 9.59931088700065e-001  
 Rate of Right Ascen(r/s): 0.00000000000000e+000  
 SQRT(A) (m 1/2): 5.15370081099980e+003  
 Right Ascen at Week(rad): 6.32605314300000e-001  
 Argument of Perigee(rad): -3.91284585000001e-001  
 Mean Anom(rad): -9.07470583900000e-001  
 Af0(s): 0.00000000000000e+000  
 Af1(s/s): 0.00000000000000e+000  
 week: 869

\*\*\*\*\* Week 869 almanac for PRN-20 \*\*\*\*\*

ID: 20  
 Health: 0  
 Eccentricity: 0.00000000000000e+000  
 Time of Applicability(s): 144000  
 Orbital Inclination(rad): 9.59931088700065e-001  
 Rate of Right Ascen(r/s): 0.00000000000000e+000  
 SQRT(A) (m 1/2): 5.15370081099980e+003

Right Ascen at Week(rad): 2.63330423800000e+000  
Argument of Perigee(rad): 1.31460762000000e+000  
Mean Anom(rad): 1.19534623600000e+000  
Af0(s): 0.00000000000000e+000  
Af1(s/s): 0.00000000000000e+000  
week: 869

\*\*\*\*\* Week 869 almanac for PRN-21 \*\*\*\*\*

ID: 21  
Health: 0  
Eccentricity: 0.00000000000000e+000  
Time of Applicability(s): 144000  
Orbital Inclination(rad): 9.59931088700065e-001  
Rate of Right Ascen(r/s): 0.00000000000000e+000  
SQRT(A) (m 1/2): 5.15370081099980e+003  
Right Ascen at Week(rad): 1.62840294800000e+000  
Argument of Perigee(rad): -2.64889907800000e+000  
Mean Anom(rad): 2.32440674300000e+000  
Af0(s): 0.00000000000000e+000  
Af1(s/s): 0.00000000000000e+000  
week: 869

\*\*\*\*\* Week 869 almanac for PRN-22 \*\*\*\*\*

ID: 22  
Health: 0  
Eccentricity: 0.00000000000000e+000  
Time of Applicability(s): 144000  
Orbital Inclination(rad): 9.59931088700065e-001  
Rate of Right Ascen(r/s): 0.00000000000000e+000  
SQRT(A) (m 1/2): 5.15370081099980e+003

Right Ascen at Week(rad): 2.69298374700000e+000  
 Argument of Perigee(rad): -1.82339680200000e+000  
 Mean Anom(rad): -7.65956640200001e-002  
 Af0(s): 0.00000000000000e+000  
 Af1(s/s): 0.00000000000000e+000  
 week: 869

\*\*\*\*\* Week 869 almanac for PRN-23 \*\*\*\*\*

ID: 23  
 Health: 0  
 Eccentricity: 0.00000000000000e+000  
 Time of Applicability(s): 144000  
 Orbital Inclination(rad): 9.59931088700065e-001  
 Rate of Right Ascen(r/s): 0.00000000000000e+000  
 SQRT(A) (m 1/2): 5.15370081099980e+003  
 Right Ascen at Week(rad): -2.57619190200000e+000  
 Argument of Perigee(rad): 2.88240265800000e+000  
 Mean Anom(rad): -1.44661092800000e+000  
 Af0(s): 0.00000000000000e+000  
 Af1(s/s): 0.00000000000000e+000  
 week: 869

\*\*\*\*\* Week 869 almanac for PRN-24 \*\*\*\*\*

ID: 24  
 Health: 0  
 Eccentricity: 0.00000000000000e+000  
 Time of Applicability(s): 144000  
 Orbital Inclination(rad): 9.59931088700065e-001  
 Rate of Right Ascen(r/s): 0.00000000000000e+000  
 SQRT(A) (m 1/2): 5.15370081099980e+003

Right Ascen at Week(rad): 1.65867066400000e+000  
 Argument of Perigee(rad): -6.39523148999999e-001  
 Mean Anom(rad): 1.03374876339972e+000  
 Af0(s): 0.00000000000000e+000  
 Af1(s/s): 0.00000000000000e+000  
 week: 869

\*\*\*\*\* Week 869 almanac for PRN-25 \*\*\*\*\*

ID: 25  
 Health: 0  
 Eccentricity: 0.00000000000000e+000  
 Time of Applicability(s): 144000  
 Orbital Inclination(rad): 9.59931088700065e-001  
 Rate of Right Ascen(r/s): 0.00000000000000e+000  
 SQRT(A) (m 1/2): 5.15370081099980e+003  
 Right Ascen at Week(rad): -1.62840080300000e+000  
 Argument of Perigee(rad): -1.22941148300000e+000  
 Mean Anom(rad): 1.46781361100000e+000  
 Af0(s): 0.00000000000000e+000  
 Af1(s/s): 0.00000000000000e+000  
 week: 869

\*\*\*\*\* Week 869 almanac for PRN-26 \*\*\*\*\*

ID: 26  
 Health: 0  
 Eccentricity: 0.00000000000000e+000  
 Time of Applicability(s): 144000  
 Orbital Inclination(rad): 9.59931088700065e-001  
 Rate of Right Ascen(r/s): 0.00000000000000e+000  
 SQRT(A) (m 1/2): 5.15370081099980e+003



Right Ascen at Week(rad): -2.52893137900000e+000  
Argument of Perigee(rad): 9.67672229000000e-001  
Mean Anom(rad): -1.88577055900000e+000  
Af0(s): 0.00000000000000e+000  
Af1(s/s): 0.00000000000000e+000  
week: 869

\*\*\*\*\* Week 869 almanac for PRN-27 \*\*\*\*\*

ID: 27  
Health: 0  
Eccentricity: 0.00000000000000e+000  
Time of Applicability(s): 144000  
Orbital Inclination(rad): 9.59931088700065e-001  
Rate of Right Ascen(r/s): 0.00000000000000e+000  
SQRT(A) (m 1/2): 5.15370081099980e+003  
Right Ascen at Week(rad): -1.59251999900000e+000  
Argument of Perigee(rad): -1.65117299600000e+000  
Mean Anom(rad): 5.39627194399999e-001  
Af0(s): 0.00000000000000e+000  
Af1(s/s): 0.00000000000000e+000  
week: 869

\*\*\*\*\* Week 869 almanac for PRN-28 \*\*\*\*\*

ID: 28  
Health: 0  
Eccentricity: 0.00000000000000e+000  
Time of Applicability(s): 144000  
Orbital Inclination(rad): 9.59931088700065e-001  
Rate of Right Ascen(r/s): 0.00000000000000e+000  
SQRT(A) (m 1/2): 5.15370081099980e+003

Right Ascen at Week(rad): -4.56912398300000e-001  
 Argument of Perigee(rad): -2.05713677400000e+000  
 Mean Anom(rad): 2.58443236400000e-001  
 Af0(s): 0.00000000000000e+000  
 Af1(s/s): 0.00000000000000e+000  
 week: 869

\*\*\*\*\* Week 869 almanac for PRN-29 \*\*\*\*\*

ID: 29  
 Health: 0  
 Eccentricity: 0.00000000000000e+000  
 Time of Applicability(s): 144000  
 Orbital Inclination(rad): 9.59931088700065e-001  
 Rate of Right Ascen(r/s): 0.00000000000000e+000  
 SQRT(A) (m 1/2): 5.15370081099980e+003  
 Right Ascen at Week(rad): 5.84426879900000e-001  
 Argument of Perigee(rad): -1.34343349900000e+000  
 Mean Anom(rad): 2.46437074459972e+000  
 Af0(s): 0.00000000000000e+000  
 Af1(s/s): 0.00000000000000e+000  
 week: 869

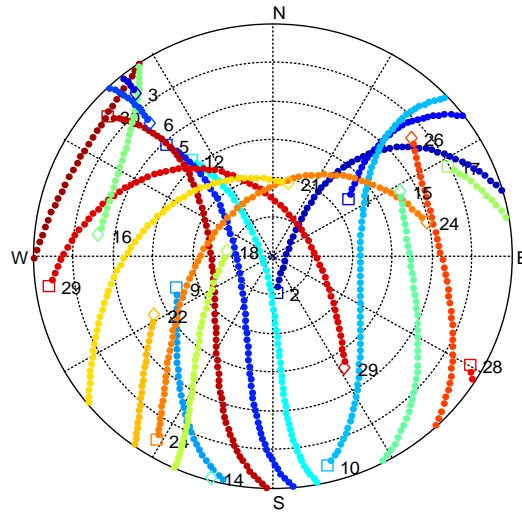
\*\*\*\*\* Week 869 almanac for PRN-30 \*\*\*\*\*

ID: 30  
 Health: 0  
 Eccentricity: 0.00000000000000e+000  
 Time of Applicability(s): 144000  
 Orbital Inclination(rad): 9.59931088700065e-001  
 Rate of Right Ascen(r/s): 0.00000000000000e+000  
 SQRT(A) (m 1/2): 5.15370081099980e+003

Right Ascen at Week(rad): -5.27972102200001e-001  
 Argument of Perigee(rad): 1.41317498700000e+000  
 Mean Anom(rad): 6.90480113000000e-001  
 Af0(s): 0.00000000000000e+000  
 Af1(s/s): 0.00000000000000e+000  
 week: 869

\*\*\*\*\* Week 869 almanac for PRN-31 \*\*\*\*\*

ID: 31  
 Health: 0  
 Eccentricity: 0.00000000000000e+000  
 Time of Applicability(s): 144000  
 Orbital Inclination(rad): 9.59931088700065e-001  
 Rate of Right Ascen(r/s): 0.00000000000000e+000  
 SQRT(A) (m 1/2): 5.15370081099980e+003  
 Right Ascen at Week(rad): -1.53629112200000e+000  
 Argument of Perigee(rad): -1.19382882100000e+000  
 Mean Anom(rad): -3.10803759100000e+000  
 Af0(s): 0.00000000000000e+000  
 Af1(s/s): 0.00000000000000e+000  
 week: 869



**GPS Satellite Visibility**  
**(PRN-24 at -10 dB,**  
**PRN-29 at -20 dB)**

### A.10.2.2 GLONASS Almanac

SV-01 was generated at -10 dB and SV-02 at -20 dB relative to the nominal received power levels (see Table 7). Both of these satellites are visible throughout the entire 6 hour simulation time.

```
***** Week 869 almanac for SV-01, slot 1 *****
ID:                101
Health:            32
Eccentricity:      2.80435376435597e-004
Time of Applicability(s): 144000
Orbital Inclination(rad): 1.12033508367946e+000
Rate of Right Ascen(r/s): 0.00000000000000e+000
SQRT(A) (m 1/2):   5.05032756696999e+003
Right Ascen at Week(rad): 7.40792320628956e-001
```

Argument of Perigee(rad): 1.04180853107395e-001  
Mean Anom(rad): 1.15091734896345e+000  
Af0(s): -1.45391561091000e-004  
Af1(s/s): 0.00000000000000e+000  
week: 869

\*\*\*\*\* Week 869 almanac for SV-02, slot -4 \*\*\*\*\*

ID: 2-4  
Health: 32  
Eccentricity: 1.33246975536473e-003  
Time of Applicability(s): 144000  
Orbital Inclination(rad): 1.12862364314003e+000  
Rate of Right Ascen(r/s): 0.00000000000000e+000  
SQRT(A) (m 1/2): 5.05064077398080e+003  
Right Ascen at Week(rad): 7.47441593549524e-001  
Argument of Perigee(rad): -2.20437677064413e+000  
Mean Anom(rad): -2.59971956740604e+000  
Af0(s): 1.79462134838000e-004  
Af1(s/s): 1.81898940355000e-012  
week: 869

\*\*\*\*\* Week 869 almanac for SV-03, slot 5 \*\*\*\*\*

ID: 305  
Health: 32  
Eccentricity: 1.32498816166167e-003  
Time of Applicability(s): 144000  
Orbital Inclination(rad): 1.12566875527212e+000  
Rate of Right Ascen(r/s): 0.00000000000000e+000  
SQRT(A) (m 1/2): 5.05066930031813e+003  
Right Ascen at Week(rad): 7.48675234560466e-001

Argument of Perigee(rad): -2.05289822822853e+000  
Mean Anom(rad): 1.69623491824316e+000  
Af0(s): 6.39893114567000e-005  
Af1(s/s): 9.09494701773000e-013  
week: 869

\*\*\*\*\* Week 869 almanac for SV-04, slot 6 \*\*\*\*\*

ID: 406  
Health: 32  
Eccentricity: 4.07477957999495e-004  
Time of Applicability(s): 144000  
Orbital Inclination(rad): 1.12598979849155e+000  
Rate of Right Ascen(r/s): 0.00000000000000e+000  
SQRT(A) (m 1/2): 5.05036637505249e+003  
Right Ascen at Week(rad): 7.47210497782127e-001  
Argument of Perigee(rad): -2.31046441525516e+000  
Mean Anom(rad): 1.15466300306374e+000  
Af0(s): 1.59780494869000e-004  
Af1(s/s): 9.09494701773000e-013  
week: 869

\*\*\*\*\* Week 869 almanac for SV-05, slot 1 \*\*\*\*\*

ID: 501  
Health: 32  
Eccentricity: 5.25326160780691e-004  
Time of Applicability(s): 144000  
Orbital Inclination(rad): 1.12011662854620e+000  
Rate of Right Ascen(r/s): 0.00000000000000e+000  
SQRT(A) (m 1/2): 5.05034296657956e+003  
Right Ascen at Week(rad): 7.39644393530448e-001

Argument of Perigee(rad): 1.23200649291355e+000  
Mean Anom(rad): 3.13126501826303e+000  
Af0(s): -3.61446291208000e-006  
Af1(s/s): -9.09494701773000e-013  
week: 869

\*\*\*\*\* Week 869 almanac for SV-06, slot -4 \*\*\*\*\*

ID: 6-4  
Health: 32  
Eccentricity: 8.53360015146096e-004  
Time of Applicability(s): 144000  
Orbital Inclination(rad): 1.12005137128198e+000  
Rate of Right Ascen(r/s): 0.00000000000000e+000  
SQRT(A) (m 1/2): 5.05065643919592e+003  
Right Ascen at Week(rad): 7.39560464322004e-001  
Argument of Perigee(rad): 2.45142186808776e+000  
Mean Anom(rad): 1.08577069852623e+000  
Af0(s): 8.49086791277000e-005  
Af1(s/s): 0.00000000000000e+000  
week: 869

\*\*\*\*\* Week 869 almanac for SV-07, slot 5 \*\*\*\*\*

ID: 705  
Health: 32  
Eccentricity: 1.10069518293223e-003  
Time of Applicability(s): 144000  
Orbital Inclination(rad): 1.12581361051808e+000  
Rate of Right Ascen(r/s): 0.00000000000000e+000  
SQRT(A) (m 1/2): 5.05066586996986e+003  
Right Ascen at Week(rad): 7.49361979736101e-001

Argument of Perigee(rad): -2.09985541861908e+000  
Mean Anom(rad): -1.40932465105142e+000  
Af0(s): -6.72508031130000e-006  
Af1(s/s): -0.00000000000000e+000  
week: 869

\*\*\*\*\* Week 869 almanac for SV-08, slot 6 \*\*\*\*\*

ID: 806  
Health: 32  
Eccentricity: 1.69977794661984e-003  
Time of Applicability(s): 144000  
Orbital Inclination(rad): 1.12591505648484e+000  
Rate of Right Ascen(r/s): 0.00000000000000e+000  
SQRT(A) (m 1/2): 5.05037218492650e+003  
Right Ascen at Week(rad): 7.49133082568086e-001  
Argument of Perigee(rad): -1.40947614523548e+000  
Mean Anom(rad): -2.86620078192880e+000  
Af0(s): -2.71061435342000e-005  
Af1(s/s): 0.00000000000000e+000  
week: 869

\*\*\*\*\* Week 869 almanac for SV-09, slot -6 \*\*\*\*\*

ID: 9-6  
Health: 32  
Eccentricity: 1.49164382262733e-003  
Time of Applicability(s): 144000  
Orbital Inclination(rad): 1.12887573482007e+000  
Rate of Right Ascen(r/s): 0.00000000000000e+000  
SQRT(A) (m 1/2): 5.05029813945331e+003  
Right Ascen at Week(rad): 2.87210862370048e+000



Argument of Perigee(rad): -2.17340232687494e+000  
Mean Anom(rad): -2.65756649912442e+000  
Af0(s): 8.67033377290000e-005  
Af1(s/s): 7.27595761418000e-012  
week: 869

\*\*\*\*\* Week 869 almanac for SV-10, slot -7 \*\*\*\*\*

ID: 10-7  
Health: 32  
Eccentricity: 1.64202181019619e-003  
Time of Applicability(s): 144000  
Orbital Inclination(rad): 1.14681706329809e+000  
Rate of Right Ascen(r/s): 0.00000000000000e+000  
SQRT(A) (m 1/2): 5.05053138049315e+003  
Right Ascen at Week(rad): 2.85464671037023e+000  
Argument of Perigee(rad): 2.65732697939073e+000  
Mean Anom(rad): -1.96468327760479e+000  
Af0(s): 1.51759013534000e-005  
Af1(s/s): 9.09494701773000e-013  
week: 869

\*\*\*\*\* Week 869 almanac for SV-11, slot 0 \*\*\*\*\*

ID: 1100  
Health: 32  
Eccentricity: 1.96070028249679e-003  
Time of Applicability(s): 144000  
Orbital Inclination(rad): 1.14010497737022e+000  
Rate of Right Ascen(r/s): 0.00000000000000e+000  
SQRT(A) (m 1/2): 5.05072659215691e+003  
Right Ascen at Week(rad): 2.84299979611610e+000

Argument of Perigee(rad): 6.59073671346432e-002  
 Mean Anom(rad): -1.57173974293076e-001  
 Af0(s): 2.48514115810000e-005  
 Af1(s/s): -0.00000000000000e+000  
 week: 869

\*\*\*\*\* Week 869 almanac for SV-12, slot -4 \*\*\*\*\*

ID: 12-4  
 Health: 32  
 Eccentricity: 3.29010000000000e-003  
 Time of Applicability(s): 144000  
 Orbital Inclination(rad): 1.13279198837290e+000  
 Rate of Right Ascen(r/s): 0.00000000000000e+000  
 SQRT(A) (m 1/2): 5.05054067518879e+003  
 Right Ascen at Week(rad): 3.09690261246385e+000  
 Argument of Perigee(rad): 2.95384060463576e+000  
 Mean Anom(rad): 1.79044601315838e-001  
 Af0(s): 5.00000000000000e-004  
 Af1(s/s): 0.00000000000000e+000  
 week: 869

\*\*\*\*\* Week 869 almanac for SV-13, slot -2 \*\*\*\*\*

ID: 13-2  
 Health: 32  
 Eccentricity: 7.99396667097814e-004  
 Time of Applicability(s): 144000  
 Orbital Inclination(rad): 1.13983784832610e+000  
 Rate of Right Ascen(r/s): 0.00000000000000e+000  
 SQRT(A) (m 1/2): 5.05028282604365e+003  
 Right Ascen at Week(rad): 2.84230006542228e+000

Argument of Perigee(rad): 1.44672167995213e+000  
Mean Anom(rad): 3.13950706608156e+000  
Af0(s): 1.00303441286000e-005  
Af1(s/s): -0.00000000000000e+000  
week: 869

\*\*\*\*\* Week 869 almanac for SV-14, slot -7 \*\*\*\*\*

ID: 14-7  
Health: 32  
Eccentricity: 1.55466745629980e-003  
Time of Applicability(s): 144000  
Orbital Inclination(rad): 1.14654884486877e+000  
Rate of Right Ascen(r/s): 0.00000000000000e+000  
SQRT(A) (m 1/2): 5.05056499236033e+003  
Right Ascen at Week(rad): 2.85343237647763e+000  
Argument of Perigee(rad): 2.62825282626368e+000  
Mean Anom(rad): 1.1464698484523e+000  
Af0(s): 2.89653427899000e-004  
Af1(s/s): 4.54747350886000e-012  
week: 869

\*\*\*\*\* Week 869 almanac for SV-15, slot 0 \*\*\*\*\*

ID: 1500  
Health: 32  
Eccentricity: 2.23977675463663e-003  
Time of Applicability(s): 144000  
Orbital Inclination(rad): 1.14653193639322e+000  
Rate of Right Ascen(r/s): 0.00000000000000e+000  
SQRT(A) (m 1/2): 5.05071089313078e+003  
Right Ascen at Week(rad): 2.85323904698924e+000

Argument of Perigee(rad): -8.70289850291570e-002  
Mean Anom(rad): -3.08905125954067e+000  
Af0(s): 6.49411231279000e-005  
Af1(s/s): 9.09494701773000e-013  
week: 869

\*\*\*\*\* Week 869 almanac for SV-16, slot -1 \*\*\*\*\*

ID: 16-1  
Health: 32  
Eccentricity: 1.83550000000000e-003  
Time of Applicability(s): 144000  
Orbital Inclination(rad): 1.13249353707081e+000  
Rate of Right Ascen(r/s): 0.00000000000000e+000  
SQRT(A) (m 1/2): 5.05054371669493e+003  
Right Ascen at Week(rad): 3.09582748965045e+000  
Argument of Perigee(rad): 2.66851068786122e+000  
Mean Anom(rad): 6.91782192978976e-001  
Af0(s): 5.00000000000000e-004  
Af1(s/s): 0.00000000000000e+000  
week: 869

\*\*\*\*\* Week 869 almanac for SV-17, slot 4 \*\*\*\*\*

ID: 1704  
Health: 32  
Eccentricity: 8.84576720774307e-004  
Time of Applicability(s): 144000  
Orbital Inclination(rad): 1.13082917946630e+000  
Rate of Right Ascen(r/s): 0.00000000000000e+000  
SQRT(A) (m 1/2): 5.05029194768975e+003  
Right Ascen at Week(rad): -1.33195554259822e+000

Argument of Perigee(rad): -2.36958530021500e+000  
Mean Anom(rad): -2.16435670581638e+000  
Af0(s): -2.28835269809000e-005  
Af1(s/s): 0.00000000000000e+000  
week: 869

\*\*\*\*\* Week 869 almanac for SV-18, slot -3 \*\*\*\*\*

ID: 18-3  
Health: 32  
Eccentricity: 1.58283047580818e-003  
Time of Applicability(s): 144000  
Orbital Inclination(rad): 1.13537186282913e+000  
Rate of Right Ascen(r/s): 0.00000000000000e+000  
SQRT(A) (m 1/2): 5.05041473916712e+003  
Right Ascen at Week(rad): -1.33706722854576e+000  
Argument of Perigee(rad): -4.70730444184711e-001  
Mean Anom(rad): 1.47504581863733e+000  
Af0(s): 9.16374847293000e-005  
Af1(s/s): 9.09494701773000e-013  
week: 869

\*\*\*\*\* Week 869 almanac for SV-19, slot 3 \*\*\*\*\*

ID: 1903  
Health: 32  
Eccentricity: 2.44352903735194e-004  
Time of Applicability(s): 144000  
Orbital Inclination(rad): 1.13925194401139e+000  
Rate of Right Ascen(r/s): 0.00000000000000e+000  
SQRT(A) (m 1/2): 5.05068914526964e+003  
Right Ascen at Week(rad): -1.32184456573935e+000

Argument of Perigee(rad): -1.18705963314368e+000  
Mean Anom(rad): 1.36025505659405e+000  
Af0(s): -1.49535015225000e-004  
Af1(s/s): -0.00000000000000e+000  
week: 869

\*\*\*\*\* Week 869 almanac for SV-20, slot 2 \*\*\*\*\*

ID: 2002  
Health: 32  
Eccentricity: 1.22842522658171e-003  
Time of Applicability(s): 144000  
Orbital Inclination(rad): 1.13945237991812e+000  
Rate of Right Ascen(r/s): 0.00000000000000e+000  
SQRT(A) (m 1/2): 5.05054064557828e+003  
Right Ascen at Week(rad): -1.32075578560146e+000  
Argument of Perigee(rad): -3.82939381582557e-001  
Mean Anom(rad): -2.46146248236104e-001  
Af0(s): -2.22451053560000e-004  
Af1(s/s): -1.81898940355000e-012  
week: 869

\*\*\*\*\* Week 869 almanac for SV-21, slot 4 \*\*\*\*\*

ID: 2104  
Health: 32  
Eccentricity: 5.31475615345574e-004  
Time of Applicability(s): 144000  
Orbital Inclination(rad): 1.13432115101620e+000  
Rate of Right Ascen(r/s): 0.00000000000000e+000  
SQRT(A) (m 1/2): 5.05029468247230e+003  
Right Ascen at Week(rad): -1.33653498898153e+000

Argument of Perigee(rad): -2.81972240040206e+000  
Mean Anom(rad): 1.44889418884053e+000  
Af0(s): 5.36972656846000e-005  
Af1(s/s): 1.81898940355000e-012  
week: 869

\*\*\*\*\* Week 869 almanac for SV-22, slot -3 \*\*\*\*\*

ID: 22-3  
Health: 32  
Eccentricity: 2.94760840310346e-003  
Time of Applicability(s): 144000  
Orbital Inclination(rad): 1.13760739536984e+000  
Rate of Right Ascen(r/s): 0.00000000000000e+000  
SQRT(A) (m 1/2): 5.05043482102626e+003  
Right Ascen at Week(rad): -1.33642892609230e+000  
Argument of Perigee(rad): -1.03944861440644e-001  
Mean Anom(rad): -2.05717394866684e+000  
Af0(s): 1.93633139133000e-004  
Af1(s/s): 9.09494701773000e-013  
week: 869

\*\*\*\*\* Week 869 almanac for SV-23, slot 3 \*\*\*\*\*

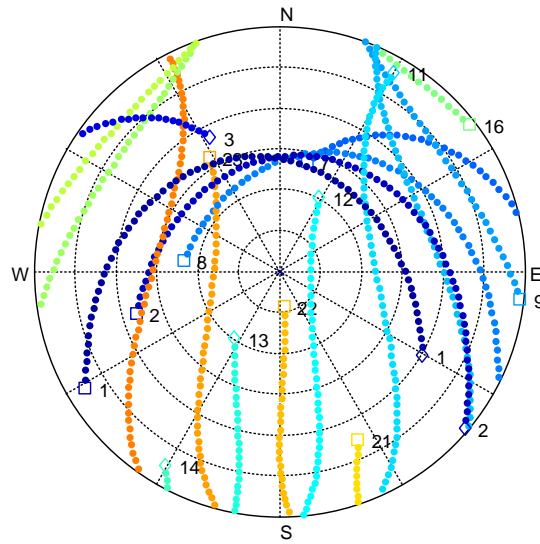
ID: 2303  
Health: 32  
Eccentricity: 3.94066120249689e-005  
Time of Applicability(s): 144000  
Orbital Inclination(rad): 1.13734058290765e+000  
Rate of Right Ascen(r/s): 0.00000000000000e+000  
SQRT(A) (m 1/2): 5.05071557599688e+003  
Right Ascen at Week(rad): -1.33712871096215e+000

Argument of Perigee(rad): -1.70246732457996e-001  
Mean Anom(rad): -2.81819268437635e+000  
Af0(s): -8.79149883986000e-005  
Af1(s/s): -3.63797880709000e-012  
week: 869

\*\*\*\*\* Week 869 almanac for SV-24, slot 2 \*\*\*\*\*

ID: 2402  
Health: 32  
Eccentricity: 6.68632423028246e-004  
Time of Applicability(s): 144000  
Orbital Inclination(rad): 1.13750141332033e+000  
Rate of Right Ascen(r/s): 0.00000000000000e+000  
SQRT(A) (m 1/2): 5.05057594902682e+003  
Right Ascen at Week(rad): -1.33677735210199e+000  
Argument of Perigee(rad): 1.12161248242197e+000  
Mean Anom(rad): 1.43907705778873e+000  
Af0(s): -1.34304165840000e-004  
Af1(s/s): 0.00000000000000e+000  
week: 869





**GLONASS Satellite Visibility**  
**(SV-01 at -10 dB,**  
**SV-02 at -20 dB)**

### A.10.2.3 Galileo Almanac

PRN-4 was generated at -10 dB and PRN-10 at -20 dB relative to the nominal received power levels (see Table 7). Both of these satellites are visible throughout the entire 6 hour simulation time.

```
***** Week 869 almanac for PRN-01 *****
ID:                                01
Health:                             0
Eccentricity:                       0.000000000000000e+000
Time of Applicability(s):           144000
Orbital Inclination(rad):           9.77384381116824e-001
Rate of Right Ascen(r/s):           0.000000000000000e+000
SQRT(A) (m 1/2):                     5.44058820349418e+003
```

Right Ascen at Week(rad): 0.00000000000000e+000  
Argument of Perigee(rad): 0.00000000000000e+000  
Mean Anom(rad): 0.00000000000000e+000  
Af0(s): 0.00000000000000e+000  
Af1(s/s): 0.00000000000000e+000  
week: 869

\*\*\*\*\* Week 869 almanac for PRN-02 \*\*\*\*\*

ID: 02  
Health: 0  
Eccentricity: 0.00000000000000e+000  
Time of Applicability(s): 144000  
Orbital Inclination(rad): 9.77384381116824e-001  
Rate of Right Ascen(r/s): 0.00000000000000e+000  
SQRT(A) (m 1/2): 5.44058820349418e+003  
Right Ascen at Week(rad): 0.00000000000000e+000  
Argument of Perigee(rad): 0.00000000000000e+000  
Mean Anom(rad): 6.98131700797731e-001  
Af0(s): 0.00000000000000e+000  
Af1(s/s): 0.00000000000000e+000  
week: 869

\*\*\*\*\* Week 869 almanac for PRN-03 \*\*\*\*\*

ID: 03  
Health: 0  
Eccentricity: 0.00000000000000e+000  
Time of Applicability(s): 144000  
Orbital Inclination(rad): 9.77384381116824e-001  
Rate of Right Ascen(r/s): 0.00000000000000e+000  
SQRT(A) (m 1/2): 5.44058820349418e+003

Right Ascen at Week(rad): 0.00000000000000e+000  
Argument of Perigee(rad): 0.00000000000000e+000  
Mean Anom(rad): 1.39626340159546e+000  
Af0(s): 0.00000000000000e+000  
Af1(s/s): 0.00000000000000e+000  
week: 869

\*\*\*\*\* Week 869 almanac for PRN-04 \*\*\*\*\*

ID: 04  
Health: 0  
Eccentricity: 0.00000000000000e+000  
Time of Applicability(s): 144000  
Orbital Inclination(rad): 9.77384381116824e-001  
Rate of Right Ascen(r/s): 0.00000000000000e+000  
SQRT(A) (m 1/2): 5.44058820349418e+003  
Right Ascen at Week(rad): 0.00000000000000e+000  
Argument of Perigee(rad): 0.00000000000000e+000  
Mean Anom(rad): 2.09439510239320e+000  
Af0(s): 0.00000000000000e+000  
Af1(s/s): 0.00000000000000e+000  
week: 869

\*\*\*\*\* Week 869 almanac for PRN-05 \*\*\*\*\*

ID: 05  
Health: 0  
Eccentricity: 0.00000000000000e+000  
Time of Applicability(s): 144000  
Orbital Inclination(rad): 9.77384381116824e-001  
Rate of Right Ascen(r/s): 0.00000000000000e+000  
SQRT(A) (m 1/2): 5.44058820349418e+003

Right Ascen at Week(rad): 0.00000000000000e+000  
Argument of Perigee(rad): 0.00000000000000e+000  
Mean Anom(rad): 2.79252680319093e+000  
Af0(s): 0.00000000000000e+000  
Af1(s/s): 0.00000000000000e+000  
week: 869

\*\*\*\*\* Week 869 almanac for PRN-06 \*\*\*\*\*

ID: 06  
Health: 0  
Eccentricity: 0.00000000000000e+000  
Time of Applicability(s): 144000  
Orbital Inclination(rad): 9.77384381116824e-001  
Rate of Right Ascen(r/s): 0.00000000000000e+000  
SQRT(A) (m 1/2): 5.44058820349418e+003  
Right Ascen at Week(rad): 0.00000000000000e+000  
Argument of Perigee(rad): 0.00000000000000e+000  
Mean Anom(rad): -2.79252680319093e+000  
Af0(s): 0.00000000000000e+000  
Af1(s/s): 0.00000000000000e+000  
week: 869

\*\*\*\*\* Week 869 almanac for PRN-07 \*\*\*\*\*

ID: 07  
Health: 0  
Eccentricity: 0.00000000000000e+000  
Time of Applicability(s): 144000  
Orbital Inclination(rad): 9.77384381116824e-001  
Rate of Right Ascen(r/s): 0.00000000000000e+000  
SQRT(A) (m 1/2): 5.44058820349418e+003

Right Ascen at Week(rad): 0.00000000000000e+000  
Argument of Perigee(rad): 0.00000000000000e+000  
Mean Anom(rad): -2.09439510239320e+000  
Af0(s): 0.00000000000000e+000  
Af1(s/s): 0.00000000000000e+000  
week: 869

\*\*\*\*\* Week 869 almanac for PRN-08 \*\*\*\*\*

ID: 08  
Health: 0  
Eccentricity: 0.00000000000000e+000  
Time of Applicability(s): 144000  
Orbital Inclination(rad): 9.77384381116824e-001  
Rate of Right Ascen(r/s): 0.00000000000000e+000  
SQRT(A) (m 1/2): 5.44058820349418e+003  
Right Ascen at Week(rad): 0.00000000000000e+000  
Argument of Perigee(rad): 0.00000000000000e+000  
Mean Anom(rad): -1.39626340159547e+000  
Af0(s): 0.00000000000000e+000  
Af1(s/s): 0.00000000000000e+000  
week: 869

\*\*\*\*\* Week 869 almanac for PRN-09 \*\*\*\*\*

ID: 09  
Health: 0  
Eccentricity: 0.00000000000000e+000  
Time of Applicability(s): 144000  
Orbital Inclination(rad): 9.77384381116824e-001  
Rate of Right Ascen(r/s): 0.00000000000000e+000  
SQRT(A) (m 1/2): 5.44058820349418e+003

Right Ascen at Week(rad): 0.00000000000000e+000  
 Argument of Perigee(rad): 0.00000000000000e+000  
 Mean Anom(rad): -6.98131700797731e-001  
 Af0(s): 0.00000000000000e+000  
 Af1(s/s): 0.00000000000000e+000  
 week: 869

\*\*\*\*\* Week 869 almanac for PRN-10 \*\*\*\*\*

ID: 10  
 Health: 0  
 Eccentricity: 0.00000000000000e+000  
 Time of Applicability(s): 144000  
 Orbital Inclination(rad): 9.77384381116824e-001  
 Rate of Right Ascen(r/s): 0.00000000000000e+000  
 SQRT(A) (m 1/2): 5.44058820349418e+003  
 Right Ascen at Week(rad): 2.09439510239320e+000  
 Argument of Perigee(rad): 0.00000000000000e+000  
 Mean Anom(rad): 2.32652389290844e-001  
 Af0(s): 0.00000000000000e+000  
 Af1(s/s): 0.00000000000000e+000  
 week: 869

\*\*\*\*\* Week 869 almanac for PRN-11 \*\*\*\*\*

ID: 11  
 Health: 0  
 Eccentricity: 0.00000000000000e+000  
 Time of Applicability(s): 144000  
 Orbital Inclination(rad): 9.77384381116824e-001  
 Rate of Right Ascen(r/s): 0.00000000000000e+000  
 SQRT(A) (m 1/2): 5.44058820349418e+003

Right Ascen at Week(rad): 2.09439510239320e+000  
 Argument of Perigee(rad): 0.00000000000000e+000  
 Mean Anom(rad): 9.30784090088577e-001  
 Af0(s): 0.00000000000000e+000  
 Af1(s/s): 0.00000000000000e+000  
 week: 869

\*\*\*\*\* Week 869 almanac for PRN-12 \*\*\*\*\*

ID: 12  
 Health: 0  
 Eccentricity: 0.00000000000000e+000  
 Time of Applicability(s): 144000  
 Orbital Inclination(rad): 9.77384381116824e-001  
 Rate of Right Ascen(r/s): 0.00000000000000e+000  
 SQRT(A) (m 1/2): 5.44058820349418e+003  
 Right Ascen at Week(rad): 2.09439510239320e+000  
 Argument of Perigee(rad): 0.00000000000000e+000  
 Mean Anom(rad): 1.62891579088631e+000  
 Af0(s): 0.00000000000000e+000  
 Af1(s/s): 0.00000000000000e+000  
 week: 869

\*\*\*\*\* Week 869 almanac for PRN-13 \*\*\*\*\*

ID: 13  
 Health: 0  
 Eccentricity: 0.00000000000000e+000  
 Time of Applicability(s): 144000  
 Orbital Inclination(rad): 9.77384381116824e-001  
 Rate of Right Ascen(r/s): 0.00000000000000e+000  
 SQRT(A) (m 1/2): 5.44058820349418e+003

Right Ascen at Week(rad): 2.09439510239320e+000  
Argument of Perigee(rad): 0.00000000000000e+000  
Mean Anom(rad): 2.32704749168404e+000  
Af0(s): 0.00000000000000e+000  
Af1(s/s): 0.00000000000000e+000  
week: 869

\*\*\*\*\* Week 869 almanac for PRN-14 \*\*\*\*\*

ID: 14  
Health: 0  
Eccentricity: 0.00000000000000e+000  
Time of Applicability(s): 144000  
Orbital Inclination(rad): 9.77384381116824e-001  
Rate of Right Ascen(r/s): 0.00000000000000e+000  
SQRT(A) (m 1/2): 5.44058820349418e+003  
Right Ascen at Week(rad): 2.09439510239320e+000  
Argument of Perigee(rad): 0.00000000000000e+000  
Mean Anom(rad): 3.02517919248177e+000  
Af0(s): 0.00000000000000e+000  
Af1(s/s): 0.00000000000000e+000  
week: 869

\*\*\*\*\* Week 869 almanac for PRN-15 \*\*\*\*\*

ID: 15  
Health: 0  
Eccentricity: 0.00000000000000e+000  
Time of Applicability(s): 144000  
Orbital Inclination(rad): 9.77384381116824e-001  
Rate of Right Ascen(r/s): 0.00000000000000e+000  
SQRT(A) (m 1/2): 5.44058820349418e+003



Right Ascen at Week(rad): 2.09439510239320e+000  
Argument of Perigee(rad): 0.00000000000000e+000  
Mean Anom(rad): -2.55987441390008e+000  
Af0(s): 0.00000000000000e+000  
Af1(s/s): 0.00000000000000e+000  
week: 869

\*\*\*\*\* Week 869 almanac for PRN-16 \*\*\*\*\*

ID: 16  
Health: 0  
Eccentricity: 0.00000000000000e+000  
Time of Applicability(s): 144000  
Orbital Inclination(rad): 9.77384381116824e-001  
Rate of Right Ascen(r/s): 0.00000000000000e+000  
SQRT(A) (m 1/2): 5.44058820349418e+003  
Right Ascen at Week(rad): 2.09439510239320e+000  
Argument of Perigee(rad): 0.00000000000000e+000  
Mean Anom(rad): -1.86174271310235e+000  
Af0(s): 0.00000000000000e+000  
Af1(s/s): 0.00000000000000e+000  
week: 869

\*\*\*\*\* Week 869 almanac for PRN-17 \*\*\*\*\*

ID: 17  
Health: 0  
Eccentricity: 0.00000000000000e+000  
Time of Applicability(s): 144000  
Orbital Inclination(rad): 9.77384381116824e-001  
Rate of Right Ascen(r/s): 0.00000000000000e+000  
SQRT(A) (m 1/2): 5.44058820349418e+003

Right Ascen at Week(rad): 2.09439510239320e+000  
Argument of Perigee(rad): 0.00000000000000e+000  
Mean Anom(rad): -1.16361101230462e+000  
Af0(s): 0.00000000000000e+000  
Af1(s/s): 0.00000000000000e+000  
week: 869

\*\*\*\*\* Week 869 almanac for PRN-18 \*\*\*\*\*

ID: 18  
Health: 0  
Eccentricity: 0.00000000000000e+000  
Time of Applicability(s): 144000  
Orbital Inclination(rad): 9.77384381116824e-001  
Rate of Right Ascen(r/s): 0.00000000000000e+000  
SQRT(A) (m 1/2): 5.44058820349418e+003  
Right Ascen at Week(rad): 2.09439510239320e+000  
Argument of Perigee(rad): 0.00000000000000e+000  
Mean Anom(rad): -4.65479311506889e-001  
Af0(s): 0.00000000000000e+000  
Af1(s/s): 0.00000000000000e+000  
week: 869

\*\*\*\*\* Week 869 almanac for PRN-19 \*\*\*\*\*

ID: 19  
Health: 0  
Eccentricity: 0.00000000000000e+000  
Time of Applicability(s): 144000  
Orbital Inclination(rad): 9.77384381116824e-001  
Rate of Right Ascen(r/s): 0.00000000000000e+000  
SQRT(A) (m 1/2): 5.44058820349418e+003

Right Ascen at Week(rad): -2.09439510239320e+000  
 Argument of Perigee(rad): 0.00000000000000e+000  
 Mean Anom(rad): 4.65304778581688e-001  
 Af0(s): 0.00000000000000e+000  
 Af1(s/s): 0.00000000000000e+000  
 week: 869

\*\*\*\*\* Week 869 almanac for PRN-20 \*\*\*\*\*

ID: 20  
 Health: 0  
 Eccentricity: 0.00000000000000e+000  
 Time of Applicability(s): 144000  
 Orbital Inclination(rad): 9.77384381116824e-001  
 Rate of Right Ascen(r/s): 0.00000000000000e+000  
 SQRT(A) (m 1/2): 5.44058820349418e+003  
 Right Ascen at Week(rad): -2.09439510239320e+000  
 Argument of Perigee(rad): 0.00000000000000e+000  
 Mean Anom(rad): 1.16343647937942e+000  
 Af0(s): 0.00000000000000e+000  
 Af1(s/s): 0.00000000000000e+000  
 week: 869

\*\*\*\*\* Week 869 almanac for PRN-21 \*\*\*\*\*

ID: 21  
 Health: 0  
 Eccentricity: 0.00000000000000e+000  
 Time of Applicability(s): 144000  
 Orbital Inclination(rad): 9.77384381116824e-001  
 Rate of Right Ascen(r/s): 0.00000000000000e+000  
 SQRT(A) (m 1/2): 5.44058820349418e+003

Right Ascen at Week(rad): -2.09439510239320e+000  
Argument of Perigee(rad): 0.00000000000000e+000  
Mean Anom(rad): 1.86156818017715e+000  
Af0(s): 0.00000000000000e+000  
Af1(s/s): 0.00000000000000e+000  
week: 869

\*\*\*\*\* Week 869 almanac for PRN-22 \*\*\*\*\*

ID: 22  
Health: 0  
Eccentricity: 0.00000000000000e+000  
Time of Applicability(s): 144000  
Orbital Inclination(rad): 9.77384381116824e-001  
Rate of Right Ascen(r/s): 0.00000000000000e+000  
SQRT(A) (m 1/2): 5.44058820349418e+003  
Right Ascen at Week(rad): -2.09439510239320e+000  
Argument of Perigee(rad): 0.00000000000000e+000  
Mean Anom(rad): 2.55969988097488e+000  
Af0(s): 0.00000000000000e+000  
Af1(s/s): 0.00000000000000e+000  
week: 869

\*\*\*\*\* Week 869 almanac for PRN-23 \*\*\*\*\*

ID: 23  
Health: 0  
Eccentricity: 0.00000000000000e+000  
Time of Applicability(s): 144000  
Orbital Inclination(rad): 9.77384381116824e-001  
Rate of Right Ascen(r/s): 0.00000000000000e+000  
SQRT(A) (m 1/2): 5.44058820349418e+003

Right Ascen at Week(rad): -2.09439510239320e+000  
Argument of Perigee(rad): 0.00000000000000e+000  
Mean Anom(rad): -3.02535372540697e+000  
Af0(s): 0.00000000000000e+000  
Af1(s/s): 0.00000000000000e+000  
week: 869

\*\*\*\*\* Week 869 almanac for PRN-24 \*\*\*\*\*

ID: 24  
Health: 0  
Eccentricity: 0.00000000000000e+000  
Time of Applicability(s): 144000  
Orbital Inclination(rad): 9.77384381116824e-001  
Rate of Right Ascen(r/s): 0.00000000000000e+000  
SQRT(A) (m 1/2): 5.44058820349418e+003  
Right Ascen at Week(rad): -2.09439510239320e+000  
Argument of Perigee(rad): 0.00000000000000e+000  
Mean Anom(rad): -2.32722202460924e+000  
Af0(s): 0.00000000000000e+000  
Af1(s/s): 0.00000000000000e+000  
week: 869

\*\*\*\*\* Week 869 almanac for PRN-25 \*\*\*\*\*

ID: 25  
Health: 0  
Eccentricity: 0.00000000000000e+000  
Time of Applicability(s): 144000  
Orbital Inclination(rad): 9.77384381116824e-001  
Rate of Right Ascen(r/s): 0.00000000000000e+000  
SQRT(A) (m 1/2): 5.44058820349418e+003

Right Ascen at Week(rad): -2.09439510239320e+000  
 Argument of Perigee(rad): 0.00000000000000e+000  
 Mean Anom(rad): -1.62909032381151e+000  
 Af0(s): 0.00000000000000e+000  
 Af1(s/s): 0.00000000000000e+000  
 week: 869

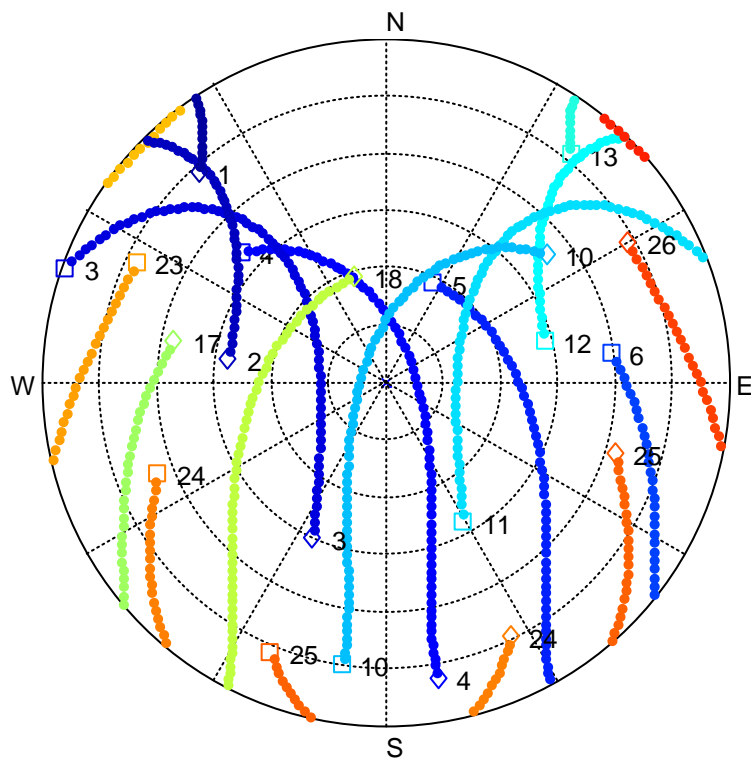
\*\*\*\*\* Week 869 almanac for PRN-26 \*\*\*\*\*

ID: 26  
 Health: 0  
 Eccentricity: 0.00000000000000e+000  
 Time of Applicability(s): 144000  
 Orbital Inclination(rad): 9.77384381116824e-001  
 Rate of Right Ascen(r/s): 0.00000000000000e+000  
 SQRT(A) (m 1/2): 5.44058820349418e+003  
 Right Ascen at Week(rad): -2.09439510239320e+000  
 Argument of Perigee(rad): 0.00000000000000e+000  
 Mean Anom(rad): -9.30958623013774e-001  
 Af0(s): 0.00000000000000e+000  
 Af1(s/s): 0.00000000000000e+000  
 week: 869

\*\*\*\*\* Week 869 almanac for PRN-27 \*\*\*\*\*

ID: 27  
 Health: 0  
 Eccentricity: 0.00000000000000e+000  
 Time of Applicability(s): 144000  
 Orbital Inclination(rad): 9.77384381116824e-001  
 Rate of Right Ascen(r/s): 0.00000000000000e+000  
 SQRT(A) (m 1/2): 5.44058820349418e+003

Right Ascen at Week(rad): -2.09439510239320e+000  
 Argument of Perigee(rad): 0.00000000000000e+000  
 Mean Anom(rad): -2.32826922216043e-001  
 Af0(s): 0.00000000000000e+000  
 Af1(s/s): 0.00000000000000e+000  
 week: 869



**Galileo Satellite Visibility**  
**(PRN-4 at -10 dB,**  
**PRN-10 at -20 dB)**

#### A.10.2.4 BeiDou Almanac

PRN-8 was generated at -10 dB and PRN-18 at -20 dB relative to the nominal received power levels (see Table 7). Both of these satellites are visible throughout the entire 6 hour simulation time.

```
***** Week 869 almanac for PRN-06 *****
ID:                06
Health:            0
Eccentricity:      0.00000000000000e+000
Time of Applicability(s): 144000
Orbital Inclination(rad): 9.59931088596883e-001
Rate of Right Ascen(r/s): 0.00000000000000e+000
SQRT(A) (m 1/2):   5.27996000000000e+003
Right Ascen at Week(rad): 0.00000000000000e+000
Argument of Perigee(rad): 0.00000000000000e+000
Mean Anom(rad):    0.00000000000000e+000
Af0(s):            0.00000000000000e+000
Af1(s/s):          0.00000000000000e+000
week:              869
```

```
***** Week 869 almanac for PRN-07 *****
ID:                07
Health:            0
Eccentricity:      0.00000000000000e+000
Time of Applicability(s): 144000
Orbital Inclination(rad): 9.59931088596883e-001
Rate of Right Ascen(r/s): 0.00000000000000e+000
SQRT(A) (m 1/2):   5.27996000000000e+003
Right Ascen at Week(rad): 0.00000000000000e+000
Argument of Perigee(rad): 7.85398163397448e-001
```



Mean Anom(rad): 0.00000000000000e+000  
Af0(s): 0.00000000000000e+000  
Af1(s/s): 0.00000000000000e+000  
week: 869

\*\*\*\*\* Week 869 almanac for PRN-08 \*\*\*\*\*

ID: 08  
Health: 0  
Eccentricity: 0.00000000000000e+000  
Time of Applicability(s): 144000  
Orbital Inclination(rad): 9.59931088596883e-001  
Rate of Right Ascen(r/s): 0.00000000000000e+000  
SQRT(A) (m 1/2): 5.27996000000000e+003  
Right Ascen at Week(rad): 0.00000000000000e+000  
Argument of Perigee(rad): 1.57079632679490e+000  
Mean Anom(rad): 0.00000000000000e+000  
Af0(s): 0.00000000000000e+000  
Af1(s/s): 0.00000000000000e+000  
week: 869

\*\*\*\*\* Week 869 almanac for PRN-09 \*\*\*\*\*

ID: 09  
Health: 0  
Eccentricity: 0.00000000000000e+000  
Time of Applicability(s): 144000  
Orbital Inclination(rad): 9.59931088596883e-001  
Rate of Right Ascen(r/s): 0.00000000000000e+000  
SQRT(A) (m 1/2): 5.27996000000000e+003  
Right Ascen at Week(rad): 0.00000000000000e+000  
Argument of Perigee(rad): 2.35619449019234e+000

Mean Anom(rad): 0.00000000000000e+000  
Af0(s): 0.00000000000000e+000  
Af1(s/s): 0.00000000000000e+000  
week: 869

\*\*\*\*\* Week 869 almanac for PRN-10 \*\*\*\*\*

ID: 10  
Health: 0  
Eccentricity: 0.00000000000000e+000  
Time of Applicability(s): 144000  
Orbital Inclination(rad): 9.59931088596883e-001  
Rate of Right Ascen(r/s): 0.00000000000000e+000  
SQRT(A) (m 1/2): 5.27996000000000e+003  
Right Ascen at Week(rad): 0.00000000000000e+000  
Argument of Perigee(rad): 3.14159265358979e+000  
Mean Anom(rad): 0.00000000000000e+000  
Af0(s): 0.00000000000000e+000  
Af1(s/s): 0.00000000000000e+000  
week: 869

\*\*\*\*\* Week 869 almanac for PRN-11 \*\*\*\*\*

ID: 11  
Health: 0  
Eccentricity: 0.00000000000000e+000  
Time of Applicability(s): 144000  
Orbital Inclination(rad): 9.59931088596883e-001  
Rate of Right Ascen(r/s): 0.00000000000000e+000  
SQRT(A) (m 1/2): 5.27996000000000e+003  
Right Ascen at Week(rad): 0.00000000000000e+000  
Argument of Perigee(rad): -2.35619449019234e+000

Mean Anom(rad): 0.00000000000000e+000  
Af0(s): 0.000000000000000e+000  
Af1(s/s): 0.000000000000000e+000  
week: 869

\*\*\*\*\* Week 869 almanac for PRN-12 \*\*\*\*\*

ID: 12  
Health: 0  
Eccentricity: 0.000000000000000e+000  
Time of Applicability(s): 144000  
Orbital Inclination(rad): 9.59931088596883e-001  
Rate of Right Ascen(r/s): 0.000000000000000e+000  
SQRT(A) (m 1/2): 5.279960000000000e+003  
Right Ascen at Week(rad): 0.000000000000000e+000  
Argument of Perigee(rad): -1.57079632679490e+000  
Mean Anom(rad): 0.000000000000000e+000  
Af0(s): 0.000000000000000e+000  
Af1(s/s): 0.000000000000000e+000  
week: 869

\*\*\*\*\* Week 869 almanac for PRN-13 \*\*\*\*\*

ID: 13  
Health: 0  
Eccentricity: 0.000000000000000e+000  
Time of Applicability(s): 144000  
Orbital Inclination(rad): 9.59931088596883e-001  
Rate of Right Ascen(r/s): 0.000000000000000e+000  
SQRT(A) (m 1/2): 5.279960000000000e+003  
Right Ascen at Week(rad): 0.000000000000000e+000  
Argument of Perigee(rad): -7.85398163397448e-001

Mean Anom(rad): 0.00000000000000e+000  
Af0(s): 0.00000000000000e+000  
Af1(s/s): 0.00000000000000e+000  
week: 869

\*\*\*\*\* Week 869 almanac for PRN-14 \*\*\*\*\*

ID: 14  
Health: 0  
Eccentricity: 0.00000000000000e+000  
Time of Applicability(s): 144000  
Orbital Inclination(rad): 9.59931088596883e-001  
Rate of Right Ascen(r/s): 0.00000000000000e+000  
SQRT(A) (m 1/2): 5.27996000000000e+003  
Right Ascen at Week(rad): 2.09439510239320e+000  
Argument of Perigee(rad): -2.87979326579064e+000  
Mean Anom(rad): 0.00000000000000e+000  
Af0(s): 0.00000000000000e+000  
Af1(s/s): 0.00000000000000e+000  
week: 869

\*\*\*\*\* Week 869 almanac for PRN-15 \*\*\*\*\*

ID: 15  
Health: 0  
Eccentricity: 0.00000000000000e+000  
Time of Applicability(s): 144000  
Orbital Inclination(rad): 9.59931088596883e-001  
Rate of Right Ascen(r/s): 0.00000000000000e+000  
SQRT(A) (m 1/2): 5.27996000000000e+003  
Right Ascen at Week(rad): 2.09439510239320e+000  
Argument of Perigee(rad): -2.09439510239321e+000

Mean Anom(rad): 0.00000000000000e+000  
Af0(s): 0.000000000000000e+000  
Af1(s/s): 0.000000000000000e+000  
week: 869

\*\*\*\*\* Week 869 almanac for PRN-16 \*\*\*\*\*

ID: 16  
Health: 0  
Eccentricity: 0.000000000000000e+000  
Time of Applicability(s): 144000  
Orbital Inclination(rad): 9.59931088596883e-001  
Rate of Right Ascen(r/s): 0.000000000000000e+000  
SQRT(A) (m 1/2): 5.279960000000000e+003  
Right Ascen at Week(rad): 2.09439510239320e+000  
Argument of Perigee(rad): -1.30899693899576e+000  
Mean Anom(rad): 0.000000000000000e+000  
Af0(s): 0.000000000000000e+000  
Af1(s/s): 0.000000000000000e+000  
week: 869

\*\*\*\*\* Week 869 almanac for PRN-17 \*\*\*\*\*

ID: 17  
Health: 0  
Eccentricity: 0.000000000000000e+000  
Time of Applicability(s): 144000  
Orbital Inclination(rad): 9.59931088596883e-001  
Rate of Right Ascen(r/s): 0.000000000000000e+000  
SQRT(A) (m 1/2): 5.279960000000000e+003  
Right Ascen at Week(rad): 2.09439510239320e+000  
Argument of Perigee(rad): -5.23598775598309e-001

Mean Anom(rad): 0.00000000000000e+000  
Af0(s): 0.000000000000000e+000  
Af1(s/s): 0.000000000000000e+000  
week: 869

\*\*\*\*\* Week 869 almanac for PRN-18 \*\*\*\*\*

ID: 18  
Health: 0  
Eccentricity: 0.000000000000000e+000  
Time of Applicability(s): 144000  
Orbital Inclination(rad): 9.59931088596883e-001  
Rate of Right Ascen(r/s): 0.000000000000000e+000  
SQRT(A) (m 1/2): 5.279960000000000e+003  
Right Ascen at Week(rad): 2.09439510239320e+000  
Argument of Perigee(rad): 2.61799387799148e-001  
Mean Anom(rad): 0.000000000000000e+000  
Af0(s): 0.000000000000000e+000  
Af1(s/s): 0.000000000000000e+000  
week: 869

\*\*\*\*\* Week 869 almanac for PRN-19 \*\*\*\*\*

ID: 19  
Health: 0  
Eccentricity: 0.000000000000000e+000  
Time of Applicability(s): 144000  
Orbital Inclination(rad): 9.59931088596883e-001  
Rate of Right Ascen(r/s): 0.000000000000000e+000  
SQRT(A) (m 1/2): 5.279960000000000e+003  
Right Ascen at Week(rad): 2.09439510239320e+000  
Argument of Perigee(rad): 1.04719755119660e+000

Mean Anom(rad): 0.00000000000000e+000  
Af0(s): 0.00000000000000e+000  
Af1(s/s): 0.00000000000000e+000  
week: 869

\*\*\*\*\* Week 869 almanac for PRN-20 \*\*\*\*\*

ID: 20  
Health: 0  
Eccentricity: 0.00000000000000e+000  
Time of Applicability(s): 144000  
Orbital Inclination(rad): 9.59931088596883e-001  
Rate of Right Ascen(r/s): 0.00000000000000e+000  
SQRT(A) (m 1/2): 5.27996000000000e+003  
Right Ascen at Week(rad): 2.09439510239320e+000  
Argument of Perigee(rad): 1.83259571459405e+000  
Mean Anom(rad): 0.00000000000000e+000  
Af0(s): 0.00000000000000e+000  
Af1(s/s): 0.00000000000000e+000  
week: 869

\*\*\*\*\* Week 869 almanac for PRN-21 \*\*\*\*\*

ID: 21  
Health: 0  
Eccentricity: 0.00000000000000e+000  
Time of Applicability(s): 144000  
Orbital Inclination(rad): 9.59931088596883e-001  
Rate of Right Ascen(r/s): 0.00000000000000e+000  
SQRT(A) (m 1/2): 5.27996000000000e+003  
Right Ascen at Week(rad): 2.09439510239320e+000  
Argument of Perigee(rad): 2.61799387799149e+000

Mean Anom(rad): 0.00000000000000e+000  
Af0(s): 0.00000000000000e+000  
Af1(s/s): 0.00000000000000e+000  
week: 869

\*\*\*\*\* Week 869 almanac for PRN-22 \*\*\*\*\*

ID: 22  
Health: 0  
Eccentricity: 0.00000000000000e+000  
Time of Applicability(s): 144000  
Orbital Inclination(rad): 9.59931088596883e-001  
Rate of Right Ascen(r/s): 0.00000000000000e+000  
SQRT(A) (m 1/2): 5.27996000000000e+003  
Right Ascen at Week(rad): -2.09439510239320e+000  
Argument of Perigee(rad): -2.61799387799148e+000  
Mean Anom(rad): 0.00000000000000e+000  
Af0(s): 0.00000000000000e+000  
Af1(s/s): 0.00000000000000e+000  
week: 869

\*\*\*\*\* Week 869 almanac for PRN-23 \*\*\*\*\*

ID: 23  
Health: 0  
Eccentricity: 0.00000000000000e+000  
Time of Applicability(s): 144000  
Orbital Inclination(rad): 9.59931088596883e-001  
Rate of Right Ascen(r/s): 0.00000000000000e+000  
SQRT(A) (m 1/2): 5.27996000000000e+003  
Right Ascen at Week(rad): -2.09439510239321e+000  
Argument of Perigee(rad): -1.83259571459404e+000



Mean Anom(rad): 0.00000000000000e+000  
Af0(s): 0.00000000000000e+000  
Af1(s/s): 0.00000000000000e+000  
week: 869

\*\*\*\*\* Week 869 almanac for PRN-24 \*\*\*\*\*

ID: 24  
Health: 0  
Eccentricity: 0.00000000000000e+000  
Time of Applicability(s): 144000  
Orbital Inclination(rad): 9.59931088596883e-001  
Rate of Right Ascen(r/s): 0.00000000000000e+000  
SQRT(A) (m 1/2): 5.27996000000000e+003  
Right Ascen at Week(rad): -2.09439510239320e+000  
Argument of Perigee(rad): -1.04719755119660e+000  
Mean Anom(rad): 0.00000000000000e+000  
Af0(s): 0.00000000000000e+000  
Af1(s/s): 0.00000000000000e+000  
week: 869

\*\*\*\*\* Week 869 almanac for PRN-25 \*\*\*\*\*

ID: 25  
Health: 0  
Eccentricity: 0.00000000000000e+000  
Time of Applicability(s): 144000  
Orbital Inclination(rad): 9.59931088596883e-001  
Rate of Right Ascen(r/s): 0.00000000000000e+000  
SQRT(A) (m 1/2): 5.27996000000000e+003  
Right Ascen at Week(rad): -2.09439510239321e+000  
Argument of Perigee(rad): -2.61799387799148e-001

Mean Anom(rad): 0.00000000000000e+000  
Af0(s): 0.00000000000000e+000  
Af1(s/s): 0.00000000000000e+000  
week: 869

\*\*\*\*\* Week 869 almanac for PRN-26 \*\*\*\*\*

ID: 26  
Health: 0  
Eccentricity: 0.00000000000000e+000  
Time of Applicability(s): 144000  
Orbital Inclination(rad): 9.59931088596883e-001  
Rate of Right Ascen(r/s): 0.00000000000000e+000  
SQRT(A) (m 1/2): 5.27996000000000e+003  
Right Ascen at Week(rad): -2.09439510239321e+000  
Argument of Perigee(rad): 5.23598775598300e-001  
Mean Anom(rad): 0.00000000000000e+000  
Af0(s): 0.00000000000000e+000  
Af1(s/s): 0.00000000000000e+000  
week: 869

\*\*\*\*\* Week 869 almanac for PRN-27 \*\*\*\*\*

ID: 27  
Health: 0  
Eccentricity: 0.00000000000000e+000  
Time of Applicability(s): 144000  
Orbital Inclination(rad): 9.59931088596883e-001  
Rate of Right Ascen(r/s): 0.00000000000000e+000  
SQRT(A) (m 1/2): 5.27996000000000e+003  
Right Ascen at Week(rad): -2.09439510239321e+000  
Argument of Perigee(rad): 1.30899693899575e+000

Mean Anom(rad): 0.00000000000000e+000  
Af0(s): 0.00000000000000e+000  
Af1(s/s): 0.00000000000000e+000  
week: 869

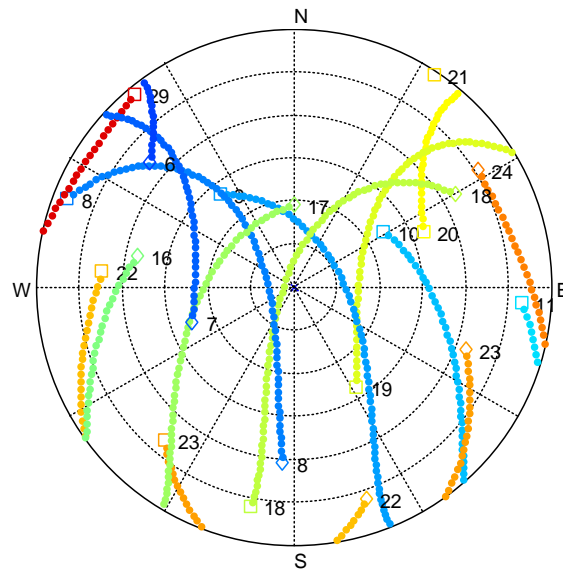
\*\*\*\*\* Week 869 almanac for PRN-28 \*\*\*\*\*

ID: 28  
Health: 0  
Eccentricity: 0.00000000000000e+000  
Time of Applicability(s): 144000  
Orbital Inclination(rad): 9.59931088596883e-001  
Rate of Right Ascen(r/s): 0.00000000000000e+000  
SQRT(A) (m 1/2): 5.27996000000000e+003  
Right Ascen at Week(rad): -2.09439510239321e+000  
Argument of Perigee(rad): 2.09439510239320e+000  
Mean Anom(rad): 0.00000000000000e+000  
Af0(s): 0.00000000000000e+000  
Af1(s/s): 0.00000000000000e+000  
week: 869

\*\*\*\*\* Week 869 almanac for PRN-29 \*\*\*\*\*

ID: 29  
Health: 0  
Eccentricity: 0.00000000000000e+000  
Time of Applicability(s): 144000  
Orbital Inclination(rad): 9.59931088596883e-001  
Rate of Right Ascen(r/s): 0.00000000000000e+000  
SQRT(A) (m 1/2): 5.27996000000000e+003  
Right Ascen at Week(rad): -2.09439510239321e+000  
Argument of Perigee(rad): 2.87979326579064e+000

Mean Anom(rad): 0.0000000000000000e+000  
 Af0(s): 0.0000000000000000e+000  
 Af1(s/s): 0.0000000000000000e+000  
 week: 869



**BeiDou Visibility**  
**(PRN-08 at -10 dB,**  
**PRN-18 at -20 dB)**

### A.10.2.5 SBAS Satellites

The two SBAS satellites were emulated in the geostationary satellite arc above 133W and 108W with PRNs 135 and 138, respectively.

### A.10.3 Emulated errors

The Spirent RTCA06 tropospheric model was utilized to generate tropospheric errors on the pseudorange and carrier phase measurements as appropriate for the emulated user location and date (32N, 106W, April 18, 2016).

Ionospheric errors were emulated using the GPS single-frequency ionospheric delay model (i.e., the Klobuchar model). The following 8 coefficients were utilized:

ALPHA0: 5.58793544769E-009

ALPHA1: 1.49011611938E-008

ALPHA2: -5.96046447754E-008

ALPHA3: -1.19209289551E-007

BETA0: 83968

BETA1: 98304

BETA2: -65536

BETA3: -524288

Galileo uses a different single-frequency ionospheric correction model known as NeQuick. NeQuick coefficients were generated, using a Spirent GSS8000 simulator software utility, to best match ionospheric delay corrections per the GPS Klobuchar model with the coefficients listed above.

#### **A.10.4**

## **APPENDIX B**

### **AGGREGATE ITM RESULTS**

## TABLE OF CONTENTS

TABLE OF CONTENTS.....	2
LIST OF FIGURES .....	3
LIST OF TABLES .....	6
REFERENCES .....	7
APPENDIX.....	8
Appendix B. Aggregate ITM Results.....	8
B.1 Statistical and Bounding ITMs for 1MHz and 10 MHz LTE Interference Signals .....	8
B.1.1 Interference Test Results for 1-MHz AWGN .....	8
B.1.2 Interference Test Results for 10-MHz LTE.....	31
<b>B.1.3</b> Combined 1 MHz AWGN Test Results and 10 MHz LTE Test Results .....	55



## LIST OF FIGURES

Figure B-1: 1 MHz GPS L1 C/A Statistical Mask Results for Cellular receivers .....	8
Figure B-2: 1 MHz All GNSS Aggregated Minimum Statistical Mask Results for Cellular receivers .....	9
Figure B-3: 1 MHz GPS L1 C/A Statistical Mask Results for General Aviation receivers .....	10
Figure B-4: 1 MHz All GNSS Aggregated Minimum Statistical Mask Results for General Aviation receivers .....	10
Figure B-5: 1 MHz GPS L1 C/A Statistical Mask Results for General Location Navigation receivers .....	11
Figure B-6: 1 MHz All GNSS Aggregated Minimum Statistical Mask Results for General Location Navigation receivers .....	12
Figure B-7: 1 MHz GPS L1 C/A Statistical Mask Results for High Precision receivers .....	12
Figure B-8: 1 MHz All GNSS Aggregated Minimum Statistical Mask Results for High Precision receivers .....	13
Figure B-9: 1 MHz GPS L1 C/A Statistical Mask Results for Space Based receivers .....	14
Figure B-10: 1 MHz All GNSS Aggregated Minimum Statistical Mask Results for Space Based receivers .....	14
Figure B-11: 1 MHz GPS L1 C/A Statistical Mask Results for Timing receivers .....	15
Figure B-12: 1 MHz All GNSS Aggregated Minimum Statistical Mask Results for Timing receivers .....	16
Figure B-13: Summary of 1 MHz and 1 MHz In-band GPS L1 C/A Bounding Masks .....	17
Figure B-14: Summary of 1 MHz and 1 MHz In-band GPS L1 P Bounding Masks .....	19
Figure B-15: Summary of 1 MHz and 1 MHz In-band GPS L1 C Bounding Masks .....	21
Figure B-16: Summary of 1 MHz and 1 MHz In-band GLONASS L1 C Bounding Masks .....	23
Figure B-17: Summary of 1 MHz and 1 MHz In-band GLONASS L1 P Bounding Masks .....	25
Figure B-18: Summary of 1 MHz and 1 MHz In-band BeiDou B1 I Bounding Masks .....	27
Figure B-19: Summary of 1 MHz and 1 MHz In-band Galileo E1 BC Bounding Masks .....	29
Figure B-20: Summary of 1 MHz and 1 MHz In-band SBAS L1 C/A Bounding Masks .....	31
Figure B-21: 10 MHz GPS L1 C/A Statistical Mask Results for Cellular receivers .....	32
Figure B-22: 10 MHz All GNSS Aggregated Minimum Statistical Mask Results for Cellular receivers .....	33
Figure B-23: 10 MHz GPS L1 C/A Statistical Mask Results for General Aviation receivers ....	33
Figure B-24: 10 MHz All GNSS Aggregated Minimum Statistical Mask Results for General Aviation receivers .....	34
Figure B-25: 10 MHz GPS L1 C/A Statistical Mask Results for General Location Navigation receivers .....	35

Figure B-26: 10 MHz All GNSS Aggregated Minimum Statistical Mask Results for General Location Navigation receivers .....	35
Figure B-27: 10 MHz GPS L1 C/A Statistical Mask Results for High Precision receivers .....	36
Figure B-28: 10 MHz All GNSS Aggregated Minimum Statistical Mask Results for High Precision receivers .....	37
Figure B-29: 10 MHz GPS L1 C/A Statistical Mask Results for Space Based receivers .....	37
Figure B-30: 10 MHz All GNSS Aggregated Minimum Statistical Mask Results for Space Based receivers .....	38
Figure B-31: 10 MHz GPS L1 C/A Statistical Mask Results for Timing receivers .....	39
Figure B-32: 10 MHz All GNSS Aggregated Minimum Statistical Mask Results for Timing receivers .....	39
Figure B-33: Summary of 10 MHz and 10MHz Intermod GPS L1 C/A Bounding Masks.....	41
Figure B-34: Summary of 10 MHz and 10 MHz Intermod GPS L1 P Bounding Masks .....	43
Figure B-35: Summary of 10 MHz and 10 MHz Intermod GPS L1 C Bounding Masks.....	45
Figure B-36: Summary of 10 MHz and 10 MHz Intermod GLONASS L1 C Bounding Masks .	47
Figure B-37: Summary of 10 MHz and 10 MHz Intermod GLONASS L1 P Bounding Masks ..	49
Figure B-38: Summary of 10 MHz and 10 MHz Intermod BeiDou B1 I Bounding Masks.....	51
Figure B-39: Summary of 10 MHz and 10 MHz Intermod Galileo E1 BC Bounding Masks .....	53
Figure B-40: Summary of 10 MHz and 10 MHz Intermod SBAS L1 C/A Bounding Masks .....	55
Figure B-41: Summary of 1&10 MHz, 1 MHz In-band, and 10 MHz Intermod GPS L1 C/A – HPR Bounding Masks.....	56
Figure B-42: Summary of 1&10 MHz, 1 MHz In-band, and 10 MHz Intermod with Certified Aviation GPS L1 C/A Bounding Masks .....	57
Figure B-43: Summary of 1&10 MHz, 1 MHz In-band, and 10 MHz Intermod GPS L1 P – HPR Bounding Masks .....	58
Figure B-44: Summary of 1&10 MHz, 1 MHz In-band, and 10 MHz Intermod GPS L1 P Bounding Masks .....	59
Figure B-45: Summary of 1&10 MHz, 1 MHz In-band, and 10 MHz Intermod GPS L1 C - GLN Bounding Masks .....	60
Figure B-46: Summary of 1&10 MHz, 1 MHz In-band, and 10 MHz Intermod GPS L1 C Bounding Masks .....	61
Figure B-47: Summary of 1&10 MHz, 1 MHz In-band, and 10 MHz Intermod GLONASS L1 C - HPR Bounding Masks .....	62
Figure B-48: Summary of 1&10 MHz, 1 MHz In-band, and 10 MHz Intermod GLONASS L1 C Bounding Masks .....	63
Figure B-49: Summary of 1&10 MHz, 1 MHz In-band, and 10 MHz Intermod GLONASS L1 P - HPR Bounding Masks .....	64
Figure B-50: Summary of 1&10 MHz, 1 MHz In-band, and 10 MHz Intermod GLONASS L1 P Bounding Masks .....	65

Figure B-51: Summary of 1&10 MHz, 1 MHz In-band, and 10 MHz Intermod BeiDou B1 I - HPR Bounding Masks.....	66
Figure B-52: Summary of 1&10 MHz, 1 MHz In-band, and 10 MHz Intermod BeiDou B1 I Bounding Masks .....	67
Figure B-53: Summary of 1&10 MHz, 1 MHz In-band, and 10 MHz Intermod Galileo E1 BC Bounding Masks .....	68
Figure B-54: Summary of 1&10 MHz, 1 MHz In-band, and 10 MHz Intermod SBAS L1 C/A - HPR Bounding Masks.....	69
Figure B-55: Summary of 1&10 MHz, 1 MHz In-band, and 10 MHz Intermod SBAS L1 C/A Bounding Masks .....	70
Figure B-56: Summary of Cellular Bounding Masks for 1 & 10 MHz, 1 MHz In-band, and 10 MHz Intermod.....	71
Figure B-57: Summary of General Aviation Bounding Masks for 1 & 10 MHz, 1 MHz In-band, and 10 MHz Intermod.....	72
Figure B-58: Summary of General Location Navigation Bounding Masks for 1 & 10 MHz, 1 MHz In-band, and 10 MHz Intermod .....	73
Figure B-59: Summary of High Precision Bounding Masks for 1 & 10 MHz, 1 MHz In-band, and 10 MHz Intermod.....	74
Figure B-60: Summary of Space Based Bounding Masks for 1 & 10 MHz, 1 MHz In-band, and 10 MHz Intermod.....	75
Figure B-61: Summary of Timing Bounding Masks for 1 & 10 MHz, 1 MHz In-band, and 10 MHz Intermod.....	76

## LIST OF TABLES

Table B-1: 1 MHz and 1 MHz In-band* GPS L1 C/A Bounding Masks (dBm).....	16
Table B-2: 1 MHz and 1 MHz In-band* GPS L1 P Bounding Masks (dBm) .....	18
Table B-3: 1 MHz and 1 MHz In-band* GPS L1 C Bounding Masks (dBm).....	20
Table B-4: 1 MHz and 1 MHz In-band* GLONASS L1 C Bounding Masks (dBm) .....	22
Table B-5: 1 MHz and 1 MHz In-band* GLONASS L1 P Bounding Masks (dBm).....	24
Table B-6: 1 MHz and 1 MHz In-band* BeiDou B1 I Bounding Masks (dBm).....	26
Table B-7: 1 MHz and 1 MHz In-band* Galileo E1 BC Bounding Masks (dBm) .....	28
Table B-8: 1 MHz and 1 MHz In-band* SBAS L1 C/A Bounding Masks (dBm).....	30
Table B-9: 10 MHz and 10 MHz Intermod* GPS L1 C/A Bounding Masks (dBm) .....	40
Table B-10: 10 MHz and 10 MHz Intermod* GPS L1 P Bounding Masks (dBm).....	42
Table B-11: 10 MHz and 10 MHz Intermod* GPS L1 C Bounding Masks (dBm) .....	44
Table B-12: 10 MHz and 10 MHz Intermod* GLONASS L1 C Bounding Masks (dBm) .....	46
Table B-13: 10 MHz and 10 MHz Intermod* GLONASS L1 P Bounding Masks (dBm).....	48
Table B-14: 10 MHz and 10 MHz Intermod* BeiDou B1 I Bounding Masks (dBm) .....	50
Table B-15: 10 MHz and 10 MHz Intermod* Galileo E1 BC Bounding Masks (dBm) .....	52
Table B-16: 10 MHz and 10 MHz Intermod* SBAS L1 C/A Bounding Masks (dBm).....	54

## **REFERENCES**

**There are no sources in the current document.**

# APPENDIX

## Appendix B. Aggregate ITM Results

### B.1 Statistical and Bounding ITMs for 1MHz and 10 MHz LTE Interference Signals

#### B.1.1 Interference Test Results for 1-MHz AWGN

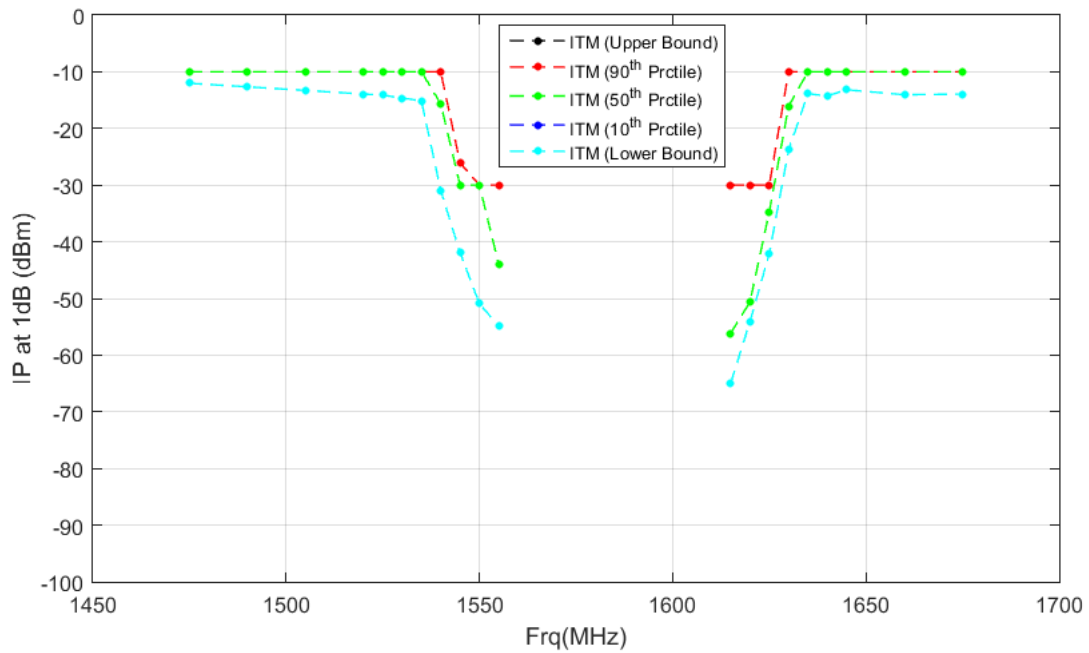


**Figure B-1: 1 MHz GPS L1 C/A Statistical Mask Results for Cellular receivers**

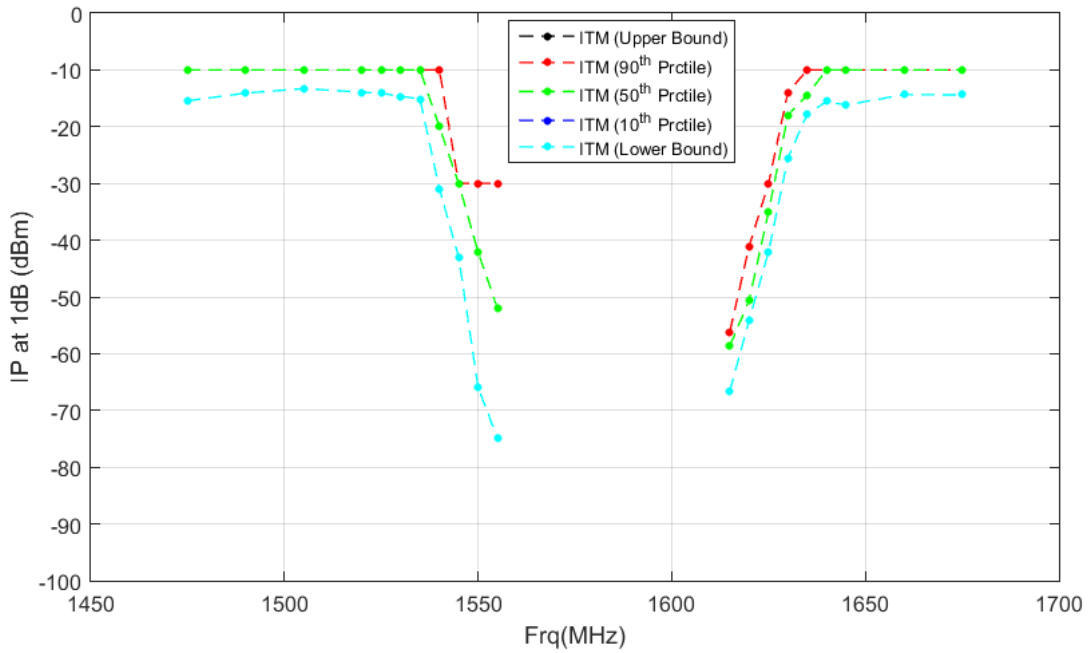


**Figure B-2: 1 MHz All GNSS Aggregated Minimum Statistical Mask Results for Cellular receivers**

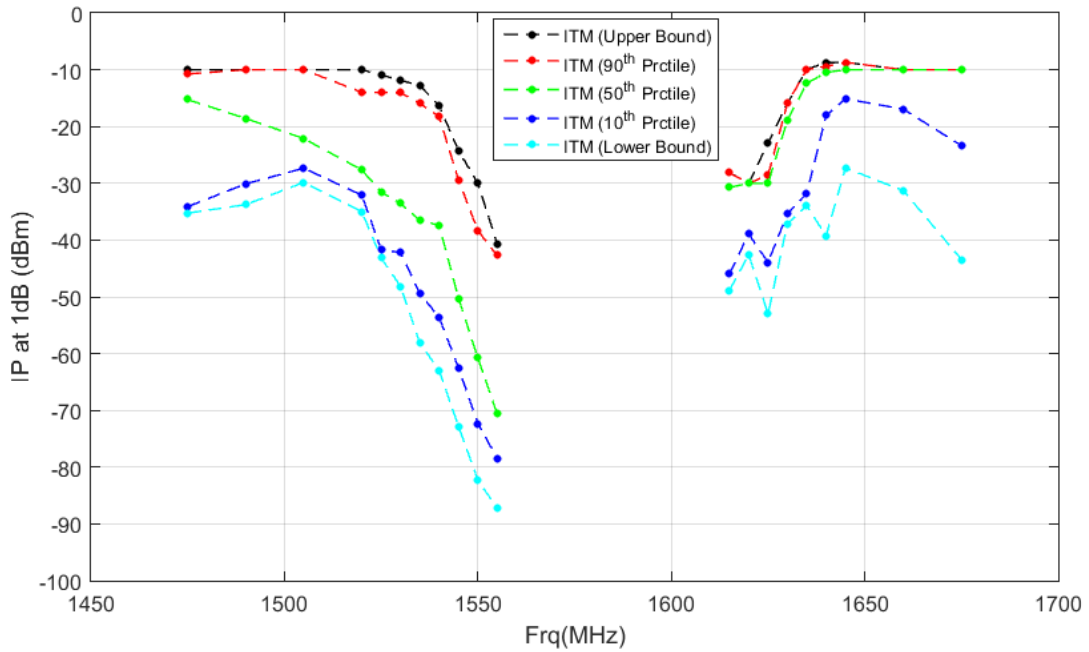


**Figure B-3: 1 MHz GPS L1 C/A Statistical Mask Results for General Aviation receivers**

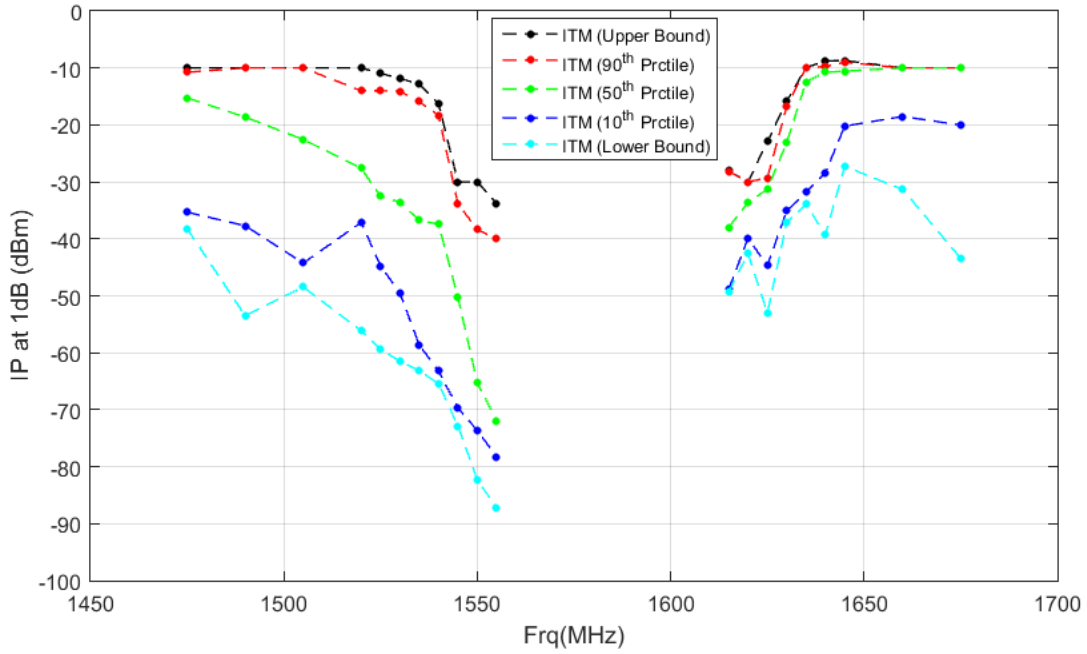


**Figure B-4: 1 MHz All GNSS Aggregated Minimum Statistical Mask Results for General Aviation receivers**



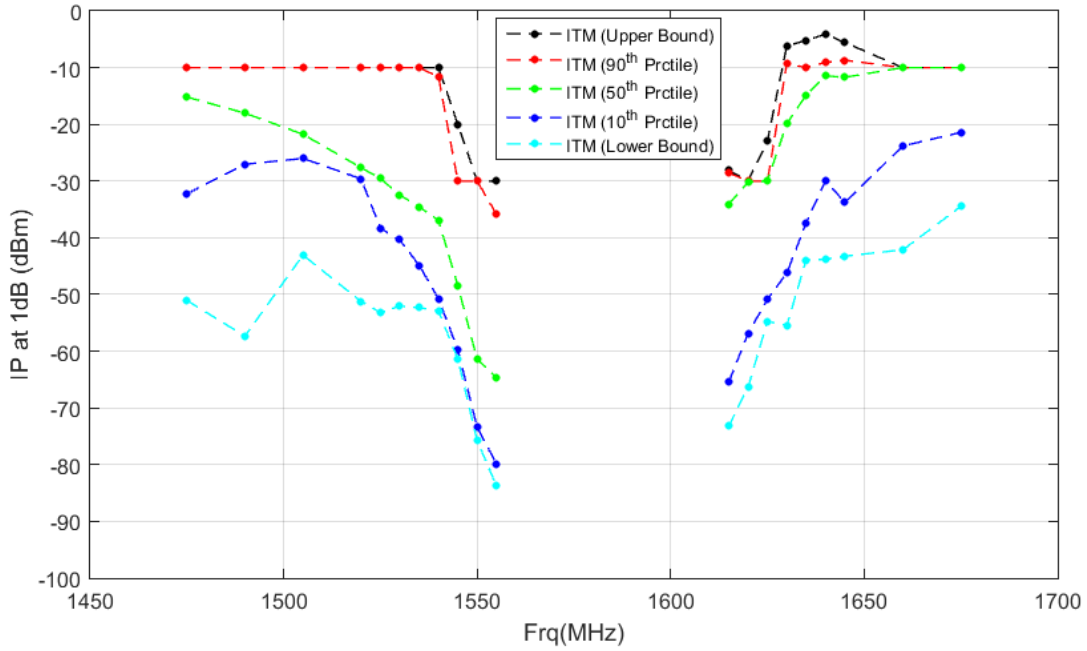


**Figure B-5: 1 MHz GPS L1 C/A Statistical Mask Results for General Location Navigation receivers**

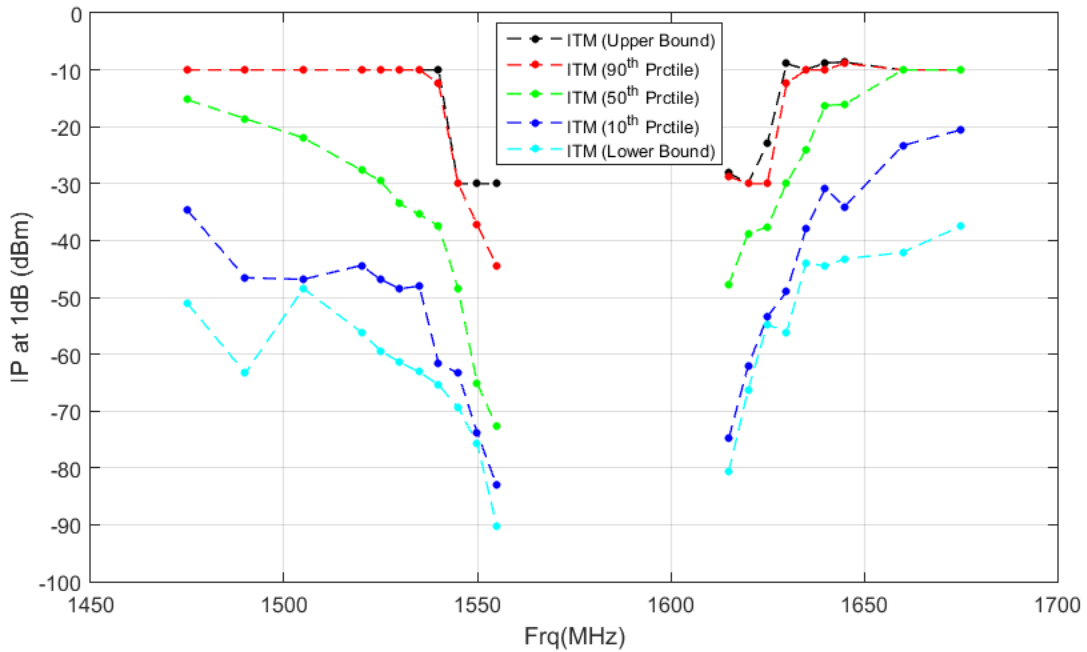


**Figure B-6: 1 MHz All GNSS Aggregated Minimum Statistical Mask Results for General Location Navigation receivers**

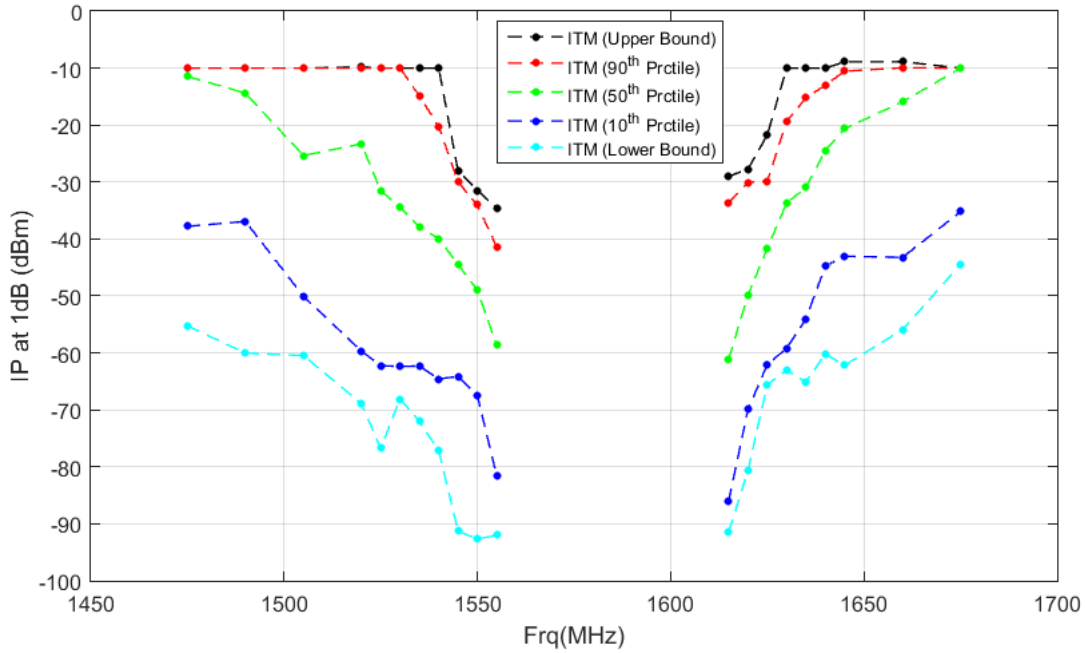


**Figure B-7: 1 MHz GPS L1 C/A Statistical Mask Results for High Precision receivers**

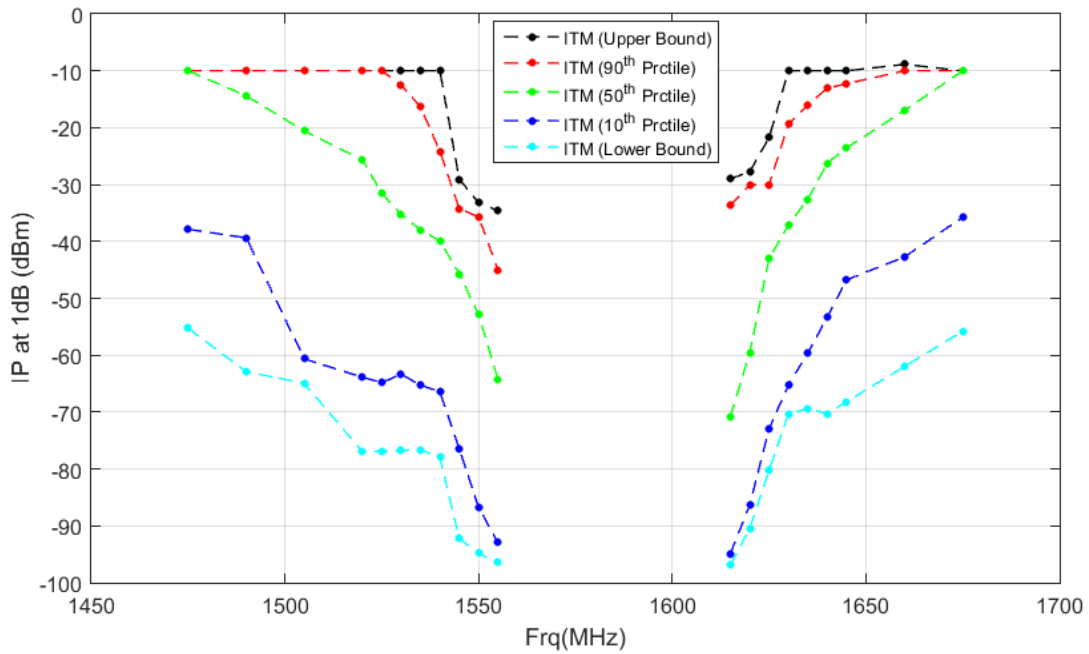


**Figure B-8: 1 MHz All GNSS Aggregated Minimum Statistical Mask Results for High Precision receivers**

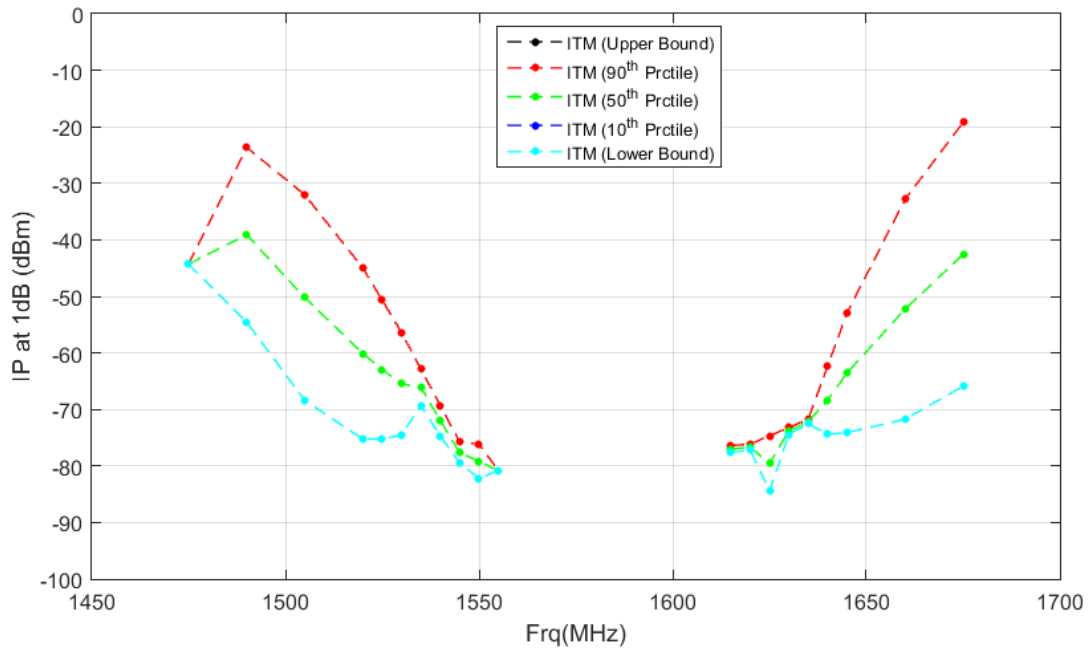


**Figure B-9: 1 MHz GPS L1 C/A Statistical Mask Results for Space Based receivers**

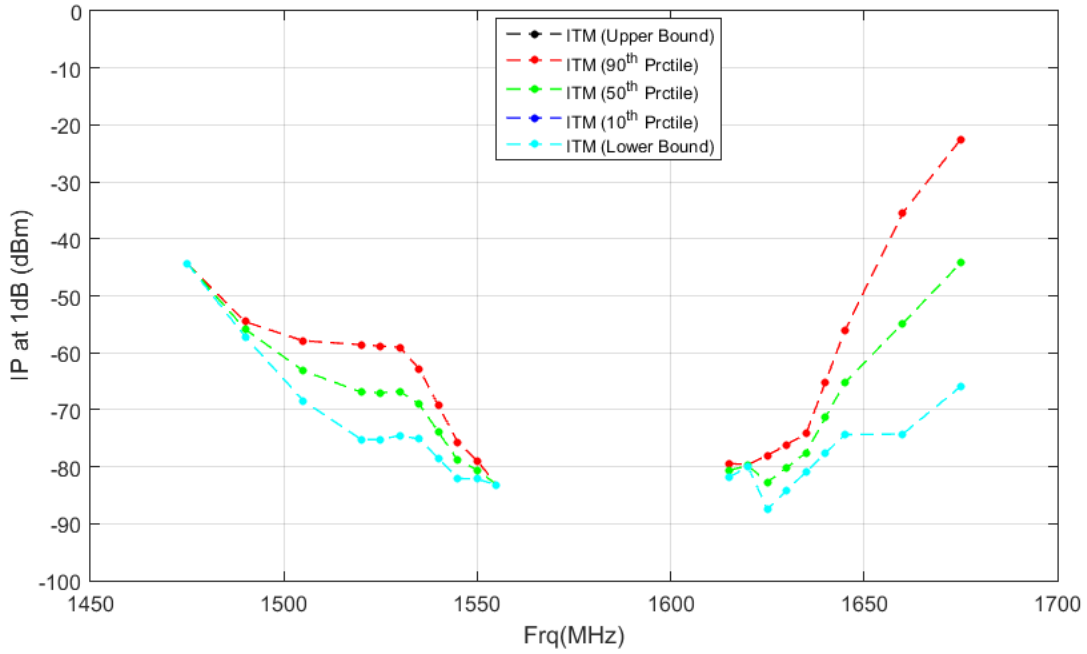


**Figure B-10: 1 MHz All GNSS Aggregated Minimum Statistical Mask Results for Space Based receivers**

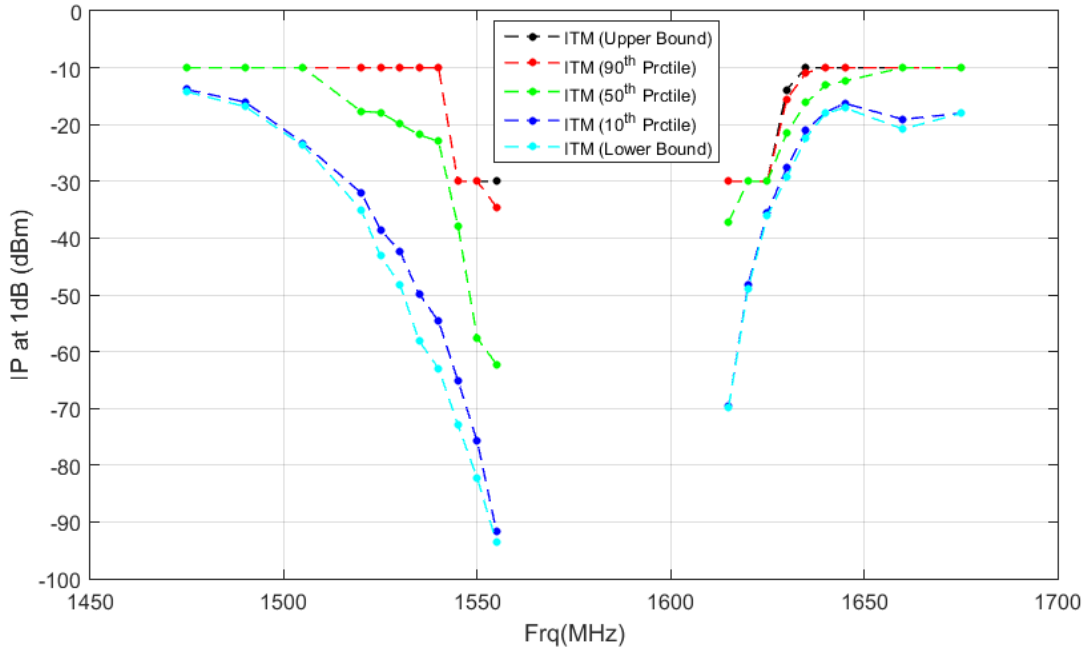


**Figure B-11: 1 MHz GPS L1 C/A Statistical Mask Results for Timing receivers**

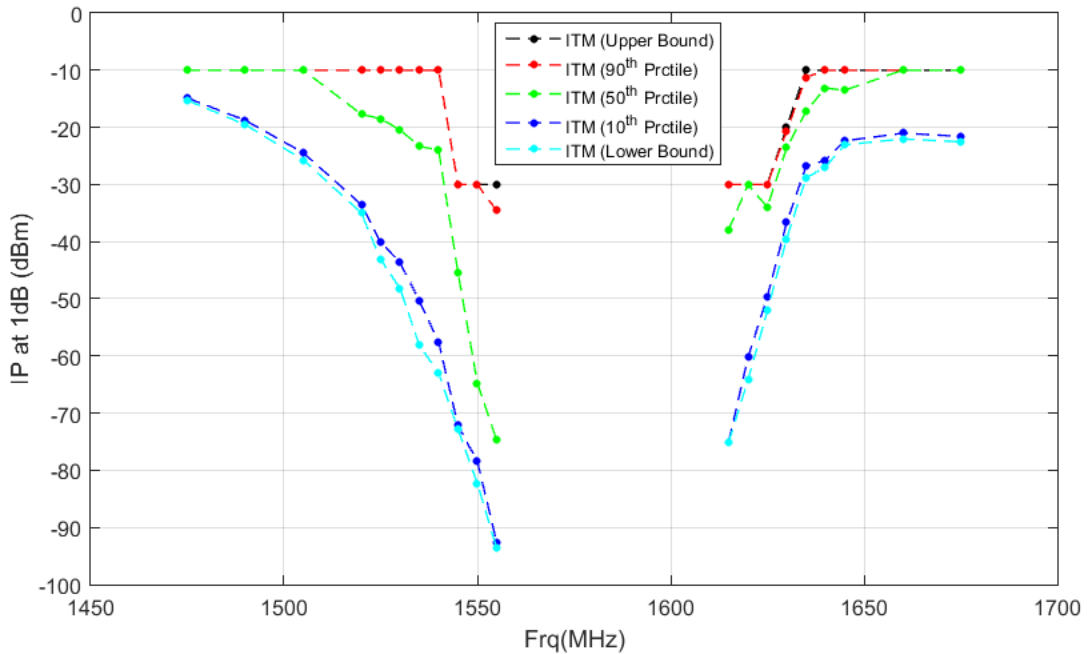


**Figure B-12: 1 MHz All GNSS Aggregated Minimum Statistical Mask Results for Timing receivers**

**Table B-1: 1 MHz and 1 MHz In-band\* GPS L1 C/A Bounding Masks (dBm)**

Frequency (MHz)	GAV	GLN	HPR	TIM	SPB	CEL
1475	-35.2559	-51.0577	-55.2458	-14.2455	-44.2989	-12.0223
1490	-33.7621	-57.3312	-60.0236	-16.8303	-54.552	-12.6553
1505	-29.8401	-43.0491	-60.4615	-23.7082	-68.4079	-13.2884
1520	-34.9844	-51.2192	-68.9024	-34.9844	-75.2401	-13.9214
1525	-43.1501	-53.1671	-76.7213	-43.1501	-75.2341	-14.1324
1530	-48.1543	-52.0402	-68.0809	-48.1543	-74.5091	-14.6318
1535	-58.124	-52.322	-72.0429	-58.124	-69.3135	-15.1311
1540	-62.9739	-52.9021	-77.1205	-62.9739	-74.6895	-30.9017
1545	-72.8509	-61.3673	-91.2872	-72.8509	-79.5006	-41.9222
1550	-82.2979	-75.7539	-92.663	-82.2979	-82.1933	-50.8924
1555	-87.2361	-83.7667	-92.0068	-93.6384	-80.8092	-54.9029
1575*	-119.066	-119.066	-116.191	-115.066	-110.143	-113.425
1595*	-82.7539	-83.6945	-99.8672	-82.7539	-81.6271	-75.4419
1615	-48.8394	-73.2344	-91.4798	-69.7614	-77.6033	-65.0079
1620	-42.5903	-66.3442	-80.6362	-48.8434	-77.2055	-54.0767
1625	-52.9903	-54.7378	-65.5759	-36.1468	-84.4141	-42.0742
1630	-37.111	-55.4588	-63.0348	-29.2349	-74.4229	-23.7846
1635	-33.9518	-43.9075	-65.1038	-22.3593	-72.5191	-13.8657
1640	-39.2495	-43.7996	-60.2043	-18.0435	-74.405	-14.2567
1645	-27.2708	-43.2334	-62.1873	-17.0656	-74.1188	-13.18
1660	-31.3256	-42.1121	-55.9123	-20.8014	-71.7159	-14.0507
1675	-43.4325	-34.4705	-44.4567	-18.0372	-65.8974	-13.9362

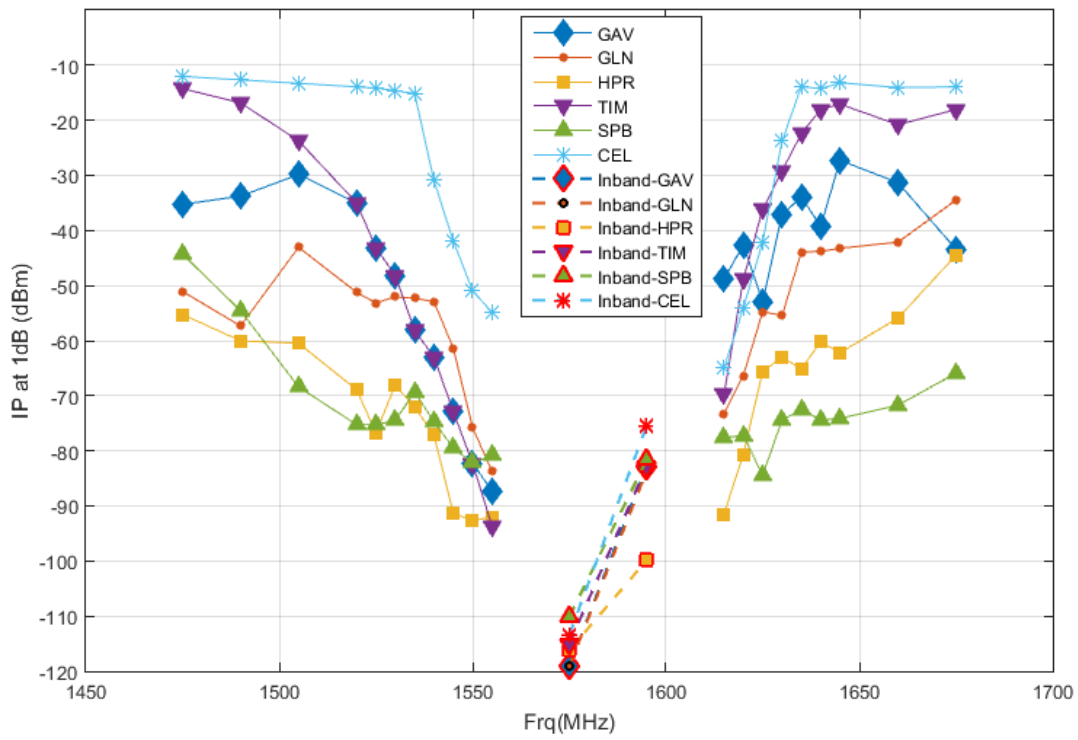


**Figure B-13: Summary of 1 MHz and 1 MHz In-band GPS L1 C/A Bounding Masks**

**Table B-2: 1 MHz and 1 MHz In-band\* GPS L1 P Bounding Masks (dBm)**

Frequency (MHz)	GLN	HPR	SPB	CEL
1475	-9.999	-54.6169	-16.4489	-12.0223
1490	-9.999	-60.4599	-57.1999	-12.6553
1505	-9.999	-62.3551	-57.8913	-13.2884
1520	-9.999	-65.2899	-58.5827	-13.9214
1525	-9.999	-62.0257	-58.8132	-14.1324
1530	-9.999	-62.0352	-59.7591	-14.6318
1535	-10.5239	-62.5546	-75.151	-15.1311
1540	-13.6638	-62.5322	-78.6008	-19.999
1545	-29.999	-62.6246	-82.0506	-29.999
1550	-40.4331	-64.2835	-78.9579	-29.999
1555	-50.8672	-66.7664	-83.1592	-29.999
1575*	-111.658	-108.025	-112.731	-113.227
1595*	-70.3132	-66.6468	NaN	-75.4419
1615	-66.3527	-63.5333	-81.9033	-65.0079
1620	-58.9925	-62.7395	-79.9751	-50.6889
1625	-43.759	-62.5091	-87.4391	-35.3214
1630	-30.4904	-61.0547	-84.1715	-23.7846
1635	-27.0752	-61.7723	-80.9039	-13.8657
1640	-23.66	-61.6717	-77.6363	-14.2567
1645	-20.2447	-62.4248	-74.3688	-13.18
1660	-9.999	-50.8114	-74.2659	-14.0507
1675	-9.999	-40.097	-65.4474	-13.9362



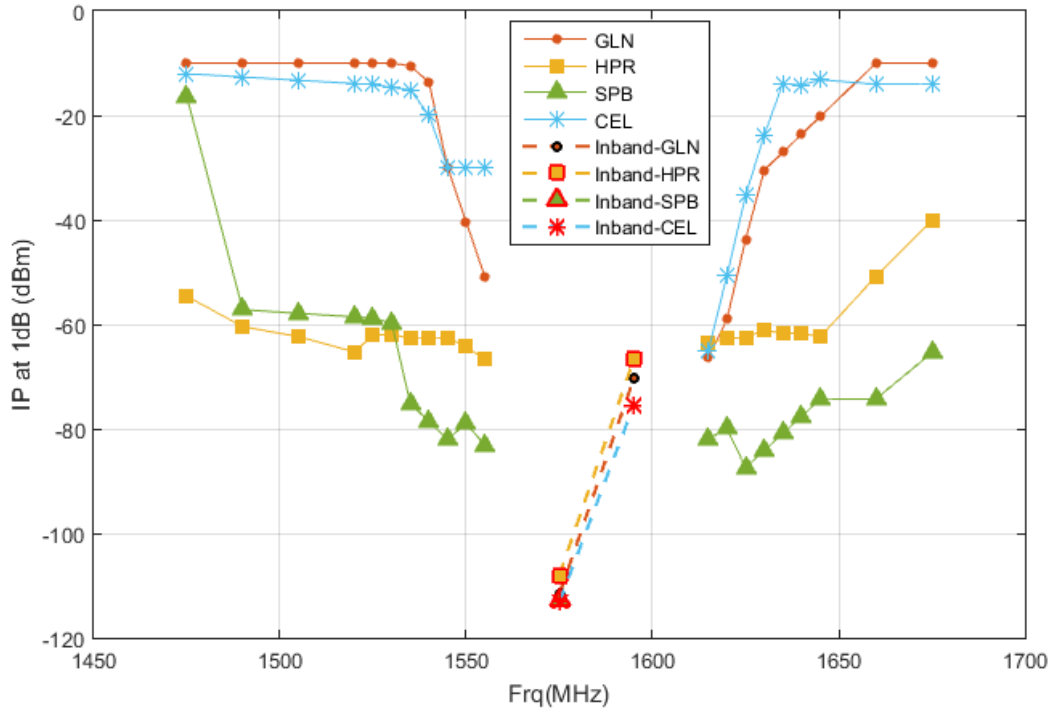


**Figure B-14: Summary of 1 MHz and 1 MHz In-band GPS L1 P Bounding Masks**

**Table B-3: 1 MHz and 1 MHz In-band\* GPS L1 C Bounding Masks (dBm)**

Frequency (MHz)	GLN	CEL
1475	-9.999	-12.0223
1490	-9.999	-12.6553
1505	-9.999	-13.2884
1520	-9.999	-13.9214
1525	-9.999	-14.1324
1530	-9.999	-14.6318
1535	-10.5239	-15.1311
1540	-13.6638	-19.999
1545	-29.999	-29.999
1550	-33.2037	-29.999
1555	-50.8672	-29.999
1575*	-111.658	-113.227
1595*	-70.3132	-75.4419
1615	-66.3527	-65.0079
1620	-58.9925	-50.6889
1625	-43.759	-35.3214
1630	-30.4904	-23.7846
1635	-27.0752	-13.8657
1640	-23.66	-14.2567
1645	-20.2447	-13.18
1660	-9.999	-14.0507
1675	-9.999	-13.9362

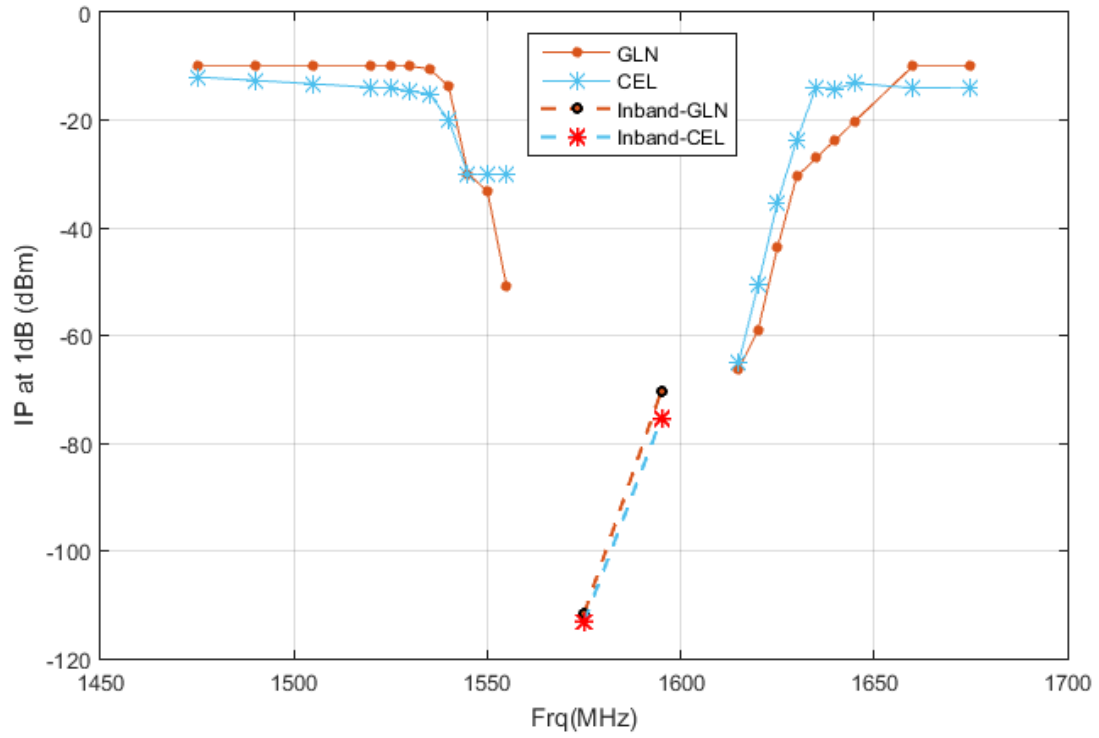


**Figure B-15: Summary of 1 MHz and 1 MHz In-band GPS L1 C Bounding Masks**

**Table B-4: 1 MHz and 1 MHz In-band\* GLONASS L1 C Bounding Masks (dBm)**

Frequency (MHz)	GAV	GLN	HPR	TIM	CEL
1475	-38.2559	-44.7577	-54.6169	-15.2559	-15.4348
1490	-53.4803	-53.4803	-62.9099	-19.5303	-14.0758
1505	-48.4582	-48.4582	-64.9422	-25.7082	-12.7169
1520	-56.1318	-56.1318	-76.9467	-31.3318	-11.3579
1525	-59.3929	-59.3929	-76.8713	-35.5429	-10.905
1530	-61.4793	-61.4793	-76.7309	-36.8043	-10.452
1535	-63.145	-63.145	-76.5364	-38.695	-9.999
1540	-65.4252	-65.4252	-76.3935	-49.3752	-21.2267
1545	-69.3673	-69.3673	-79.0175	-71.1694	-38.8222
1550	-72.6693	-72.6693	-86.7862	-72.6693	-42.0942
1555	-77.2525	-77.2525	-92.9286	-90.0964	-50.9955
1575*	-74.1159	-77.5833	-106.008	-90.6933	-73.3266
1595*	-98.5561	-101.975	-113.167	-110.561	-79.5011
1615	-49.3102	-75.1443	-96.917	-75.1443	-66.5954
1620	-39.5942	-64.2107	-90.419	-64.2107	-47.9014
1625	-43.7848	-52.0968	-80.2284	-52.0968	-37.3339
1630	-30.8828	-44.72	-70.3042	-39.5099	-25.5447
1635	-29.1745	-42.9075	-69.3723	-28.8593	-17.7719
1640	-25.6797	-44.4996	-70.2717	-26.931	-15.5567
1645	-18.4429	-37.7709	-68.1748	-23.0656	-16.18
1660	-15.3092	-40.1121	-61.9614	-22.0264	-14.3642
1675	-9.999	-37.4705	-55.797	-22.5372	-14.3862

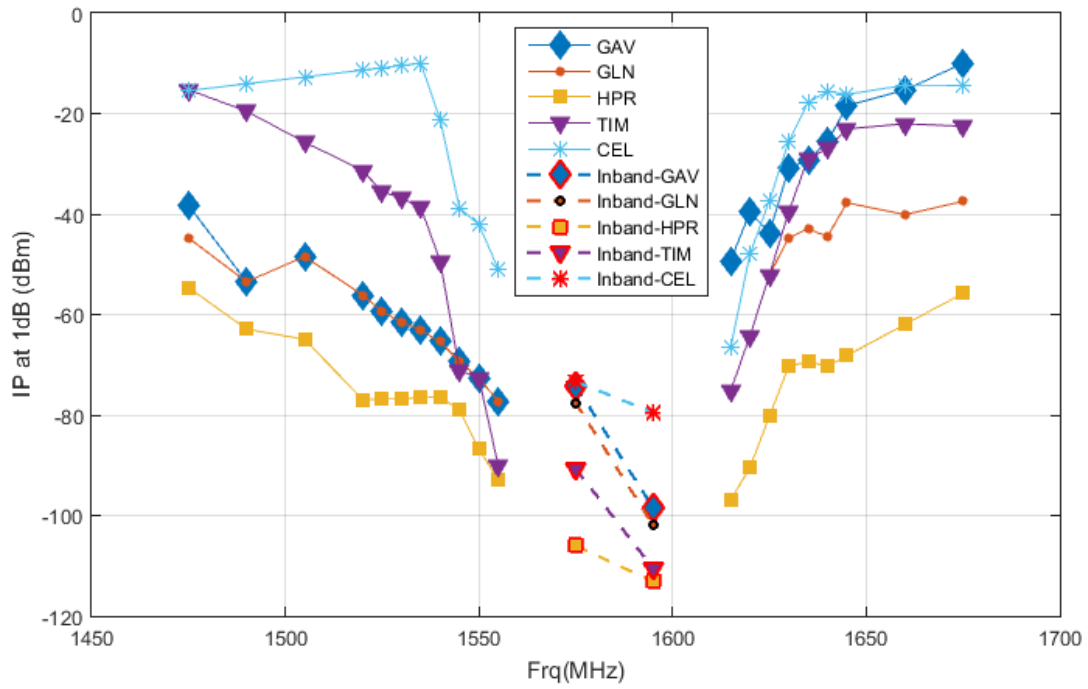


**Figure B-16: Summary of 1 MHz and 1 MHz In-band GLONASS L1 C Bounding Masks**

**Table B-5: 1 MHz and 1 MHz In-band\* GLONASS L1 P Bounding Masks (dBm)**

Frequency (MHz)	GLN	HPR	CEL
1475	-9.999	-9.999	-15.4348
1490	-9.999	-9.999	-14.0758
1505	-9.999	-11.8353	-12.7169
1520	-12.0311	-13.6716	-11.3579
1525	-9.999	-18.1971	-10.905
1530	-9.999	-26.0448	-10.452
1535	-9.999	-27.7146	-9.999
1540	-12.7888	-30.2492	-19.999
1545	-29.999	-38.772	-29.999
1550	-37.5179	-51.3101	-29.999
1555	-50.9922	-58.7847	-29.999
1575*	-77.5833	-100.344	-73.3266
1595*	-101.975	-105.436	-75.3544
1615	-64.1152	-91.7591	-66.5954
1620	-59.0175	-76.0987	-47.9014
1625	-45.8712	-48.0537	-37.3339
1630	-33.3779	-30.6987	-21.0846
1635	-27.6843	-24.6631	-16.1157
1640	-12.8654	-20.8626	-15.5567
1645	-12.1488	-19.2505	-16.18
1660	-9.999	-14.6248	-14.3642
1675	-9.999	-9.999	-14.3862

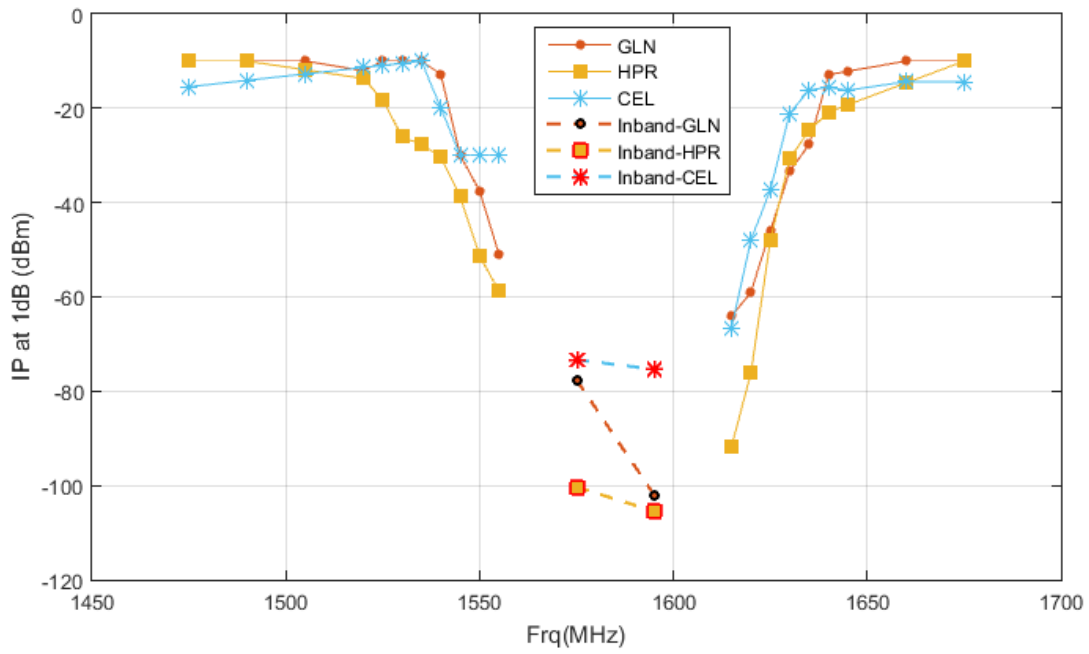


**Figure B-17: Summary of 1 MHz and 1 MHz In-band GLONASS L1 P Bounding Masks**

**Table B-6: 1 MHz and 1 MHz In-band\* BeiDou B1 I Bounding Masks (dBm)**

Frequency (MHz)	GLN	HPR	CEL
1475	-15.2553	-9.999	-9.999
1490	-18.5174	-26.9935	-9.999
1505	-22.5464	-49.829	-9.999
1520	-28.4477	-63.8777	-9.999
1525	-29.3591	-71.0896	-9.999
1530	-34.3999	-76.0923	-9.999
1535	-35.2722	-76.6179	-14.7446
1540	-36.3339	-77.9462	-19.4902
1545	-61.2885	-87.3658	-42.9971
1550	-71.2057	-94.8011	-65.9259
1555	-90.2237	-96.4363	-74.9061
1575*	-78.1883	-100.556	-65.7427
1595*	-77.9432	-93.2012	NaN
1615	-80.688	-79.3254	-33.2232
1620	-53.752	-76.038	-29.999
1625	-37.6608	-68.782	-29.999
1630	-36.7556	-59.2317	-9.999
1635	-32.3209	-48.1514	-9.999
1640	-22.7274	-41.544	-9.999
1645	-17.6939	-34.8068	-9.999
1660	-9.999	-15.0115	-9.999
1675	-9.999	-9.999	-9.999



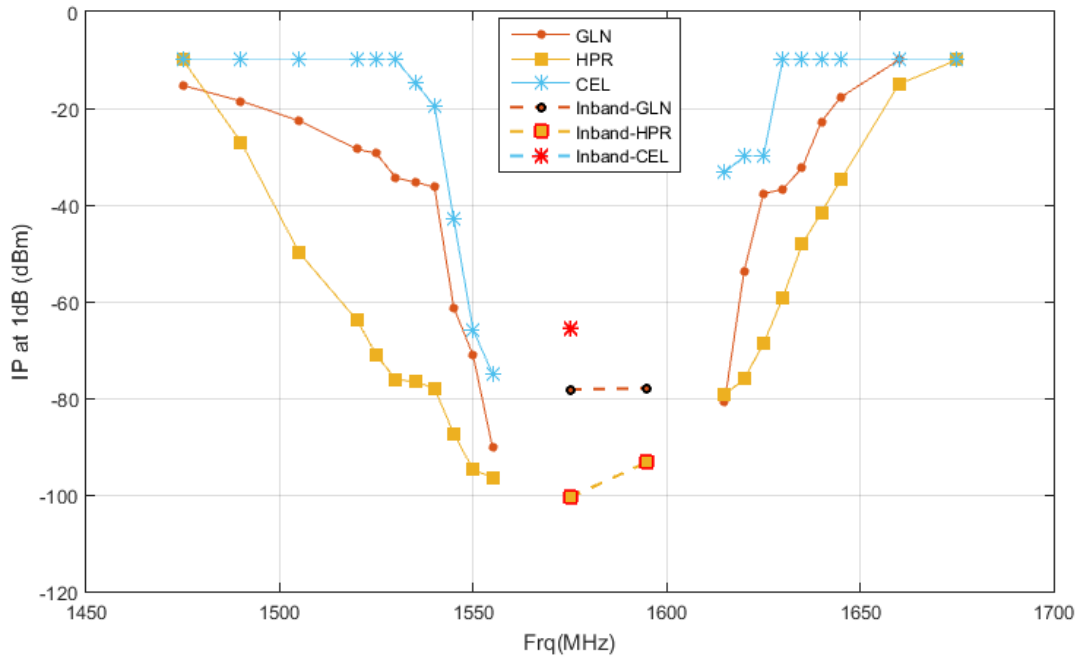


**Figure B-18: Summary of 1 MHz and 1 MHz In-band BeiDou B1 I Bounding Masks**

**Table B-7: 1 MHz and 1 MHz In-band\* Galileo E1 BC Bounding Masks (dBm)**

Frequency (MHz)	HPR
1475	-35.2548
1490	-40.5603
1505	-54.5503
1520	-67.9842
1525	-73.9463
1530	-71.4059
1535	-71.6929
1540	-76.3935
1545	-90.805
1550	-93.463
1555	-93.9953
1575*	-111.593
1595*	-98.7922
1615	-91.4673
1620	-86.9953
1625	-72.9294
1630	-66.8658
1635	-59.6178
1640	-53.3542
1645	-46.7501
1660	-40.3065
1675	-36.0584

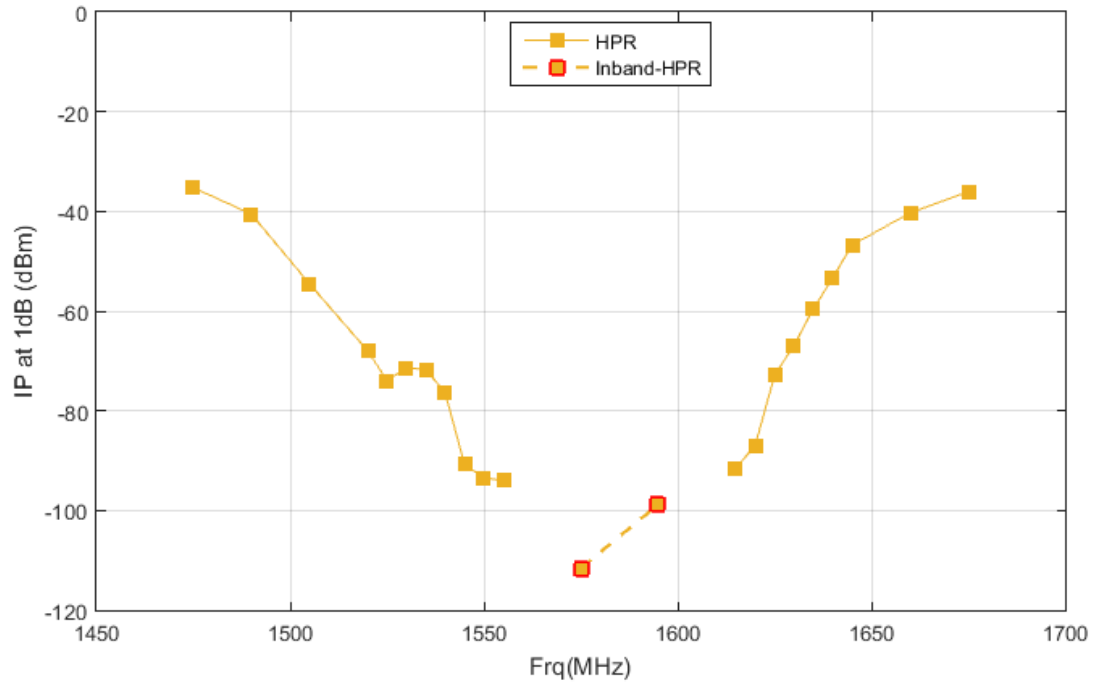


**Figure B-19: Summary of 1 MHz and 1 MHz In-band Galileo E1 BC Bounding Masks**

**Table B-8: 1 MHz and 1 MHz In-band\* SBAS L1 C/A Bounding Masks (dBm)**

Frequency (MHz)	GLN	HPR	TIM
1475	-51.0577	-36.3048	-9.999
1490	-63.3312	-36.2106	-9.999
1505	-43.0991	-54.7003	-9.999
1520	-51.2192	-66.2717	-18.1846
1525	-53.1171	-68.445	-17.8801
1530	-52.0402	-70.6184	-19.9122
1535	-52.3345	-72.0554	-21.82
1540	-52.9021	-76.3935	-27.8443
1545	-57.8562	-92.255	-36.8048
1550	-75.2539	-92.7255	-60.008
1555	-83.7667	-92.7703	-64.5788
1575*	-118.108	-116.304	-111.015
1595*	-71.7432	-98.7297	-65.1566
1615	-74.2469	-91.5423	-45.1318
1620	-66.3442	-82.5362	-46.3982
1625	-54.2824	-66.4259	-37.1343
1630	-56.1713	-61.6283	-29.2349
1635	-43.9075	-55.9303	-22.8593
1640	-43.7996	-44.6667	-18.0685
1645	-43.1834	-48.7722	-14.134
1660	-42.1121	-40.0315	-10.9981
1675	-34.4705	-35.6063	NaN

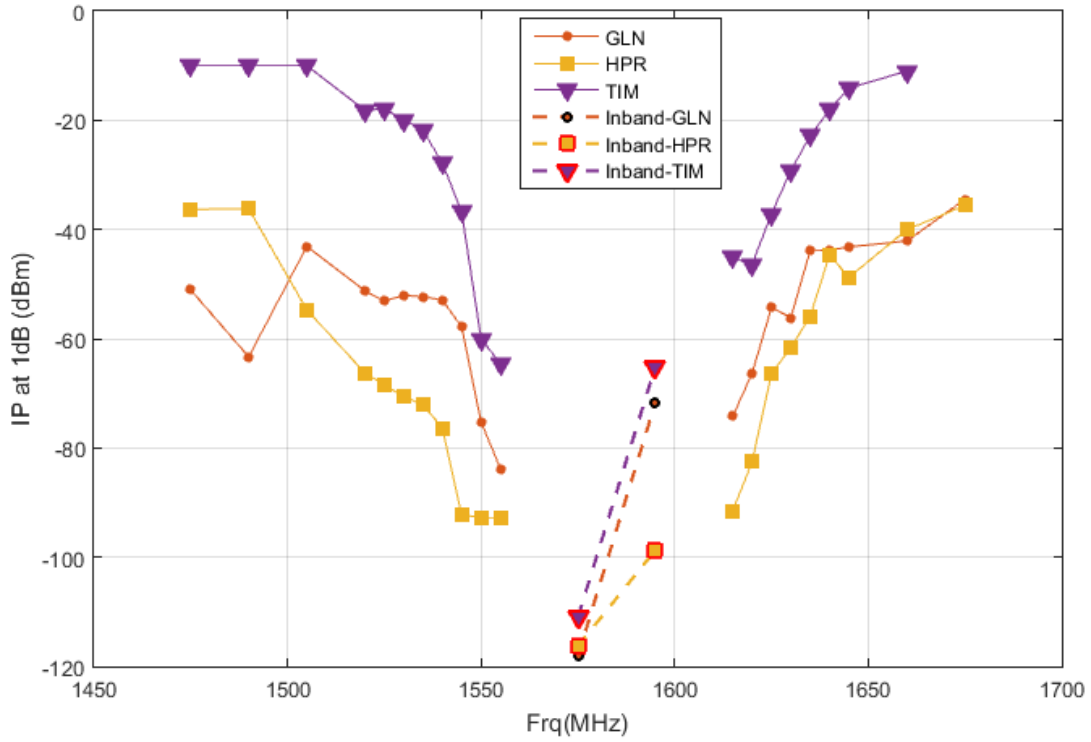


**Figure B-20: Summary of 1 MHz and 1 MHz In-band SBAS L1 C/A Bounding Masks**

**B.1.2 Interference Test Results for 10-MHz LTE**

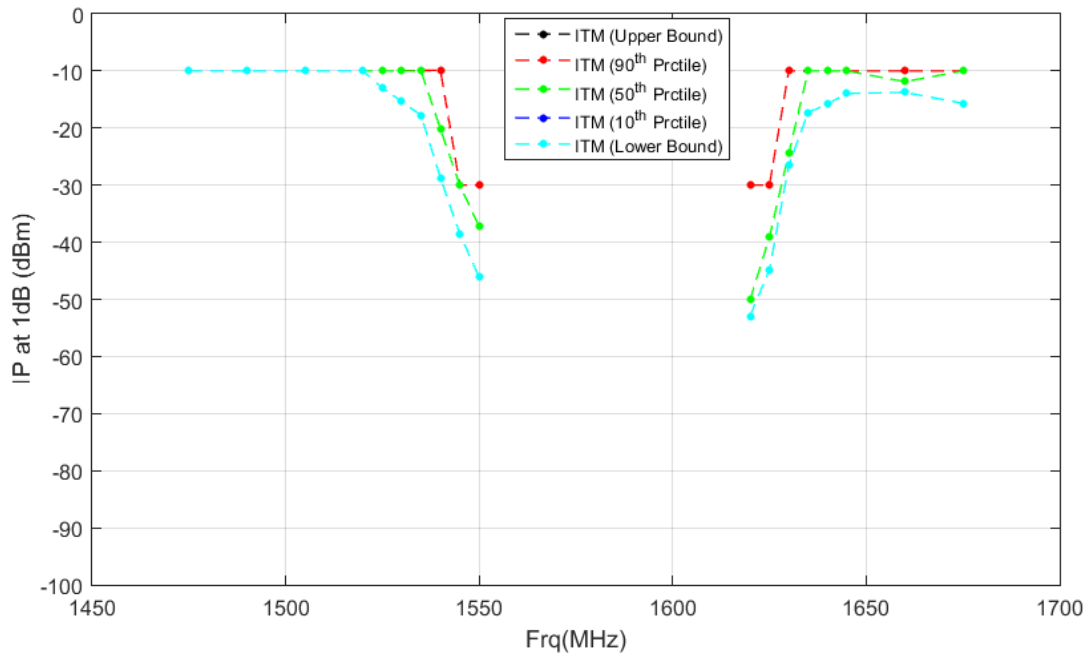


**Figure B-21: 10 MHz GPS L1 C/A Statistical Mask Results for Cellular receivers**

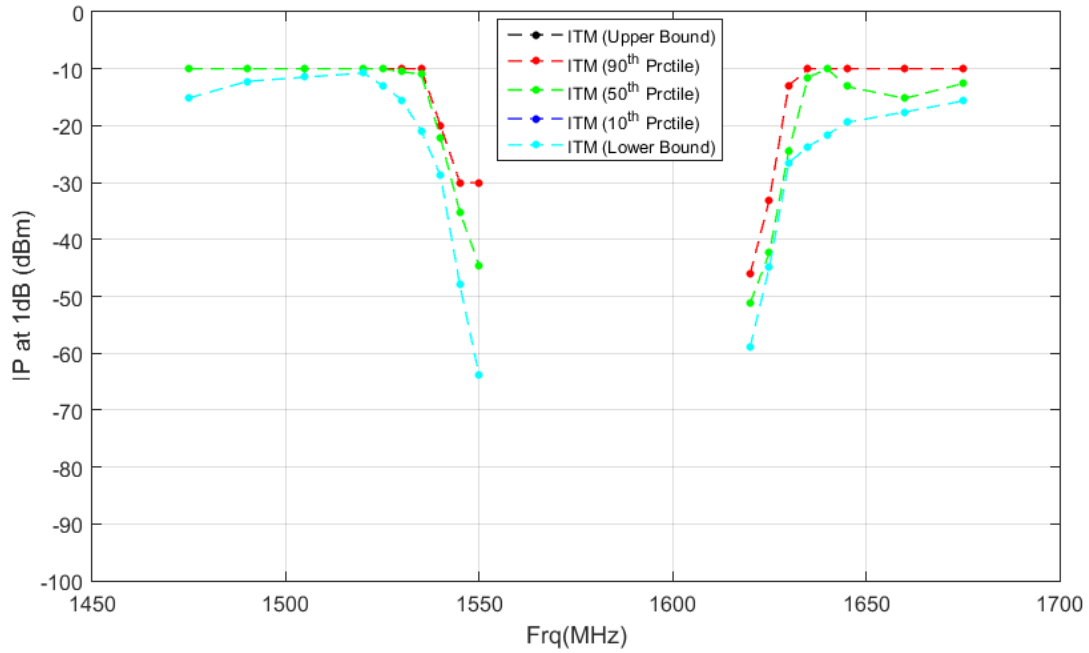


**Figure B-22: 10 MHz All GNSS Aggregated Minimum Statistical Mask Results for Cellular receivers**

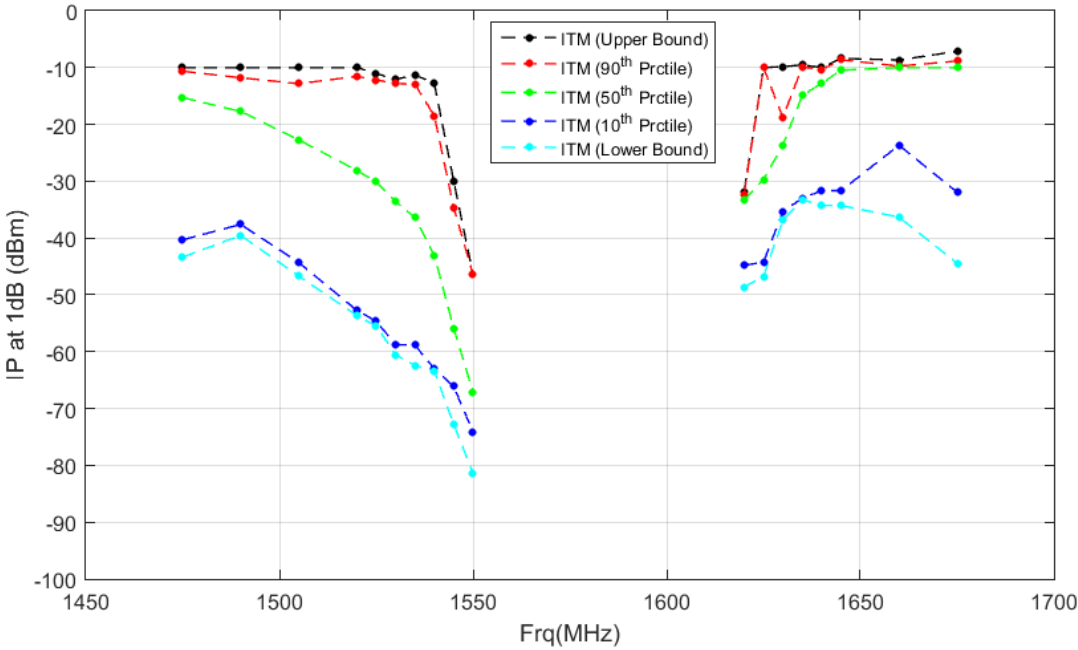


**Figure B-23: 10 MHz GPS L1 C/A Statistical Mask Results for General Aviation receivers**

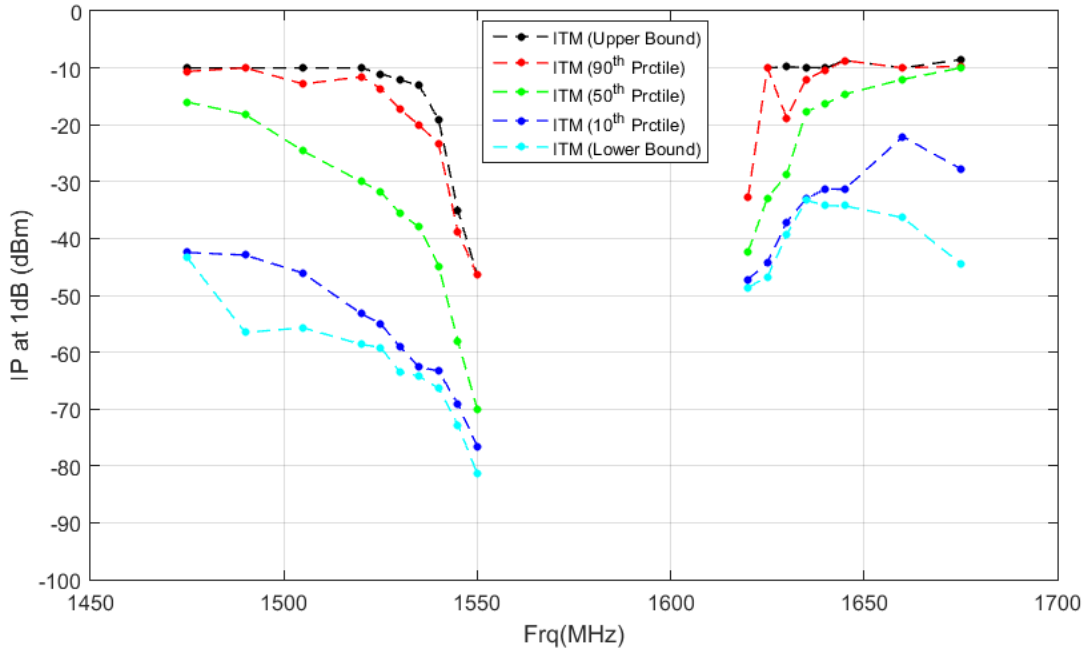


**Figure B-24: 10 MHz All GNSS Aggregated Minimum Statistical Mask Results for General Aviation receivers**

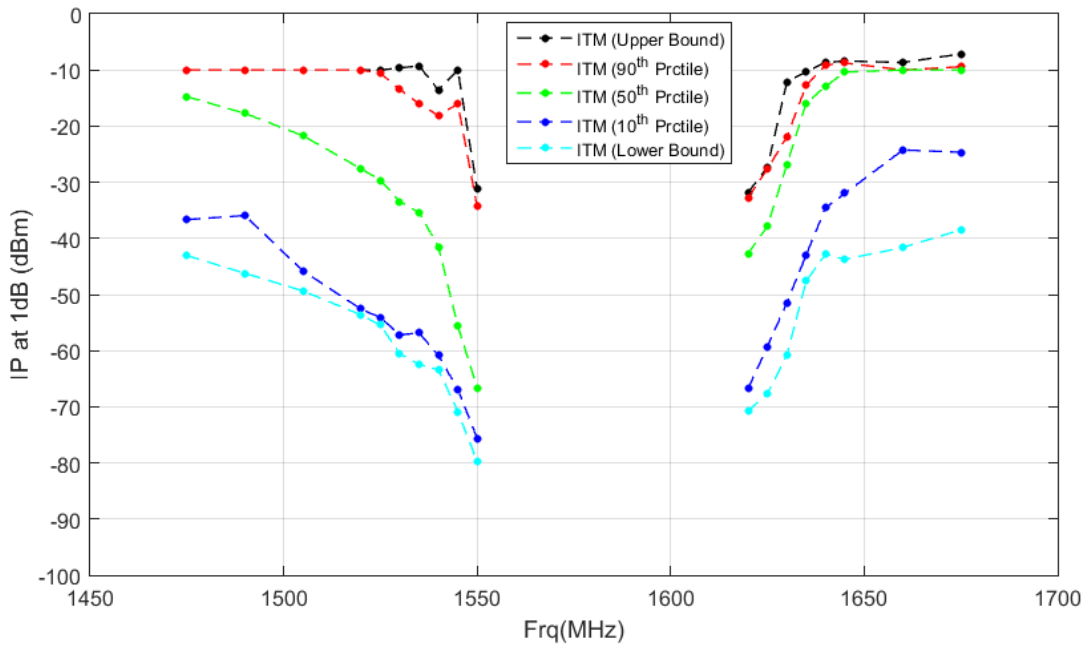




**Figure B-25: 10 MHz GPS L1 C/A Statistical Mask Results for General Location Navigation receivers**

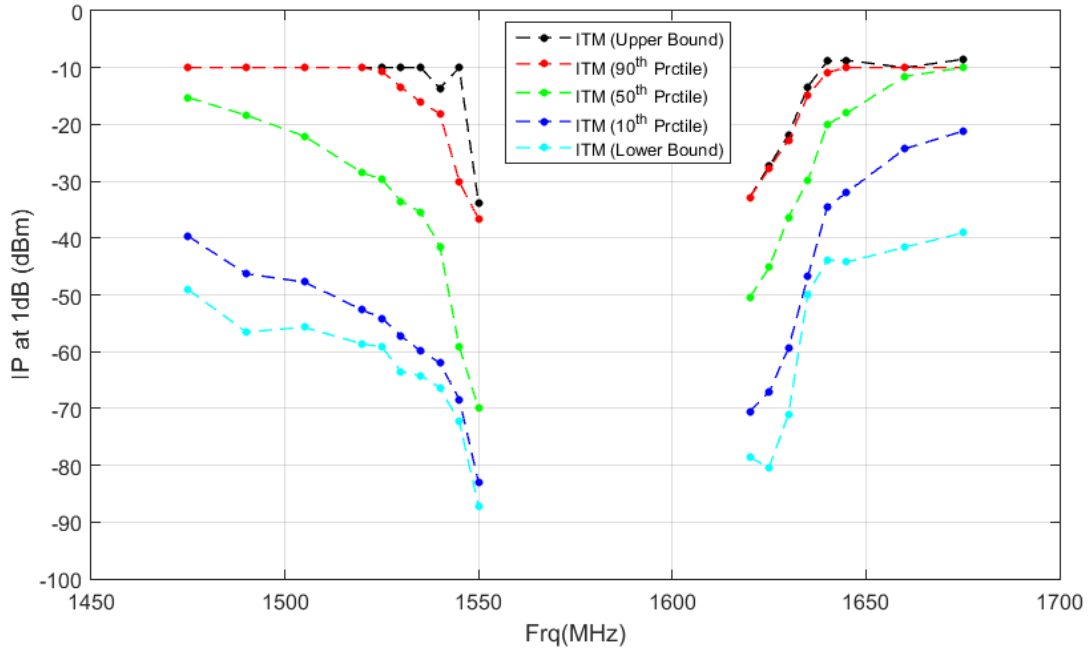


**Figure B-26: 10 MHz All GNSS Aggregated Minimum Statistical Mask Results for General Location Navigation receivers**

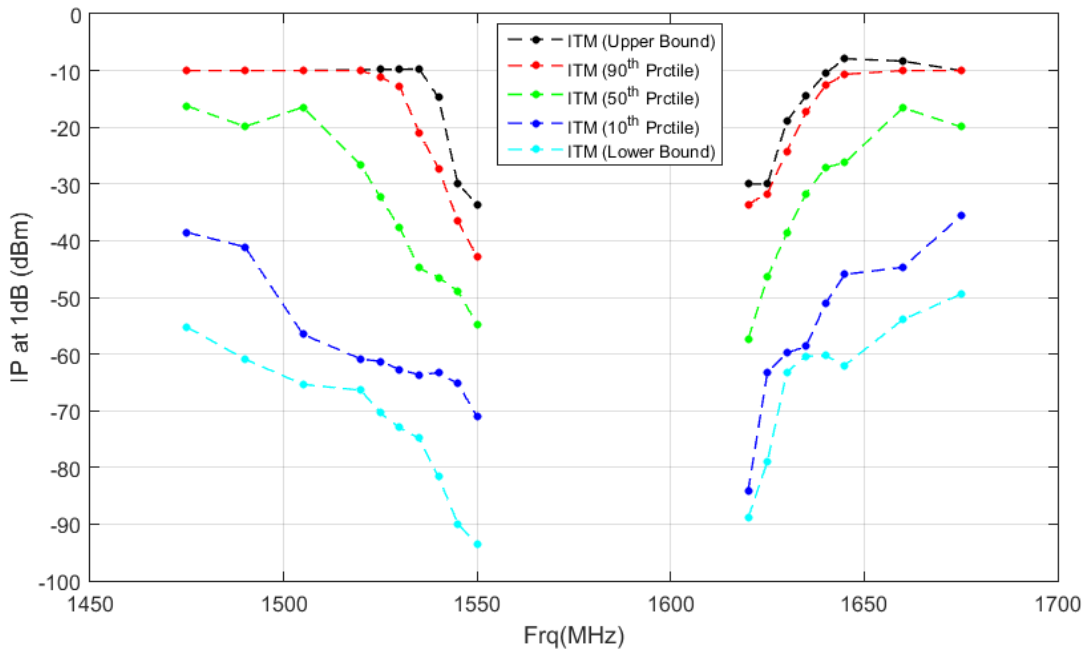


**Figure B-27: 10 MHz GPS L1 C/A Statistical Mask Results for High Precision receivers**

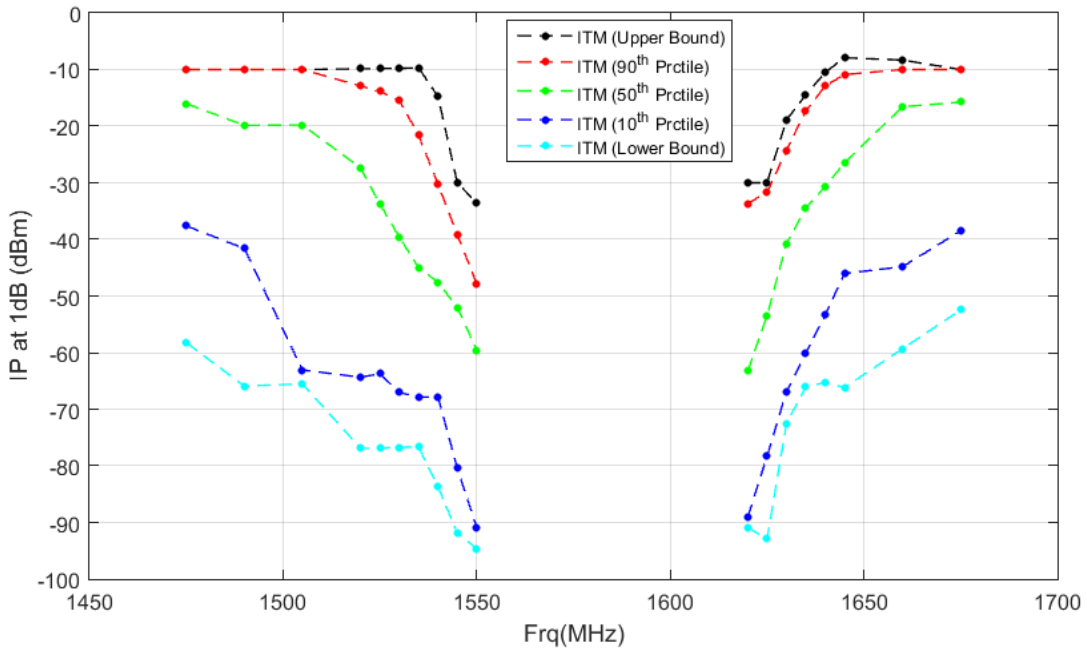


**Figure B-28: 10 MHz All GNSS Aggregated Minimum Statistical Mask Results for High Precision receivers**

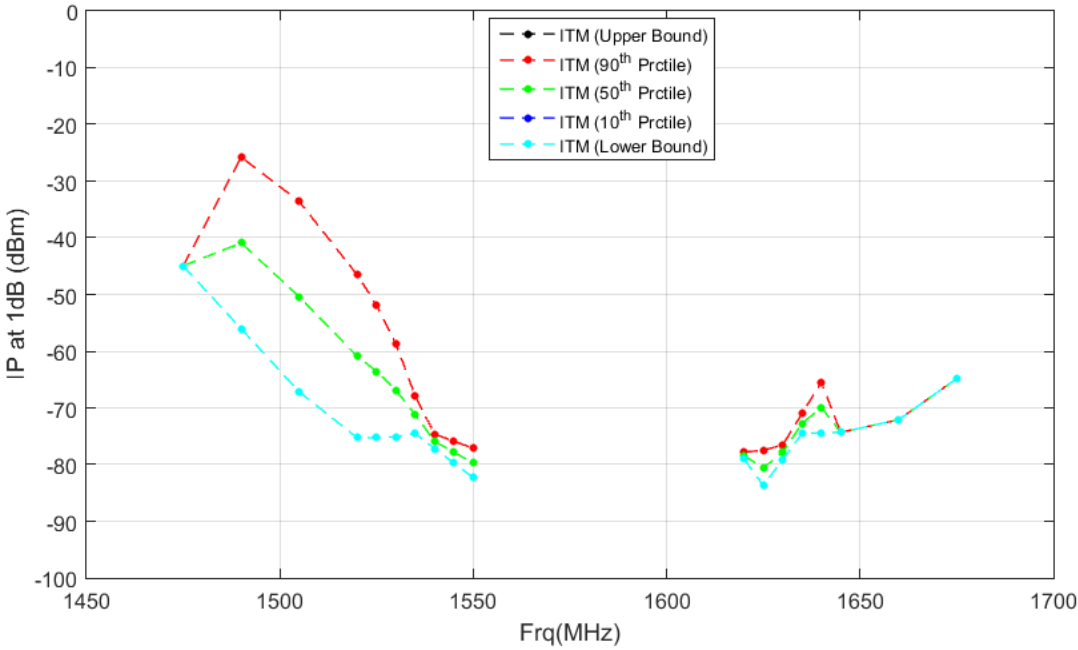


**Figure B-29: 10 MHz GPS L1 C/A Statistical Mask Results for Space Based receivers**

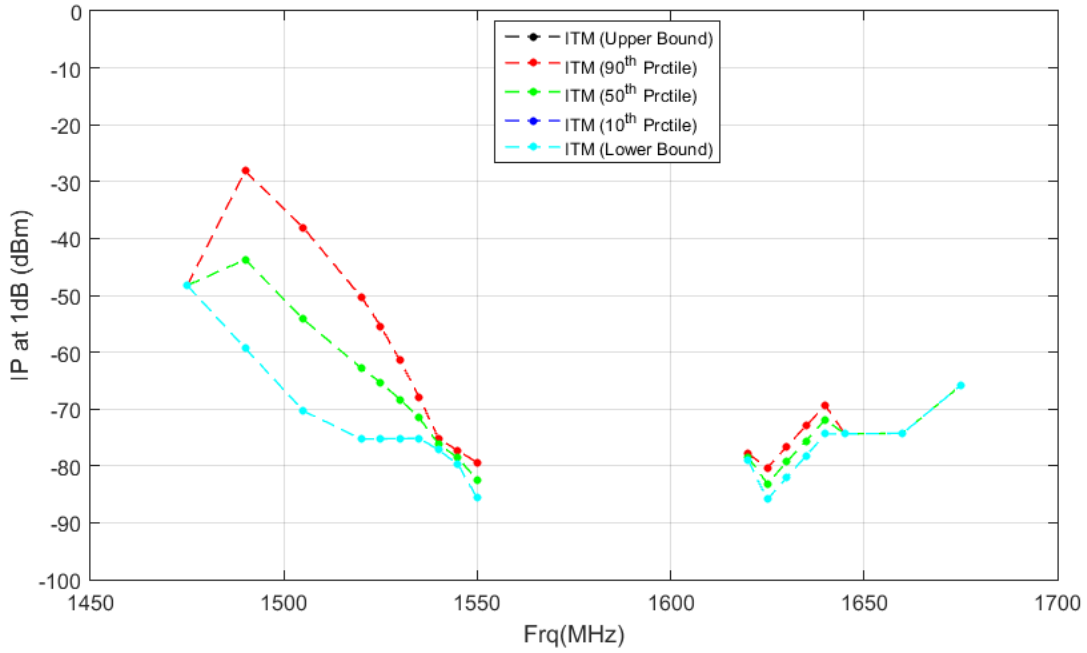


**Figure B-30: 10 MHz All GNSS Aggregated Minimum Statistical Mask Results for Space Based receivers**

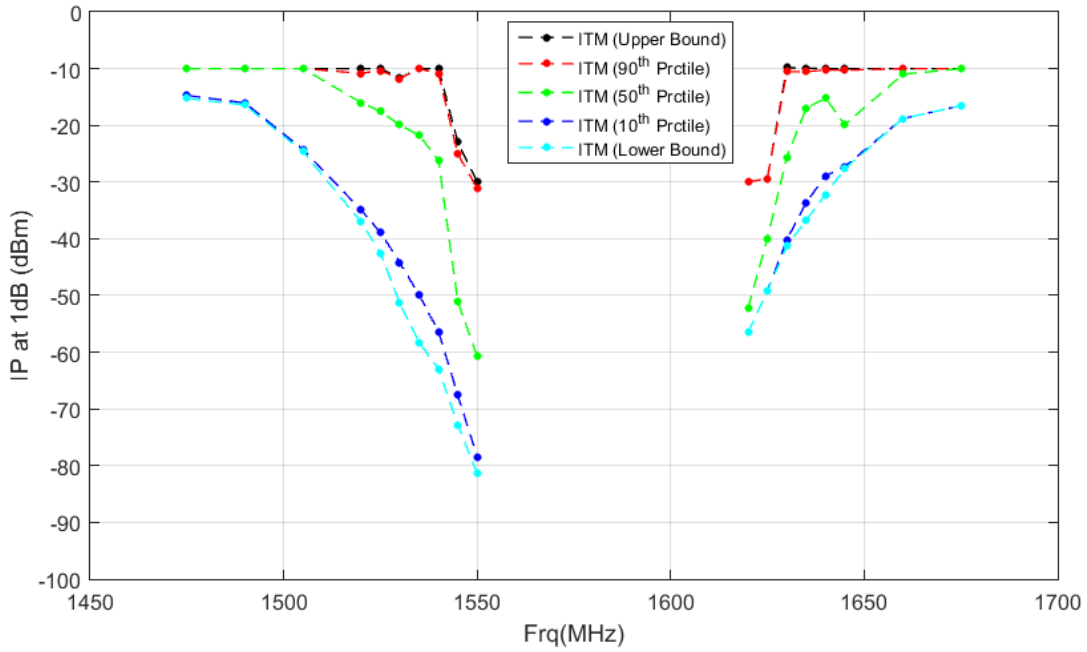


**Figure B-31: 10 MHz GPS L1 C/A Statistical Mask Results for Timing receivers**

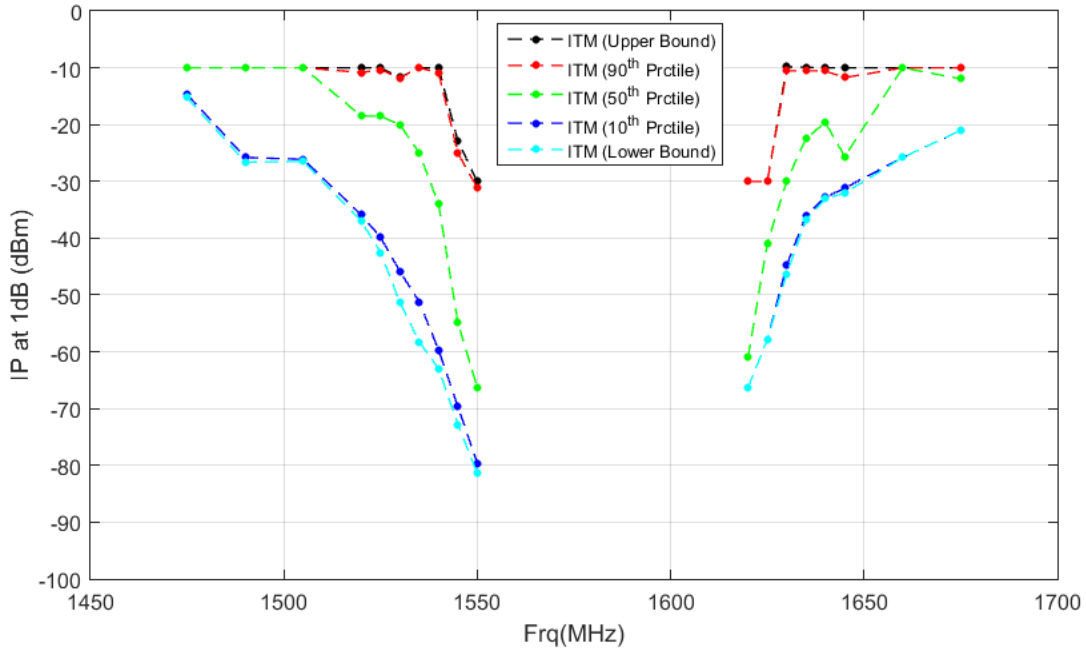


**Figure B-32: 10 MHz All GNSS Aggregated Minimum Statistical Mask Results for Timing receivers**

Using this approach a bounding ITM was produced for each category and signal type combination. Figure B-33 illustrates how the L1 C/A bounding ITMs compare across the six categories of receivers. This plot shows the HPR and SPB categories to be the most susceptible in terms of received interference power levels with the cellular category generally being the most tolerant of LTE interference.

**Table B-9: 10 MHz and 10 MHz Intermod\* GPS L1 C/A Bounding Masks (dBm)**

Frequency (MHz)	GAV	GLN	HPR	TIM	SPB	CEL
1475	-43.3646	-43.0577	-55.2458	-15.2559	-44.9489	-9.999
1490	-39.5303	-46.2115	-60.9099	-16.4053	-56.0659	-9.999
1505	-46.7082	-49.3654	-65.3551	-24.6328	-67.1829	-9.999
1520	-53.6318	-53.6318	-66.3967	-37.0094	-75.2901	-9.999
1525	-55.4429	-55.4429	-70.4213	-42.5001	-75.2341	-12.9574
1530	-60.5293	-60.5293	-72.9934	-51.3793	-75.1091	-15.3651
1530*	-73.6293	-75.91	-78.9673	-73.6293	-76.5937	-36.467
1535	-62.445	-62.445	-74.8804	-58.249	-74.501	-17.7728
1540	-63.4002	-63.4002	-81.6489	-62.9739	-77.1892	-28.7517
1545	-72.8009	-70.8562	-89.9247	-72.8009	-79.7538	-38.5472
1550	-81.3979	-79.7539	-93.538	-81.3979	-82.3183	-46.0942
1550*	-82.7979	-85.2039	-88.2261	-82.7979	-86.1433	-45.5942
1620	-48.6403	-70.7486	-88.9203	-56.5041	-79.0305	-52.9139
1625	-46.7292	-67.6878	-78.9544	-49.1718	-83.6891	-44.7992
1630	-36.8823	-60.8322	-63.1922	-41.2976	-79.1041	-26.5096
1635	-33.2516	-47.6279	-60.3723	-36.7448	-74.5191	-17.2657
1640	-34.2495	-42.7996	-60.2717	-32.192	-74.405	-15.8067
1645	-34.2708	-43.7334	-61.9748	-27.6393	-74.3188	-13.9425
1660	-36.3256	-41.6121	-53.9123	-18.8014	-72.0909	-13.7382
1675	-44.4325	-38.4705	-49.4567	-16.5372	-64.8224	-15.6612

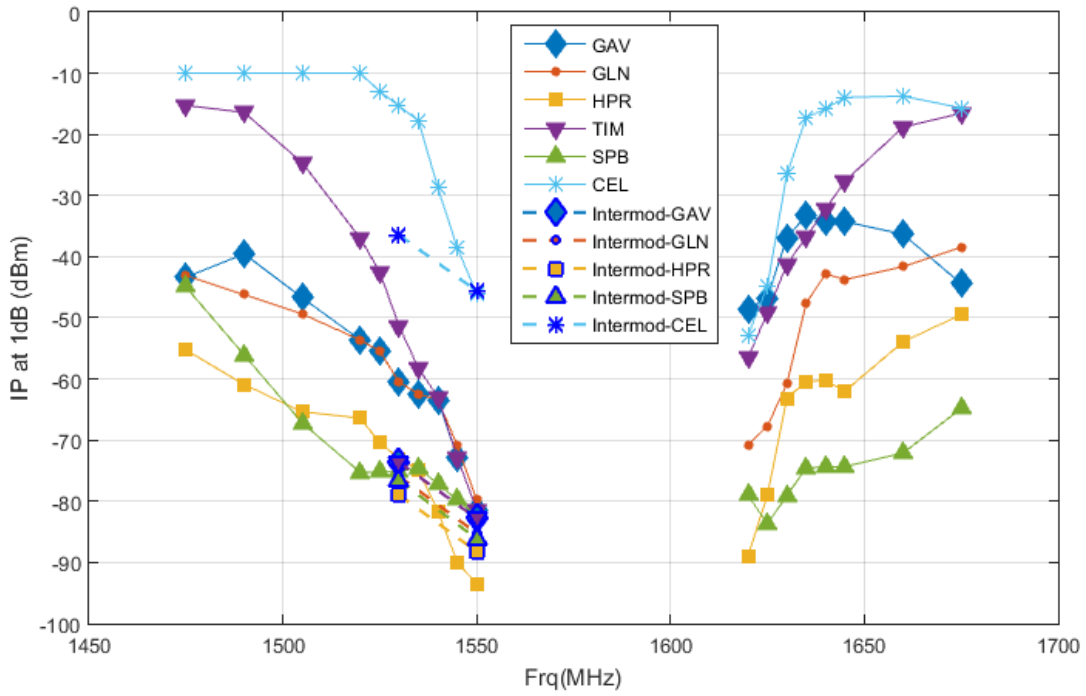


**Figure B-33: Summary of 10 MHz and 10MHz Intermod GPS L1 C/A Bounding Masks**

**Table B-10: 10 MHz and 10 MHz Intermod\* GPS L1 P Bounding Masks (dBm)**

Frequency (MHz)	GLN	HPR	SPB	CEL
1475	-9.999	-58.2419	-48.2739	-9.999
1490	-9.999	-65.9099	-59.2909	-9.999
1505	-9.999	-65.5172	-70.3079	-9.999
1520	-9.999	-63.7114	-74.0025	-9.999
1525	-12.1984	-65.1348	-75.2341	-12.9574
1530	-14.3977	-64.8352	-75.2091	-15.3651
1530*	-27.9178	-68.2977	NaN	NaN
1535	-16.5971	-65.3046	-75.151	-17.7728
1540	-19.7263	-66.7822	-75.2145	-20.1804
1545	-29.999	-65.5121	-79.6059	-29.999
1550	-41.6162	-68.946	-85.6683	-29.999
1550*	-37.2516	-77.621	NaN	NaN
1620	-52.0646	-62.4395	NaN	-52.9139
1625	-48.234	-62.7591	-85.8891	-42.7839
1630	-32.0891	-62.2422	-82.0611	-26.5096
1635	-16.731	-61.4098	-78.233	-17.2657
1640	-13.365	-63.4217	-74.405	-15.8067
1645	-9.999	-62.9873	-74.3688	-13.9425
1660	-9.999	-49.5114	-74.2659	-13.7382
1675	-9.999	-46.3192	-65.8474	-15.6612



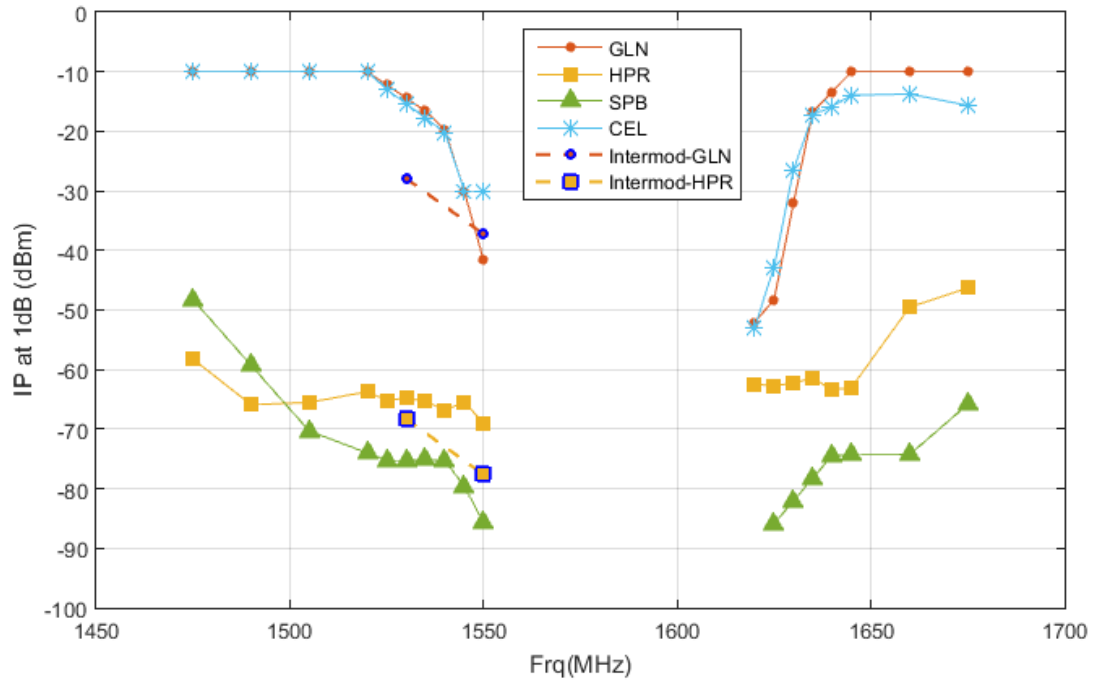


**Figure B-34: Summary of 10 MHz and 10 MHz Intermod GPS L1 P Bounding Masks**

**Table B-11: 10 MHz and 10 MHz Intermod\* GPS L1 C Bounding Masks (dBm)**

Frequency (MHz)	GLN	CEL
1475	-9.999	-9.999
1490	-9.999	-9.999
1505	-9.999	-9.999
1520	-9.999	-9.999
1525	-12.1984	-12.9574
1530	-14.3977	-15.3651
1530*	-27.9178	NaN
1535	-16.5971	-17.7728
1540	-19.7263	-20.1804
1545	-29.999	-29.999
1550	-41.6162	-29.999
1550*	-37.2516	NaN
1620	-52.0646	-52.9139
1625	-48.234	-42.7839
1630	-32.0891	-26.5096
1635	-16.731	-17.2657
1640	-13.365	-15.8067
1645	-9.999	-13.9425
1660	-9.999	-13.7382
1675	-9.999	-15.6612

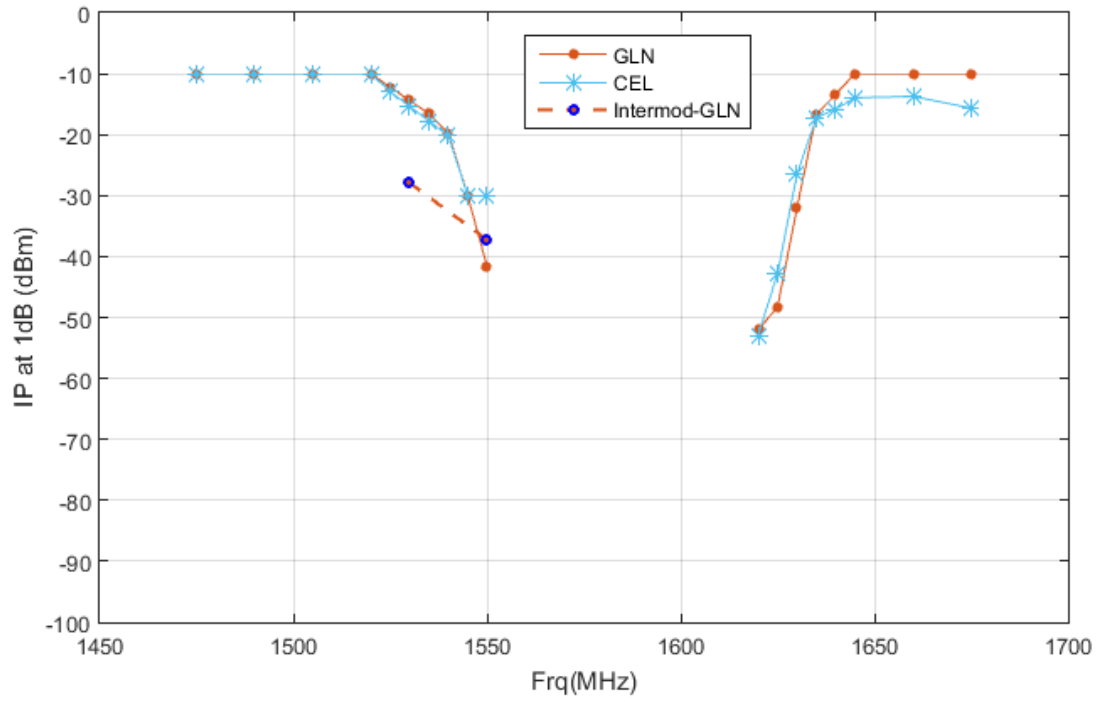


**Figure B-35: Summary of 10 MHz and 10 MHz Intermod GPS L1 C Bounding Masks**

**Table B-12: 10 MHz and 10 MHz Intermod\* GLONASS L1 C Bounding Masks (dBm)**

Frequency (MHz)	GAV	GLN	HPR	TIM	CEL
1475	-41.5559	-49.0577	-57.1169	-14.6684	-15.1348
1490	-56.5303	-56.5303	-63.9099	-26.6126	-12.2023
1505	-55.7082	-55.7082	-65.1422	-26.4832	-11.4679
1520	-58.6318	-58.6318	-76.9217	-31.4068	-10.7334
1525	-59.1679	-59.1679	-76.8713	-33.7179	-10.4886
1530	-63.5043	-63.5043	-76.7309	-37.5543	-15.4582
1530*	-63.4418	-63.4418	-79.6515	-63.4418	-32.967
1535	-64.22	-64.22	-76.5364	-40.595	-20.9174
1540	-66.3502	-66.3502	-76.381	-54.7114	-26.3767
1545	-68.7673	-68.7673	-80.4122	-62.3673	-37.5972
1550	-75.3943	-75.3943	-88.6362	-75.3943	-45.0942
1550*	-72.6568	-72.6568	-89.0612	-72.6568	-42.1424
1620	-45.8192	-78.6146	-89.2958	-66.2982	-58.9889
1625	-40.1098	-80.4061	-92.9202	-57.8343	-42.9589
1630	-39.3828	-71.0266	-72.5692	-46.2599	-25.8346
1635	-30.9245	-49.925	-66.0598	-34.1262	-23.6998
1640	-27.7297	-43.7996	-65.2717	-33.0535	-21.5649
1645	-23.4929	-42.2334	-66.1748	-32.0656	-19.43
1660	-16.7459	-39.5371	-59.3114	-25.8014	-17.5882
1675	-9.999	-39.108	-52.4567	-21.0372	-15.177

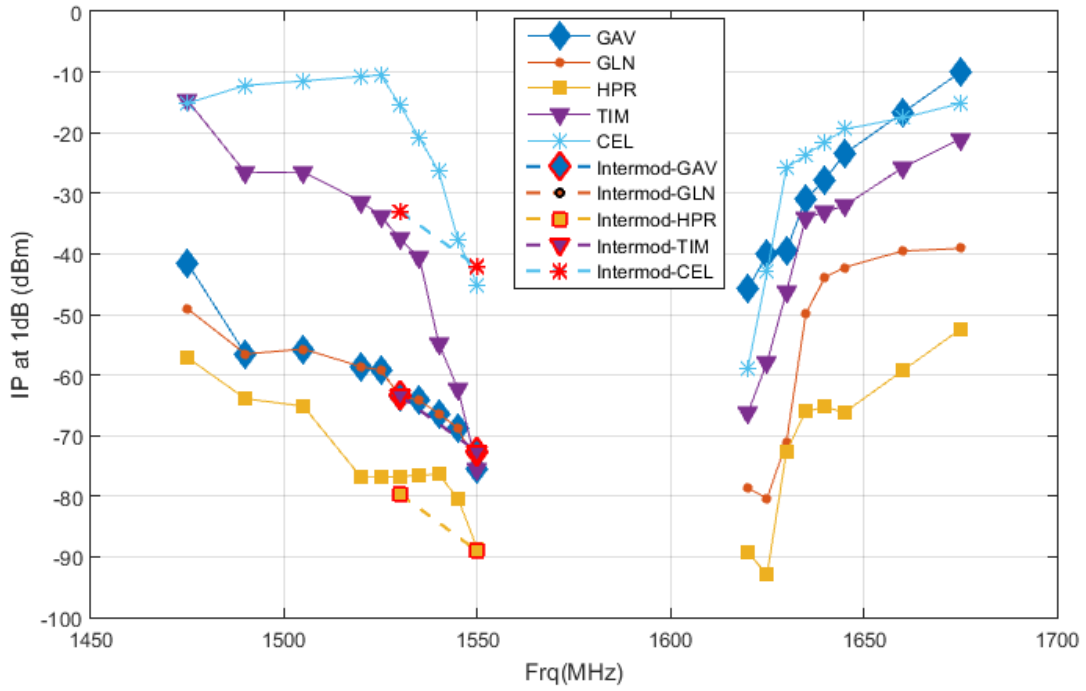


**Figure B-36: Summary of 10 MHz and 10 MHz Intermod GLONASS L1 C Bounding Masks**

**Table B-13: 10 MHz and 10 MHz Intermod\* GLONASS L1 P Bounding Masks (dBm)**

Frequency (MHz)	GLN	HPR	CEL
1475	-9.999	-9.999	-15.1348
1490	-9.999	-11.2502	-12.2023
1505	-12.1713	-16.534	-11.4679
1520	-14.3436	-24.3966	-10.7334
1525	-13.6543	-29.9846	-10.4886
1530	-12.965	-35.0448	-10.2438
1530*	-29.5678	-47.5536	-9.999
1535	-12.6165	-38.3146	-9.999
1540	-16.0238	-40.9242	-19.999
1545	-29.999	-43.472	-29.999
1550	-38.8287	-56.6851	-29.999
1550*	-38.9037	-56.8351	-29.999
1620	-78.6146	-84.0237	-58.9889
1625	-80.4061	-63.1057	-42.9589
1630	-71.0266	-40.6515	-25.8346
1635	-49.925	-33.9881	-23.6998
1640	-16.666	-28.7876	-21.5649
1645	-19.0538	-24.6255	-19.43
1660	-9.999	-12.3051	-17.5882
1675	-9.999	-9.999	-15.177

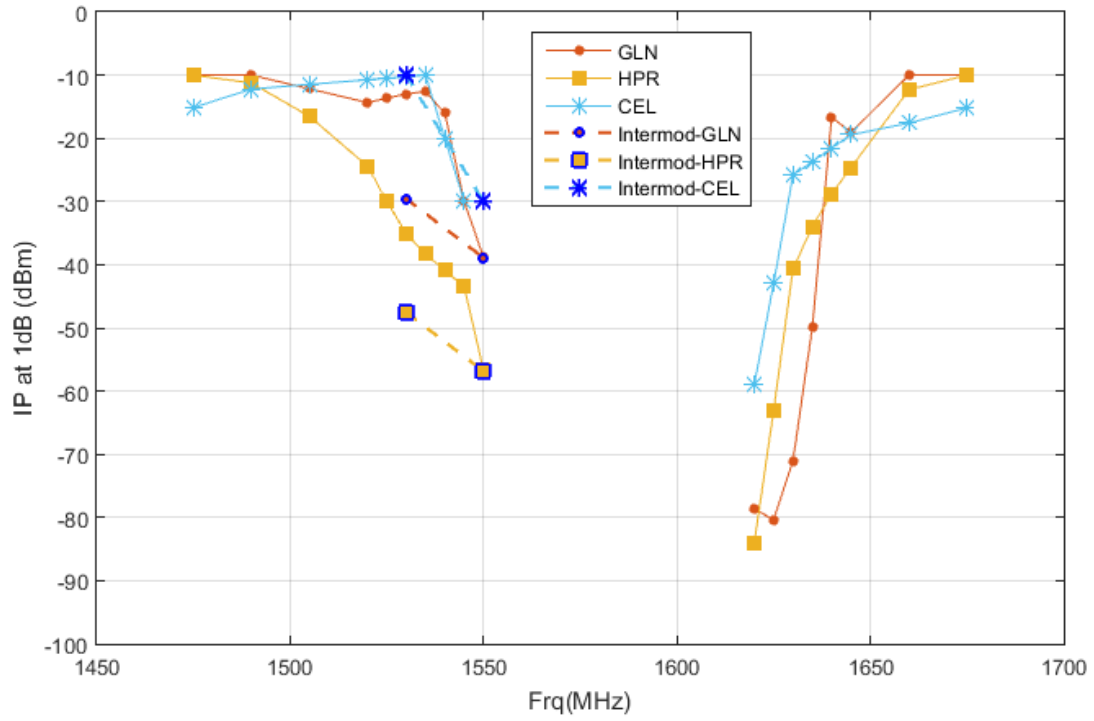
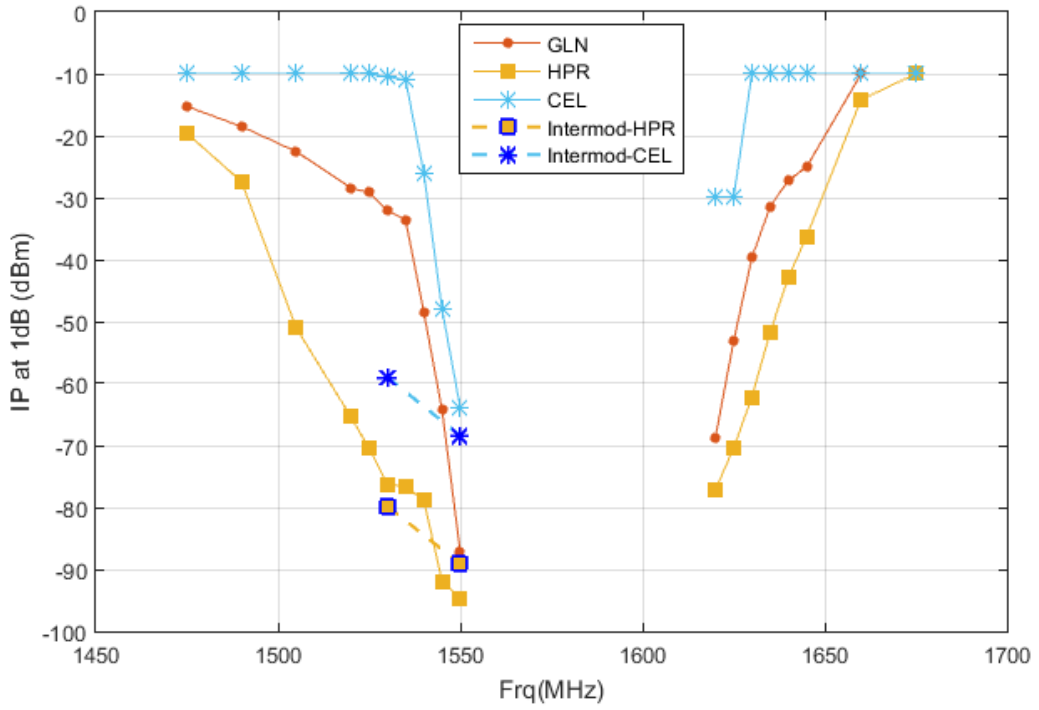


**Figure B-37: Summary of 10 MHz and 10 MHz Intermod GLONASS L1 P Bounding Masks**

**Table B-14: 10 MHz and 10 MHz Intermod\* BeiDou B1 I Bounding Masks (dBm)**

Frequency (MHz)	GLN	HPR	CEL
1475	-15.2553	-19.5883	-9.999
1490	-18.5174	-27.4185	-9.999
1505	-22.5464	-51.029	-9.999
1520	-28.4227	-65.3777	-9.999
1525	-29.1841	-70.5146	-9.999
1530	-32.0749	-76.2673	-10.4945
1530*	NaN	-79.8286	-58.9725
1535	-33.6097	-76.6679	-10.9901
1540	-48.4839	-78.8212	-26.0027
1545	-64.2635	-91.9158	-47.9971
1550	-87.2057	-94.6261	-63.9259
1550*	NaN	-89.1101	-68.4259
1620	-68.727	-77.163	-29.999
1625	-53.1608	-70.407	-29.999
1630	-39.7056	-62.1942	-9.999
1635	-31.4209	-51.7889	-9.999
1640	-27.2274	-42.9315	-9.999
1645	-25.0439	-36.2818	-9.999
1660	-9.999	-14.1615	-9.999
1675	-9.999	-9.999	-9.999

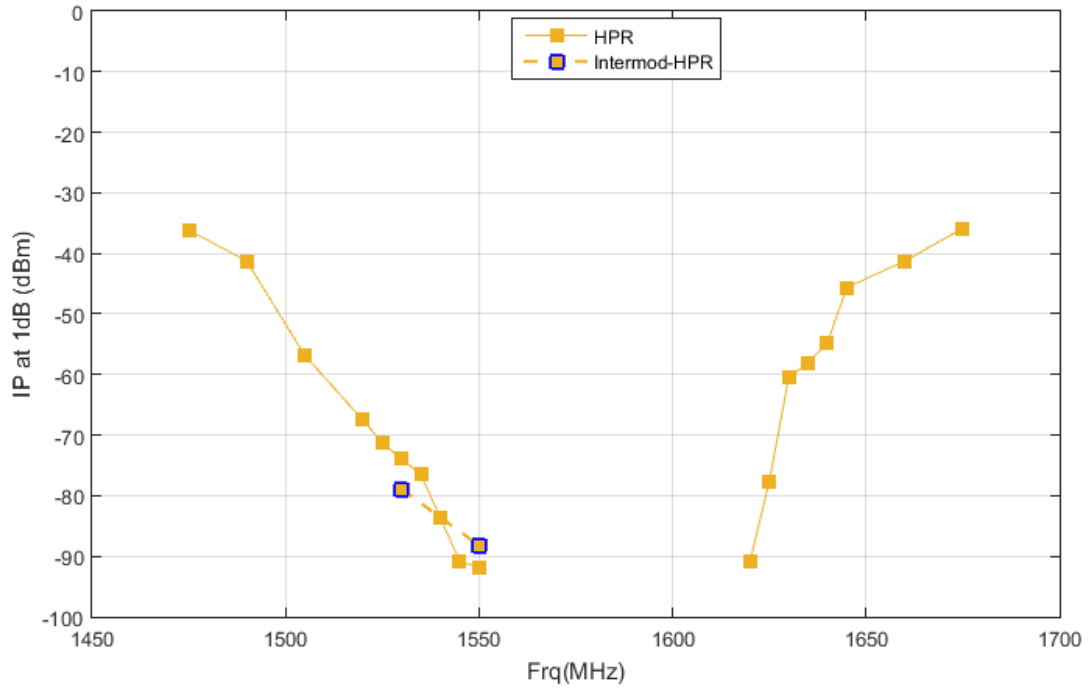




**Figure B-38: Summary of 10 MHz and 10 MHz Intermod BeiDou B1 I Bounding Masks**

**Table B-15: 10 MHz and 10 MHz Intermod\* Galileo E1 BC Bounding Masks (dBm)**

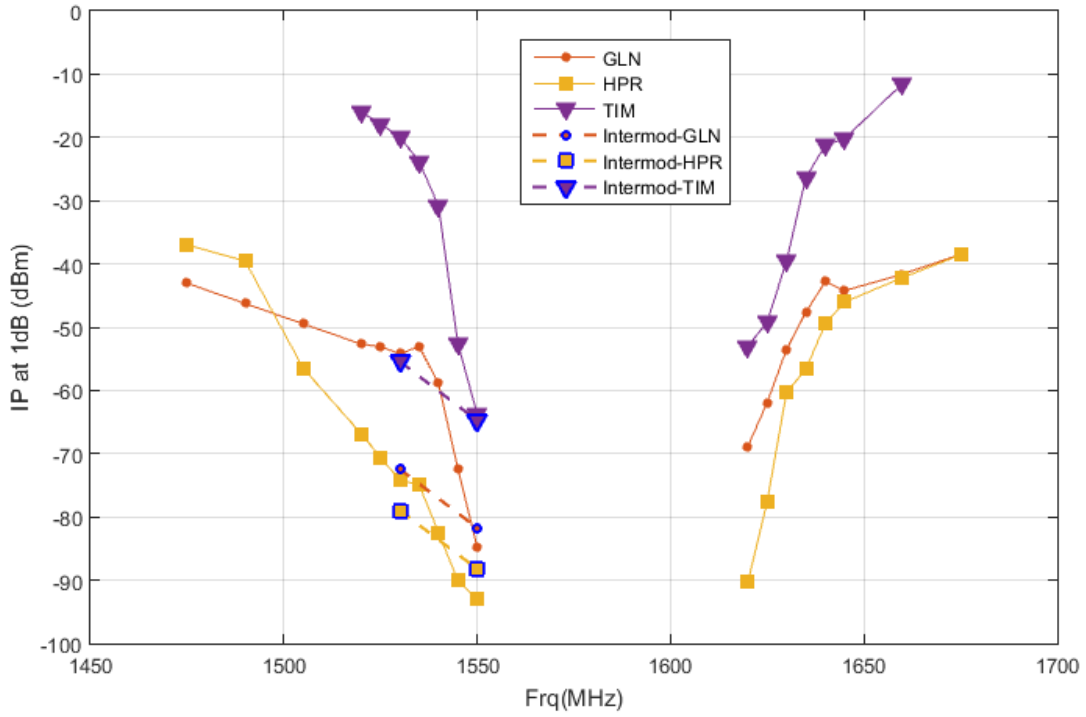
Frequency (MHz)	HPR
1475	-36.1449
1490	-41.2853
1505	-56.8628
1520	-67.5092
1525	-71.2713
1530	-73.8934
1530*	-78.9423
1535	-76.5364
1540	-83.6832
1545	-90.83
1550	-91.788
1550*	-88.2011
1620	-90.8953
1625	-77.6544
1630	-60.4783
1635	-58.0303
1640	-54.8042
1645	-45.6251
1660	-41.2507
1675	-35.8563



**Figure B-39: Summary of 10 MHz and 10 MHz Intermod Galileo E1 BC Bounding Masks**

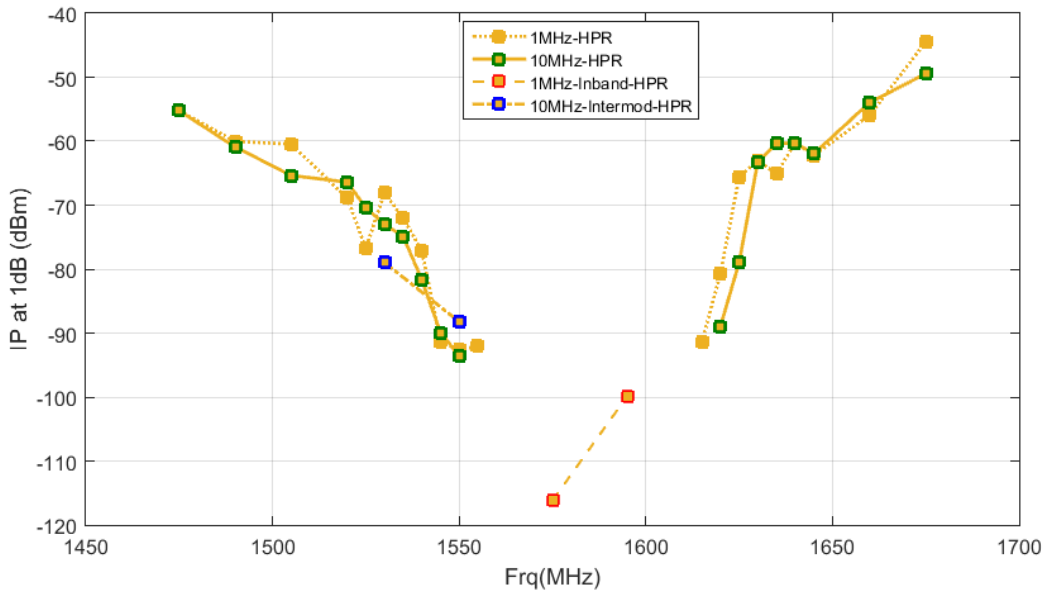
**Table B-16: 10 MHz and 10 MHz Intermod\* SBAS L1 C/A Bounding Masks (dBm)**

Frequency (MHz)	GLN	HPR	TIM
1475	-43.0577	-36.9968	NaN
1490	-46.2615	-39.5353	NaN
1505	-49.4654	-56.4753	NaN
1520	-52.6692	-66.8467	-15.9846
1525	-53.0921	-70.5588	-17.8801
1530	-54.2027	-74.2059	-19.9122
1530*	-72.4225	-78.9673	-55.4372
1535	-53.0595	-74.9054	-23.82
1540	-58.906	-82.4582	-30.8443
1545	-72.3562	-90.03	-52.5923
1550	-84.7539	-93.013	-63.7205
1550*	-81.7289	-88.2261	-64.7455
1620	-68.8442	-90.2953	-53.0107
1625	-61.8949	-77.5544	-49.1718
1630	-53.4838	-60.2533	-39.5099
1635	-47.6279	-56.6803	-26.3593
1640	-42.7996	-49.4667	-21.231
1645	-44.2334	-46.0279	-20.184
1660	-41.6121	-42.1585	-11.4981
1675	-38.4705	-38.5679	NaN

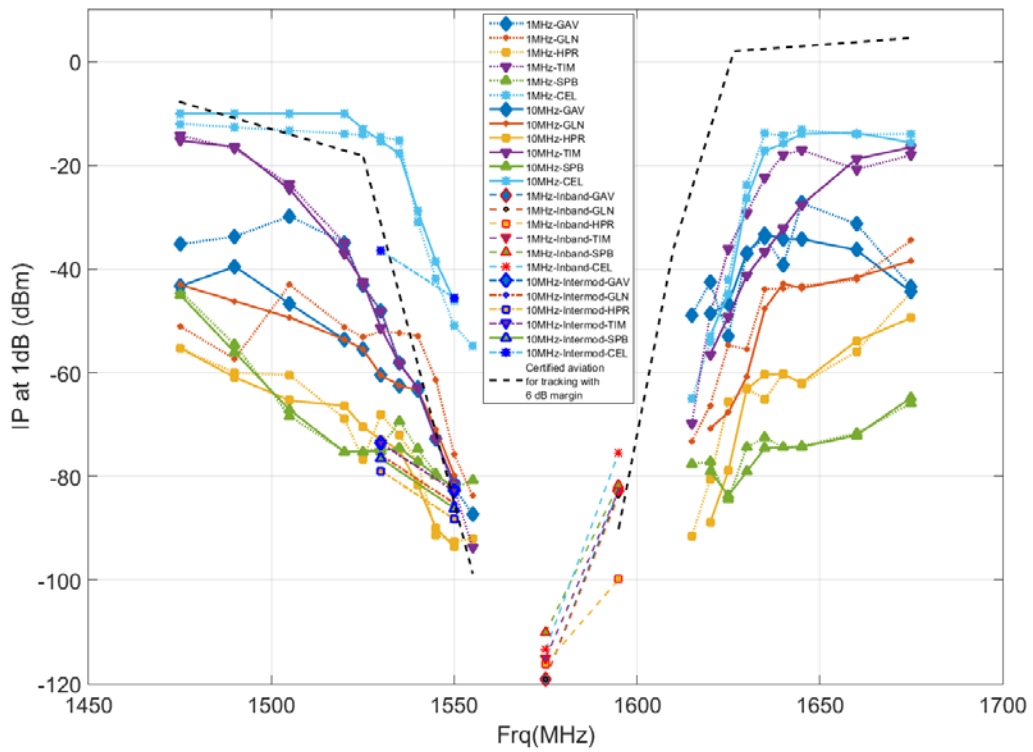


**Figure B-40: Summary of 10 MHz and 10 MHz Intermod SBAS L1 C/A Bounding Masks**

**B.1.3 Combined 1 MHz AWGN Test Results and 10 MHz LTE Test Results**

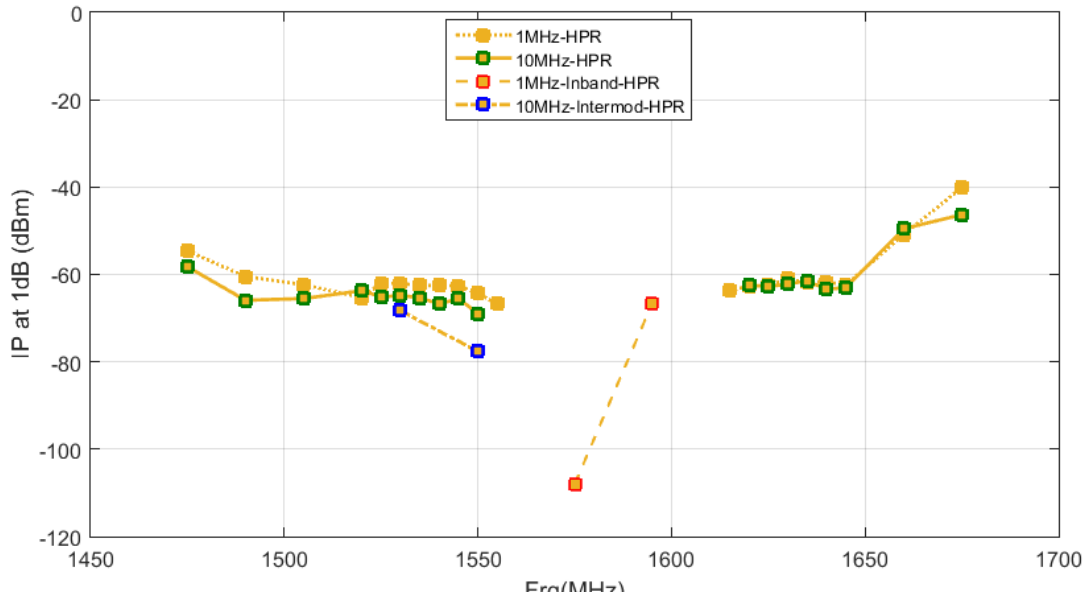


**Figure B-41: Summary of 1&10 MHz, 1 MHz In-band, and 10 MHz Intermod GPS L1 C/A – HPR Bounding Masks**



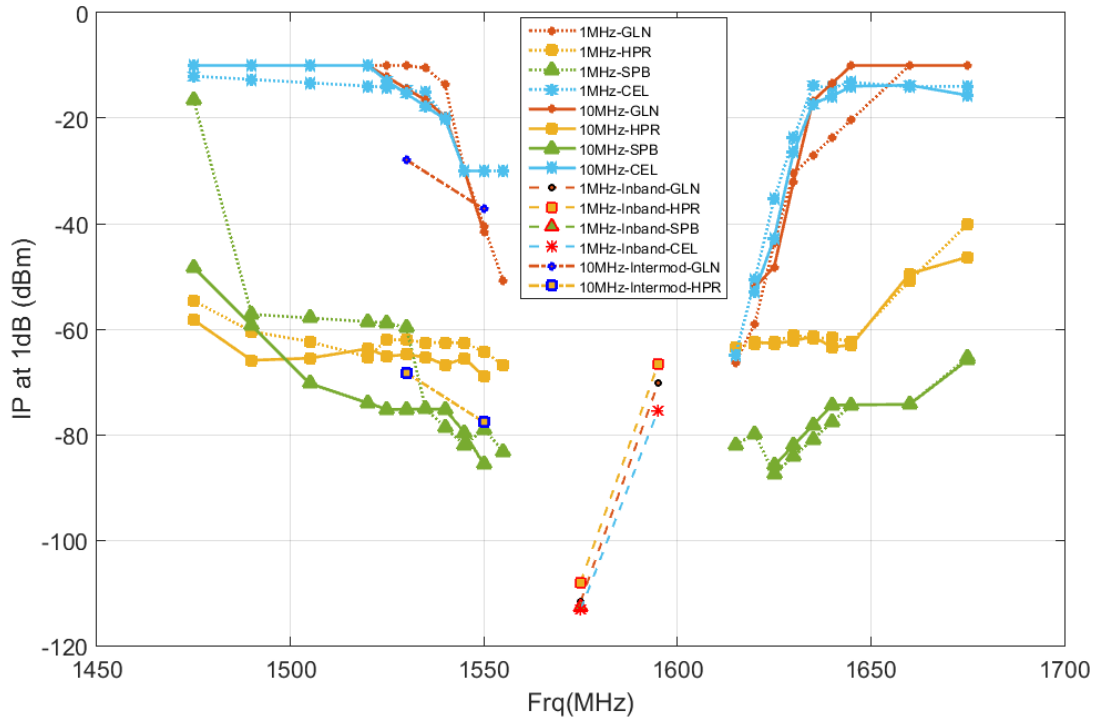
**Figure B-42: Summary of 1&10 MHz, 1 MHz In-band, and 10 MHz Intermod with Certified Aviation GPS L1 C/A Bounding Masks**

Note: Certified Aviation Mask has a value of -110 dBm for 1 MHz in band interference

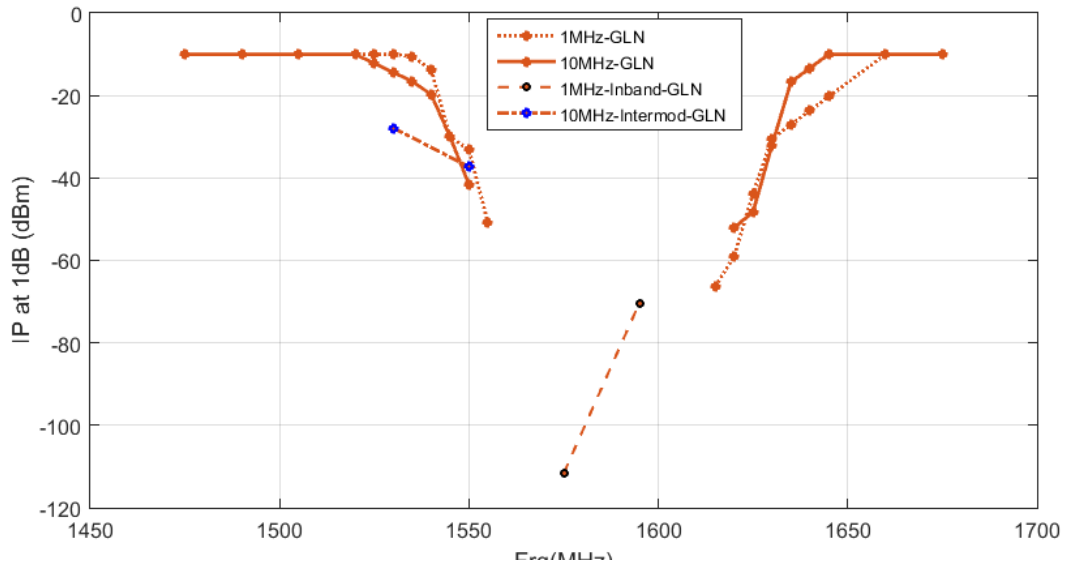


**Figure B-43: Summary of 1&10 MHz, 1 MHz In-band, and 10 MHz Intermod GPS L1 P – HPR Bounding Masks**

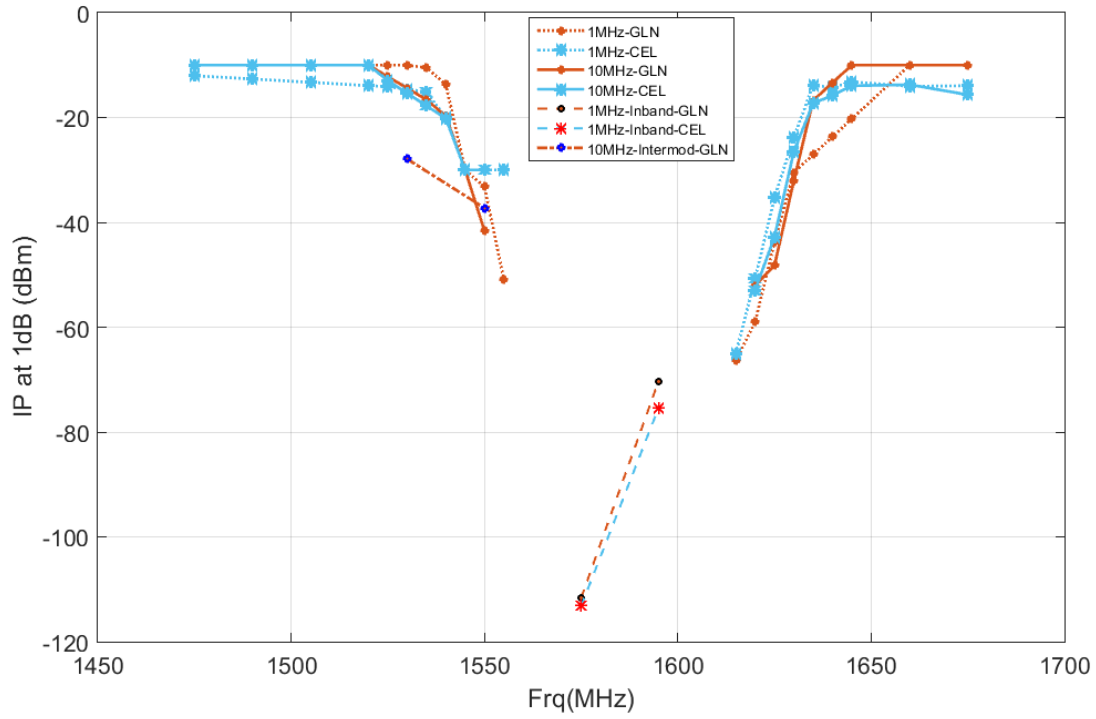




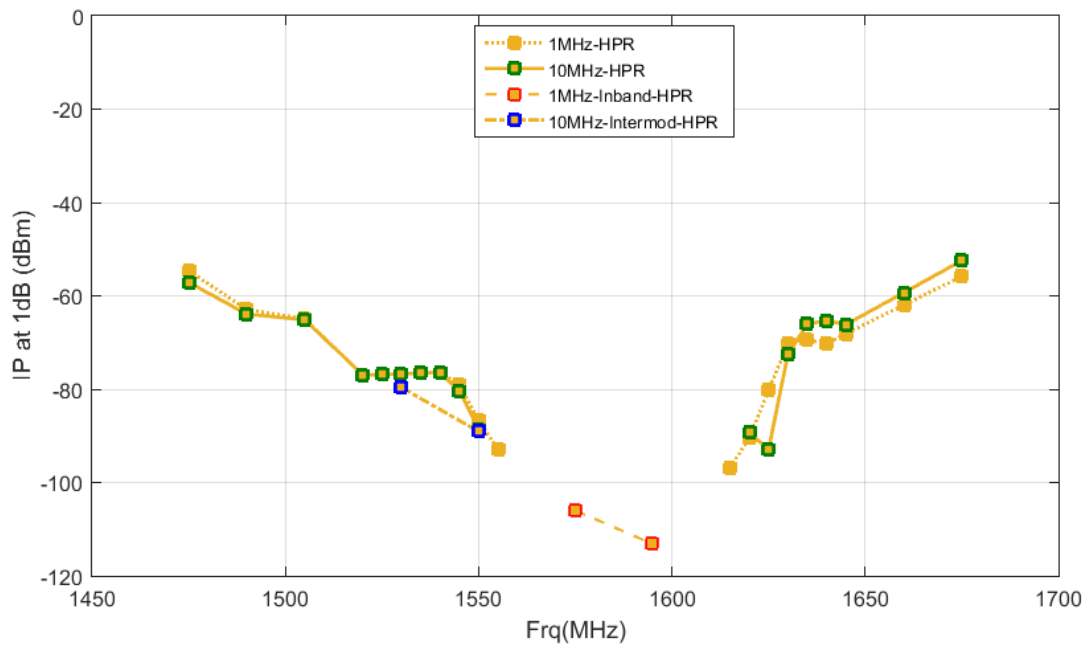
**Figure B-44: Summary of 1&10 MHz, 1 MHz In-band, and 10 MHz Intermod GPS L1 P Bounding Masks**



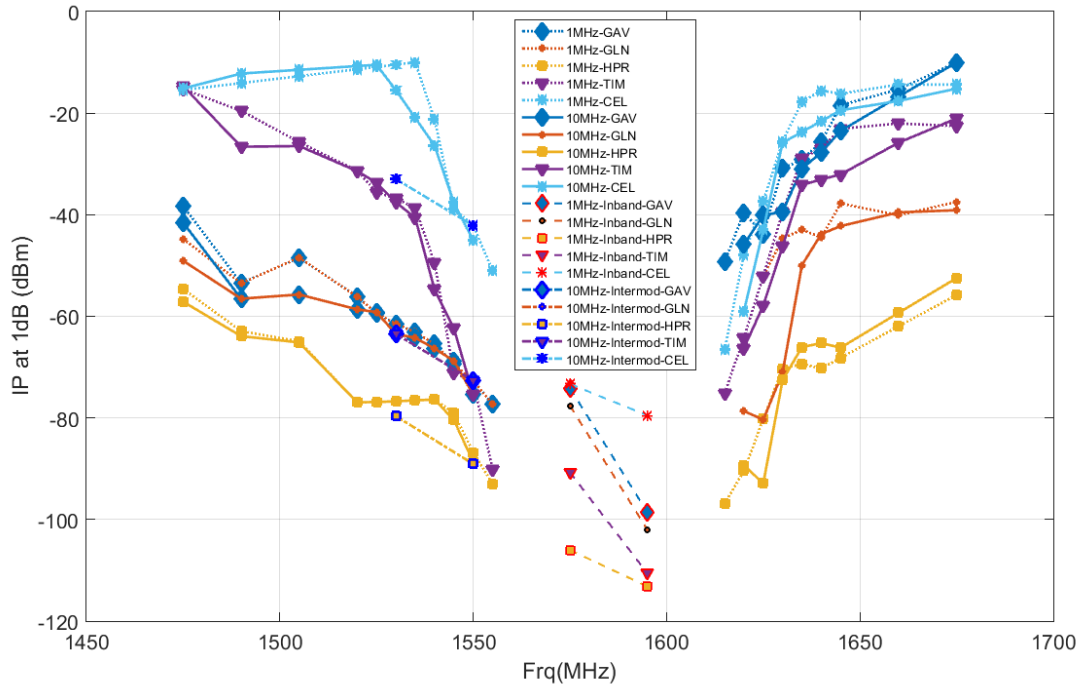
**Figure B-45: Summary of 1&10 MHz, 1 MHz In-band, and 10 MHz Intermod GPS L1 C - GLN Bounding Masks**



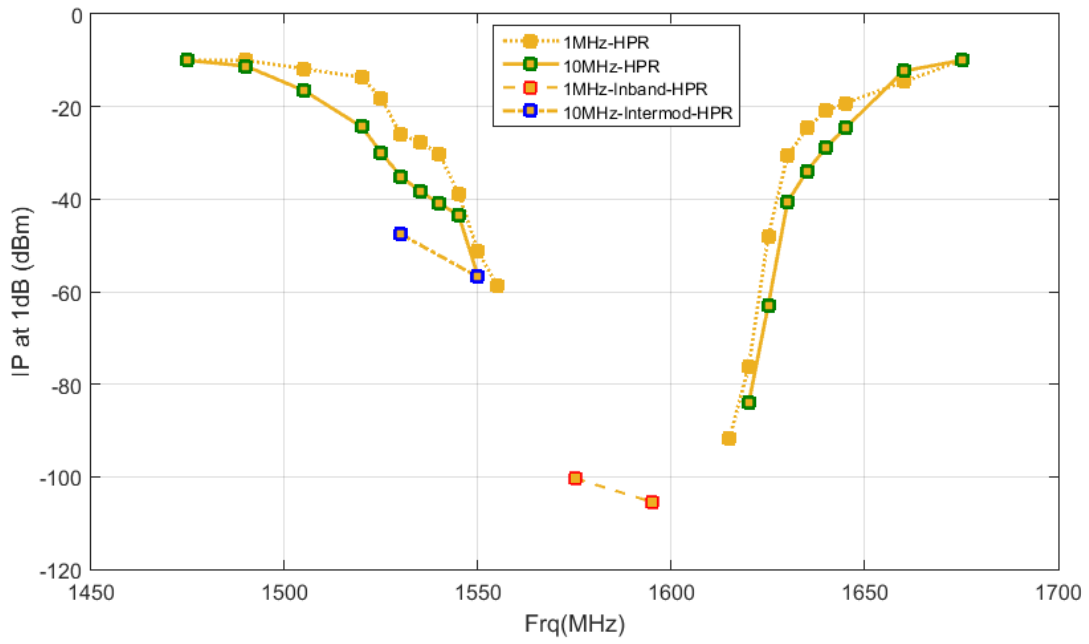
**Figure B-46: Summary of 1&10 MHz, 1 MHz In-band, and 10 MHz Intermod GPS L1 C Bounding Masks**



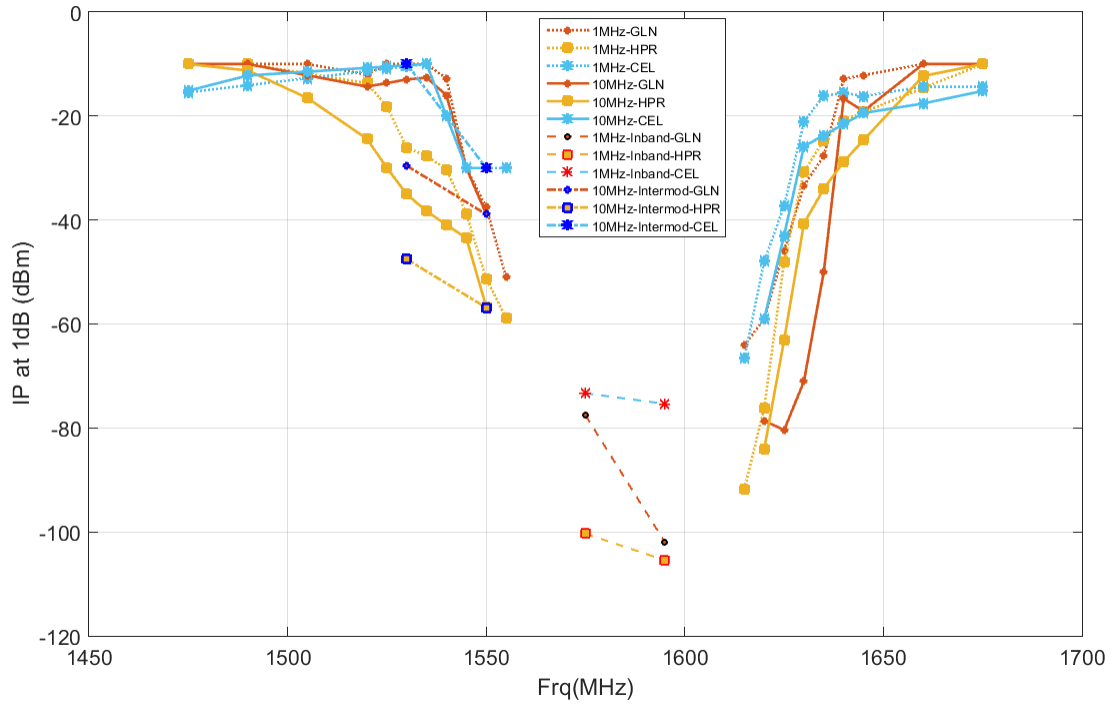
**Figure B-47: Summary of 1&10 MHz, 1 MHz In-band, and 10 MHz Intermod GLONASS L1 C - HPR Bounding Masks**



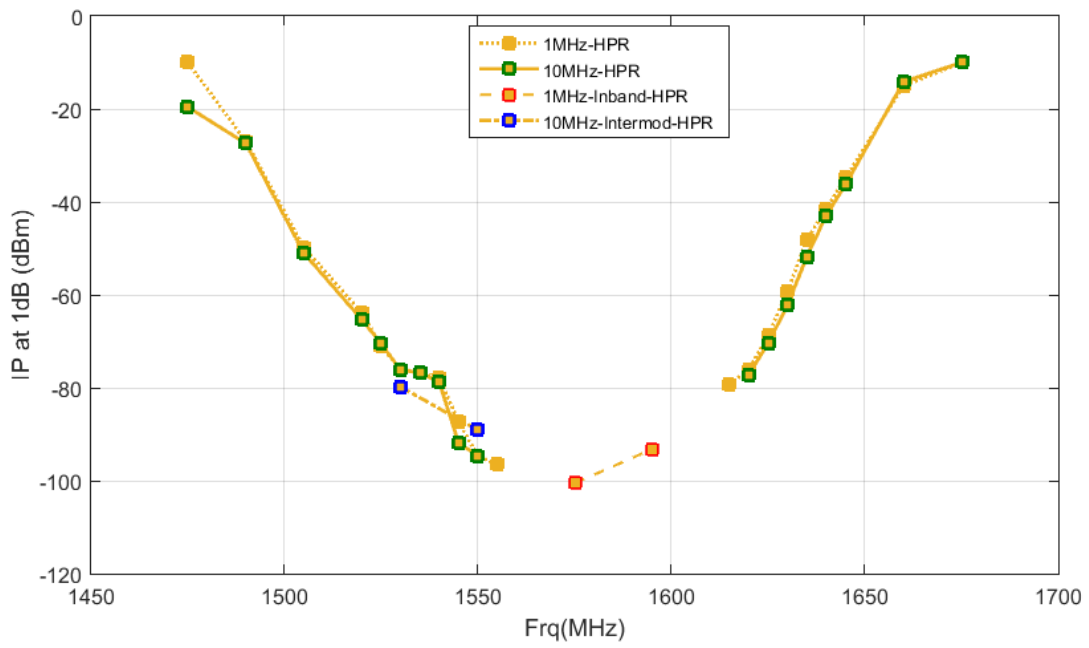
**Figure B-48: Summary of 1&10 MHz, 1 MHz In-band, and 10 MHz Intermod GLONASS L1 C Bounding Masks**



**Figure B-49: Summary of 1&10 MHz, 1 MHz In-band, and 10 MHz Intermod GLONASS L1 P - HPR Bounding Masks**

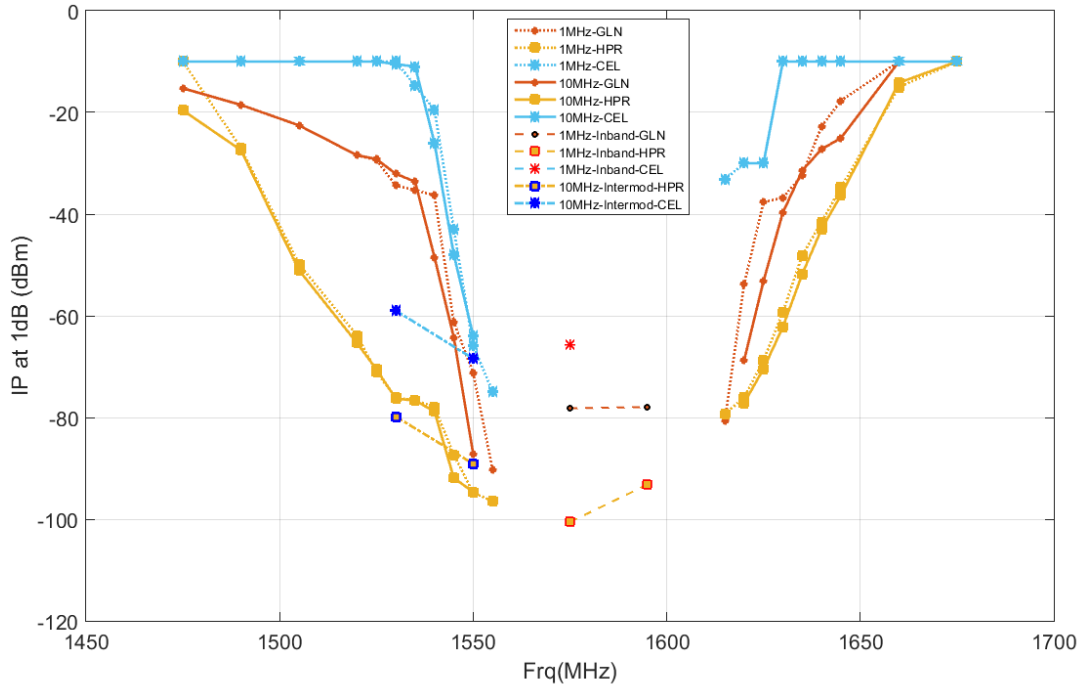


**Figure B-50: Summary of 1&10 MHz, 1 MHz In-band, and 10 MHz Intermod GLONASS L1 P Bounding Masks**

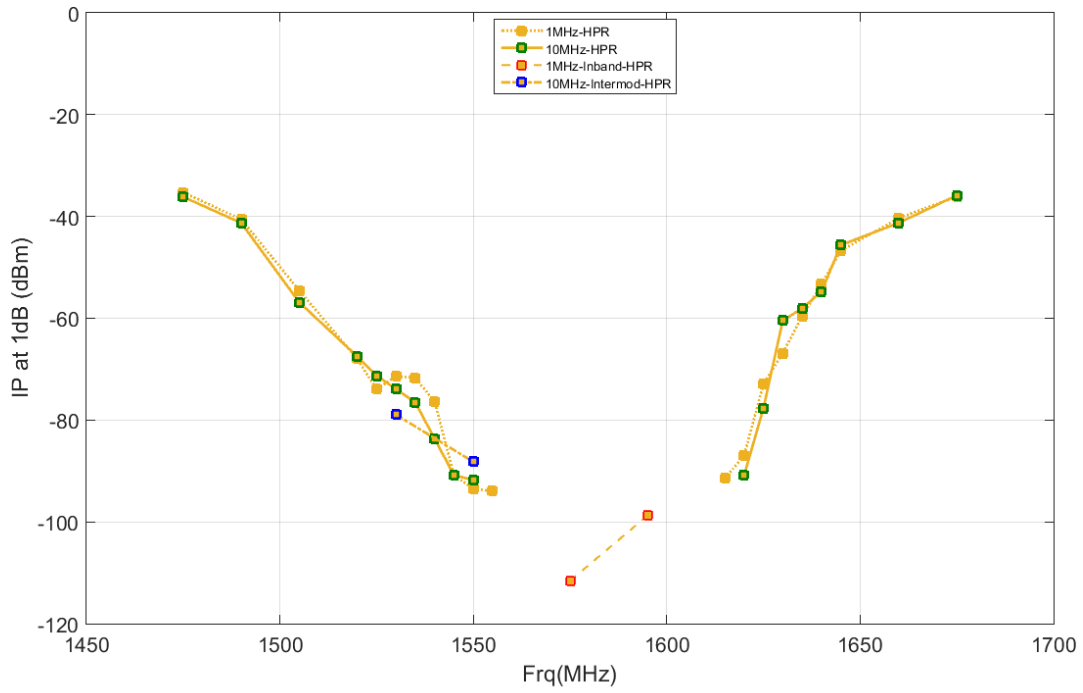


**Figure B-51: Summary of 1&10 MHz, 1 MHz In-band, and 10 MHz Intermod BeiDou B1 I - HPR Bounding Masks**

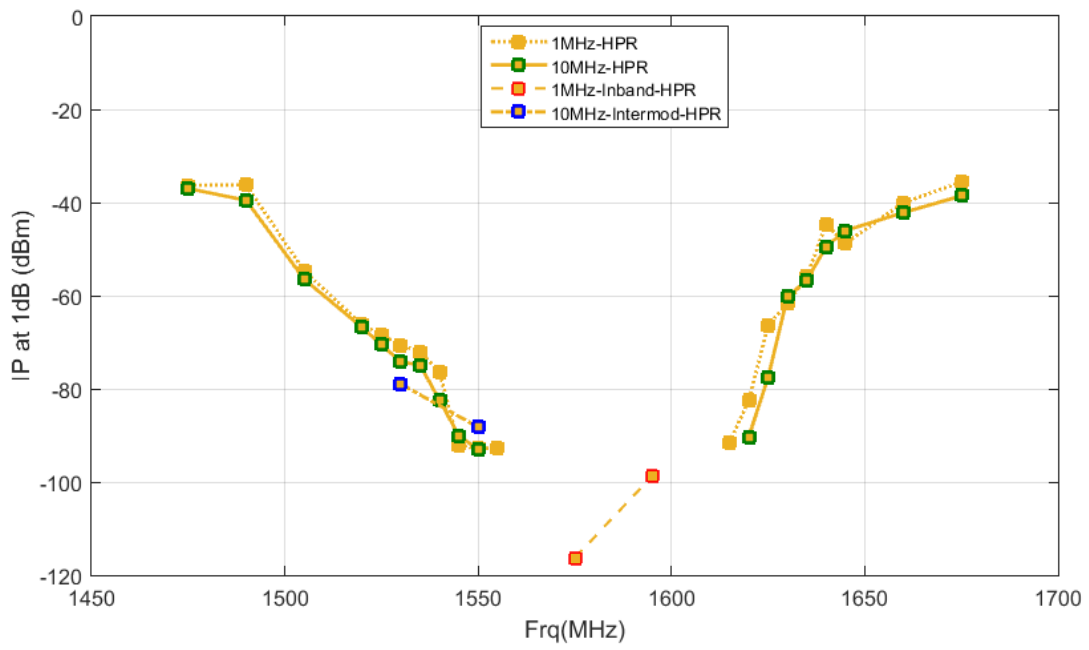




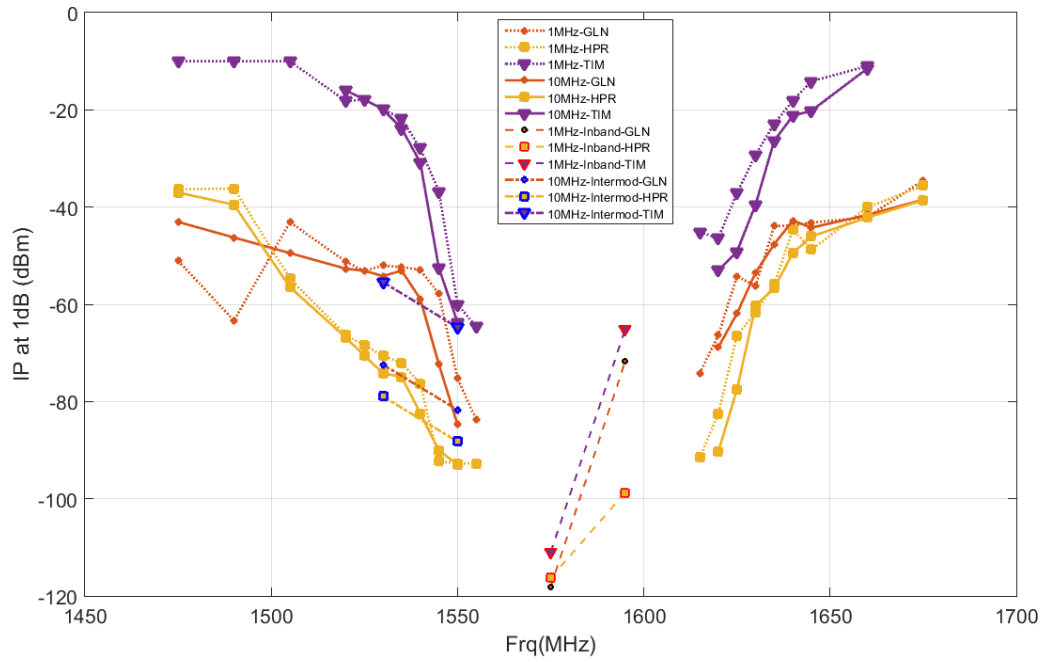
**Figure B-52: Summary of 1&10 MHz, 1 MHz In-band, and 10 MHz Intermod BeiDou B1 I Bounding Masks**



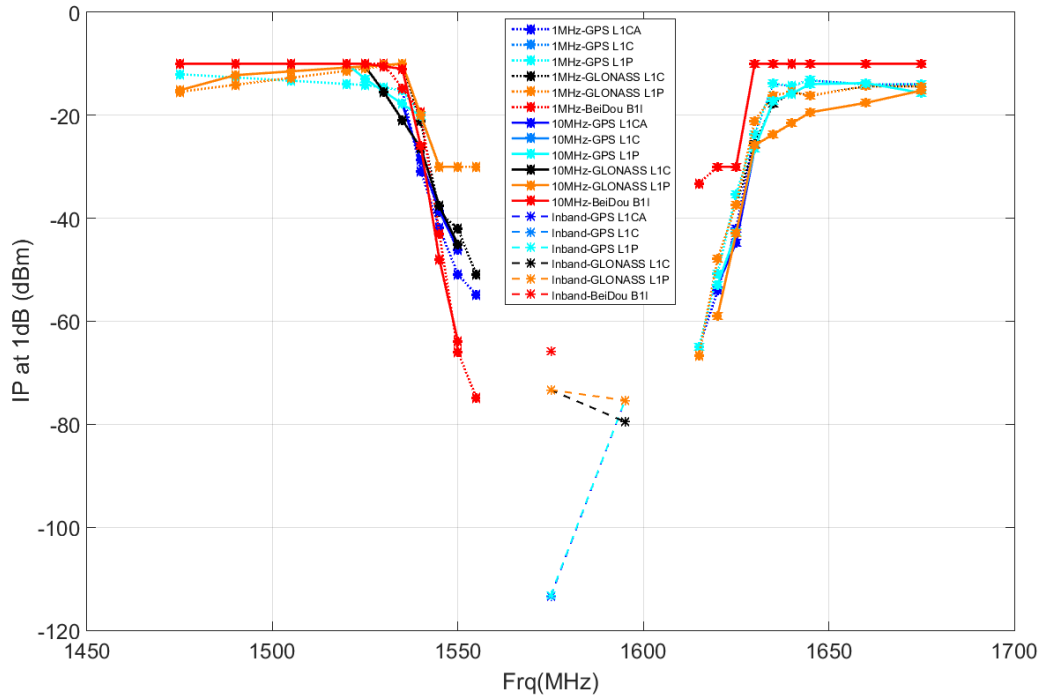
**Figure B-53: Summary of 1&10 MHz, 1 MHz In-band, and 10 MHz Intermod Galileo E1 BC Bounding Masks**



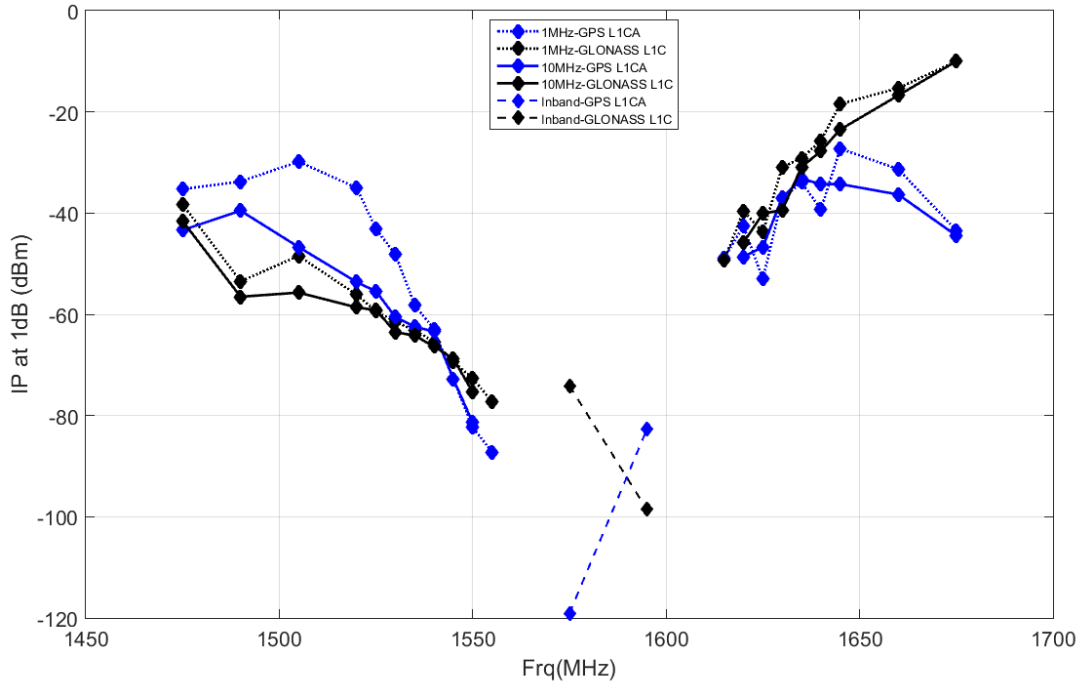
**Figure B-54: Summary of 1&10 MHz, 1 MHz In-band, and 10 MHz Intermod SBAS L1 C/A - HPR Bounding Masks**



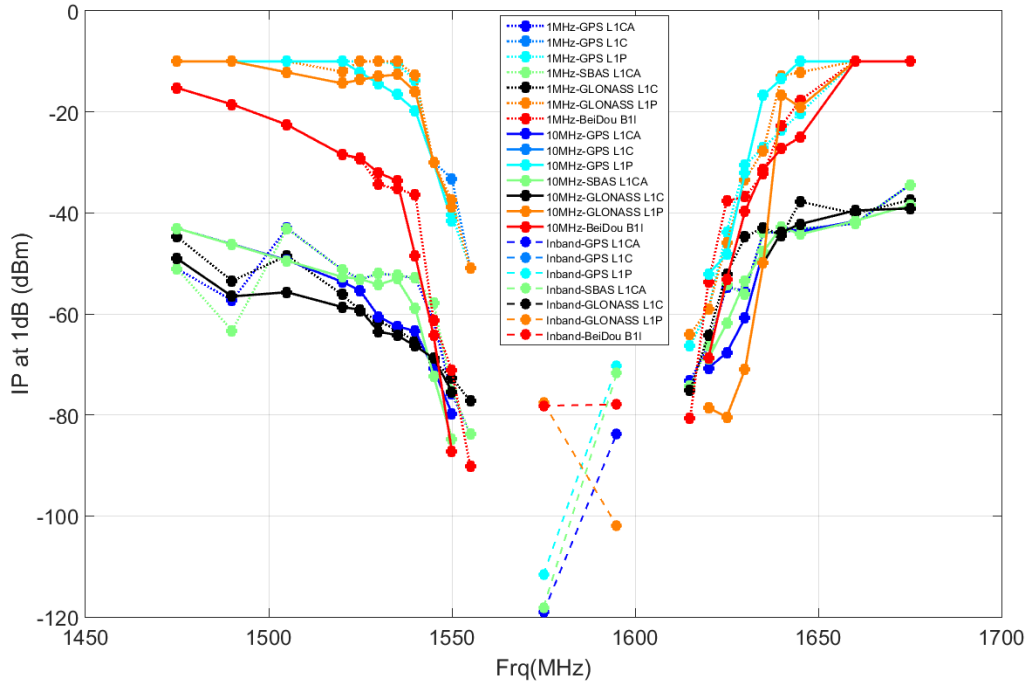
**Figure B-55: Summary of 1&10 MHz, 1 MHz In-band, and 10 MHz Intermod SBAS L1 C/A Bounding Masks**



**Figure B-56: Summary of Cellular Bounding Masks for 1 & 10 MHz, 1 MHz In-band, and 10 MHz Intermod**

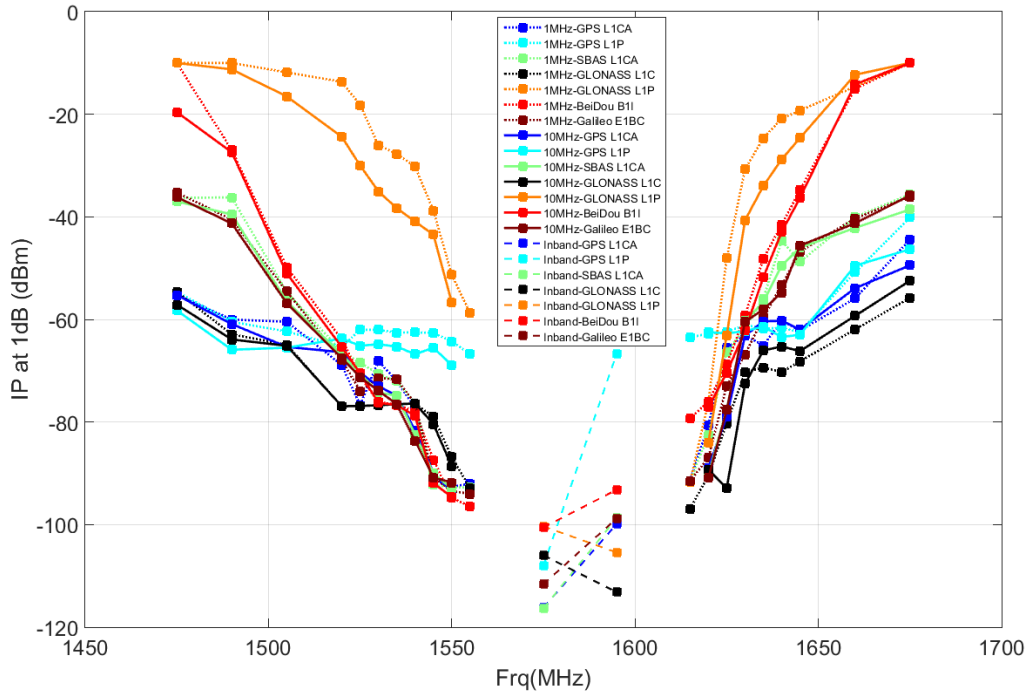


**Figure B-57: Summary of General Aviation Bounding Masks for 1 & 10 MHz, 1 MHz In-band, and 10 MHz Intermod**



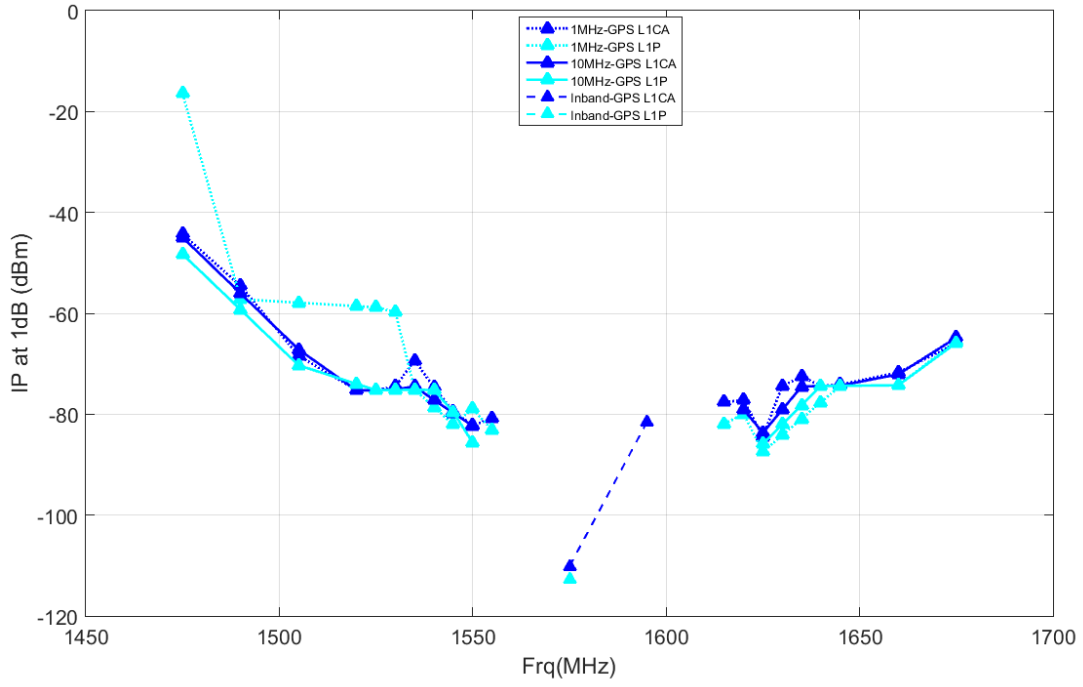
**Figure B-58: Summary of General Location Navigation Bounding Masks for 1 & 10 MHz, 1 MHz In-band, and 10 MHz Intermod**

Figure B-59 compares the ITMs across all emulated GNSS signal types for the HPR receiver category. The receive interference level from an LTE type signal should not exceed any of the masks in if all GNSS operation is to be ensured for the HPR category.



**Figure B-59: Summary of High Precision Bounding Masks for 1 & 10 MHz, 1 MHz In-band, and 10 MHz Intermod**





**Figure B-60: Summary of Space Based Bounding Masks for 1 & 10 MHz, 1 MHz In-band, and 10 MHz Intermod**

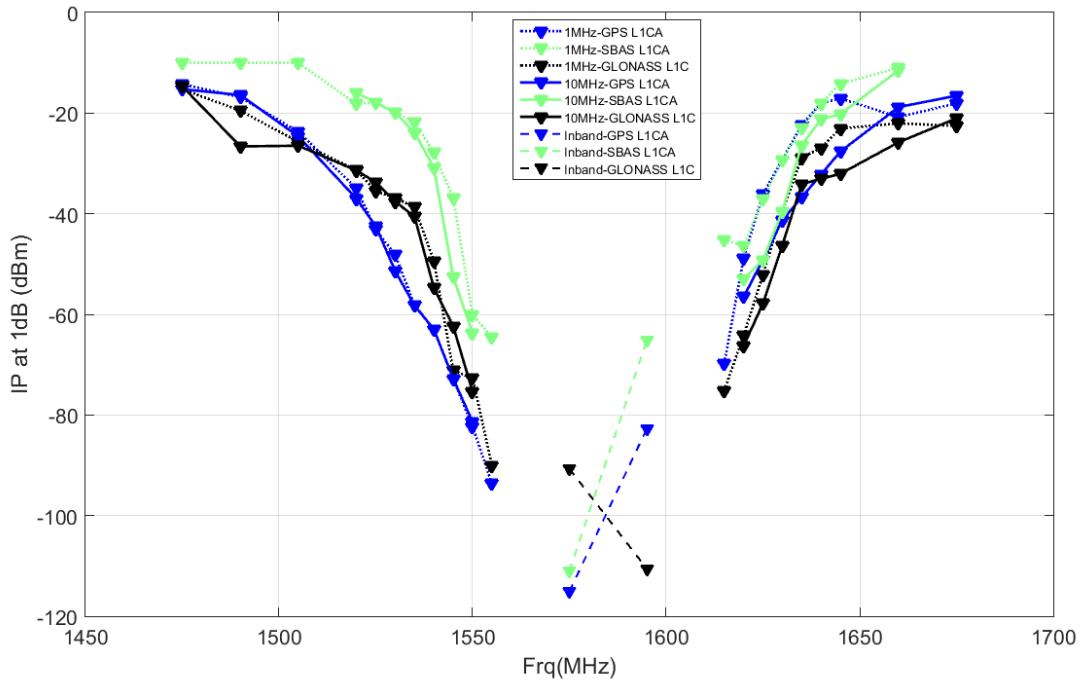


**Figure B-61: Summary of Timing Bounding Masks for 1 & 10 MHz, 1 MHz In-band, and 10 MHz Intermod**



## **APPENDIX C**

### **LOSS OF LOCK RESULTS**

# TABLE OF CONTENTS

TABLE OF CONTENTS.....	2
LIST OF FIGURES .....	4
LIST OF TABLES.....	5
REFERENCES .....	6
APPENDIX.....	7
Appendix C. Loss of Lock Results.....	7
C.1 Summary of Bounding Masks.....	7
C.1.1 GPS L1 C/A.....	7
C.1.2 GPS L1 P .....	8
C.1.3 GPS L1 C.....	9
C.1.4 GLONASS L1 C.....	10
C.1.5 GLONASS L1 P .....	11
C.1.6 BeiDou B1I.....	12
C.1.7 Galileo E1 BC.....	13
C.1.8 SBAS L1 C/A .....	14
C.2 Summary of Loss-of-Lock Analysis .....	15
C.2.1 GPS L1 C/A.....	15
C.2.1.1 Nominal SVs.....	15
C.2.1.2 Low Elevation SVs .....	17
C.2.2 GPS L1 P .....	19
C.2.2.1 Nominal SVs.....	19
C.2.2.2 Low Elevation SVs .....	21
C.2.3 GPS L1 C.....	24
C.2.3.1 Nominal SVs.....	24
C.2.3.2 Low Elevation SVs .....	26
C.2.4 GLONASS L1 C.....	29
C.2.4.1 Nominal SVs.....	29

C.2.4.2	Low Elevation SVs .....	31
C.2.5	GLONASS L1 P .....	34
C.2.5.1	Nominal SVs .....	34
C.2.5.2	Low Elevation SVs .....	36
C.2.6	BeiDou B1I.....	38
C.2.6.1	Nominal SVs .....	38
C.2.6.2	Low Elevation SVs .....	40
C.2.7	Galileo E1 BC.....	43
C.2.7.1	Nominal SVs .....	43
C.2.7.2	Low Elevation SVs .....	45
C.2.8	SBAS L1 C/A .....	47
C.2.8.1	Nominal SVs .....	47

## LIST OF FIGURES

Figure C-1: Bounding Masks for GPS L1 C/A with 10 MHz LTE Interference.....	7
Figure C-2: Bounding Masks for GPS L1 P with 10 MHz LTE Interference .....	8
Figure C-3: Bounding Masks for GPS L1 C with 10 MHz LTE Interference.....	9
Figure C-4: Bounding Masks for GLONASS L1 C with 10 MHz LTE Interference.....	10
Figure C-5: Bounding Masks for GLONASS L1 P with 10 MHz LTE Interference .....	11
Figure C-6: Bounding Masks for BeiDou B1I with 10 MHz LTE Interference.....	12
Figure C-7: Bounding Masks for Galileo E1 BC with 10 MHz LTE Interference.....	13
Figure C-8: Bounding Masks for SBAS L1 C/A with 10 MHz LTE Interference .....	14
Figure C-9: Nominal SVs (a) GPS L1 C/A Bounding Masks and (b) GPS L1 C/A Median .....	16
Figure C-10: Low Elevation SVs (a) GPS L1 C/A Bounding Masks and (b) GPS L1 C/A Median .....	18
Figure C-11: Nominal SVs (a) GPS L1 P Bounding Masks and (b) GPS L1 P Median.....	21
Figure C-12: Low Elevation SVs (a) GPS L1 P Bounding Masks and (b) GPS L1 P Median ...	23
Figure C-13: Nominal SVs (a) GPS L1 C Bounding Masks and (b) GPS L1 C Median .....	26
Figure C-14: Low Elevation SVs (a) GPS L1 C Bounding Masks and (b) GPS L1 C Median ..	28
Figure C-15: Nominal SVs (a) GLONASS L1 C Bounding Masks and (b) GLONASS L1 C Median .....	31
Figure C-16: Low Elevation SVs (a) GLONASS L1 C Bounding Masks and (b) GLONASS L1 C Median.....	33
Figure C-17: Nominal SVs (a) GLONASS L1 P Bounding Masks and (b) GLONASS L1 P Median .....	35
Figure C-18: Low Elevation SVs (a) GLONASS L1 P Bounding Masks and (b) GLONASS L1 P Median .....	37
Figure C-19: Nominal SVs (a) BeiDou B1I Bounding Masks and (b) BeiDou B1I Median .....	40
Figure C-20: Low Elevation SVs (a) BeiDou B1I Bounding Masks and (b) BeiDou B1I Median .....	42
Figure C-21: Nominal SVs (a) Galileo E1 BC Bounding Masks and (b) Galileo E1 BC Median .....	44
Figure C-22: Low Elevation SVs (a) Galileo E1 BC Bounding Masks and (b) Galileo E1 BC Median .....	46
Figure C-23: Nominal SVs (a) SBAS L1 C/A Bounding Masks and (b) SBAS L1 C/A Median	49

## LIST OF TABLES

Table C-1: Nominal SVs GPS L1 C/A Bounding Masks (dBm).....	15
Table C-2: Nominal SVs GPS L1 C/A Median (dBm).....	16
Table C-3: Low Elevation SVs GPS L1 C/A Bounding Masks (dBm).....	17
Table C-4: Low Elevation SVs GPS L1 C/A Median (dBm).....	18
Table C-5: Nominal SVs GPS L1 P Bounding Masks (dBm).....	19
Table C-6: Nominal SVs GPS L1 P Median (dBm).....	20
Table C-7: Low Elevation SVs GPS L1 P Bounding Masks (dBm).....	22
Table C-8: Low Elevation SVs GPS L1 P Median (dBm).....	23
Table C-9: Nominal SVs GPS L1 C Bounding Masks (dBm).....	24
Table C-10: Nominal SVs GPS L1 C Median (dBm).....	25
Table C-11: Low Elevation SVs GPS L1 C Bounding Masks (dBm).....	27
Table C-12: Low Elevation SVs GPS L1 P Median (dBm).....	28
Table C-13: Nominal SVs GLONASS L1 C Bounding Masks (dBm).....	29
Table C-14: Nominal SVs GLONASS L1 C Median (dBm).....	30
Table C-15: Low Elevation SVs GLONASS L1 C Bounding Masks (dBm).....	32
Table C-16: Low Elevation SVs GLONASS L1 C Median (dBm).....	33
Table C-17: Nominal SVs GLONASS L1 P Bounding Masks (dBm).....	34
Table C-18: Nominal SVs GLONASS L1 P Median (dBm).....	35
Table C-19: Low Elevation SVs GLONASS L1 P Bounding Masks (dBm).....	36
Table C-20: Low Elevation SVs GLONASS L1 P Median (dBm).....	37
Table C-21: Nominal SVs BeiDou B1I Bounding Masks (dBm).....	38
Table C-22: Nominal SVs BeiDou B1I Median (dBm).....	39
Table C-23: Low Elevation SVs BeiDou B1I Bounding Masks (dBm).....	41
Table C-24: Low Elevation SVs BeiDou B1I Median (dBm).....	42
Table C-25: Nominal SVs Galileo E1 BC Bounding Masks (dBm).....	43
Table C-26: Nominal SVs Galileo E1 BC Median (dBm).....	44
Table C-27: Low Elevation SVs Galileo E1 BC Bounding Masks (dBm).....	45
Table C-28: Low Elevation SVs Galileo E1 BC Median (dBm).....	46
Table C-29: Nominal SVs SBAS L1 C/A Bounding Masks (dBm).....	47
Table C-30: Nominal SVs SBAS L1 C/A Median (dBm).....	48



## **REFERENCES**

**There are no sources in the current document.**

# APPENDIX

## Appendix C. Loss of Lock Results

### C.1 Summary of Bounding Masks

#### C.1.1 GPS L1 C/A

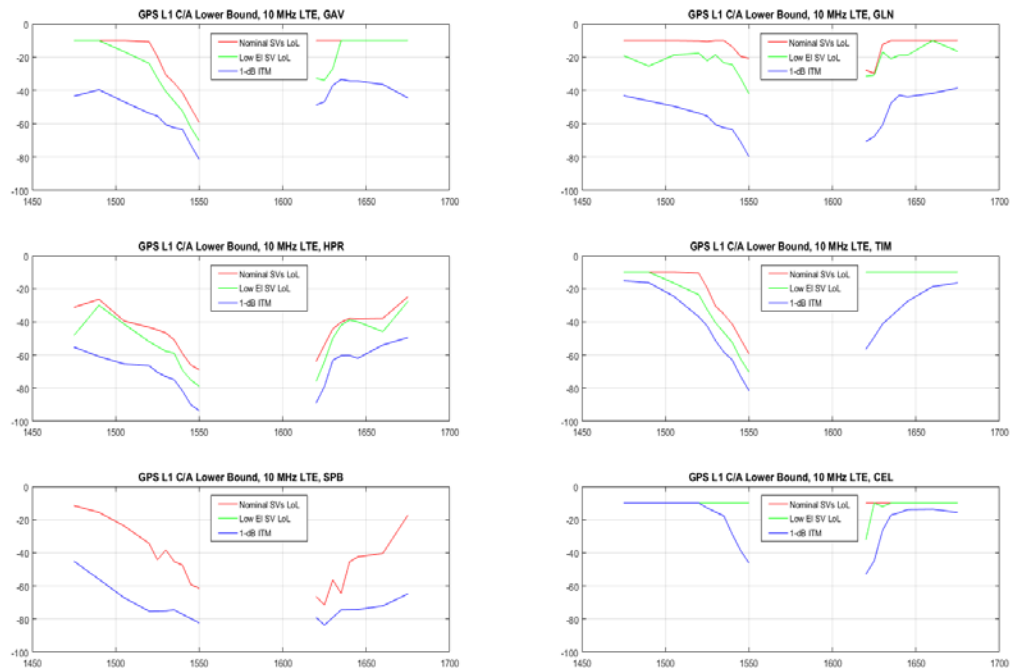
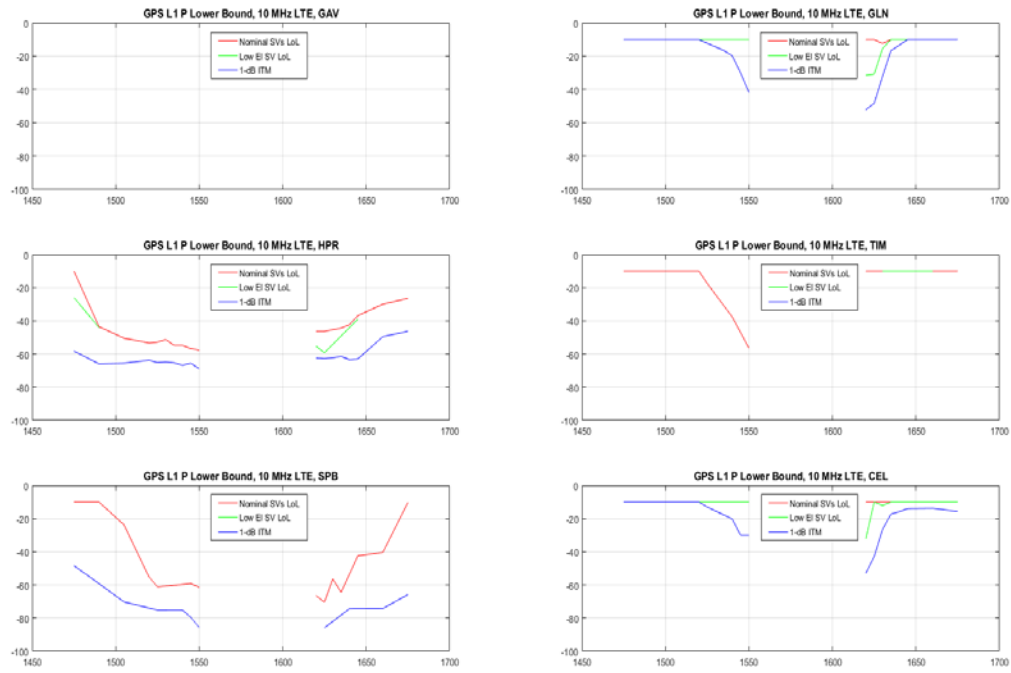


Figure C-1: Bounding Masks for GPS L1 C/A with 10 MHz LTE Interference

## C.1.2 GPS L1 P



**Figure C-2: Bounding Masks for GPS L1 P with 10 MHz LTE Interference**

### C.1.3 GPS L1 C

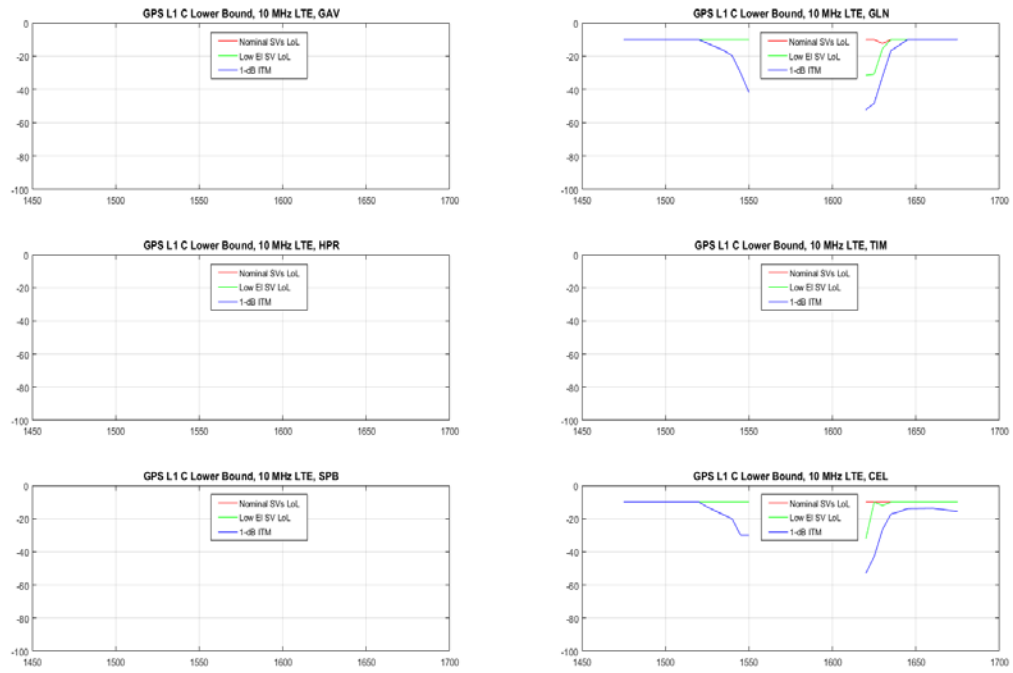


Figure C-3: Bounding Masks for GPS L1 C with 10 MHz LTE Interference

## C.1.4 GLONASS L1 C

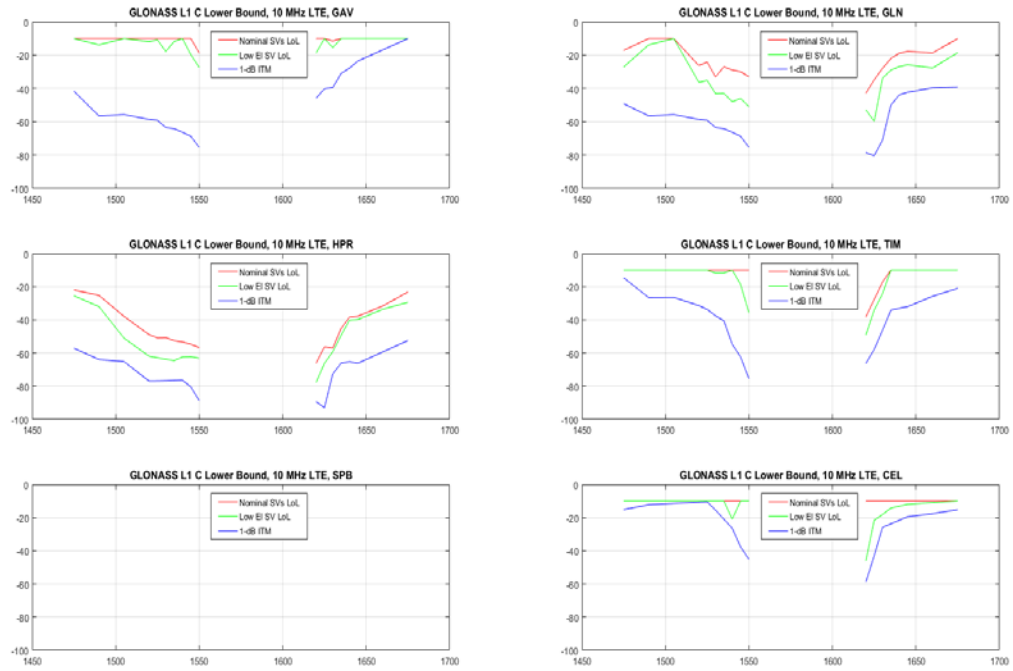


Figure C-4: Bounding Masks for GLONASS L1 C with 10 MHz LTE Interference

## C.1.5 GLONASS L1 P

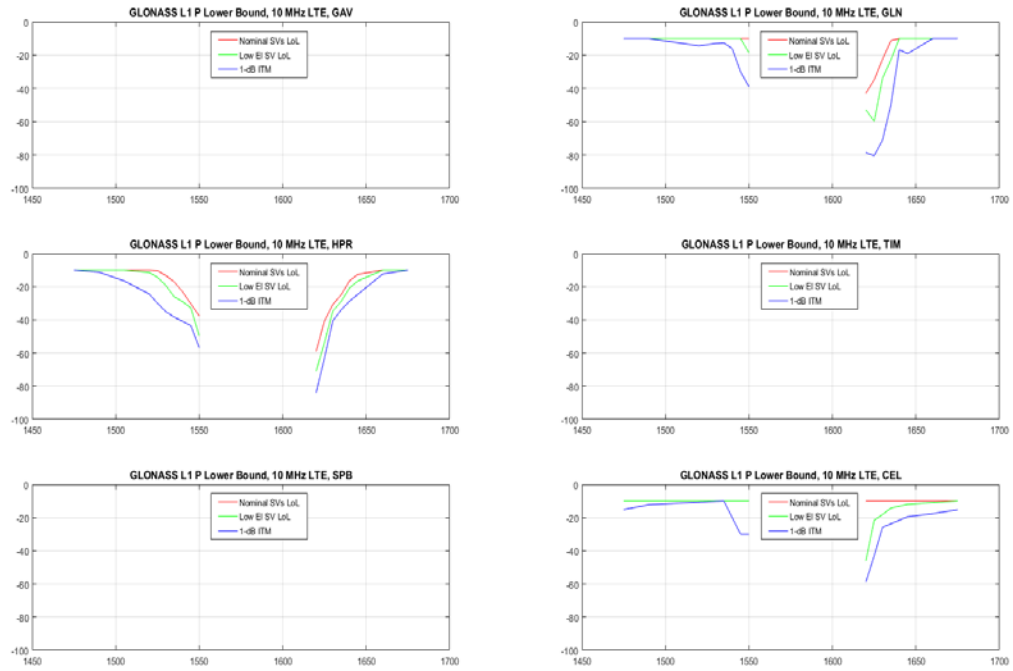


Figure C-5: Bounding Masks for GLONASS L1 P with 10 MHz LTE Interference

## C.1.6 BeiDou B1I

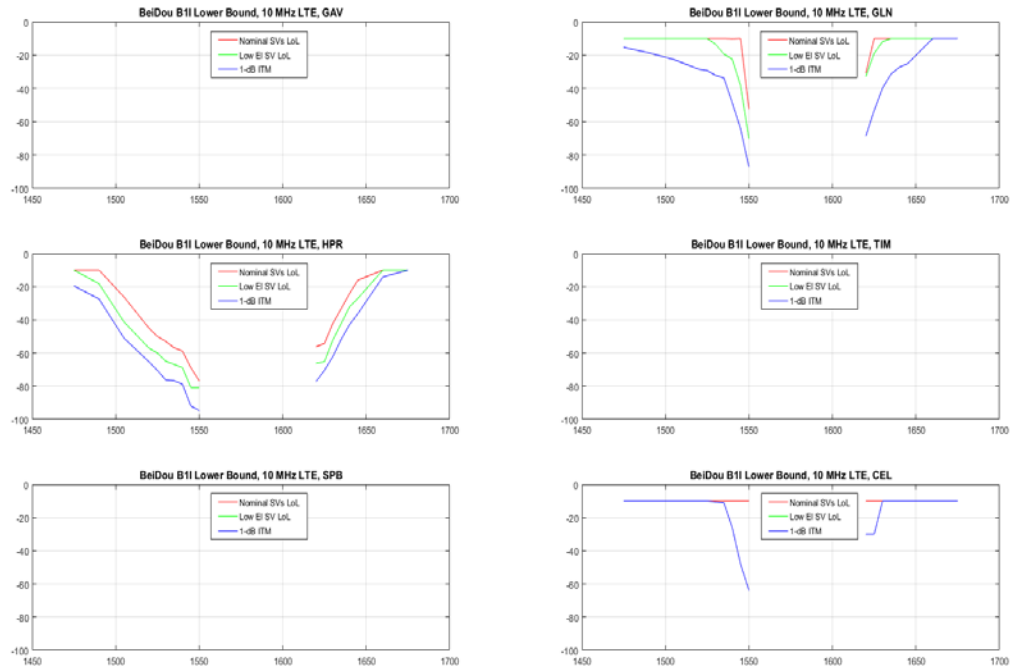


Figure C-6: Bounding Masks for BeiDou B1I with 10 MHz LTE Interference

## C.1.7 Galileo E1 BC

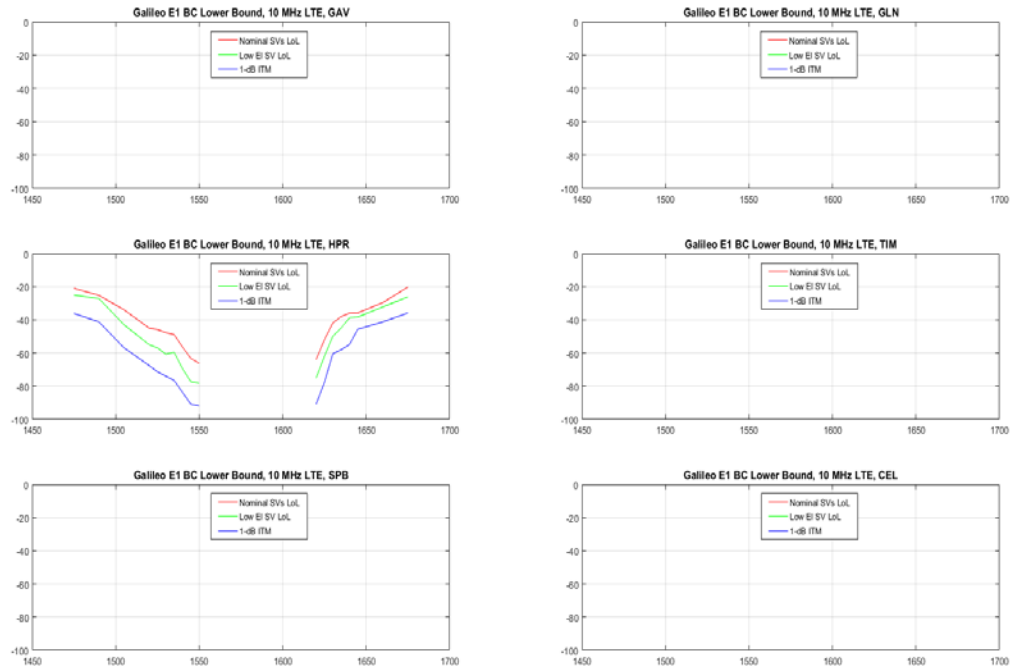


Figure C-7: Bounding Masks for Galileo E1 BC with 10 MHz LTE Interference



## C.1.8 SBAS L1 C/A

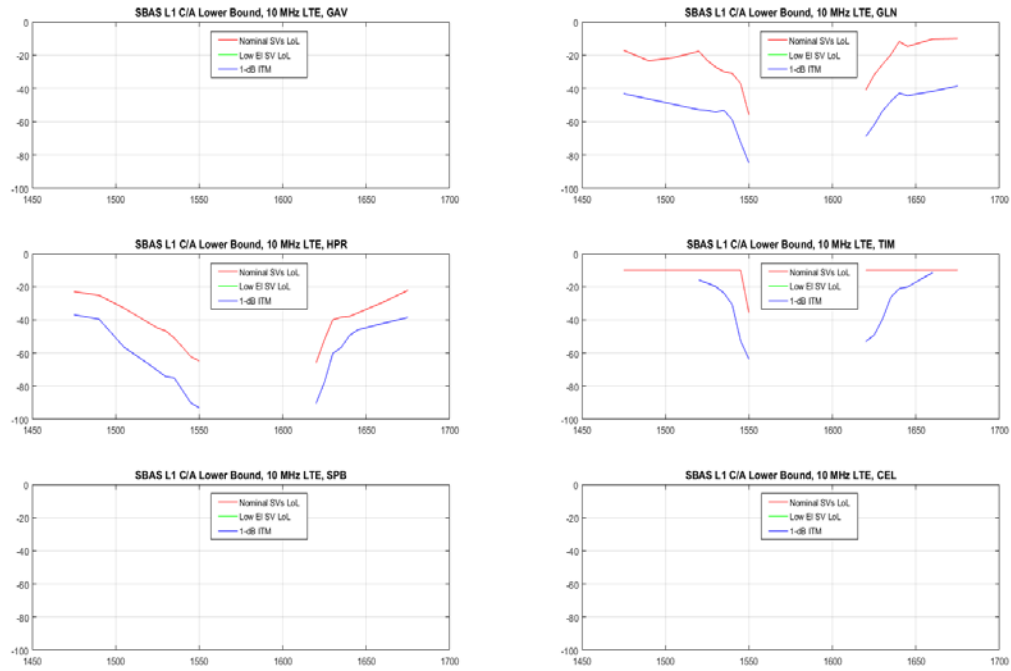


Figure C-8: Bounding Masks for SBAS L1 C/A with 10 MHz LTE Interference

## C.2 Summary of Loss-of-Lock Analysis

### C.2.1 GPS L1 C/A

#### C.2.1.1 Nominal SVs

Loss-of-Lock ITM computed using only “nominally” powered GPS signals

**Table C-1: Nominal SVs GPS L1 C/A Bounding Masks (dBm)**

Frequency (MHz)	GAV	GLN	HPR	TIM	SPB	CEL
1475	-9.999	-9.999	-31.2458	-9.999	-11.5239	-9.999
1490	-9.999	-9.999	-26.4447	-9.999	-15.602	-9.999
1505	-9.999	-9.999	-39.4615	-9.999	-23.7284	-9.999
1520	-10.7094	-10.2192	-43.3004	-10.7094	-34.2901	-9.999
1525	-19.6251	-10.5456	-44.8713	-19.6251	-44.2341	-9.999
1530	-30.5543	-9.999	-46.7309	-30.5543	-38.2091	-9.999
1535	-35.399	-9.999	-50.8679	-35.399	-45.151	-9.999
1540	-41.3614	-13.7121	-59.1205	-41.3614	-47.3892	-9.999
1545	-50.3634	-19.4403	-66.0247	-50.3634	-59.2506	-9.999
1550	-59.2229	-20.705	-68.8667	-59.2229	-61.4683	-9.999
1620	-9.999	-27.7486	-63.9203	-9.999	-66.5055	-9.999
1625	-9.999	-29.7378	-53.9544	-9.999	-71.4891	-9.999
1630	-9.999	-12.4154	-44.3042	-9.999	-56.4729	-9.999
1635	-9.999	-9.999	-40.1698	-9.999	-64.5191	-9.999
1640	-9.999	-9.999	-37.9451	-9.999	-45.405	-9.999
1645	-9.999	-9.999	-38.1748	-9.999	-42.3688	-9.999
1660	-9.999	-9.999	-37.9123	-9.999	-40.2659	-9.999
1675	-9.999	-9.999	-24.847	-9.999	-17.1974	-9.999

**Table C-2: Nominal SVs GPS L1 C/A Median (dBm)**

Frequency (MHz)	GAV	GLN	HPR	TIM	SPB	CEL
1475	-9.999	-9.999	-9.999	-9.999	-10.7615	-9.999
1490	-9.999	-9.999	-9.999	-9.999	-12.8005	-9.999
1505	-9.999	-9.999	-9.999	-9.999	-16.8637	-9.999
1520	-9.999	-9.999	-13.4422	-9.999	-22.8703	-9.999
1525	-9.999	-9.999	-16.8264	-9.999	-31.8007	-9.999
1530	-9.999	-9.999	-21.2618	-9.999	-32.8139	-9.999
1535	-9.999	-9.999	-26.9407	-9.999	-45.151	-9.999
1540	-9.999	-9.999	-31.4524	-9.999	-45.8019	-9.999
1545	-9.999	-9.999	-34.4658	-9.999	-59.2506	-9.999
1550	-9.999	-9.999	-40.9653	-9.999	-59.3381	-9.999
1620	-9.999	-9.999	-36.5694	-9.999	-56.5085	-9.999
1625	-9.999	-9.999	-31.9266	-9.999	-59.0085	-9.999
1630	-9.999	-9.999	-22.2095	-9.999	-50.5324	-9.999
1635	-9.999	-9.999	-14.6811	-9.999	-64.5191	-9.999
1640	-9.999	-9.999	-10.551	-9.999	-38.9629	-9.999
1645	-9.999	-9.999	-9.999	-9.999	-42.3688	-9.999
1660	-9.999	-9.999	-9.999	-9.999	-26.3502	-9.999
1675	-9.999	-9.999	-9.999	-9.999	-13.5982	-9.999

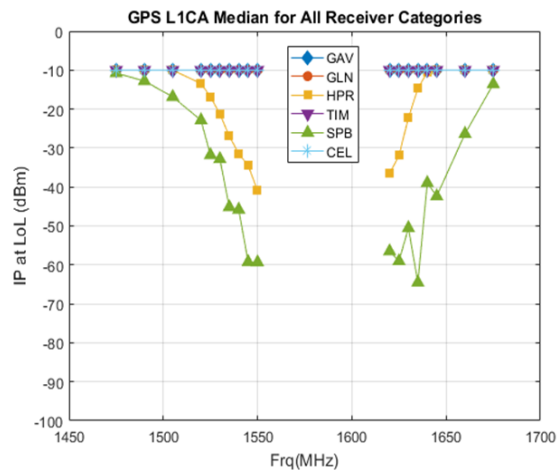
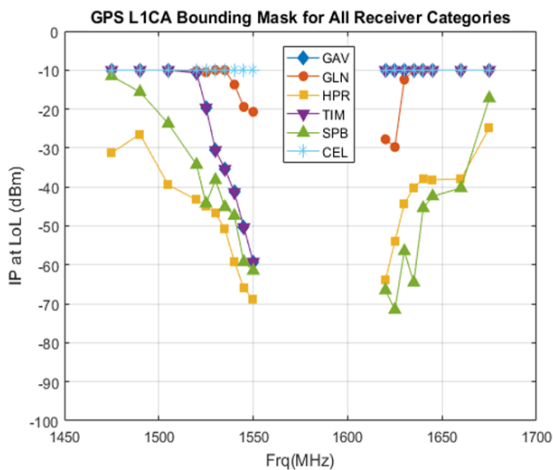


**Figure C-9: Nominal SVs (a) GPS L1 C/A Bounding Masks and (b) GPS L1 C/A Median**

### C.2.1.2 Low Elevation SVs

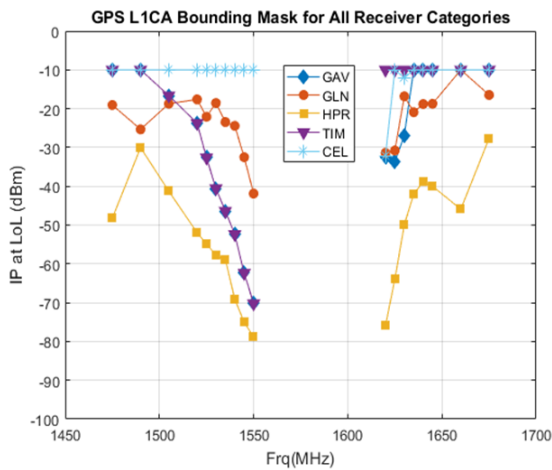
Loss-of-Lock ITM computed using only PRN-24 fixed at -10 dB relative to the nominal received power levels.

**Table C-3: Low Elevation SVs GPS L1 C/A Bounding Masks (dBm)**

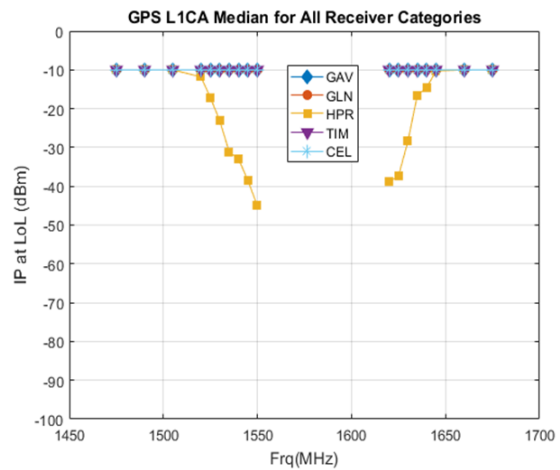
Frequency (MHz)	GAV	GLN	HPR	TIM	SPB	CEL
1475	-9.999	-19.0577	-48.2458	-9.999	NaN	-9.999
1490	-9.999	-25.3312	-30.0449	-9.999	NaN	-9.999
1505	-16.6328	-18.724	-41.279	-16.6328	NaN	-9.999
1520	-23.7094	-17.6091	-51.9467	-23.7094	NaN	-9.999
1525	-32.6251	-22.0921	-54.8713	-32.6251	NaN	-9.999
1530	-40.5543	-18.5543	-57.7309	-40.5543	NaN	-9.999
1535	-46.399	-23.445	-58.8679	-46.399	NaN	-9.999
1540	-52.3614	-24.4252	-69.1205	-52.3614	NaN	-9.999
1545	-62.3634	-32.507	-75.0247	-62.3634	NaN	-9.999
1550	-70.2229	-41.8765	-78.8667	-70.2229	NaN	-9.999
1620	-32.6403	-31.3943	-75.9203	-9.999	NaN	-32.1514
1625	-33.7292	-30.7686	-63.9544	-9.999	NaN	-9.999
1630	-26.8823	-16.82	-49.9352	-9.999	NaN	-12.0846
1635	-9.999	-20.9075	-42.0443	-9.999	NaN	-9.999
1640	-9.999	-18.7996	-38.8251	-9.999	NaN	-9.999
1645	-9.999	-18.7334	-40.0116	-9.999	NaN	-9.999
1660	-9.999	-9.999	-45.9123	-9.999	NaN	-9.999
1675	-9.999	-16.4705	-27.6572	-9.999	NaN	-9.999

**Table C-4: Low Elevation SVs GPS L1 C/A Median (dBm)**

Frequency (MHz)	GAV	GLN	HPR	TIM	SPB	CEL
1475	-9.999	-9.999	-9.999	-9.999	NaN	-9.999
1490	-9.999	-9.999	-9.999	-9.999	NaN	-9.999
1505	-9.999	-9.999	-9.999	-9.999	NaN	-9.999
1520	-9.999	-9.999	-11.8129	-9.999	NaN	-9.999
1525	-9.999	-9.999	-17.1529	-9.999	NaN	-9.999
1530	-9.999	-9.999	-23.1472	-9.999	NaN	-9.999
1535	-9.999	-9.999	-31.1458	-9.999	NaN	-9.999
1540	-9.999	-9.999	-32.9976	-9.999	NaN	-9.999
1545	-9.999	-9.999	-38.5907	-9.999	NaN	-9.999
1550	-9.999	-9.999	-45.0672	-9.999	NaN	-9.999
1620	-9.999	-9.999	-38.8637	-9.999	NaN	-9.999
1625	-9.999	-9.999	-37.3521	-9.999	NaN	-9.999
1630	-9.999	-9.999	-28.4308	-9.999	NaN	-9.999
1635	-9.999	-9.999	-16.5783	-9.999	NaN	-9.999
1640	-9.999	-9.999	-14.5126	-9.999	NaN	-9.999
1645	-9.999	-9.999	-10.2873	-9.999	NaN	-9.999
1660	-9.999	-9.999	-9.999	-9.999	NaN	-9.999
1675	-9.999	-9.999	-9.999	-9.999	NaN	-9.999



(a)



(b)

**Figure C-10: Low Elevation SVs (a) GPS L1 C/A Bounding Masks and (b) GPS L1 C/A Median**

## C.2.2 GPS L1 P

### C.2.2.1 Nominal SVs

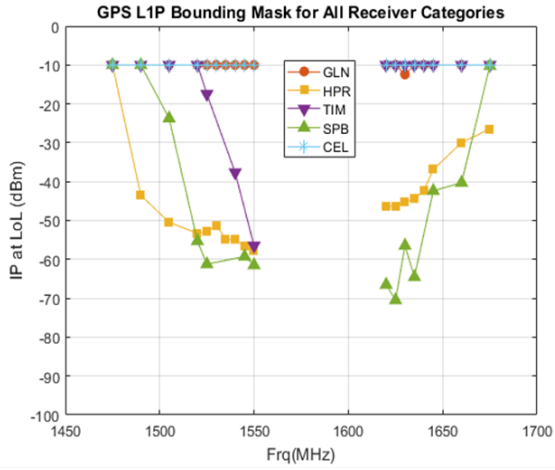
Loss-of-Lock ITM computed using only “nominally” powered GPS signals

**Table C-5: Nominal SVs GPS L1 P Bounding Masks (dBm)**

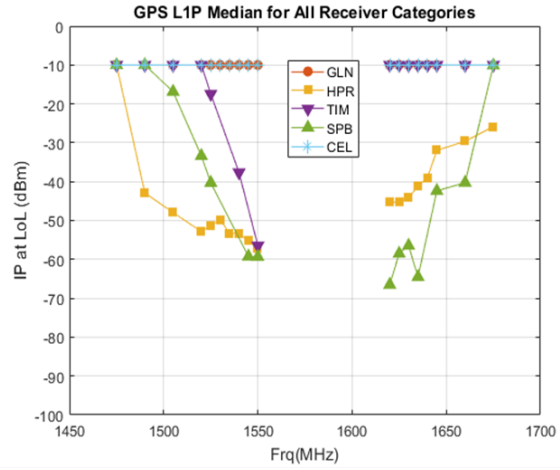
Frequency (MHz)	GAV	GLN	HPR	TIM	SPB	CEL
1475	NaN	-9.999	-9.999	-9.999	-9.999	-9.999
1490	NaN	-9.999	-43.5111	-9.999	-9.999	-9.999
1505	NaN	-9.999	-50.4615	-9.999	-23.7284	-9.999
1520	NaN	-9.999	-53.3004	-9.999	-55.2901	-9.999
1525	NaN	-9.999	-52.8098	-17.4427	-61.2341	-9.999
1530	NaN	-9.999	-51.2816	NaN	NaN	-9.999
1535	NaN	-9.999	-54.8046	NaN	NaN	-9.999
1540	NaN	-9.999	-54.7822	-37.657	NaN	-9.999
1545	NaN	-9.999	-56.7246	NaN	-59.2506	-9.999
1550	NaN	-9.999	-57.6585	-56.4707	-61.4683	-9.999
1620	NaN	-9.999	-46.3395	-9.999	-66.5055	-9.999
1625	NaN	-9.999	-46.3261	-9.999	-70.4891	-9.999
1630	NaN	-12.4154	-45.3042	-9.999	-56.4729	-9.999
1635	NaN	-9.999	-44.3723	-9.999	-64.5191	-9.999
1640	NaN	-9.999	-42.2717	-9.999	NaN	-9.999
1645	NaN	-9.999	-36.8869	-9.999	-42.3688	-9.999
1660	NaN	-9.999	-29.9614	-9.999	-40.2659	-9.999
1675	NaN	-9.999	-26.4567	-9.999	-10.1974	-9.999

**Table C-6: Nominal SVs GPS L1 P Median (dBm)**

Frequency (MHz)	GAV	GLN	HPR	TIM	SPB	CEL
1475	NaN	-9.999	-9.999	-9.999	-9.999	-9.999
1490	NaN	-9.999	-42.9099	-9.999	-9.999	-9.999
1505	NaN	-9.999	-47.9422	-9.999	-16.8637	-9.999
1520	NaN	-9.999	-52.8489	-9.999	-33.3703	-9.999
1525	NaN	-9.999	-51.2298	-17.4427	-40.3007	-9.999
1530	NaN	-9.999	-49.8352	NaN	NaN	-9.999
1535	NaN	-9.999	-53.2823	NaN	NaN	-9.999
1540	NaN	-9.999	-53.3135	-37.657	NaN	-9.999
1545	NaN	-9.999	-55.2629	NaN	-59.2506	-9.999
1550	NaN	-9.999	-57.2322	-56.4707	-59.3381	-9.999
1620	NaN	-9.999	-45.2663	-9.999	-66.5055	-9.999
1625	NaN	-9.999	-45.2341	-9.999	-58.5085	-9.999
1630	NaN	-9.999	-44.1922	-9.999	-56.4729	-9.999
1635	NaN	-9.999	-41.1038	-9.999	-64.5191	-9.999
1640	NaN	-9.999	-39.0043	-9.999	NaN	-9.999
1645	NaN	-9.999	-31.9579	-9.999	-42.3688	-9.999
1660	NaN	-9.999	-29.6232	-9.999	-40.2659	-9.999
1675	NaN	-9.999	-25.847	-9.999	-10.0982	-9.999



(a)



(b)

**Figure C-11: Nominal SVs (a) GPS L1 P Bounding Masks and (b) GPS L1 P Median**

### C.2.2.2 Low Elevation SVs

Loss-of-Lock ITM computed using only PRN-24 fixed at -10 dB relative to the nominal received power levels.



**Table C-7: Low Elevation SVs GPS L1 P Bounding Masks (dBm)**

Frequency (MHz)	GAV	GLN	HPR	TIM	SPB	CEL
1475	NaN	-9.999	-25.96	NaN	NaN	-9.999
1490	NaN	-9.999	-44.0449	NaN	NaN	-9.999
1505	NaN	-9.999	NaN	NaN	NaN	-9.999
1520	NaN	-9.999	NaN	NaN	NaN	-9.999
1525	NaN	-9.999	NaN	NaN	NaN	-9.999
1530	NaN	-9.999	NaN	NaN	NaN	-9.999
1535	NaN	-9.999	NaN	NaN	NaN	-9.999
1540	NaN	-9.999	NaN	NaN	NaN	-9.999
1545	NaN	-9.999	NaN	NaN	NaN	-9.999
1550	NaN	-9.999	NaN	NaN	NaN	-9.999
1620	NaN	-31.3943	-55.2663	NaN	NaN	-32.1514
1625	NaN	-30.7686	-59.2341	NaN	NaN	-9.999
1630	NaN	-15.4154	NaN	-9.999	NaN	-12.0846
1635	NaN	-9.999	NaN	NaN	NaN	-9.999
1640	NaN	-9.999	NaN	NaN	NaN	-9.999
1645	NaN	-9.999	-39.029	NaN	NaN	-9.999
1660	NaN	-9.999	NaN	-9.999	NaN	-9.999
1675	NaN	-9.999	NaN	NaN	-26.1974	-9.999

**Table C-8: Low Elevation SVs GPS L1 P Median (dBm)**

Frequency (MHz)	GAV	GLN	HPR	TIM	SPB	CEL
1475	NaN	-9.999	-25.96	NaN	NaN	-9.999
1490	NaN	-9.999	-44.0449	NaN	NaN	-9.999
1505	NaN	-9.999	NaN	NaN	NaN	-9.999
1520	NaN	-9.999	NaN	NaN	NaN	-9.999
1525	NaN	-9.999	NaN	NaN	NaN	-9.999
1530	NaN	-9.999	NaN	NaN	NaN	-9.999
1535	NaN	-9.999	NaN	NaN	NaN	-9.999
1540	NaN	-9.77771	NaN	NaN	NaN	-9.999
1545	NaN	-9.999	NaN	NaN	NaN	-9.999
1550	NaN	-9.999	NaN	NaN	NaN	-9.999
1620	NaN	-19.675	-55.2663	NaN	NaN	-26.0967
1625	NaN	-14.0983	-59.2341	NaN	NaN	-9.999
1630	NaN	-13.8262	NaN	-9.999	NaN	-11.0418
1635	NaN	-9.999	NaN	NaN	NaN	-9.999
1640	NaN	-9.999	NaN	NaN	NaN	-9.999
1645	NaN	-9.999	-39.029	NaN	NaN	-9.999
1660	NaN	-9.999	NaN	-9.999	NaN	-9.999
1675	NaN	-9.999	NaN	NaN	-18.0982	-9.999

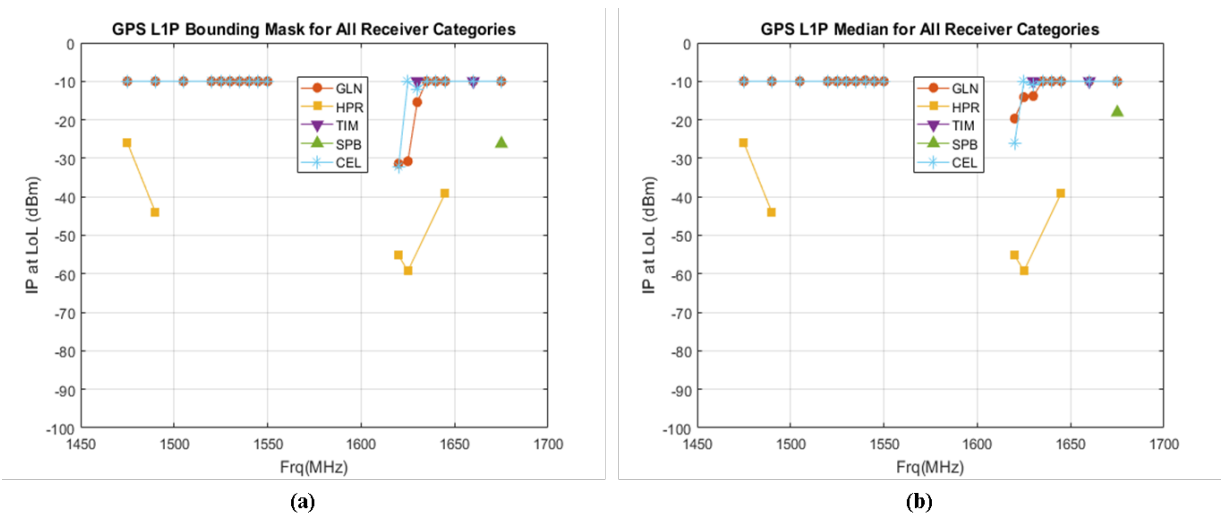


**Figure C-12: Low Elevation SVs (a) GPS L1 P Bounding Masks and (b) GPS L1 P Median**

### C.2.3 GPS L1 C

#### C.2.3.1 Nominal SVs

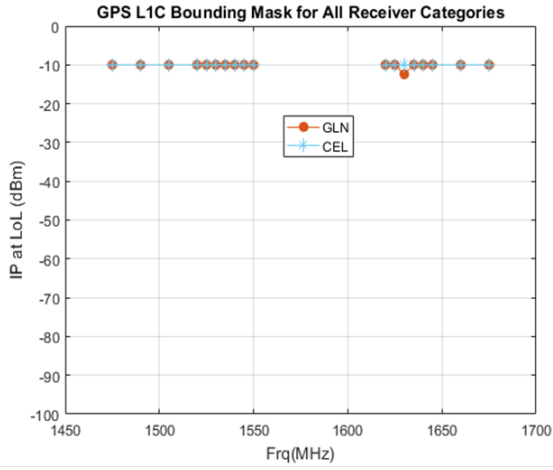
Loss-of-Lock ITM computed using only “nominally” powered GPS signals

**Table C-9: Nominal SVs GPS L1 C Bounding Masks (dBm)**

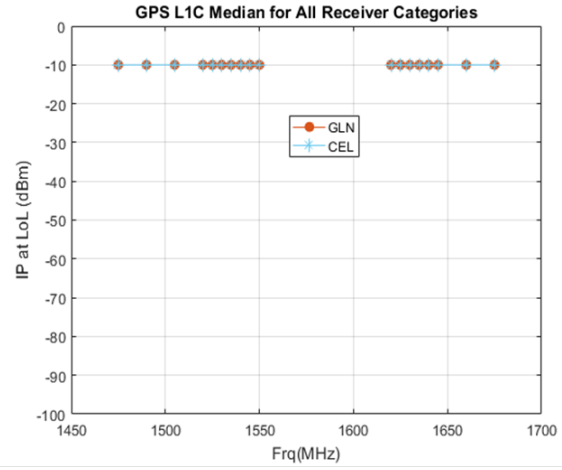
Frequency (MHz)	GAV	GLN	HPR	TIM	SPB	CEL
1475	NaN	-9.999	NaN	NaN	NaN	-9.999
1490	NaN	-9.999	NaN	NaN	NaN	-9.999
1505	NaN	-9.999	NaN	NaN	NaN	-9.999
1520	NaN	-9.999	NaN	NaN	NaN	-9.999
1525	NaN	-9.999	NaN	NaN	NaN	-9.999
1530	NaN	-9.999	NaN	NaN	NaN	-9.999
1535	NaN	-9.999	NaN	NaN	NaN	-9.999
1540	NaN	-9.999	NaN	NaN	NaN	-9.999
1545	NaN	-9.999	NaN	NaN	NaN	-9.999
1550	NaN	-9.999	NaN	NaN	NaN	-9.999
1620	NaN	-9.999	NaN	NaN	NaN	-9.999
1625	NaN	-9.999	NaN	NaN	NaN	-9.999
1630	NaN	-12.4154	NaN	NaN	NaN	-9.999
1635	NaN	-9.999	NaN	NaN	NaN	-9.999
1640	NaN	-9.999	NaN	NaN	NaN	-9.999
1645	NaN	-9.999	NaN	NaN	NaN	-9.999
1660	NaN	-9.999	NaN	NaN	NaN	-9.999
1675	NaN	-9.999	NaN	NaN	NaN	-9.999

**Table C-10: Nominal SVs GPS L1 C Median (dBm)**

Frequency (MHz)	GAV	GLN	HPR	TIM	SPB	CEL
1475	NaN	-9.999	NaN	NaN	NaN	-9.999
1490	NaN	-9.999	NaN	NaN	NaN	-9.999
1505	NaN	-9.999	NaN	NaN	NaN	-9.999
1520	NaN	-9.999	NaN	NaN	NaN	-9.999
1525	NaN	-9.999	NaN	NaN	NaN	-9.999
1530	NaN	-9.999	NaN	NaN	NaN	-9.999
1535	NaN	-9.999	NaN	NaN	NaN	-9.999
1540	NaN	-9.999	NaN	NaN	NaN	-9.999
1545	NaN	-9.999	NaN	NaN	NaN	-9.999
1550	NaN	-9.999	NaN	NaN	NaN	-9.999
1620	NaN	-9.999	NaN	NaN	NaN	-9.999
1625	NaN	-9.999	NaN	NaN	NaN	-9.999
1630	NaN	-9.999	NaN	NaN	NaN	-9.999
1635	NaN	-9.999	NaN	NaN	NaN	-9.999
1640	NaN	-9.999	NaN	NaN	NaN	-9.999
1645	NaN	-9.999	NaN	NaN	NaN	-9.999
1660	NaN	-9.999	NaN	NaN	NaN	-9.999
1675	NaN	-9.999	NaN	NaN	NaN	-9.999



(a)



(b)

**Figure C-13: Nominal SVs (a) GPS L1 C Bounding Masks and (b) GPS L1 C Median**

### C.2.3.2 Low Elevation SVs

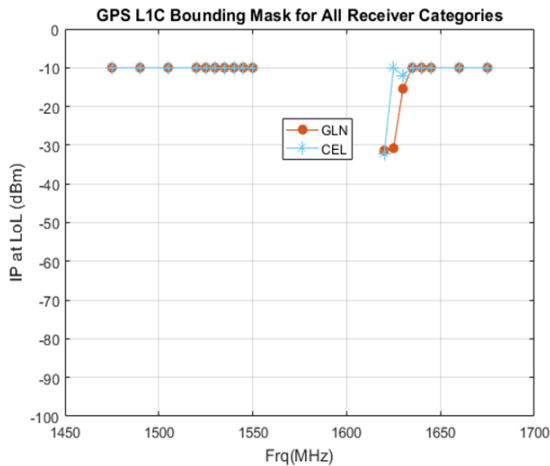
Loss-of-Lock ITM computed using only PRN-24 fixed at -10 dB relative to the nominal received power levels.

**Table C-11: Low Elevation SVs GPS L1 C Bounding Masks (dBm)**

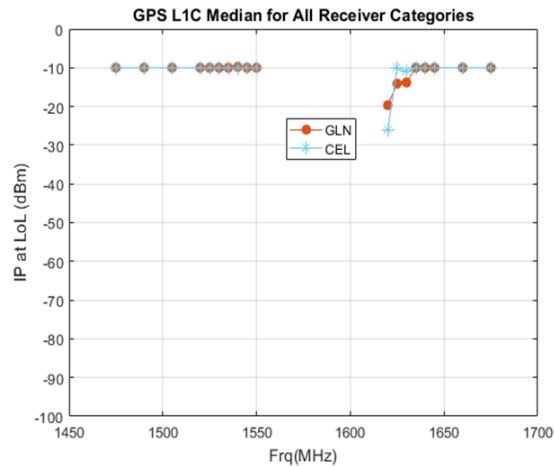
Frequency (MHz)	GAV	GLN	HPR	TIM	SPB	CEL
1475	NaN	-9.999	NaN	NaN	NaN	-9.999
1490	NaN	-9.999	NaN	NaN	NaN	-9.999
1505	NaN	-9.999	NaN	NaN	NaN	-9.999
1520	NaN	-9.999	NaN	NaN	NaN	-9.999
1525	NaN	-9.999	NaN	NaN	NaN	-9.999
1530	NaN	-9.999	NaN	NaN	NaN	-9.999
1535	NaN	-9.999	NaN	NaN	NaN	-9.999
1540	NaN	-9.999	NaN	NaN	NaN	-9.999
1545	NaN	-9.999	NaN	NaN	NaN	-9.999
1550	NaN	-9.999	NaN	NaN	NaN	-9.999
1620	NaN	-31.3943	NaN	NaN	NaN	-32.1514
1625	NaN	-30.7686	NaN	NaN	NaN	-9.999
1630	NaN	-15.4154	NaN	NaN	NaN	-12.0846
1635	NaN	-9.999	NaN	NaN	NaN	-9.999
1640	NaN	-9.999	NaN	NaN	NaN	-9.999
1645	NaN	-9.999	NaN	NaN	NaN	-9.999
1660	NaN	-9.999	NaN	NaN	NaN	-9.999
1675	NaN	-9.999	NaN	NaN	NaN	-9.999

**Table C-12: Low Elevation SVs GPS L1 P Median (dBm)**

Frequency (MHz)	GAV	GLN	HPR	TIM	SPB	CEL
1475	NaN	-9.999	NaN	NaN	NaN	-9.999
1490	NaN	-9.999	NaN	NaN	NaN	-9.999
1505	NaN	-9.999	NaN	NaN	NaN	-9.999
1520	NaN	-9.999	NaN	NaN	NaN	-9.999
1525	NaN	-9.999	NaN	NaN	NaN	-9.999
1530	NaN	-9.999	NaN	NaN	NaN	-9.999
1535	NaN	-9.999	NaN	NaN	NaN	-9.999
1540	NaN	-9.77771	NaN	NaN	NaN	-9.999
1545	NaN	-9.999	NaN	NaN	NaN	-9.999
1550	NaN	-9.999	NaN	NaN	NaN	-9.999
1620	NaN	-19.675	NaN	NaN	NaN	-26.0967
1625	NaN	-14.0983	NaN	NaN	NaN	-9.999
1630	NaN	-13.8262	NaN	NaN	NaN	-11.0418
1635	NaN	-9.999	NaN	NaN	NaN	-9.999
1640	NaN	-9.999	NaN	NaN	NaN	-9.999
1645	NaN	-9.999	NaN	NaN	NaN	-9.999
1660	NaN	-9.999	NaN	NaN	NaN	-9.999
1675	NaN	-9.999	NaN	NaN	NaN	-9.999



(a)



(b)

**Figure C-14: Low Elevation SVs (a) GPS L1 C Bounding Masks and (b) GPS L1 C Median**

## C.2.4 GLONASS L1 C

### C.2.4.1 Nominal SVs

Loss-of-Lock ITM computed using only “nominally” powered GPS signals

**Table C-13: Nominal SVs GLONASS L1 C Bounding Masks (dBm)**

Frequency (MHz)	GAV	GLN	HPR	TIM	SPB	CEL
1475	-9.999	-17.0577	-22.0199	-9.999	NaN	-9.999
1490	-9.999	-9.999	-25.2549	-9.999	NaN	-9.999
1505	-9.999	-9.999	-37.9422	-9.999	NaN	-9.999
1520	-9.999	-26.2192	-48.9467	-9.999	NaN	-9.999
1525	-9.999	-24.0921	-50.8713	-9.999	NaN	-9.999
1530	-9.999	-33.0652	-50.7309	-9.999	NaN	-9.999
1535	-9.999	-26.897	-52.5364	-9.999	NaN	-9.999
1540	-9.999	-28.9021	-53.3135	-9.999	NaN	-9.999
1545	-9.999	-29.8816	-54.7246	-9.999	NaN	-9.999
1550	-18.6341	-32.884	-56.6585	-9.999	NaN	-9.999
1620	-9.999	-42.7896	-66.188	-38.2107	NaN	-9.999
1625	-9.999	-34.7686	-56.207	NaN	NaN	-9.999
1630	-11.4378	-27.82	-57.0348	-17.2599	NaN	-9.999
1635	-9.999	-21.9075	-45.1698	-9.999	NaN	-9.999
1640	-9.999	-18.7996	-38.3831	-9.999	NaN	-9.999
1645	-9.999	-17.7334	-37.8222	-9.999	NaN	-9.999
1660	-9.999	-18.6121	-31.6007	-9.999	NaN	-9.999
1675	-9.999	-9.999	-23.2063	-9.999	NaN	-9.999



**Table C-14: Nominal SVs GLONASS L1 C Median (dBm)**

Frequency (MHz)	GAV	GLN	HPR	TIM	SPB	CEL
1475	-9.999	-9.999	-9.999	-9.999	NaN	-9.999
1490	-9.999	-9.999	-9.999	-9.999	NaN	-9.999
1505	-9.999	-9.999	-9.999	-9.999	NaN	-9.999
1520	-9.999	-9.999	-16.3549	-9.999	NaN	-9.999
1525	-9.999	-9.999	-16.3513	-9.999	NaN	-9.999
1530	-9.999	-9.999	-20.7887	-9.999	NaN	-9.999
1535	-9.999	-9.999	-25.2012	-9.999	NaN	-9.999
1540	-9.999	-9.999	-23.0492	-9.999	NaN	-9.999
1545	-9.999	-9.999	-9.999	-9.999	NaN	-9.999
1550	-9.999	-9.999	-38.8832	-9.999	NaN	-9.999
1620	-9.999	-15.0761	-53.4166	-9.999	NaN	-9.999
1625	-9.999	-9.999	-37.9896	NaN	NaN	-9.999
1630	-9.999	-9.999	-33.3659	-9.999	NaN	-9.999
1635	-9.999	-9.999	-23.4376	-9.999	NaN	-9.999
1640	-9.999	-9.999	-15.6777	-9.999	NaN	-9.999
1645	-9.999	-9.999	-9.999	-9.999	NaN	-9.999
1660	-9.999	-9.999	-9.999	-9.999	NaN	-9.999
1675	-9.999	-9.999	-9.999	-9.999	NaN	-9.999

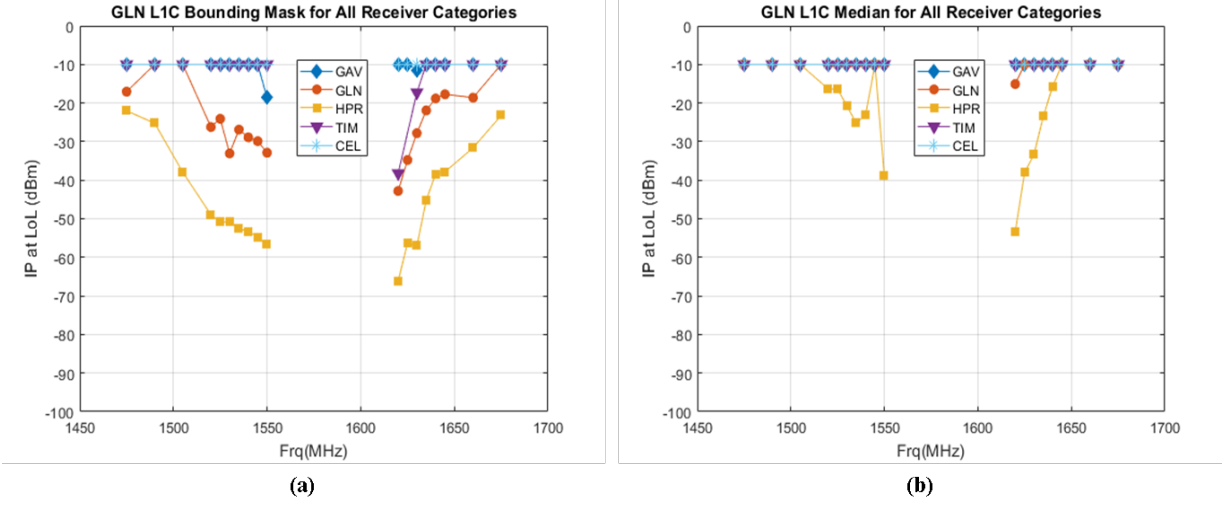


**Figure C-15: Nominal SVs (a) GLONASS L1 C Bounding Masks and (b) GLONASS L1 C Median**

**C.2.4.2 Low Elevation SVs**

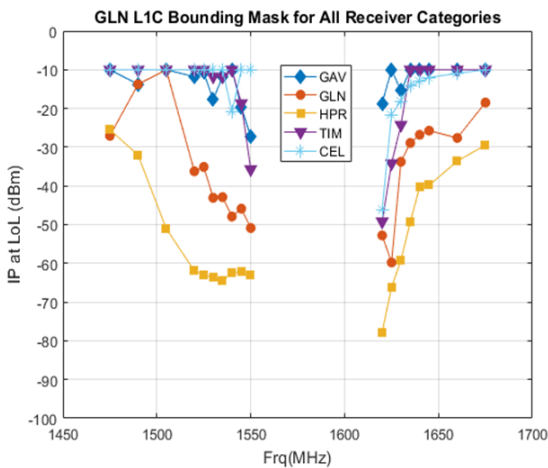
Loss-of-Lock ITM computed using only SV-01 fixed at -10 dB relative to the nominal received power levels.

**Table C-15: Low Elevation SVs GLONASS L1 C Bounding Masks (dBm)**

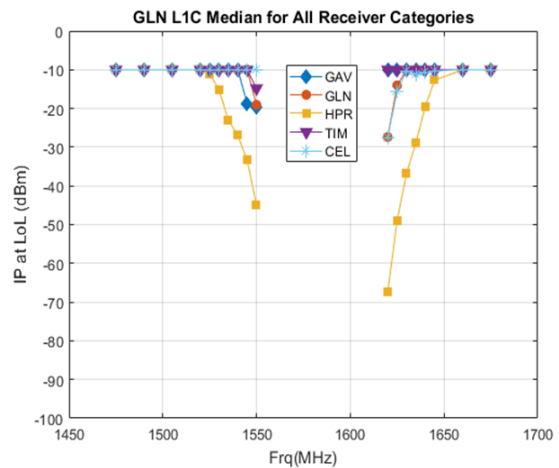
Frequency (MHz)	GAV	GLN	HPR	TIM	SPB	CEL
1475	-9.999	-27.0577	-25.4968	-9.999	NaN	-9.999
1490	-13.7647	-13.7647	-32.0449	-9.999	NaN	-9.999
1505	-9.999	-9.999	-51.0301	-9.999	NaN	-9.999
1520	-11.8154	-36.2192	-61.9467	-9.999	NaN	-9.999
1525	-10.771	-35.0921	-62.8713	-9.999	NaN	-9.999
1530	-17.7766	-43.0652	-63.7309	-11.7766	NaN	-9.999
1535	-11.722	-42.897	-64.5364	-11.722	NaN	-9.999
1540	-9.999	-47.9021	-62.3935	-9.999	NaN	-20.9017
1545	-19.6831	-45.8816	-62.2675	-18.6831	NaN	-9.999
1550	-27.2693	-50.884	-63.138	-35.7205	NaN	-9.999
1620	-18.6707	-52.7896	-77.7669	-49.2107	NaN	-46.1514
1625	-9.999	-59.7686	-66.207	-34.1718	NaN	-21.579
1630	-15.4378	-33.7641	-59.1922	-24.2599	NaN	-18.0846
1635	-9.999	-28.9075	-49.3014	-9.999	NaN	-14.2157
1640	-9.999	-26.7996	-40.194	-9.999	NaN	-13.0403
1645	-9.999	-25.7334	-39.8279	-9.999	NaN	-12.005
1660	-9.999	-27.6121	-33.6007	-9.999	NaN	-10.9311
1675	-9.999	-18.4705	-29.4429	-9.999	NaN	-9.999

**Table C-16: Low Elevation SVs GLONASS L1 C Median (dBm)**

Frequency (MHz)	GAV	GLN	HPR	TIM	SPB	CEL
1475	-9.999	-9.999	-9.999	-9.999	NaN	-9.999
1490	-9.999	-9.999	-9.999	-9.999	NaN	-9.999
1505	-9.999	-9.999	-9.999	-9.999	NaN	-9.999
1520	-9.999	-9.999	-9.999	-9.999	NaN	-9.999
1525	-9.999	-9.999	-11.1529	-9.999	NaN	-9.999
1530	-9.999	-9.999	-15.1472	-9.999	NaN	-9.999
1535	-9.999	-9.999	-23.0548	-9.999	NaN	-9.999
1540	-9.999	-9.999	-26.9976	-9.999	NaN	-9.999
1545	-18.6831	-9.999	-33.3833	-9.999	NaN	-9.999
1550	-19.6341	-19.0674	-44.8832	-14.8166	NaN	-9.999
1620	-9.999	-27.3583	-67.4381	-9.999	NaN	-27.5419
1625	-9.999	-14.064	-48.9016	-9.999	NaN	-15.5228
1630	-9.999	-10.0739	-36.8036	-9.999	NaN	-10.2921
1635	-9.999	-9.999	-28.9246	-9.999	NaN	-11.1461
1640	-9.999	-9.999	-19.5126	-9.999	NaN	-10.7826
1645	-9.999	-9.999	-12.6969	-9.999	NaN	-10.2662
1660	-9.999	-9.999	-9.999	-9.999	NaN	-9.999
1675	-9.999	-9.999	-9.999	-9.999	NaN	-9.999



(a)



(b)

**Figure C-16: Low Elevation SVs (a) GLONASS L1 C Bounding Masks and (b) GLONASS L1 C Median**

## C.2.5 GLONASS L1 P

### C.2.5.1 Nominal SVs

Loss-of-Lock ITM computed using only “nominally” powered GPS signals

**Table C-17: Nominal SVs GLONASS L1 P Bounding Masks (dBm)**

Frequency (MHz)	GAV	GLN	HPR	TIM	SPB	CEL
1475	NaN	-9.999	-9.999	NaN	NaN	-9.999
1490	NaN	-9.999	-9.999	NaN	NaN	-9.999
1505	NaN	-9.999	-9.999	NaN	NaN	-9.999
1520	NaN	-9.999	-9.999	NaN	NaN	-9.999
1525	NaN	-9.999	-10.3721	NaN	NaN	-9.999
1530	NaN	-9.999	-13.2698	NaN	NaN	-9.999
1535	NaN	-9.999	-17.1146	NaN	NaN	-9.999
1540	NaN	-9.999	-23.0492	NaN	NaN	-9.999
1545	NaN	-9.999	NaN	NaN	NaN	-9.999
1550	NaN	-9.999	-37.6101	NaN	NaN	-9.999
1620	NaN	-42.7896	-59.0987	NaN	NaN	-9.999
1625	NaN	-34.7686	-40.7037	NaN	NaN	-9.999
1630	NaN	-22.4154	-30.8015	NaN	NaN	-9.999
1635	NaN	-11.24	-24.9246	NaN	NaN	-9.999
1640	NaN	-9.999	-16.5126	NaN	NaN	-9.999
1645	NaN	-9.999	-12.5755	NaN	NaN	-9.999
1660	NaN	-9.999	-9.999	NaN	NaN	-9.999
1675	NaN	-9.999	-9.999	NaN	NaN	-9.999

**Table C-18: Nominal SVs GLONASS L1 P Median (dBm)**

Frequency (MHz)	GAV	GLN	HPR	TIM	SPB	CEL
1475	NaN	-9.999	-9.999	NaN	NaN	-9.999
1490	NaN	-9.999	-9.999	NaN	NaN	-9.999
1505	NaN	-9.999	-9.999	NaN	NaN	-9.999
1520	NaN	-9.999	-9.999	NaN	NaN	-9.999
1525	NaN	-9.999	-9.999	NaN	NaN	-9.999
1530	NaN	-9.999	-9.999	NaN	NaN	-9.999
1535	NaN	-9.999	-11.5269	NaN	NaN	-9.999
1540	NaN	-9.999	-13.4983	NaN	NaN	-9.999
1545	NaN	-9.999	NaN	NaN	NaN	-9.999
1550	NaN	-9.999	-30.364	NaN	NaN	-9.999
1620	NaN	-21.685	-49.7287	NaN	NaN	-9.999
1625	NaN	-14.0983	-36.9373	NaN	NaN	-9.999
1630	NaN	-11.1903	-25.1865	NaN	NaN	-9.999
1635	NaN	-9.999	-16.2811	NaN	NaN	-9.999
1640	NaN	-9.999	-12.4209	NaN	NaN	-9.999
1645	NaN	-9.999	-9.999	NaN	NaN	-9.999
1660	NaN	-9.999	-9.999	NaN	NaN	-9.999
1675	NaN	-9.999	-9.999	NaN	NaN	-9.999

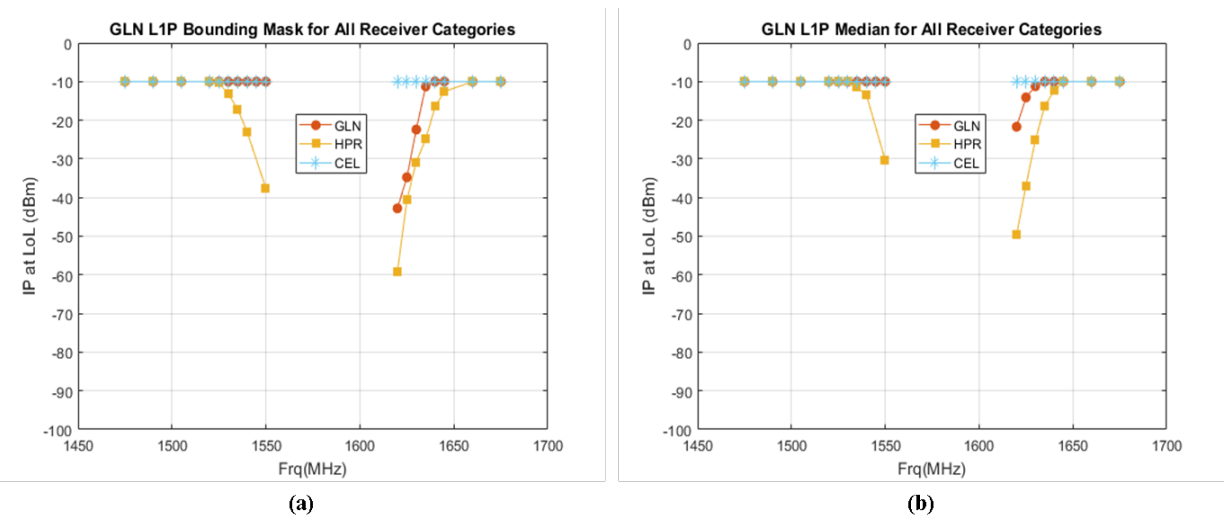


**Figure C-17: Nominal SVs (a) GLONASS L1 P Bounding Masks and (b) GLONASS L1 P Median**

### C.2.5.2 Low Elevation SVs

Loss-of-Lock ITM computed using only SV-01 fixed at -10 dB relative to the nominal received power levels.

**Table C-19: Low Elevation SVs GLONASS L1 P Bounding Masks (dBm)**

Frequency (MHz)	GAV	GLN	HPR	TIM	SPB	CEL
1475	NaN	-9.999	-9.999	NaN	NaN	-9.999
1490	NaN	-9.999	-9.999	NaN	NaN	-9.999
1505	NaN	-9.999	-9.999	NaN	NaN	-9.999
1520	NaN	-9.999	-11.4466	NaN	NaN	-9.999
1525	NaN	-9.999	-14.3721	NaN	NaN	-9.999
1530	NaN	-9.999	-19.2698	NaN	NaN	-9.999
1535	NaN	-9.999	-26.1146	NaN	NaN	-9.999
1540	NaN	-9.999	-29.0492	NaN	NaN	-9.999
1545	NaN	-9.999	-32.772	NaN	NaN	-9.999
1550	NaN	-18.5007	-49.6101	NaN	NaN	-9.999
1620	NaN	-52.7896	-71.0987	NaN	NaN	-46.1514
1625	NaN	-59.7686	-53.7037	NaN	NaN	-21.579
1630	NaN	-33.7641	-34.8015	NaN	NaN	-18.0846
1635	NaN	-22.8	-28.9246	NaN	NaN	-14.2157
1640	NaN	-9.999	-20.8429	NaN	NaN	-13.0403
1645	NaN	-9.999	-16.5755	NaN	NaN	-12.005
1660	NaN	-9.999	-9.999	NaN	NaN	-10.9311
1675	NaN	-9.999	-9.999	NaN	NaN	-9.999

**Table C-20: Low Elevation SVs GLONASS L1 P Median (dBm)**

Frequency (MHz)	GAV	GLN	HPR	TIM	SPB	CEL
1475	NaN	-9.999	-9.999	NaN	NaN	-9.999
1490	NaN	-9.999	-9.999	NaN	NaN	-9.999
1505	NaN	-9.999	-9.999	NaN	NaN	-9.999
1520	NaN	-9.999	-9.999	NaN	NaN	-9.999
1525	NaN	-9.999	-11.5759	NaN	NaN	-9.999
1530	NaN	-9.999	-9.999	NaN	NaN	-9.999
1535	NaN	-9.999	-16.5269	NaN	NaN	-9.999
1540	NaN	-9.999	-22.4202	NaN	NaN	-9.999
1545	NaN	-9.999	-31.4723	NaN	NaN	-9.999
1550	NaN	-9.999	-36.364	NaN	NaN	-9.999
1620	NaN	-36.371	-57.7287	NaN	NaN	-45.6181
1625	NaN	-24.7626	-45.4373	NaN	NaN	-21.3128
1630	NaN	-18.2821	-31.1865	NaN	NaN	-14.3349
1635	NaN	-11.74	-21.7009	NaN	NaN	-13.2545
1640	NaN	-9.999	-15.2558	NaN	NaN	-12.3033
1645	NaN	-9.999	-10.4087	NaN	NaN	-11.2692
1660	NaN	-9.999	-9.999	NaN	NaN	-10.4651
1675	NaN	-9.999	-9.999	NaN	NaN	-9.91455

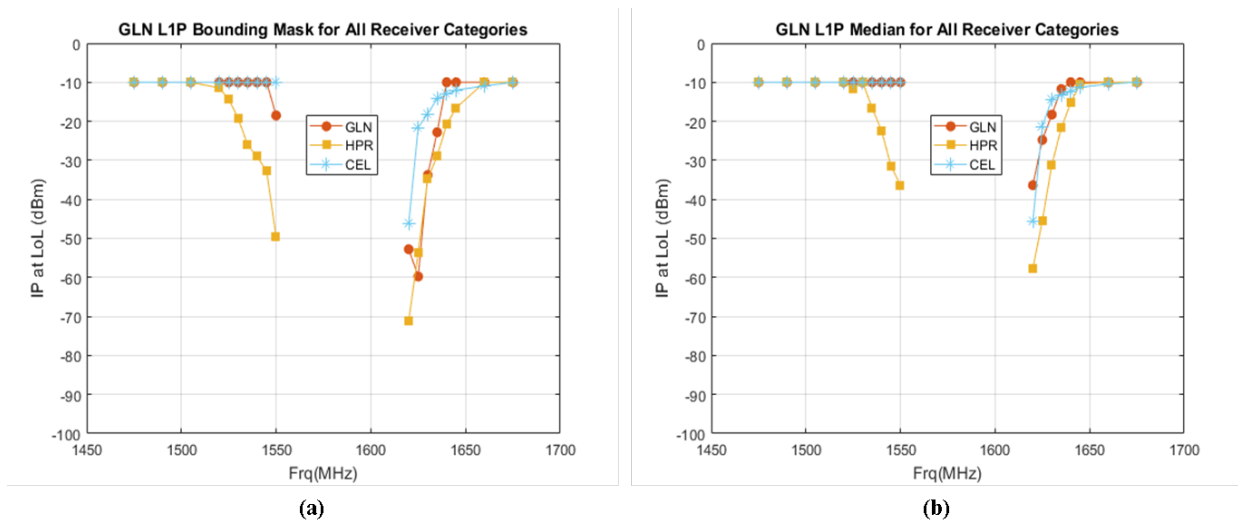


**Figure C-18: Low Elevation SVs (a) GLONASS L1 P Bounding Masks and (b) GLONASS L1 P Median**



## C.2.6 BeiDou B1I

### C.2.6.1 Nominal SVs

Loss-of-Lock ITM computed using only “nominally” powered GPS signals

**Table C-21: Nominal SVs BeiDou B1I Bounding Masks (dBm)**

Frequency (MHz)	GAV	GLN	HPR	TIM	SPB	CEL
1475	NaN	-9.999	-9.999	NaN	NaN	-9.999
1490	NaN	-9.999	-9.999	NaN	NaN	-9.999
1505	NaN	-9.999	-26.279	NaN	NaN	-9.999
1520	NaN	-9.999	-45.1027	NaN	NaN	-9.999
1525	NaN	NaN	-50.0021	NaN	NaN	-9.999
1530	NaN	-9.999	-52.9673	NaN	NaN	-9.999
1535	NaN	-9.999	-56.8679	NaN	NaN	-9.999
1540	NaN	-10.1664	-58.8462	NaN	NaN	-9.999
1545	NaN	-9.999	-68.8158	NaN	NaN	-9.999
1550	NaN	-52.2057	-76.7261	NaN	NaN	-9.999
1620	NaN	-30.752	-56.188	NaN	NaN	-9.999
1625	NaN	-9.999	-54.207	NaN	NaN	-9.999
1630	NaN	-9.999	-42.2442	NaN	NaN	-9.999
1635	NaN	-9.999	-33.3014	NaN	NaN	-9.999
1640	NaN	-9.999	-24.194	NaN	NaN	-9.999
1645	NaN	-9.999	-16.1068	NaN	NaN	-9.999
1660	NaN	-9.999	-9.999	NaN	NaN	-9.999
1675	NaN	-9.999	-9.999	NaN	NaN	-9.999

**Table C-22: Nominal SVs BeiDou B1I Median (dBm)**

Frequency (MHz)	GAV	GLN	HPR	TIM	SPB	CEL
1475	NaN	-9.999	-9.999	NaN	NaN	-9.999
1490	NaN	-9.999	-9.999	NaN	NaN	-9.999
1505	NaN	-9.999	-9.999	NaN	NaN	-9.999
1520	NaN	-9.999	-9.999	NaN	NaN	-9.999
1525	NaN	NaN	-9.999	NaN	NaN	-9.999
1530	NaN	-9.999	-9.999	NaN	NaN	-9.999
1535	NaN	-9.999	-9.999	NaN	NaN	-9.999
1540	NaN	-10.1664	-19.99	NaN	NaN	-9.999
1545	NaN	-9.999	-43.4035	NaN	NaN	-9.999
1550	NaN	-52.2057	-69.2392	NaN	NaN	-9.999
1620	NaN	-30.752	-9.999	NaN	NaN	-9.999
1625	NaN	-9.999	-9.999	NaN	NaN	-9.999
1630	NaN	-9.999	-9.999	NaN	NaN	-9.999
1635	NaN	-9.999	-9.999	NaN	NaN	-9.999
1640	NaN	-9.999	-9.999	NaN	NaN	-9.999
1645	NaN	-9.999	-9.999	NaN	NaN	-9.999
1660	NaN	-9.999	-9.999	NaN	NaN	-9.999
1675	NaN	-9.999	-9.999	NaN	NaN	-9.999

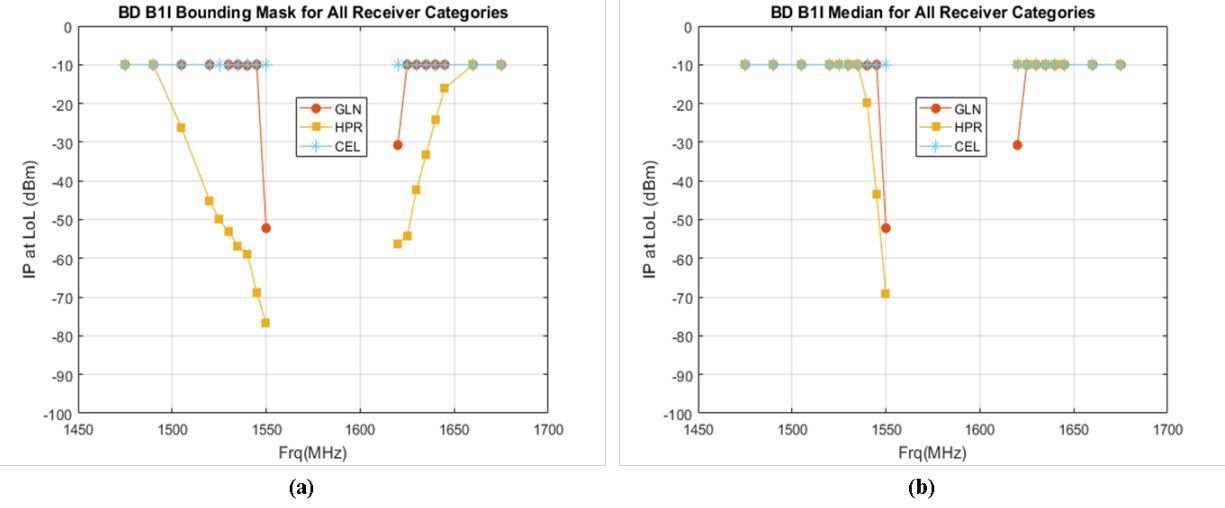


**Figure C-19: Nominal SVs (a) BeiDou B1I Bounding Masks and (b) BeiDou B1I Median**

**C.2.6.2 Low Elevation SVs**

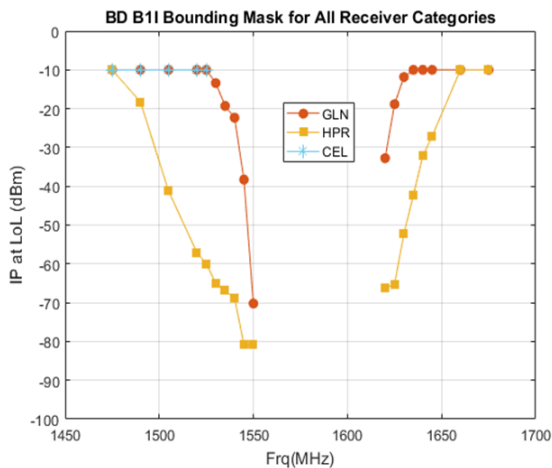
Loss-of-Lock ITM computed using only PRN-08 fixed at -10 dB relative to the nominal received power levels.

**Table C-23: Low Elevation SVs BeiDou B1I Bounding Masks (dBm)**

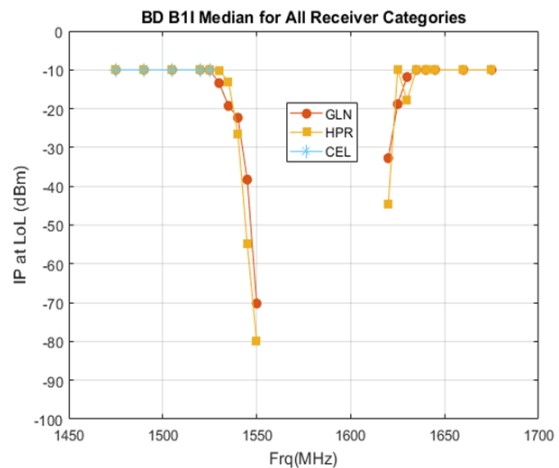
Frequency (MHz)	GAV	GLN	HPR	TIM	SPB	CEL
1475	NaN	-9.999	-9.999	NaN	NaN	-9.999
1490	NaN	-9.999	-18.2685	NaN	NaN	-9.999
1505	NaN	-9.999	-41.279	NaN	NaN	-9.999
1520	NaN	-9.999	-57.1027	NaN	NaN	-9.999
1525	NaN	-9.999	-60.0021	NaN	NaN	-9.999
1530	NaN	-13.3999	-64.9673	NaN	NaN	NaN
1535	NaN	-19.2972	-66.8679	NaN	NaN	NaN
1540	NaN	-22.3339	-68.8462	NaN	NaN	NaN
1545	NaN	-38.2885	-80.8158	NaN	NaN	NaN
1550	NaN	-70.2057	-80.8683	NaN	NaN	NaN
1620	NaN	-32.752	-66.188	NaN	NaN	NaN
1625	NaN	-18.8299	-65.207	NaN	NaN	NaN
1630	NaN	-11.8523	-52.2442	NaN	NaN	NaN
1635	NaN	-9.999	-42.3014	NaN	NaN	NaN
1640	NaN	-9.999	-32.194	NaN	NaN	NaN
1645	NaN	-9.999	-27.1068	NaN	NaN	NaN
1660	NaN	-9.999	-9.999	NaN	NaN	NaN
1675	NaN	-9.999	-9.999	NaN	NaN	NaN

**Table C-24: Low Elevation SVs BeiDou B1I Median (dBm)**

Frequency (MHz)	GAV	GLN	HPR	TIM	SPB	CEL
1475	NaN	-9.999	-9.999	NaN	NaN	-9.999
1490	NaN	-9.999	-9.999	NaN	NaN	-9.999
1505	NaN	-9.999	-9.999	NaN	NaN	-9.999
1520	NaN	-9.999	-9.999	NaN	NaN	-9.999
1525	NaN	-9.999	-9.999	NaN	NaN	-9.999
1530	NaN	-13.3999	-10.1063	NaN	NaN	NaN
1535	NaN	-19.2972	-13.0842	NaN	NaN	NaN
1540	NaN	-22.3339	-26.49	NaN	NaN	NaN
1545	NaN	-38.2885	-54.9035	NaN	NaN	NaN
1550	NaN	-70.2057	-79.9274	NaN	NaN	NaN
1620	NaN	-32.752	-44.695	NaN	NaN	NaN
1625	NaN	-18.8299	-9.999	NaN	NaN	NaN
1630	NaN	-11.8523	-17.801	NaN	NaN	NaN
1635	NaN	-9.999	-9.999	NaN	NaN	NaN
1640	NaN	-9.999	-9.999	NaN	NaN	NaN
1645	NaN	-9.999	-9.999	NaN	NaN	NaN
1660	NaN	-9.999	-9.999	NaN	NaN	NaN
1675	NaN	-9.999	-9.999	NaN	NaN	NaN



(a)



(b)

**Figure C-20: Low Elevation SVs (a) BeiDou B1I Bounding Masks and (b) BeiDou B1I Median**

## C.2.7 Galileo E1 BC

### C.2.7.1 Nominal SVs

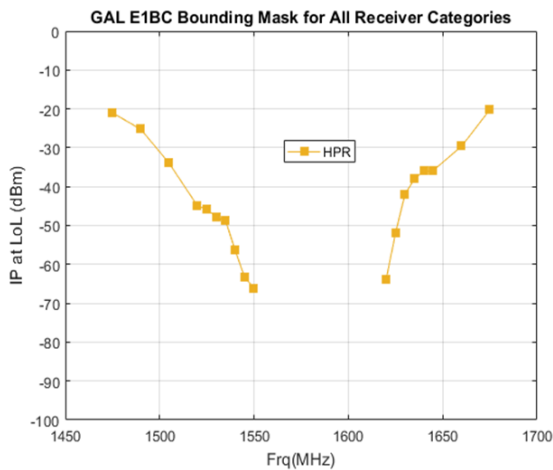
Loss-of-Lock ITM computed using only “nominally” powered GPS signals

**Table C-25: Nominal SVs Galileo E1 BC Bounding Masks (dBm)**

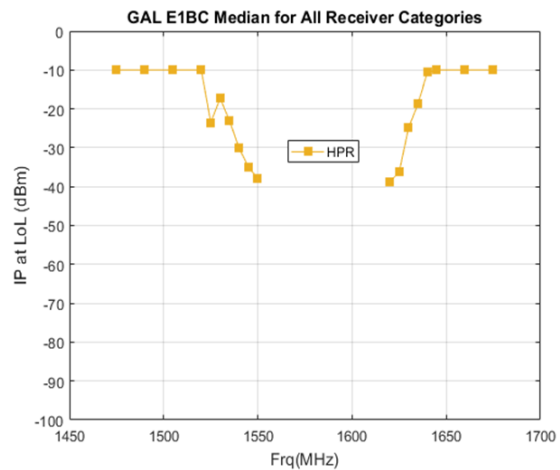
Frequency (MHz)	GAV	GLN	HPR	TIM	SPB	CEL
1475	NaN	NaN	-21.0199	NaN	NaN	NaN
1490	NaN	NaN	-25.2549	NaN	NaN	NaN
1505	NaN	NaN	-33.9753	NaN	NaN	NaN
1520	NaN	NaN	-44.9467	NaN	NaN	NaN
1525	NaN	NaN	-45.8713	NaN	NaN	NaN
1530	NaN	NaN	-47.7309	NaN	NaN	NaN
1535	NaN	NaN	-48.8679	NaN	NaN	NaN
1540	NaN	NaN	-56.3935	NaN	NaN	NaN
1545	NaN	NaN	-63.2675	NaN	NaN	NaN
1550	NaN	NaN	-66.138	NaN	NaN	NaN
1620	NaN	NaN	-63.9203	NaN	NaN	NaN
1625	NaN	NaN	-51.9544	NaN	NaN	NaN
1630	NaN	NaN	-41.9352	NaN	NaN	NaN
1635	NaN	NaN	-38.0443	NaN	NaN	NaN
1640	NaN	NaN	-35.9451	NaN	NaN	NaN
1645	NaN	NaN	-35.8279	NaN	NaN	NaN
1660	NaN	NaN	-29.6007	NaN	NaN	NaN
1675	NaN	NaN	-20.2063	NaN	NaN	NaN

**Table C-26: Nominal SVs Galileo E1 BC Median (dBm)**

Frequency (MHz)	GAV	GLN	HPR	TIM	SPB	CEL
1475	NaN	NaN	-9.999	NaN	NaN	NaN
1490	NaN	NaN	-9.999	NaN	NaN	NaN
1505	NaN	NaN	-9.999	NaN	NaN	NaN
1520	NaN	NaN	-9.999	NaN	NaN	NaN
1525	NaN	NaN	-23.5116	NaN	NaN	NaN
1530	NaN	NaN	-17.2698	NaN	NaN	NaN
1535	NaN	NaN	-23.1146	NaN	NaN	NaN
1540	NaN	NaN	-30.0492	NaN	NaN	NaN
1545	NaN	NaN	-34.991	NaN	NaN	NaN
1550	NaN	NaN	-37.8596	NaN	NaN	NaN
1620	NaN	NaN	-38.7558	NaN	NaN	NaN
1625	NaN	NaN	-36.3017	NaN	NaN	NaN
1630	NaN	NaN	-24.8276	NaN	NaN	NaN
1635	NaN	NaN	-18.7342	NaN	NaN	NaN
1640	NaN	NaN	-10.5126	NaN	NaN	NaN
1645	NaN	NaN	-9.999	NaN	NaN	NaN
1660	NaN	NaN	-9.999	NaN	NaN	NaN
1675	NaN	NaN	-9.999	NaN	NaN	NaN



(a)



(b)

**Figure C-21: Nominal SVs (a) Galileo E1 BC Bounding Masks and (b) Galileo E1 BC Median**

### C.2.7.2 Low Elevation SVs

Loss-of-Lock ITM computed using only PRN-04 fixed at -10 dB relative to the nominal received power levels.

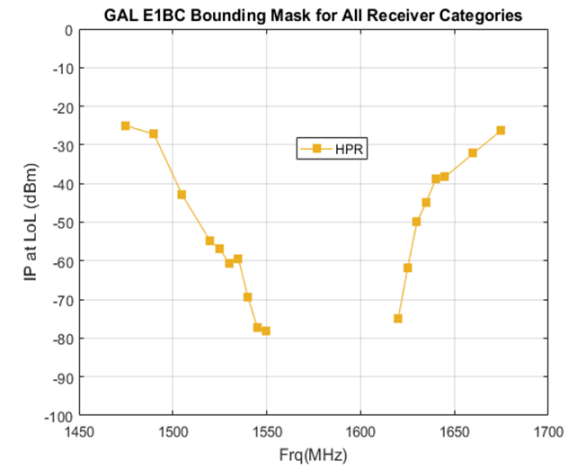
**Table C-27: Low Elevation SVs Galileo E1 BC Bounding Masks (dBm)**

Frequency (MHz)	GAV	GLN	HPR	TIM	SPB	CEL
1475	NaN	NaN	-25.0199	NaN	NaN	NaN
1490	NaN	NaN	-27.2549	NaN	NaN	NaN
1505	NaN	NaN	-42.9753	NaN	NaN	NaN
1520	NaN	NaN	-54.9467	NaN	NaN	NaN
1525	NaN	NaN	-56.8713	NaN	NaN	NaN
1530	NaN	NaN	-60.7309	NaN	NaN	NaN
1535	NaN	NaN	-59.5364	NaN	NaN	NaN
1540	NaN	NaN	-69.3935	NaN	NaN	NaN
1545	NaN	NaN	-77.2675	NaN	NaN	NaN
1550	NaN	NaN	-78.138	NaN	NaN	NaN
1620	NaN	NaN	-75.0987	NaN	NaN	NaN
1625	NaN	NaN	-61.9544	NaN	NaN	NaN
1630	NaN	NaN	-49.9352	NaN	NaN	NaN
1635	NaN	NaN	-44.9053	NaN	NaN	NaN
1640	NaN	NaN	-38.7792	NaN	NaN	NaN
1645	NaN	NaN	-38.3086	NaN	NaN	NaN
1660	NaN	NaN	-32.2085	NaN	NaN	NaN
1675	NaN	NaN	-26.2063	NaN	NaN	NaN

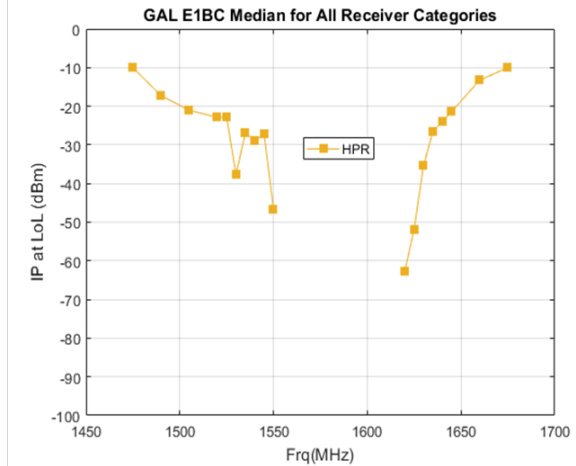


**Table C-28: Low Elevation SVs Galileo E1 BC Median (dBm)**

Frequency (MHz)	GAV	GLN	HPR	TIM	SPB	CEL
1475	NaN	NaN	-9.999	NaN	NaN	NaN
1490	NaN	NaN	-17.2685	NaN	NaN	NaN
1505	NaN	NaN	-21.0294	NaN	NaN	NaN
1520	NaN	NaN	-22.8807	NaN	NaN	NaN
1525	NaN	NaN	-22.825	NaN	NaN	NaN
1530	NaN	NaN	-37.6765	NaN	NaN	NaN
1535	NaN	NaN	-26.9013	NaN	NaN	NaN
1540	NaN	NaN	-28.8764	NaN	NaN	NaN
1545	NaN	NaN	-27.2681	NaN	NaN	NaN
1550	NaN	NaN	-46.564	NaN	NaN	NaN
1620	NaN	NaN	-62.7254	NaN	NaN	NaN
1625	NaN	NaN	-51.8027	NaN	NaN	NaN
1630	NaN	NaN	-35.4037	NaN	NaN	NaN
1635	NaN	NaN	-26.5766	NaN	NaN	NaN
1640	NaN	NaN	-23.9544	NaN	NaN	NaN
1645	NaN	NaN	-21.3745	NaN	NaN	NaN
1660	NaN	NaN	-13.2377	NaN	NaN	NaN
1675	NaN	NaN	-9.999	NaN	NaN	NaN



(a)



(b)

**Figure C-22: Low Elevation SVs (a) Galileo E1 BC Bounding Masks and (b) Galileo E1 BC Median**

## C.2.8 SBAS L1 C/A

### C.2.8.1 Nominal SVs

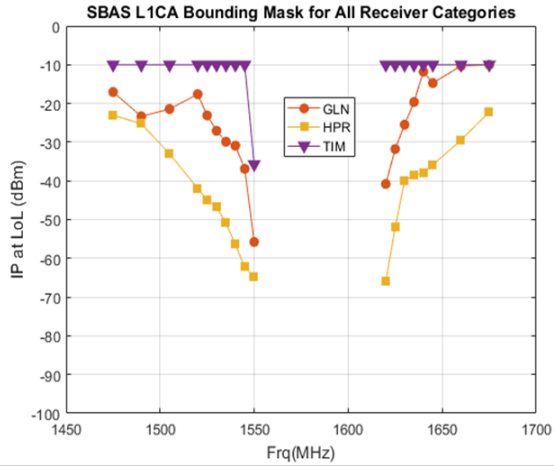
Loss-of-Lock ITM computed using only “nominally” powered GPS signals

**Table C-29: Nominal SVs SBAS L1 C/A Bounding Masks (dBm)**

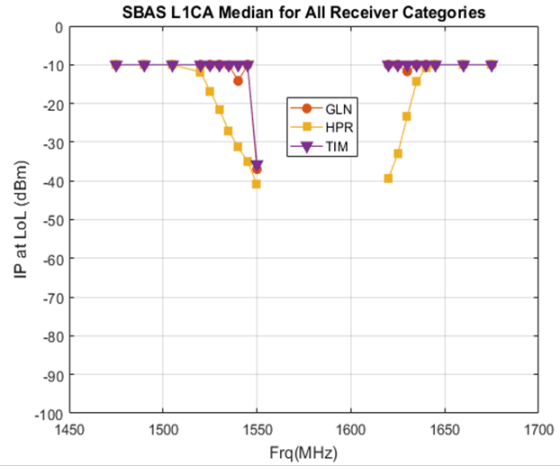
Frequency (MHz)	GAV	GLN	HPR	TIM	SPB	CEL
1475	NaN	-17.0577	-23.0199	-9.999	NaN	NaN
1490	NaN	-23.3312	-25.2549	-9.999	NaN	NaN
1505	NaN	-21.4491	-32.9753	-9.999	NaN	NaN
1520	NaN	-17.6091	-41.9467	-9.999	NaN	NaN
1525	NaN	-23.0921	-44.8713	-9.999	NaN	NaN
1530	NaN	-27.0652	-46.7309	-9.999	NaN	NaN
1535	NaN	-29.897	-50.8679	-9.999	NaN	NaN
1540	NaN	-30.9021	-56.3935	-9.999	NaN	NaN
1545	NaN	-36.8816	-62.2675	-9.999	NaN	NaN
1550	NaN	-55.7539	-64.7261	-35.7205	NaN	NaN
1620	NaN	-40.7896	-65.9203	-9.999	NaN	NaN
1625	NaN	-31.7686	-51.9544	-9.999	NaN	NaN
1630	NaN	-25.4838	-39.9352	-9.999	NaN	NaN
1635	NaN	-19.6279	-38.4688	-9.999	NaN	NaN
1640	NaN	-11.7996	-37.9451	-9.999	NaN	NaN
1645	NaN	-14.7334	-35.8279	-9.999	NaN	NaN
1660	NaN	-10.3055	-29.4585	-9.999	NaN	NaN
1675	NaN	-9.999	-22.2063	-9.999	NaN	NaN

**Table C-30: Nominal SVs SBAS L1 C/A Median (dBm)**

Frequency (MHz)	GAV	GLN	HPR	TIM	SPB	CEL
1475	NaN	-9.999	-9.999	-9.999	NaN	NaN
1490	NaN	-9.999	-9.999	-9.999	NaN	NaN
1505	NaN	-9.999	-9.999	-9.999	NaN	NaN
1520	NaN	-9.999	-11.8986	-9.999	NaN	NaN
1525	NaN	-9.999	-16.8264	-9.999	NaN	NaN
1530	NaN	-9.999	-21.6315	-9.999	NaN	NaN
1535	NaN	-10.1481	-27.116	-9.999	NaN	NaN
1540	NaN	-14.1664	-31.3096	-9.999	NaN	NaN
1545	NaN	-9.999	-34.9536	-9.999	NaN	NaN
1550	NaN	-36.9631	-40.9457	-35.7205	NaN	NaN
1620	NaN	-9.999	-39.4386	-9.999	NaN	NaN
1625	NaN	-9.999	-32.9266	-9.999	NaN	NaN
1630	NaN	-11.6903	-23.4623	-9.999	NaN	NaN
1635	NaN	-9.999	-14.4376	-9.999	NaN	NaN
1640	NaN	-9.999	-10.8429	-9.999	NaN	NaN
1645	NaN	-9.999	-9.999	-9.999	NaN	NaN
1660	NaN	-9.999	-9.999	-9.999	NaN	NaN
1675	NaN	-9.999	-9.999	-9.999	NaN	NaN



(a)



(b)

**Figure C-23: Nominal SVs (a) SBAS L1 C/A Bounding Masks and (b) SBAS L1 C/A Median**

# **APPENDIX D**

## **CONDUCTED TEST DETAILS**

**TABLE OF CONTENTS**

TABLE OF CONTENTS..... 2  
LIST OF FIGURES ..... 3  
LIST OF TABLES ..... 4  
REFERENCES ..... 5  
APPENDIX..... 6  
Appendix D. Conducted Test..... 6  
    D.1 OOB Level Settings..... 6

## **LIST OF FIGURES**

**No table of figures entries found.**

## LIST OF TABLES

Table D-1: Ratio of OOBE limit density to LTE power for setting OOBE testing levels .....	6
Table D-2: OOBE levels (in dBm/MHz) for the LTE tests ranges.....	6



## **REFERENCES**

**There are no sources in the current document.**

# APPENDIX

## Appendix D. Conducted Test

### D.1 OOB Level Settings

The key points associated with wired testing were largely covered in the main body of the report or in the previous section with review of SPIGAT. One area that generated much discussion was simulation of FCC and Proposed OOB limits in the wired testing. The OOB levels to be generated were determined by assuming a fixed ratio between OOB limit and LTE signal power for each of the four cases (from the combination of transmitter type and OOB limit sponsor) as summarized in Table D-1. The appropriate ratio was applied (added) to the target LTE signal power at each point in the test to determine the corresponding OOB level to generate. Each ratio was determined by assuming OOB is at the limit when LTE power levels are at the specified maximums of 62 dBm (32 dBW) for base stations and 23 dBm (-7 dBW) for handsets. All limits were taken without consideration for sloping specified within (or any levels specified outside) the RNSS band. Therefore, the FCC limit was taken as -40 dBm/MHz for both handsets and base stations and the Proposed limits was taken as -70 dBm/MHz for base stations and -75 dBm/MHz for handsets.

**Table D-1: Ratio of OOB limit density to LTE power for setting OOB testing levels**

	OOB density [dBm/MHz]	LTE power [dBm]	ratio OOB/LTE [dB/MHz]
FCC base station	-40	62	-102
FCC handset	-40	23	-63
Proposed base station	-70	62	-132
Proposed handset	-75	23	-98

The appropriate ratio was applied to the target LTE signal power at each point in the test to determine the corresponding OOB level to generate. For example, the LTE uplink at 1630 MHz was tested in a power range from -80 to -10 dBm. For the FCC limit (adding the ratio -63 dB/MHz), the OOB range was -143 to -73 dBm/MHz (-233 to -163 dBW/Hz). For the Proposed limit (adding the ratio -98 dB/MHz), the corresponding OOB range was -178 to -108 dBm/MHz (-268 to -198 dBW/Hz). Table D-2 shows the OOB levels generated for each of the LTE test ranges.

**Table D-2: OOB levels (in dBm/MHz) for the LTE tests ranges**

	LTE power [dBm]	FCC OOB density [dBm/MHz]	Proposed OOB density [dBm/MHz]
base station 1475	-80 To -10	-182 to -112	-212 to -142

	1490	-80 To -10	-182 to -112	-212 to -142
	1505	-80 to -10	-182 to -112	-212 to -142
	1520	-80 to -10	-182 to -112	-212 to -142
	1525	-80 to -10	-182 to -112	-212 to -142
	1530	-80 to -10	-182 to -112	-212 to -142
	1535	-80 to -10	-182 to -112	-212 to -142
	1540	-80 to -10	-182 to -112	-212 to -142
	1545	-100 to -30	-202 to -132	-232 to -162
	1550	-100 to -30	-202 to -132	-232 to -162
handset	1620	-100 to -30	-163 to -93	-198 to -128
	1625	-100 to -30	-163 to -93	-198 to -128
	1630	-80 to -10	-143 to -73	-178 to -108
	1635	-80 to -10	-143 to -73	-178 to -108
	1640	-80 to -10	-143 to -73	-178 to -108
	1645	-80 to -10	-143 to -73	-178 to -108
	1660	-80 to -10	-143 to -73	-178 to -108
base station	1675	-80 to -10	-182 to -112	-212 to -142



# **APPENDIX E**

## **ANTENNA CHARACTERIZATION DETAILS**

## TABLE OF CONTENTS

TABLE OF CONTENTS.....	2
LIST OF FIGURES .....	3
LIST OF TABLES .....	5
REFERENCES .....	6
APPENDIX.....	7
Appendix E. Antenna Characterization Details .....	7
E.1 Anechoic Chamber Measurements.....	7

## LIST OF FIGURES

Figure E-1: VPOL Gain Patterns for 14 External Antennas (1475 MHz).....	7
Figure E-2: HPOL Gain Patterns for 14 External Antennas (1475 MHz).....	8
Figure E-3: VPOL Gain Patterns for 14 External Antennas (1490 MHz).....	9
Figure E-4: HPOL Gain Patterns for 14 External Antennas (1490 MHz).....	10
Figure E-5: VPOL Gain Patterns for 14 External Antennas (1495 MHz).....	11
Figure E-6: HPOL Gain Patterns for 14 External Antennas (1495 MHz).....	12
Figure E-7: VPOL Gain Patterns for 14 External Antennas (1505 MHz).....	13
Figure E-8: HPOL Gain Patterns for 14 External Antennas (1505 MHz).....	14
Figure E-9: VPOL Gain Patterns for 14 External Antennas (1520 MHz).....	15
Figure E-10: HPOL Gain Patterns for 14 External Antennas (1520 MHz).....	16
Figure E-11: VPOL Gain Patterns for 14 External Antennas (1530 MHz).....	17
Figure E-12: HPOL Gain Patterns for 14 External Antennas (1530 MHz).....	18
Figure E-13: VPOL Gain Patterns for 14 External Antennas (1535 MHz).....	19
Figure E-14: HPOL Gain Patterns for 14 External Antennas (1535 MHz).....	20
Figure E-15: VPOL Gain Patterns for 14 External Antennas (1540 MHz).....	21
Figure E-16: HPOL Gain Patterns for 14 External Antennas (1540 MHz).....	22
Figure E-17: VPOL Gain Patterns for 14 External Antennas (1545 MHz).....	23
Figure E-18: HPOL Gain Patterns for 14 External Antennas (1545 MHz).....	24
Figure E-19: VPOL Gain Patterns for 14 External Antennas (1550 MHz).....	25
Figure E-20: HPOL Gain Patterns for 14 External Antennas (1550 MHz).....	26
Figure E-21: VPOL Gain Patterns for 14 External Antennas (1555 MHz).....	27
Figure E-22: HPOL Gain Patterns for 14 External Antennas (1555 MHz).....	28
Figure E-23: VPOL Gain Patterns for 14 External Antennas (1575 MHz).....	29
Figure E-24: HPOL Gain Patterns for 14 External Antennas (1575 MHz).....	30
Figure E-25: RHCP Gain Patterns for 14 External Antennas (1575 MHz).....	31
Figure E-26: VPOL Gain Patterns for 14 External Antennas (1595 MHz).....	32
Figure E-27: HPOL Gain Patterns for 14 External Antennas (1595 MHz).....	33
Figure E-28: VPOL Gain Patterns for 14 External Antennas (1615 MHz).....	34
Figure E-29: HPOL Gain Patterns for 14 External Antennas (1615 MHz).....	35
Figure E-30: VPOL Gain Patterns for 14 External Antennas (1620 MHz).....	36
Figure E-31: HPOL Gain Patterns for 14 External Antennas (1620 MHz).....	37
Figure E-32: VPOL Gain Patterns for 14 External Antennas (1625 MHz).....	38
Figure E-33: HPOL Gain Patterns for 14 External Antennas (1625 MHz).....	39
Figure E-34: VPOL Gain Patterns for 14 External Antennas (1630 MHz).....	40
Figure E-35: HPOL Gain Patterns for 14 External Antennas (1630 MHz).....	41
Figure E-36: VPOL Gain Patterns for 14 External Antennas (1635 MHz).....	42

Figure E-37: HPOL Gain Patterns for 14 External Antennas (1635 MHz).....	43
Figure E-38: VPOL Gain Patterns for 14 External Antennas (1640 MHz).....	44
Figure E-39: HPOL Gain Patterns for 14 External Antennas (1640 MHz).....	45
Figure E-40: VPOL Gain Patterns for 14 External Antennas (1645 MHz).....	46
Figure E-41: HPOL Gain Patterns for 14 External Antennas (1645 MHz).....	47
Figure E-42: VPOL Gain Patterns for 14 External Antennas (1660 MHz).....	48
Figure E-43: HPOL Gain Patterns for 14 External Antennas (1660 MHz).....	49
Figure E-44: VPOL Gain Patterns for 14 External Antennas (1675 MHz).....	50
Figure E-45: HPOL Gain Patterns for 14 External Antennas (1675 MHz).....	51



## **LIST OF TABLES**

No table of figures entries found.

## **REFERENCES**

**There are no sources in the current document.**

# APPENDIX

## Appendix E. Antenna Characterization Details

### E.1 Anechoic Chamber Measurements

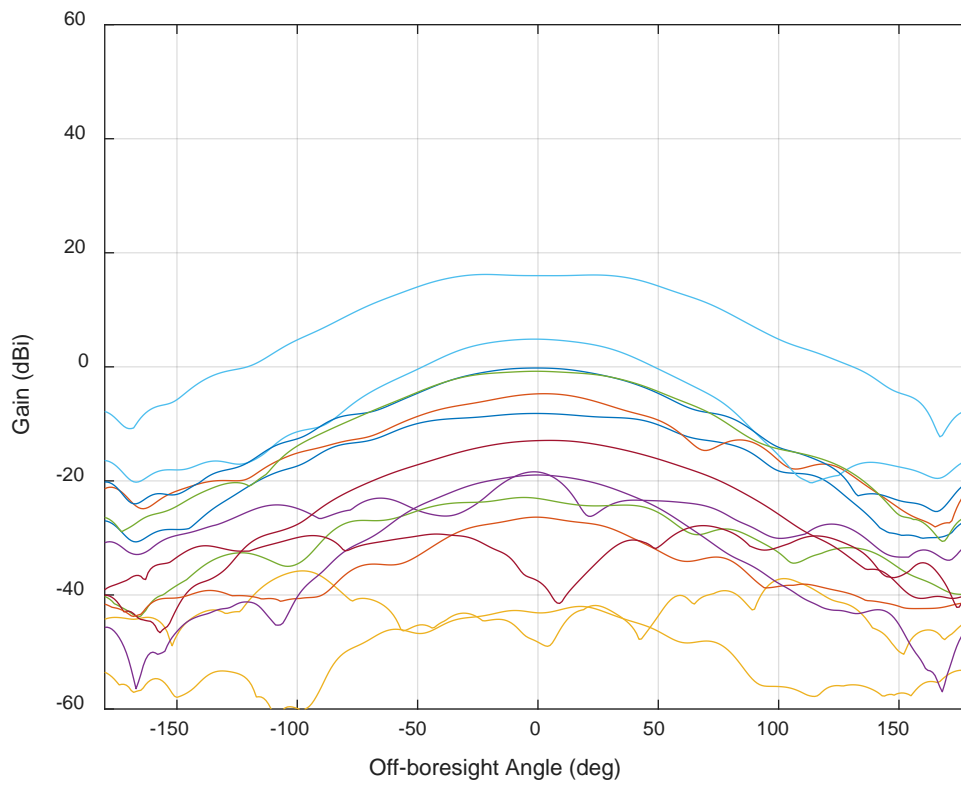


**Figure E-1: VPOL Gain Patterns for 14 External Antennas (1475 MHz)**

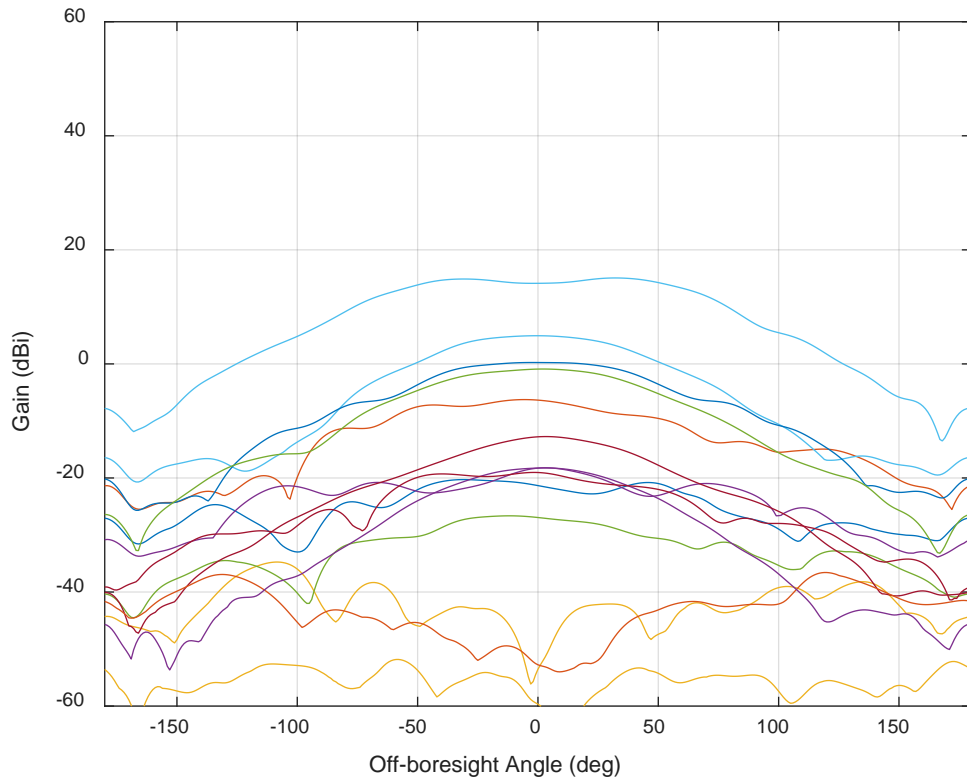


**Figure E-2: HPOL Gain Patterns for 14 External Antennas (1475 MHz)**

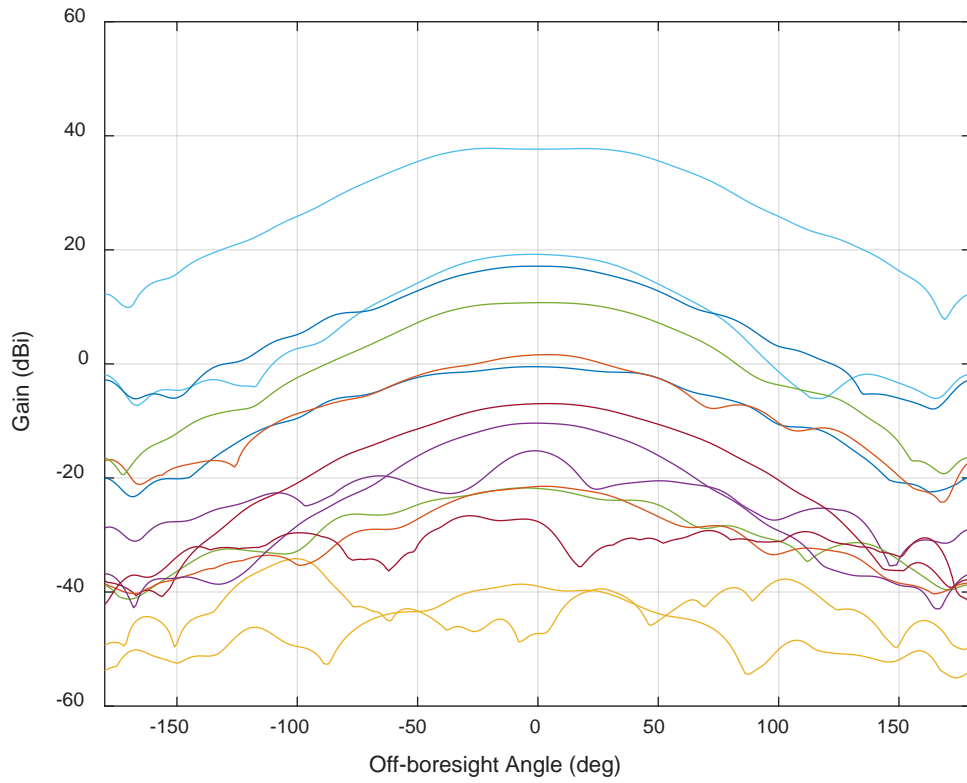


**Figure E-3: VPOL Gain Patterns for 14 External Antennas (1490 MHz)**

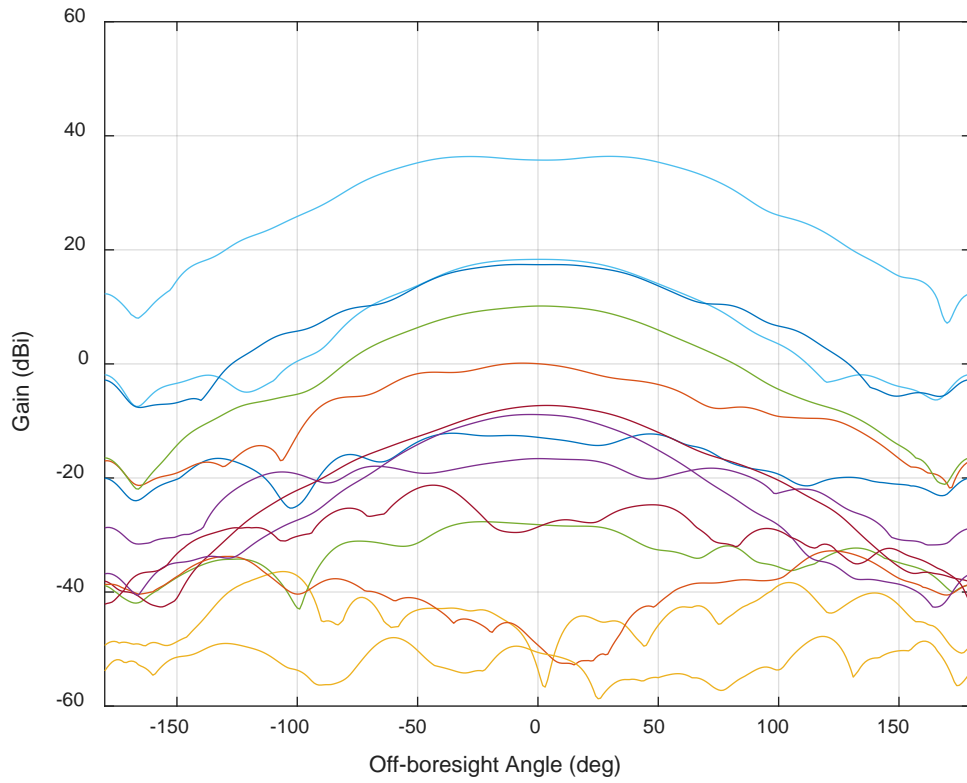


**Figure E-4: HPOL Gain Patterns for 14 External Antennas (1490 MHz)**

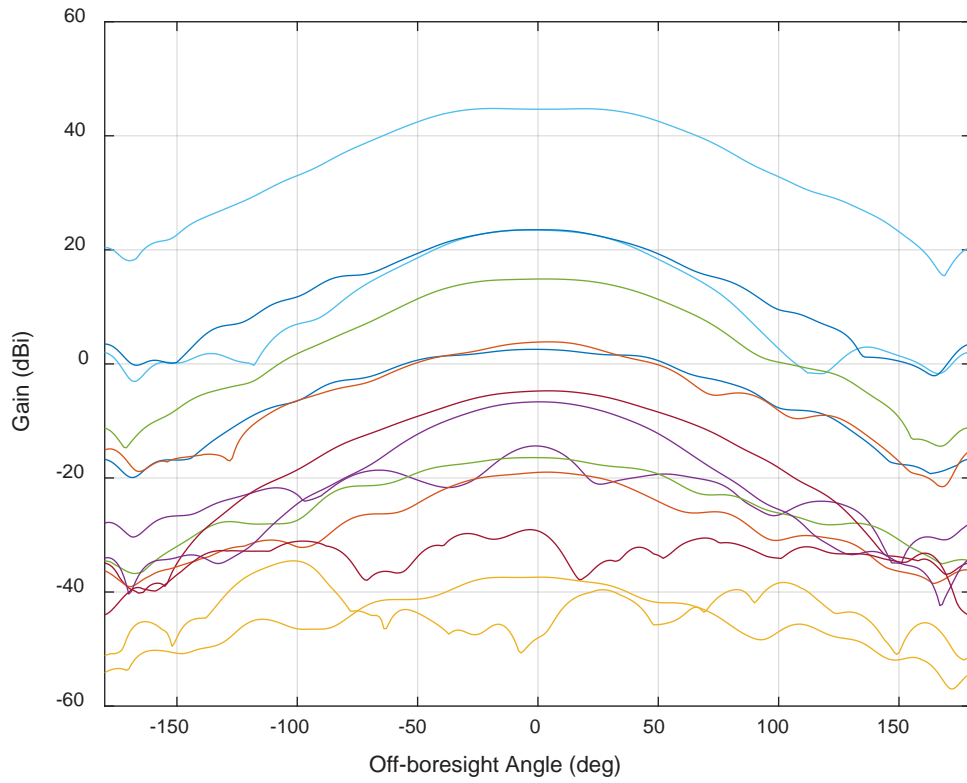


**Figure E-5: VPOL Gain Patterns for 14 External Antennas (1495 MHz)**

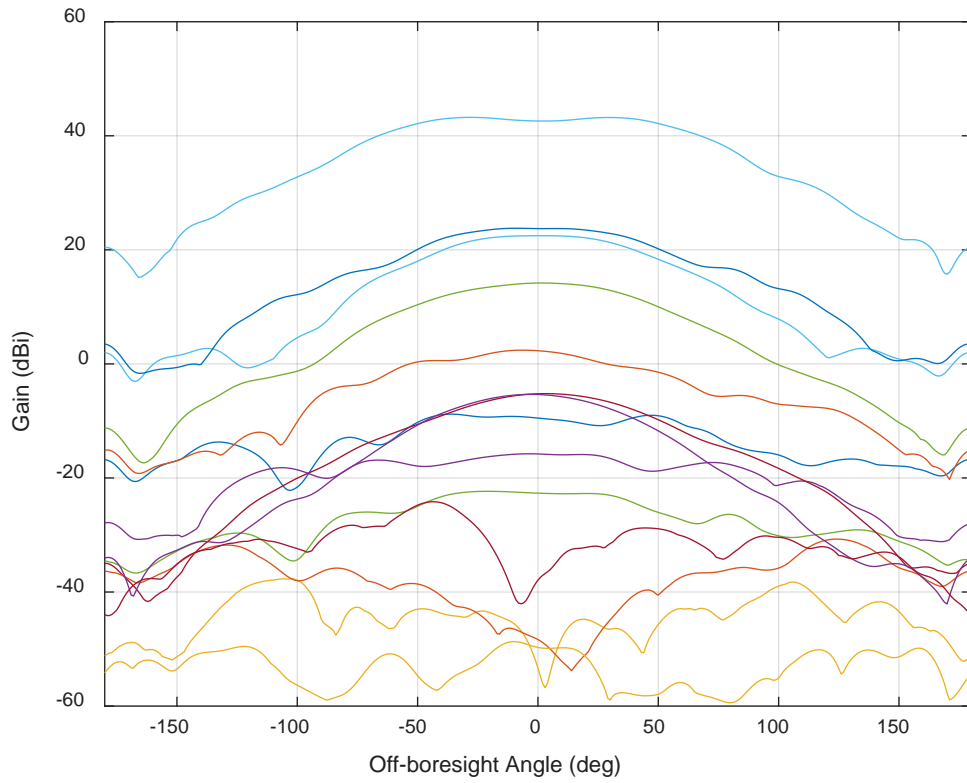


**Figure E-6: HPOL Gain Patterns for 14 External Antennas (1495 MHz)**



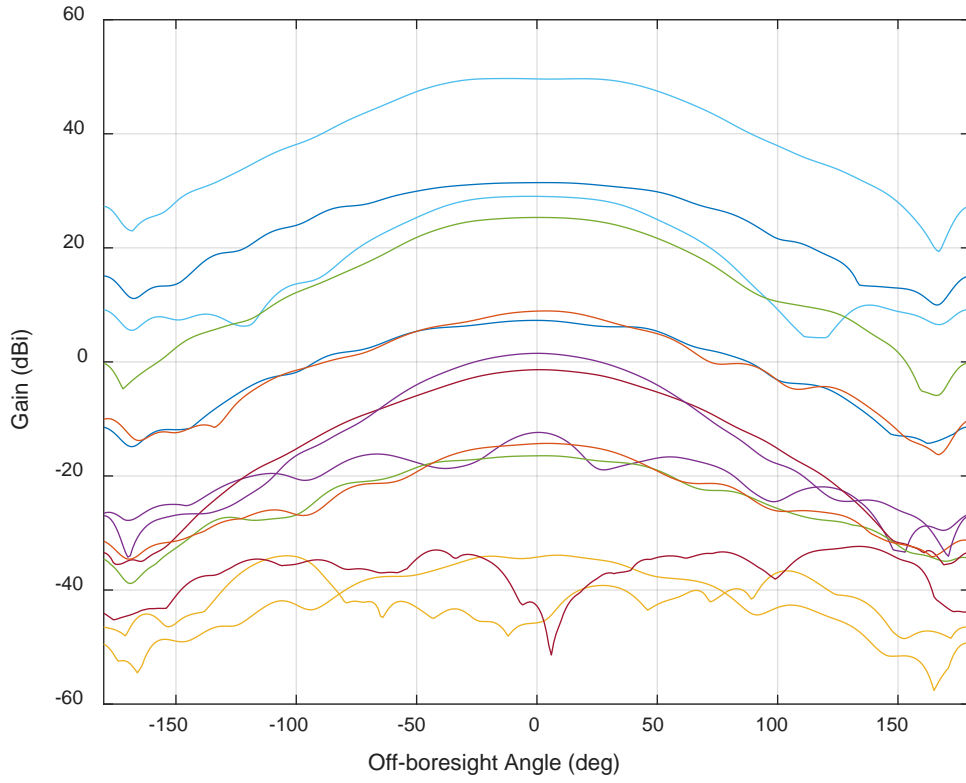


**Figure E-7: VPOL Gain Patterns for 14 External Antennas (1505 MHz)**

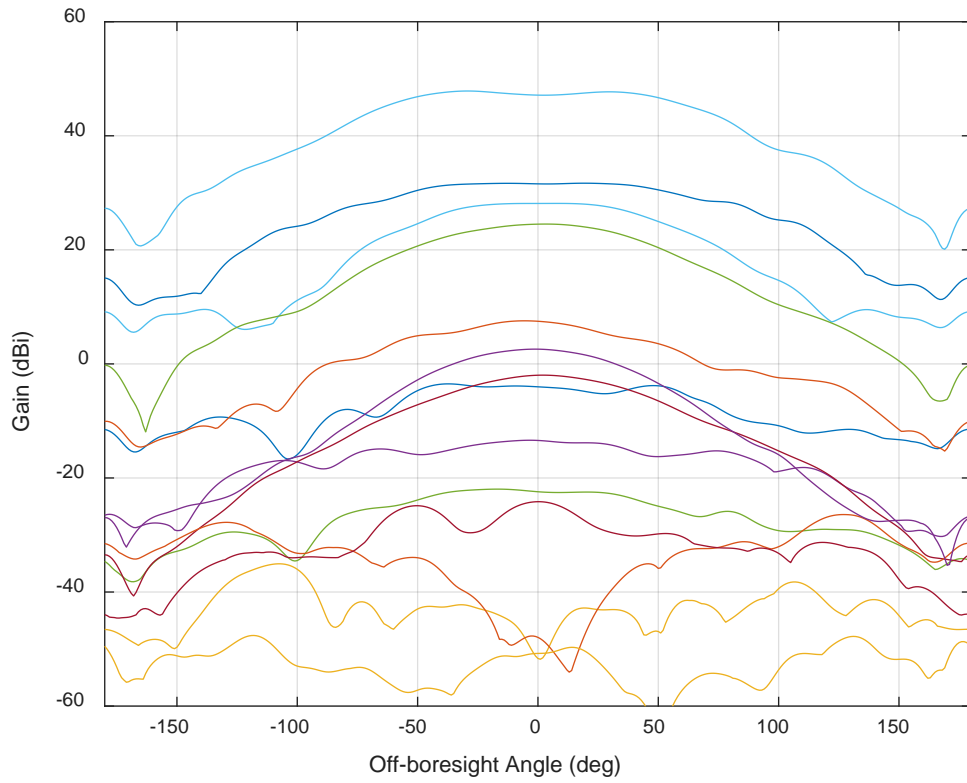


**Figure E-8: HPOL Gain Patterns for 14 External Antennas (1505 MHz)**

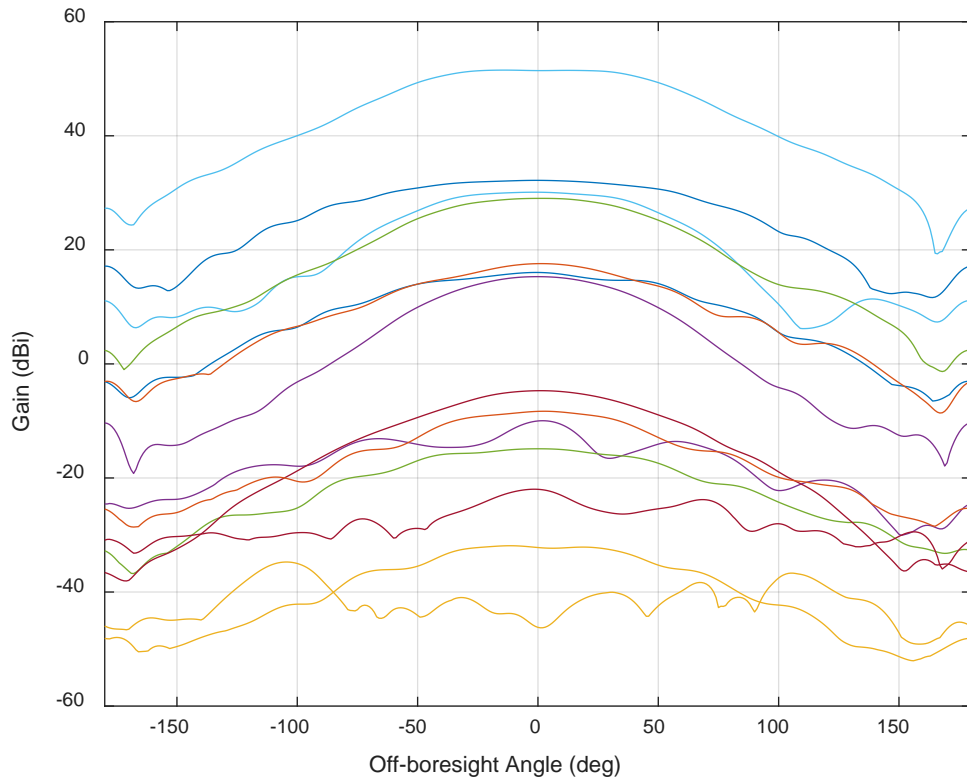


**Figure E-9: VPOL Gain Patterns for 14 External Antennas (1520 MHz)**

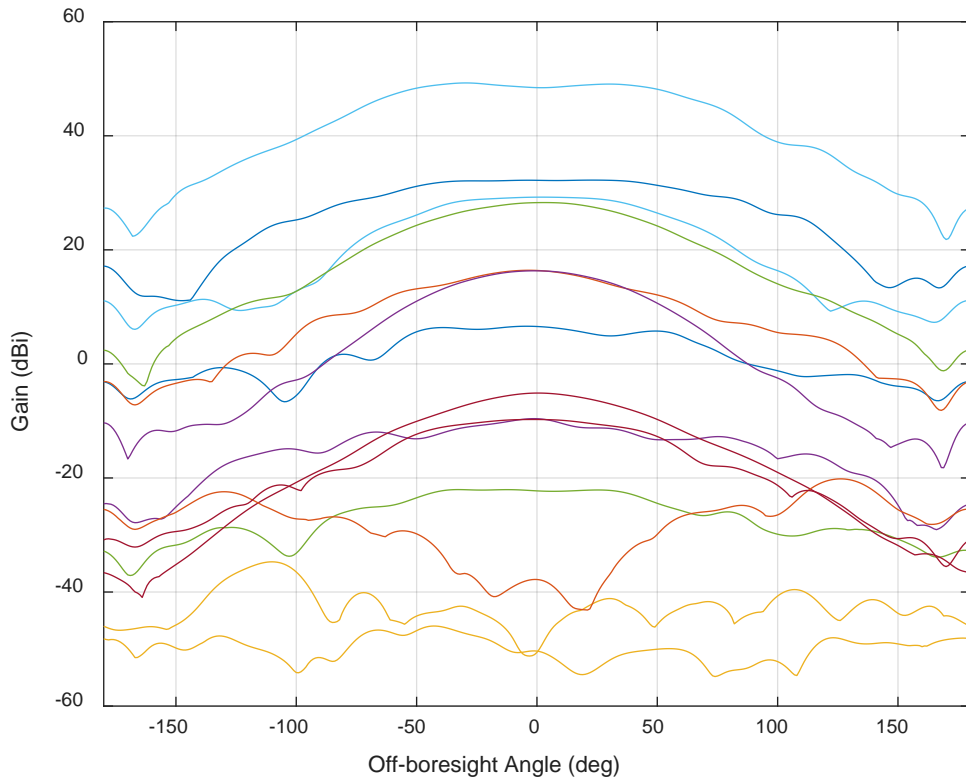


**Figure E-10: HPOL Gain Patterns for 14 External Antennas (1520 MHz)**

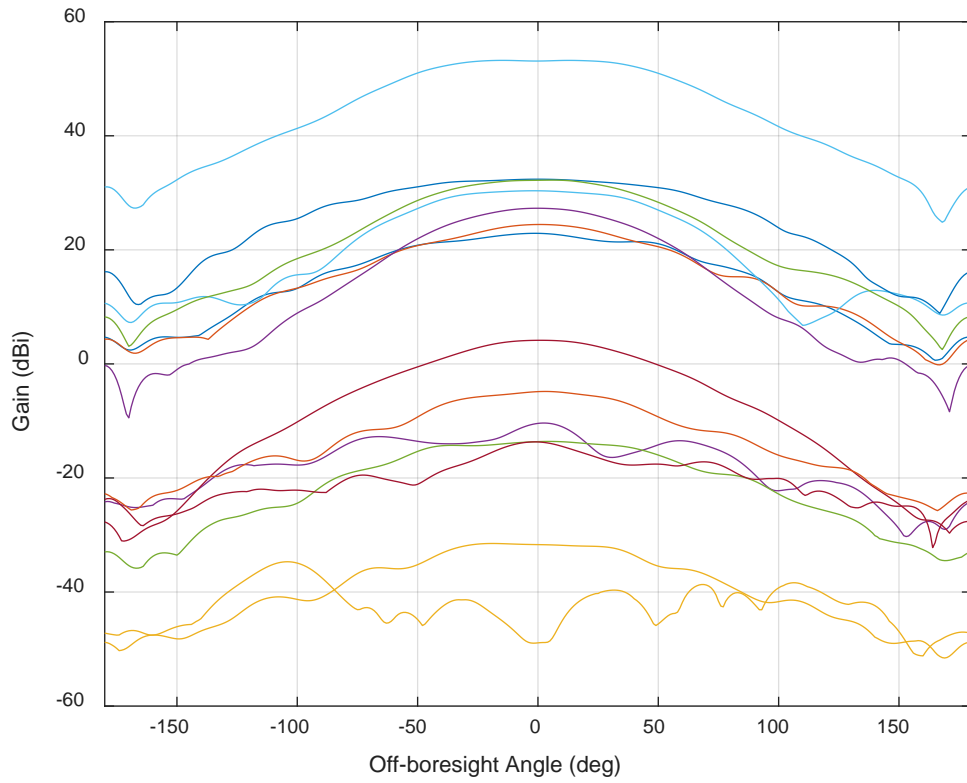


**Figure E-11: VPOL Gain Patterns for 14 External Antennas (1530 MHz)**

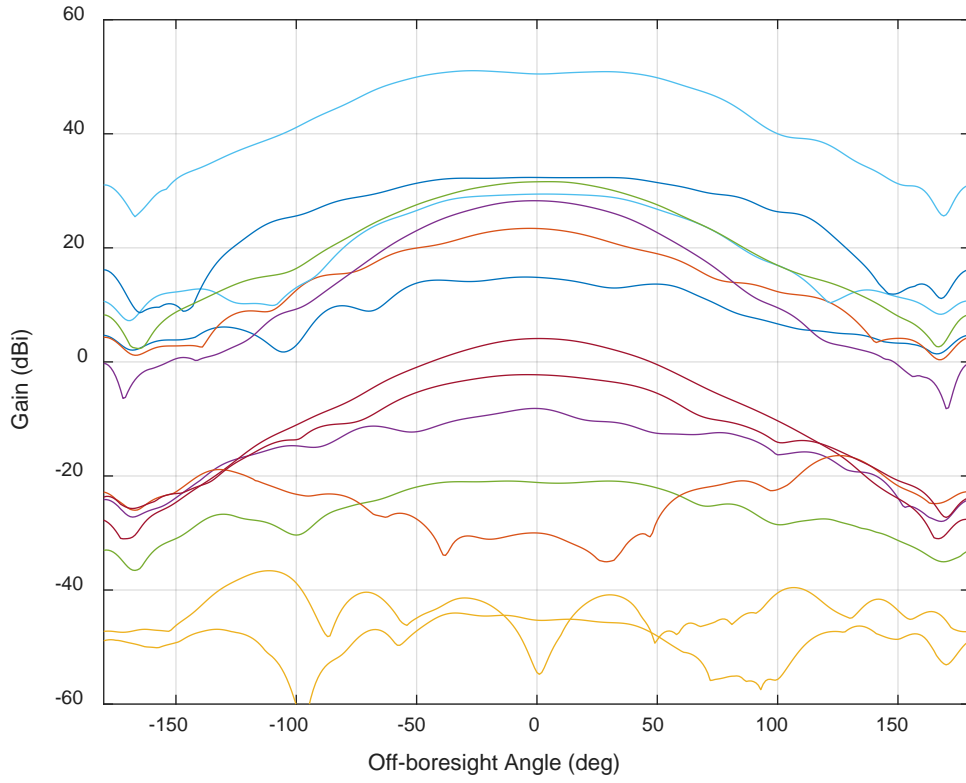


**Figure E-12: HPOL Gain Patterns for 14 External Antennas (1530 MHz)**

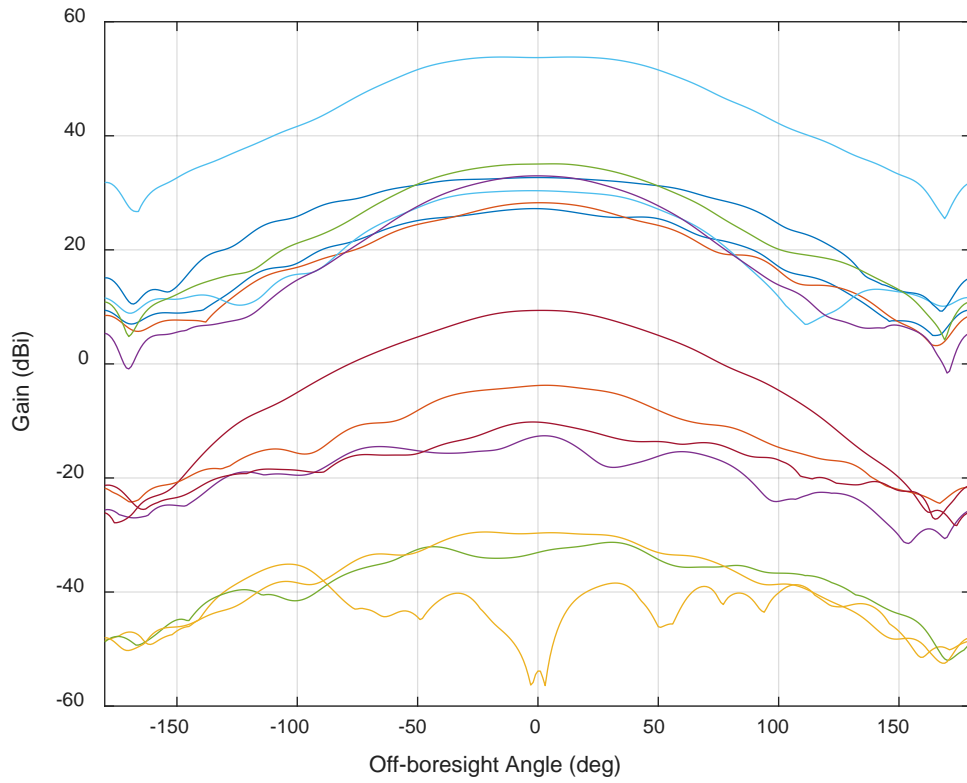


**Figure E-13: VPOL Gain Patterns for 14 External Antennas (1535 MHz)**

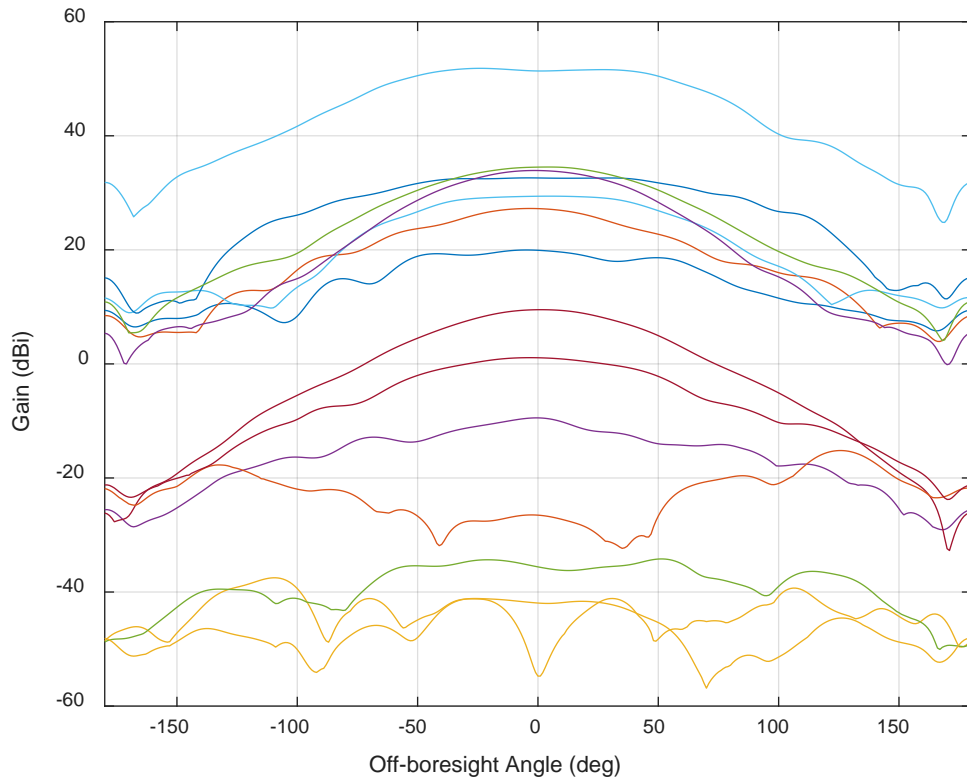


**Figure E-14: HPOL Gain Patterns for 14 External Antennas (1535 MHz)**



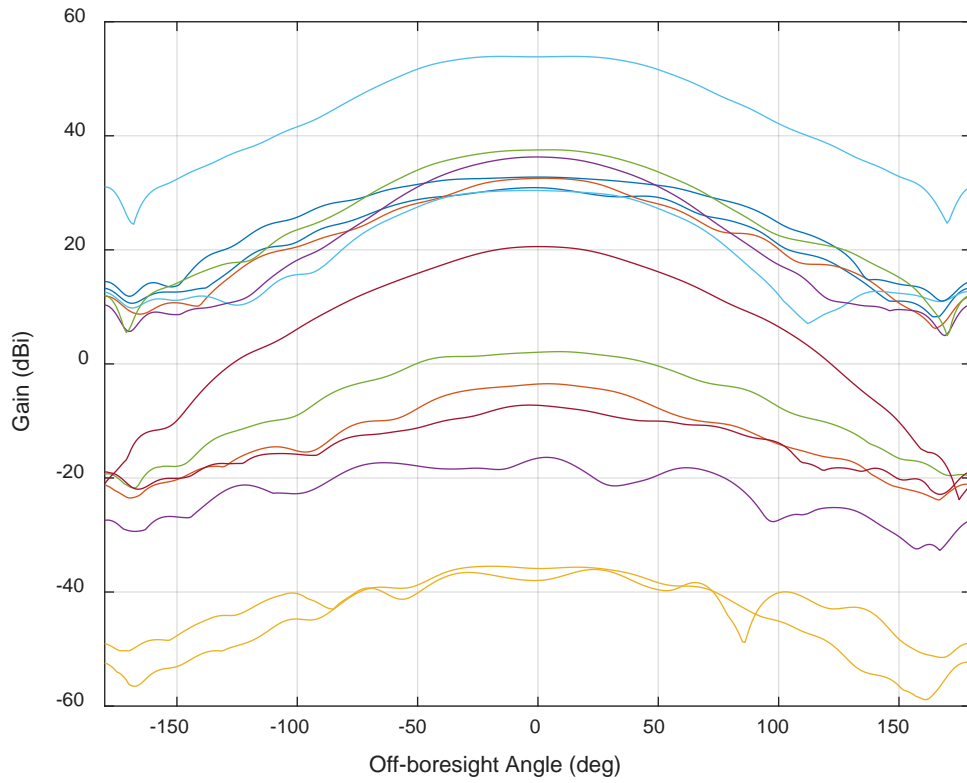


**Figure E-15: VPOL Gain Patterns for 14 External Antennas (1540 MHz)**

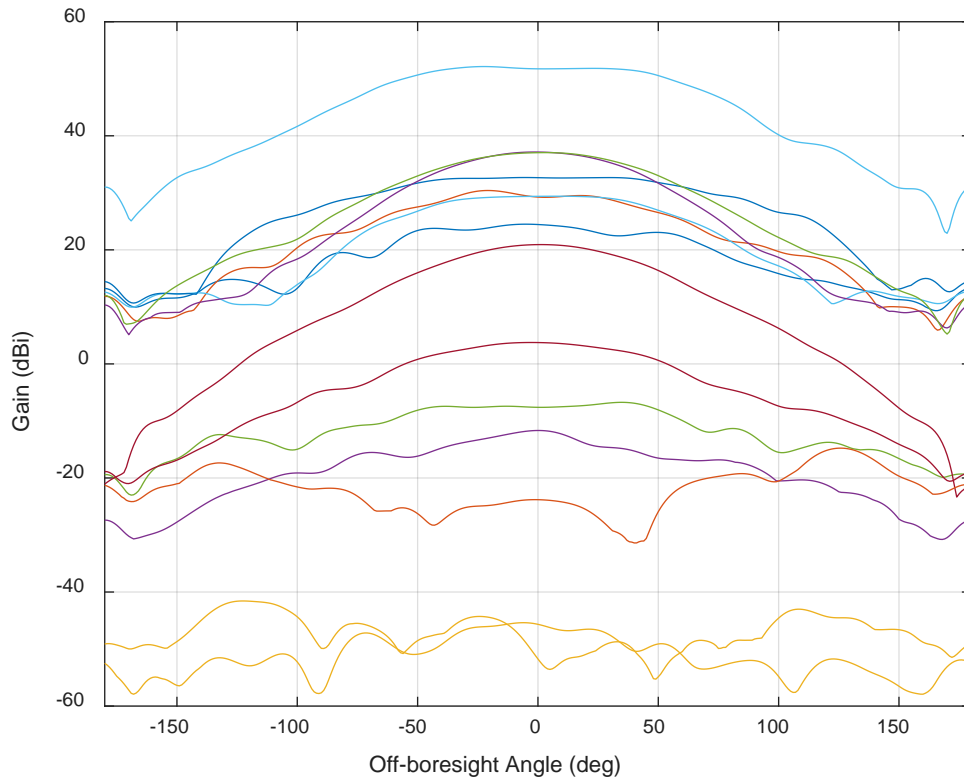


**Figure E-16: HPOL Gain Patterns for 14 External Antennas (1540 MHz)**

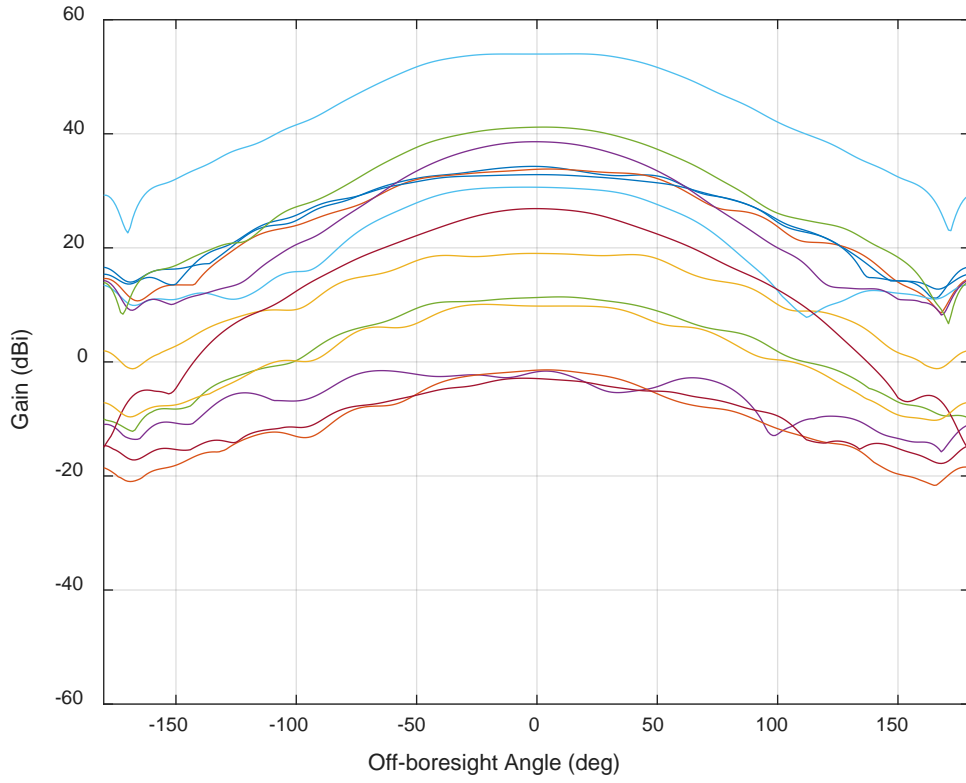


**Figure E-17: VPOL Gain Patterns for 14 External Antennas (1545 MHz)**

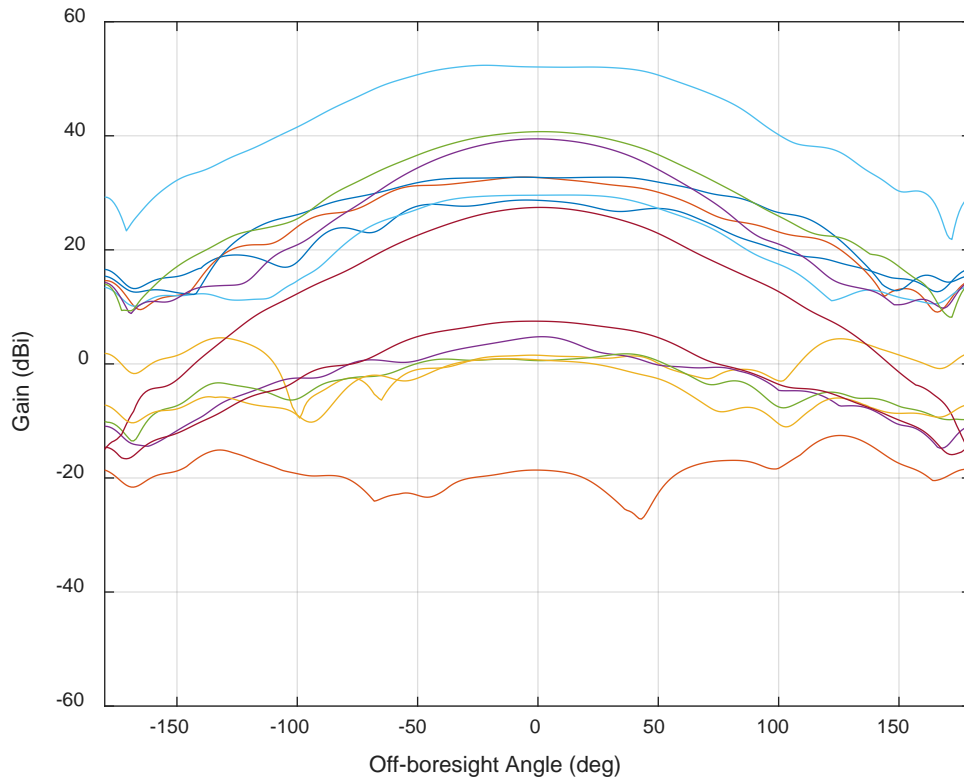


**Figure E-18: HPOL Gain Patterns for 14 External Antennas (1545 MHz)**

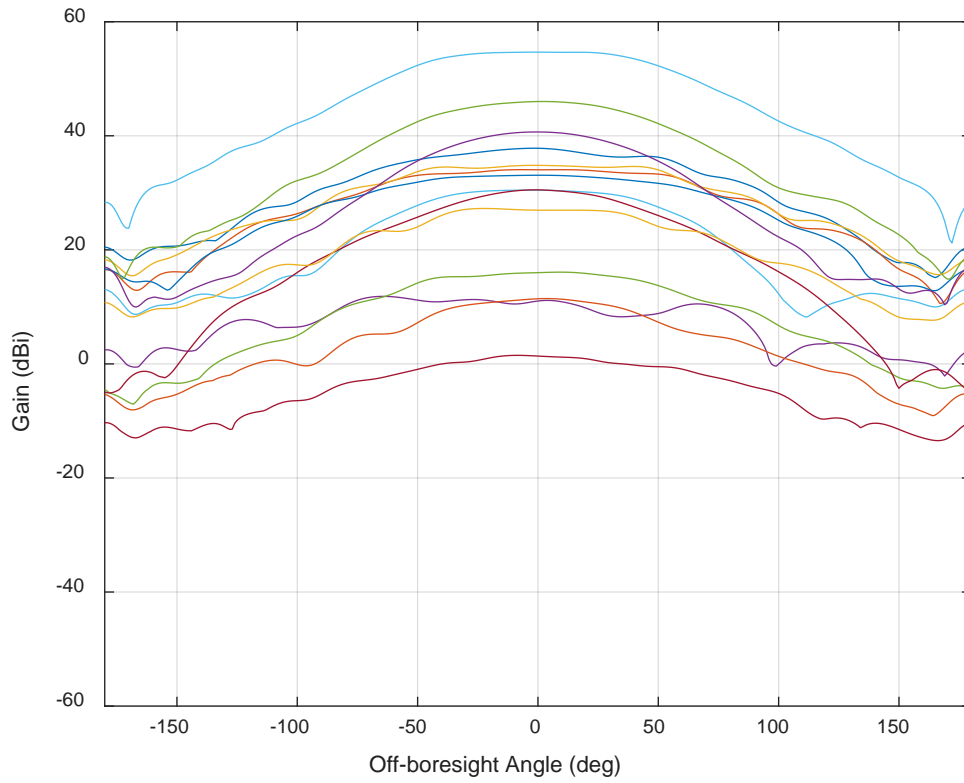


**Figure E-19: VPOL Gain Patterns for 14 External Antennas (1550 MHz)**

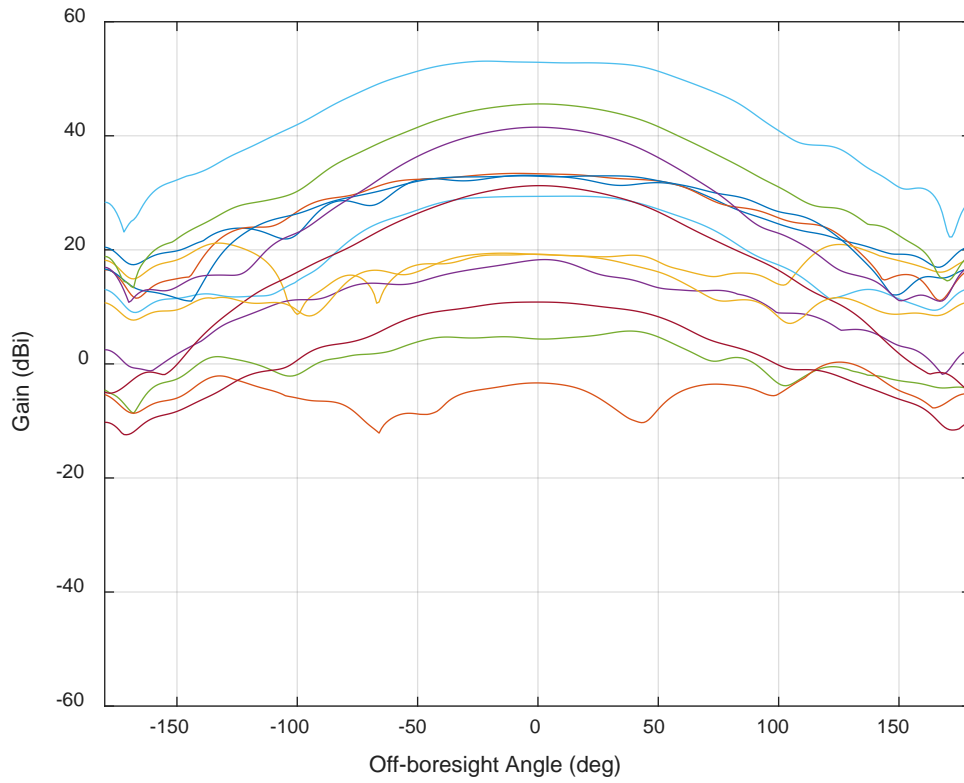


**Figure E-20: HPOL Gain Patterns for 14 External Antennas (1550 MHz)**

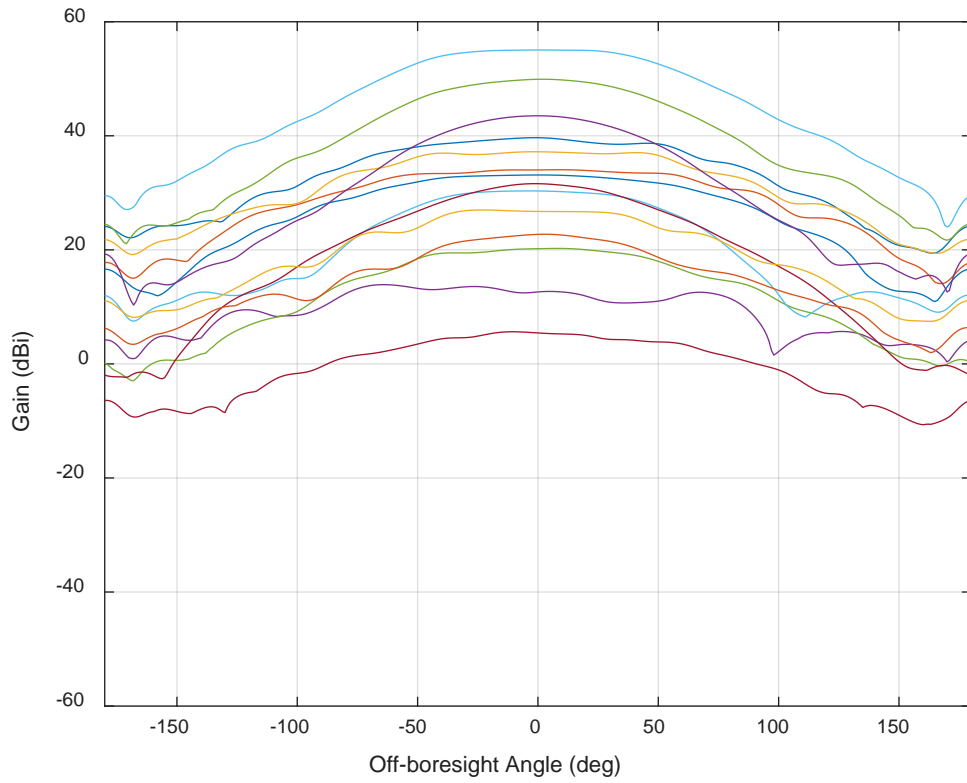


**Figure E-21: VPOL Gain Patterns for 14 External Antennas (1555 MHz)**

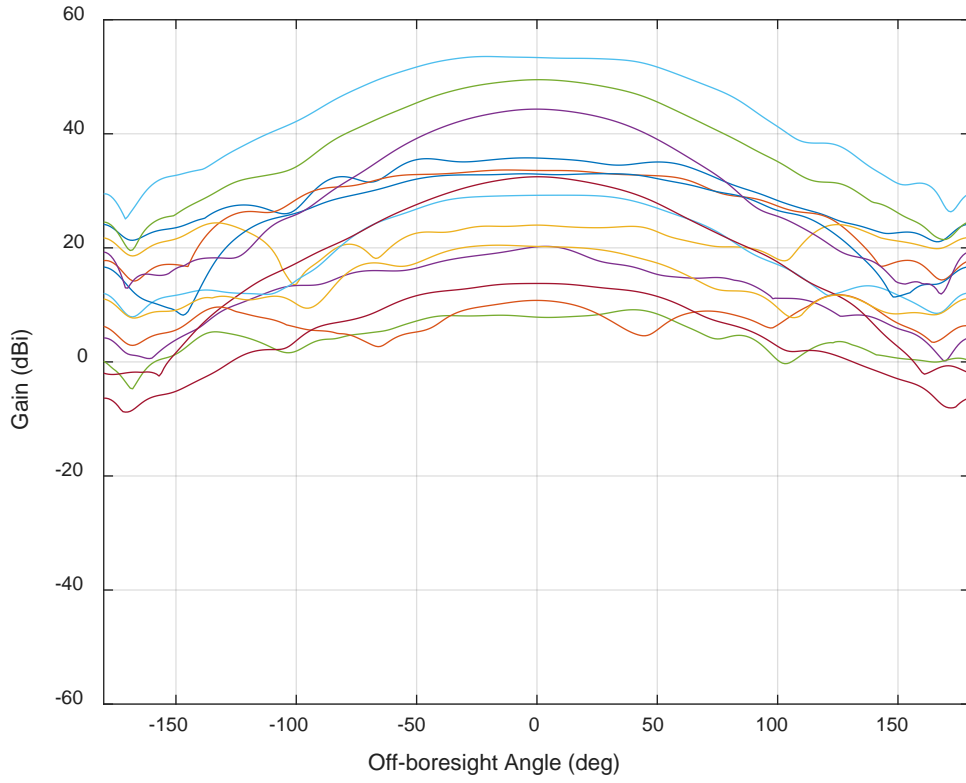


**Figure E-22: HPOL Gain Patterns for 14 External Antennas (1555 MHz)**



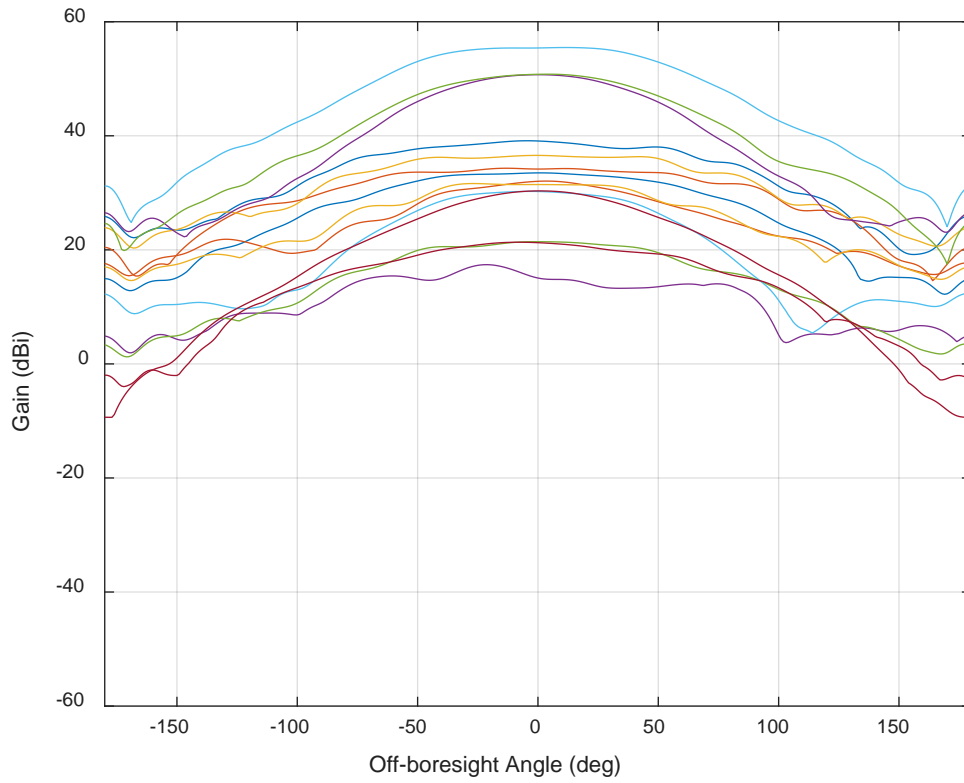


**Figure E-23: VPOL Gain Patterns for 14 External Antennas (1575 MHz)**

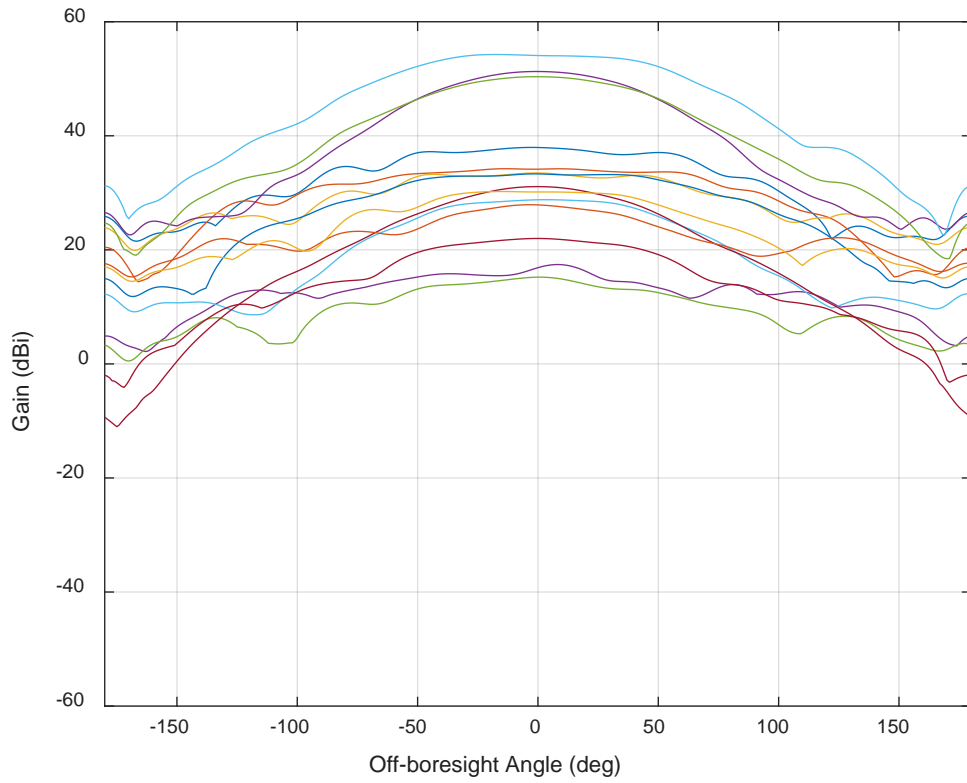


**Figure E-24: HPOL Gain Patterns for 14 External Antennas (1575 MHz)**

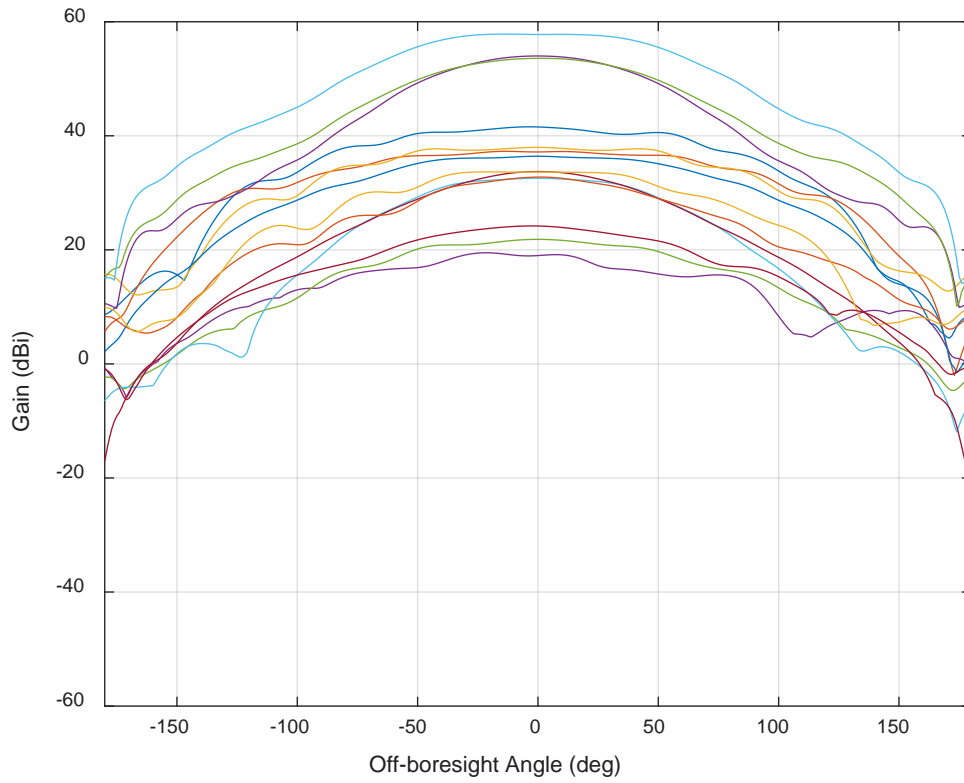


**Figure E-25: RHCP Gain Patterns for 14 External Antennas (1575 MHz)**

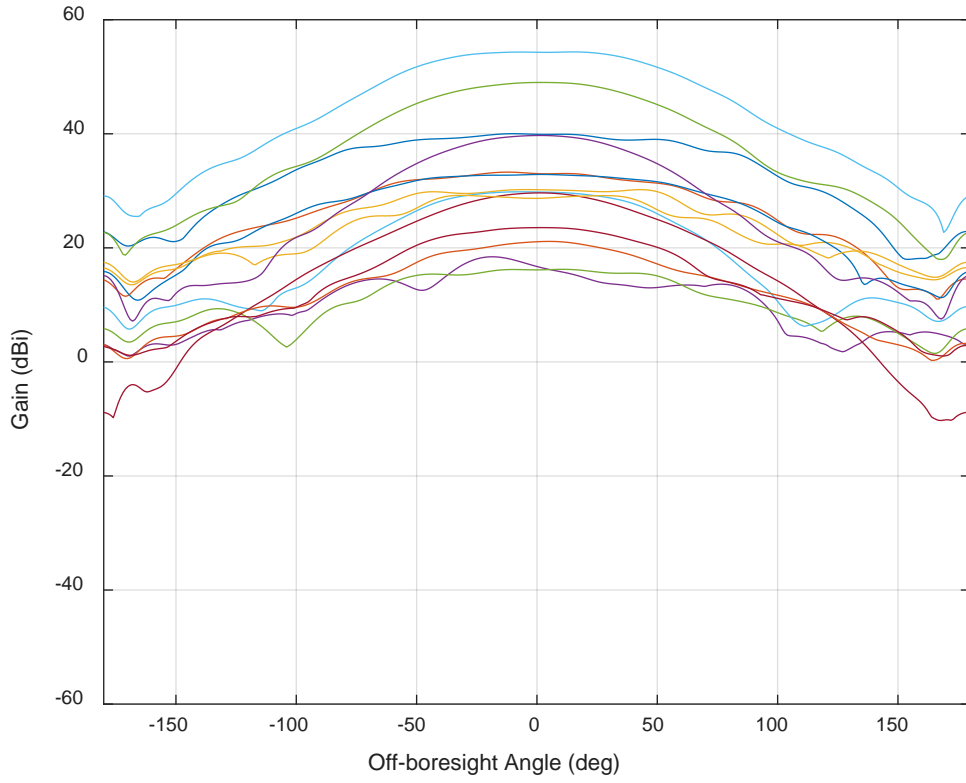


**Figure E-26: VPOL Gain Patterns for 14 External Antennas (1595 MHz)**

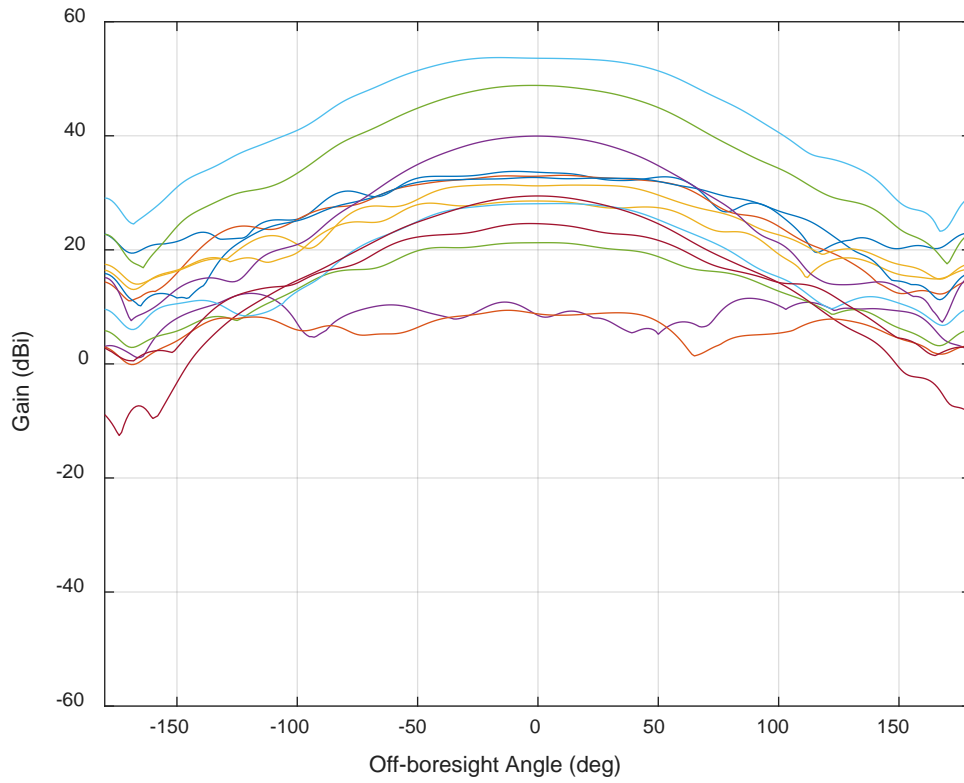


**Figure E-27: HPOL Gain Patterns for 14 External Antennas (1595 MHz)**

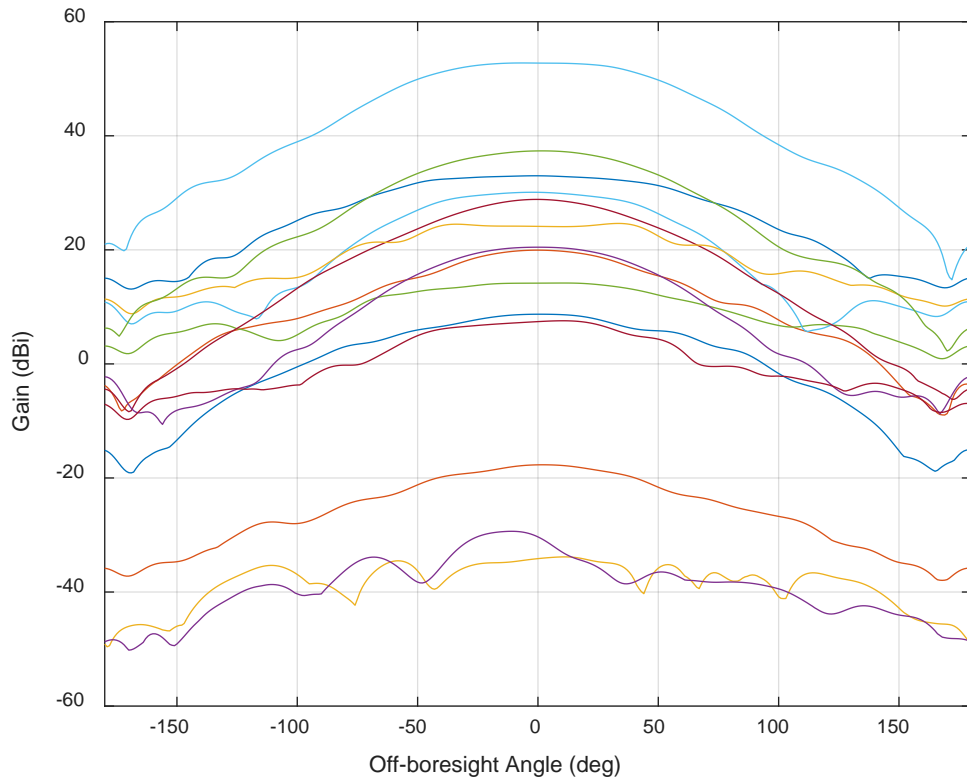


**Figure E-28: VPOL Gain Patterns for 14 External Antennas (1615 MHz)**

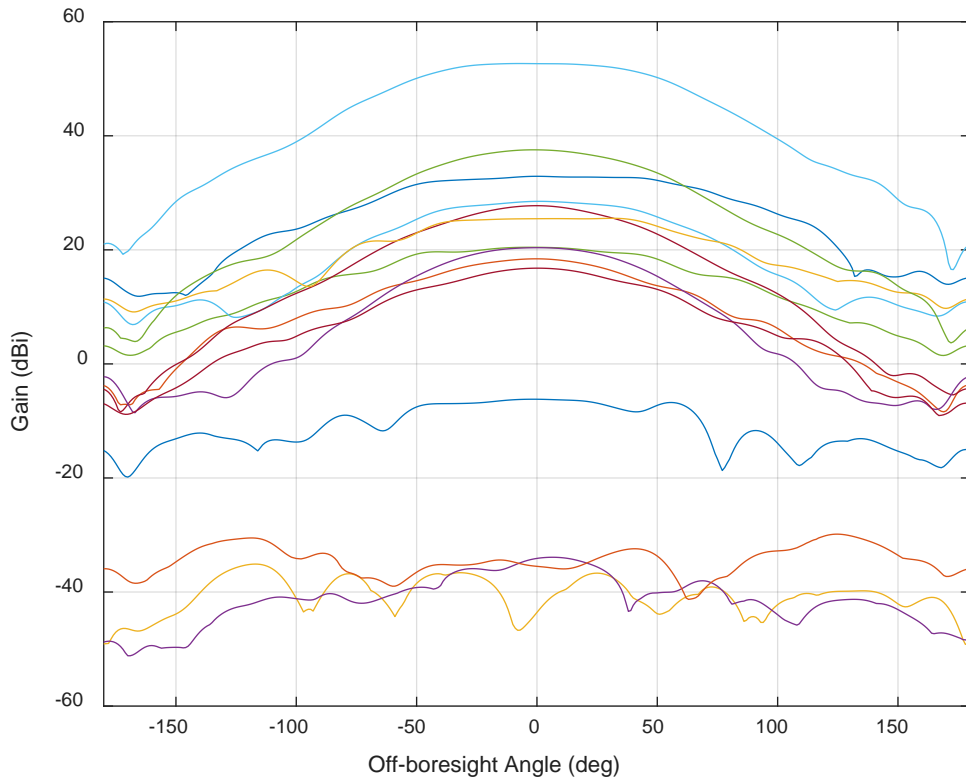


**Figure E-29: HPOL Gain Patterns for 14 External Antennas (1615 MHz)**

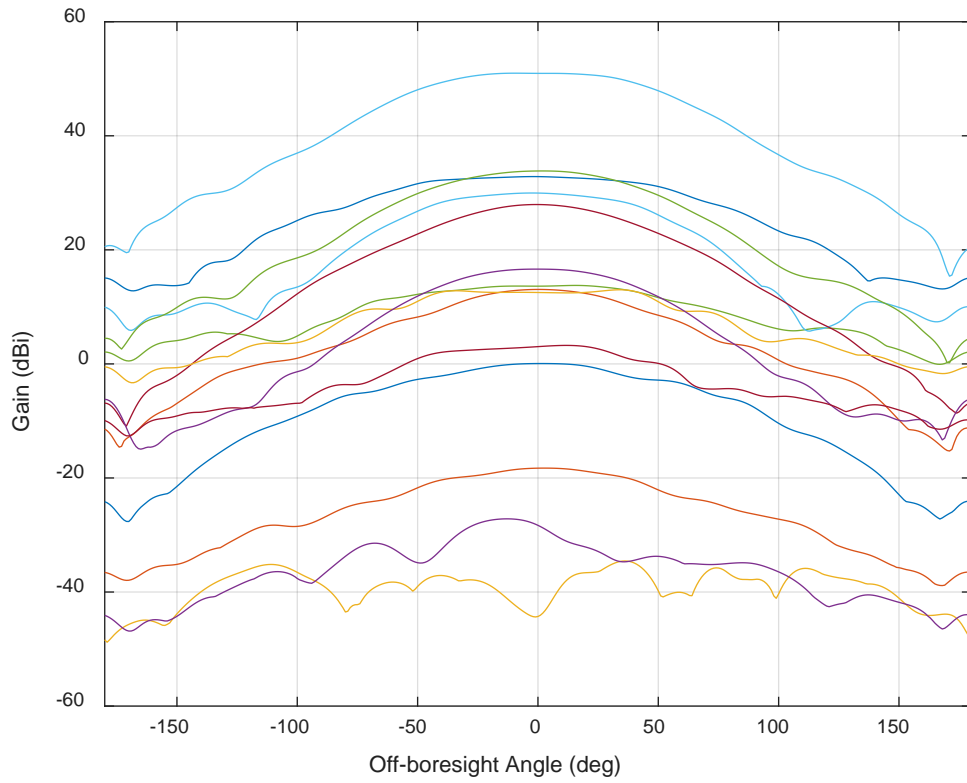


**Figure E-30: VPOL Gain Patterns for 14 External Antennas (1620 MHz)**



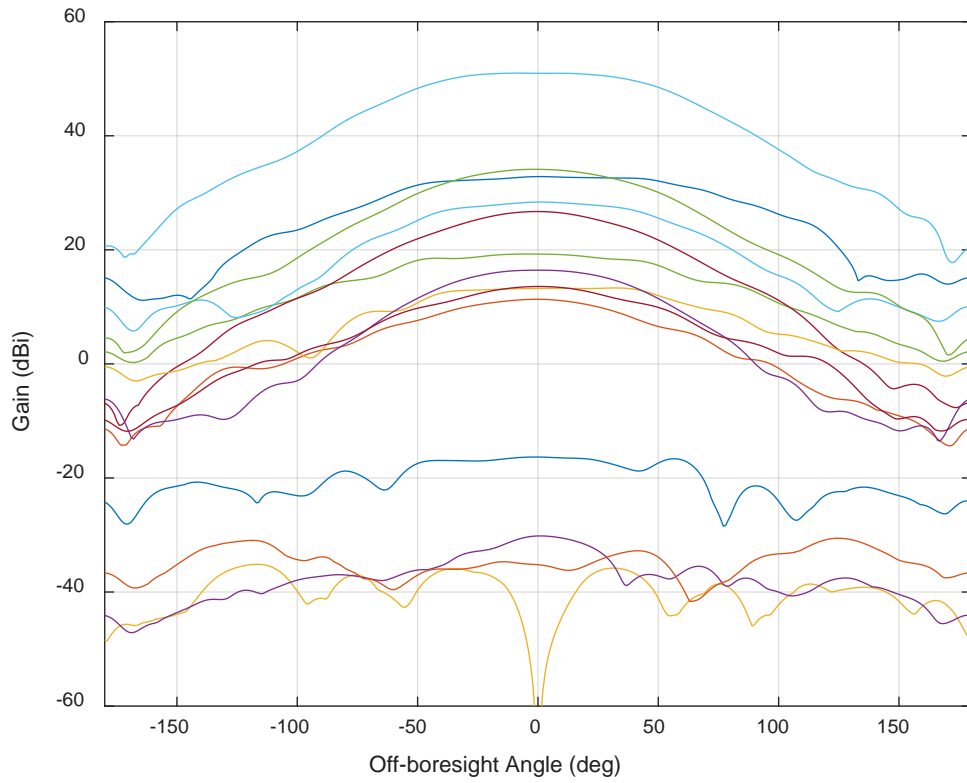


**Figure E-31: HPOL Gain Patterns for 14 External Antennas (1620 MHz)**

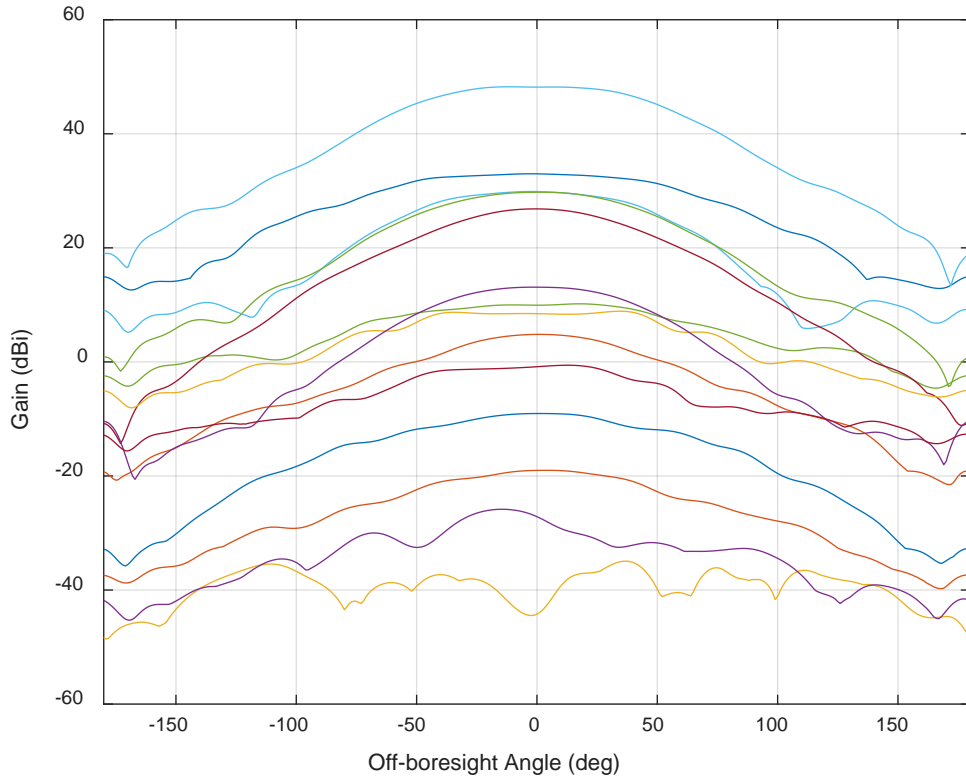


**Figure E-32: VPOL Gain Patterns for 14 External Antennas (1625 MHz)**

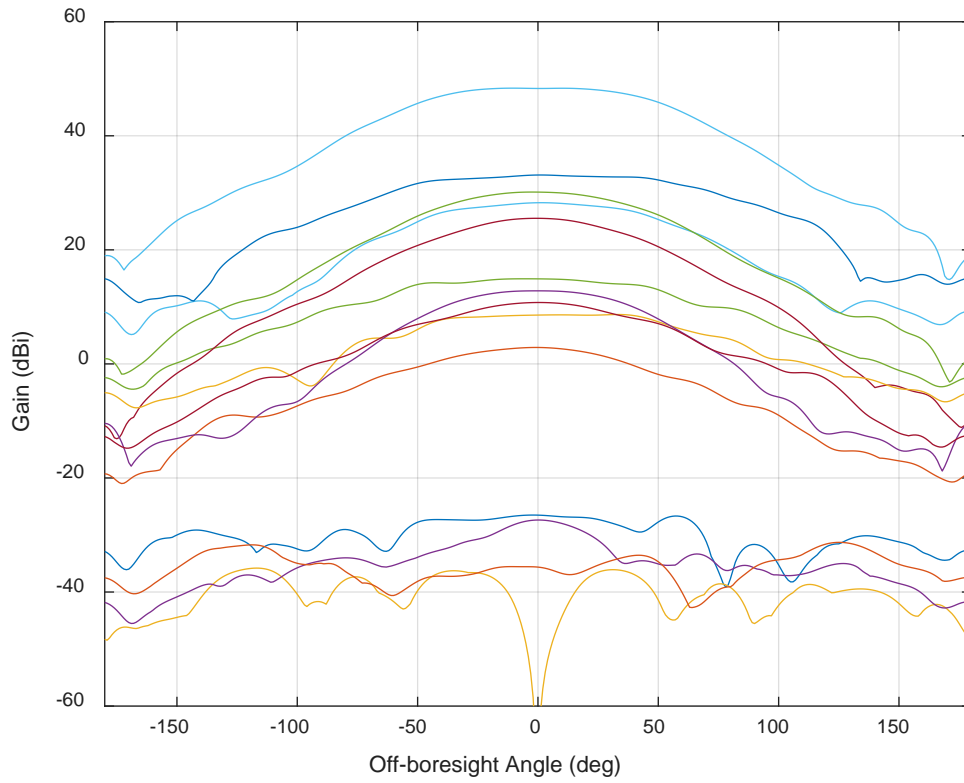


**Figure E-33: HPOL Gain Patterns for 14 External Antennas (1625 MHz)**

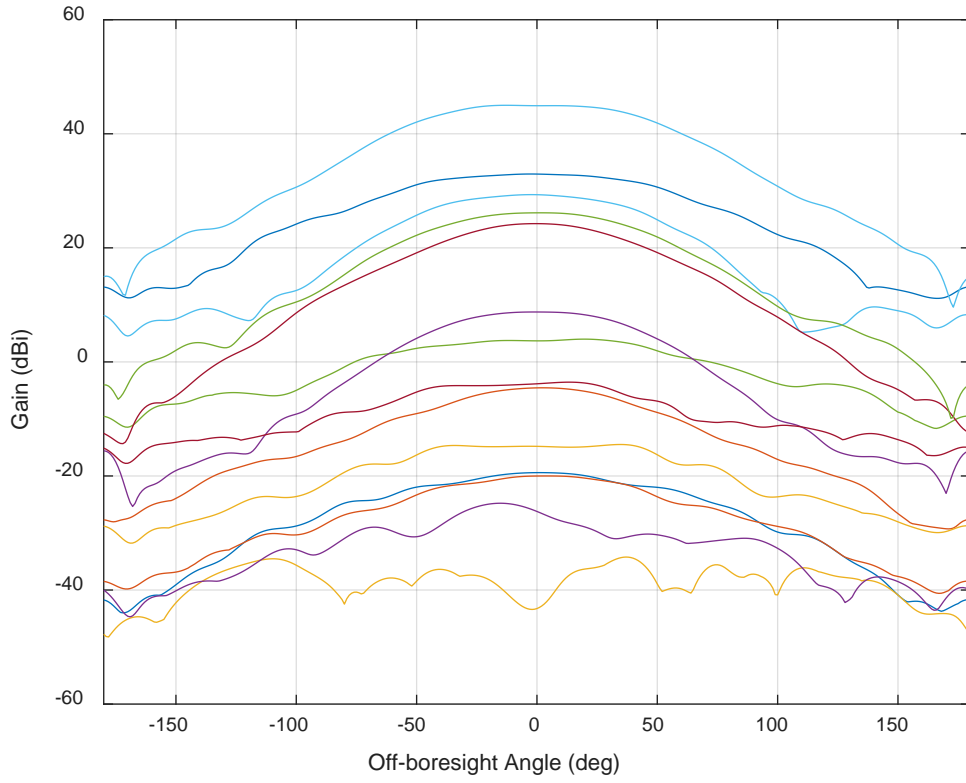


**Figure E-34: VPOL Gain Patterns for 14 External Antennas (1630 MHz)**

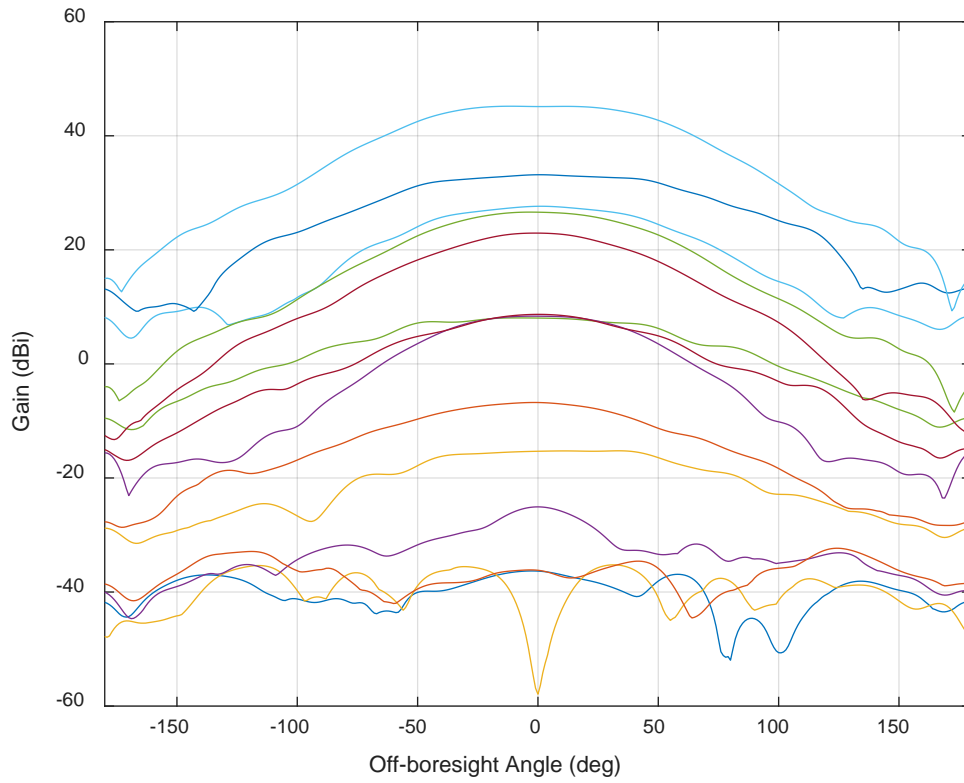


**Figure E-35: HPOL Gain Patterns for 14 External Antennas (1630 MHz)**

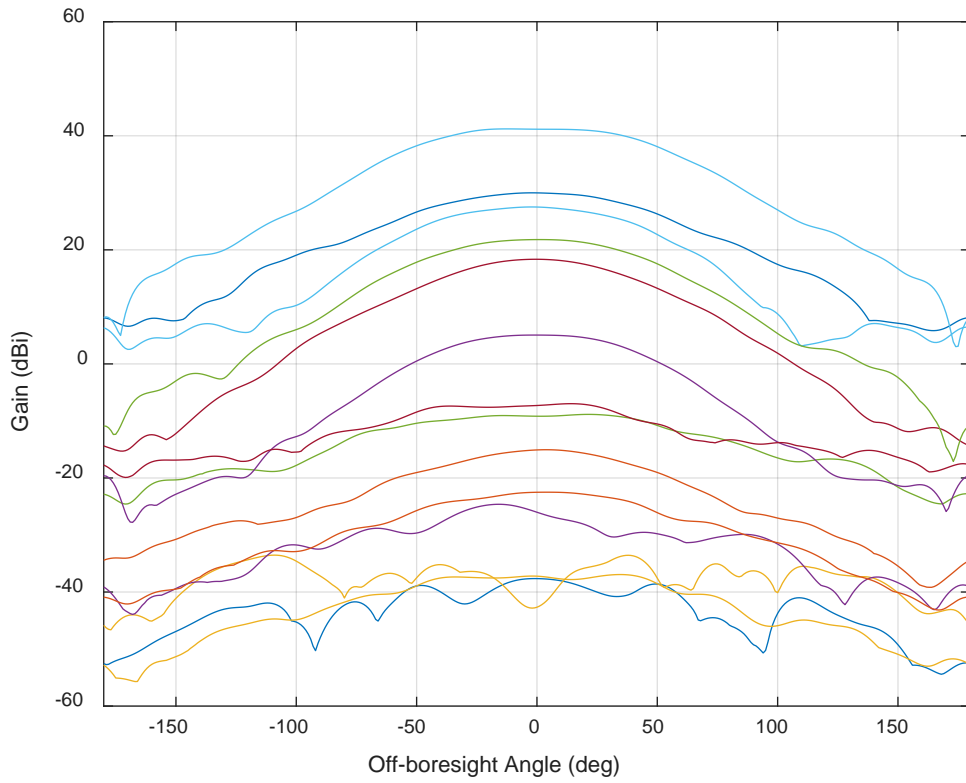


**Figure E-36: VPOL Gain Patterns for 14 External Antennas (1635 MHz)**

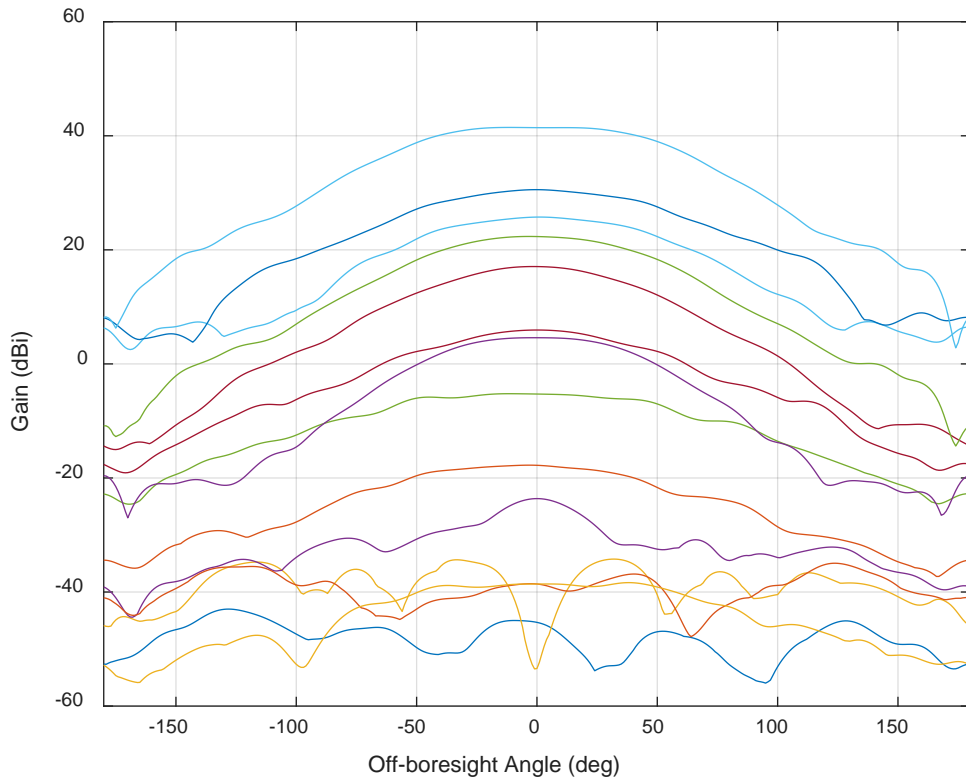


**Figure E-37: HPOL Gain Patterns for 14 External Antennas (1635 MHz)**

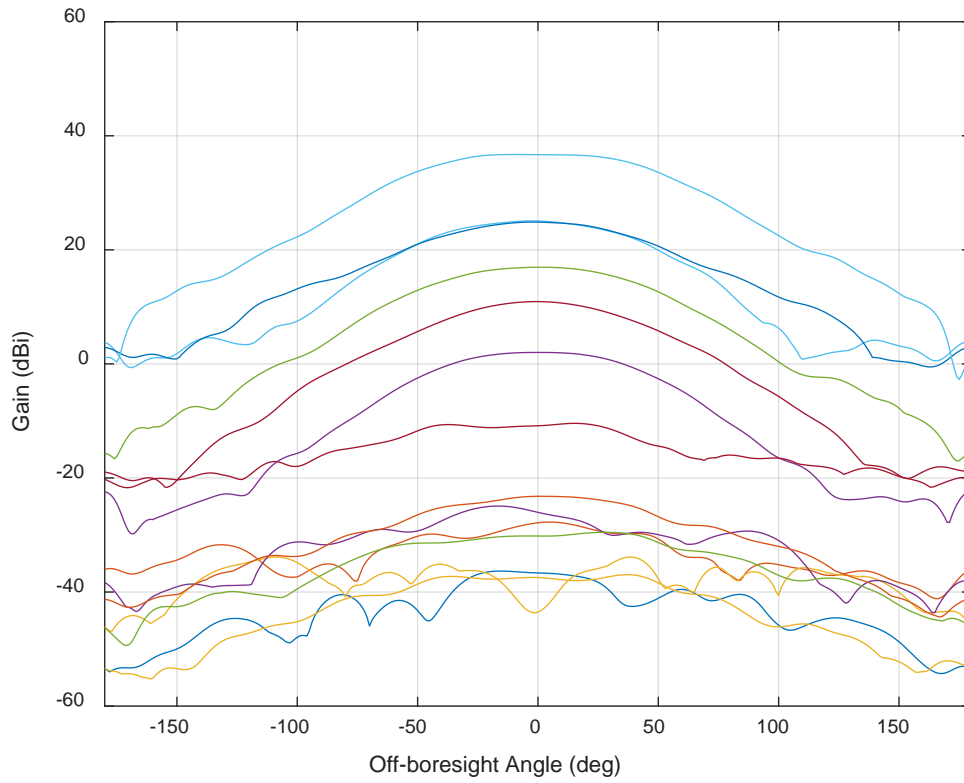


**Figure E-38: VPOL Gain Patterns for 14 External Antennas (1640 MHz)**



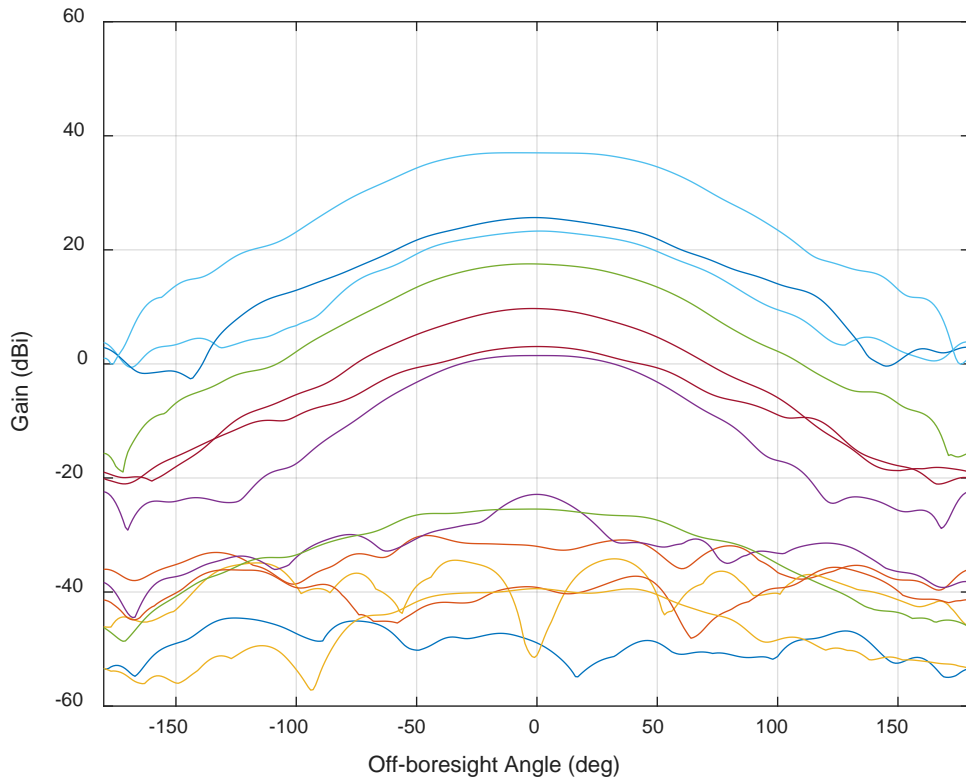


**Figure E-39: HPOL Gain Patterns for 14 External Antennas (1640 MHz)**

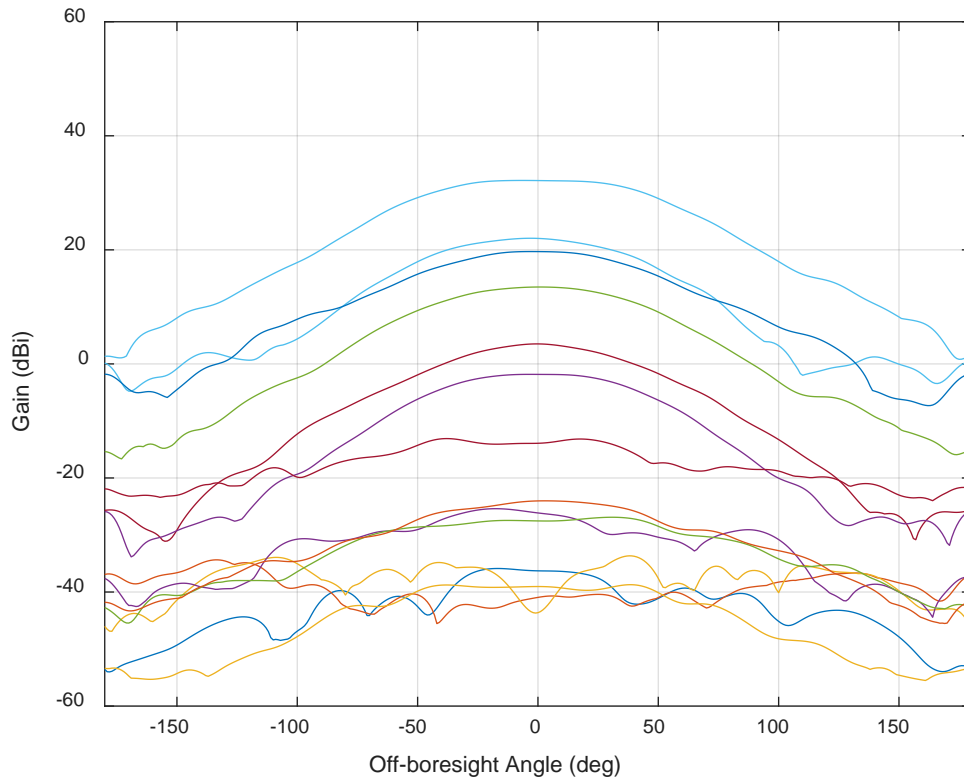


**Figure E-40: VPOL Gain Patterns for 14 External Antennas (1645 MHz)**

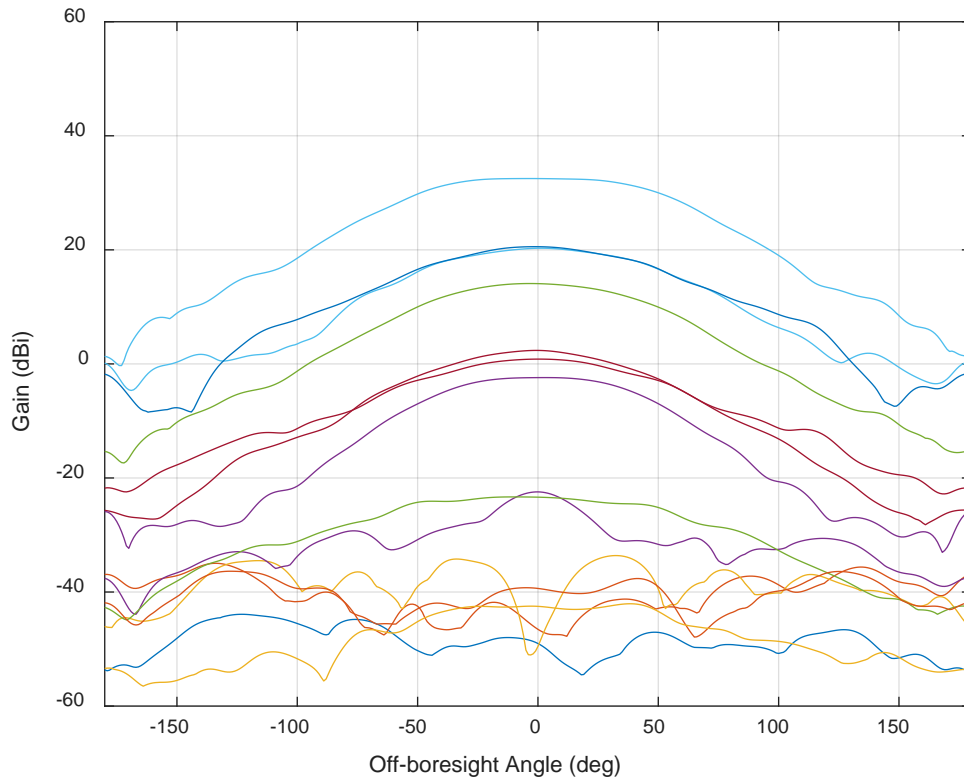


**Figure E-41: HPOL Gain Patterns for 14 External Antennas (1645 MHz)**

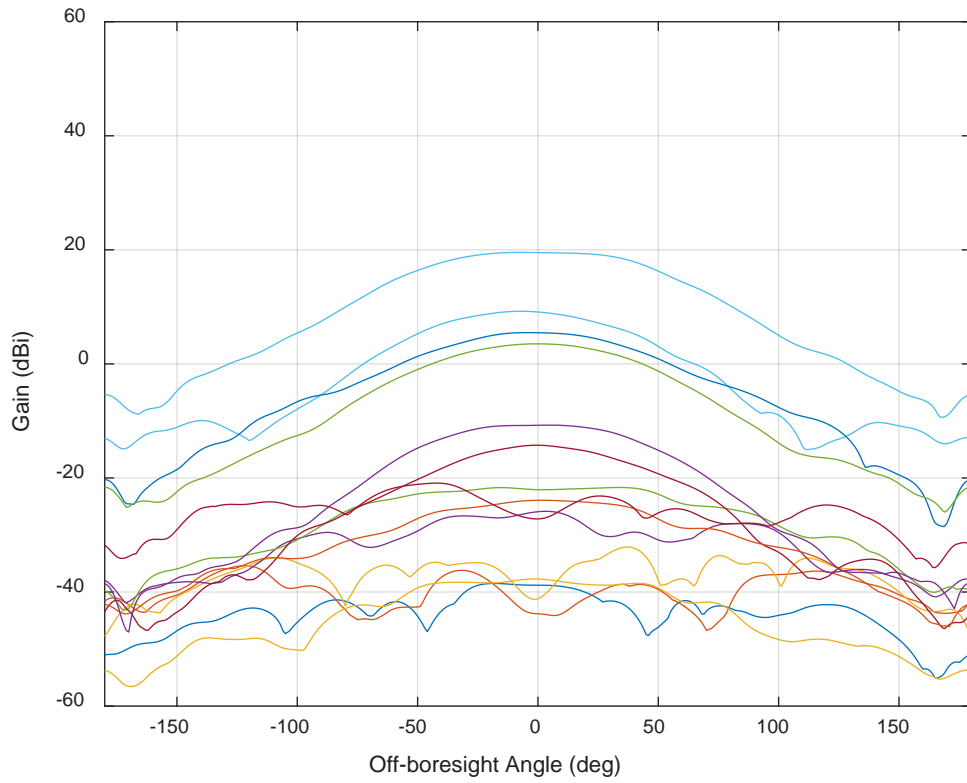


**Figure E-42: VPOL Gain Patterns for 14 External Antennas (1660 MHz)**

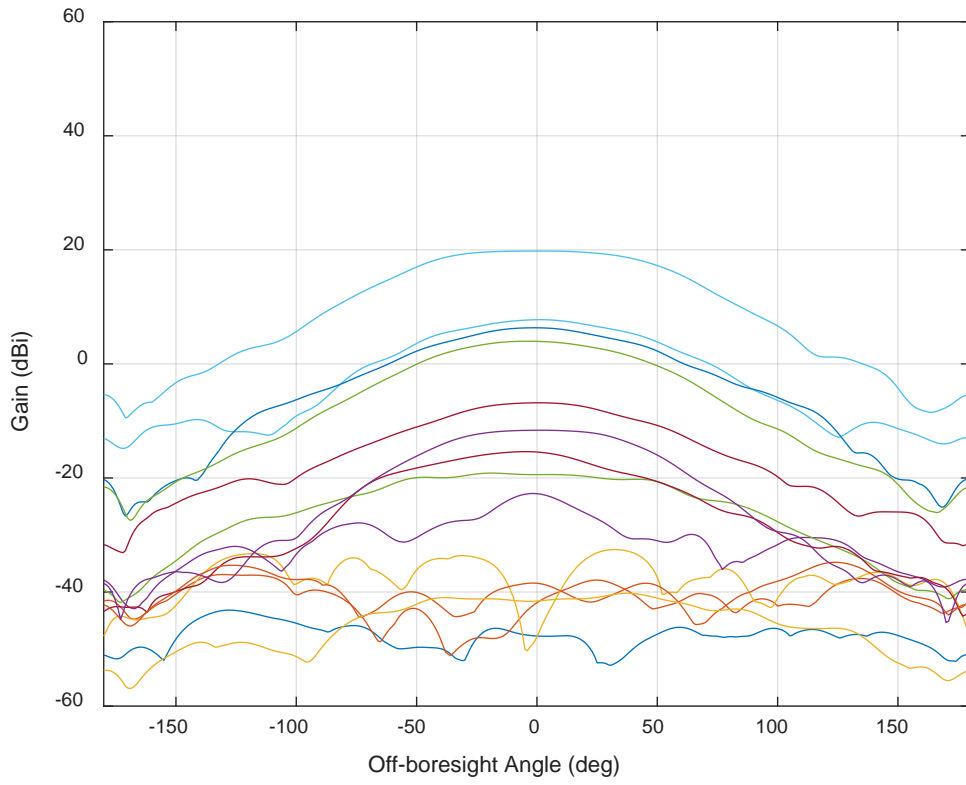


**Figure E-43: HPOL Gain Patterns for 14 External Antennas (1660 MHz)**

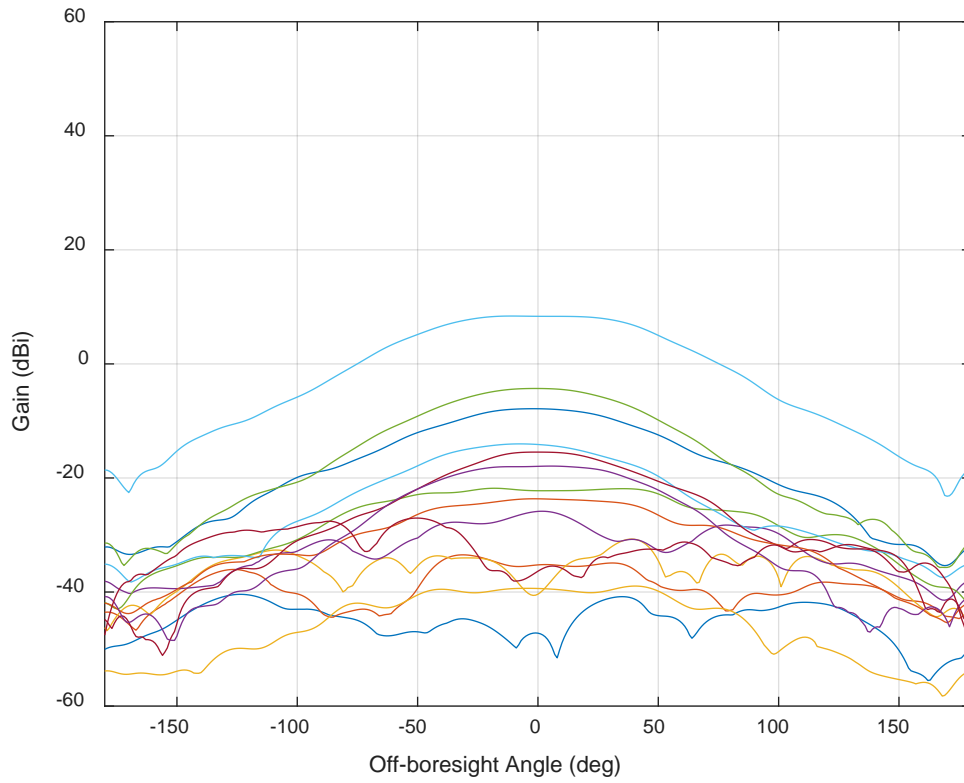


**Figure E-44: VPOL Gain Patterns for 14 External Antennas (1675 MHz)**

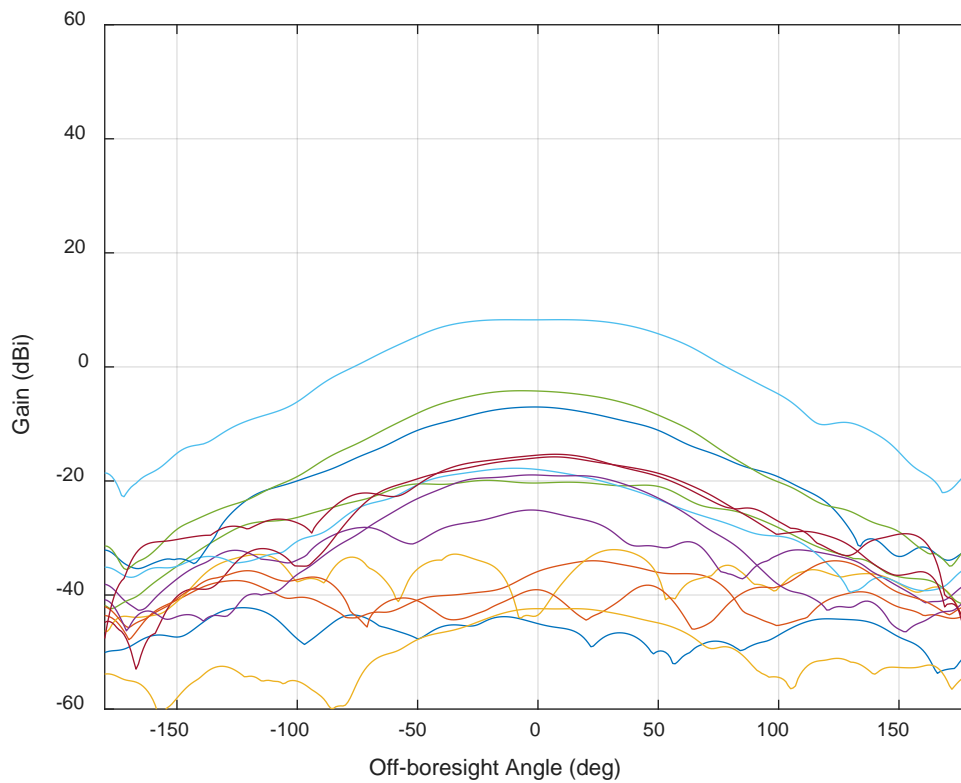


**Figure E-45: HPOL Gain Patterns for 14 External Antennas (1675 MHz)**

## **APPENDIX F**

# **PROPAGATION PATH AND AGGREGATE EFFECT COMPUTATION MODELS**



## TABLE OF CONTENTS

TABLE OF CONTENTS.....	2
LIST OF FIGURES .....	4
LIST OF TABLES .....	5
REFERENCES .....	6
APPENDIX.....	8
Appendix F. Propagation Path and Aggregate Effect Computation Models .....	8
F.1 Propagation Path Model General Aspects .....	8
F.2 Single Path Model .....	8
F.2.1 Single Path Median Isotropic Propagation Model .....	8
F.2.1.1 Short Range Path Segment (Two-Ray) Isotropic Model .....	9
F.2.1.1.1 Short Range Path Segment (Level-Terrain Two-Ray) Isotropic Model .....	9
F.2.1.1.2 Sloping Terrain Two-Ray Isotropic Path Model .....	11
F.2.1.1.3 Two-Ray Path Model Aspects for Directive, Dual-Polarization Source Antennas	13
F.2.1.2 Medium Range Path Segment Erceg-Greenstein Isotropic Model .....	15
F.2.1.3 Medium Range Path Segment Exponential Fit Isotropic Model .....	16
F.2.1.4 Long Range Segment Path Isotropic Model .....	16
F.2.1.5 Free Space Path Isotropic Model .....	19
F.2.2 Single Path Probabilistic Propagation Model .....	19
F.2.2.1 Single Path Probabilistic Propagation Model Basic Aspects.....	19
F.2.2.2 Median Path Segment Propagation Parameters and Segment Break Points	20
F.2.2.3 Single Path Probabilistic Propagation Slow Fading Parameters, $\mu$ and $\sigma$ ...	22
F.2.2.4 Single Path Probabilistic Propagation Fast-Fading Parameters, $L$ , $\psi_0$ , $\rho_0$ ...	23
F.3 Aggregate Propagation Effects Computation Methods .....	25
F.3.1 Randomly-Located Source Statistics .....	25
F.3.1.1 Randomly-Located Source Mean Aggregate Interference Power .....	25

F.3.1.2	Randomly-Located Source Aggregate Interference Power Standard Deviation	25
F.3.1.3	Randomly-Located Source Aggregate Interference Power Probability Distribution.....	26
F.3.2	Discretely-Located Source Statistics .....	27
F.3.2.1	Discrete Source Mean Aggregate Interference Power.....	27
F.3.2.2	Discrete Source Aggregate Interference Power Probability Distribution....	28
F.3.2.2.1	General Discrete Source Aggregate Interference Power Probability Distribution.....	28
F.3.2.2.2	Discrete Source Aggregate Characteristic Function with Sectorization.....	28

## LIST OF FIGURES

Figure F-1: Level-Terrain Two-Ray Path Model Geometry.....	10
Figure F-2: Example Level Terrain Two-Ray Isotropic Median Path Spreading Factor .....	11
Figure F-3: Sloping Terrain Two-Ray Path Model Geometry.....	12
Figure F-4: Example Erceg-Greenstein Isotropic Median Path Spreading Factor .....	16
Figure F-5: Example Hata-Okumura Median Isotropic Path Spreading Factor .....	17
Figure F-6: Okumura Slope Correction Factor Data Points and Fit Equations .....	18

## **LIST OF TABLES**

No table of figures entries found.

## REFERENCES

- [1] M. Hata, "Empirical formula for propagation loss in land mobile radio services," *IEEE Trans. Veh. Technol.*, vol. 29, pp. 317-325, Aug. 1980.
- [2] Y. Okumura, E. Ohmor, T. Kawano and K. Fukua, "Field strength and its variability in UHF and VHF land-mobile radio service," *Review of Electrical Communications Lab.*, vol. 16, no. 9, 1968.
- [3] D. Parsons, *The Mobile Radio Propagation Channel*, Chichester, England: John Wiley & Sons, 1996.
- [4] V. Erceg, L. J. Greenstein, S. Y. Tjandra, S. R. Parkoff, A. Gupta, B. Kulic, A. Julius and R. Bianchi, "An Empirically Based Path Loss Model for Wireless Channels in Suburban Environments," *IEEE Journal on Selected Areas in Communications*, vol. 17, no. 7, July 1999.
- [5] Status Report: Assessment of Compatibility of Planned LightSquared Ancillary Terrestrial Component Transmissions in the 1526-1536 MHz Band with Certified Aviation GPS Receivers, FAA Report PR 25, January 25, 2012.
- [6] Handout for wireless comm. graduate course, University of Illinois (ECE559), Professor V. V. Veeraldi pp. 53-56.
- [7] C. Loo, "A Statistical Model for a Land Mobile Satellite Link," *IEEE Transactions on Vehicle Technology*, vol. 34, no. 3, Aug. 1985.
- [8] K. M. Peterson and R. J. Erlandson, "Analytic Statistical Model for Aggregate Radio Frequency Interference to Airborne GPS Receivers from Ground-Based Emitters," *Journal of the Institute of Navigation*, vol. 59, no. 1, Spring, 2012.
- [9] Final Report: A Generalized Statistical Model for Aggregate Radio Frequency Interference to Airborne GPS Receivers from Ground Based Emitters (DOT/FAA/TC-14/30, Rev. 1), August 7, 2017.
- [10] J. A. Gubner, "A New Formula for Lognormal Characteristic Function," *IEEE Transactions on Vehicle Technology*, vol. 55, no. 5, pp. 1668- 1671, Sept. 2006.
- [11] K. Chung, *A Course In Probability Theory*, New York: Academic Press, 1974.



## APPENDIX

### Appendix F. Propagation Path and Aggregate Effect Computation Models

#### F.1 Propagation Path Model General Aspects

All the RFI propagation path models used herein are based on the flat-earth approximation. In other words, the ground under the aircraft is assumed to be essentially smooth and flat out to a radio horizon from the point on the ground directly under the aircraft. In line-of-sight propagation conditions at radio frequencies near the GPS carrier, this radio horizon value depends, in general, on the aircraft GNSS and RFI source antenna heights and the amount of atmospheric refraction along the propagation path. A 4/3 Earth radius approximation for the refractive effect on the radio horizon will be used in all propagation models.

The propagation model described in this document basically consists of two different types of models. Those scenarios where blockage is a factor are typically evaluated using probabilistic models while clear line-of-sight scenarios are analyzed using free space path loss.

For scenarios that involve environments in which emissions from adjacent channel systems undergo scattering, reflections, and absorption prior to arriving at an aircraft's GPS antenna, a probabilistic propagation model must be used. These propagation environments were the subject of much research during the development of cellular radio systems. As a result, the cellular radio community has over the years developed propagation models which for the most part are applicable to the present RFI scenarios under consideration.

Generally, in this document the point at which free space propagation path model is used occurs at an aircraft antenna height of 550 meters. Above 550 meters, various parameter limits associated with the probabilistic models are exceeded thereby making the model use problematic. Also at these aircraft heights, line-of-sight conditions generally prevail which means that free space path loss is the most appropriate model to apply.

Below the 550 meter aircraft antenna height the probabilistic models developed by the cellular radio community become applicable. Each of these models have one feature in common; the probabilistic nature of the propagation path model is well approximated by the product of a slow fading process and a fast fading process. The slow fading process is very well approximated by a log-normal distribution while the fast fading process is described by a non-central Chi-Squared distribution. The log-normal component is completely determined by two parameters,  $\mu$  and  $\sigma$  and the Chi-Squared process by the parameters  $L$ ,  $\psi_0$  and  $\rho_0$ . The range dependent median path model between the GPS antenna and the interference source determines the parameter  $\mu$  while the remaining parameters vary with range depending on the scenario. In some special cases below 550 m aircraft antenna height, free-space ( $1/r^2$ ) propagation is assumed.

#### F.2 Single Path Model

##### F.2.1 Single Path Median Isotropic Propagation Model

The single path median isotropic propagation model used depends upon the GPS aircraft antenna height and emitter source antenna height above ground. For aircraft antenna heights greater than or equal to 550 meters, a free space propagation model is used. The median isotropic propagation path model for aircraft antenna heights below 550 meters consists in general of three segments, depending on the scenario, appropriately blended together. They form a continuous function of the lateral separation radius  $r$  (in meters) between the aircraft and RFI source antennas. At the shorter radial distances, conventional two-ray propagation is used. That model assumes a direct path between the two antennas interacts with one other path reflected from the ground between antennas. For radii greater than about 1 km, the Hata-Okumura suburban propagation model ([1], [2]) is used. At radii beyond 20 km, a long distance extension is made to the standard Hata-Okumura formulation. If necessary to achieve propagation path model continuity, the two-ray and Hata-Okumura model segments are connected together by one of two means. One method uses a single, constant slope exponential fit function that covers radius values in between segments. The other method, used in mobile broadband handset station scenarios with aircraft antenna heights below 80 meters and source antennas less than 2 meters, is a modified Erceg-Greenstein path loss segment. Since median isotropic propagation path model is generally a function of the aircraft and RFI source antenna heights, the path loss is adapted to each specific RFI scenario.

For convenience, this Appendix generally uses the term "path spreading factor" ( $PF$ ), which is the algebraic reciprocal of the path loss.

### **F.2.1.1 Short Range Path Segment (Two-Ray) Isotropic Model**

#### **F.2.1.1.1 Short Range Path Segment (Level-Terrain Two-Ray) Isotropic Model**

Measurements indicate that at short ranges, where few obstructions are present, the GPS antenna receives interference from an RFI source by both a direct and reflected path [3]. On the reflected path, the electromagnetic wave is reflected from the earth's surface with a range-dependent complex reflection coefficient  $\rho_v(r)$ <sup>1</sup>. In addition to the relative phase delay between the direct and reflected rays, the complex reflection coefficient both attenuates and adds phase shift to the reflected ray. When the two rays additively combine at the receive antenna, the resulting received power fluctuates with lateral separation range  $r$ . Figure F-1 illustrates the direct and indirect reflected ray geometry.

---

<sup>1</sup>The equations that follow from this model are a first-order approximation to a more complicated possible derivation. This approximation is considered acceptable for the aviation-related analyses in this report.



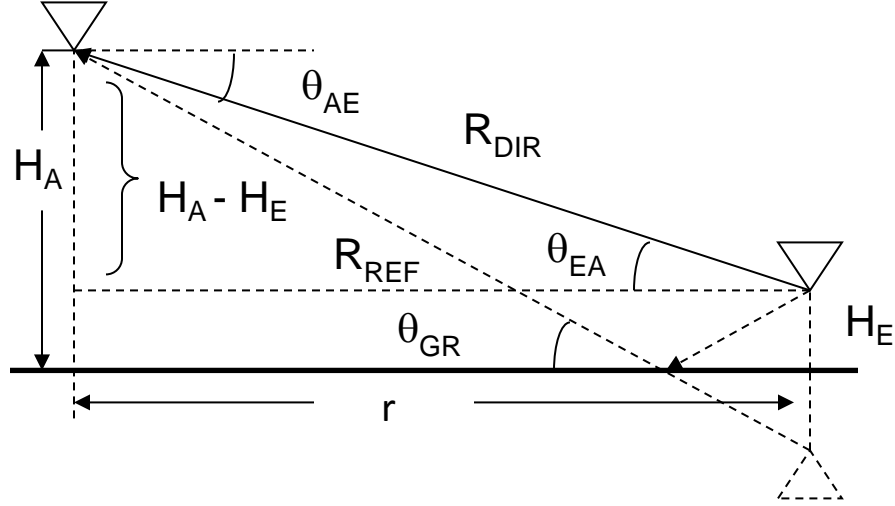


**Figure F-1: Level-Terrain Two-Ray Path Model Geometry**

With the aircraft antenna height denoted by  $H_A$  and the interference source antenna height by  $H_E$  the direct and reflected ray path lengths are defined respectively as:  $R_{DIR}(r) = \sqrt{(H_A - H_E)^2 + (r)^2}$

and  $R_{REFL}(r) = \sqrt{(H_A + H_E)^2 + (r)^2}$ . The reflected ray relative phase lag is determined by

$\phi(r) = \left( \frac{2\pi}{\lambda_c(f_c)} \right) (R_{REFL}(r) - R_{DIR}(r))$ , where  $\lambda_c$  is the free-space wavelength at the receiver center

frequency,  $f_c$ . The grazing angle,  $\theta_{GR}(r)$ , of the reflected ray with the concrete reflecting surface is given as  $\theta_{GR}(r) = \sin^{-1}((H_A + H_E) / R_{REFL}(r))$ . Two electrical parameters of concrete (relative

dielectric constant,  $\epsilon_r = 7.0$ , conductivity,  $\sigma_{cc} = 0.15$  S/m) are used to form a constituent ratio parameter,  $x(f_c) = \frac{\sigma_{cc}}{2\pi f_c \epsilon_0}$ , where  $\epsilon_0$  is the free space permittivity. With the ratio parameter  $x$

defined, the complex reflection coefficient for vertical polarized waves,  $\rho_v(r)$ , is given as:

$$\rho_v(r, f_c) = \frac{(\epsilon_r - i \cdot x(f_c)) \sin(\theta_{GR}(r)) - \sqrt{(\epsilon_r - i \cdot x(f_c)) - \cos^2(\theta_{GR}(r))}}{(\epsilon_r - i \cdot x(f_c)) \sin(\theta_{GR}(r)) + \sqrt{(\epsilon_r - i \cdot x(f_c)) - \cos^2(\theta_{GR}(r))}};$$

where the imaginary constant,  $i = \sqrt{-1}$ . The complex multipath field factor at the receive antenna

is then given by  $P_v(r, f_c) = 1 + \left( \frac{R_{DIR}(r)}{R_{REFL}(r)} \right) \rho_v(r, f_c) \cdot e^{-i\phi(r)}$ . With these definitions the two-

ray isotropic median path spreading factor (reciprocal of path loss) is written (algebraic terms) as:

$$PF_{2Ray}(r, f_c) = \left( \frac{\lambda_c(f_c)}{4\pi} \cdot \frac{|P_v(r, f_c)|}{R_{DIR}(r)} \right)^2 \text{ for } 0 \leq r < r_I. \quad (\text{F-1})$$

The aircraft and source antenna gains for the direct ray path can be computed from the direct ray elevation angle,  $\theta_{AE}(r) = -\sin^{-1}((H_A - H_E)/R_{DIR}(r))$ . Note that  $\theta_{EA} = -\theta_{AE}$ . The break point  $r_I$  is described in Section F.2.2.2. Figure F-2 shows a typical two-ray model path spreading factor plotted in dB as a function of the range  $r$  in meters for  $f_c = 1575.42$  MHz

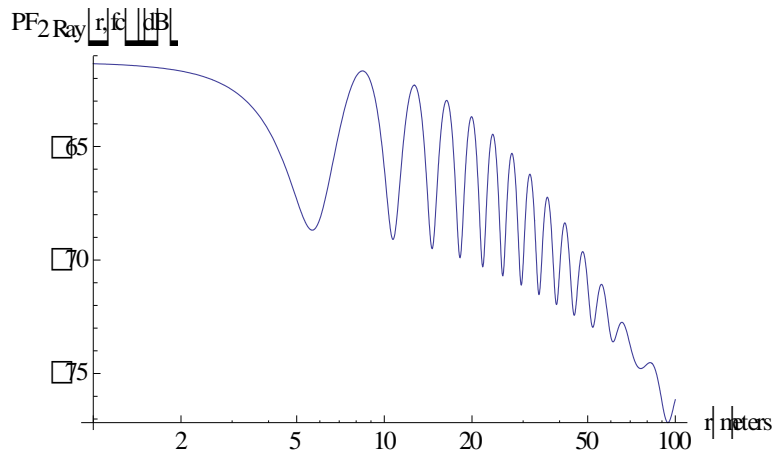


**Figure F-2: Example Level Terrain Two-Ray Isotropic Median Path Spreading Factor**

#### F.2.1.1.2 Sloping Terrain Two-Ray Isotropic Path Model

A more general purpose two-ray isotropic path model for use in some scenarios is one with sloping terrain between emitter and aircraft. The simpler two-ray level terrain model discussed in Section F.2.1.1.1 must be adjusted as shown in Figure F-3. The sloping terrain grazing angle,  $\theta_{GRS}(r)$ , as a function of the lateral separation radius,  $r$ , is derived in terms of known path parameters:  $R_{DIR}$ ,  $H_E$  (as defined in level terrain case), terrain slope angle  $\theta_S$ , and the aircraft height above the local terrain,  $h_A$ . While the triangles formed by the antennas, ray paths, and level terrain in Figure B-1 are right similar triangles, the associated triangles in Figure B-3 on sloping terrain are not right similar. Thus derivation of  $\theta_{GRS}(r)$  will involve use of the Law of Sines.

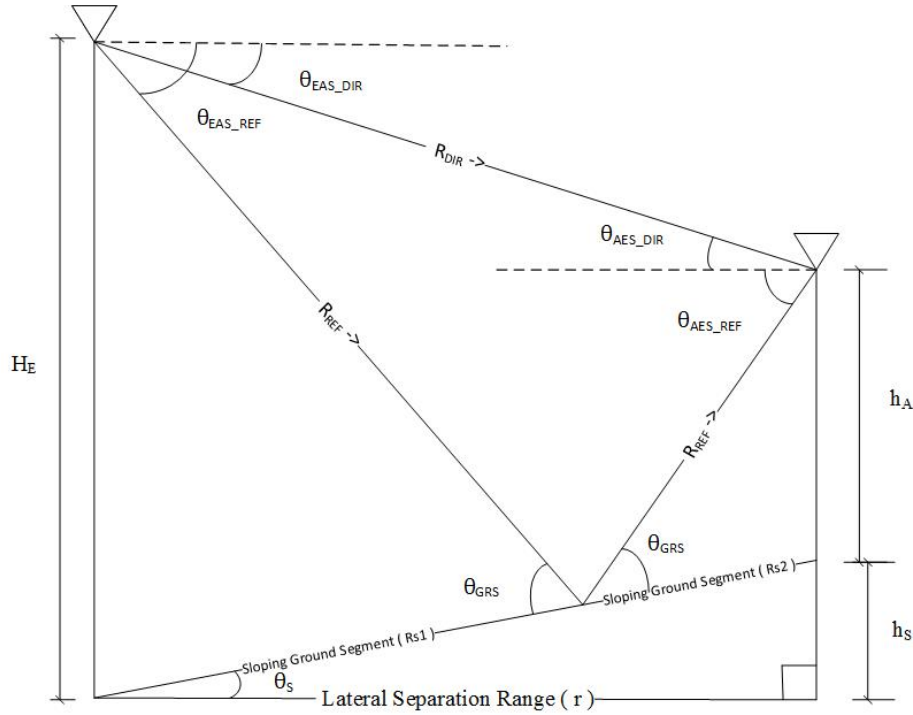


**Figure F-3: Sloping Terrain Two-Ray Path Model Geometry**

The derivation begins by applying the Pythagorean Theorem to four ground segments,  

$$r^2 + h_s^2 = (Rs1 + Rs2)^2.$$

Using the Law of Sines, the two sloping ground segments  $Rs1$  and  $Rs2$  can be defined in terms of ground slope and grazing angles and the closer of the emitter or aircraft height;

$$Rs1 = H_E \sin(\pi/2 - (\theta_{GRS}(r) - \theta_s)) / \sin(\theta_{GRS}(r)) \text{ and}$$

$$Rs2 = h_A \sin(\pi/2 - (\theta_{GRS}(r) + \theta_s)) / \sin(\theta_{GRS}(r)).$$

With  $a = \pi/2$  and  $b = (\theta_{GRS}(r) \pm \theta_s)$  used in the identity  $\sin(a - b) = \sin(a)\cos(b) - \cos(a)\sin(b)$ , the relationships for  $Rs1$  and  $Rs2$  simplify to:

$$Rs1 = H_E \cos(\theta_{GRS}(r) - \theta_s) / \sin(\theta_{GRS}(r)) \text{ and}$$

$$Rs2 = h_A \cos(\theta_{GRS}(r) + \theta_s) / \sin(\theta_{GRS}(r)).$$

Applying the identity,  $\cos(a - b) = \cos(a)\cos(b) + \sin(a)\sin(b)$ , to the expression for  $Rs1$  and the identity,  $\cos(a + b) = \cos(a)\cos(b) - \sin(a)\sin(b)$ , to the expression for  $Rs2$ , then substituting both results back into the original Pythagorean Theorem expression of the four ground segments, and taking the square root of both sides of the expression yields:

$$(r^2 + h_s^2)^{1/2} = \{ H_E [\cos(\theta_{GRS}(r))\cos(\theta_s) + \sin(\theta_{GRS}(r))\sin(\theta_s)]$$

$$+ h_A [\cos(\theta_{GRS}(r))\cos(\theta_s) - \sin(\theta_{GRS}(r))\sin(\theta_s)] \} / \sin(\theta_{GRS}(r)).$$

Finally, applying the trigonometric relationship  $h_s = r[\tan(\theta_s)]$  for the slope height above level terrain assumption at the aircraft nadir, and the identity,  $\cos(a)/\sin(a) = 1/\tan(a)$ , and performing algebraic simplifications the resulting expression is:

$$\theta_{GRS}(r) = \tan^{-1} \left( \frac{(H_E + h_A) \cos(\theta_s)}{r \sqrt{1 + \tan^2(\theta_s)} - (H_E - h_A) \sin(\theta_s)} \right).$$

The direct path length,  $R_{DIR,S}(r)$ , needed for the sloping terrain two-ray path loss is determined by first noting that the aircraft antenna height above level terrain in Figure F-3 is given by  $H_A(r) = h_A + r \tan(\theta_s)$ . Then the level terrain expression,  $R_{DIR}(r) = \sqrt{(H_A - H_E)^2 + r^2}$ , after substitution becomes, on the sloping terrain,  $R_{DIR,S}(r) = \sqrt{(h_A + r \cdot \tan(\theta_s) - H_E)^2 + r^2}$ . The reflected ray path length,  $R_{REF,S}(r)$ , is determined from Law of Sines relations to be  $R_{REF,S}(r) = (H_E + h_A) \cos(\theta_s) / \sin(\theta_{GRS}(r))$ . With these revised sloping terrain parameter definitions, the remaining two-ray path loss factors can be determined from the same expression forms as in Section F.2.1.1.1.

Once  $\theta_{GRS}(r)$  is determined, four elevation angles,  $\theta_{EAS\_DIR}$ ,  $\theta_{EAS\_REF}$ ,  $\theta_{AES\_DIR}$ ,  $\theta_{AES\_REF}$ , can be derived for use to compute the antenna gains in the scenario. By definition,  $\theta_s \geq 0$ ,  $\theta_{GRS} > 0$ ,  $\theta_{EAS\_REF} < 0$ , and  $\theta_{AES\_REF} < 0$ . It is also true that  $\theta_{AES\_DIR} = -\theta_{EAS\_DIR}$ . However, the direct ray elevation angles  $\theta_{EAS\_DIR}$  and  $\theta_{AES\_DIR}$  can be either positive or negative depending on the relative heights of  $H_E$  vs.  $(h_A + h_s)$ . The emitter direct path elevation angle,  $\theta_{EAS\_DIR}(r)$ , for sloping terrain is given by:  $\theta_{EAS\_DIR}(r) = -\tan^{-1} \{ [(H_E - h_A) - r \tan(\theta_s)] / r \}$  for  $H_E > (h_A + h_s)$  and  $r \leq r_1$ . Expressions for the two reflected path elevation angles are  $\theta_{EAS\_REF}(r) = -(\theta_{GRS}(r) - \theta_s)$  and  $\theta_{AES\_REF}(r) = -(\theta_{GRS}(r) + \theta_s)$ .

### F.2.1.1.3 Two-Ray Path Model Aspects for Directive, Dual-Polarization Source Antennas

Although RFI sources in some scenarios can be modelled with vertically polarized emissions, other scenarios call for the use of relatively directive base station source antennas that transmit a  $\pm 45^\circ$  cross-polarized signal. This type of signal is modelled for aviation GPS RFI analyses as a dual vertically- and horizontally-polarized signal. Each polarization component is assumed to contain half the total emission power. This signal type causes increased complexity especially in the two-ray path loss segment. Compared to the formulation in Section F.2.1.1.1, one extra parameter needed in the two-ray zone is the horizontal-polarized reflection coefficient expressed as

$$\rho_h(r, f_c) = \frac{\sin(\theta_{GR}(r)) - \sqrt{(\epsilon_r - i \cdot x(f_c)) - \cos^2(\theta_{GR}(r))}}{\sin(\theta_{GR}(r)) + \sqrt{(\epsilon_r - i \cdot x(f_c)) - \cos^2(\theta_{GR}(r))}}.$$

Without accounting yet for any source antenna directivity, the associated horizontal polarized

multi-path field factor is expressed in similar form to Section F.2.1.1.1 as

$$P_h(r, f_c) = 1 + \left( \frac{R_{DIR}(r)}{R_{REFL}(r)} \right) \rho_h(r, f_c) \cdot e^{-i\phi(r)}; \text{ where the direct and reflected}$$

ray path lengths,  $R_{DIR}(r)$  and  $R_{REFL}(r)$ , and the reflected ray path relative phase lag,  $\phi(r)$ , are the same as for vertical polarization.

To properly account for the source and receive antenna pattern effects on the reflected ray relative strength compared to the direct ray at the receive antenna, the ray angles need to be determined. The ray angle expressions in Section F.2.1.1.2 above can be adapted as needed for flat or sloping ground (flat ground has  $\theta_s=0$ ). The source side ray angles, once determined, are then transformed as in Appendix G into the tilted beam coordinates and used to determine the source antenna power gain in the direct and reflected ray directions. The source antenna power gain in any direction is assumed to be independent of polarization. The receive side ray angles are used with the receive antenna equations in Section 4.1.2 to determine the receive antenna power gain to both direct and reflected vertical and horizontal polarization ray components.

The source transmit direct- and reflected-ray power gain values,  $G_{td}(r)$  and  $G_{tr}(r)$ , are then formed into a transmit voltage gain ratio,  $VG_{trd}(r) = \sqrt{G_{tr}(r)/G_{td}(r)}$  (same value for both v-pol. and h-pol.). Similarly the receive direct- and reflected-ray vertical- and horizontal-polarized power gain values,  $G_{rd_v}(r)$ ,  $G_{rr_v}(r)$ ,  $G_{rd_h}(r)$ , and  $G_{rr_h}(r)$  are formed into receive voltage gain ratios  $VG_{rd_v}(r) = \sqrt{G_{rr_v}(r)/G_{rd_v}(r)}$  and  $VG_{rd_h}(r) = \sqrt{G_{rr_h}(r)/G_{rd_h}(r)}$ . These voltage gain ratios are used to modify the multi-path field factor and yield the directive multi-path factors:

$$P_{d_h}(r, f_c) = 1 + VG_{trd}(r) \cdot VG_{rd_h}(r) \cdot \left( \frac{R_{DIR}(r)}{R_{REFL}(r)} \right) \rho_h(r, f_c) \cdot e^{-i\phi(r)} \text{ and}$$

$$P_{d_v}(r, f_c) = 1 + VG_{trd}(r) \cdot VG_{rd_v}(r) \cdot \left( \frac{R_{DIR}(r)}{R_{REFL}(r)} \right) \rho_v(r, f_c) \cdot e^{-i\phi(r)}.$$

Since the voltage gain ratios are less than unity, their effect in the above expressions is to diminish the magnitude of the fluctuating component in the multi-path field factor at a given radius compared to the initial value without the directivity correction.

When these modified multi-path field factor expressions are substituted into the basic two-ray path factor Equation (F-1), the resulting vertical and horizontal polarization path factors are:

$$PF_{2Ray,v}(r, f_c) = \left( \frac{\lambda_c(f_c)}{4\pi} \cdot \frac{|P_{d_v}(r, f_c)|}{R_{DIR}(r)} \right)^2 \text{ and } PF_{2Ray,h}(r, f_c) = \left( \frac{\lambda_c(f_c)}{4\pi} \cdot \frac{|P_{d_h}(r, f_c)|}{R_{DIR}(r)} \right)^2.$$

When the effects of a directive dual-polarized base station source antenna are incorporated, as discussed above, an additional complication occurs in the determination of the outer radius limit,  $r_l$ , for the two-ray path model. Investigation of the path factor expressions indicates that at any

particular given radius the horizontal and vertical path factors may have different values. However, there are certain radius values at which the path factors are equal, a feature which is necessary for the starting radius of the mid-range path model zone.

For sources emitting only vertically polarized signals, the  $r_I$  value is the radius at which the complex vertical polarization reflection coefficient,  $\rho_v(r, f_c)$ , is purely imaginary (phase of  $\rho_v = -90^\circ$ ) very near the minimum magnitude. At this radius, the grazing angle for the reflecting surface is at a critical value,  $\theta_{CRIT}$ , that depends on only the surface electrical parameters. With the critical grazing angle known along with antenna heights, the expression for grazing angle in Section F.2.1.1.2 can be inverted to solve for the associated vertical polarization radius,  $r_{IV}$ . The strategy for the dual polarization radius,  $r_{Id}$  is to determine from the path factor equations, the first radius beyond  $r_{IV}$  at which the vertical and horizontal polarization path factors are equal (usually a few centimeters beyond  $r_{IV}$ ). The two-ray path factor value at  $r_{Id}$  is used in the formula for the mid-range path factor.

### F.2.1.2 Medium Range Path Segment Erceg-Greenstein Isotropic Model

Median path propagation models were initially developed for cellular mobile phones at lateral separation ranges beyond 1 km and out to 20 km. This left a need for some type of model to cover ranges from 100 meters to 1 km. In the mid-1990's this need was met by researchers from ATT Laboratories who developed a mid-range model that came to be known as the Erceg-Greenstein model [4]. Their model pertains to ranges from 100 meters to 8 km with base station antenna heights between 10 and 80 meters and a mobile unit antenna height of 2 meters. The model was developed for suburban environments using three different terrain categories to make it more flexible. An operating frequency of 1.9 GHz was used in developing the model although extrapolations to other frequencies are possible. In the Erceg-Greenstein model the median path loss is proportional to  $(r/r_0)^\gamma$  where  $r_0$  is usually taken to be 100 meters. The loss exponent  $\gamma$  changes with terrain type but is greater than 2 meaning that the path loss is more severe than that associated with a free space model. The classic Erceg-Greenstein model has the actual path loss increasing slightly as the range increases, however the modified model used in this analysis holds this constant with range.

The modified Erceg-Greenstein model has a median isotropic path spreading factor (in algebraic terms) given by:

$$PF_{EG,mod}(r, f_c) = 1 / \left[ A^2(f_c) \cdot \left( \frac{r}{r_0} \right)^{a-bH_A+c_{EG}/H_A} \right], \text{ for } r_1 \leq r < r_2 \quad (\text{F-2})$$

In Equation (F-2),  $A(f_c) = 4\pi r_0 / \lambda_c(f_c)$  with  $r_0 = 100$  m. Values for constants  $a$  (3.6),  $b$  (0.005), and  $c_{EG}$  (20.0) are chosen to represent the area in the vicinity of an airport (terrain model C (flat, light tree cover)). The break points  $r_1$  and  $r_2$  are described in Section F.2.2.2. Figure F-4 shows a

sample median path spreading factor produced by the Erceg-Greenstein model at  $f_c = 1575.42$  MHz.

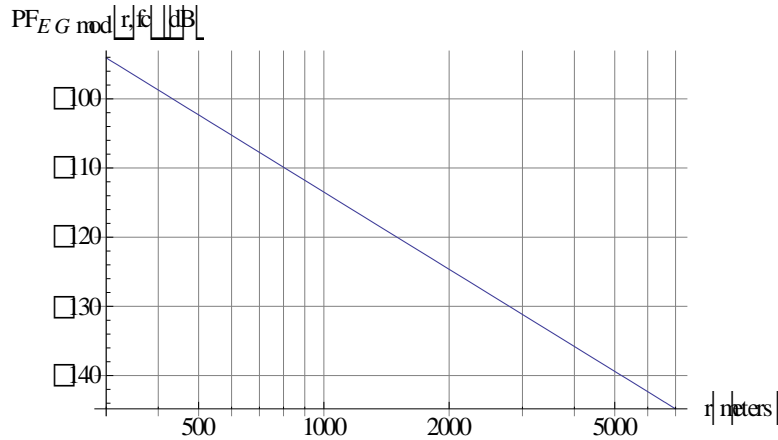


**Figure F-4: Example Erceg-Greenstein Isotropic Median Path Spreading Factor**

### F.2.1.3 Medium Range Path Segment Exponential Fit Isotropic Model

For cases when  $H_A > 80$  m (e.g., the FAF Waypoint) or  $H_E > 2$  m, an exponential, constant slope blending function is used. The function's constant exponent and intercept point are chosen to achieve continuity at either end with the short- and long-range path loss functions given appropriate segment breakpoints,  $r_1$  and  $r_2$ . For handset interference sources, the exponential constant slope path loss model is given by:

$$PF_{\text{exp fit1}}(r, f_c) = PF_{2\text{Ray}}(r_1, f_c)(r / r_1)^{-\Gamma_1(f_c)} \quad (\text{F-3})$$

The exponent is expressed as:

$$\Gamma_1(r_1, r_2, f_c) = [\alpha(f_c) + \beta_c \cdot \log_{10}(r_2 / 1000) + \log_{10}(PF_{2\text{Ray}}(r_1, f_c))] / \log_{10}(r_2 / r_1)$$

where  $r_2 < 20,000$  m, and  $\alpha(f_c)$ , and  $\beta_c$ , are parameters associated with the Hata-Okumura model discussed in Section F.2.1.4.

For base station interference sources there is a single exponential constant slope model given in similar form but with different parameter values by

$$PF_{\text{exp fit1}}(r, f_c) = PF_{2\text{Ray}}(r_1, f_c)(r / r_1)^{-\Gamma_1(r_1, r_2, f_c)} \quad (\text{F-4})$$

where  $\Gamma_1(r_1, r_2, f_c)$  has the same form as in Equation (F-3).

### F.2.1.4 Long Range Segment Path Isotropic Model

For propagation over “flat earth” terrain from RFI sources at distances beyond 1 km from the aircraft antenna, the Hata-Okumura median path propagation model is used. It was originally developed for predicting UHF cellular mobile telephone propagation at distances beyond 1 km from the base station for three terrain types: urban areas, suburban areas and open areas. In this Report the suburban terrain parameters are used to represent the environment around a large metropolitan airport. As with the Erceg-Greenstein model, the Hata-Okumura path median spreading factor is inversely proportional to  $(r/r_0)^\gamma$  but in this case  $r_0$  is set to 1000 meters. The exponent  $\gamma$  varies with antenna height as well as range and for distances beyond 20 km it also varies with operating frequency. With the ITU-R extension to the original model, it is usable to ranges of 100 km. Figure F-5 shows the median path spreading factor generated by the Hata-Okumura model for an operating frequency  $f_c = 1575.42$  MHz.

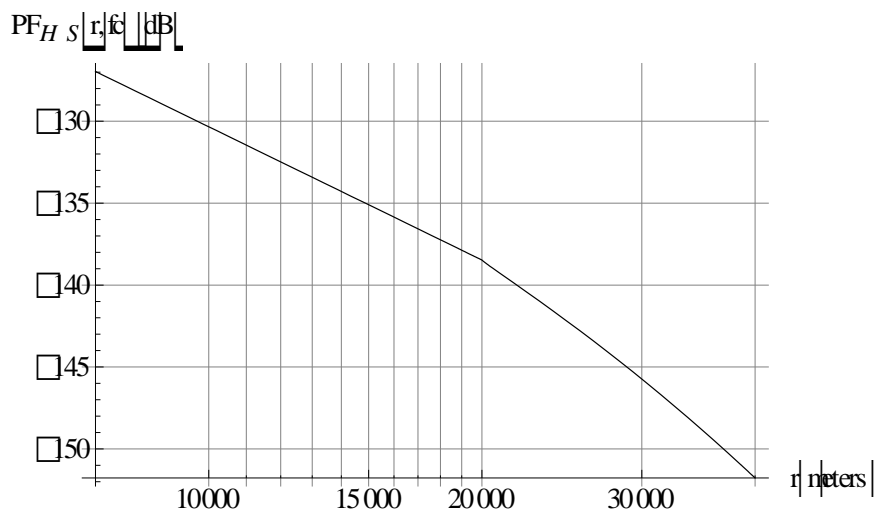


**Figure F-5: Example Hata-Okumura Median Isotropic Path Spreading Factor**

The Hata suburban median isotropic path spreading factor (in algebraic terms) is given by:

$$PF_{HS}(r, f_c) = 10^{(K_{sp}(r)/10 - (\alpha(f_c) + \beta_c \cdot \log(r/1000)) \cdot F(r, f_c, H_A))} \quad (\text{F-5})$$

for  $r_2 \leq r \leq R_0$  as appropriate where  $K_{sp}(r)$  (in dB) denotes a range-dependent slope correction factor (0 dB for “flat-earth”),

$$\alpha(f_c) = 0.1 \left[ 69.12 + 26.16 \cdot \log(f_c) - 2 \cdot \log^2\left(\frac{f_c}{28}\right) - 13.82 \cdot \log(H_A) - 3.2 \cdot \log^2(11.75 H_E) \right],$$

$$\beta_c = 0.1 \cdot [44.9 - 6.55 \cdot \log(H_A)] \text{ and } F(r, f_c, H_A) = 1, r \leq 20 \text{ km, or:}$$

$$F(r, f_c, H_A) = 1 + \left[ 0.14 + 1.87 \cdot 10^{-4} (f_c) + \frac{1.07 \cdot 10^{-3} H_A}{(1 + 7 \cdot 10^{-6} H_A^2)} \right] (\log_{10}(r / 2 \cdot 10^4))^{0.8} \text{ for } r > 20 \text{ km.}$$



For the certified aviation equipment analyses in this report, the Hata “base station” antenna height,  $H_A$ , in the long range model segment is assumed to be the greater of the aircraft or interference source antenna height. The Hata “mobile station” height,  $H_E$ , is the lesser of the two antenna heights. In addition, the propagation is assumed to be reciprocal.

When applying the Hata suburban median isotropic spreading factor to certain discrete base station scenarios on irregular, sloping terrain, it may be necessary to apply a non-zero slope correction factor  $K_{sp}(r)$  to the model. This correction factor, derived from the work of Okumura [2], was chosen as the principal factor and other smaller ones were considered negligible. These terrain slopes are averages computed over a significant distance (Okumura suggests distances of 5-10 km). The correction as given in [2] shows that positive (upward, away from the aircraft) slopes reduce the path loss while negative (downward) slopes yield increased path loss. Steep slopes produce increased correction whether they are positive or negative. The correction is given in dB as a function of slope angle in milliradians and distance in kilometers. Correction factor data points presented graphically in [ 2], (Figure 34)] have been extracted and fit with an equation for ease of use. The Okumura data points and fit equations for several distances (10, 30 , 60 km) are plotted in Figure F-6. The fit equation  $K_{sp}(\theta, d)$  in dB as a function of slope angle  $\theta$  (milliradians) and distance  $d$  (m) is:

$$K_{sp}(\theta, d) = \begin{cases} a_1 + (a_2 + a_3(d/1000))\theta - (a_4 + a_5(d/1000))\theta^2, & \theta < 0 \\ b_1 + (b_2 + b_3(d/1000) + b_4(d/1000)^2)\theta - (b_5 + b_6(d/1000) + b_7(d/1000)^2)\theta^2, & 0 \leq \theta \end{cases}$$

where  $a_1 = 0.052857$ ,  $a_2 = -0.105285$ ,  $a_3 = 0.0288714$ ,  $a_4 = 0.0027143$ ,  $a_5 = 7.14265 \times 10^{-5}$ ,  $b_1 = 0.018567$ ,  $b_2 = 0.01394$ ,  $b_3 = 0.0193213$ ,  $b_4 = -9.1533 \times 10^{-5}$ ,  $b_5 = -1.94286 \times 10^{-3}$ ,  $b_6 = 4.25715 \times 10^{-4}$ , and  $b_7 = -3.14287 \times 10^{-6}$ .

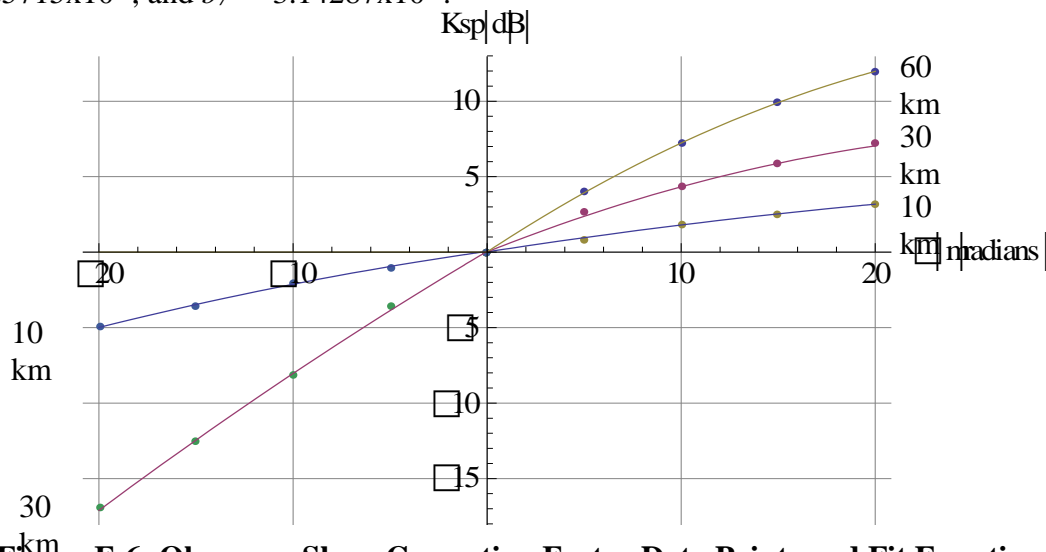


**Figure F-6: Okumura Slope Correction Factor Data Points and Fit Equations**

In applying this factor, it proved useful to divide the terrain into angular sectors about the aircraft nadir point. These sectors were chosen so as to provide as much terrain uniformity as possible

when traversing outward from aircraft nadir along any given radial line. Within a given sector, an average ground height was determined extending to some appropriate radial distance from aircraft nadir followed by a slope determination, if one exists beyond such distance.

### F.2.1.5 Free Space Path Isotropic Model

For aircraft antenna heights generally greater than 550 meters and certain special cases below 550 m, there is predominately a clear line of sight to all RFI sources other than ground based mobile sources whose interference impact has been shown to be negligible at these altitudes from previous analysis [5]. In such cases, a free space path propagation model is most appropriate. Free space propagation is the most basic model in which the path isotropic spreading factor is proportional to the inverse square of the separation range. This is a deterministic model with no associated probability distribution. Hence the path spreading factor can be exactly determined once the range between GPS antenna and interfering source is known. The free space isotropic spreading factor is given by:

$$PF_{FSP}(r, f_c) = (c / 4\pi R_{DIR}(r) f_c)^2 \quad (F-6)$$

where, as previously defined,  $R_{DIR}(r) = \sqrt{(H_A - H_E)^2 + (r)^2}$  and  $c$  is the speed of light in vacuum.

## F.2.2 Single Path Probabilistic Propagation Model

### F.2.2.1 Single Path Probabilistic Propagation Model Basic Aspects

The probabilistic propagation channel is typically modeled as a product of a slow fading process (log-normal power distribution) and a fast fading process [3]. The fast fading portion may be either "flat" (maximum delay spread,  $\tau_{ds} \ll 1/W$ , where  $W$ =interference signal base-bandwidth) or it may be frequency selective. The simplest case to model is the case where the fast fading is flat. In that case, the received interference from a single emitter,  $\gamma(t)$ , may be written as

$$\gamma(t) = \text{Re} \left\{ \bar{\alpha}(t) \bar{\beta}(t) s_E(t) \right\} \text{ where } \text{Re} \{ \} \text{ denotes the real part, while } \bar{\alpha}, \bar{\beta}, \text{ and } s_E \text{ are}$$

independent complex random processes. The term  $\bar{\alpha}(t)$  denotes the fast fading process,  $\bar{\beta}(t)$  the slow fading component, and  $s_E(t)$  the portion of the interfering emitter signal arriving at the GPS receiver antenna at center frequency  $f_c$ , ( $s_E(t) = u(t) \exp(i2\pi f_c t)$ , where  $u(t)$  is complex).

In the propagation model,  $\bar{\alpha}$  has independent normally distributed real and imaginary parts each with mean values that may be different from zero to account for the presence of a strong line-of-sight component at shorter ranges. Thus,  $|\bar{\alpha}(t)|^2$ , has a non-central Chi-squared distribution with two degrees of freedom. Although  $|s_E(t)|^2$  is a random process, to avoid dealing with those statistics the instantaneous power associated with the single source emission (unwanted emission in this analysis) is deemed to be constant as in most of the literature on path loss models. In the

model used for this analysis, power was assumed to be  $2P_oW$  watts; i.e., an rms power spectral density of  $P_o$  watts/Hz over a signal base-bandwidth,  $W$ . Under these assumptions, the random process  $|\beta(t)s_E(t)|^2$  is log-normally distributed and the received single emitter interference power  $|\gamma(t)|^2$  becomes the product of two random variables, one having a non-central Chi-squared distribution while the other is log-normally distributed.

For a scenario with frequency selective fast fading, it is shown [6] that  $\gamma$  can be approximated as the sum of several independent flat fading processes. Thus,  $\gamma(t)$  is written as

$$\gamma(t) = \left( \sum_{l=0}^{L-1} \alpha_l(t) s_E(t - \tau_l) \right) \beta(t);$$

where the channel parameter,  $L$ , is the number of resolvable fast

fading paths and the  $\tau_l$  are chosen such that  $E[s_E(t - \tau_i)s_E(t - \tau_k)] = 0$  for  $k \neq l$ . Then the

instantaneous power,  $|\gamma(t)|^2$ , becomes  $|\gamma(t)|^2 = \left( \sum_{l=0}^{L-1} |\alpha_l(t)|^2 |s_E(t - \tau_l)|^2 \right) |\beta(t)|^2 \dots$

Using the same assumption as above regarding the single emitter power, the received single emitter power density may be written as:

$$|\gamma(t)|_{density}^2 = \underbrace{\left( \sum_{l=0}^{L-1} |\alpha_l(t)|^2 \right)}_{FastFading} \overbrace{|\beta(t)|^2 P_o}^{SlowFading}.$$

This form for the received single emitter power density is the most flexible and is the form adopted in the present model. The slow fading portion is log-normally distributed with parameters  $\mu$  and  $\sigma$  while the fast fading process has a non-central Chi-squared distribution with  $2L$  degrees of freedom and parameters  $\rho_o$  and  $\psi_o$ .

The propagation model assumes each of these parameters to be range dependent hence we may express the received single emitter power spectral density as:

$$P_E(r) = \Sigma(r)\Omega(r),$$

where  $\Sigma$  denotes the fast fading component and  $\Omega$  the slow fading. Note all time dependence has been dropped as all of the constituent processes are assumed to be stationary.

### F.2.2.2 Median Path Segment Propagation Parameters and Segment Break Points

The propagation environment is modeled probabilistically with a range and height-dependent median path loss to an individual RFI source. Based on a flat-earth assumption, a continuous median path spreading factor function,  $PF(r, f_c)$ , is generated by combining three range segment models taken in part from mobile radiotelephone propagation studies. The long range segment model ( $r$  typically greater than 1 km) is based on the Hata-Okumura model [ [1], (suburban

case)]. Two options are used for the mid-range segment model depending on aircraft antenna height: Erceg/Greenstein ( $H_A \leq 80$  m), and an exponential constant slope blend models for  $H_A > 80$  m. The short range segment model (ranges less than a few hundred meters) is the classic two-ray with concrete as the single reflecting surface. Reciprocity is assumed to hold as it relates to the probabilistic modeling of the propagation channel. The median path isotropic spreading factor is then expressed for handset interference sources as:

$$PF(r, f_c) = \left\{ \begin{array}{ll} PF_{2Ray}(r, f_c), & 0 \leq r < r_1 \\ PF_{EG,mod}(r, f_c) \text{ or } PF_{exp fit1}(r, f_c), & r_1 \leq r < r_2 \\ PF_{HS}(r, f_c), & r_2 \leq r \leq R_o \end{array} \right\} \quad (F-7)$$

while, for base station interference, sources:

$$PF(r, f_c) = \left\{ \begin{array}{ll} PF_{2Ray}(r, f_c), & 0 \leq r < r_1 \\ PF_{exp fit1}(r, f_c), & r_1 \leq r < r_2 \\ PF_{HS}(r, f_c), & r_2 \leq r \leq R_o \end{array} \right\} \quad (F-8)$$

For handset interference sources, the following set of guidelines was used for the isotropic median path loss break points.

- At short ranges a two-ray median path propagation model is used up to the range  $r_1$  where the two ray and Erceg-Greenstein and/or exponential fit models join. This break point varies with aircraft antenna height and is computed so as to produce a continuous path spreading factor function. When the Erceg-Greenstein model is used, this break point is usually near 100 meters. When the exponential fit model is used, as in the FAF scenario, this break point is near where the two ray vertically polarized component reflection coefficient is at minimum magnitude.
- The second segment uses the Erceg-Greenstein model, if applicable, up to the point  $r_2$  where it intersects the Hata-Okumura median path propagation model. When the exponential fit model is used, to preserve some consistency with the lower height cases, the mid-range segment inner radius,  $r_1$ , is set to give a two-ray segment grazing angle,  $\theta_{GR}(r)$  such that  $\tan(\theta_{GR}(r_1)) \cong 0.5$ . Some slight adjustment of the  $r_1$  value may be done, if needed, to reduce the spreading factor slope change at the junction with the two-ray segment. In a similar way, the outer radius,  $r_2$ , is set to give an elevation angle from the source to the receive antenna,  $\mathcal{E}(r)$ , such that  $\tan(\mathcal{E}(r_2)) = 1/14$  (i.e.;  $\mathcal{E}(r_2) \cong 4^\circ$ ). An exponential fit mid-range segment is also used for very low aircraft antenna heights (e.g.  $< 10$  m). In these instances,  $r_1$  is set for the radius at which the two ray vertically polarized component reflection coefficient is at minimum magnitude. The outer radius,  $r_2$ , is set at 1 km (the minimum applicable radius for the Hata model).
- Beyond  $r_2$  the Hata-Okumura suburban median path propagation model is used.
- The radio horizon is given by  $R_o = 4124.12 \left( \sqrt{H_A} + \sqrt{H_E} \right)$  (all dimensions in meters).

For base station interference sources, two basic breakpoints were defined as follows.

- At short ranges a two-ray median path propagation model is used up to the radius  $r_1$  where the vertically polarized component reflection coefficient is at minimum magnitude. This break point varies with aircraft antenna height.
- Beyond  $r_1$ , the median path spreading factor is modelled as an exponential constant-slope blending function out to radius,  $r_2$  (details in Section F.2.1.3), where it intersects the Hata-Okumura long range segment.
- Beyond  $r_2$ , the Hata-Okumura suburban median path propagation model is used.

### F.2.2.3 Single Path Probabilistic Propagation Slow Fading Parameters, $\mu$ and $\sigma$

With the median path spreading factor,  $PF(r, f_c)$ , defined for any individual source, the single-path slow fading parameter,  $\mu(r, f_c)$ , can be written in general as:

$$\mu(r, f_c) = \ln[P_{xmit} \cdot G_{xmit}(\theta_{elev}(r), \phi_{az}) \cdot PF(r, f_c) \cdot G_{rcv}(\zeta_{elev}(r))]$$

This expression can be rewritten and further simplified to:

$$\mu(r, f_c) = \ln(P_0) + \mu'(r, f_c) \quad (\text{F-9})$$

where  $\mu'(r, f_c) = \ln[G_{norm}(\theta_{elev}(r), \phi_{az}) \cdot PF(r, f_c) \cdot G_{rcv}(\zeta_{elev}(r))]$  is a unitless mean fading factor,  $\ln()$  denotes natural logarithm and  $P_0 (P_{xmit} \eta G_0)$  is the RFI source effective isotropic radiated power (EIRP) or power spectra density at the transmit beam center (Appendix G.1). The antenna gain factors are:  $G_{xmit}()$  the interfering emitter antenna gain,  $\theta_{elev}(r)$  the transmit elevation angle, and  $\phi_{az}$  the azimuth angle toward the receive antenna,  $G_{norm}()$  is the normalized transmit gain ( $G_{xmit}() / \eta G_0$ ),  $G_{rcv}()$  the receive antenna gain, and  $\zeta_{elev}(r)$  the receive elevation angle toward the interfering emitter antenna. Note that  $G_{norm}()$  is set to unity independent of angle for handset emitters.

The single-path slow fading parameter,  $\sigma$ , is generally range dependent and hence is written as  $\sigma(r)$ . Its range dependence varies with the interference scenario, i.e., whether the interference is from a base station source or from a handset source. For a handset source, a linear transition region is used between the very short range condition and the onset of significant scattering (chosen to be the mid-range segment inner radius) [5]. The transition region starting point is chosen as the radius,  $r_s$ , such that the elevation angle from the source to the receive antenna,  $\mathcal{E}(r_s)$  is  $45^\circ$  (i.e.;  $r_s = H_A - H_E$ )<sup>2</sup>. The transition end point is the radius,  $r_1$ , previously defined in Section B.2.2.2 for handset sources. For convenience, the single-path standard deviation,  $\sigma(r)$ , is

<sup>2</sup> For handset scenarios when the aircraft antenna height is very low (e.g. < 10 m), the transition region start point radius,  $r_s$  is set equal to  $r_1$  and the end point radius is  $r_2$ .

described in decibel terms. Similar to the strategy used in [B-5], the short-range and full-scattering  $\sigma(r)$  limits used in this analysis are 0.5 dB and 6.4 dB<sup>3</sup>, respectively. Thus:

$$\sigma_{dB}(r) = \begin{cases} 0.5, & 0 \leq r \leq r_s \\ 0.5 + 5.9 \frac{(r - r_s)}{(r_1 - r_s)}, & r_s < r \leq r_1 \\ 6.4, & r > r_1 \end{cases} \quad (\text{F-10})$$

Note that  $\sigma(r) = (Ln(10)/10)\sigma_{dB}(r)$ .

For base station sources the method used in [5] is modified somewhat in this analysis. Instead of a stepped or polynomial function for the radial variation, a linear function for  $\sigma_{dB}(r)$  similar to that used for handsets is used. A standard deviation for "light shadowing" is given as 0.5 dB, which is similar to the handset scenario is assumed for short distances ( $< r_1$ ), in agreement with Loo's result [7]. Beyond the  $r_1$  breakpoint,  $\sigma_{dB}(r)$  rises linearly in  $r$  up to 6.4 dB at the  $r_2$  breakpoint (start of Hata Okumura path segment). (See Section F.2.2.2 for base station sources). Thus:

$$\sigma_{dB}(r) = \begin{cases} 0.5, & 0 \leq r \leq r_1 \\ 0.5 + 5.9 \frac{(r - r_1)}{(r_2 - r_1)}, & r_1 < r \leq r_2 \\ 6.4, & r > r_2 \end{cases} \quad (\text{F-11})$$

#### F.2.2.4 Single Path Probabilistic Propagation Fast-Fading Parameters, $L$ , $\psi_0$ , $\rho_0$

For handset interference sources, the unitless diffuse scattering parameter<sup>4</sup>,  $\psi_0(r)$ , is specified in terms of a product with channel parameter,  $L$ , as:

---

<sup>3</sup> The 6.4 dB standard deviation value used in the Log-Normal slow fading component of the certified avionics analysis model comes from measurements made around London by M.F. Ibrahim and J.D. Parsons [3]. This 6.4 dB was applicable for London type terrain and measured at a frequency of 900 MHz. As shown in [2], the standard deviation does not change much with frequency, so a 6.4 dB standard deviation was also assumed for the certified avionics analysis around 1531 MHz. In reality the standard deviation may be around 0.5 dB greater at 1531 MHz than at 900 MHz.

<sup>4</sup> For handset scenarios when the aircraft antenna height is very low (e.g.  $< 10$  m), the fast fading parameters transition region start point radius,  $r_s$  is set equal to  $r_1$  and the end point radius is  $r_2$ .

$$2L\psi_0(r) = \begin{cases} 0.1, & 0 \leq r \leq r_s \\ 0.1 + 0.9 \frac{(r - r_s)}{(r_1 - r_s)}, & r_s < r \leq r_1 \\ 1.0, & r > r_1 \end{cases} \quad (\text{F-12})$$

Note in Equation (F-12) that the composite parameter  $2L\psi_0(r)$  is non-zero at short ranges ( $< r_s$ ). This aspect provides consistency with the assumption that  $\sigma(r)$  is also non-zero over the same ranges. This result associates the small  $\sigma(r)$  value with a small amount of diffuse scattering in the propagation loss at short ranges. For this analysis  $L = \lceil \tau_{DS} W \rceil$  where the operator  $\lceil \cdot \rceil$  implies rounding up the operand to the next integer,  $\tau_{DS}$  is the spread in channel delay time, and  $W$  is the channel baseband bandwidth. Thus  $L$  denotes the number of resolvable paths associated with the fast fading component (see Section F.2.2.1).

In a similar manner then have for base station interference sources:

$$2L\psi_0(r) = \begin{cases} 0.1, & 0 \leq r \leq r_1 \\ 0.1 + 0.9 \frac{(r - r_1)}{(r_2 - r_1)}, & r_1 < r \leq r_2 \\ 1.0, & r > r_2 \end{cases} \quad (\text{F-13})$$

For handset sources the unitless line-of-sight parameter,  $\rho_0(r)$ , is specified as:

$$\rho_0^2(r) = \begin{cases} 1.0, & 0 \leq r \leq r_s \\ 1.0 - \frac{(r - r_s)}{(r_1 - r_s)}, & r_s < r \leq r_1 \\ 0, & r > r_1 \end{cases} \quad (\text{F-14})$$

Again, for the base station scenario using the break point definitions given in Section F.2.2.2:

$$\rho_0^2(r) = \begin{cases} 1.0, & 0 \leq r \leq r_1 \\ 1.0 - \frac{(r-r_1)}{(r_2-r_1)}, & r_1 < r \leq r_2 \\ 0, & r > r_2 \end{cases} \quad (\text{F-15})$$

### F.3 Aggregate Propagation Effects Computation Methods

Aggregate propagation effects are treated differently depending upon whether the interference sources are randomly distributed or have discrete known locations. Although there are exceptions, most handset sources use randomly distributed sources while base station sources have known locations. For uniformly-distributed, randomly-located interference sources, it is shown ([8], [9]) that once the single path interference characteristics have been determined, it is possible to determine the mean power, standard deviation, and cumulative probability distribution associated with aggregate received interference power. The same holds true for sources that have discrete known locations although the method used to determine mean power and cumulative probability distribution is different.

#### F.3.1 Randomly-Located Source Statistics

##### F.3.1.1 Randomly-Located Source Mean Aggregate Interference Power

As noted, for uniformly-distributed, randomly-located interference sources, once the single path interference characteristics have been determined, it is possible to determine the mean power, standard deviation, and cumulative probability distribution associated with aggregate received interference power by the ‘‘Analytic Statistical’’ method. For example, the aggregate mean power is given by:

$$\overline{P_I} = P_o \overline{n} \int_0^{R_o} (2L\psi_o(r) + \rho_o^2(r)) \exp[\sigma^2(r)/2 + \mu'(r, f_c)] f(r) dr \quad (\text{F-16})$$

where  $\overline{n}$  is the mean number of active emitters (Poisson-distributed) within the radio horizon radius,  $R_o$ , and  $f(r)$  is the radial location probability density function for uniformly distributed emitters. (More details in [9]). The expression,  $(2L\psi_o(r) + \rho_o^2(r))$ , is the first moment (mean) of the non-central Chi-squared fast-fading distribution and the expression,  $\exp[\sigma^2(r)/2 + \mu'(r, f_c)]$ , is the log-normal slow-fading distribution unitless mean.

##### F.3.1.2 Randomly-Located Source Aggregate Interference Power Standard Deviation

For randomly-located interference sources, the normalized standard deviation (normalized by the aggregate mean power) has been determined as in [9] by:



$$\sigma_I = P_0 \cdot \sqrt{n \int_0^{R_0} ((2L\psi_o(r) + \rho_o^2(r))^2 + 4L\psi_o^2(r) + 4\psi_o(r)\rho_o^2(r)) \exp[2\mu'(r, f_c) + 2\sigma^2(r)] f(r) dr / \overline{P_I}} \quad (\text{F-17})$$

where the parameters  $L$ ,  $\mu$ ,  $\sigma$ ,  $\psi_o$ , and  $\rho_o$  are as defined previously.

### F.3.1.3 Randomly-Located Source Aggregate Interference Power Probability Distribution

Following the methodology described in [9] for randomly-located sources, the characteristic function associated with the normalized aggregate interference power is expressed as:

$$C(\tau) = \exp[-\overline{n}(1 - \phi(\tau))] \quad (\text{F-18})$$

where  $\phi(\tau) = E[\exp(i\tau P_E(r) / \overline{P_I})]$ , i.e.,  $\phi(\tau)$  is the characteristic function of the interference from a single emitter normalized by the mean aggregate interference power.

It is shown in [B-9], after some manipulation it is possible to write:

$$\phi(\tau) = \int_{-\infty}^{\infty} \int_0^{R_0} (1/\sqrt{\pi}) \Phi(\tau, y, r) f(r) \text{Exp}(-y^2) dr dy ; \text{ where}$$

$$\Phi(\tau, y, r) = [1 / (1 - 2i\tau\psi_o(r)\Gamma(r, f_c) \exp(\sqrt{2}\sigma(r)y))^L] \exp[i\tau\Gamma(r, f_c) \exp(\sqrt{2}\sigma(r)y)\rho_o^2(r) / (1 - 2i\tau\psi_o(r)\Gamma(r, f_c) \exp(\sqrt{2}\sigma(r)y))]$$

$$\text{and } \Gamma(r, f_c) = P_o \cdot G_{norm}(\theta_{elev}(r), \phi_{az}) \cdot PF(r, f_c) \cdot G_{rcv}(\zeta_{elev}(r)) / \overline{P_I}$$

Then as in [10], the K-point Hermite-Gauss quadrature method with weights  $w_k$  and nodes  $y_k$  may be used to write:

$$\phi(\tau) \approx \sum_{k=1}^K (w_k / \sqrt{\pi}) \int_0^{R_0} \Phi(\tau, y_k, r) f(r) dr \quad (\text{F-19})$$

A value of 65 has been used for  $K$  to obtain very good accuracy in Equation (F-19).

Finally using Equation (F-18), we obtain the desired cumulative distribution function for the random variable  $P_I / \overline{P_I}$  as in [11] by the following:

$$\Pr(P_I / \overline{P_I} > z) = 1 - (1 / (2\pi)) \lim_{A \rightarrow \infty} \int_{-A}^A ((1 - \exp(-i\tau z)) / (i\tau)) C(\tau) d\tau + (1/2) \exp(-\overline{n}) \quad (\text{F-20})$$

for  $z > 0$ .

In those instances where randomly-located handsets are considered and where there is an already established level of unwanted interference from existing baseline sources, the procedure below may be used to determine the cumulative distribution function for the total aggregate interference.

Let  $P_{I_1} / \overline{P_{I_1}}$  denote the normalized aggregate interference from existing baseline sources and  $P_{I_2} / \overline{P_{I_2}}$  that from the new handset sources. Also let  $\overline{n} = \overline{n_1} + \overline{n_2}$  where  $\overline{n_1}$  and  $\overline{n_2}$  are the mean number of active emitters within the radio horizon associated with existing baseline sources and new handsets, respectively. The mean number of active emitters may be computed as described in [9] using parameters applicable to either existing sources or new handsets. The characteristic function  $C_1(\tau)$  associated with existing baseline sources is then given by:

$$C_1(\tau) = \text{Exp}[-\overline{n_1}(1 - \phi_1(\overline{P_{I_1}}\tau / (\overline{P_{I_1}} + \overline{P_{I_2}})))]$$

where  $\phi_1(\bullet)$  is the normalized single emitter interference characteristic function determined using the methodology described above with the parameters provided in [9]. The function  $\phi_1(\bullet)$  must be computed for whatever flight scenario is applicable (see, for example, [9]).

Similarly,

$$C_2(\tau) = \text{Exp}[-\overline{n_2}(1 - \phi_2(\overline{P_{I_2}}\tau / (\overline{P_{I_1}} + \overline{P_{I_2}})))]$$

where  $\phi_2(\bullet)$  is determined using parameters applicable to the new handsets under consideration.

The characteristic function  $C(\tau)$  associated with the total normalized aggregate interference,  $(P_{I_1} + P_{I_2}) / (\overline{P_{I_1}} + \overline{P_{I_2}})$ , is then given by  $C(\tau) = C_1(\tau)C_2(\tau)$ , which may be inverted to give the desired cumulative distribution function using Equation (F-20).

## F.3.2 Discretely-Located Source Statistics

### F.3.2.1 Discrete Source Mean Aggregate Interference Power

For sources having a known discrete distribution (e.g., the relative location (range) and height parameters associated with each source are known), two possible approaches may be used to determine the aggregate interference power, its mean and cumulative distribution function. Since the single source interference power in this case is still a random variable and is described by the product of a slow fading process and a fast fading process, similar to the case with randomly-located sources, the aggregate mean power may be computed as:

$$\overline{P_I} = P_o \sum_{k=1}^n (2L\psi_o(r_k) + \rho_o^2(r_k)) \exp[\sigma^2(r_k) / 2 + \mu'(r_k, H_{E_k}, H_A, f_c)] \quad (\text{F-21})$$

where  $r_k$  and  $H_{E_k}$  denote the lateral range to and height of the kth emitter antenna,  $H_A$  is the aircraft antenna height, and  $n$  is the known number of discrete interference sources (Analytic Statistical method).

Alternatively, it is also possible to use a Monte Carlo simulation to determine the mean aggregate interference power. In this alternative, the received power from the  $k$ th interfering emitter is modeled as the product of a slow fading process (log-normally distributed) and a fast fading process having a non-central Chi-Squared distribution. The log-normal component is generated using the same two parameters,  $\mu$  and  $\sigma$  as in the random source distribution while the Chi-Squared process uses the parameters,  $L$ ,  $\psi_o$  and  $\rho_o$ .

### F.3.2.2 Discrete Source Aggregate Interference Power Probability Distribution

#### F.3.2.2.1 General Discrete Source Aggregate Interference Power Probability Distribution

For discretely distributed interference sources, the characteristic function,  $\phi_k(\tau)$ , for the  $k$ th single emitter interference power can be computed as  $\phi_k(\tau) = E[\exp(i\tau P_{E_k}(r_k, H_{E_k}) / \bar{P}_I)]$ . This characteristic function can be written as:

$$\phi_k(\tau) \approx \sum_{m=1}^M (w_m / \sqrt{\pi}) \Phi(\tau, y_m, r_k)$$

where the weights  $w_m$  and nodes  $y_m$  are as defined previously and  $r_k$  is the distance to the  $k$ th interference source. A good value for  $M$  would be 65 as in the case of randomly-located, uniformly distributed interference sources.

The characteristic function for the normalized aggregate interference,  $C(\tau)$ , can then be determined from:

$$C(\tau) = \prod_{k=1}^n \phi_k(\tau).$$

Similar to the uniform randomly distributed interference case, the distribution function is

$$\Pr(P_I / \bar{P}_I > z) = 1 - (1 / (2\pi)) \lim_{A \rightarrow \infty} \int_{-A}^A ((1 - \exp(-i\tau z)) / (i\tau)) C(\tau) d\tau \quad (\text{F-22})$$

#### F.3.2.2.2 Discrete Source Aggregate Characteristic Function with Sectorization

The previous subsection describes in general the method to compute the aggregate characteristic function  $C(\tau)$  from the discretely-located individual base station characteristic functions  $\phi_k(\tau)$ . However, in the discrete location cases where several angular sectors are defined to enable terrain modeling, some alterations need to be made. The method described above may be used to determine the characteristic function  $C_n(\tau)$  for an individual sector assuming each of these characteristic functions have been normalized using the mean received aggregate factor for the

nth sector  $Fd_{AGGn}$  (used in place of  $\bar{P}_I$  in previous section). Then the composite characteristic function  $C(\tau)$  is defined in terms of the individual sector characteristic functions  $C_n(\tau)$  by

$$C(\tau) = \prod_{n=1}^N C_n((Fd_{AGGn}/MF_{AGG}) \cdot \tau)$$

where  $n$  is the individual sector number,  $N$  is the total number of sectors, and  $MF_{AGG}$  is the overall mean aggregate factor for all the sectors. Once  $C(\tau)$  is determined, the desired cumulative probability distribution function for the location can be computed with the inverse Fourier transform as in Equation (F-22) above.

## **APPENDIX G**

### **FAA BASE STATION ANTENNA MODEL**

**TABLE OF CONTENTS**

TABLE OF CONTENTS..... 2

LIST OF FIGURES ..... 3

LIST OF TABLES..... 4

REFERENCES ..... 5

APPENDIX..... 6

Appendix G. Base Station Transmit Antenna Far-Field Gain Pattern Model..... 6

    G.1 Gain Pattern Model Derivation..... 6

    G.2 Usage of Antenna Gain Pattern Model ..... 8

## LIST OF FIGURES

Figure A-1: Far Field Pattern Coordinate System .....	6
Figure A-2: Base Station Transmit Broad beam Elevation Pattern .....	7
Figure A-3: Base Station Transmit Broad beam Azimuth Pattern .....	8

## LIST OF TABLES

Table A-1: Base Station Transmit Antenna Parameters .....	6
---	---



## **REFERENCES**

**There are no sources in the current document.**

# APPENDIX

## Appendix G. Base Station Transmit Antenna Far-Field Gain Pattern Model

### G.1 Gain Pattern Model Derivation

The base station transmit antenna far field pattern model<sup>1</sup> is that associated with a uniformly illuminated rectangular aperture of width "a" and height "b". The aperture is centered on the "xy" coordinate center shown in Figure G-1 with the width "a" being co aligned with the "x" axis and the height "b" with the "y" axis. (Figure G-1 depicts general angular coordinates relative to the indicated axes.)

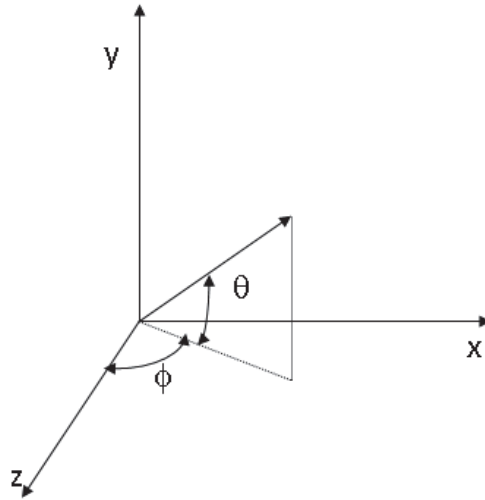


**Figure G-1: Far Field Pattern Coordinate System**

The beam is centered on the "z" axis with a peak gain, elevation beamwidth and azimuth beamwidth as shown in Table G-1. Table G-1 also lists other important parameters associated with the far field pattern. Table G-1 values are shown for the "narrow beam" (i.e., the study described in 5.3.3.3, Results for Inflight Aircraft Ground Based Base Station Cases) and "broad beam" (i.e., the study described in 5.3.3.6, Results for Inflight Aircraft TAWS/HTAWS and Low Altitude Pos/Nav) cases.

**Table G-1: Base Station Transmit Antenna Parameters**

Parameter	"Narrow Beam" Value	"Broad Beam" Value
$a/\lambda$	0.8278	0.7722535
$b/\lambda$	5.7	2.641574
$G_o$	72.5344	31.8649
$\eta$	0.681491	0.686578
Peak Gain	16.94 dB	13.4 dB
Elevation Beamwidth	8.8 deg	18.6 deg

<sup>1</sup> Pattern based on uniformly illuminated rectangular aperture as described in C. A. Balanis, "Antenna Theory: Analysis and Design", John Wiley & Sons, 2005 while accounting for a change in coordinate systems from that used in the book.

Azimuth Beamwidth	64.6 deg	70.0 deg
-------------------	----------	----------

The equations shown below are used by both the “narrow beam” and “broad beam” models and the dual use is true for all equations in this appendix unless otherwise indicated.

$$g(\theta', \phi') = \begin{cases} 1, & \theta' = 0 \text{ and } \phi' \in \{0\}, \{\pi\} \\ [\sin^2(\phi') + \cos^4(\theta') \sin^2(\theta') \cos^2(\phi')] / [\sin^2(\phi') \cos^2(\theta') + \sin^2(\theta')], & \text{elsewhere} \end{cases}$$

$$h(\theta', \phi') = \text{sinc}^2[\pi(a/\lambda)\sin(\phi')\cos(\theta')] \text{sinc}^2[\pi(b/\lambda)\sin(\theta')] g(\theta', \phi') \gamma(\phi')$$

A variation between the antenna equations of the “narrow beam” and “broad beam” models for the function,  $\gamma(\phi')$ , is that an exponential coefficient has a value of either a 3 or 4, as shown below.

$$\text{Narrow Beam Model: } \gamma(\phi') = \begin{cases} 1, & |\phi'| \leq \pi/2 \\ \exp[-3(|\phi'| - \pi/2)], & \pi/2 < |\phi'| \leq \pi \end{cases}$$

$$\text{Broad Beam Model: } \gamma(\phi') = \begin{cases} 1, & |\phi'| \leq \pi/2 \\ \exp[-3(|\phi'| - \pi/2)], & \pi/2 < |\phi'| \leq \pi \end{cases}$$

Then the far field base station antenna gain pattern is given by  $G_{xmit}(\theta', \phi') = \eta G_0 h(\theta', \phi')$

Figure G-2 shows an elevation cut of the pattern while Figure G-3 shows the azimuth cut. Note the gain is shown in dB in both figures while the angles are in degrees.

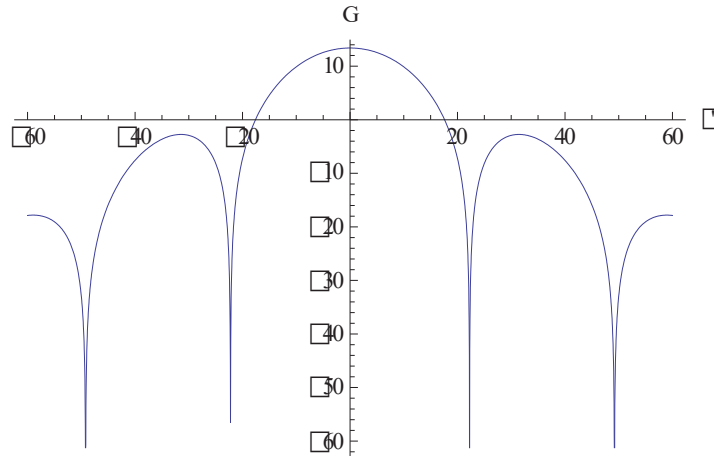


**Figure G-2: Base Station Transmit Broad beam Elevation Pattern**

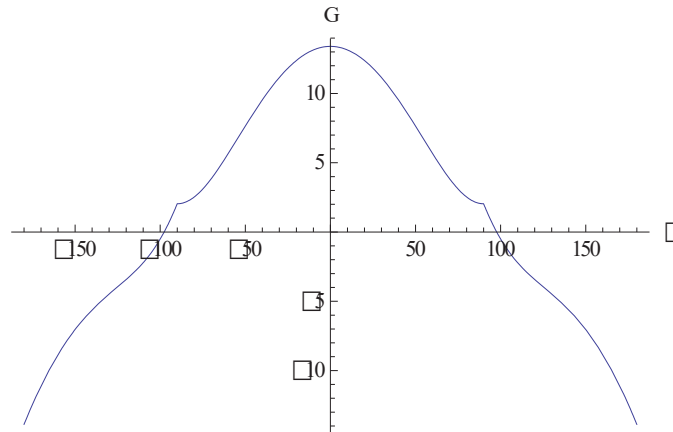


**Figure G-3: Base Station Transmit Broad beam Azimuth Pattern**

## G.2 Usage of Antenna Gain Pattern Model

The coordinate system described above will be tilted down (with respect to the local horizon)  $\xi$  degrees ( $\xi^\circ$  rotation about "x" axis) at each base station location in a practical application. Hence to use the above derived gain pattern in a typical "flat earth" untilted coordinate system  $(\theta, \phi)$ , a transformation of variables must be made. The gain in the untilted coordinate system is given by  $G_{xmit}[\theta'(\theta, \phi), \phi'(\theta, \phi)]$ ; where the elevation and azimuth angle transformation expressions are, respectively

$$\theta'(\theta, \phi) = \sin^{-1}[\cos(\xi\pi/180)\sin(\theta) + \sin(\xi\pi/180)\cos(\theta)\cos(\phi)] \text{ and}$$

$$\phi'(\theta, \phi) = \tan^{-1}[-\sin(\xi\pi/180)\sin(\theta) + \cos(\xi\pi/180)\cos(\theta)\cos(\phi), \cos(\theta)\sin(\phi)]$$

Note that  $\theta, \phi$  denote the elevation and azimuth angles respectively in the untilted coordinate system. For EIRP limit computation the relative pattern is normalized to beam center peak gain value:  $G_{norm}(\cdot) = G_{xmit}(\cdot)/\eta G_0$ .

# **APPENDIX H**

## **USE CASE DEVELOPMENT**

**TABLE OF CONTENTS**

TABLE OF CONTENTS..... 2  
LIST OF FIGURES ..... 3  
LIST OF TABLES ..... 4  
REFERENCES ..... 5  
APPENDIX..... 6  
Appendix H. Use Case Development..... 6

## **LIST OF FIGURES**

**No table of figures entries found.**

## **LIST OF TABLES**

No table of figures entries found.



## **REFERENCES**

**There are no sources in the current document.**

# **APPENDIX**

## **Appendix H. Use Case Development**



## Use Case Outreach

- ❑ Worked closely with our federal partners to understand their use case applications
- ❑ Conducted outreach with manufacturers who provided use case applications
- ❑ Results from these efforts can be located at:
  - [Workshop I](#)
  - [Workshop II](#)
  - [Workshop III](#)
  - [Workshop V](#)

## Incorporation of Use Cases

- Use cases will be used in conjunction with Interference Tolerance Masks (ITM) and propagation models to provide the power levels that can be tolerated adjacent to GPS/GNSS signals
- Use cases are assembled from DOT's federal partners & industry responses and aggregated by six (6) GPS/GNSS categories:
  - General Aviation [non certified] (GAV)
  - General Location/Navigation (GLN)
  - High Precision & Networks (HPR)
  - Timing (TIM)
  - Cellular (CEL)
  - Space Based (SPB)

# Use-Case Summary

Category	Height (feet AGL)		Speed (mph)	Urbanization	Terrain	Antenna Integration	Antenna Orientation
	Min	Max					
GAV	0	40k	920	Urban/Suburban/Rural	Flat/Sloped/Canyon – Open/Impeded - Land/Water	Yes/No	Variable
GLN	0	1,000	600	Urban/Suburban/Rural	Flat/Sloped/Canyon – Open/Impeded - Land/Water	Yes/No	Variable
HPR	0	20,000	180	Urban/Suburban/Rural	Flat/Sloped/Canyon – Open/Impeded - Land/Water	Yes/No	Variable
TIM	0	1000s	100	Urban/Suburban/rural	Flat – Open - Land	No	Fixed
CEL	0	100s	100s	Urban/Suburban/rural	Flat/Sloped/Canyon – Open/Impeded - Land/Water	Yes	Variable
SPB	1,700k	4,300k	16k	n/a	n/a	No	Variable

# Selection of Use Case Priorities





## PNTAB's View: Minimum Criteria for Testing/Evaluation of Interference Potential of High Power Terrestrial Transmitters in Repurposed Radio Bands

1. **Accept and strictly apply the 1 dB degradation** Interference Protection Criterion (IPC) for worst case conditions (This is the accepted, world-wide standard for PNT and many other radiocommunication applications)
2. Verify interference for **all classes of GPS receivers** is below criteria, **especially precision** (Real Time Kinematic - requires both user and reference station to be interference-free) and **timing receivers** (economically these two classes are the highest payoff applications – many \$B/year)
3. Test and **verify interference for receivers in all operating modes** is less than criteria, particularly **acquisition** and **reacquisition** of GNSS signals under difficult conditions (see attachment of representative interference cases)
4. **Focus analysis on worst cases**: use **maximum** authorized transmitted interference powers and **smallest-attenuation** propagation models (antennas and space losses) that do not underrepresent the maximum power of the interfering signal (including multiple transmitters)
5. Ensure **interference to emerging Global Navigation Satellite System (GNSS) signals** (particularly wider bandwidth GPS L1C – Galileo, GLONASS), is less than criteria
6. All testing must include **GNSS expertise** and be open to public comment and scrutiny.

# Why HPR as an Important Use Case?

## □ EXCOM Priorities

- Focus on existing uses ✓
- Vital Needs:
  - Economic ✓
  - Public Safety ✓
  - Scientific ✓
  - National Security ✓

## □ PNT Advisory Board Priorities

- Focus on HPR and TIM ✓
- Focus analysis on most sensitive case ✓
- Apply the 1 dB degradation ✓
- Include GNSS ✓

Category	Existing Uses	Vital Needs				Most Sensitive ITM
		Economic	Public Safety	Scientific	National Security	
GAV	✓	✓	✓	✓	✓	
GLN	✓	✓	✓	✓	✓	
HPR	✓	✓	✓	✓	✓	✓
TIM	✓	✓	✓	✓	✓	
CEL	✓	✓	✓	✓		
SPB	✓	✓	✓	✓	✓	✓

# Use Case Scenario Focus

Agriculture/Farming  
Construction/Infrastructure  
Emergency Response

# Agriculture/Farming

## □ Benefits of GPS:

- Precise operation/auto-steering for tractors, combines and sprayers
- Non-restrictive operations (e.g. fog and night)
- Coordinate movements of multiple tractors or other equipment
- Optimize seed, fertilizer and pesticides placement based on soil conditions and temperature.
- Precise planting and watering
- Yield and crop monitoring

## □ Makes use of augmentation systems:

- OmniSTAR, StarFire, Terrestar
- Real Time Kinematic (RTK)

# Agriculture/Farming Scenario – Basic Components



Photo courtesy AbeSnap23/ThinkStock  
LTE Cellular Tower



Photo courtesy Valio84s/ThinkStock  
Drone/Crop Monitoring



Photo courtesy of John Deere  
GPS Guidance System



Photo courtesy of John Deere  
High Precision Farming

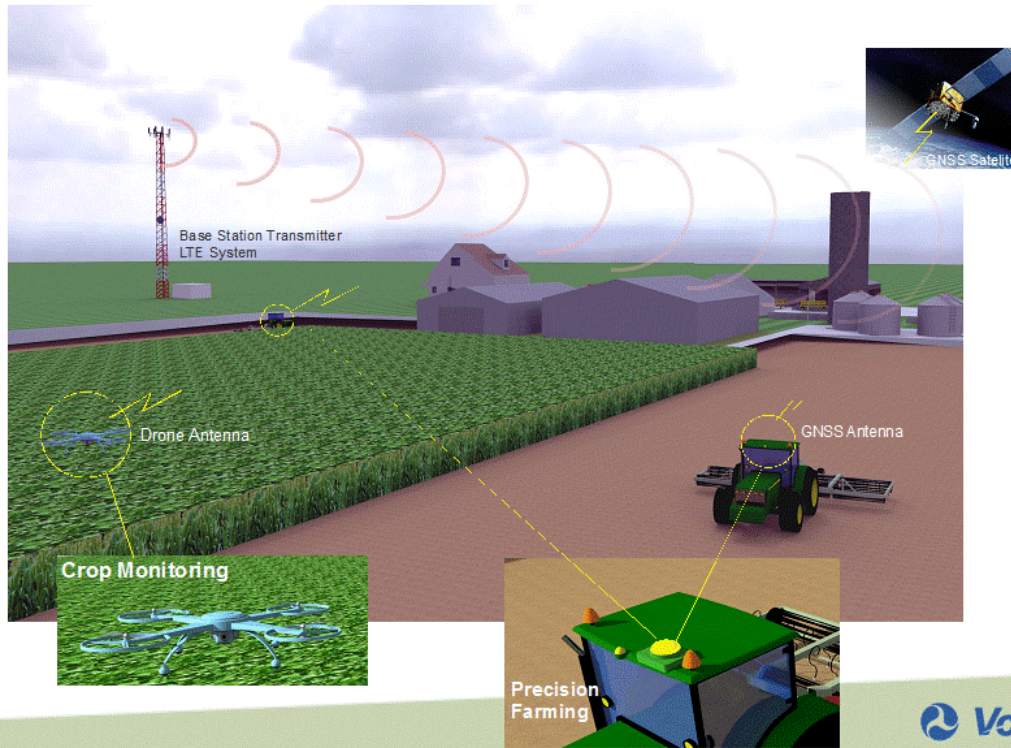


Photo courtesy of John Deere  
High Precision Farming



Photo courtesy Bennymarty/ThinkStock  
Drone/Crop Monitoring

# Agriculture/Farming Scenario



# Agriculture/Farming Summary

- Categories included are HPR and GLN/GAV
- Precision Farming (HPR)
  - Vital Needs: Economic
  - Lateral distances down to 10 feet from the base station
  - Vertical heights within 0-20 of feet above the ground
- Crop Health Monitoring (GLN/GAV)
  - Vital Needs: Economic
  - Lateral distances down to 10 feet from the base station
  - Vertical heights up to (and above) the base station height

## Construction/Infrastructure

### □ Benefits of GPS:

- Precise machine control for many different type of heavy equipment (e.g. dozers, excavators, pavers, scrapers, compactors)
- Placement of blades/heavy machinery give precise results (less rework)
- Improved process control through equipment location monitoring
- Virtual staking (view points on a screen vs. physical stakes)
- Time saving from traditional surveying

### □ Surveyor setup (3d geodetic control area) and monitor machine control operations



# Construction/Infrastructure Scenarios - Basic Components



Photo courtesy of WSP Canada Inc  
GPS HPR receiver used in  
construction/surveying



Photo courtesy of WSP Canada Inc  
GPS HPR receiver used in  
construction/surveying



Photo courtesy Medvedkov/ThinkStock  
Construction/Surveying



Photo courtesy ThinkStock  
GPS HPR receiver used in  
construction guidance



Photo courtesy AbeSnap23/ThinkStock  
LTE Cellular Tower



Photo courtesy Kadmy/ThinkStock  
Surveying

# Construction/Infrastructure Scenario



## Construction/Infrastructure (HPR) Summary

- ❑ Construction/infrastructure (HPR)
- ❑ Vital Needs: Economic
- ❑ Lateral distances down to 1 – 2 city blocks from the base station
- ❑ Vertical heights up to (and above) the base station height

## Emergency Services

- ❑ Medical and police personnel are increasingly using GPS to locate patients both during emergencies and regular activities
- ❑ Police resource tracking (increased awareness of where their officers are located)
- ❑ Drones/UAV/UAS will take on increasing importance in dealing with natural and other disasters/incidents

# Emergency Services Scenarios - Basic Components



Photo courtesy Tiero/ThinkStock

Drone/Emergency  
Response/Disasters



Photo courtesy StockSolutions/ThinkStock

Ankle Bracelet  
Monitoring



Photo courtesy Mokee81/ThinkStock

Police/Emergency  
Response/Resource Tracking



Photo courtesy Mrdoomits/ThinkStock

Emergency Response/  
Resource Tracking



Photo courtesy AbeSnap23/ThinkStock

LTE Cellular Tower



Photo courtesy ThinkStock

Drone/Emergency  
Response/Disasters

# Emergency Response Scenario



# Emergency Response Summary

- ❑ Two categories included GAV and GLN
  - UAS/UAV/Drone (GLN/GAV)
  - Emergency Services/Asset Tracking (GLN)
  - Emergency Response/Asset Tracking (GLN)
- ❑ Lateral distances down to 10 feet from the base station
- ❑ Vertical heights up to (and above) the base station height
- ❑ Vital Needs:
  - Public safety / Safety of life
  - National Security

## Other Considerations



# GPS/GNSS Receiver Modification

- ❑ Receiver modification to reduce susceptibility to out of band emissions?
- ❑ Many receivers are sealed and modification are complicated if not impossible
- ❑ Even if you can modify the receivers, how do identify “all” users?
- ❑ May result in loss of augmentation (e.g., Mobile Satellite Service delivered corrections) capability



Photo courtesy Scanrai/ThinkStock



Photo courtesy Comstock/ThinkStock



\* [http://www.deere.com/en\\_US/docs/html/brochures/publication.html?id=004d03e7#14](http://www.deere.com/en_US/docs/html/brochures/publication.html?id=004d03e7#14)

\*\* [http://www.trimble.com/mappingGIS/pro6-Pro-Series-Receiver.aspx?tab=Features\\_and\\_Benefits](http://www.trimble.com/mappingGIS/pro6-Pro-Series-Receiver.aspx?tab=Features_and_Benefits)

## Summary

- ❑ Every possible use case is not covered - as there are thousands of use cases
- ❑ Cases illustrated are applications that happen routinely and can bound the results/impact of base station transmitters
- ❑ Inverse and propagation modeling will utilize the height and location limits of the these use case application to determine worst case base station transmit power levels

# **APPENDIX I**

## **FORWARD MODELING RESULTS**

# TABLE OF CONTENTS

TABLE OF CONTENTS.....	2
LIST OF FIGURES .....	4
LIST OF TABLES.....	9
REFERENCES .....	10
APPENDIX.....	11
Appendix I. Forward Modeling Results.....	11
I.1 Macro Urban Base Station, GPS C/A-code.....	11
I.1.1 GAV .....	11
I.1.2 GLN .....	16
I.1.3 HPR.....	21
I.1.4 TIM .....	27
I.1.5 CEL.....	32
I.2 Small Cell Outdoor/Urban Micro Urban Base Station, GPS C/A-code.....	36
I.2.1 GAV .....	36
I.2.2 GLN .....	41
I.2.3 HPR.....	46
I.2.4 TIM .....	50
I.2.5 CEL.....	56
I.3 Handsets, GPS C/A-code.....	61
I.3.1 GAV .....	61
I.3.2 GLN .....	65
I.3.3 HPR.....	70
I.3.4 TIM .....	73
I.3.5 CEL.....	77
I.4 Sensitivity Analyses .....	82
I.4.1 Non-bounding DUTs .....	82
I.4.2 Other GNSS Signal Types .....	87

I.4.3 Propagation Models ..... 88

## LIST OF FIGURES

Figure I-1: Maximum Impacted Lateral Distance for Bounding GAV, Macro Urban Base Station (EIRP = 59 dBm) .....	12
Figure I-2: Macro Urban Base Station (EIRP = 59 dBm), Bounding GAV, 1475 MHz.....	12
Figure I-3: Macro Urban Base Station (EIRP = 59 dBm), Bounding GAV, 1490 MHz.....	13
Figure I-4: Macro Urban Base Station (EIRP = 59 dBm), Bounding GAV, 1505 MHz.....	13
Figure I-5: Macro Urban Base Station (EIRP = 59 dBm), Bounding GAV, 1520 MHz.....	13
Figure I-6: Macro Urban Base Station (EIRP = 59 dBm), Bounding GAV, 1525 MHz.....	14
Figure I-7: Macro Urban Base Station (EIRP = 59 dBm), Bounding GAV, 1530 MHz.....	14
Figure I-8: Macro Urban Base Station (EIRP = 59 dBm), Bounding GAV, 1535 MHz.....	14
Figure I-9: Macro Urban Base Station (EIRP = 59 dBm), Bounding GAV, 1540 MHz.....	15
Figure I-10: Macro Urban Base Station (EIRP = 59 dBm), Bounding GAV, 1545 MHz.....	15
Figure I-11: Macro Urban Base Station (EIRP = 59 dBm), Bounding GAV, 1550 MHz.....	15
Figure I-12: Macro Urban Base Station (EIRP = 59 dBm), Bounding GAV, 1675 MHz.....	16
Figure I-13: Maximum Impacted Lateral Distance for Bounding GLN, Macro Urban Base Station with EIRP of 59 dBm/sector.....	17
Figure I-14: Macro Urban Base Station (EIRP = 59 dBm), Bounding GLN, 1475 MHz .....	17
Figure I-15: Macro Urban Base Station (EIRP = 59 dBm), Bounding GLN, 1490 MHz .....	18
Figure I-16: Macro Urban Base Station (EIRP = 59 dBm), Bounding GLN, 1505 MHz .....	18
Figure I-17: Macro Urban Base Station (EIRP = 59 dBm), Bounding GLN, 1520 MHz .....	18
Figure I-18: Macro Urban Base Station (EIRP = 59 dBm), Bounding GLN, 1525 MHz .....	19
Figure I-19: Macro Urban Base Station (EIRP = 59 dBm), Bounding GLN, 1530 MHz .....	19
Figure I-20: Macro Urban Base Station (EIRP = 59 dBm), Bounding GLN, 1535 MHz .....	19
Figure I-21: Macro Urban Base Station (EIRP = 59 dBm), Bounding GLN, 1540 MHz .....	20
Figure I-22: Macro Urban Base Station (EIRP = 59 dBm), Bounding GLN, 1545 MHz .....	20
Figure I-23: Macro Urban Base Station (EIRP = 59 dBm), Bounding GLN, 1550 MHz .....	20
Figure I-24: Macro Urban Base Station (EIRP = 59 dBm), Bounding GLN, 1675 MHz .....	21
Figure I-25: Maximum Impacted Lateral Distance for Bounding HPR, Macro Urban Base Station with EIRP of 59 dBm/sector .....	22
Figure I-26: Macro Urban Base Station (EIRP = 59 dBm), Bounding HPR, 1475 MHz.....	22
Figure I-27: Macro Urban Base Station (EIRP = 59 dBm), Bounding HPR, 1490 MHz.....	23
Figure I-28: Macro Urban Base Station (EIRP = 59 dBm), Bounding HPR, 1505 MHz.....	23
Figure I-29: Macro Urban Base Station (EIRP = 59 dBm), Bounding HPR, 1520 MHz.....	23
Figure I-30: Macro Urban Base Station (EIRP = 59 dBm), Bounding HPR, 1525 MHz.....	24
Figure I-31: Macro Urban Base Station (EIRP = 59 dBm), Bounding HPR, 1530 MHz.....	24
Figure I-32: Macro Urban Base Station (EIRP = 59 dBm), Bounding HPR, 1535 MHz.....	24
Figure I-33: Macro Urban Base Station (EIRP = 59 dBm), Bounding HPR, 1540 MHz.....	25

Figure I-34: Macro Urban Base Station (EIRP = 59 dBm), Bounding HPR, 1545 MHz.....	25
Figure I-35: Macro Urban Base Station (EIRP = 59 dBm), Bounding HPR, 1550 MHz.....	25
Figure I-36: Macro Urban Base Station (EIRP = 59 dBm), Bounding HPR, 1675 MHz.....	26
Figure I-37: Maximum Impacted Lateral Distance for Bounding TIM, Macro Urban Base Station with EIRP of 59 dBm/sector.....	27
Figure I-38: Macro Urban Base Station (EIRP = 59 dBm), Bounding TIM, 1475 MHz .....	28
Figure I-39: Macro Urban Base Station (EIRP = 59 dBm), Bounding TIM, 1490 MHz .....	28
Figure I-40: Macro Urban Base Station (EIRP = 59 dBm), Bounding TIM, 1505 MHz .....	29
Figure I-41: Macro Urban Base Station (EIRP = 59 dBm), Bounding TIM, 1520 MHz .....	29
Figure I-42: Macro Urban Base Station (EIRP = 59 dBm), Bounding TIM, 1525 MHz .....	29
Figure I-43: Macro Urban Base Station (EIRP = 59 dBm), Bounding TIM, 1530 MHz .....	30
Figure I-44: Macro Urban Base Station (EIRP = 59 dBm), Bounding TIM, 1535 MHz .....	30
Figure I-45: Macro Urban Base Station (EIRP = 59 dBm), Bounding TIM, 1540 MHz .....	30
Figure I-46: Macro Urban Base Station (EIRP = 59 dBm), Bounding TIM, 1545 MHz .....	31
Figure I-47: Macro Urban Base Station (EIRP = 59 dBm), Bounding TIM, 1550 MHz .....	31
Figure I-48: Macro Urban Base Station (EIRP = 59 dBm), Bounding TIM, 1675 MHz .....	31
Figure I-49: Maximum Impacted Lateral Distance for Bounding CEL, Macro Urban Base Station with EIRP of 59 dBm/sector.....	33
Figure I-50: Macro Urban Base Station (EIRP = 59 dBm), Bounding CEL, 1525 MHz.....	34
Figure I-51: Macro Urban Base Station (EIRP = 59 dBm), Bounding CEL, 1530 MHz.....	34
Figure I-52: Macro Urban Base Station (EIRP = 59 dBm), Bounding CEL, 1535 MHz.....	35
Figure I-53: Macro Urban Base Station (EIRP = 59 dBm), Bounding CEL, 1540 MHz.....	35
Figure I-54: Macro Urban Base Station (EIRP = 59 dBm), Bounding CEL, 1545 MHz.....	35
Figure I-55: Macro Urban Base Station (EIRP = 59 dBm), Bounding CEL, 1550 MHz.....	36
Figure I-56: Macro Urban Base Station (EIRP = 59 dBm), Bounding CEL, 1675 MHz.....	36
Figure I-57: Small Cell Outdoor/Micro Urban (EIRP = 40 dBm), Bounding GAV .....	37
Figure I-58: Small Cell Outdoor/Micro Urban (EIRP = 40 dBm), Bounding GAV, 1475 MHz	37
Figure I-59: Small Cell Outdoor/Micro Urban (EIRP = 40 dBm), Bounding GAV, 1490 MHz	38
Figure I-60: Small Cell Outdoor/Micro Urban (EIRP = 40 dBm), Bounding GAV, 1505 MHz	38
Figure I-61: Small Cell Outdoor/Micro Urban (EIRP = 40 dBm), Bounding GAV, 1520 MHz	38
Figure I-62: Small Cell Outdoor/Micro Urban (EIRP = 40 dBm), Bounding GAV, 1525 MHz	39
Figure I-63: Small Cell Outdoor/Micro Urban (EIRP = 40 dBm), Bounding GAV, 1530 MHz	39
Figure I-64: Small Cell Outdoor/Micro Urban (EIRP = 40 dBm), Bounding GAV, 1535 MHz	39
Figure I-65: Small Cell Outdoor/Micro Urban (EIRP = 40 dBm), Bounding GAV, 1540 MHz	40
Figure I-66: Small Cell Outdoor/Micro Urban (EIRP = 40 dBm), Bounding GAV, 1545 MHz	40
Figure I-67: Small Cell Outdoor/Micro Urban (EIRP = 40 dBm), Bounding GAV, 1550 MHz	40
Figure I-68: Small Cell Outdoor/Micro Urban (EIRP = 40 dBm), Bounding GAV, 1675 MHz	41
Figure I-69: Small Cell Outdoor/Micro Urban (EIRP = 40 dBm), Bounding GLN.....	41
Figure I-70: Small Cell Outdoor/Micro Urban (EIRP = 40 dBm), Bounding GLN, 1475 MHz	42

Figure I-71: Small Cell Outdoor/Micro Urban (EIRP = 40 dBm), Bounding GLN, 1490 MHz	42
Figure I-72: Small Cell Outdoor/Micro Urban (EIRP = 40 dBm), Bounding GLN, 1505 MHz	42
Figure I-73: Small Cell Outdoor/Micro Urban (EIRP = 40 dBm), Bounding GLN, 1520 MHz	43
Figure I-74: Small Cell Outdoor/Micro Urban (EIRP = 40 dBm), Bounding GLN, 1525 MHz	43
Figure I-75: Small Cell Outdoor/Micro Urban (EIRP = 40 dBm), Bounding GLN, 1530 MHz	43
Figure I-76: Small Cell Outdoor/Micro Urban (EIRP = 40 dBm), Bounding GLN, 1535 MHz	44
Figure I-77: Small Cell Outdoor/Micro Urban (EIRP = 40 dBm), Bounding GLN, 1540 MHz	44
Figure I-78: Small Cell Outdoor/Micro Urban (EIRP = 40 dBm), Bounding GLN, 1545 MHz	44
Figure I-79: Small Cell Outdoor/Micro Urban (EIRP = 40 dBm), Bounding GLN, 1550 MHz	45
Figure I-80: Small Cell Outdoor/Micro Urban (EIRP = 40 dBm), Bounding GLN, 1675 MHz	45
Figure I-81: Small Cell Outdoor/Micro Urban, Bounding HPR.....	46
Figure I-82: Small Cell Outdoor/Micro Urban (EIRP = 40 dBm), Bounding HPR, 1475 MHz.	46
Figure I-83: Small Cell Outdoor/Micro Urban (EIRP = 40 dBm), Bounding HPR, 1490 MHz.	47
Figure I-84: Small Cell Outdoor/Micro Urban (EIRP = 40 dBm), Bounding HPR, 1505 MHz.	47
Figure I-85: Small Cell Outdoor/Micro Urban (EIRP = 40 dBm), Bounding HPR, 1520 MHz.	47
Figure I-86: Small Cell Outdoor/Micro Urban (EIRP = 40 dBm), Bounding HPR, 1525 MHz.	48
Figure I-87: Small Cell Outdoor/Micro Urban (EIRP = 40 dBm), Bounding HPR, 1530 MHz.	48
Figure I-88: Small Cell Outdoor/Micro Urban (EIRP = 40 dBm), Bounding HPR, 1535 MHz.	48
Figure I-89: Small Cell Outdoor/Micro Urban (EIRP = 40 dBm), Bounding HPR, 1540 MHz.	49
Figure I-90: Small Cell Outdoor/Micro Urban (EIRP = 40 dBm), Bounding HPR, 1545 MHz.	49
Figure I-91: Small Cell Outdoor/Micro Urban (EIRP = 40 dBm), Bounding HPR, 1550 MHz.	49
Figure I-92: Small Cell Outdoor/Micro Urban (EIRP = 40 dBm), Bounding HPR, 1675 MHz.	50
Figure I-93: Small Cell Outdoor/Micro Urban (EIRP = 40 dBm), Bounding TIM.....	50
Figure I-94: Small Cell Outdoor/Micro Urban (EIRP = 40 dBm), Bounding TIM, 1475 MHz .	51
Figure I-95: Small Cell Outdoor/Micro Urban (EIRP = 40 dBm), Bounding TIM, 1490 MHz .	52
Figure I-96: Small Cell Outdoor/Micro Urban (EIRP = 40 dBm), Bounding TIM, 1505 MHz .	53
Figure I-97: Small Cell Outdoor/Micro Urban (EIRP = 40 dBm), Bounding TIM, 1520 MHz .	53
Figure I-98: Small Cell Outdoor/Micro Urban (EIRP = 40 dBm), Bounding TIM, 1525 MHz .	54
Figure I-99: Small Cell Outdoor/Micro Urban (EIRP = 40 dBm), Bounding TIM, 1530 MHz .	54
Figure I-100: Small Cell Outdoor/Micro Urban (EIRP = 40 dBm), Bounding TIM, 1535 MHz	54
Figure I-101: Small Cell Outdoor/Micro Urban (EIRP = 40 dBm), Bounding TIM, 1540 MHz	55
Figure I-102: Small Cell Outdoor/Micro Urban (EIRP = 40 dBm), Bounding TIM, 1545 MHz	55
Figure I-103: Small Cell Outdoor/Micro Urban (EIRP = 40 dBm), Bounding TIM, 1550 MHz	55
Figure I-104: Small Cell Outdoor/Micro Urban (EIRP = 40 dBm), Bounding TIM, 1675 MHz	56
Figure I-105: Small Cell Outdoor/Micro Urban (EIRP = 40 dBm), Bounding CEL .....	57
Figure I-106: Small Cell Outdoor/Micro Urban (EIRP = 40 dBm), Bounding CEL, 1525 MHz	58
Figure I-107: Small Cell Outdoor/Micro Urban (EIRP = 40 dBm), Bounding CEL, 1530 MHz	59
Figure I-108: Small Cell Outdoor/Micro Urban (EIRP = 40 dBm), Bounding CEL, 1535 MHz	59
Figure I-109: Small Cell Outdoor/Micro Urban (EIRP = 40 dBm), Bounding CEL, 1540 MHz	60



Figure I-110: Small Cell Outdoor/Micro Urban (EIRP = 40 dBm), Bounding CEL, 1545 MHz	60
Figure I-111: Small Cell Outdoor/Micro Urban (EIRP = 40 dBm), Bounding CEL, 1550 MHz	60
Figure I-112: Small Cell Outdoor/Micro Urban (EIRP = 40 dBm), Bounding CEL, 1675 MHz	61
Figure I-113: Handset (EIRP = 23 dBm), Bounding GAV	62
Figure I-114: Handset (EIRP = 23 dBm), Bounding GAV, 1620 MHz	62
Figure I-115: Handset (EIRP = 23 dBm), Bounding GAV, 1625 MHz	63
Figure I-116: Handset (EIRP = 23 dBm), Bounding GAV, 1630 MHz	63
Figure I-117: Handset (EIRP = 23 dBm), Bounding GAV, 1635 MHz	64
Figure I-118: Handset (EIRP = 23 dBm), Bounding GAV, 1640 MHz	64
Figure I-119: Handset (EIRP = 23 dBm), Bounding GAV, 1645 MHz	65
Figure I-120: Handset (EIRP = 23 dBm), Bounding GAV, 1660 MHz	65
Figure I-121: Handset (EIRP = 23 dBm), Bounding GLN	66
Figure I-122: Handset (EIRP = 23 dBm), Bounding GLN, 1620 MHz	66
Figure I-123: Handset (EIRP = 23 dBm), Bounding GLN, 1625 MHz	67
Figure I-124: Handset (EIRP = 23 dBm), Bounding GLN, 1630 MHz	67
Figure I-125: Handset (EIRP = 23 dBm), Bounding GLN, 1635 MHz	68
Figure I-126: Handset (EIRP = 23 dBm), Bounding GLN, 1640 MHz	68
Figure I-127: Handset (EIRP = 23 dBm), Bounding GLN, 1645 MHz	69
Figure I-128: Handset (EIRP = 23 dBm), Bounding GLN, 1660 MHz	69
Figure I-129: Handset (EIRP = 23 dBm), Bounding HPR	70
Figure I-130: Handset (EIRP = 23 dBm), Bounding HPR, 1620 MHz	70
Figure I-131: Handset (EIRP = 23 dBm), Bounding HPR, 1625 MHz	71
Figure I-132: Handset (EIRP = 23 dBm), Bounding HPR, 1630 MHz	71
Figure I-133: Handset (EIRP = 23 dBm), Bounding HPR, 1635 MHz	71
Figure I-134: Handset (EIRP = 23 dBm), Bounding HPR, 1640 MHz	72
Figure I-135: Handset (EIRP = 23 dBm), Bounding HPR, 1645 MHz	72
Figure I-136: Handset (EIRP = 23 dBm), Bounding HPR, 1660 MHz	72
Figure I-137: Handset (EIRP = 23 dBm), Bounding TIM	73
Figure I-138: Handset (EIRP = 23 dBm), Bounding TIM, 1620 MHz	74
Figure I-139: Handset (EIRP = 23 dBm), Bounding TIM, 1625 MHz	74
Figure I-140: Handset (EIRP = 23 dBm), Bounding TIM, 1630 MHz	75
Figure I-141: Handset (EIRP = 23 dBm), Bounding TIM, 1635 MHz	75
Figure I-142: Handset (EIRP = 23 dBm), Bounding TIM, 1640 MHz	76
Figure I-143: Handset (EIRP = 23 dBm), Bounding TIM, 1645 MHz	76
Figure I-144: Handset (EIRP = 23 dBm), Bounding TIM, 1660 MHz	77
Figure I-145: Handset (EIRP = 23 dBm), Bounding CEL	78
Figure I-146: Handset (EIRP = 23 dBm), Bounding CEL, 1620 MHz	79
Figure I-147: Handset (EIRP = 23 dBm), Bounding CEL, 1625 MHz	79
Figure I-148: Handset (EIRP = 23 dBm), Bounding CEL, 1630 MHz	80

Figure I-149: Handset (EIRP = 23 dBm), Bounding CEL, 1635 MHz .....	80
Figure I-150: Handset (EIRP = 23 dBm), Bounding CEL, 1640 MHz .....	81
Figure I-151: Handset (EIRP = 23 dBm), Bounding CEL, 1645 MHz .....	81
Figure I-152: Handset (EIRP = 23 dBm), Bounding CEL, 1660 MHz .....	82
Figure I-153: Maximum Impacted Lateral Distance for GAV, Macro Urban Base Station (EIRP = 59 dBm) .....	83
Figure I-154: Maximum Impacted Lateral Distance for GLN, Macro Urban Base Station (EIRP = 59 dBm) .....	84
Figure I-155: Maximum Impacted Lateral Distance for HPR, Macro Urban Base Station (EIRP = 59 dBm) .....	85
Figure I-156: Maximum Impacted Lateral Distance for TIM, Macro Urban Base Station (EIRP = 59 dBm) .....	86
Figure I-157: Maximum Impacted Lateral Distance for CEL, Macro Urban Base Station (EIRP = 59 dBm) .....	87
Figure I-158: Small Cell Outdoor/Micro Urban (EIRP = 40 dBm), Bounding GLN, 1530 MHz: (a) GPS C/A-code (b) GLONASS L1C .....	88
Figure I-159: Impacted Area for Cellular DUT from 23 dBm EIRP Mobile Device at 1550 MHz (a) as predicted using free-space propagation model, (b) as predicted using two-ray propagation model.....	89

## **LIST OF TABLES**

No table of figures entries found.

## **REFERENCES**

**There are no sources in the current document.**

## **APPENDIX**

### **Appendix I. Forward Modeling Results**

This appendix presents forward modeling results. Section I.1 provides results for macro urban base stations (EIRP = 59 dBm, antenna height = 25 m). Section I.2 provides results for micro urban/small cell outdoor base stations (EIRP = 40 dBm, antenna height = 6 m). Section I.3 provides results for mobile devices (EIRP = 23 dBm, antenna height = 2 m). These three sections (Sections I.1, I.2, and I.3) only include results for the most sensitive (bounding) GPS C/A-code receiver for each frequency in each receiver category (except certified-aviation and spaceborne).

Section I.4 provides the results of a sensitivity analysis. This section explores the variability in forward modeling results with input assumptions including: (1) percentile of DUTs protected (e.g., protecting the median DUT vs. the bounding DUT for each frequency and each receiver category), (2) consideration of other GNSS signal types besides the GPS C/A-code, and (3) propagation model.

#### **I.1 Macro Urban Base Station, GPS C/A-code**

This section presents results for 10-MHz LTE signals broadcast by macro urban base stations (three sectors with 59 dBm EIRP/sector, 16 dBi antennas at 25 m AGL with 10 deg downtilt), free-space propagation, and bounding mask.

##### **I.1.1 GAV**

Figure I-1 plots the maximum impacted lateral distance for three types of impact to the most sensitive (bounding) DUT for each frequency: (1) interference results in a 1-dB CNR degradation (blue), (2) interference results in loss of lock on low-elevation angle satellites (red), and (3) interference results in loss of lock for high-elevation angle satellites (orange). Figure I-2 to Figure I-12 show the two-dimensional impacted area regions for tested frequencies from 1475 MHz to 1675 MHz.

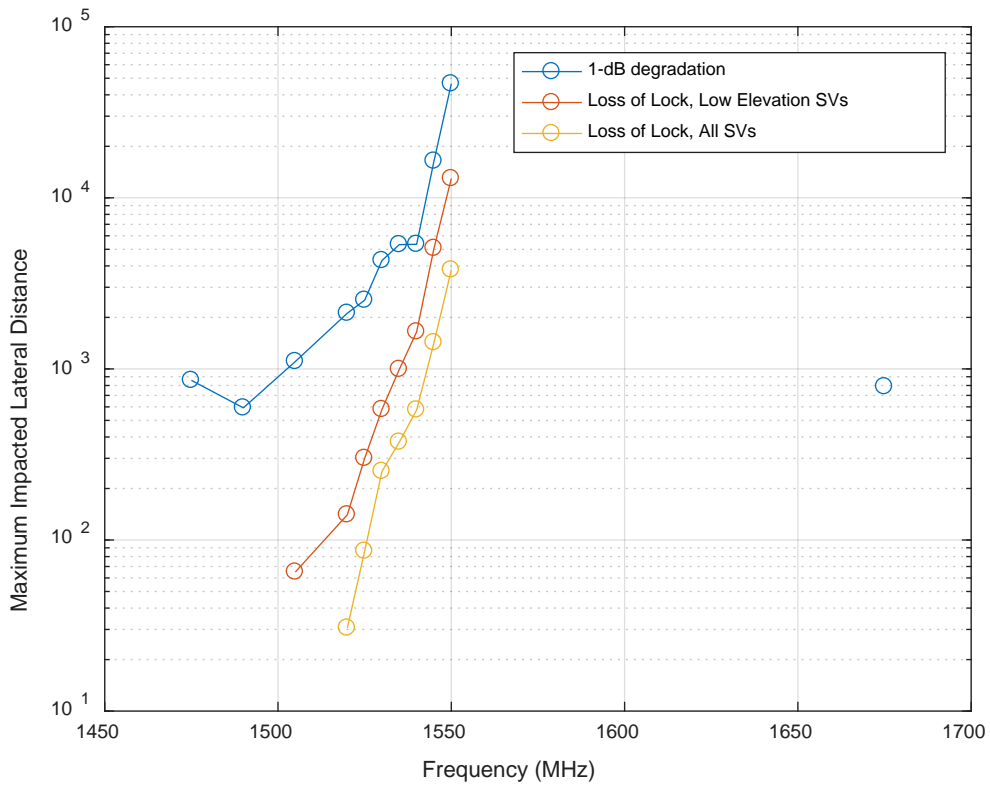


**Figure I-1: Maximum Impacted Lateral Distance for Bounding GAV, Macro Urban Base Station (EIRP = 59 dBm)**

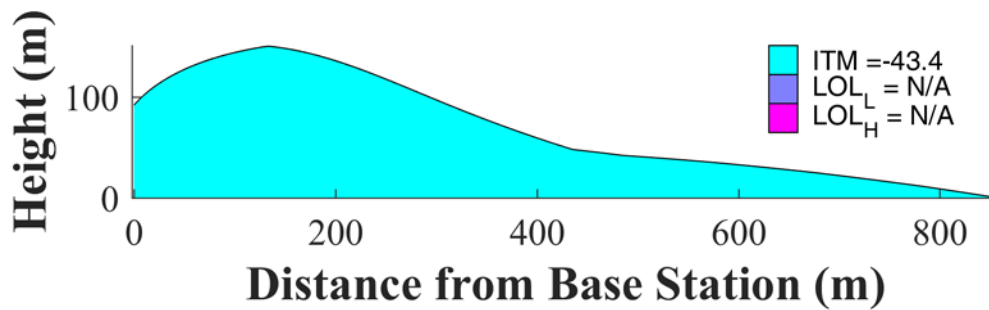


**Figure I-2: Macro Urban Base Station (EIRP = 59 dBm), Bounding GAV, 1475 MHz**

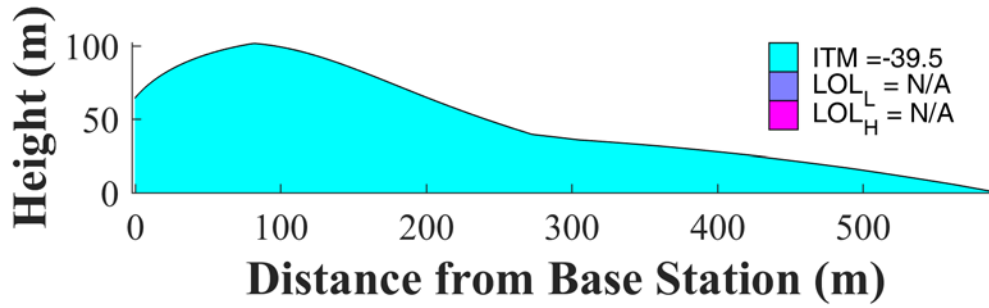


Figure I-3: Macro Urban Base Station (EIRP = 59 dBm), Bounding GAV, 1490 MHz

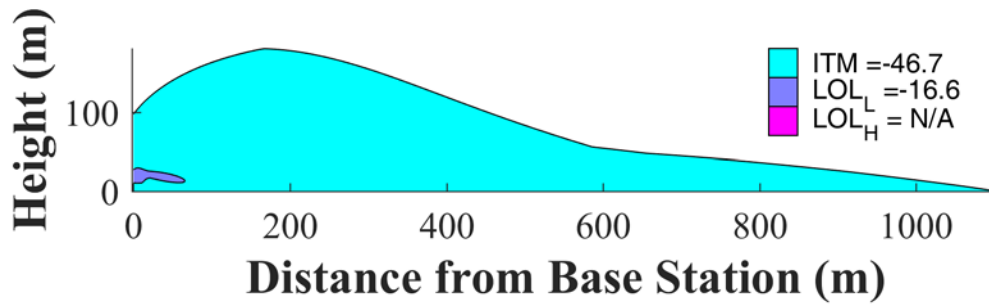


Figure I-4: Macro Urban Base Station (EIRP = 59 dBm), Bounding GAV, 1505 MHz

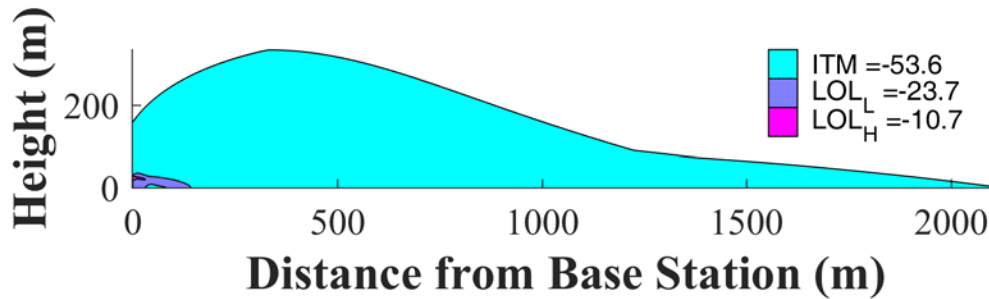


Figure I-5: Macro Urban Base Station (EIRP = 59 dBm), Bounding GAV, 1520 MHz

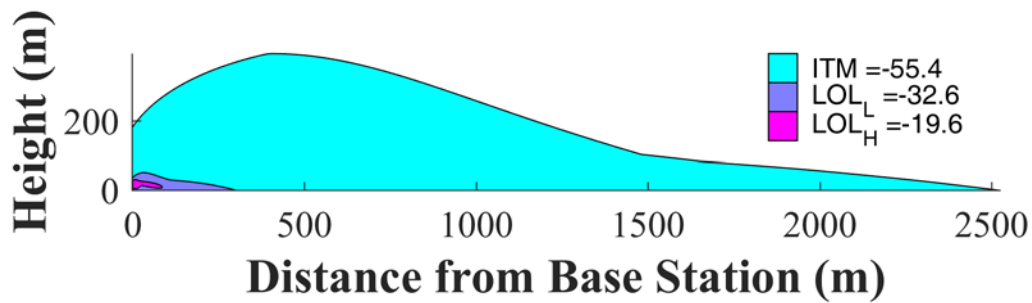


Figure I-6: Macro Urban Base Station (EIRP = 59 dBm), Bounding GAV, 1525 MHz

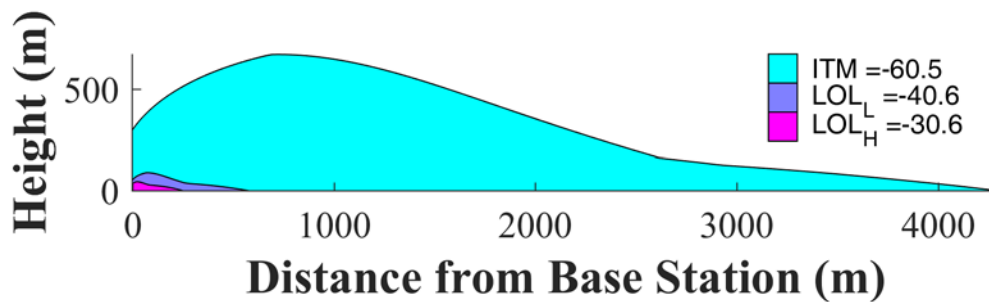


Figure I-7: Macro Urban Base Station (EIRP = 59 dBm), Bounding GAV, 1530 MHz

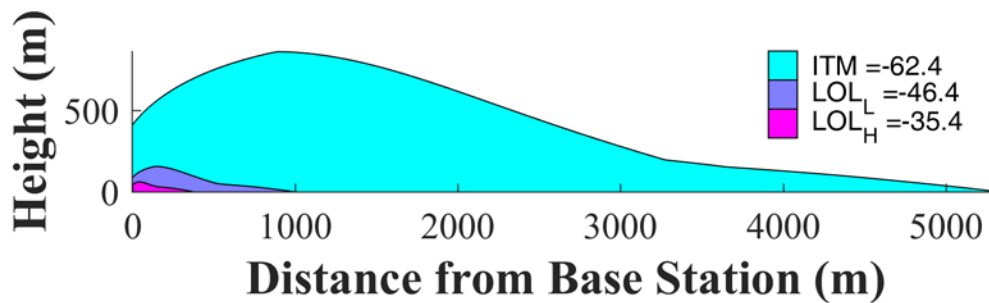


Figure I-8: Macro Urban Base Station (EIRP = 59 dBm), Bounding GAV, 1535 MHz



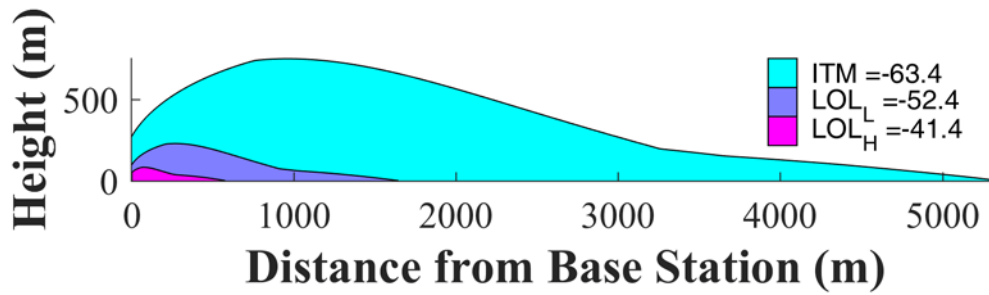


Figure I-9: Macro Urban Base Station (EIRP = 59 dBm), Bounding GAV, 1540 MHz

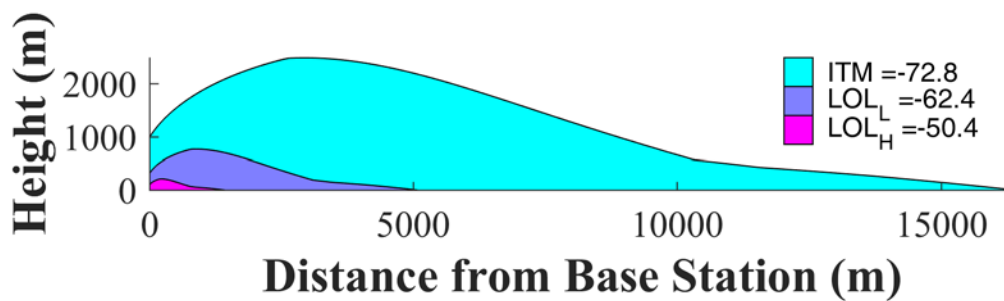


Figure I-10: Macro Urban Base Station (EIRP = 59 dBm), Bounding GAV, 1545 MHz

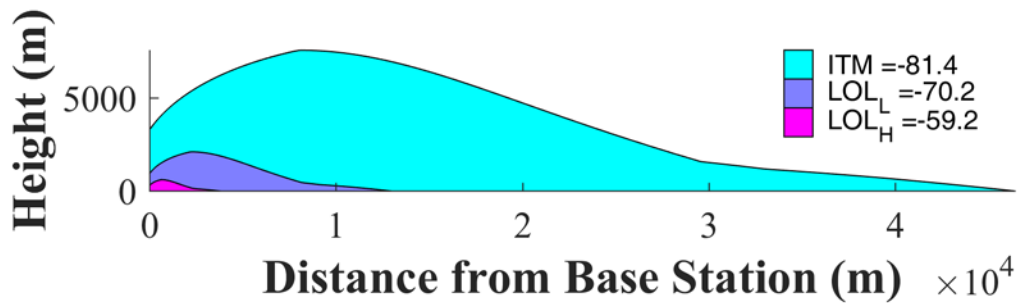
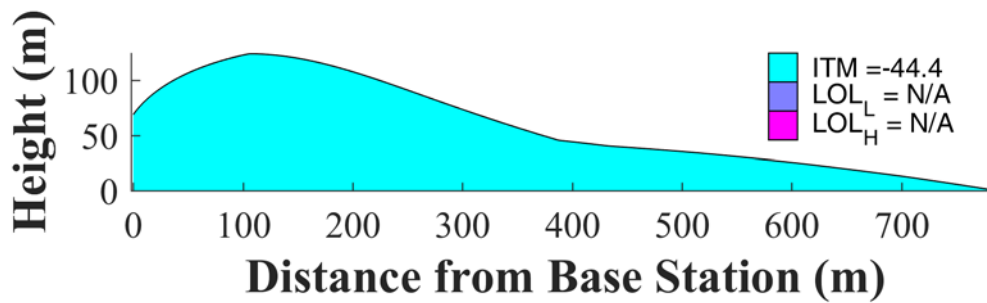


Figure I-11: Macro Urban Base Station (EIRP = 59 dBm), Bounding GAV, 1550 MHz



**Figure I-12: Macro Urban Base Station (EIRP = 59 dBm), Bounding GAV, 1675 MHz**

### I.1.2 GLN

Figure I-13 plots the maximum impacted lateral distance for three types of impact to the most sensitive (bounding) DUT for each frequency: (1) interference results in a 1-dB CNR degradation (blue), (2) interference results in loss of lock on low-elevation angle satellites (red), and (3) interference results in loss of lock for high-elevation angle satellites (orange). Figure I-14 to Figure I-24 show the two-dimensional impacted area regions for tested frequencies from 1475 MHz to 1675 MHz.

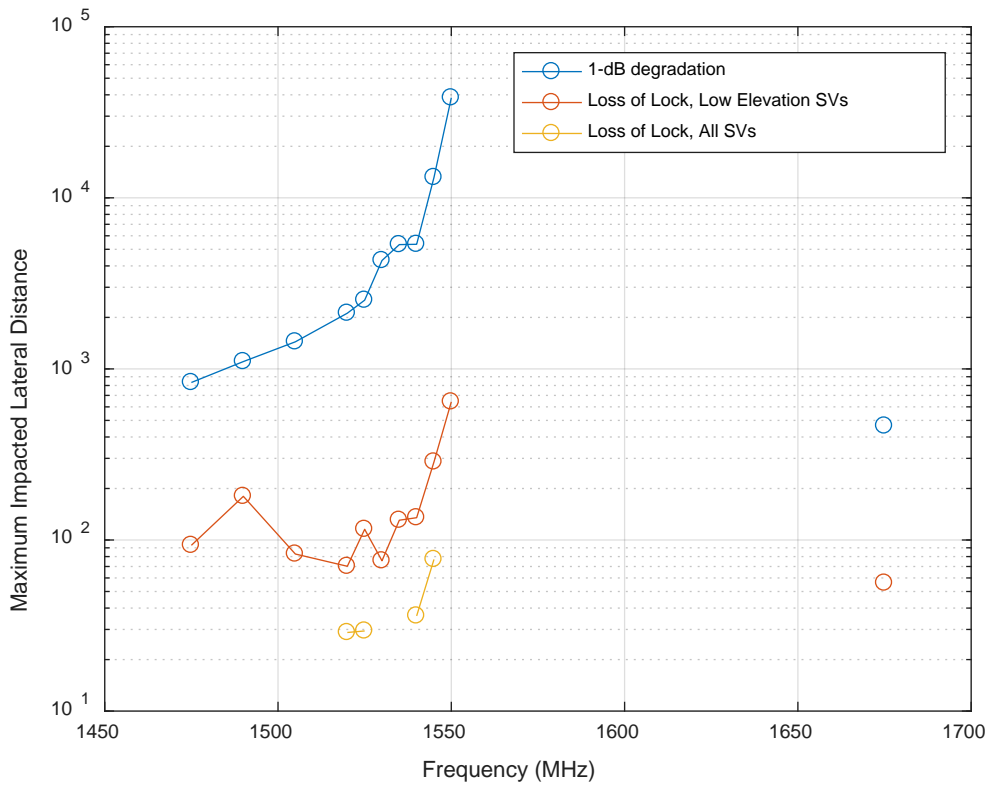


**Figure I-13: Maximum Impacted Lateral Distance for Bounding GLN, Macro Urban Base Station with EIRP of 59 dBm/sector**

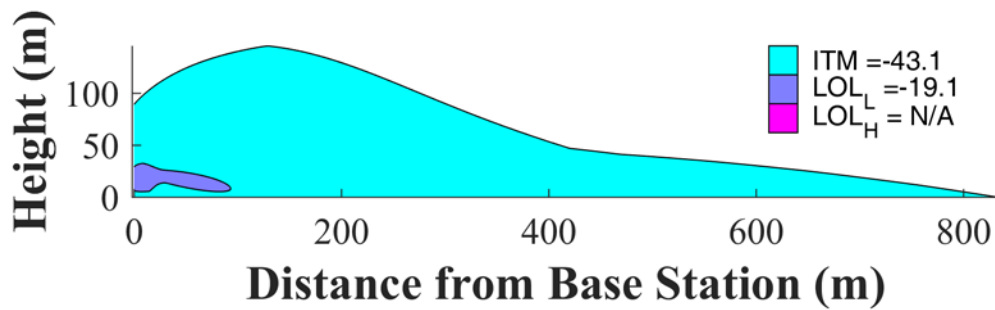


**Figure I-14: Macro Urban Base Station (EIRP = 59 dBm), Bounding GLN, 1475 MHz**

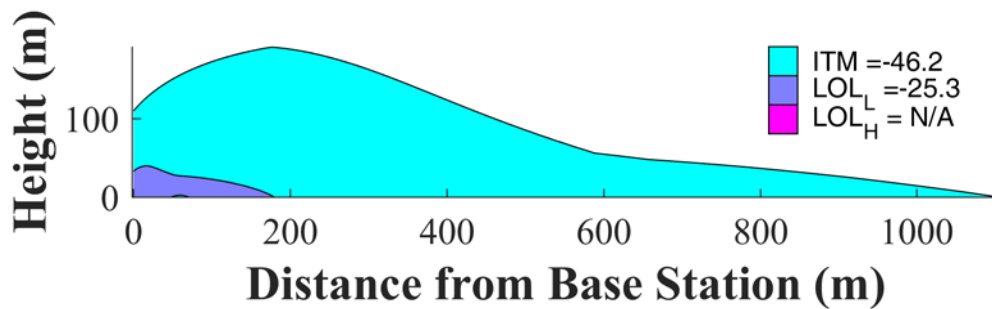


Figure I-15: Macro Urban Base Station (EIRP = 59 dBm), Bounding GLN, 1490 MHz

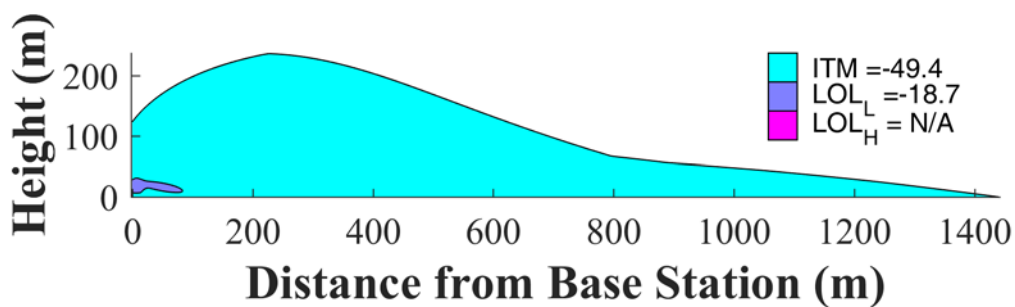


Figure I-16: Macro Urban Base Station (EIRP = 59 dBm), Bounding GLN, 1505 MHz

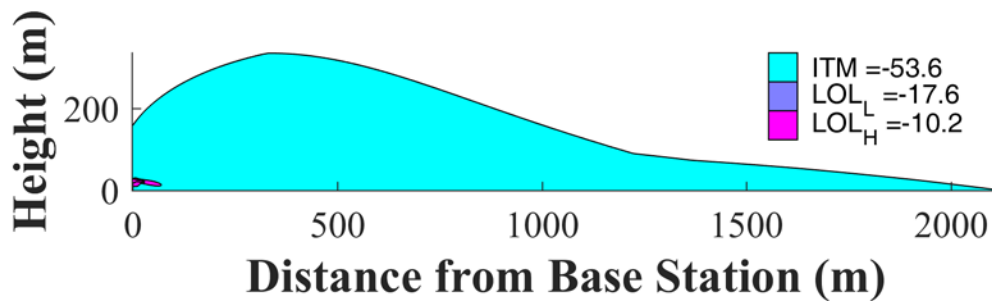


Figure I-17: Macro Urban Base Station (EIRP = 59 dBm), Bounding GLN, 1520 MHz

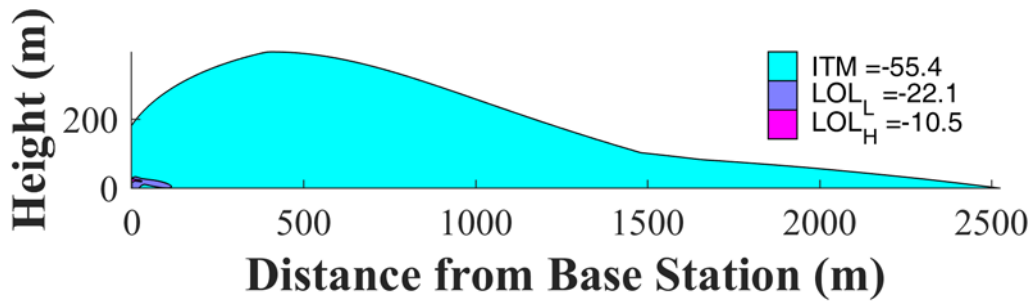


Figure I-18: Macro Urban Base Station (EIRP = 59 dBm), Bounding GLN, 1525 MHz

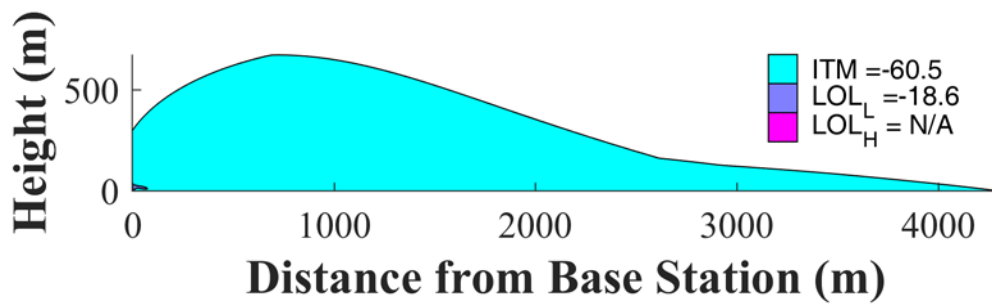


Figure I-19: Macro Urban Base Station (EIRP = 59 dBm), Bounding GLN, 1530 MHz

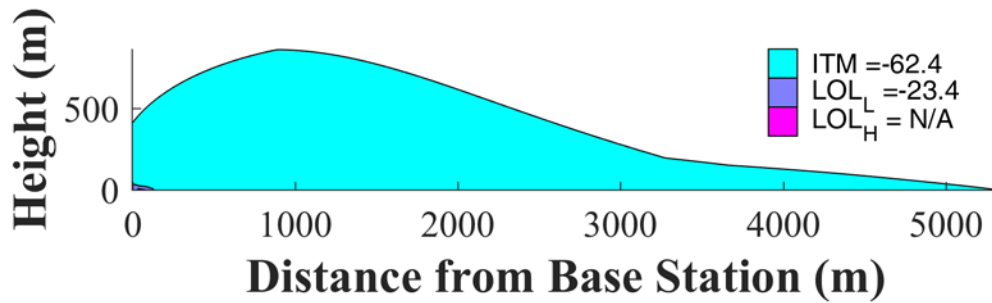


Figure I-20: Macro Urban Base Station (EIRP = 59 dBm), Bounding GLN, 1535 MHz

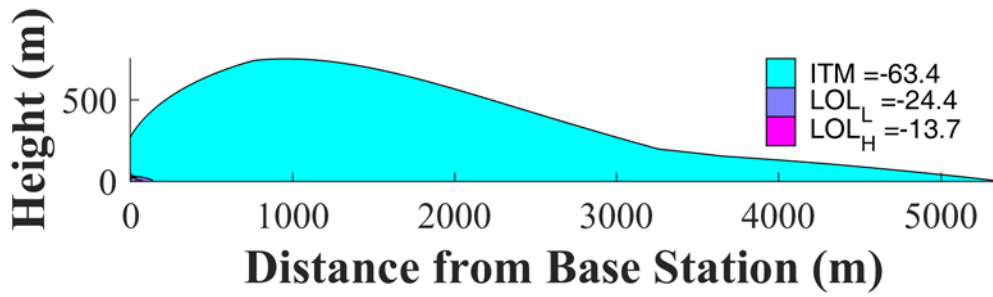


Figure I-21: Macro Urban Base Station (EIRP = 59 dBm), Bounding GLN, 1540 MHz

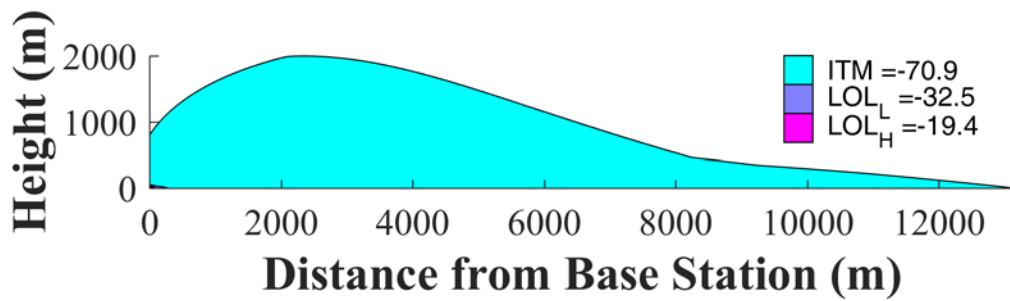


Figure I-22: Macro Urban Base Station (EIRP = 59 dBm), Bounding GLN, 1545 MHz

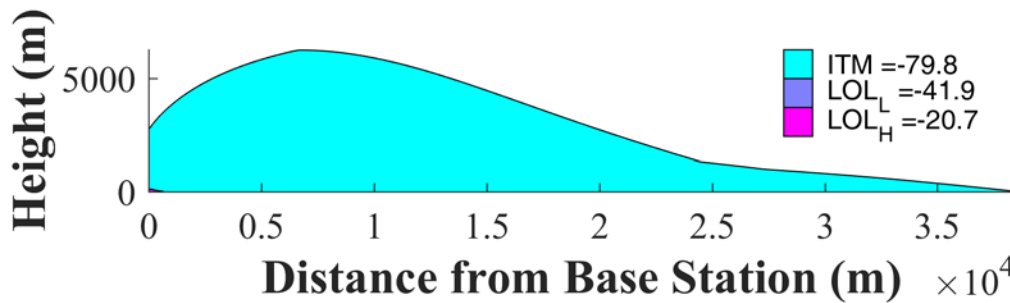
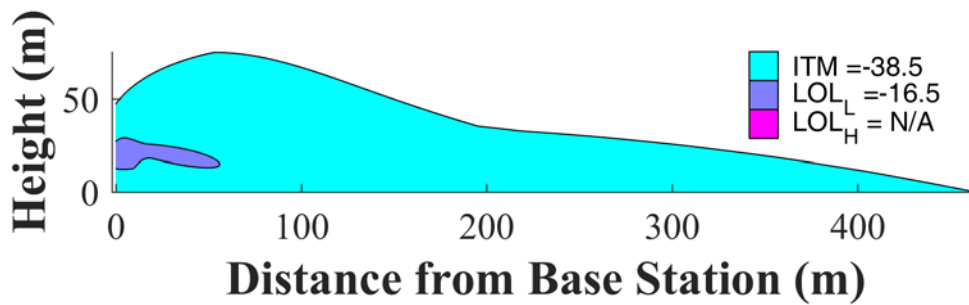


Figure I-23: Macro Urban Base Station (EIRP = 59 dBm), Bounding GLN, 1550 MHz



**Figure I-24: Macro Urban Base Station (EIRP = 59 dBm), Bounding GLN, 1675 MHz**

### I.1.3 HPR

Figure I-25 plots the maximum impacted lateral distance for three types of impact to the most sensitive (bounding) DUT for each frequency: (1) interference results in a 1-dB CNR degradation (blue), (2) interference results in loss of lock on low-elevation angle satellites (red), and (3) interference results in loss of lock for high-elevation angle satellites (orange). Figure I-26 to Figure I-36 show the two-dimensional impacted area regions for tested frequencies from 1475 MHz to 1675 MHz.

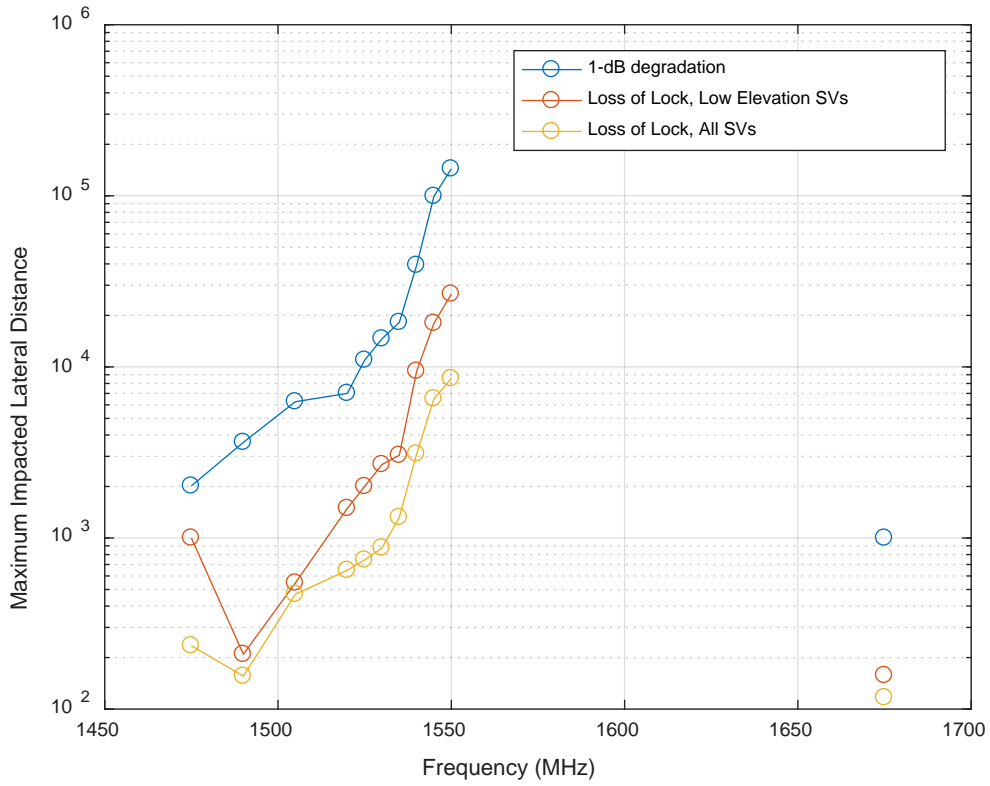


**Figure I-25: Maximum Impacted Lateral Distance for Bounding HPR, Macro Urban Base Station with EIRP of 59 dBm/sector**

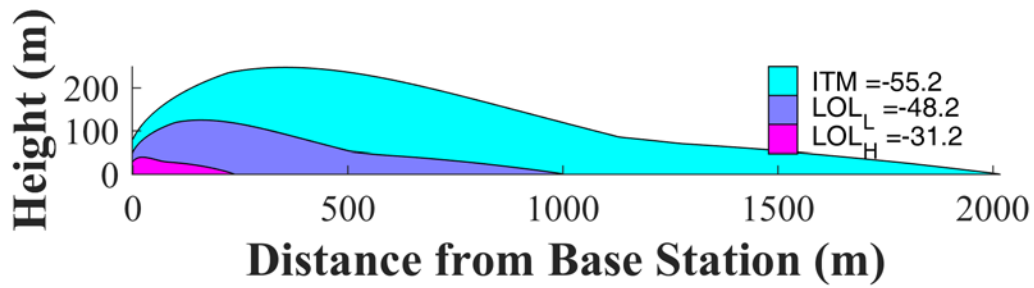


**Figure I-26: Macro Urban Base Station (EIRP = 59 dBm), Bounding HPR, 1475 MHz**



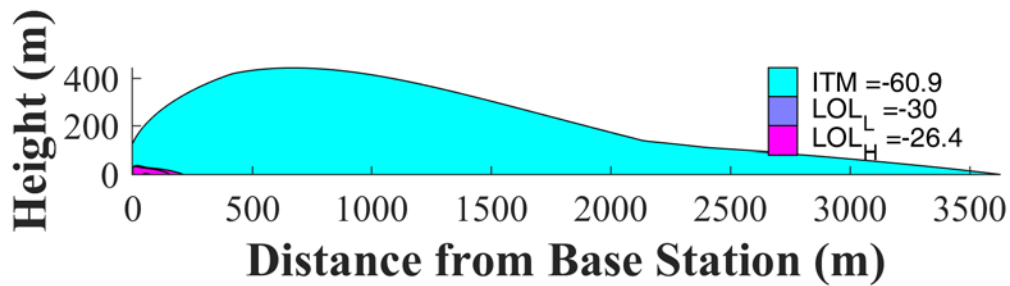


Figure I-27: Macro Urban Base Station (EIRP = 59 dBm), Bounding HPR, 1490 MHz

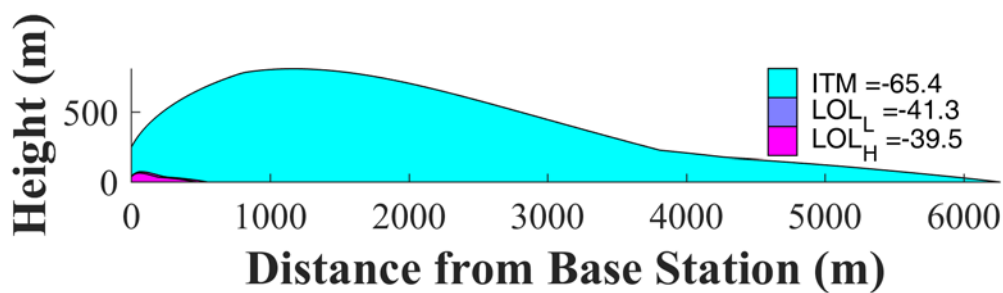


Figure I-28: Macro Urban Base Station (EIRP = 59 dBm), Bounding HPR, 1505 MHz

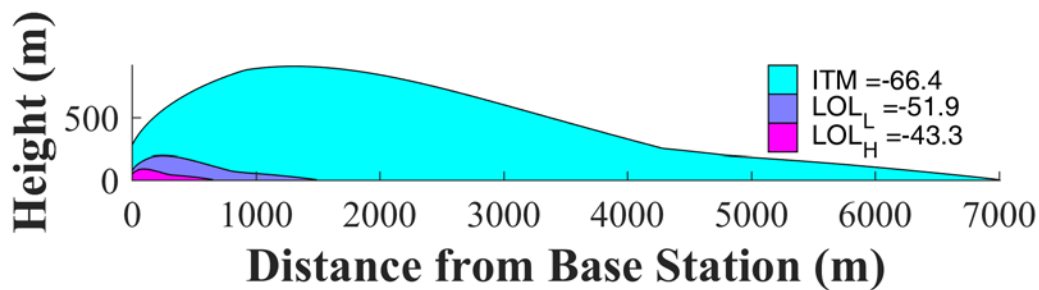


Figure I-29: Macro Urban Base Station (EIRP = 59 dBm), Bounding HPR, 1520 MHz

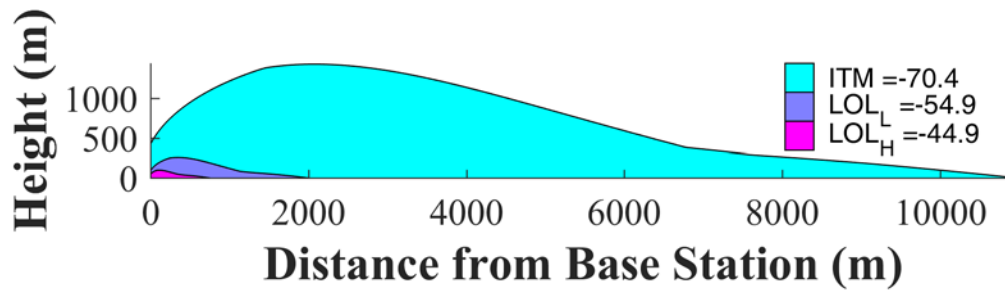


Figure I-30: Macro Urban Base Station (EIRP = 59 dBm), Bounding HPR, 1525 MHz

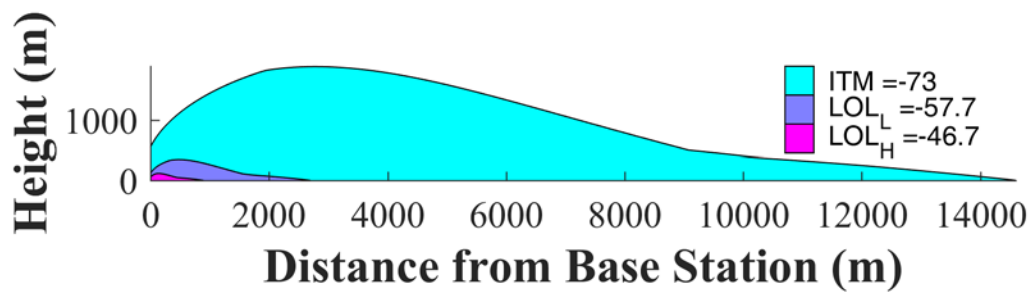


Figure I-31: Macro Urban Base Station (EIRP = 59 dBm), Bounding HPR, 1530 MHz

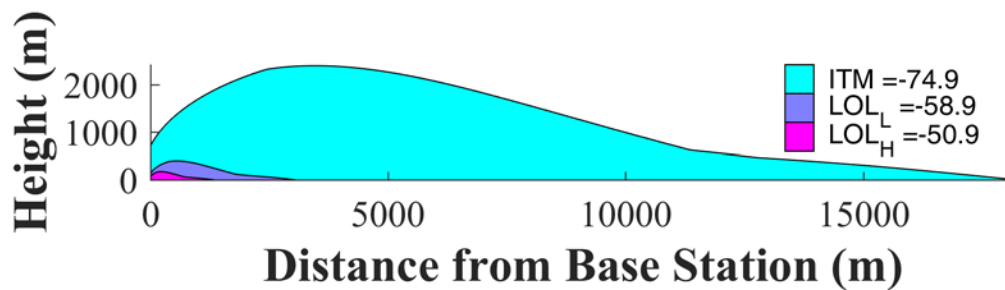


Figure I-32: Macro Urban Base Station (EIRP = 59 dBm), Bounding HPR, 1535 MHz

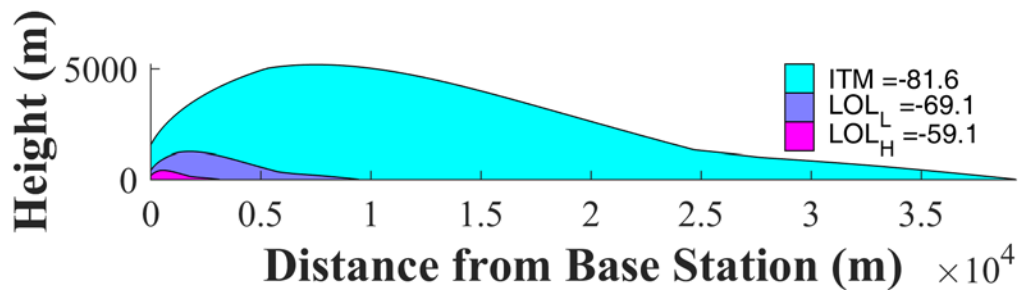


Figure I-33: Macro Urban Base Station (EIRP = 59 dBm), Bounding HPR, 1540 MHz

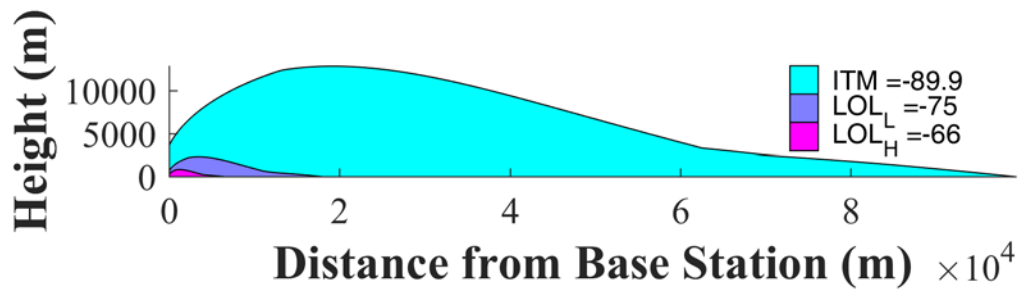


Figure I-34: Macro Urban Base Station (EIRP = 59 dBm), Bounding HPR, 1545 MHz

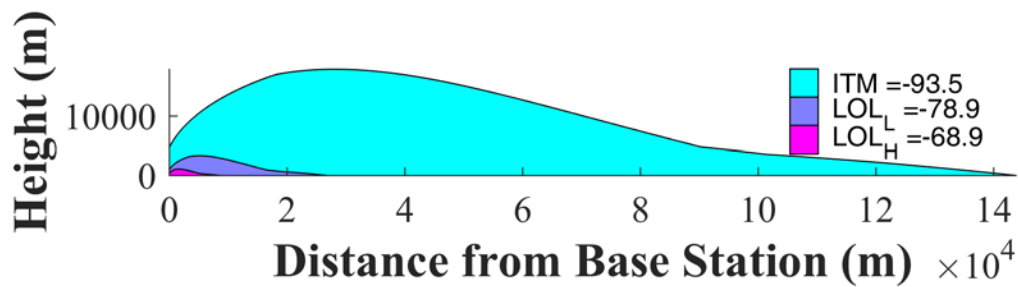
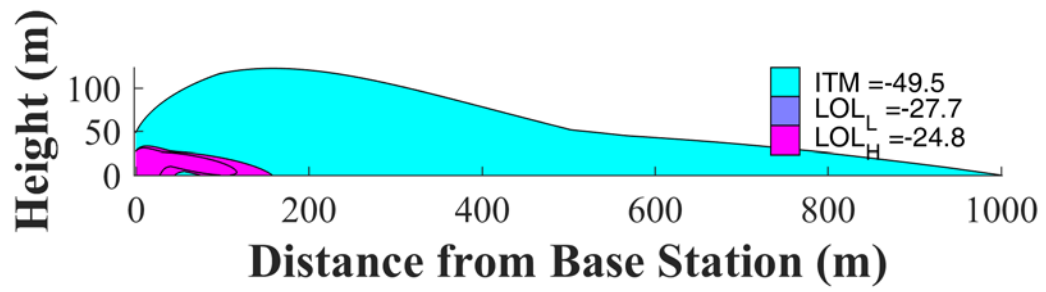


Figure I-35: Macro Urban Base Station (EIRP = 59 dBm), Bounding HPR, 1550 MHz



**Figure I-36: Macro Urban Base Station (EIRP = 59 dBm), Bounding HPR, 1675 MHz**

### I.1.4 TIM

Figure I-37 plots the maximum impacted lateral distance for three types of impact to the most sensitive (bounding) DUT for each frequency: (1) interference results in a 1-dB CNR degradation (blue), (2) interference results in loss of lock on low-elevation angle satellites (red), and (3) interference results in loss of lock for high-elevation angle satellites (orange). Figure I-38 to Figure I-48 show the two-dimensional impacted area regions for tested frequencies from 1475 MHz to 1675 MHz.

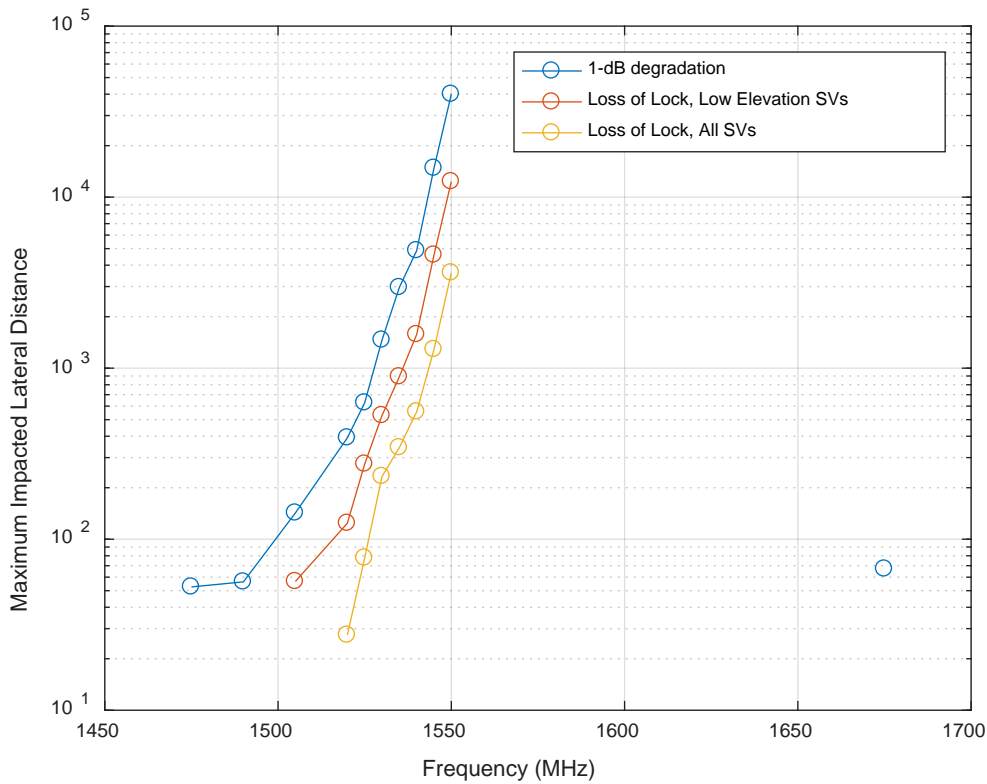


**Figure I-37: Maximum Impacted Lateral Distance for Bounding TIM, Macro Urban Base Station with EIRP of 59 dBm/sector**

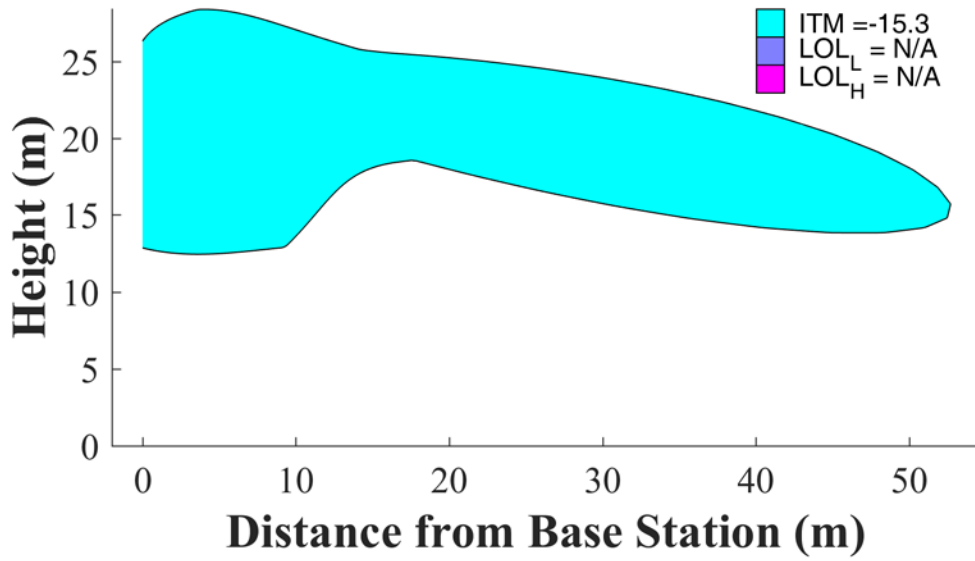


Figure I-38: Macro Urban Base Station (EIRP = 59 dBm), Bounding TIM, 1475 MHz

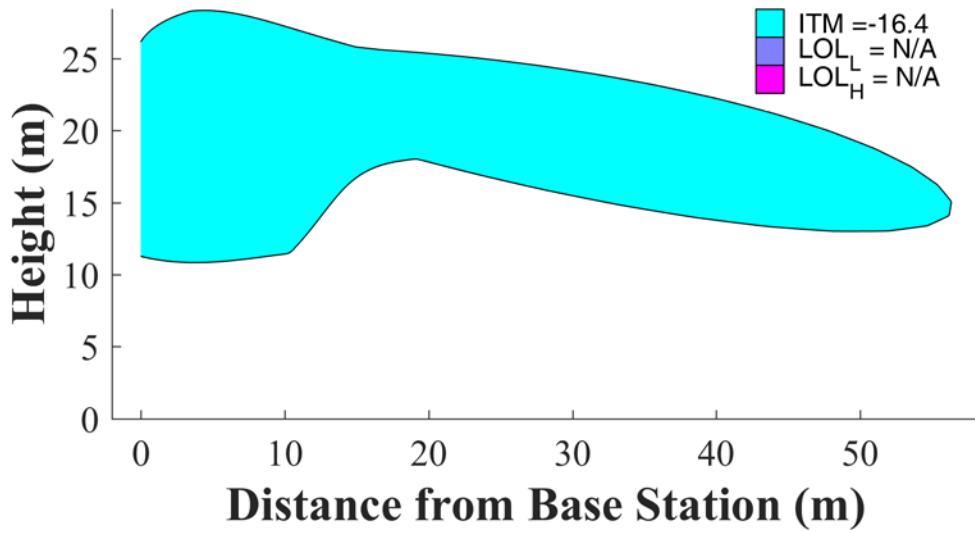


Figure I-39: Macro Urban Base Station (EIRP = 59 dBm), Bounding TIM, 1490 MHz

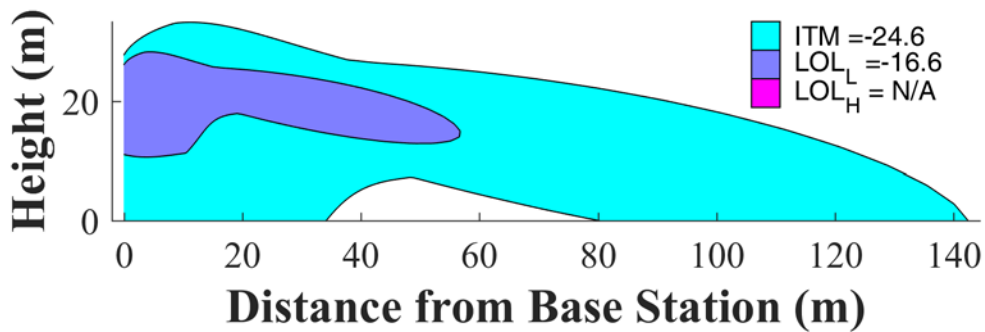


Figure I-40: Macro Urban Base Station (EIRP = 59 dBm), Bounding TIM, 1505 MHz

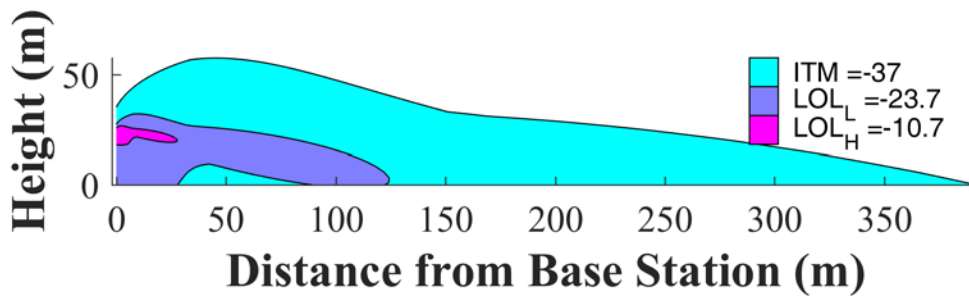


Figure I-41: Macro Urban Base Station (EIRP = 59 dBm), Bounding TIM, 1520 MHz

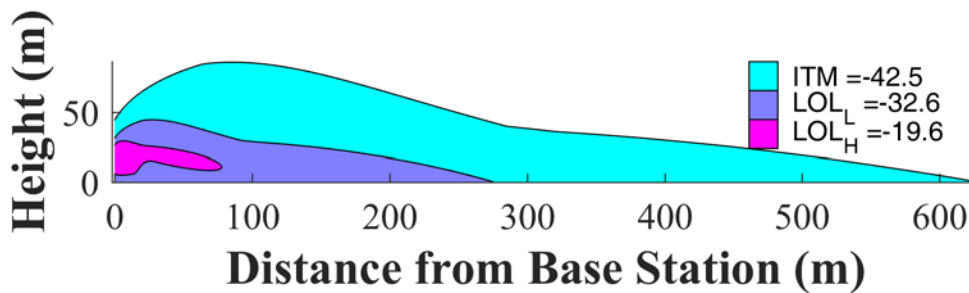


Figure I-42: Macro Urban Base Station (EIRP = 59 dBm), Bounding TIM, 1525 MHz

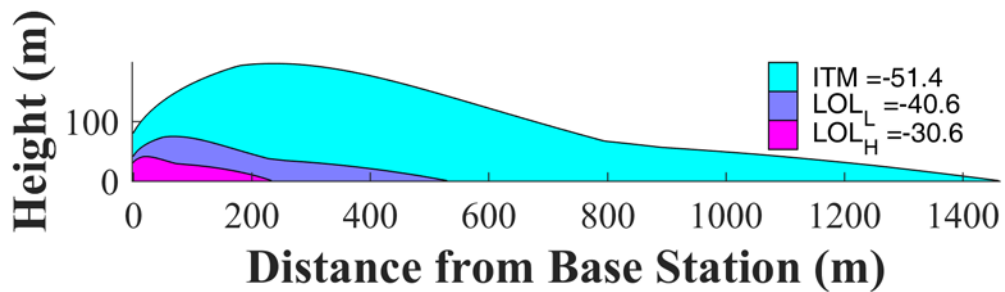


Figure I-43: Macro Urban Base Station (EIRP = 59 dBm), Bounding TIM, 1530 MHz

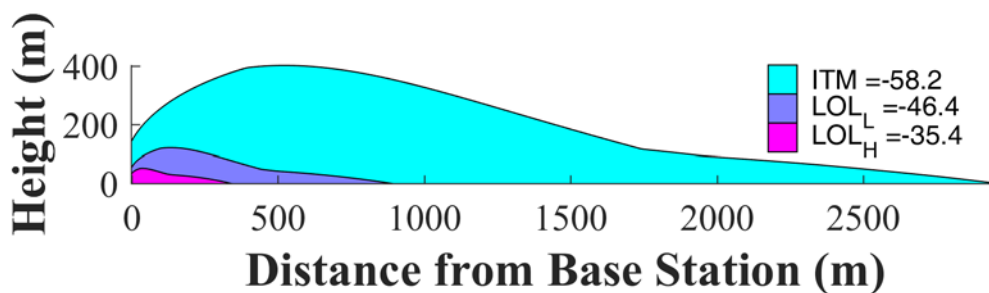


Figure I-44: Macro Urban Base Station (EIRP = 59 dBm), Bounding TIM, 1535 MHz

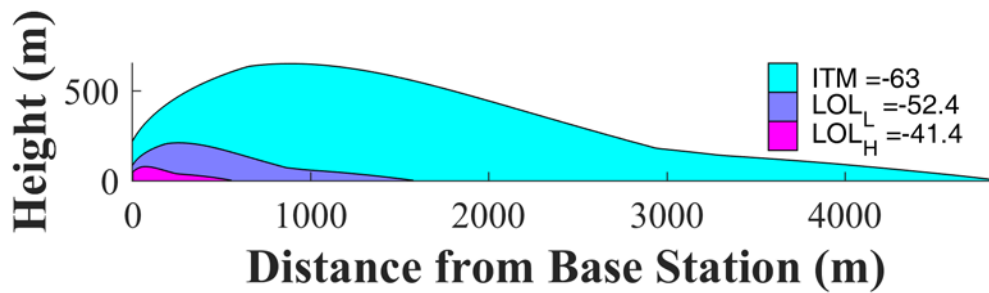


Figure I-45: Macro Urban Base Station (EIRP = 59 dBm), Bounding TIM, 1540 MHz



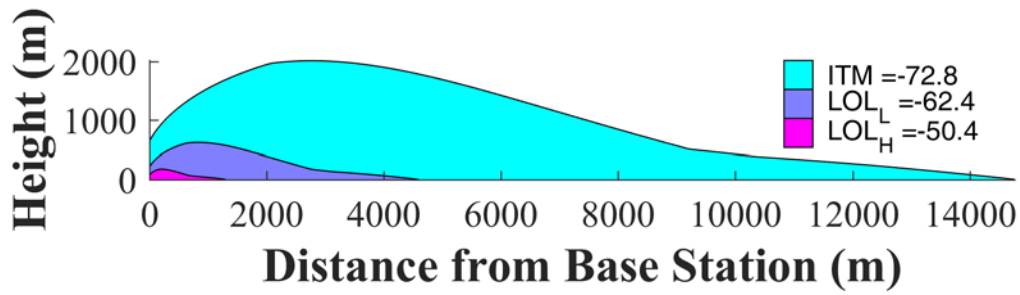


Figure I-46: Macro Urban Base Station (EIRP = 59 dBm), Bounding TIM, 1545 MHz

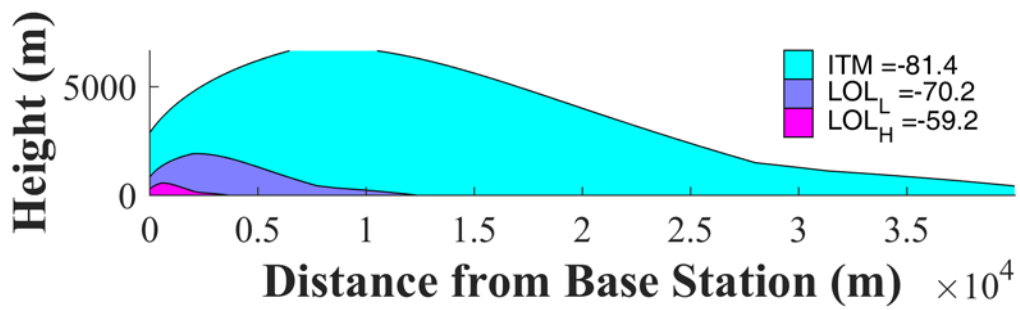


Figure I-47: Macro Urban Base Station (EIRP = 59 dBm), Bounding TIM, 1550 MHz

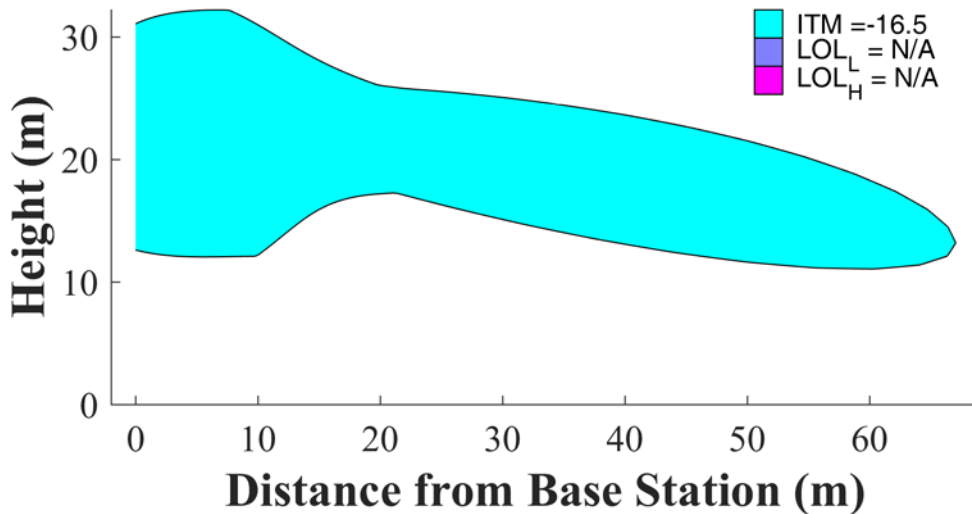


Figure I-48: Macro Urban Base Station (EIRP = 59 dBm), Bounding TIM, 1675 MHz

### I.1.5 CEL

Figure I-49 plots the maximum impacted lateral distance for three types of impact to the most sensitive (bounding) DUT for each frequency: (1) interference results in a 1-dB CNR degradation (blue), (2) interference results in loss of lock on -10 dB satellites<sup>1</sup> (red), and (3) interference results in loss of lock for high-elevation angle satellites (orange). Figure I-50 to Figure I-56 show the two-dimensional impacted area regions for tested frequencies from 1525 MHz to 1675 MHz. (Note that for the other LTE frequencies tested, there was no impact).

---

<sup>1</sup> All of the plots in this Appendix that use the loss-of-lock interference level towards nominally powered satellites are referred to as “all SVs” and towards -10 dB satellites as “low elevation SVs” since a typical DUT antenna exhibited 10 dB less gain towards low elevation angles as compared to its gain at zenith. However, these curves should be interpreted differently for CEL devices since as described in the main body of this report, CEL antennas were modeled as isotropic. The “all SVs” curve can still be interpreted as the interference level that would result in loss of tracking of all satellites, but the “low elevation SVs” curve should be interpreted as the interference level that would result in the device losing lock on satellite signals that are attenuated by 10 dB due, e.g., to line-of-sight blockage.

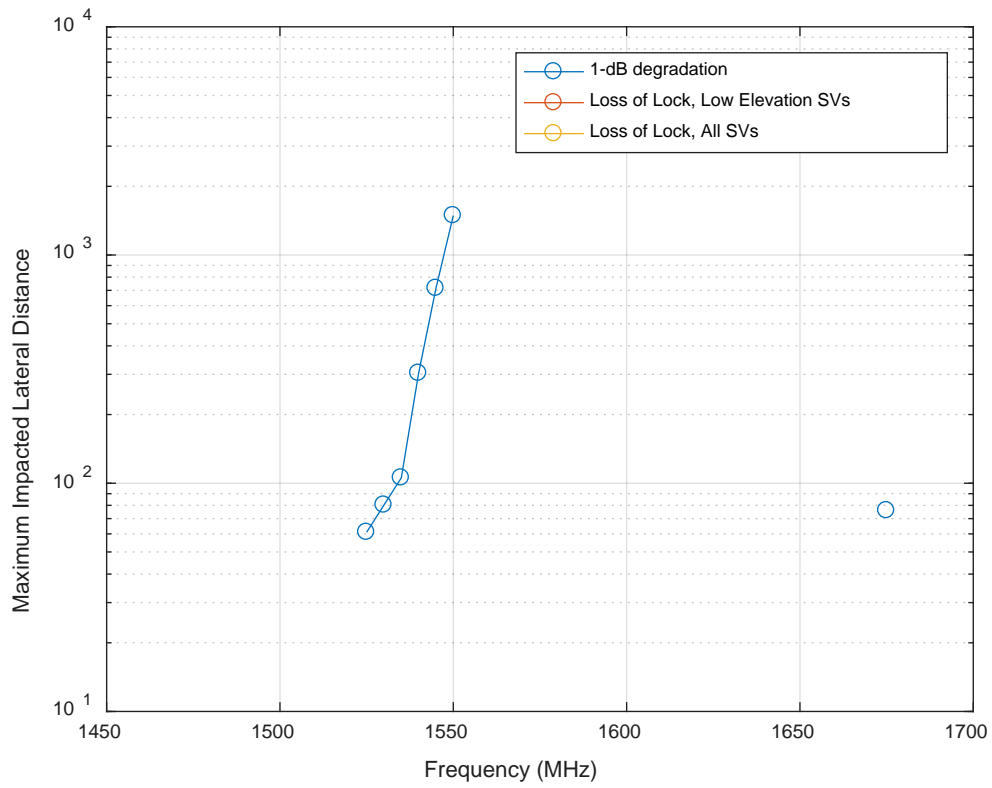


**Figure I-49: Maximum Impacted Lateral Distance for Bounding CEL, Macro Urban Base Station with EIRP of 59 dBm/sector**

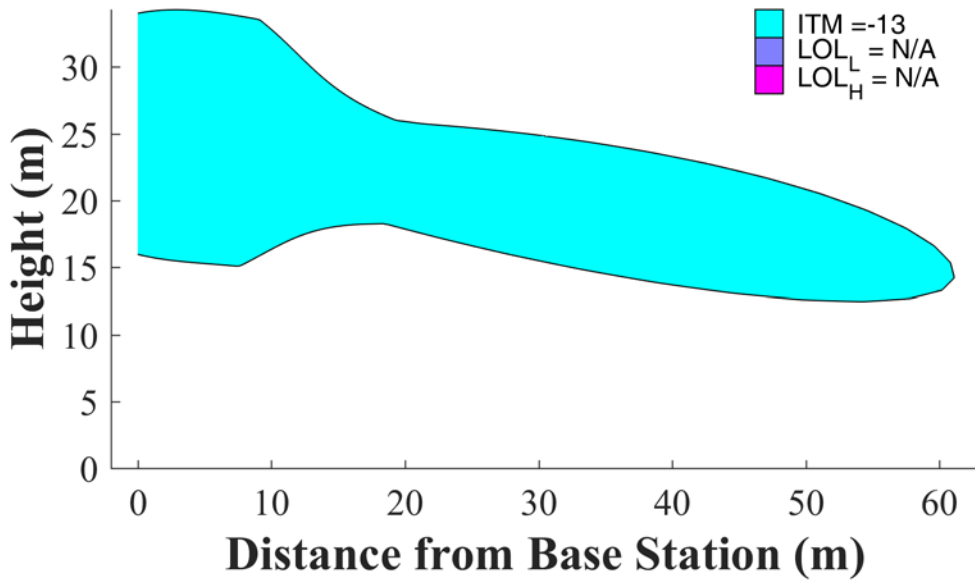


**Figure I-50: Macro Urban Base Station (EIRP = 59 dBm), Bounding CEL, 1525 MHz**

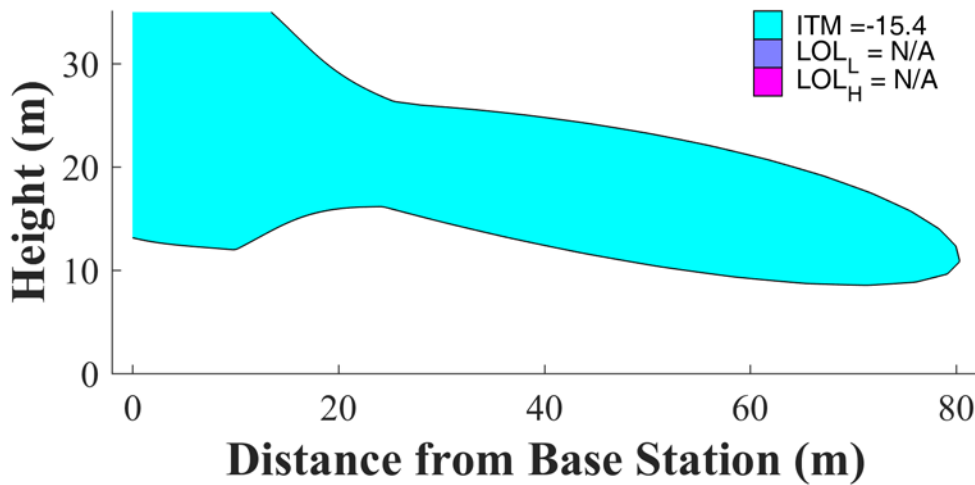


**Figure I-51: Macro Urban Base Station (EIRP = 59 dBm), Bounding CEL, 1530 MHz**

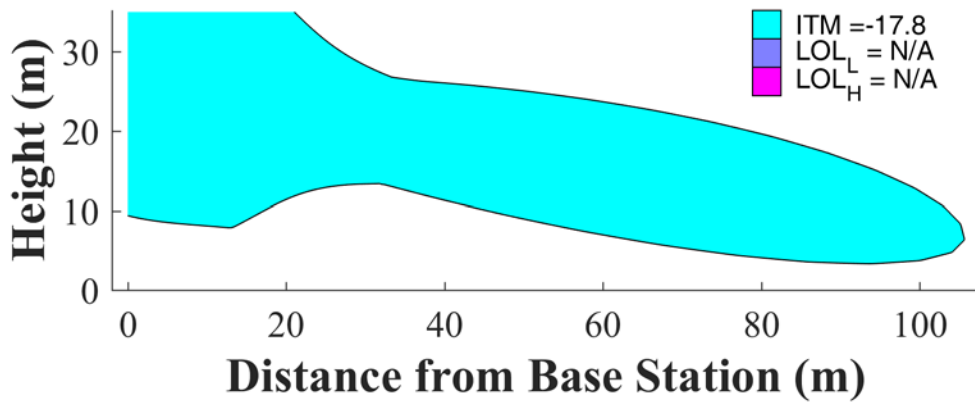


Figure I-52: Macro Urban Base Station (EIRP = 59 dBm), Bounding CEL, 1535 MHz

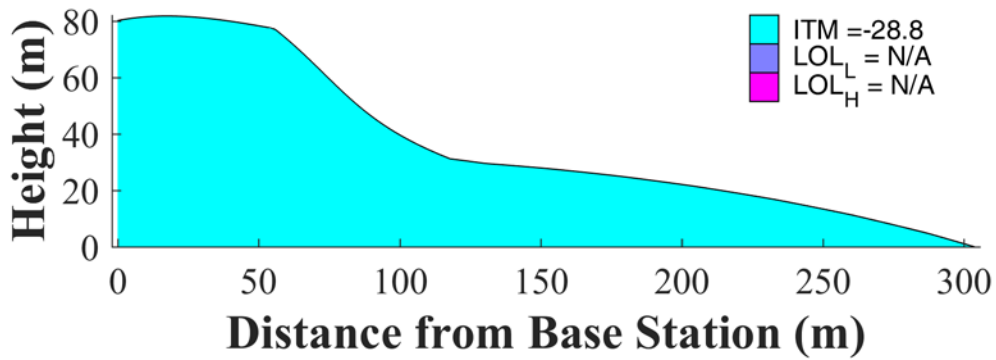


Figure I-53: Macro Urban Base Station (EIRP = 59 dBm), Bounding CEL, 1540 MHz

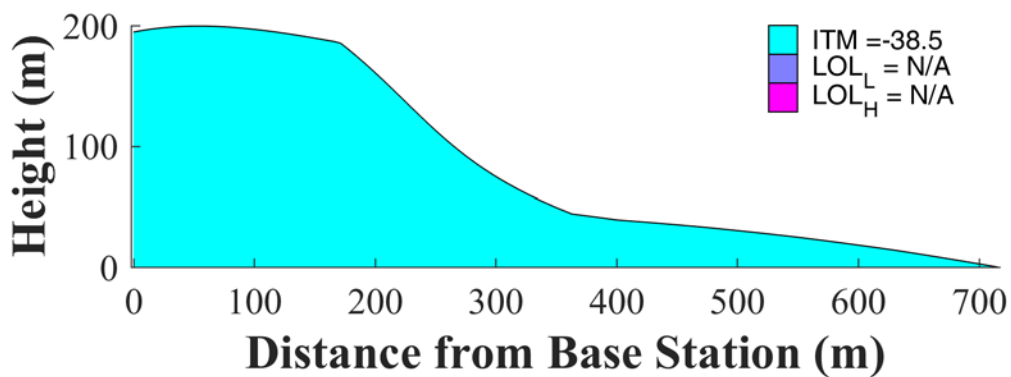
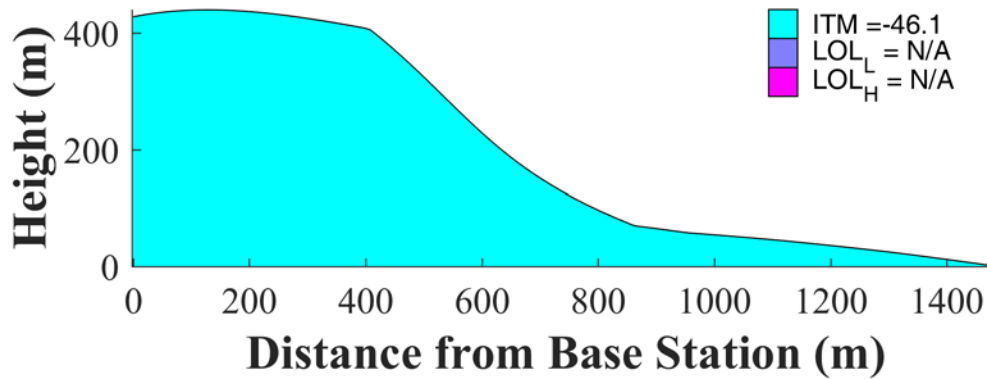
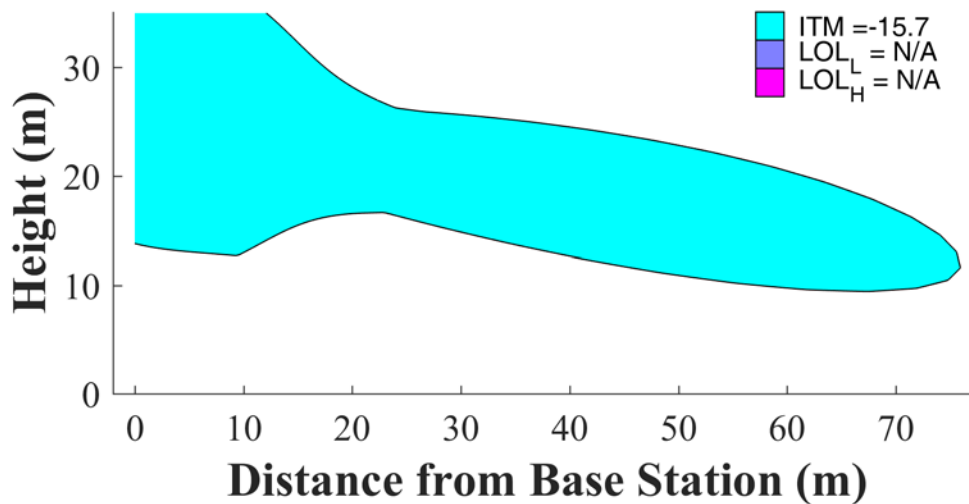


Figure I-54: Macro Urban Base Station (EIRP = 59 dBm), Bounding CEL, 1545 MHz



**Figure I-55: Macro Urban Base Station (EIRP = 59 dBm), Bounding CEL, 1550 MHz**



**Figure I-56: Macro Urban Base Station (EIRP = 59 dBm), Bounding CEL, 1675 MHz**

## **I.2 Small Cell Outdoor/Urban Micro Urban Base Station, GPS C/A-code**

This section presents results for 10-MHz LTE signals broadcast by small cell outdoor/micro urban base stations (one sector with 40 dBm EIRP, 5 dBi antenna at 6 m AGL), free-space propagation, bounding mask.

### **I.2.1 GAV**

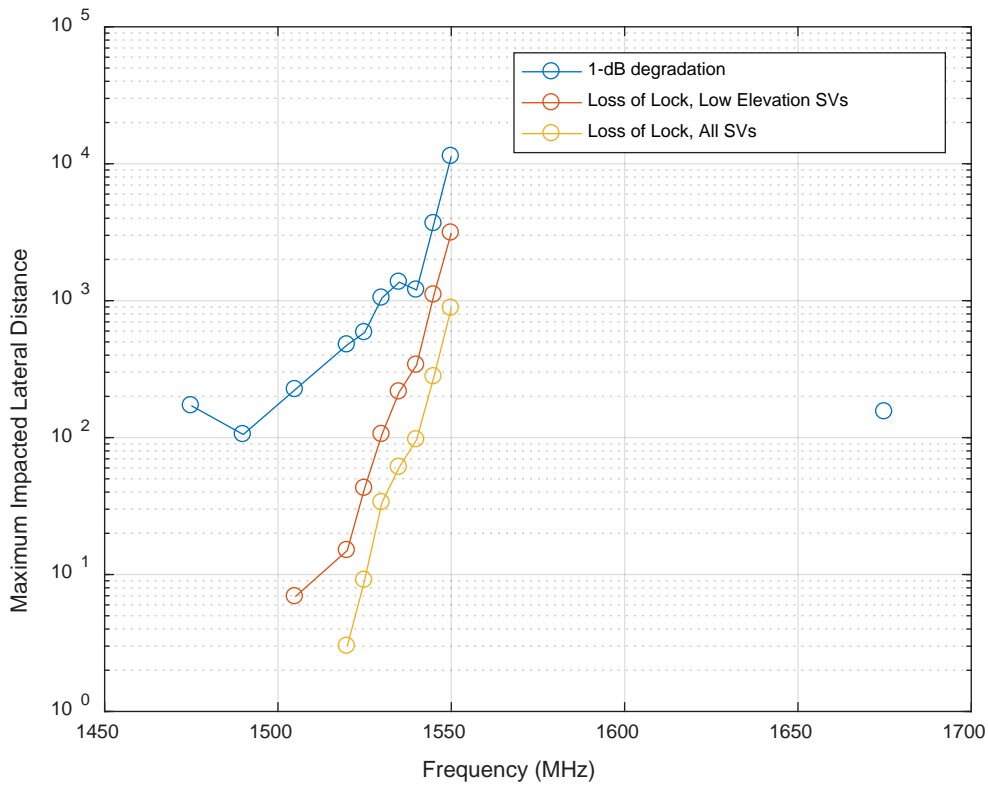


**Figure I-57: Small Cell Outdoor/Micro Urban (EIRP = 40 dBm), Bounding GAV**

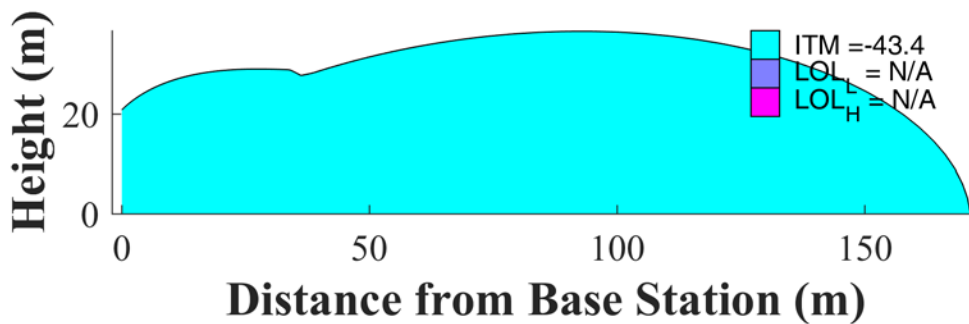


**Figure I-58: Small Cell Outdoor/Micro Urban (EIRP = 40 dBm), Bounding GAV, 1475 MHz**

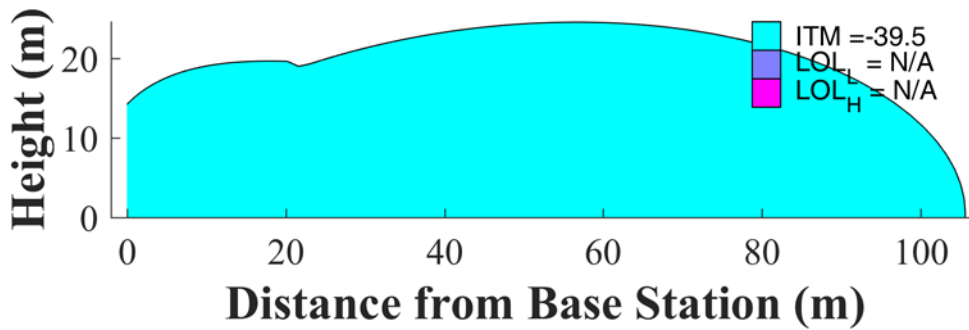


**Figure I-59: Small Cell Outdoor/Micro Urban (EIRP = 40 dBm), Bounding GAV, 1490 MHz**

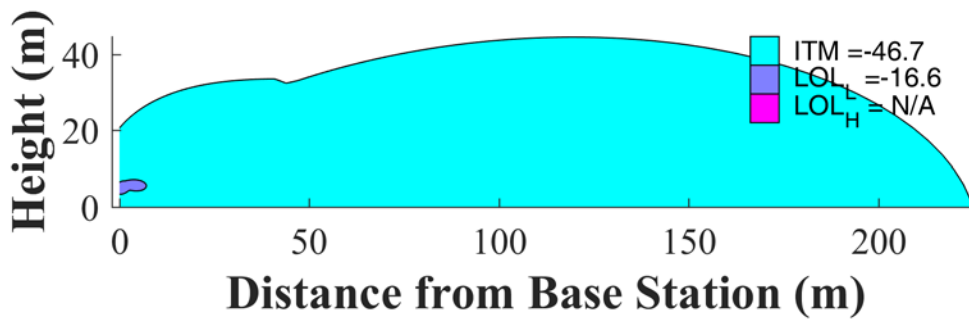


**Figure I-60: Small Cell Outdoor/Micro Urban (EIRP = 40 dBm), Bounding GAV, 1505 MHz**

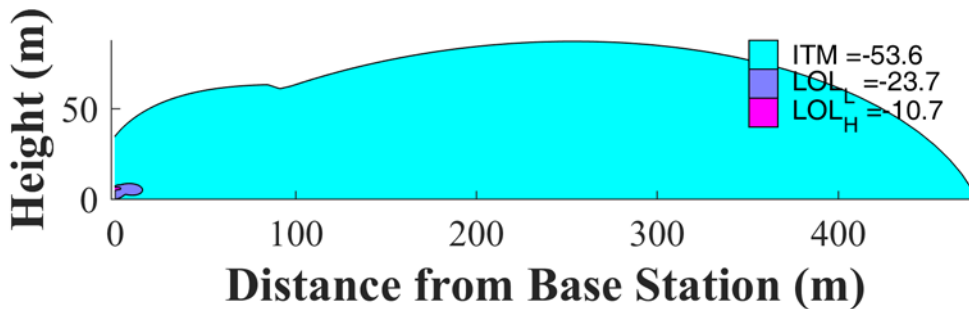


**Figure I-61: Small Cell Outdoor/Micro Urban (EIRP = 40 dBm), Bounding GAV, 1520 MHz**



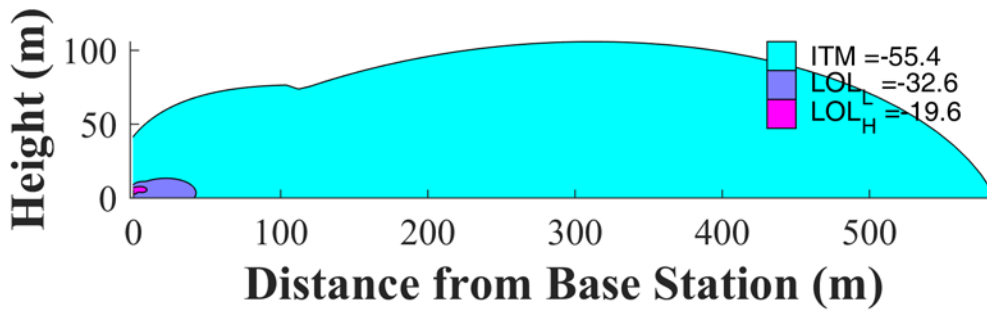


Figure I-62: Small Cell Outdoor/Micro Urban (EIRP = 40 dBm), Bounding GAV, 1525 MHz

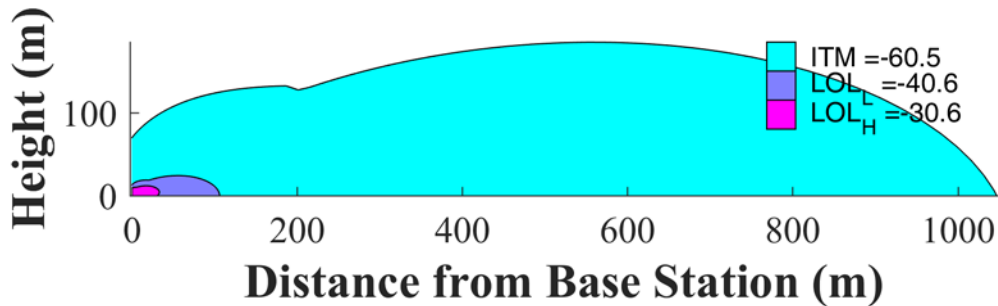


Figure I-63: Small Cell Outdoor/Micro Urban (EIRP = 40 dBm), Bounding GAV, 1530 MHz

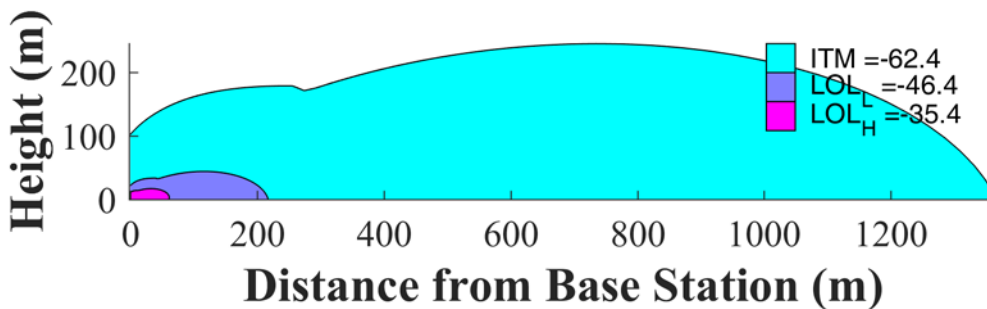
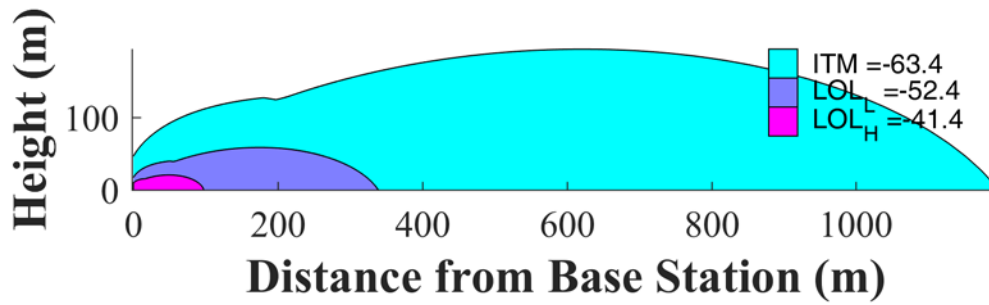
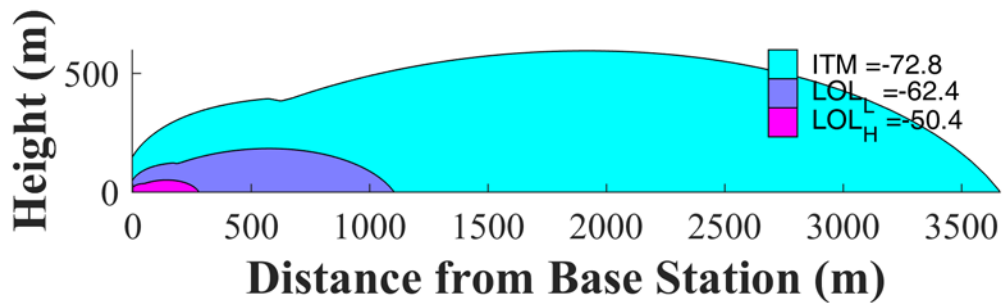


Figure I-64: Small Cell Outdoor/Micro Urban (EIRP = 40 dBm), Bounding GAV, 1535 MHz



**Figure I-65: Small Cell Outdoor/Micro Urban (EIRP = 40 dBm), Bounding GAV, 1540 MHz**



**Figure I-66: Small Cell Outdoor/Micro Urban (EIRP = 40 dBm), Bounding GAV, 1545 MHz**

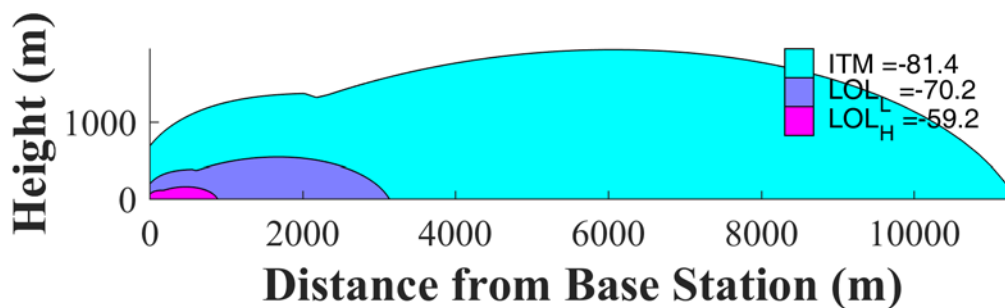


**Figure I-67: Small Cell Outdoor/Micro Urban (EIRP = 40 dBm), Bounding GAV, 1550 MHz**

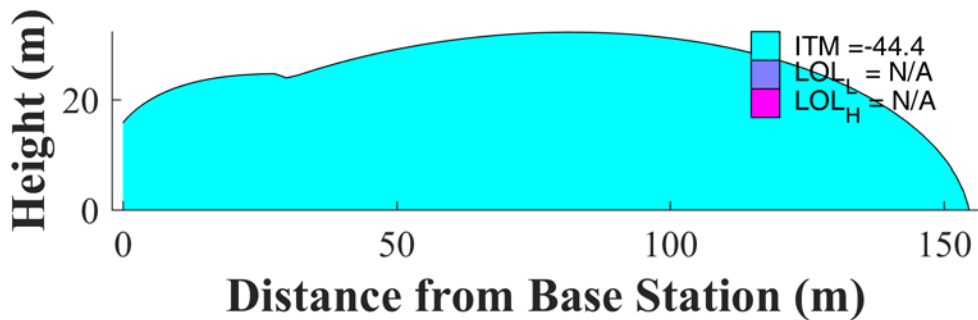


**Figure I-68: Small Cell Outdoor/Micro Urban (EIRP = 40 dBm), Bounding GAV, 1675 MHz**

**I.2.2 GLN**

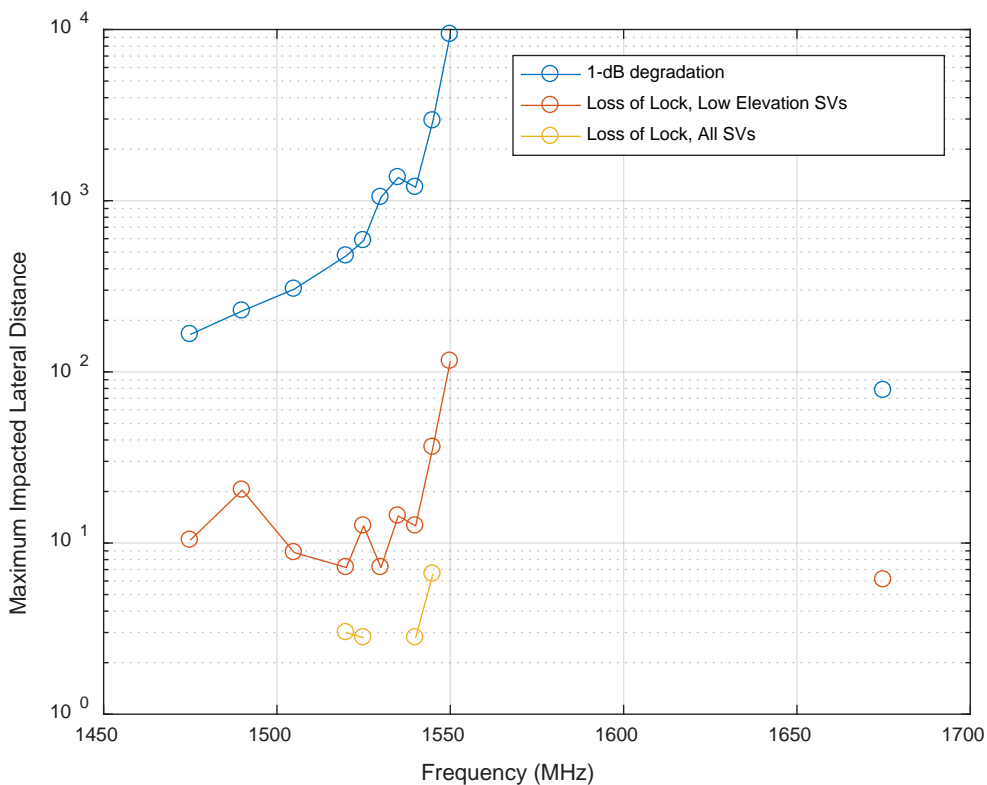


**Figure I-69: Small Cell Outdoor/Micro Urban (EIRP = 40 dBm), Bounding GLN**

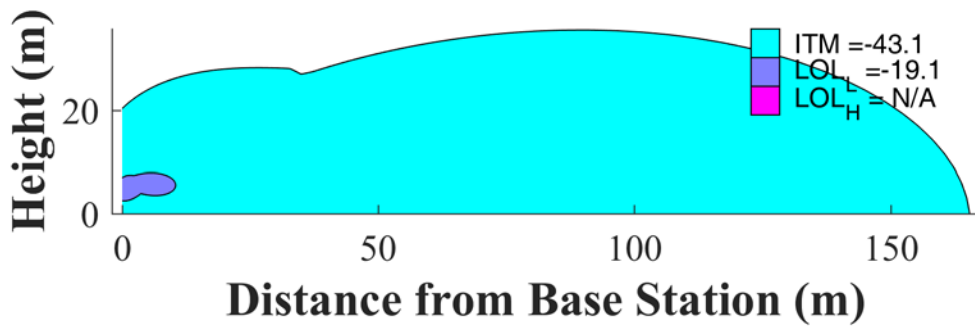


Figure I-70: Small Cell Outdoor/Micro Urban (EIRP = 40 dBm), Bounding GLN, 1475 MHz

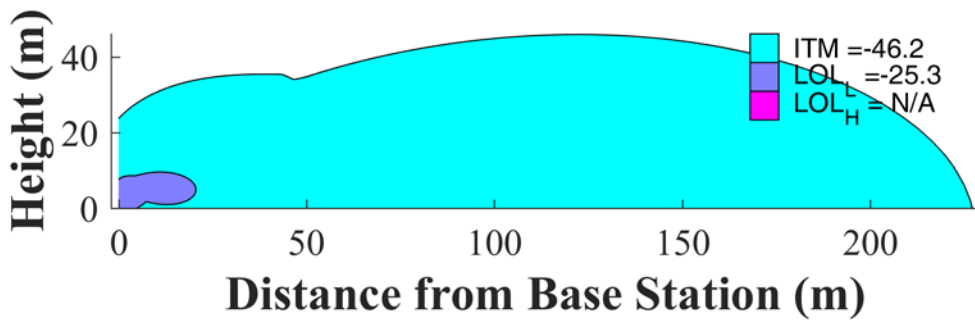


Figure I-71: Small Cell Outdoor/Micro Urban (EIRP = 40 dBm), Bounding GLN, 1490 MHz

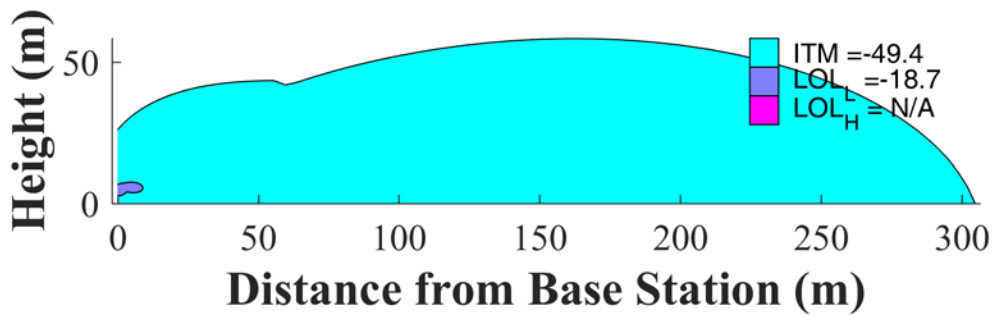


Figure I-72: Small Cell Outdoor/Micro Urban (EIRP = 40 dBm), Bounding GLN, 1505 MHz

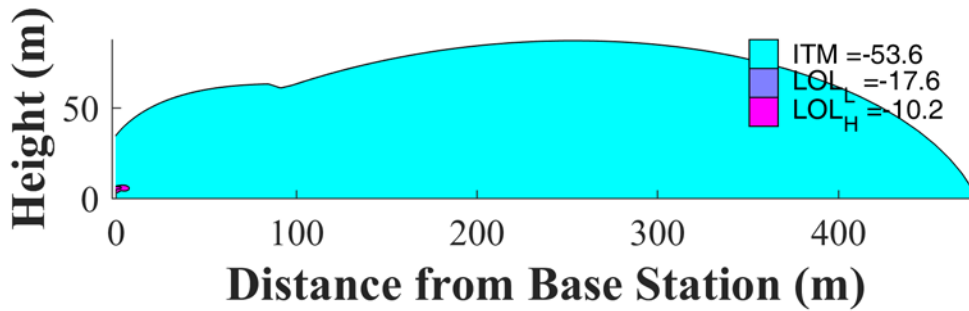


Figure I-73: Small Cell Outdoor/Micro Urban (EIRP = 40 dBm), Bounding GLN, 1520 MHz

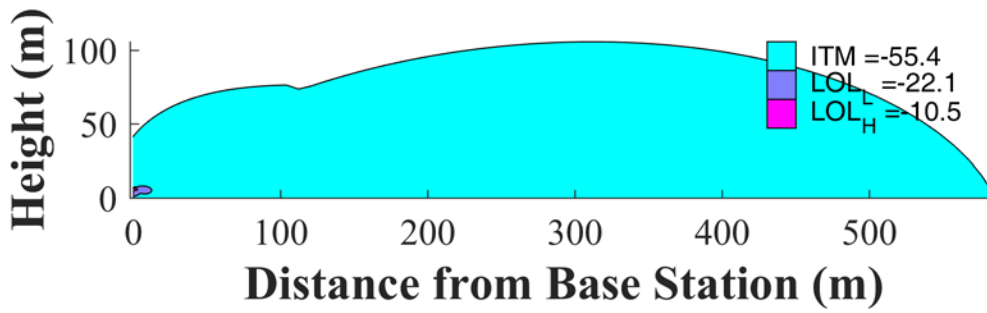


Figure I-74: Small Cell Outdoor/Micro Urban (EIRP = 40 dBm), Bounding GLN, 1525 MHz

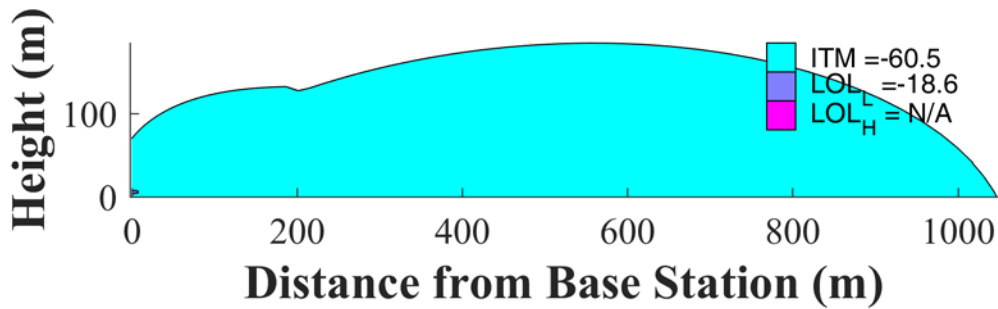
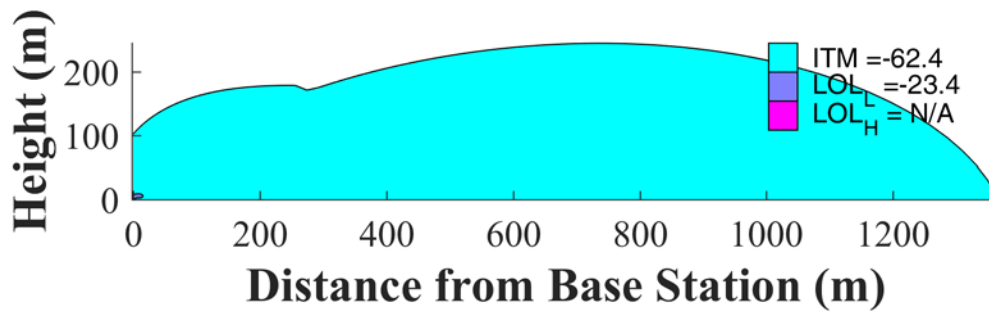
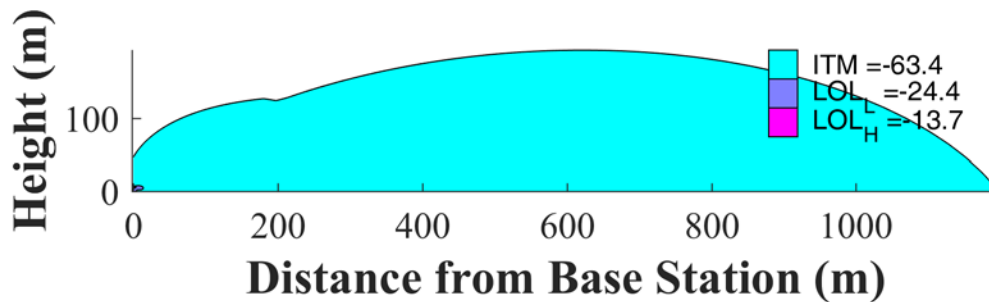


Figure I-75: Small Cell Outdoor/Micro Urban (EIRP = 40 dBm), Bounding GLN, 1530 MHz



**Figure I-76: Small Cell Outdoor/Micro Urban (EIRP = 40 dBm), Bounding GLN, 1535 MHz**



**Figure I-77: Small Cell Outdoor/Micro Urban (EIRP = 40 dBm), Bounding GLN, 1540 MHz**

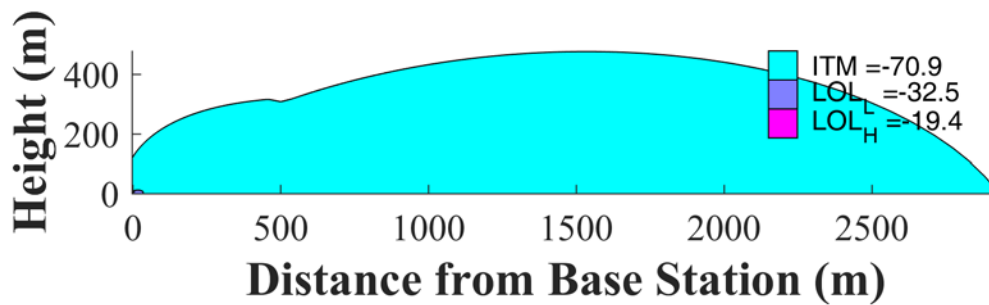


**Figure I-78: Small Cell Outdoor/Micro Urban (EIRP = 40 dBm), Bounding GLN, 1545 MHz**

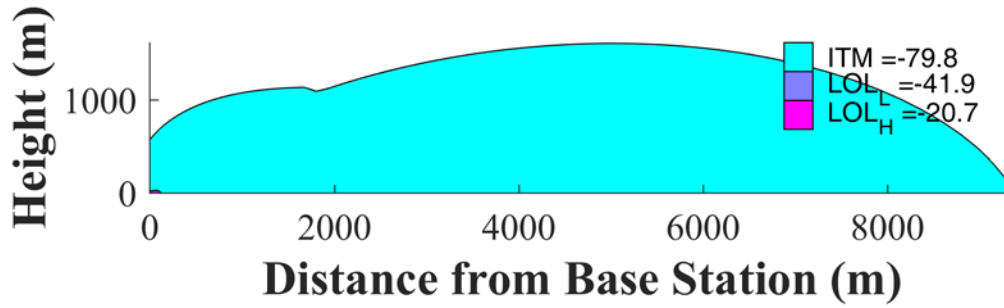


**Figure I-79: Small Cell Outdoor/Micro Urban (EIRP = 40 dBm), Bounding GLN, 1550 MHz**

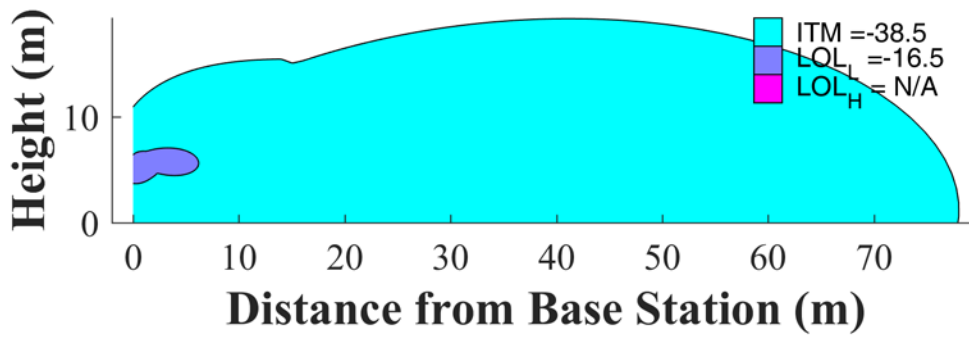


**Figure I-80: Small Cell Outdoor/Micro Urban (EIRP = 40 dBm), Bounding GLN, 1675 MHz**

### I.2.3 HPR

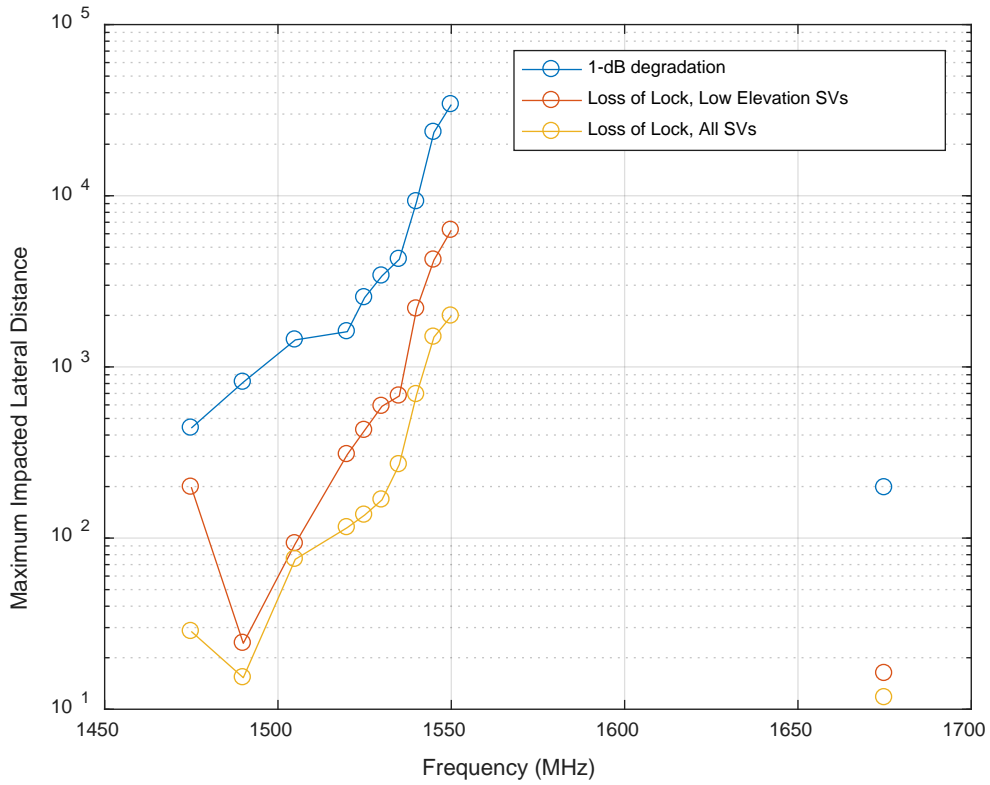


**Figure I-81: Small Cell Outdoor/Micro Urban, Bounding HPR**

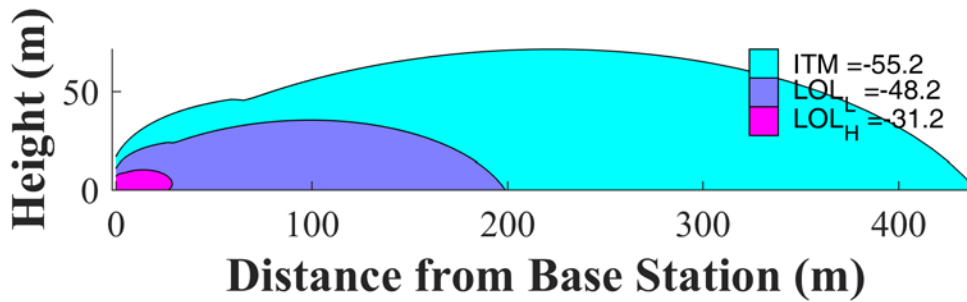


**Figure I-82: Small Cell Outdoor/Micro Urban (EIRP = 40 dBm), Bounding HPR, 1475 MHz**



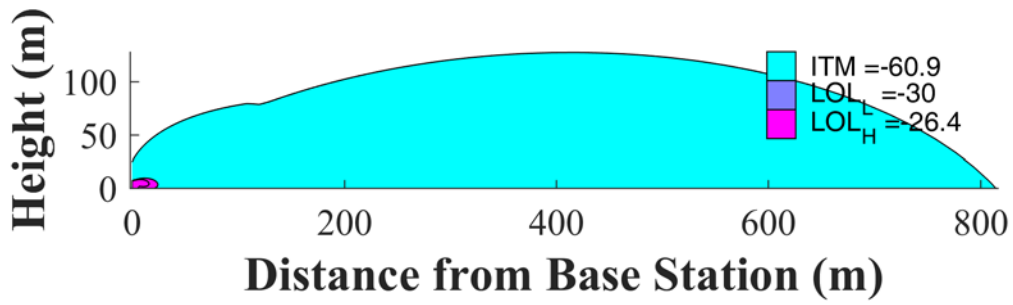


**Figure I-83: Small Cell Outdoor/Micro Urban (EIRP = 40 dBm), Bounding HPR, 1490 MHz**

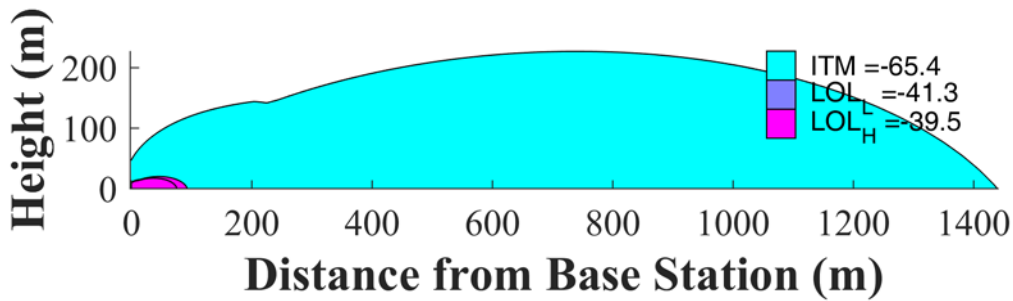


**Figure I-84: Small Cell Outdoor/Micro Urban (EIRP = 40 dBm), Bounding HPR, 1505 MHz**

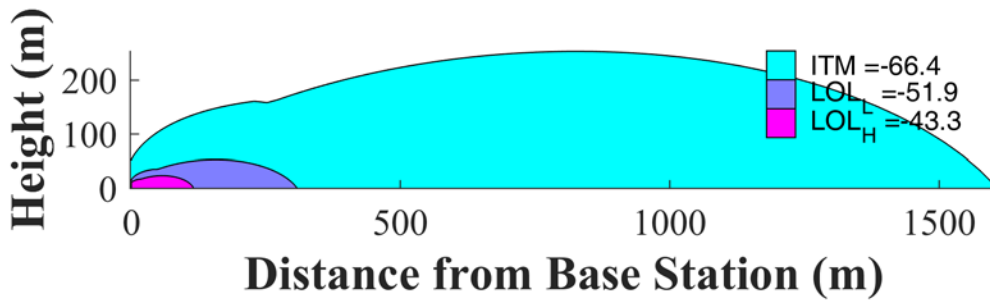


**Figure I-85: Small Cell Outdoor/Micro Urban (EIRP = 40 dBm), Bounding HPR, 1520 MHz**

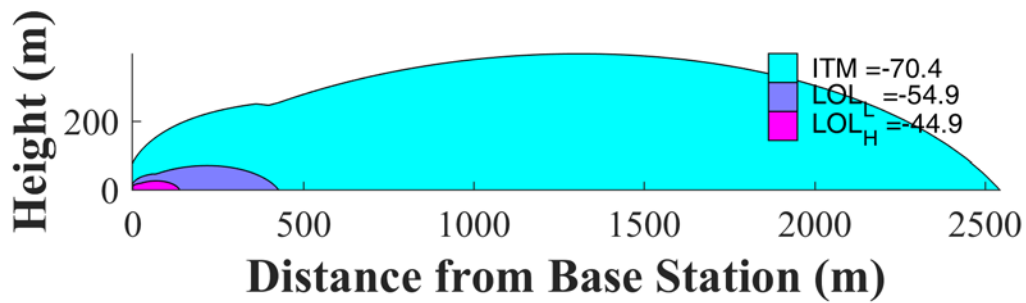


**Figure I-86: Small Cell Outdoor/Micro Urban (EIRP = 40 dBm),  
Bounding HPR, 1525 MHz**

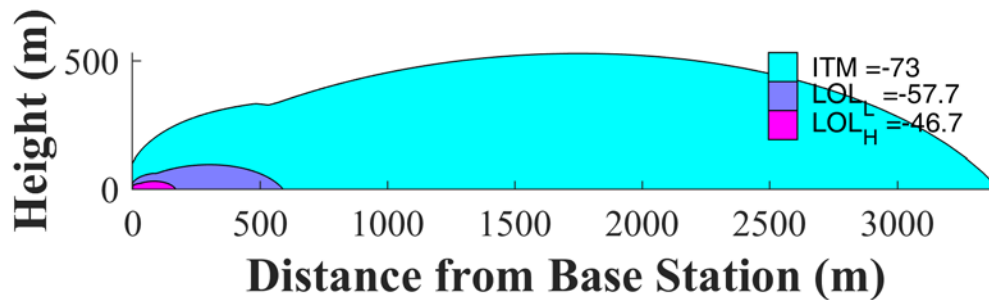


**Figure I-87: Small Cell Outdoor/Micro Urban (EIRP = 40 dBm),  
Bounding HPR, 1530 MHz**

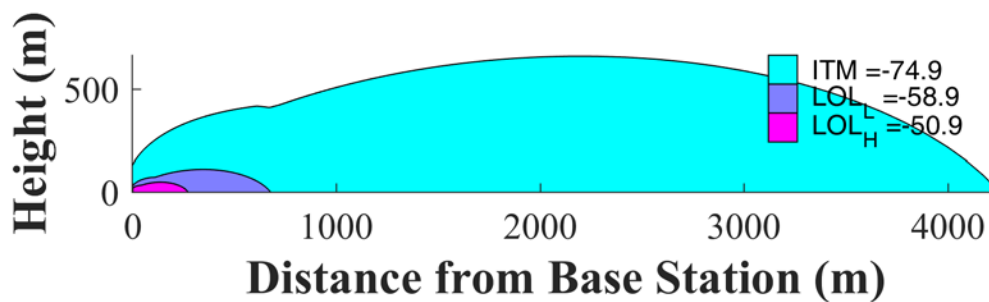


**Figure I-88: Small Cell Outdoor/Micro Urban (EIRP = 40 dBm),  
Bounding HPR, 1535 MHz**

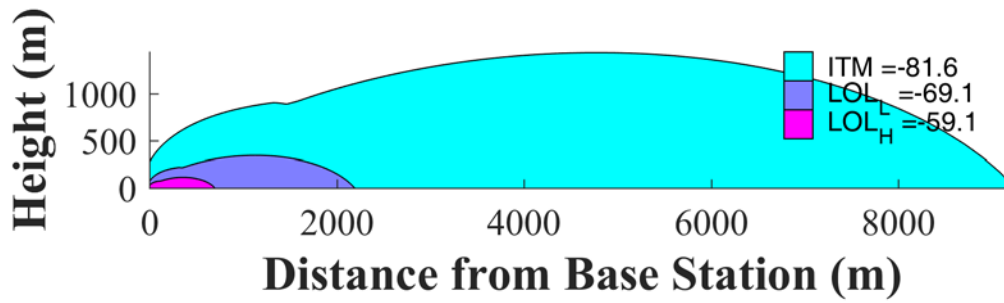


**Figure I-89: Small Cell Outdoor/Micro Urban (EIRP = 40 dBm), Bounding HPR, 1540 MHz**

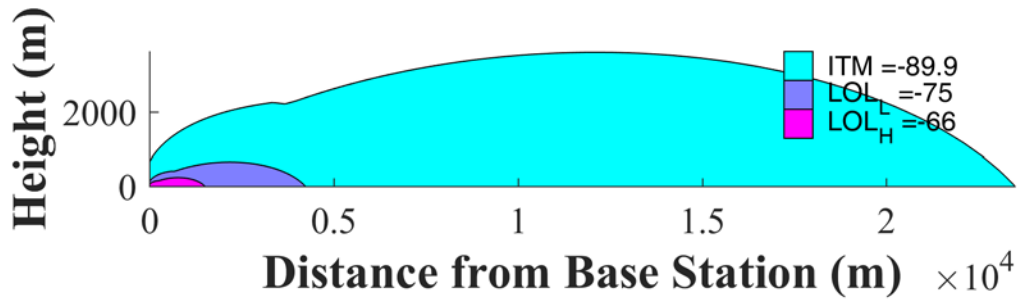


**Figure I-90: Small Cell Outdoor/Micro Urban (EIRP = 40 dBm), Bounding HPR, 1545 MHz**

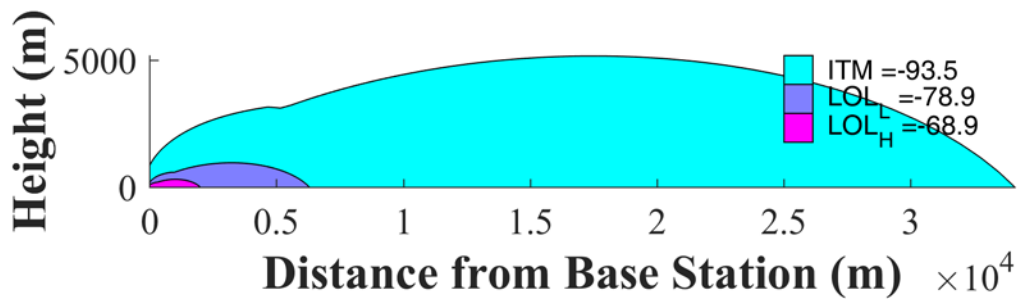


**Figure I-91: Small Cell Outdoor/Micro Urban (EIRP = 40 dBm), Bounding HPR, 1550 MHz**

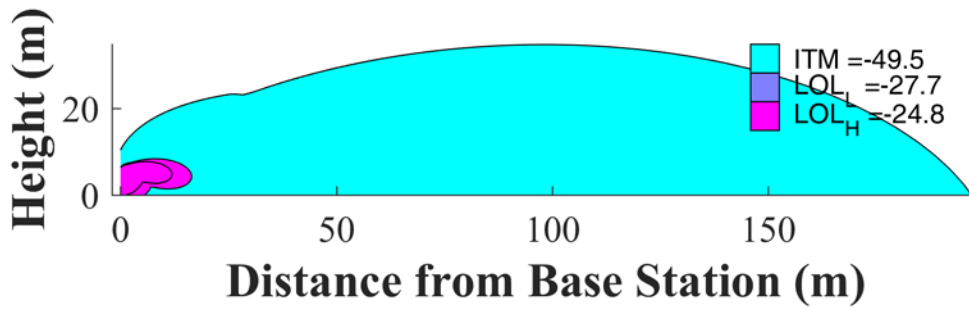


**Figure I-92: Small Cell Outdoor/Micro Urban (EIRP = 40 dBm), Bounding HPR, 1675 MHz**

#### I.2.4 TIM

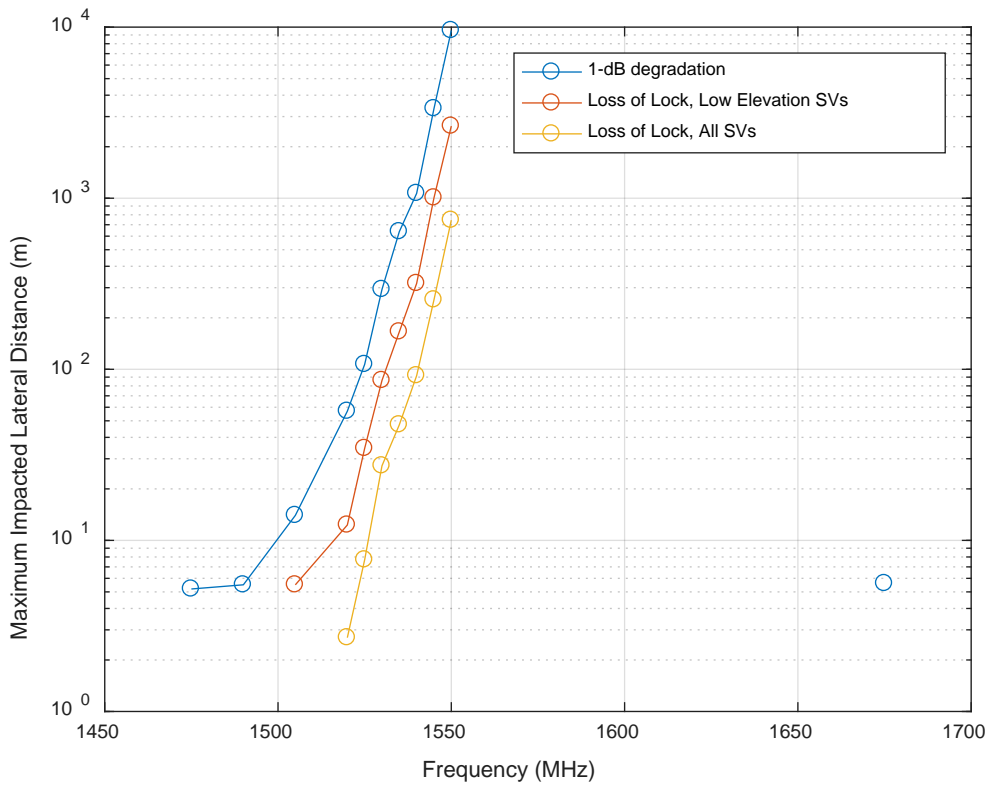


**Figure I-93: Small Cell Outdoor/Micro Urban (EIRP = 40 dBm), Bounding TIM**

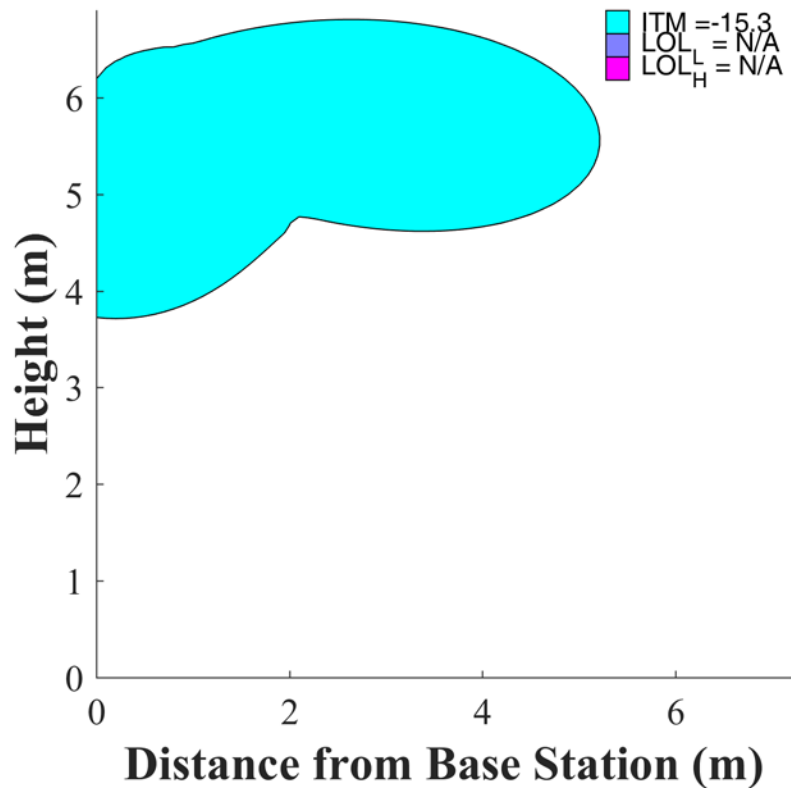


**Figure I-94: Small Cell Outdoor/Micro Urban (EIRP = 40 dBm),  
Bounding TIM, 1475 MHz**

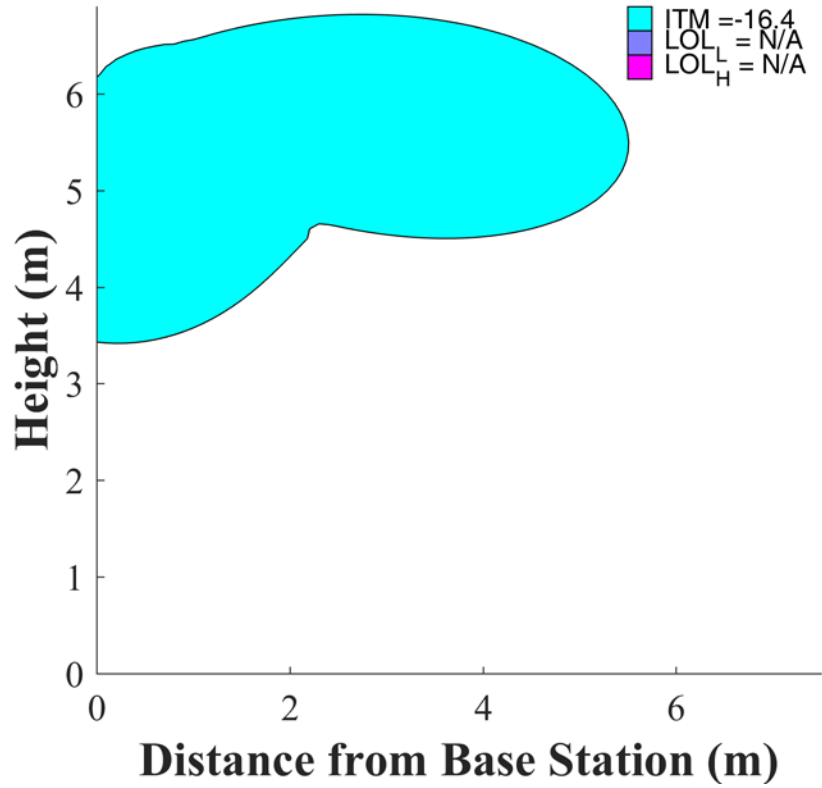


**Figure I-95: Small Cell Outdoor/Micro Urban (EIRP = 40 dBm),  
Bounding TIM, 1490 MHz**

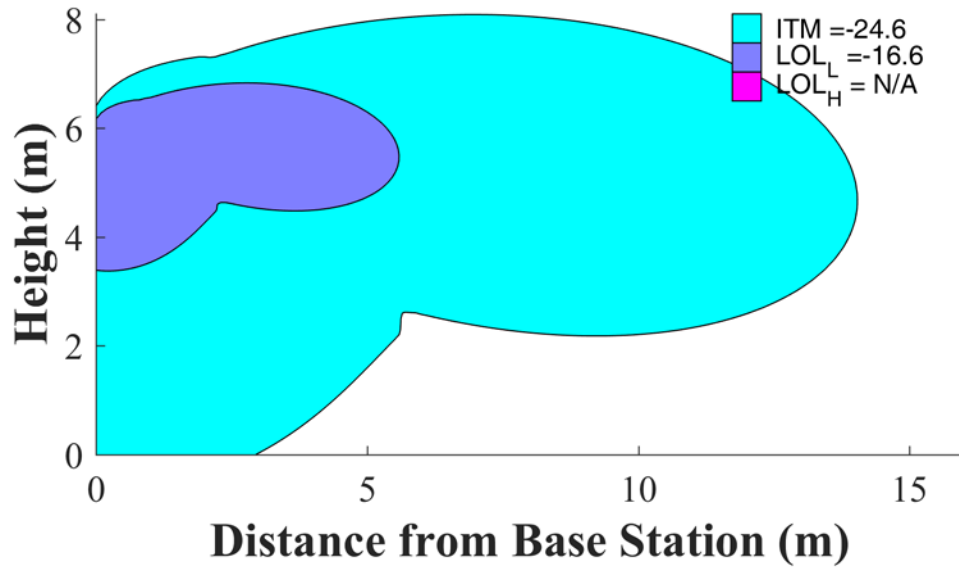


**Figure I-96: Small Cell Outdoor/Micro Urban (EIRP = 40 dBm),  
Bounding TIM, 1505 MHz**

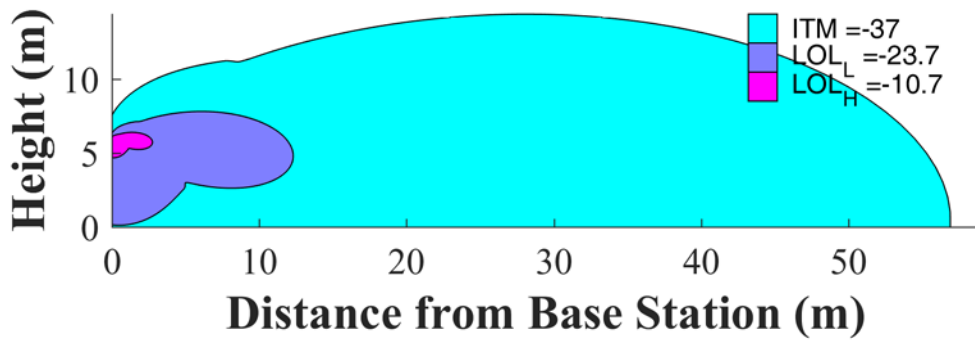


**Figure I-97: Small Cell Outdoor/Micro Urban (EIRP = 40 dBm),  
Bounding TIM, 1520 MHz**

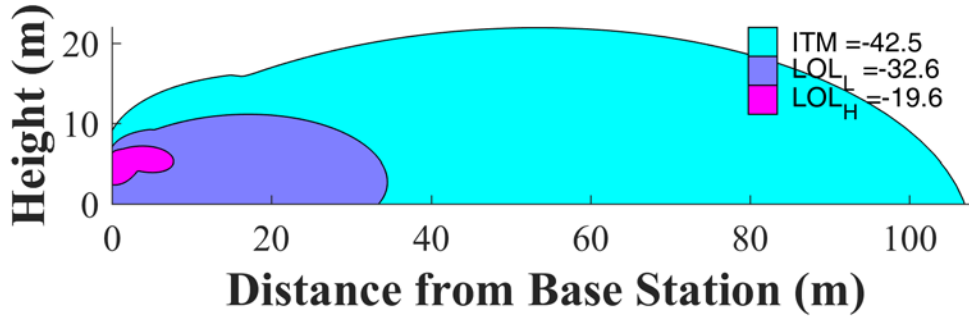


**Figure I-98: Small Cell Outdoor/Micro Urban (EIRP = 40 dBm), Bounding TIM, 1525 MHz**

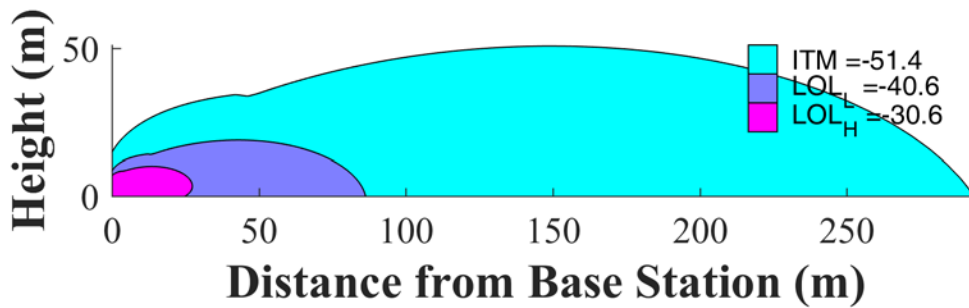


**Figure I-99: Small Cell Outdoor/Micro Urban (EIRP = 40 dBm), Bounding TIM, 1530 MHz**

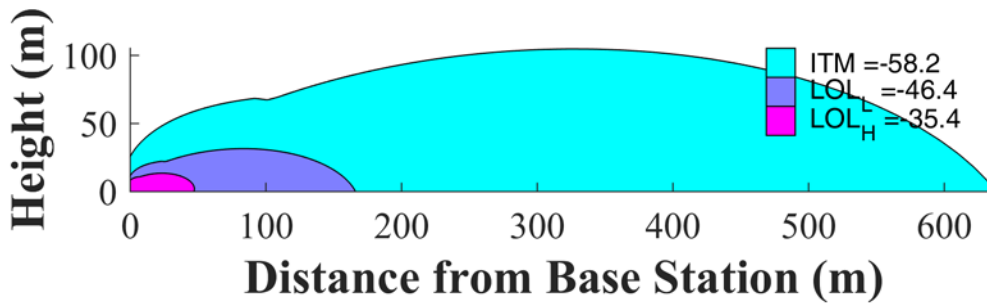


**Figure I-100: Small Cell Outdoor/Micro Urban (EIRP = 40 dBm), Bounding TIM, 1535 MHz**



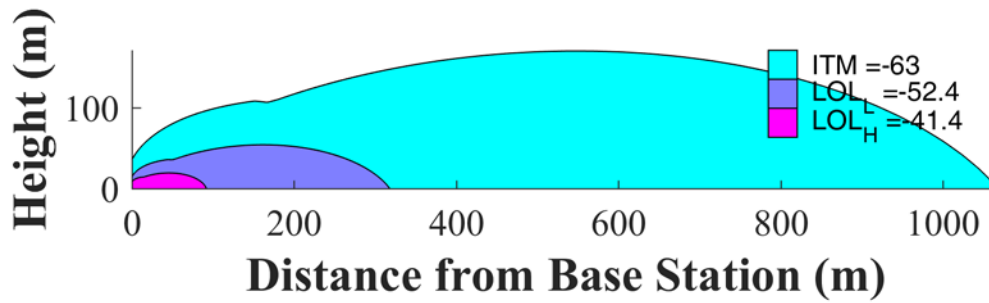


Figure I-101: Small Cell Outdoor/Micro Urban (EIRP = 40 dBm), Bounding TIM, 1540 MHz

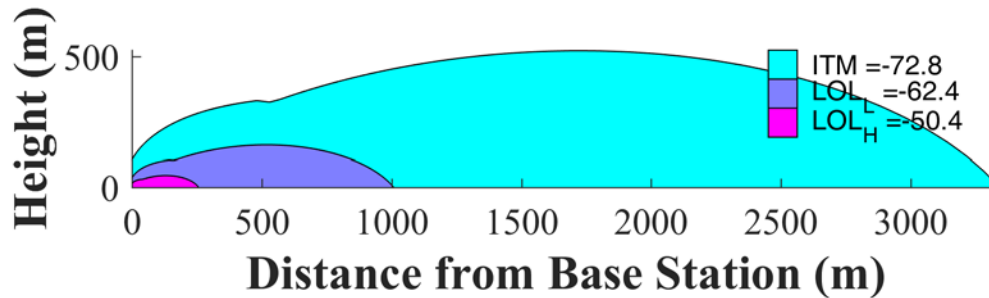


Figure I-102: Small Cell Outdoor/Micro Urban (EIRP = 40 dBm), Bounding TIM, 1545 MHz

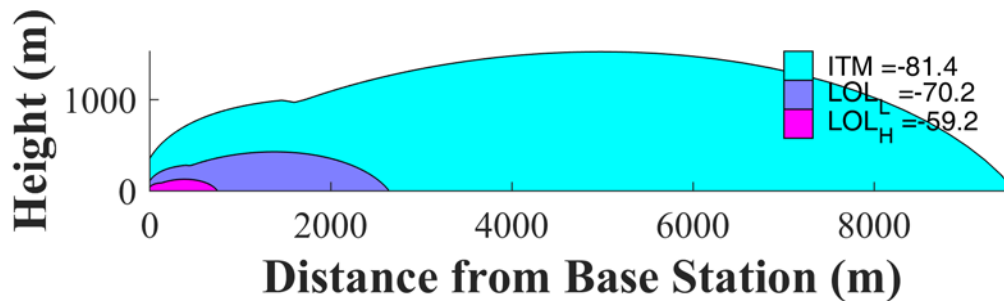
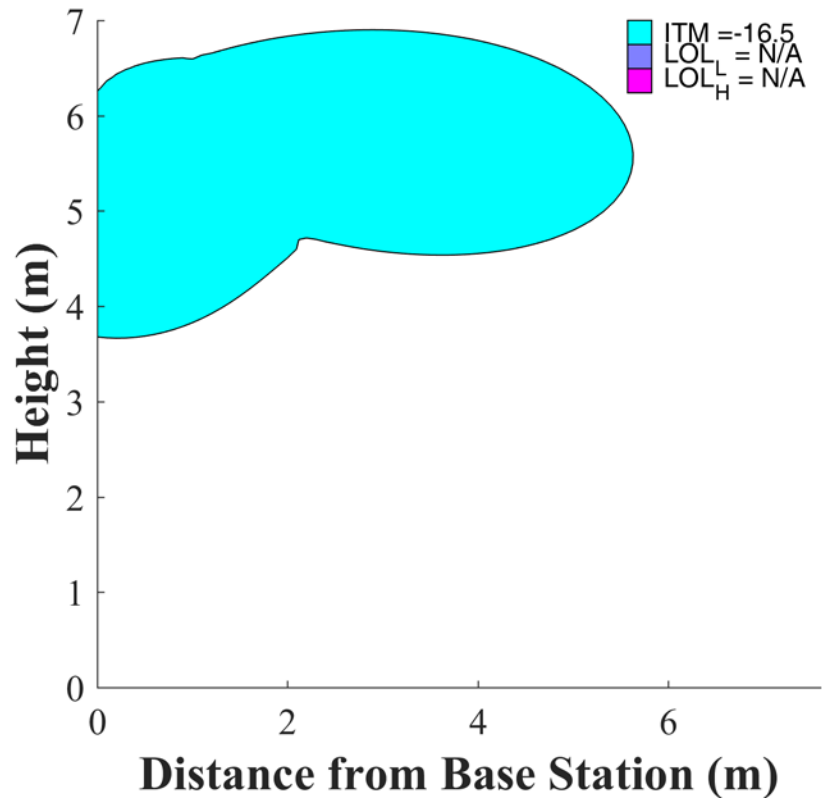
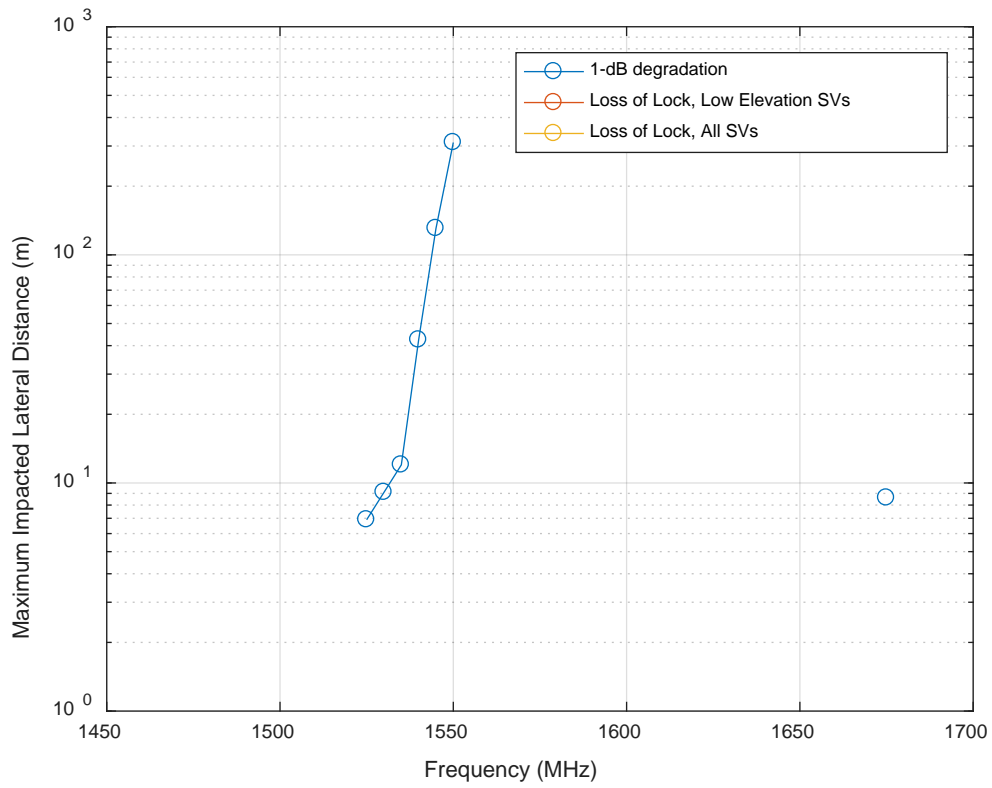


Figure I-103: Small Cell Outdoor/Micro Urban (EIRP = 40 dBm), Bounding TIM, 1550 MHz



**Figure I-104: Small Cell Outdoor/Micro Urban (EIRP = 40 dBm),  
Bounding TIM, 1675 MHz**

**I.2.5 CEL**



**Figure I-105: Small Cell Outdoor/Micro Urban (EIRP = 40 dBm), Bounding CEL**

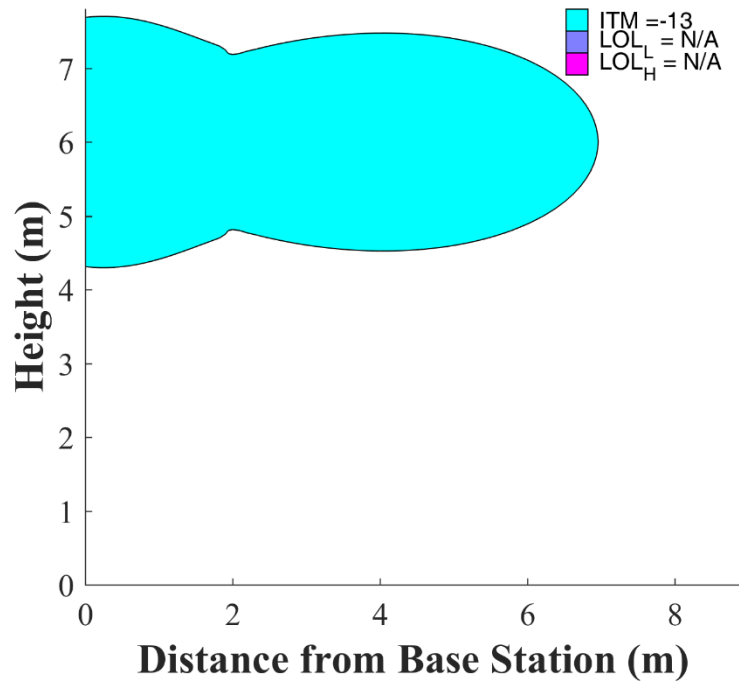


**Figure I-106: Small Cell Outdoor/Micro Urban (EIRP = 40 dBm),  
Bounding CEL, 1525 MHz**

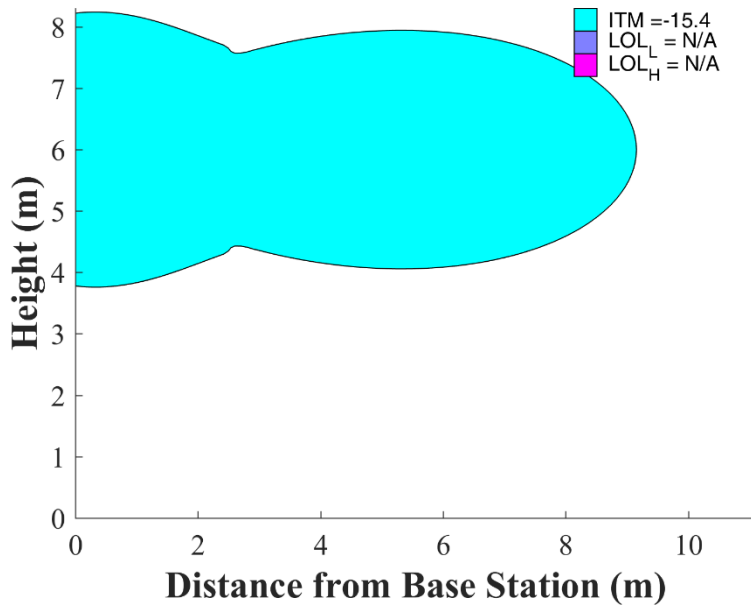


**Figure I-107: Small Cell Outdoor/Micro Urban (EIRP = 40 dBm),  
Bounding CEL, 1530 MHz**

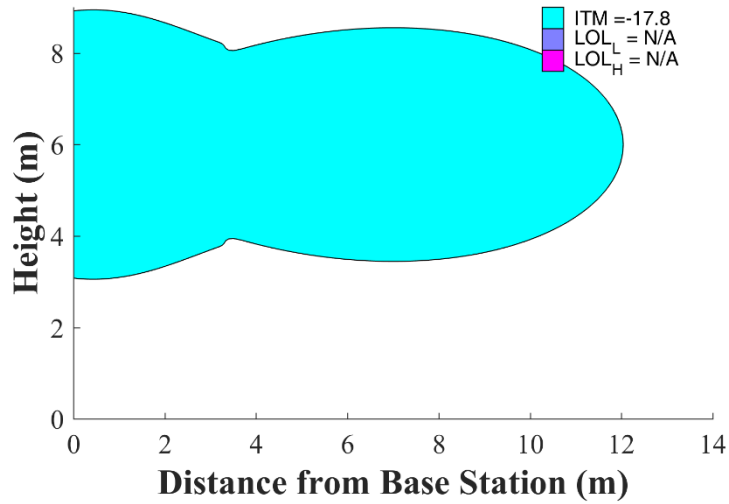


**Figure I-108: Small Cell Outdoor/Micro Urban (EIRP = 40 dBm),  
Bounding CEL, 1535 MHz**

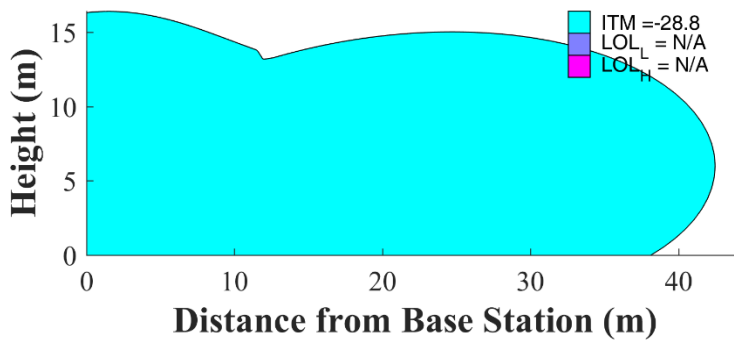


**Figure I-109: Small Cell Outdoor/Micro Urban (EIRP = 40 dBm), Bounding CEL, 1540 MHz**

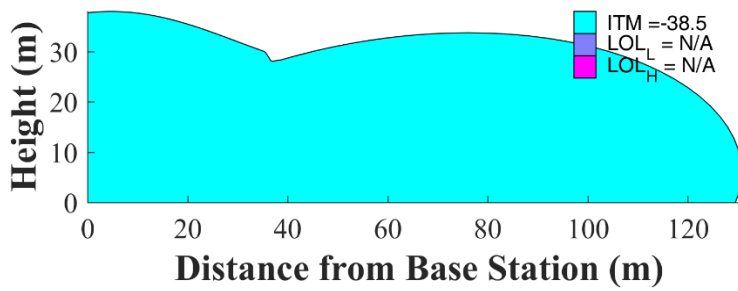


**Figure I-110: Small Cell Outdoor/Micro Urban (EIRP = 40 dBm), Bounding CEL, 1545 MHz**

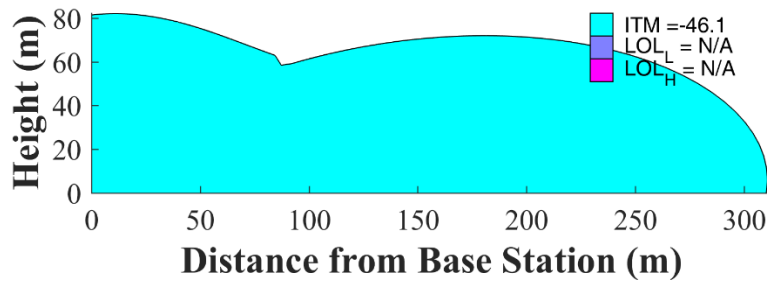


**Figure I-111: Small Cell Outdoor/Micro Urban (EIRP = 40 dBm), Bounding CEL, 1550 MHz**

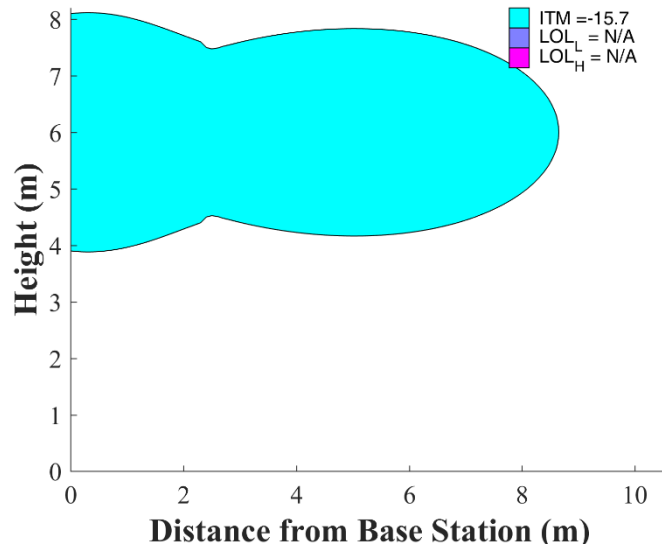


**Figure I-112: Small Cell Outdoor/Micro Urban (EIRP = 40 dBm), Bounding CEL, 1675 MHz**

**Figure X. Small Cell Outdoor/Micro Urban (EIRP = 40 dBm), Bounding CEL**

### I.3 Handsets, GPS C/A-code

This section presents results for 10-MHz LTE signals broadcast by handsets (EIRP = 23 dBm, isotropic antenna at 2 m AGL), free-space propagation, bounding mask.

#### I.3.1 GAV

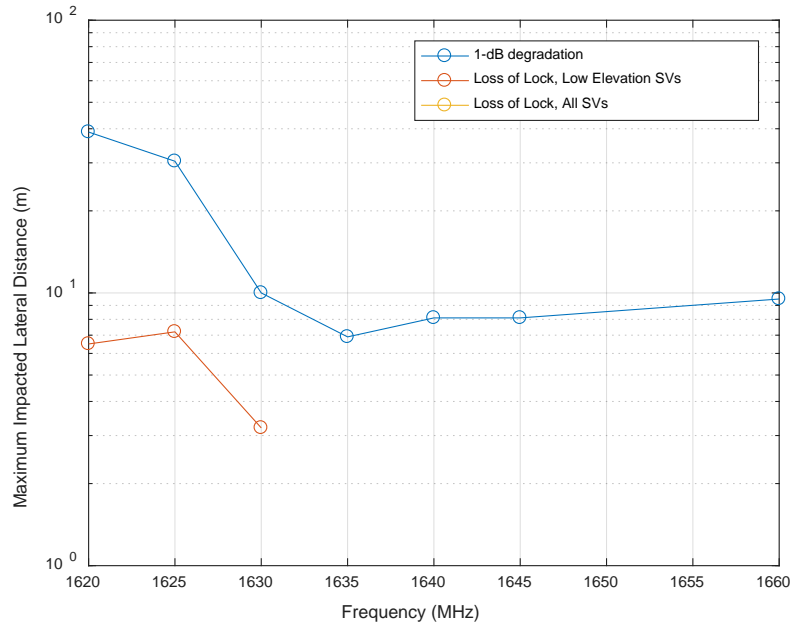


**Figure I-113: Handset (EIRP = 23 dBm), Bounding GAV**

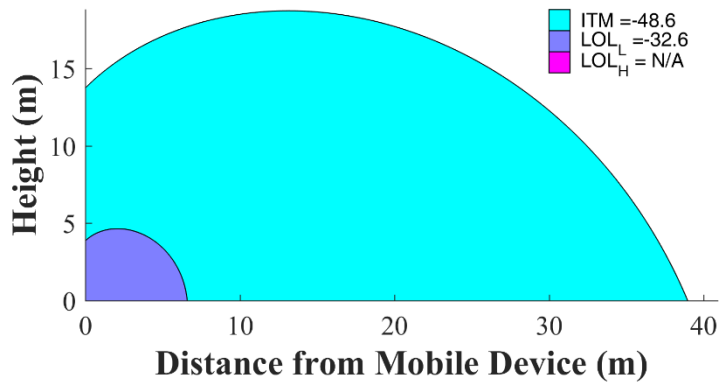


**Figure I-114: Handset (EIRP = 23 dBm), Bounding GAV, 1620 MHz**



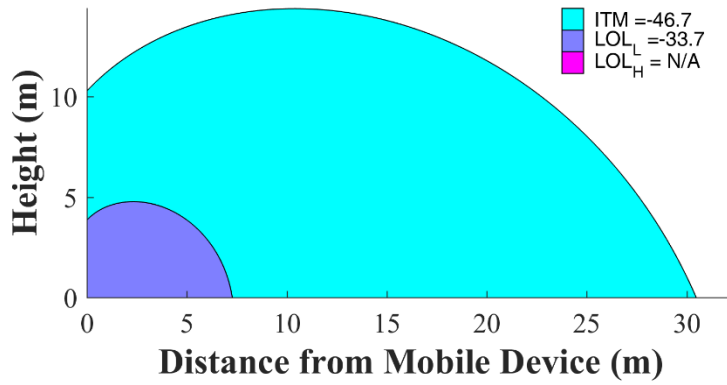


**Figure I-115: Handset (EIRP = 23 dBm), Bounding GAV, 1625 MHz**

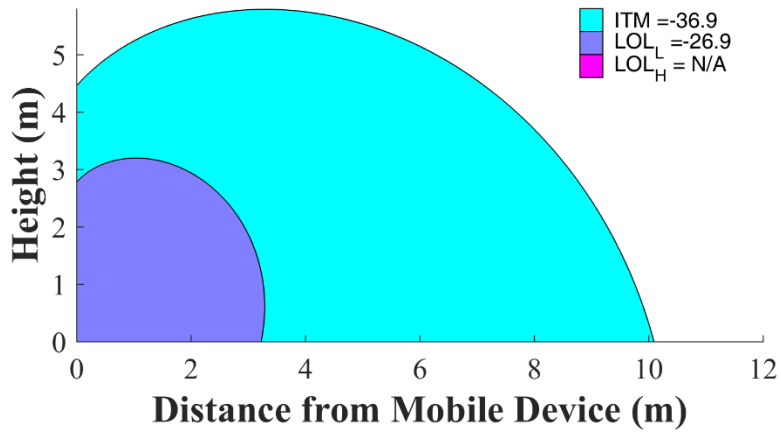


**Figure I-116: Handset (EIRP = 23 dBm), Bounding GAV, 1630 MHz**

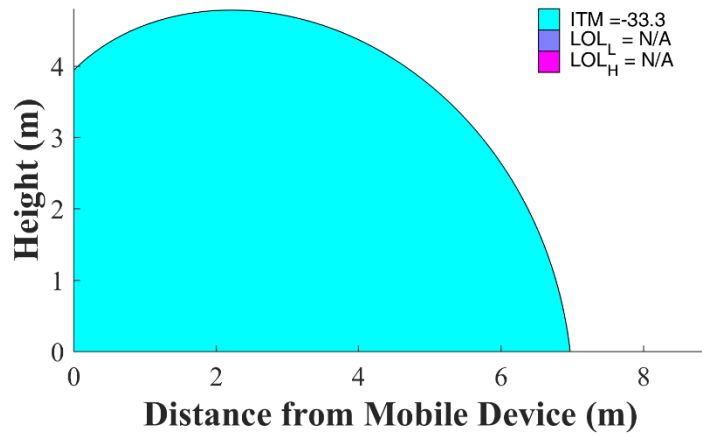


**Figure I-117: Handset (EIRP = 23 dBm), Bounding GAV, 1635 MHz**

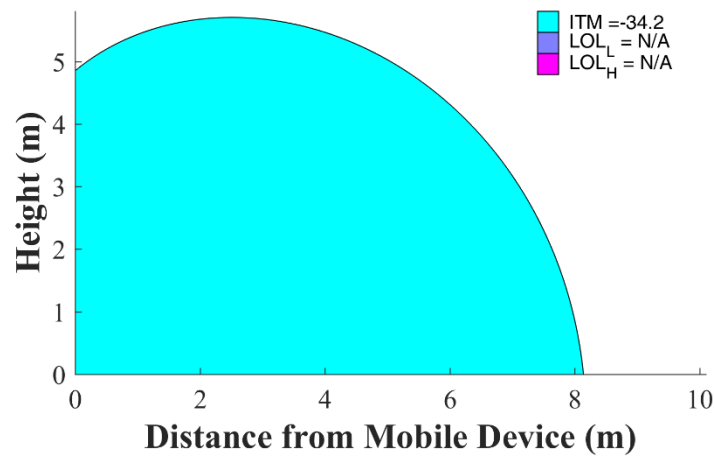


**Figure I-118: Handset (EIRP = 23 dBm), Bounding GAV, 1640 MHz**

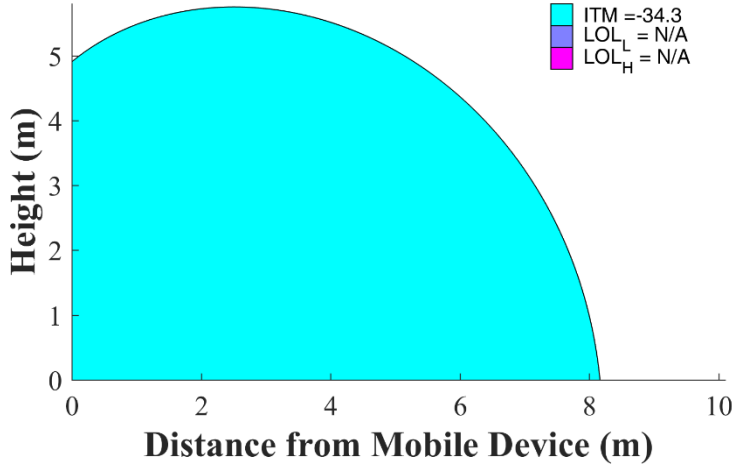


**Figure I-119: Handset (EIRP = 23 dBm), Bounding GAV, 1645 MHz**

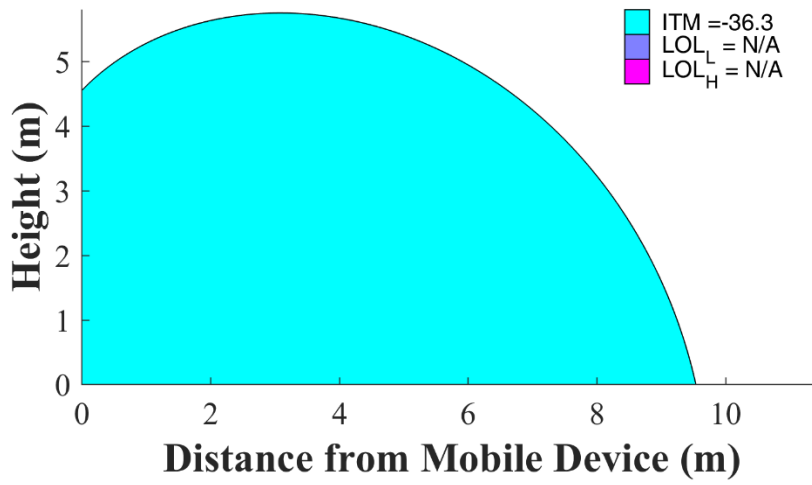


**Figure I-120: Handset (EIRP = 23 dBm), Bounding GAV, 1660 MHz**

**I.3.2 GLN**

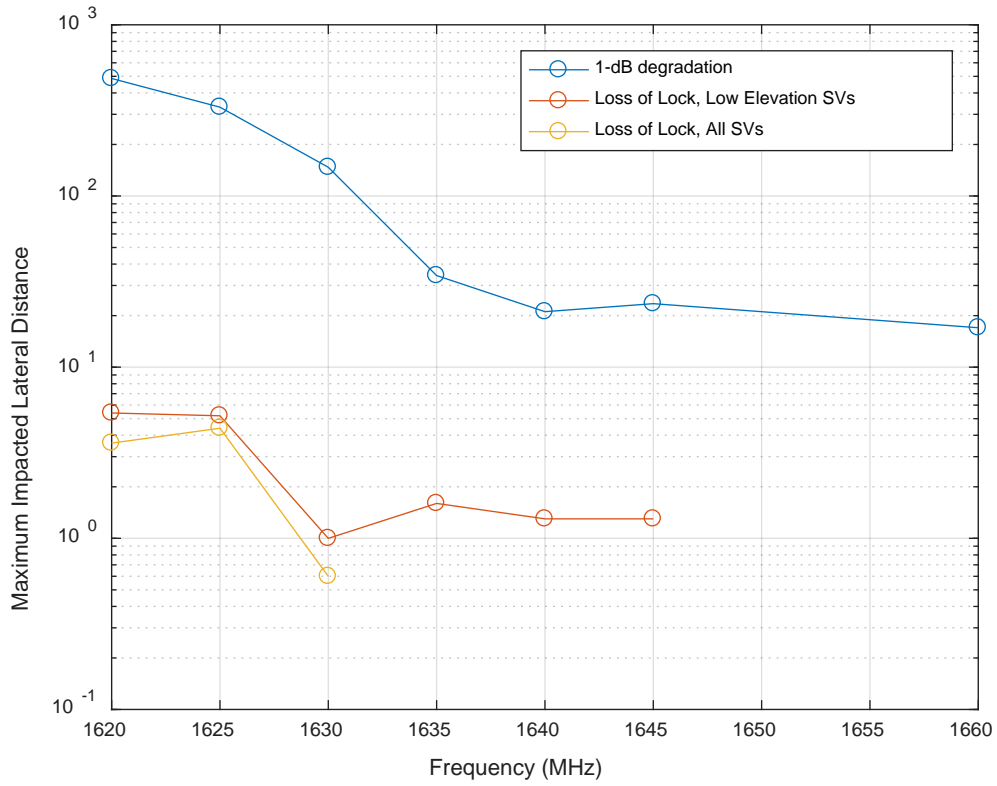


**Figure I-121: Handset (EIRP = 23 dBm), Bounding GLN**

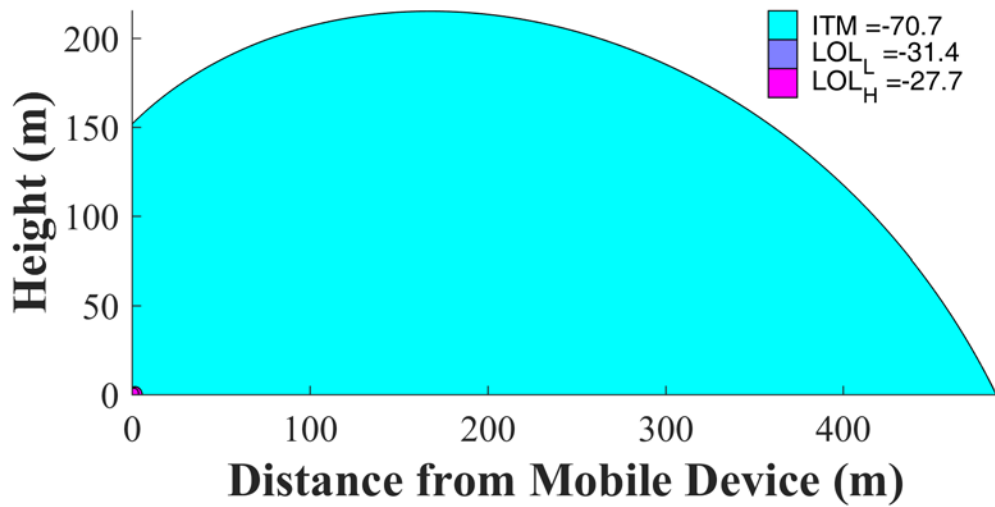


**Figure I-122: Handset (EIRP = 23 dBm), Bounding GLN, 1620 MHz**

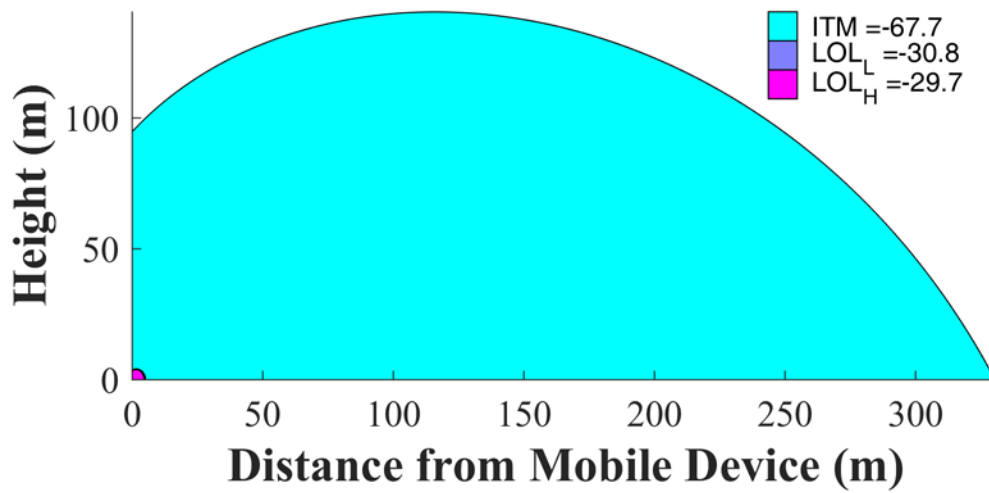


Figure I-123: Handset (EIRP = 23 dBm), Bounding GLN, 1625 MHz

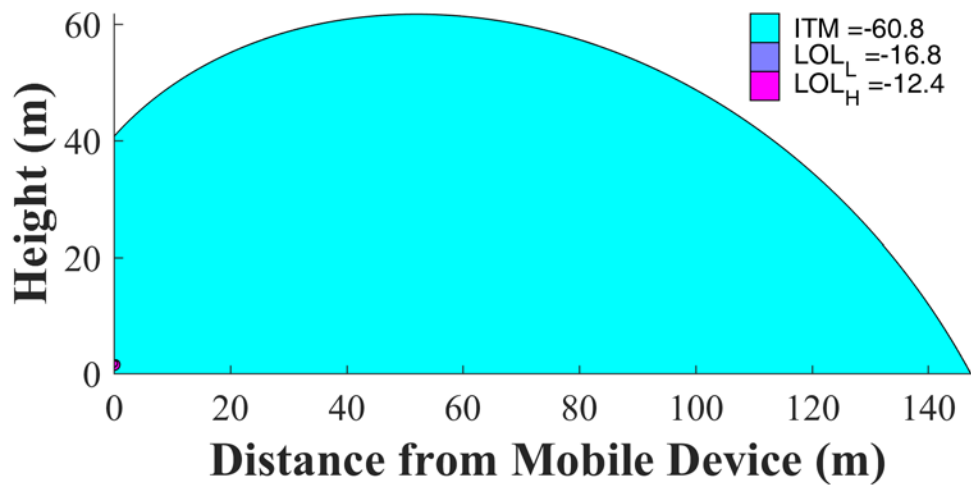


Figure I-124: Handset (EIRP = 23 dBm), Bounding GLN, 1630 MHz

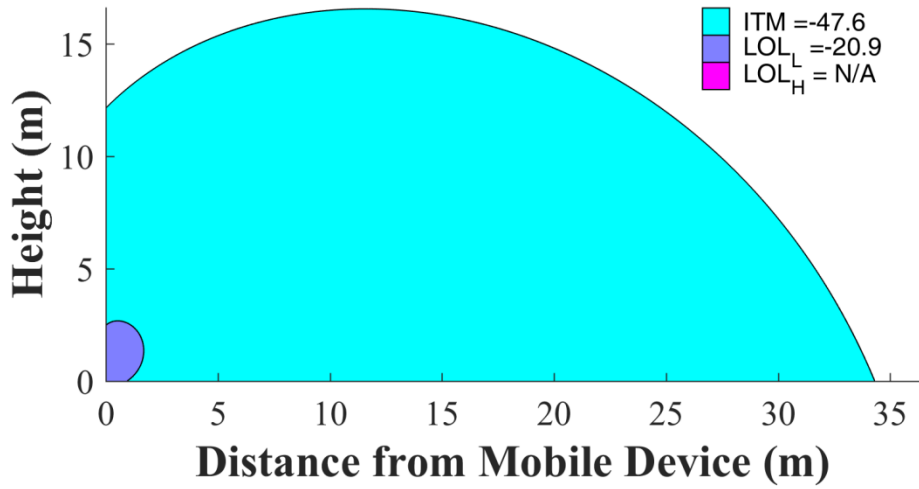


Figure I-125: Handset (EIRP = 23 dBm), Bounding GLN, 1635 MHz

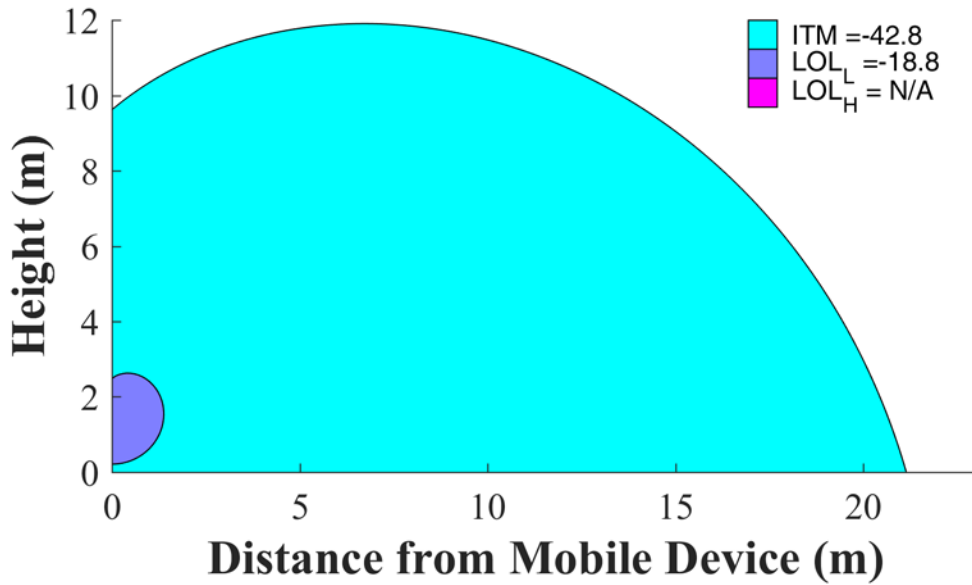


Figure I-126: Handset (EIRP = 23 dBm), Bounding GLN, 1640 MHz

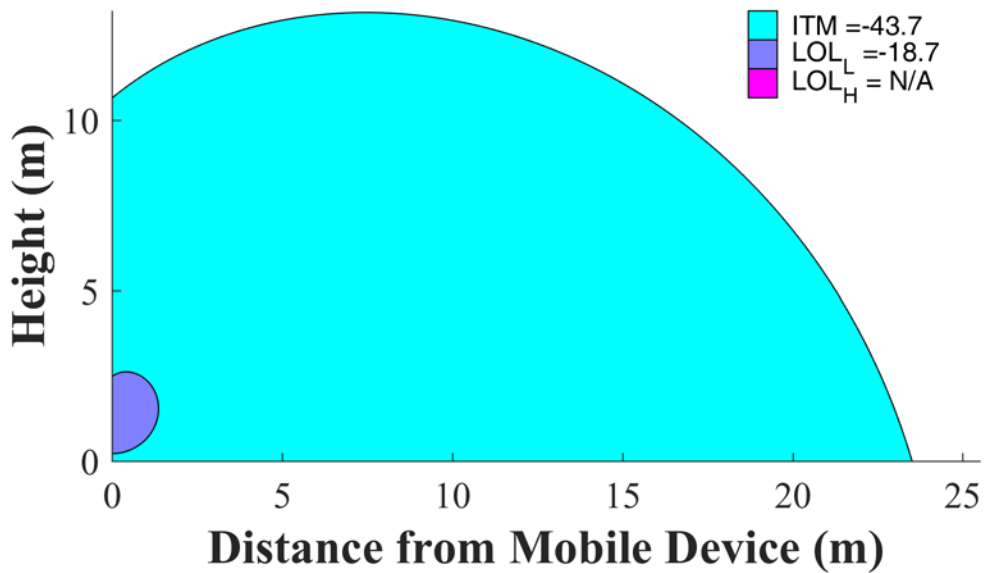


Figure I-127: Handset (EIRP = 23 dBm), Bounding GLN, 1645 MHz

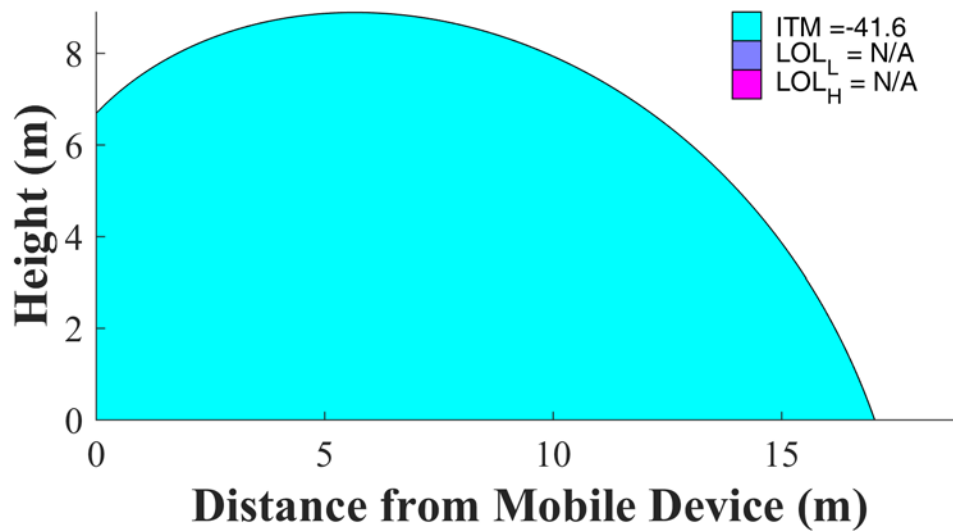
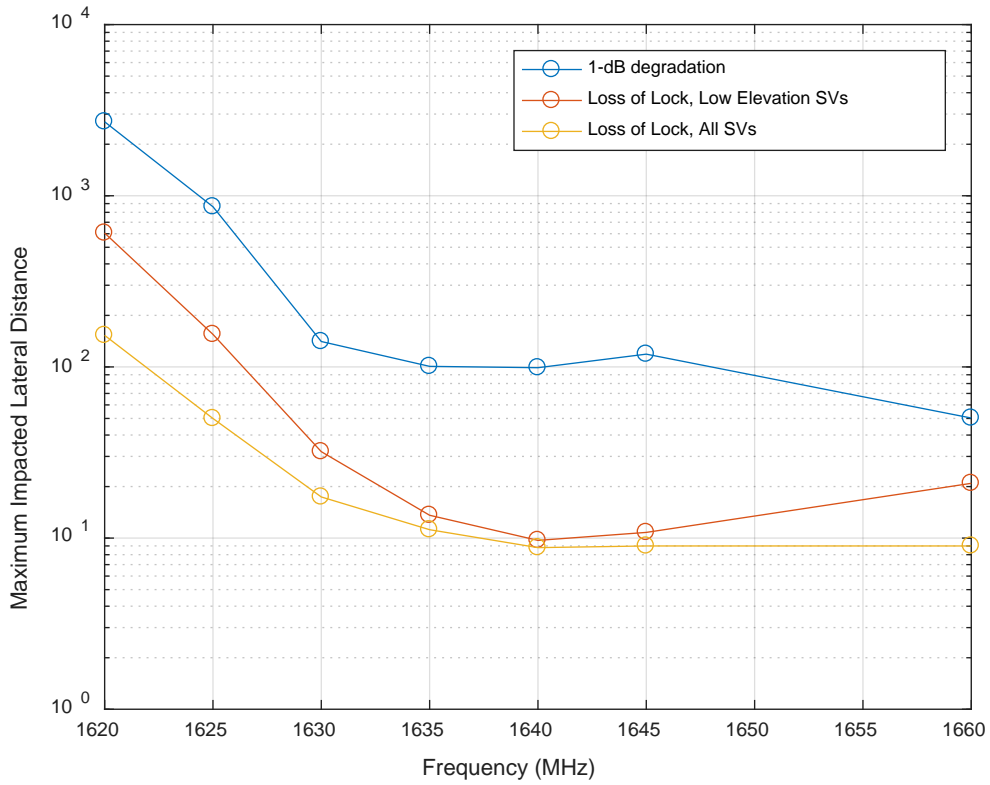
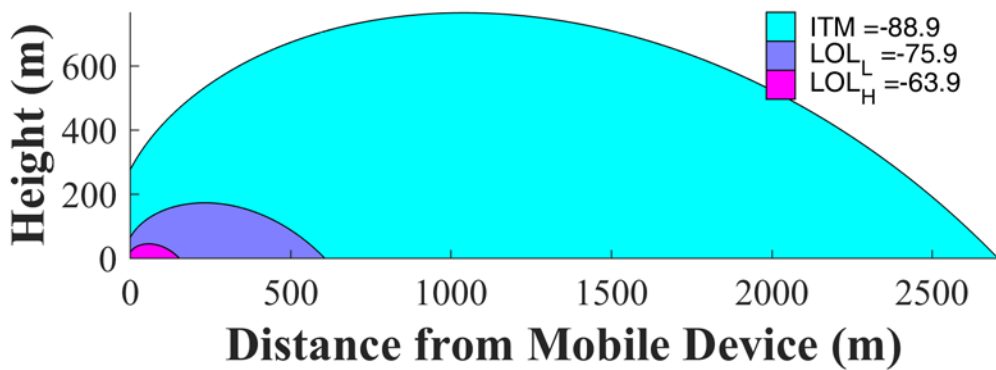


Figure I-128: Handset (EIRP = 23 dBm), Bounding GLN, 1660 MHz

### I.3.3 HPR



**Figure I-129: Handset (EIRP = 23 dBm), Bounding HPR**



**Figure I-130: Handset (EIRP = 23 dBm), Bounding HPR, 1620 MHz**



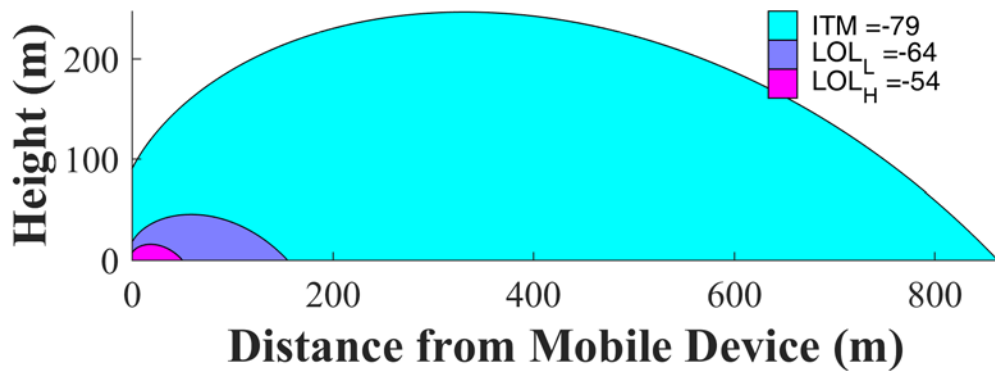


Figure I-131: Handset (EIRP = 23 dBm), Bounding HPR, 1625 MHz

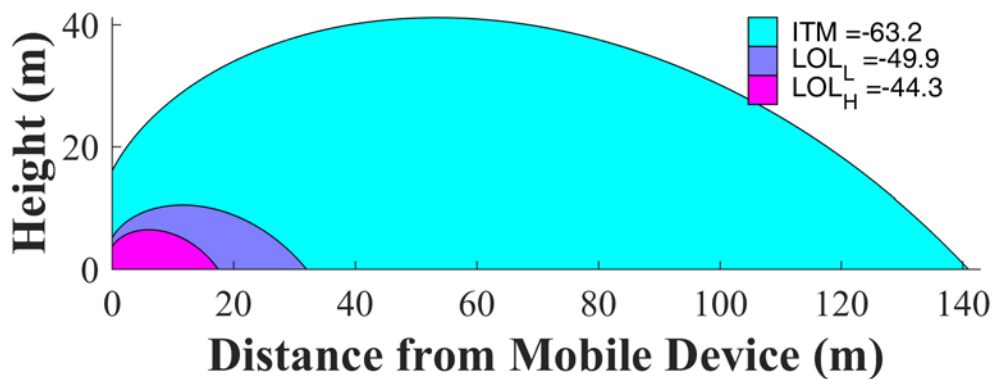


Figure I-132: Handset (EIRP = 23 dBm), Bounding HPR, 1630 MHz

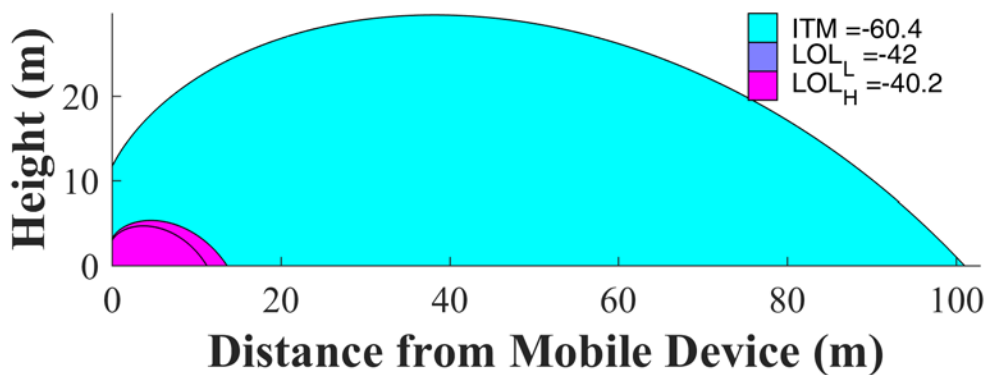


Figure I-133: Handset (EIRP = 23 dBm), Bounding HPR, 1635 MHz

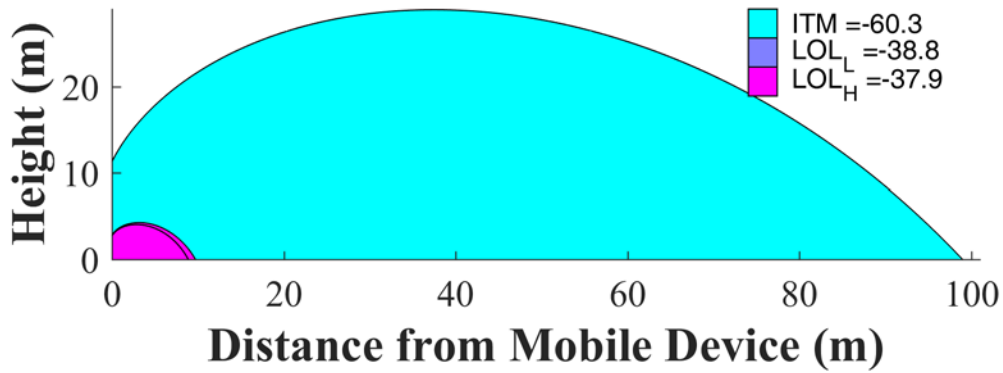


Figure I-134: Handset (EIRP = 23 dBm), Bounding HPR, 1640 MHz

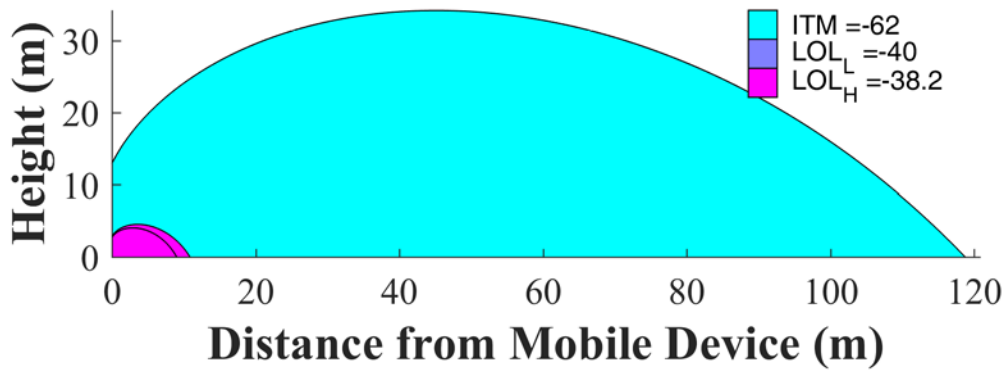


Figure I-135: Handset (EIRP = 23 dBm), Bounding HPR, 1645 MHz

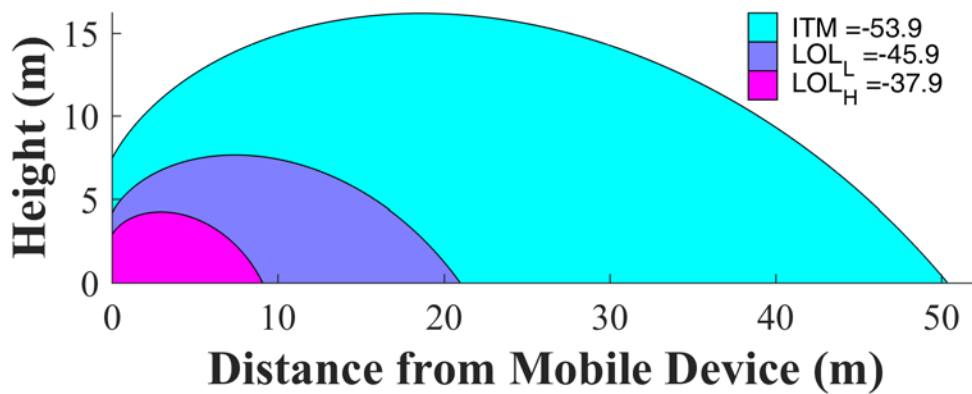
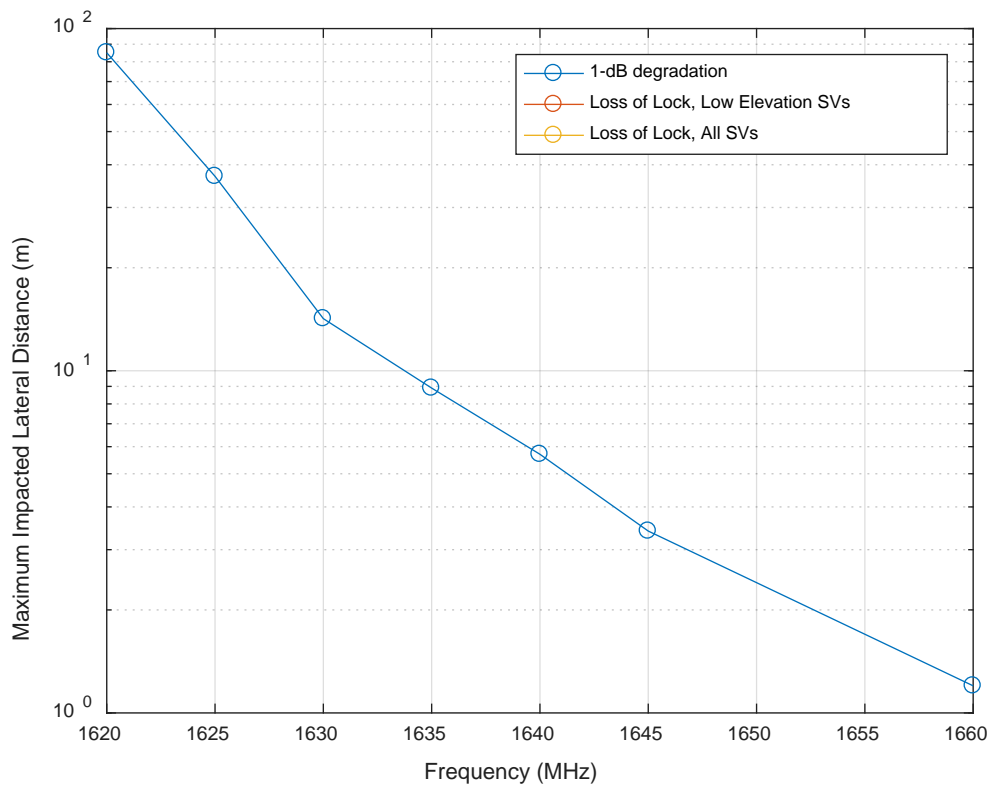


Figure I-136: Handset (EIRP = 23 dBm), Bounding HPR, 1660 MHz

### I.3.4 TIM



**Figure I-137: Handset (EIRP = 23 dBm), Bounding TIM**

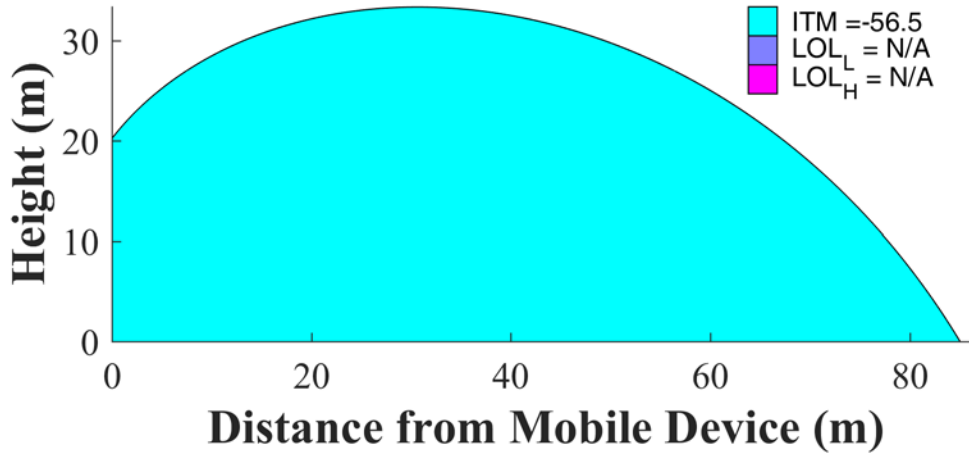


Figure I-138: Handset (EIRP = 23 dBm), Bounding TIM, 1620 MHz

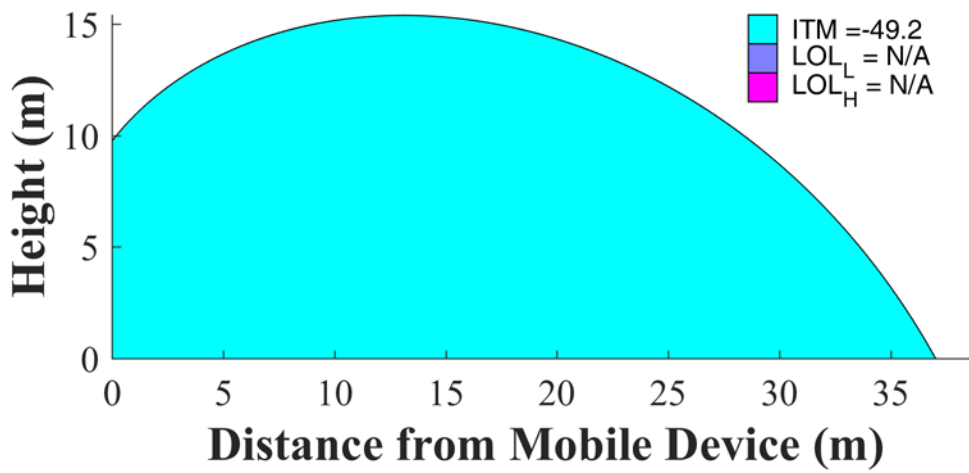


Figure I-139: Handset (EIRP = 23 dBm), Bounding TIM, 1625 MHz

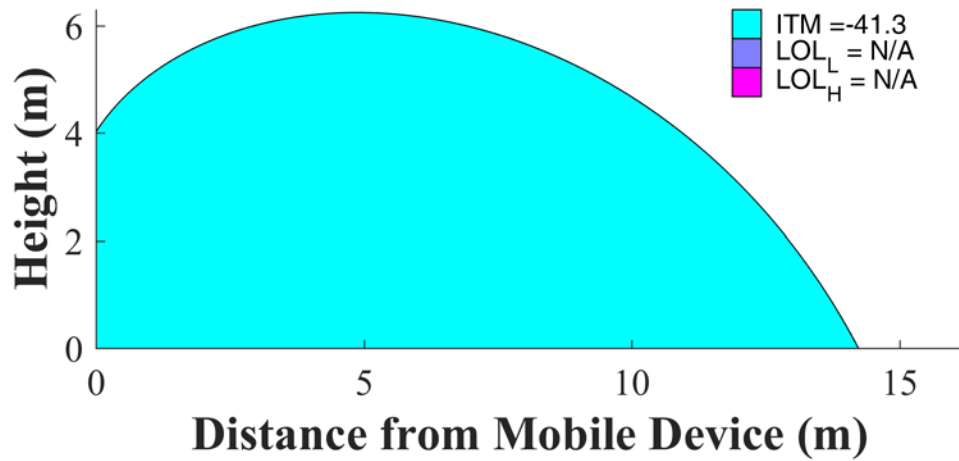


Figure I-140: Handset (EIRP = 23 dBm), Bounding TIM, 1630 MHz

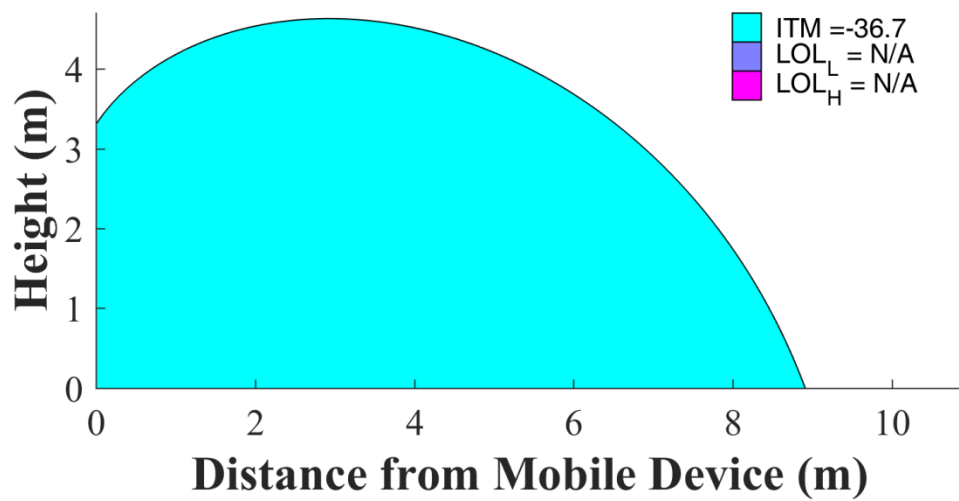


Figure I-141: Handset (EIRP = 23 dBm), Bounding TIM, 1635 MHz

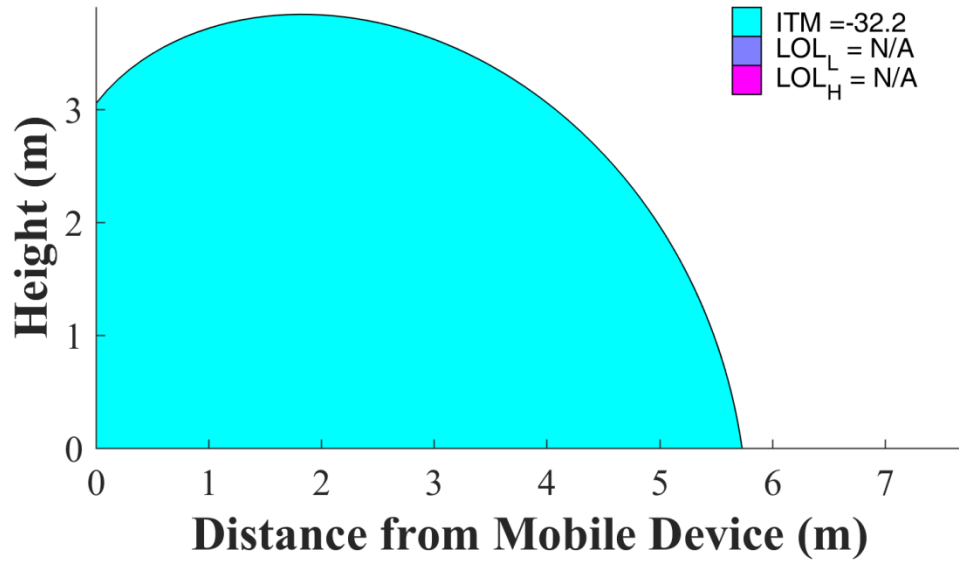


Figure I-142: Handset (EIRP = 23 dBm), Bounding TIM, 1640 MHz

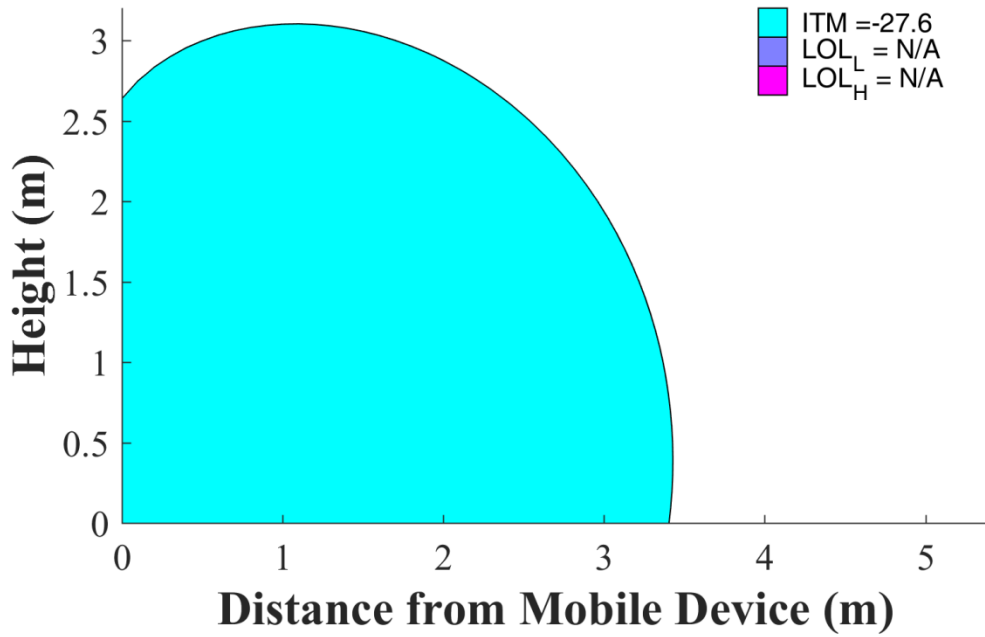
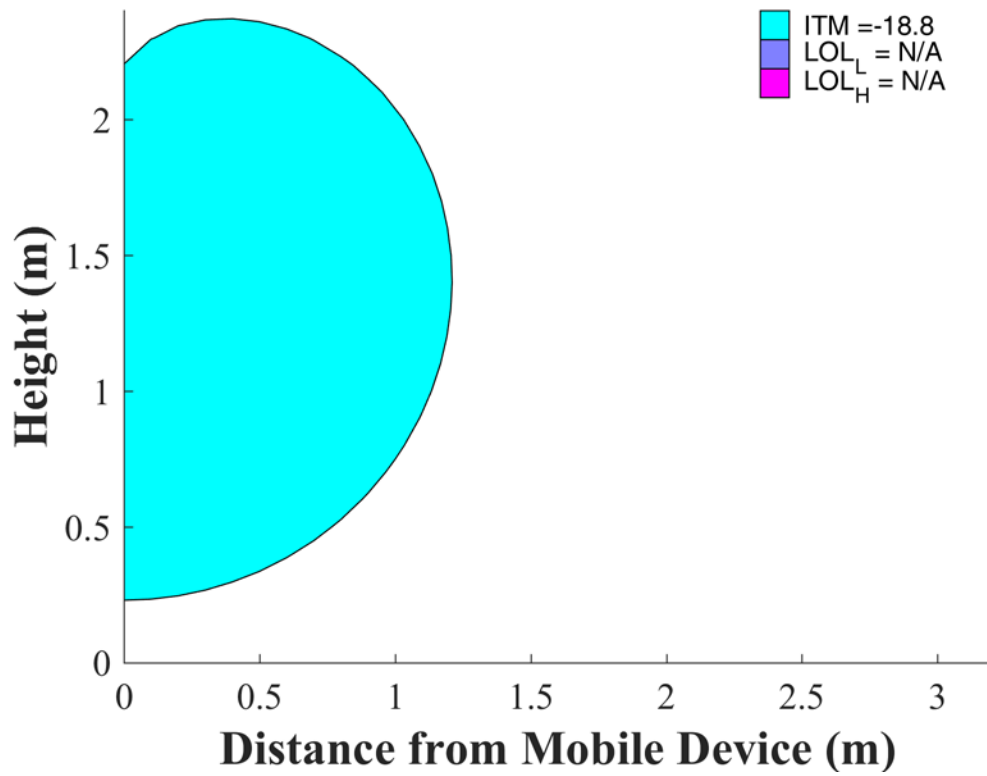
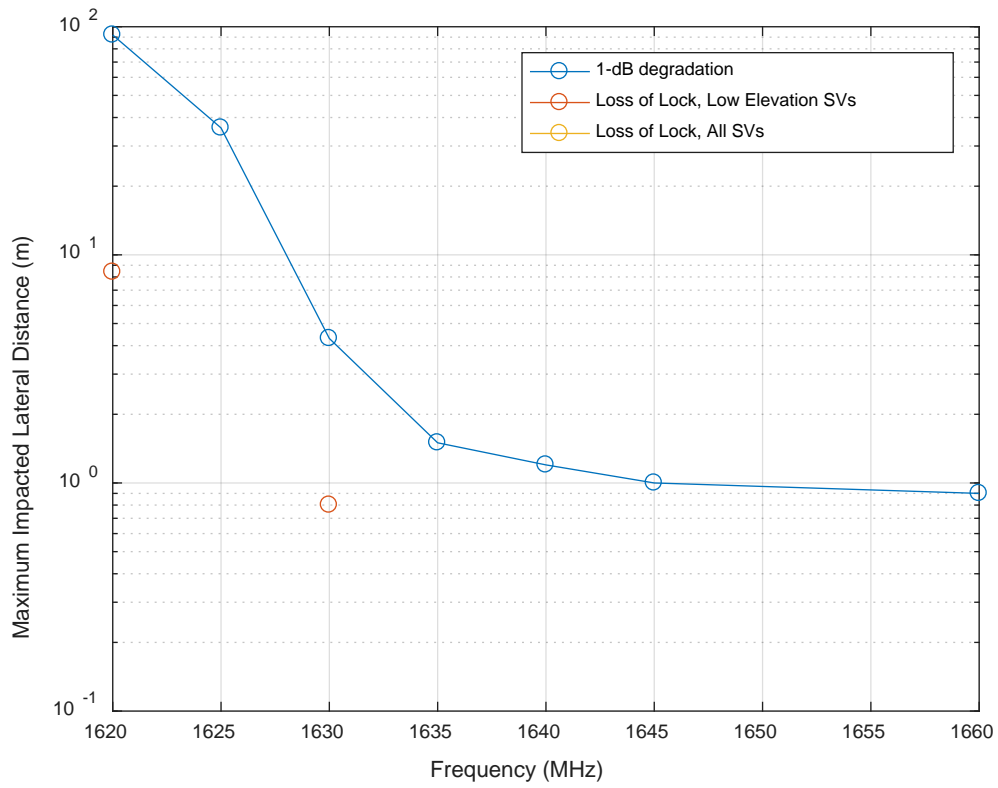


Figure I-143: Handset (EIRP = 23 dBm), Bounding TIM, 1645 MHz



**Figure I-144: Handset (EIRP = 23 dBm), Bounding TIM, 1660 MHz**

### I.3.5 CEL



**Figure I-145: Handset (EIRP = 23 dBm), Bounding CEL**



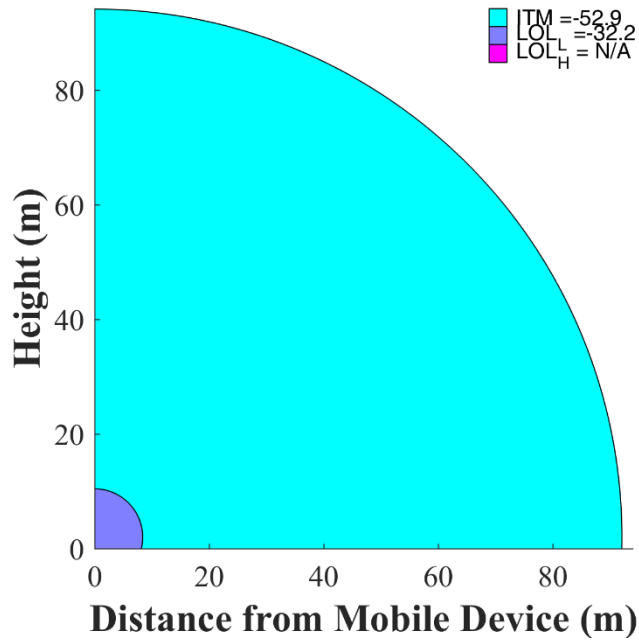


**Figure I-146: Handset (EIRP = 23 dBm), Bounding CEL, 1620 MHz**

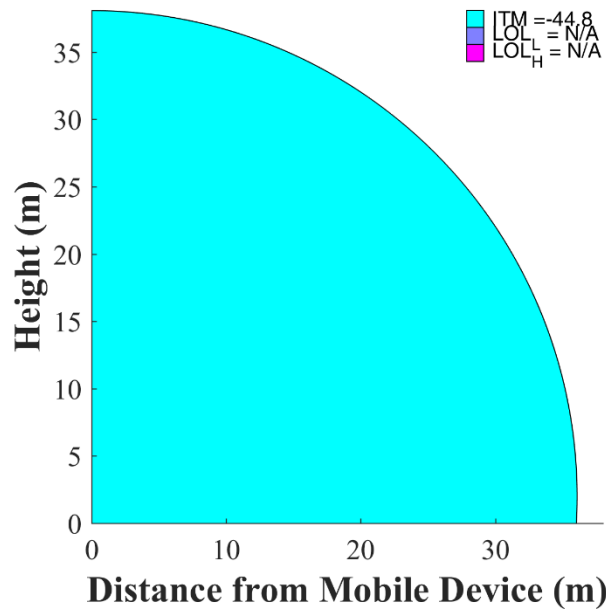


**Figure I-147: Handset (EIRP = 23 dBm), Bounding CEL, 1625 MHz**

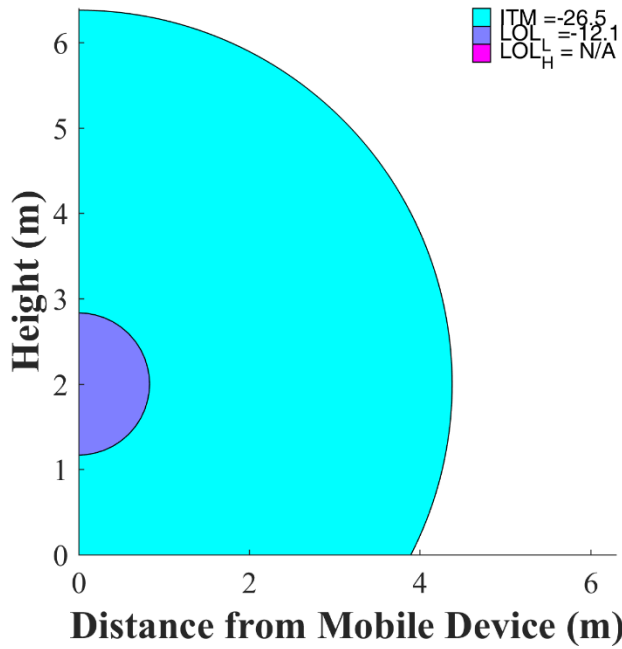


**Figure I-148: Handset (EIRP = 23 dBm), Bounding CEL, 1630 MHz**

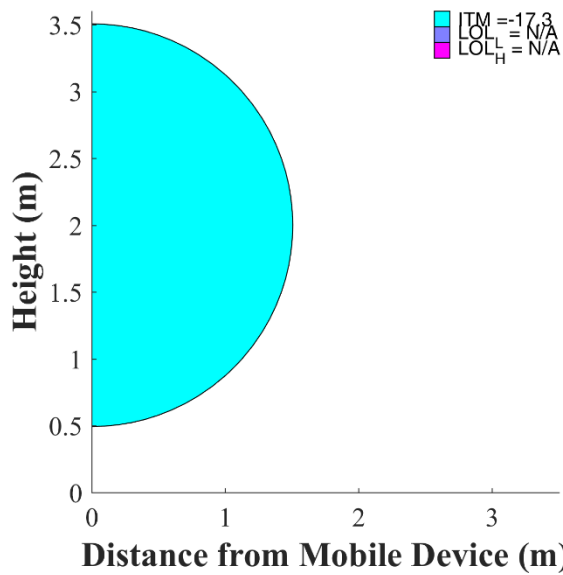


**Figure I-149: Handset (EIRP = 23 dBm), Bounding CEL, 1635 MHz**

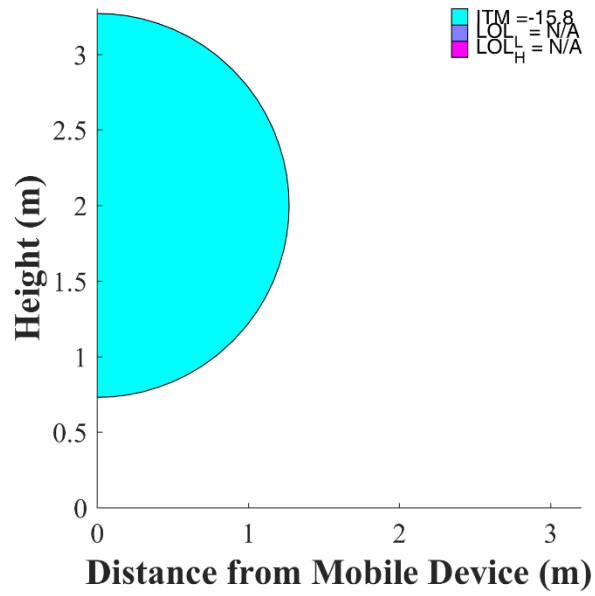


**Figure I-150: Handset (EIRP = 23 dBm), Bounding CEL, 1640 MHz**

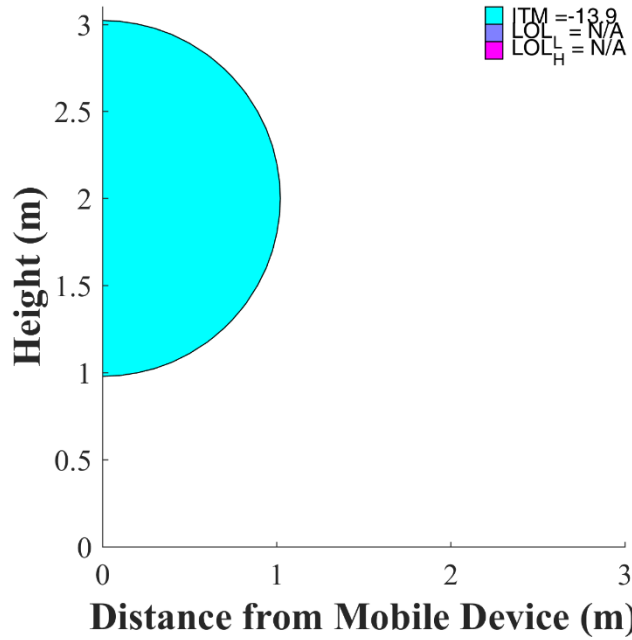


**Figure I-151: Handset (EIRP = 23 dBm), Bounding CEL, 1645 MHz**

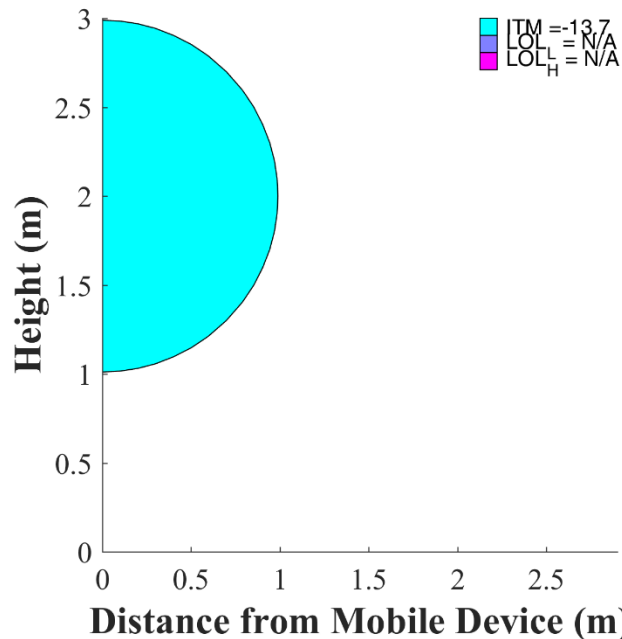


**Figure I-152: Handset (EIRP = 23 dBm), Bounding CEL, 1660 MHz**

## I.4 Sensitivity Analyses

Sections I.1 to I.3 presented results that were applicable for:

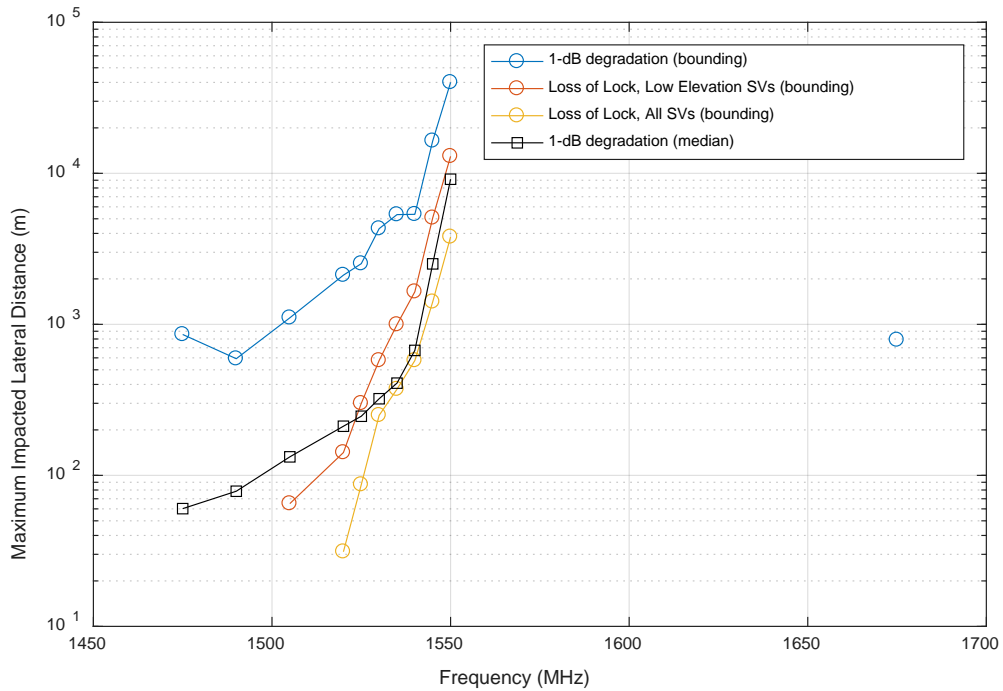
- The most sensitive (bounding) DUT of each receiver category for each frequency.
- GPS C/A-code tracking.
- Environments where the free-space path loss model is appropriate.

This section examines sensitivity of the results to these assumptions.

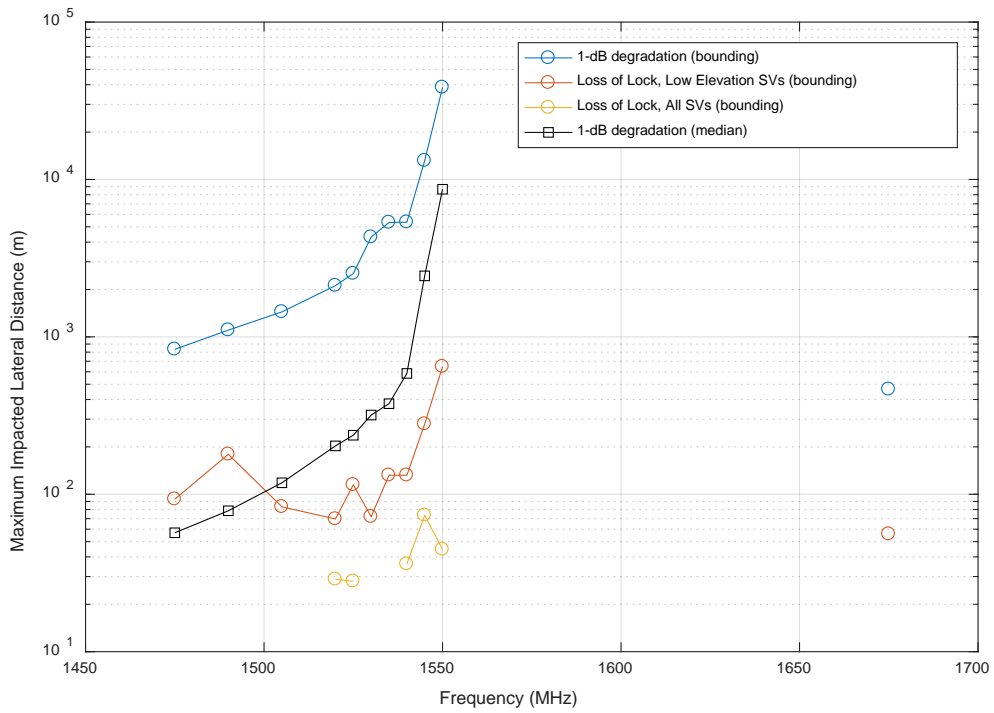
### I.4.1 Non-bounding DUTs

Figure I-153 to Figure I-157 provide results for the maximum impacted lateral distance for both the bounding and median DUTs for each receiver category and frequency. The results in these plots are applicable for a single macro urban base station (EIRP = 59 dBm) and for reception of the GPS C/A-code. It is important to note that “median” pertains only to the set of devices tested

at WSMR for each category, and these results should not be interpreted as being applicable to the “median” of fielded GPS/GNSS receivers. As expected, the impacted distances are significantly smaller for the median vs bounding DUTs. Loss-of-lock curves are only included in the HPR plot (Figure I-155) since the median DUTs for all of the other receiver categories did not lose lock on either the nominal or -10 dB satellite signals at any tested frequency.



**Figure I-153: Maximum Impacted Lateral Distance for GAV, Macro Urban Base Station (EIRP = 59 dBm)**



**Figure I-154: Maximum Impacted Lateral Distance for GLN, Macro Urban Base Station (EIRP = 59 dBm)**

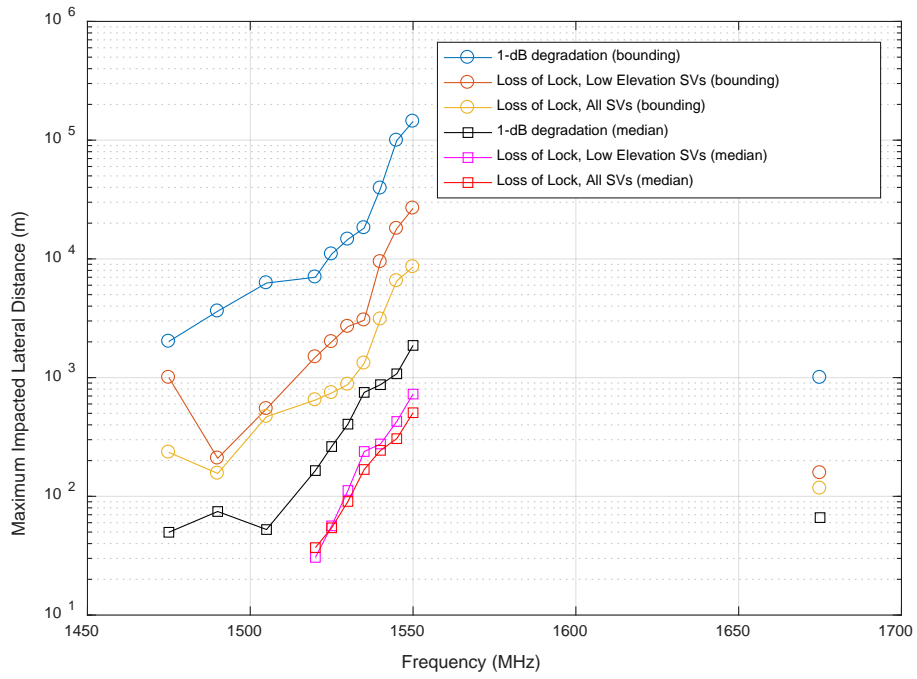


**Figure I-155: Maximum Impacted Lateral Distance for HPR, Macro Urban Base Station (EIRP = 59 dBm)**

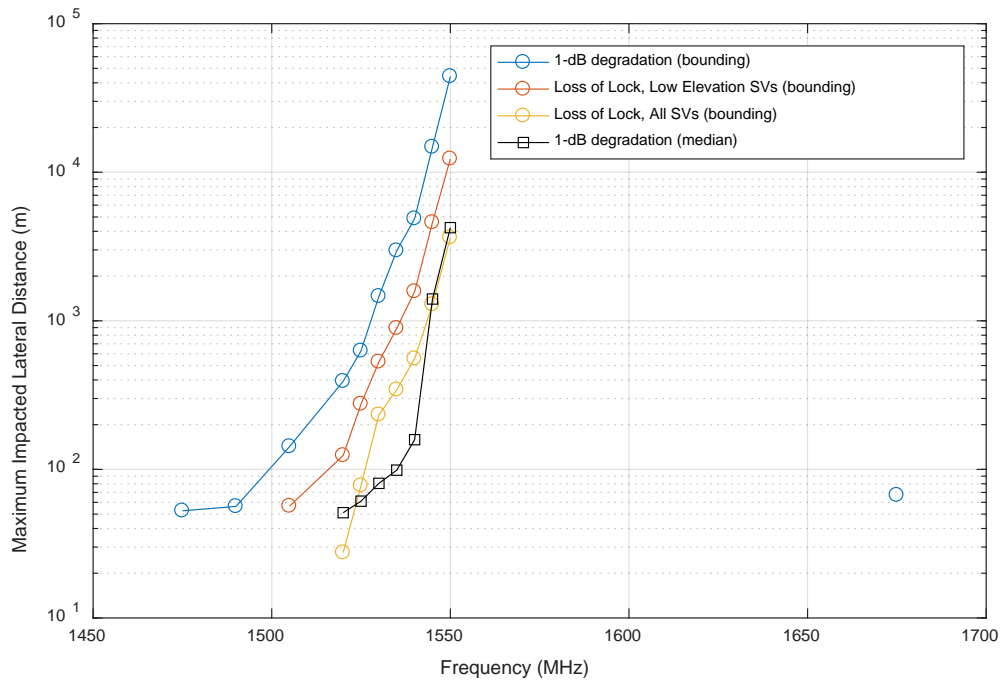


**Figure I-156: Maximum Impacted Lateral Distance for TIM, Macro Urban Base Station (EIRP = 59 dBm)**



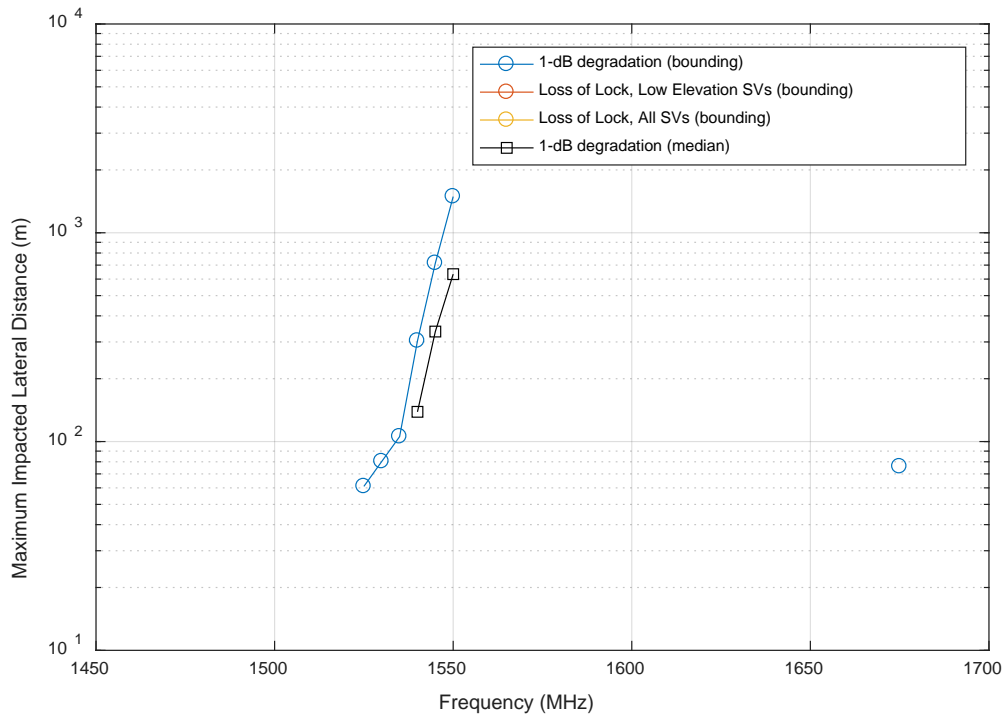
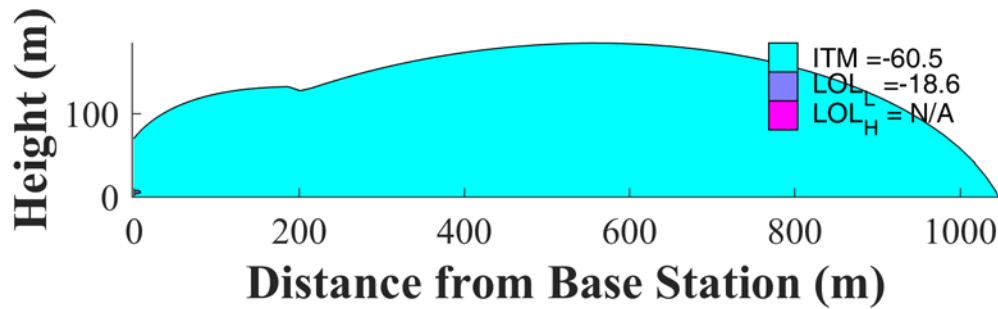


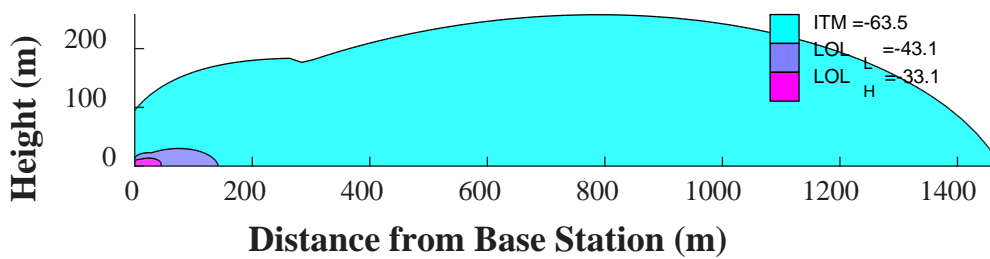
**Figure I-157: Maximum Impacted Lateral Distance for CEL, Macro Urban Base Station (EIRP = 59 dBm)**

#### I.4.2 Other GNSS Signal Types

Sections I.1 through I.3 presented results only for GPS C/A-code reception. Oftentimes, DUTs that were capable of tracking other GNSS signal types were more sensitive to interference for the processing of the other signals. As an example, Figure I-158 shows the impacted areas for a small cell outdoor base station operating at 1530 MHz for the most-sensitive GLN DUT. The top figure (a) is for GPS C/A-code, and the bottom figure (b) for GLONASS L1C.



(a)



(b)

**Figure I-158: Small Cell Outdoor/Micro Urban (EIRP = 40 dBm), Bounding GLN, 1530 MHz: (a) GPS C/A-code (b) GLONASS L1C**

### I.4.3 Propagation Models

Sections I.1 through I.3 presented forward modeling results that presumed free-space propagation. Depending on the operational environment, these results can be excessively optimistic or pessimistic.

When there is a clear line-of-sight path between the transmitting and receiving antennas and additionally a strong ground reflection, the free-space propagation model can yield optimistic results (i.e., the maximum impacted distance may be greater than predicted). In such environments, a two-ray path model may provide greater accuracy in predicting received power levels. Figure I-159 provides an example of the difference in impacted areas between free-space propagation and two-ray propagation. The two-ray result presumes that the reflecting ground surface is smooth concrete. As a second example, received power levels from an LTE base station in a rural area near Las Vegas were observed at power levels significantly greater than

predicted using the free-space path loss model at lateral distances of up to 9 km.<sup>2</sup> The base station antenna height was 18 m and the received power was measured at a height of around 2 m.

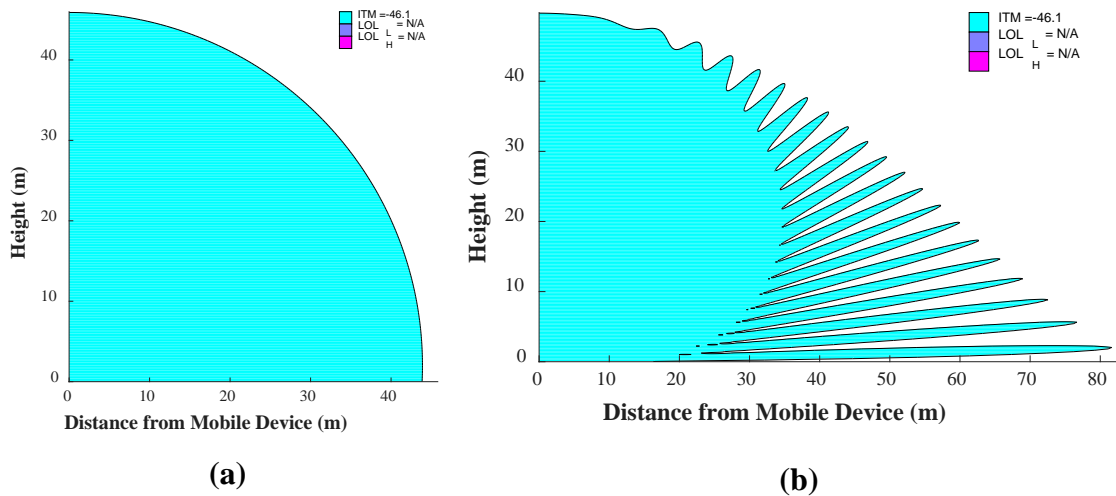


**Figure I-159: Impacted Area for Cellular DUT from 23 dBm EIRP Mobile Device at 1550 MHz (a) as predicted using free-space propagation model, (b) as predicted using two-ray propagation model**

When there is significant blockage between the transmitting and receiving antennas, the free-space propagation model can at times yield pessimistic results (i.e., the maximum impacted distance may be far smaller than predicted). For example, received power measurements from an LTE base station in a dense urban area within Las Vegas were typically observed to be 10 – 20 dB below those levels predicted using free-space propagation for lateral distances of up to 2 km.<sup>3</sup> The base station antenna height was 72 m and the received power was measured at a height of around 2 m. It should be noted that, even though the received power was most frequently less than predicted using free-space, in some locations far from the base station (> 1 km) power levels were observed to be as high as or exceeding the free-space propagation model predictions. Such observations were much more frequent within 500 km of the base station.

Given the prevalence of line-of-sight blockages in urban and dense suburban areas, the free-space results in Sections I.1 through I.3 are likely to be significantly pessimistic for distances

<sup>2</sup> See p. 110 of <https://ecfsapi.fcc.gov/file/7021690471.pdf>.

<sup>3</sup> See p. 107 of <https://ecfsapi.fcc.gov/file/7021690471.pdf>.

exceeding a few hundred meters for all azimuths and significantly pessimistic for some azimuths at shorter distances. Importantly, however, LTE macro base stations may be separated by distances as small as 250 m and small cell outdoor base stations even shorter distances (see Table 3-13). Over several hundred meters in all environments including dense urban, the free-space propagation and two-ray propagation models are appropriately conservative models to protect GPS/GNSS receivers from interference from adjacent band mobile broadband systems.

## **APPENDIX J**

### **INVERSE MODELING RESULTS**

# TABLE OF CONTENTS

TABLE OF CONTENTS.....	2
LIST OF FIGURES .....	4
LIST OF TABLES .....	6
REFERENCES .....	7
APPENDIX.....	8
Appendix J. Bounding and Median EIRP Tolerance Masks (ETM) for Single Transmitter .....	8
J.1 GPS L1 C/A ETMs .....	8
J.1.1 Micro Urban Deployment.....	8
J.1.1.1 Bounding ETMs.....	8
J.1.1.1.1 FSPL Propagation Model.....	8
J.1.1.1.2 2-Ray Path loss model .....	10
J.1.1.2 Median ETMs .....	11
J.1.1.2.1 FSPL Propagation Model.....	12
J.1.1.2.2 2-Ray Path loss model .....	13
J.1.2 Macro Urban Deployment .....	14
J.1.2.1 Bounding ETMs.....	15
J.1.2.1.1 FSPL Propagation Model.....	15
J.1.2.1.2 2-Ray Path loss model .....	16
J.1.2.2 Median ETMs .....	18
J.1.2.2.1 FSPL Propagation Model.....	18
J.1.2.2.2 2-Ray Path loss model .....	20
J.2 All GNSS services.....	22
J.2.1 Micro Urban Deployment.....	22
J.2.1.1 Bounding ETMs.....	22
J.2.1.1.1 FSPL Propagation Model.....	22
J.2.1.1.2 2-Ray Path loss model .....	24
J.2.1.2 Median ETMs .....	26

J.2.1.2.1	FSPL Propagation Model.....	26
J.2.1.2.2	2-Ray Path loss model .....	28
J.2.2	Macro Urban Deployment .....	29
J.2.2.1	Bounding ETMs.....	30
J.2.2.1.1	FSPL Propagation Model.....	30
J.2.2.1.2	2-Ray Path loss model .....	31
J.2.2.2	Median ETMs .....	33
J.2.2.2.1	FSPL Propagation Model.....	33
J.2.2.2.2	2-Ray Path loss model .....	35

## LIST OF FIGURES

Figure J-1: GPS L1 C/A, Micro Urban, Bounding EIRP Mask: FSPL, $d_{\text{Standoff}} = 500$ m.....	8
Figure J-2: GPS L1 C/A, Micro Urban, Bounding EIRP Mask: FSPL, $d_{\text{Standoff}} = 100$ m.....	9
Figure J-3: GPS L1 C/A, Micro Urban, Bounding EIRP Mask: FSPL, $d_{\text{Standoff}} = 10$ m.....	9
Figure J-4: GPS L1 C/A, Micro Urban, Bounding EIRP Mask: 2-Ray, $d_{\text{Standoff}} = 500$ m.....	10
Figure J-5: GPS L1 C/A, Micro Urban, Bounding EIRP Mask: 2-Ray, $d_{\text{Standoff}} = 100$ m.....	10
Figure J-6: GPS L1 C/A, Micro Urban, Bounding EIRP Mask: 2-Ray, $d_{\text{Standoff}} = 10$ m.....	11
Figure J-7: GPS L1 C/A, Micro Urban, Median EIRP Mask: FSPL, $d_{\text{Standoff}} = 500$ m.....	12
Figure J-8: GPS L1 C/A, Micro Urban, Median EIRP Mask: FSPL, $d_{\text{Standoff}} = 100$ m.....	12
Figure J-9: GPS L1 C/A, Micro Urban, Median EIRP Mask: FSPL, $d_{\text{Standoff}} = 10$ m.....	13
Figure J-10: GPS L1 C/A, Micro Urban, Median EIRP Mask: 2-Ray, $d_{\text{Standoff}} = 500$ m.....	13
Figure J-11: GPS L1 C/A, Micro Urban, Median EIRP Mask: 2-Ray, $d_{\text{Standoff}} = 100$ m.....	14
Figure J-12: GPS L1 C/A, Micro Urban, Median EIRP Mask: 2-Ray, $d_{\text{Standoff}} = 10$ m.....	14
Figure J-13: GPS L1 C/A, Macro Urban, Bounding EIRP Mask: FSPL, $d_{\text{Standoff}} = 1000$ m.....	15
Figure J-14: GPS L1 C/A, Macro Urban, Bounding EIRP Mask: FSPL, $d_{\text{Standoff}} = 100$ m.....	16
Figure J-15: GPS L1 C/A, Macro Urban, Bounding EIRP Mask: FSPL, $d_{\text{Standoff}} = 10$ m.....	16
Figure J-16: GPS L1 C/A, Macro Urban, Bounding EIRP Mask: 2-Ray, $d_{\text{Standoff}} = 1000$ m.....	17
Figure J-17: GPS L1 C/A, Macro Urban, Bounding EIRP Mask: 2-Ray, $d_{\text{Standoff}} = 100$ m.....	17
Figure J-18: GPS L1 C/A, Macro Urban, Bounding EIRP Mask: 2-Ray, $d_{\text{Standoff}} = 10$ m.....	18
Figure J-19: GPS L1 C/A, Macro Urban, Median EIRP Mask: FSPL, $d_{\text{Standoff}} = 1000$ m.....	19
Figure J-20: GPS L1 C/A, Macro Urban, Median EIRP Mask: FSPL, $d_{\text{Standoff}} = 100$ m.....	19
Figure J-21: GPS L1 C/A, Macro Urban, Median EIRP Mask: FSPL, $d_{\text{Standoff}} = 10$ m.....	20
Figure J-22: GPS L1 C/A, Macro Urban, Median EIRP Mask: 2-Ray, $d_{\text{Standoff}} = 1000$ m.....	21
Figure J-23: GPS L1 C/A, Macro Urban, Median EIRP Mask: 2-Ray, $d_{\text{Standoff}} = 100$ m.....	21
Figure J-24: GPS L1 C/A, Macro Urban, Median EIRP Mask: 2-Ray, $d_{\text{Standoff}} = 10$ m.....	22
Figure J-25: All GNSS, Micro Urban, Bounding EIRP Mask: FSPL, $d_{\text{Standoff}} = 500$ m.....	23
Figure J-26: All GNSS, Micro Urban, Bounding EIRP Mask: FSPL, $d_{\text{Standoff}} = 100$ m.....	23
Figure J-27: All GNSS, Micro Urban, Bounding EIRP Mask: FSPL, $d_{\text{Standoff}} = 10$ m.....	24
Figure J-28: All GNSS, Micro Urban, Bounding EIRP Mask: 2-Ray, $d_{\text{Standoff}} = 500$ m.....	25
Figure J-29: All GNSS, Micro Urban, Bounding EIRP Mask: 2-Ray, $d_{\text{Standoff}} = 100$ m.....	25
Figure J-30: All GNSS, Micro Urban, Bounding EIRP Mask: 2-Ray, $d_{\text{Standoff}} = 10$ m.....	26
Figure J-31: All GNSS, Micro Urban, Median EIRP Mask: FSPL, $d_{\text{Standoff}} = 500$ m.....	27
Figure J-32: All GNSS, Micro Urban, Median EIRP Mask: FSPL, $d_{\text{Standoff}} = 100$ m.....	27
Figure J-33: All GNSS, Micro Urban, Median EIRP Mask: FSPL, $d_{\text{Standoff}} = 10$ m.....	28
Figure J-34: All GNSS, Micro Urban, Median EIRP Mask: 2-Ray, $d_{\text{Standoff}} = 500$ m.....	28
Figure J-35: All GNSS, Micro Urban, Median EIRP Mask: 2-Ray, $d_{\text{Standoff}} = 100$ m.....	29
Figure J-36: All GNSS, Micro Urban, Median EIRP Mask: 2-Ray, $d_{\text{Standoff}} = 10$ m.....	29



Figure J-37: All GNSS, Macro Urban, Bounding EIRP Mask: FSPL, $d_{\text{Standoff}} = 1000$ m .....	30
Figure J-38: All GNSS, Macro Urban, Bounding EIRP Mask: FSPL, $d_{\text{Standoff}} = 100$ m .....	31
Figure J-39: All GNSS, Macro Urban, Bounding EIRP Mask: FSPL, $d_{\text{Standoff}} = 10$ m .....	31
Figure J-40: All GNSS, Macro Urban, Bounding EIRP Mask: 2-Ray, $d_{\text{Standoff}} = 1000$ m.....	32
Figure J-41: All GNSS, Macro Urban, Bounding EIRP Mask: 2-Ray, $d_{\text{Standoff}} = 100$ m.....	32
Figure J-42: All GNSS, Macro Urban, Bounding EIRP Mask: 2-Ray, $d_{\text{Standoff}} = 10$ m.....	33
Figure J-43: All GNSS, Macro Urban, Median EIRP Mask: FSPL, $d_{\text{Standoff}} = 1000$ m.....	34
Figure J-44: All GNSS, Macro Urban, Median EIRP Mask: FSPL, $d_{\text{Standoff}} = 100$ m.....	34
Figure J-45: All GNSS, Macro Urban, Median EIRP Mask: FSPL, $d_{\text{Standoff}} = 10$ m.....	35
Figure J-46: All GNSS, Macro Urban, Median EIRP Mask: 2-Ray, $d_{\text{Standoff}} = 1000$ m .....	36
Figure J-47: All GNSS, Macro Urban, Median EIRP Mask: 2-Ray, $d_{\text{Standoff}} = 100$ m .....	36
Figure J-48: All GNSS, Macro Urban, Median EIRP Mask: 2-Ray, $d_{\text{Standoff}} = 10$ m .....	37

## **LIST OF TABLES**

No table of figures entries found.

## **REFERENCES**

**There are no sources in the current document.**

# APPENDIX

## Appendix J. Bounding and Median EIRP Tolerance Masks (ETM) for Single Transmitter

### J.1 GPS L1 C/A ETMs

#### J.1.1 Micro Urban Deployment

##### J.1.1.1 Bounding ETMs

##### J.1.1.1.1 FSPL Propagation Model

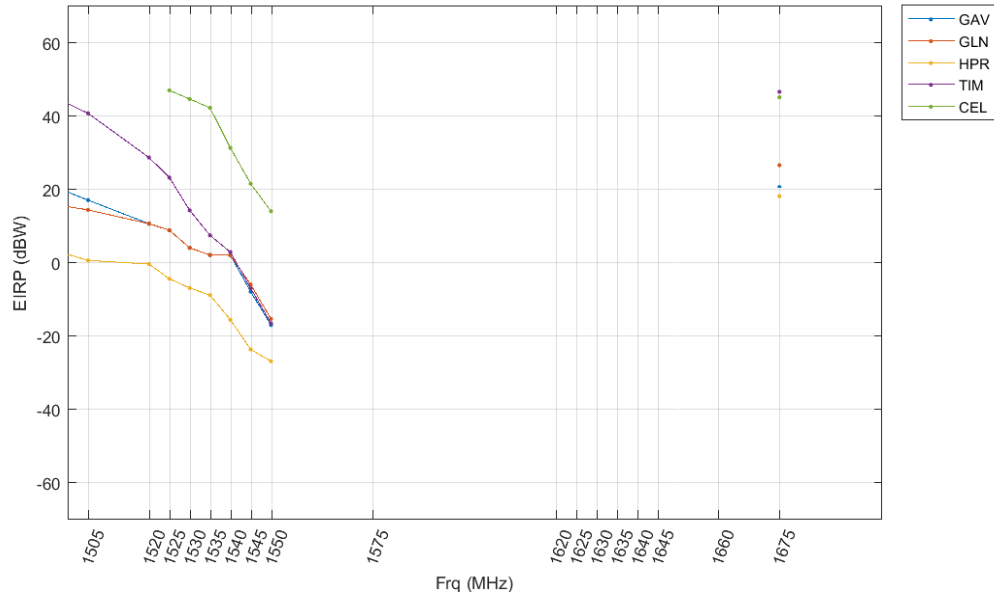
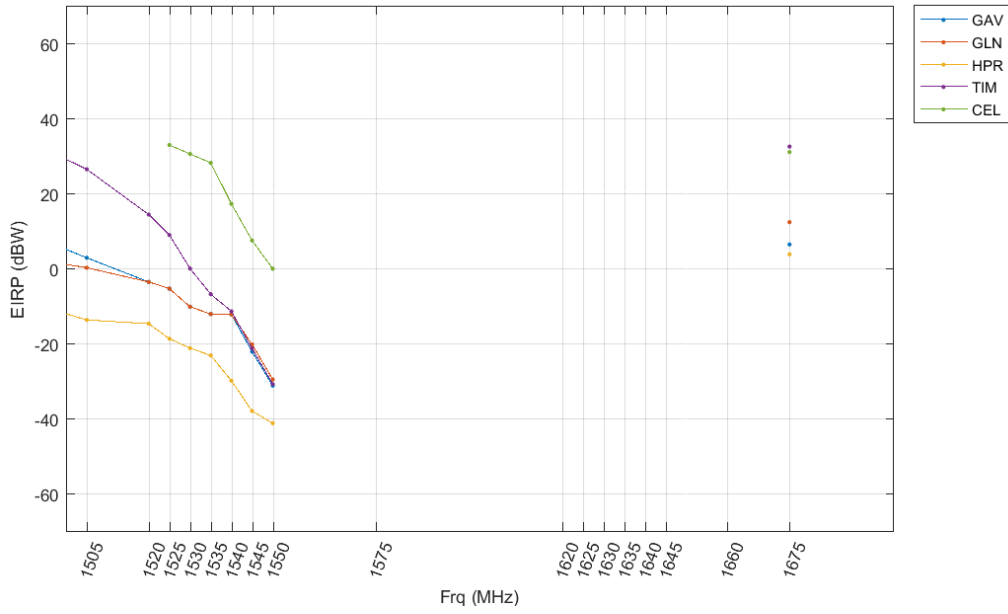
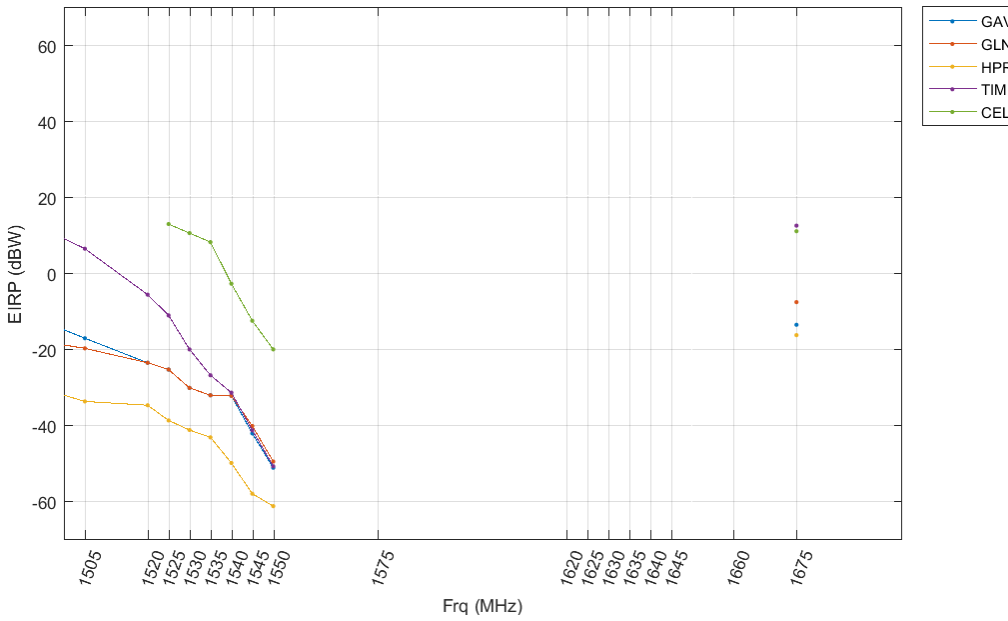


Figure J-1: GPS L1 C/A, Micro Urban, Bounding EIRP Mask: FSPL,  $d_{\text{Standoff}} = 500$  m



**Figure J-2: GPS L1 C/A, Micro Urban, Bounding EIRP Mask: FSPL,  $d_{\text{standoff}} = 100 \text{ m}$**



**Figure J-3: GPS L1 C/A, Micro Urban, Bounding EIRP Mask: FSPL,  $d_{\text{standoff}} = 10 \text{ m}$**

### J.1.1.1.2 2-Ray Path loss model

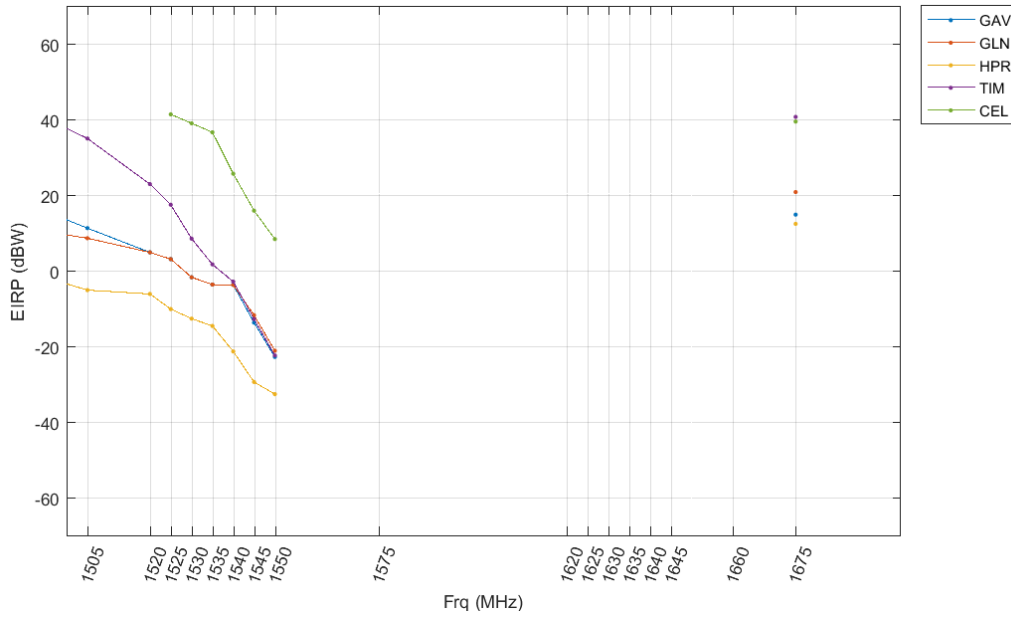


Figure J-4: GPS L1 C/A, Micro Urban, Bounding EIRP Mask: 2-Ray,  $d_{\text{standoff}} = 500 \text{ m}$

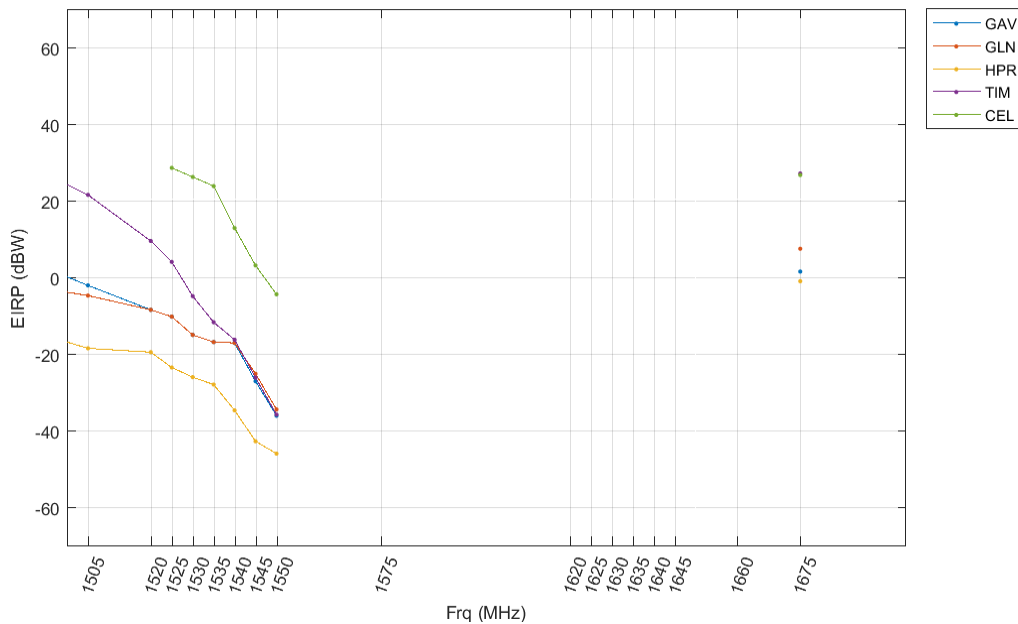
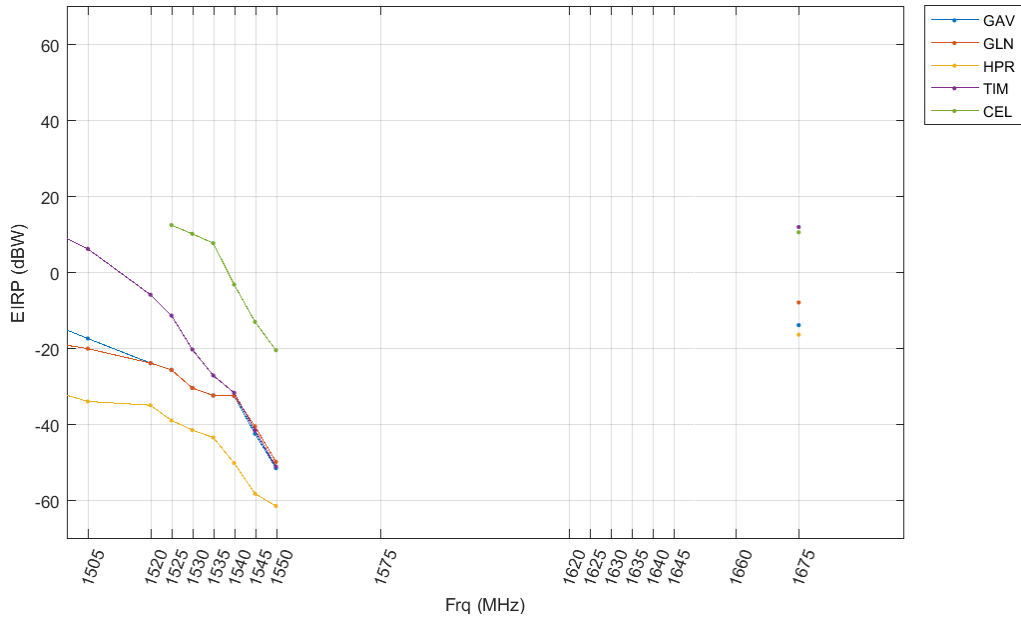


Figure J-5: GPS L1 C/A, Micro Urban, Bounding EIRP Mask: 2-Ray,  $d_{\text{standoff}} = 100 \text{ m}$



**Figure J-6: GPS L1 C/A, Micro Urban, Bounding EIRP Mask: 2-Ray,  $d_{\text{Standoff}} = 10 \text{ m}$**

### J.1.1.2 Median ETMs

### J.1.1.2.1 FSPL Propagation Model

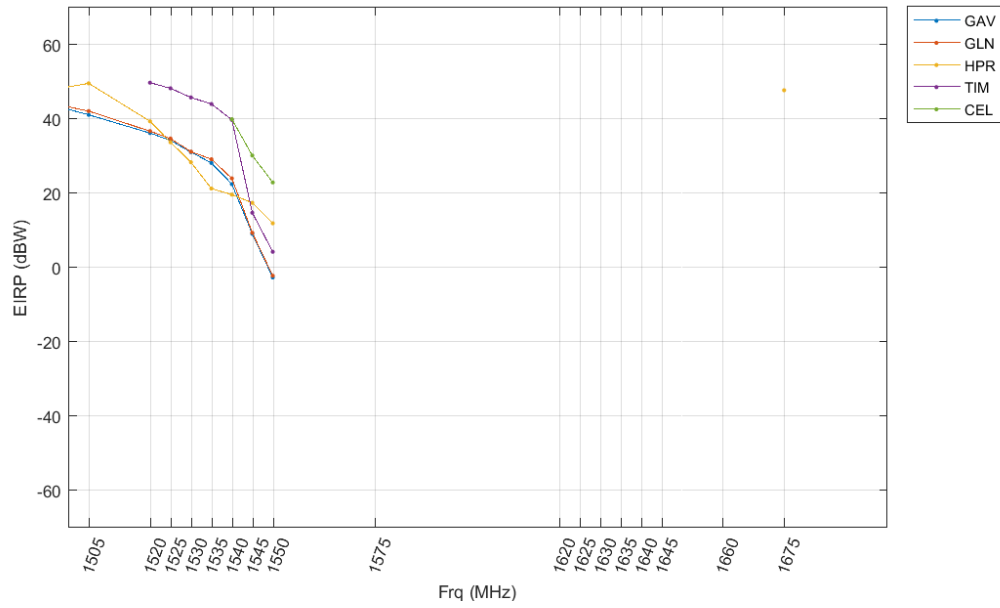


Figure J-7: GPS L1 C/A, Micro Urban, Median EIRP Mask: FSPL,  $d_{\text{standoff}} = 500 \text{ m}$

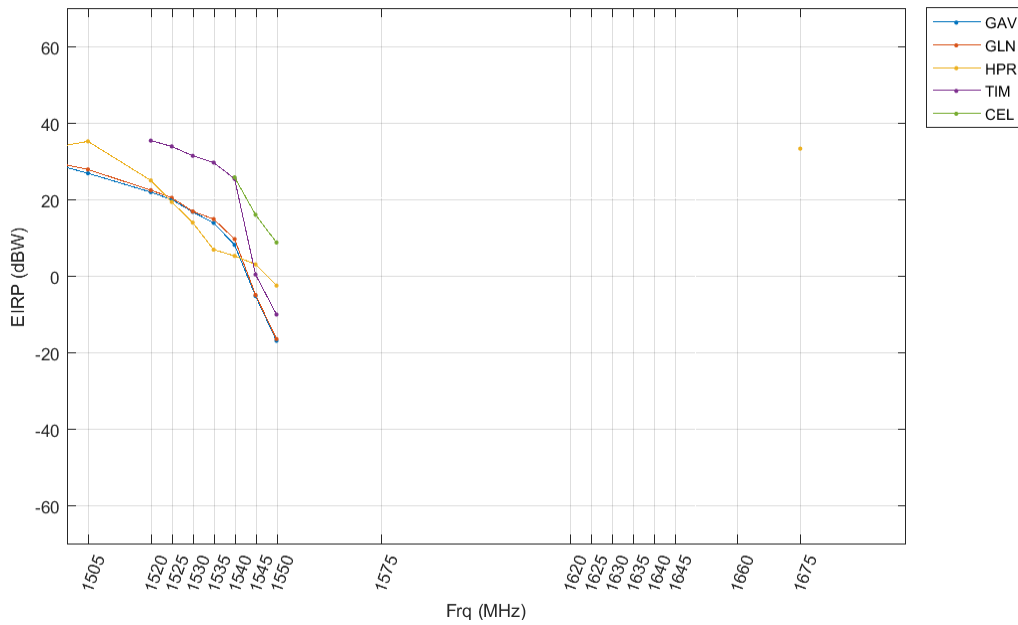
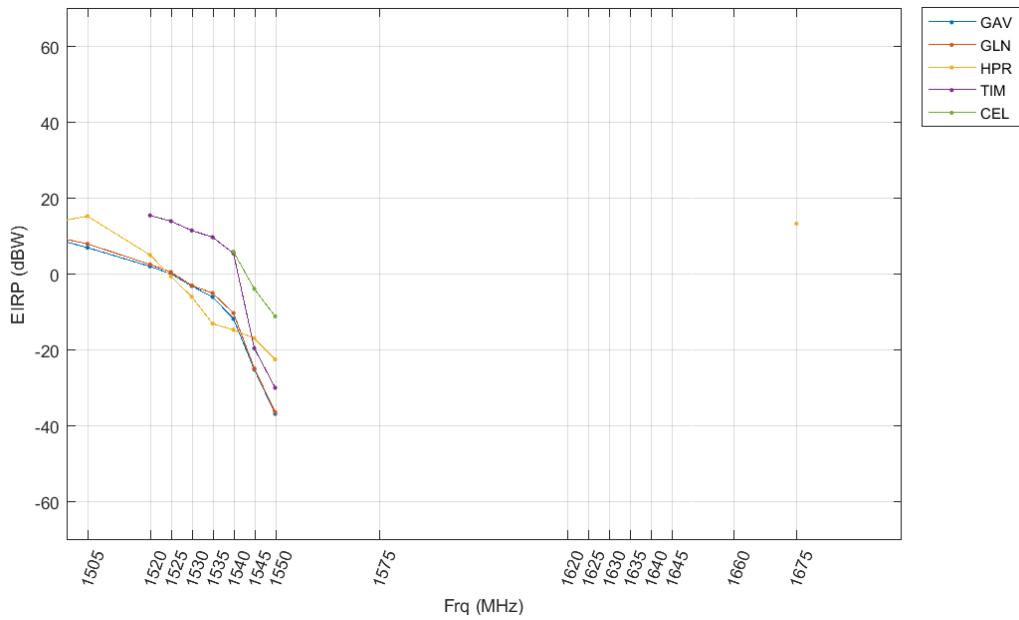


Figure J-8: GPS L1 C/A, Micro Urban, Median EIRP Mask: FSPL,  $d_{\text{standoff}} = 100 \text{ m}$





**Figure J-9: GPS L1 C/A, Micro Urban, Median EIRP Mask: FSPL,  $d_{\text{Standoff}} = 10 \text{ m}$**

**J.1.1.2.2 2-Ray Path loss model**

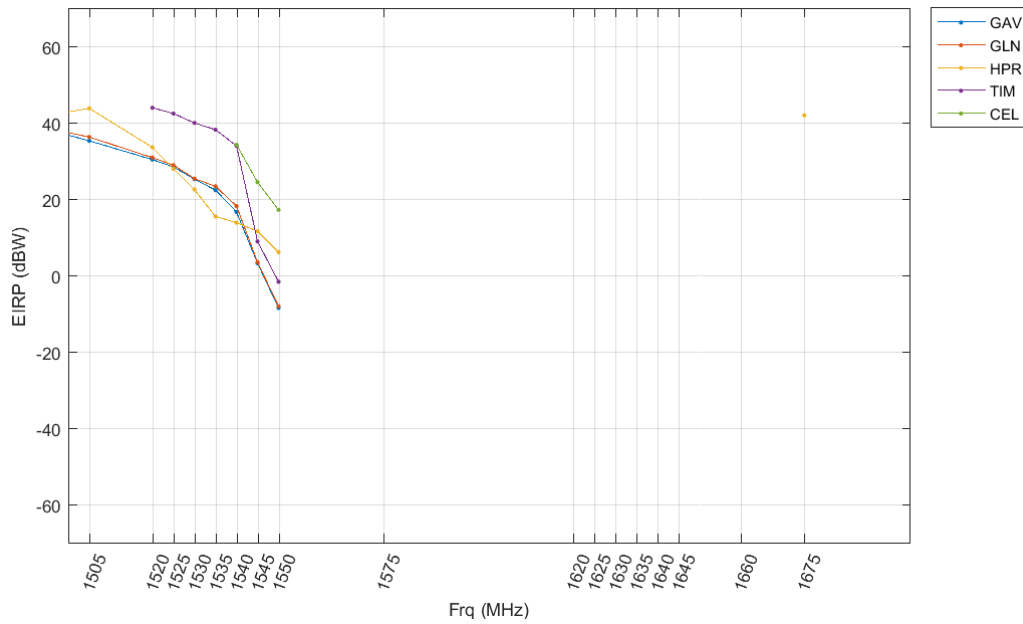


**Figure J-10: GPS L1 C/A, Micro Urban, Median EIRP Mask: 2-Ray,  $d_{\text{Standoff}} = 500 \text{ m}$**

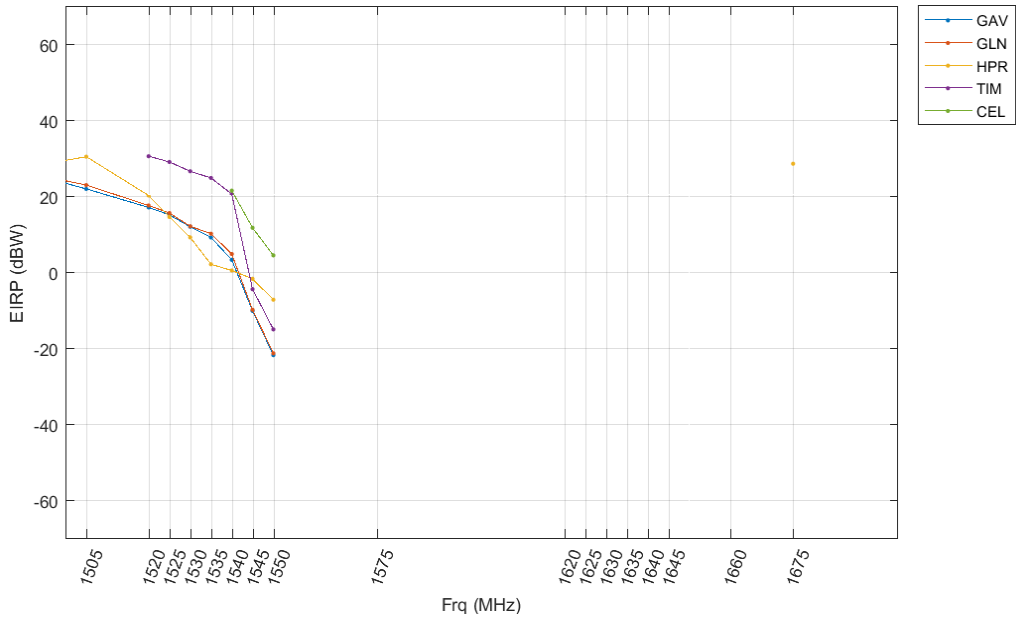


**Figure J-11: GPS L1 C/A, Micro Urban, Median EIRP Mask: 2-Ray,  $d_{\text{Standoff}} = 100 \text{ m}$**

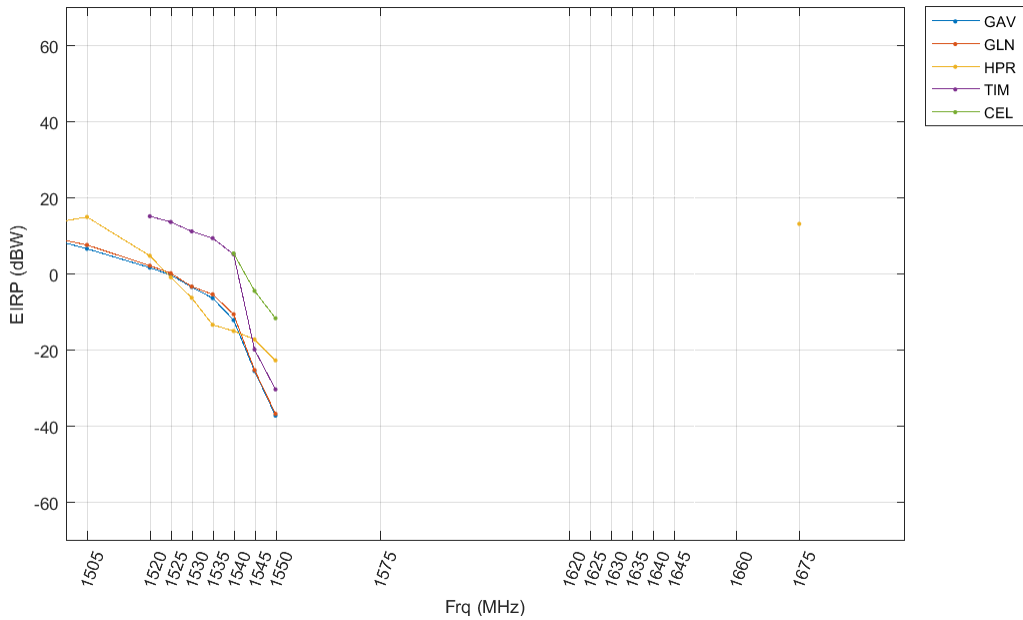


**Figure J-12: GPS L1 C/A, Micro Urban, Median EIRP Mask: 2-Ray,  $d_{\text{Standoff}} = 10 \text{ m}$**

### J.1.2 Macro Urban Deployment

### J.1.2.1 Bounding ETMs

#### J.1.2.1.1 FSPL Propagation Model

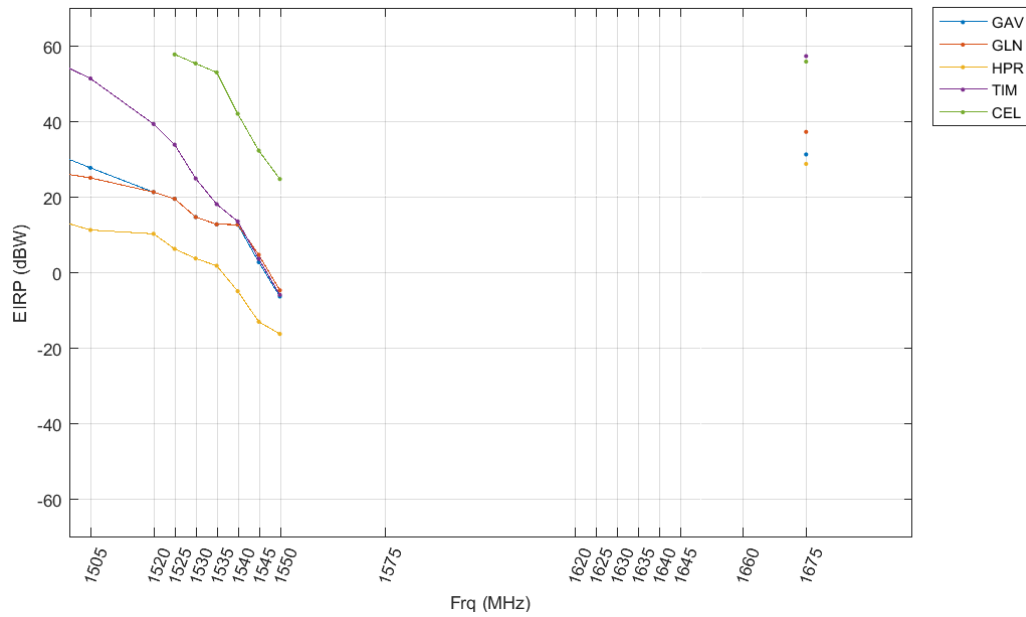


**Figure J-13: GPS L1 C/A, Macro Urban, Bounding EIRP Mask: FSPL,  $d_{\text{Standoff}} = 1000$  m**

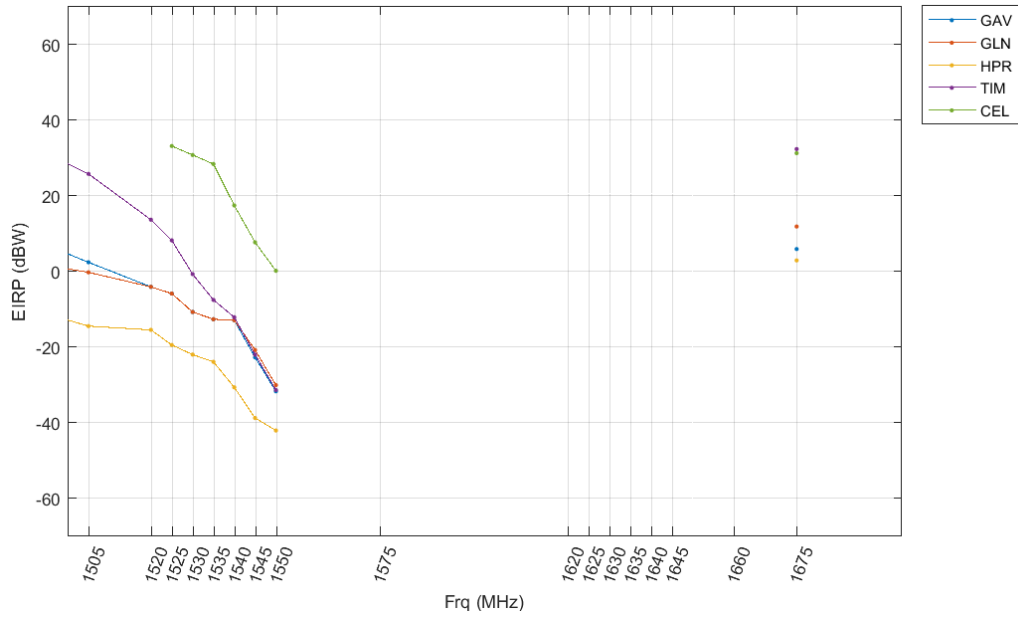


**Figure J-14: GPS L1 C/A, Macro Urban, Bounding EIRP Mask: FSPL,  $d_{\text{Standoff}} = 100$  m**

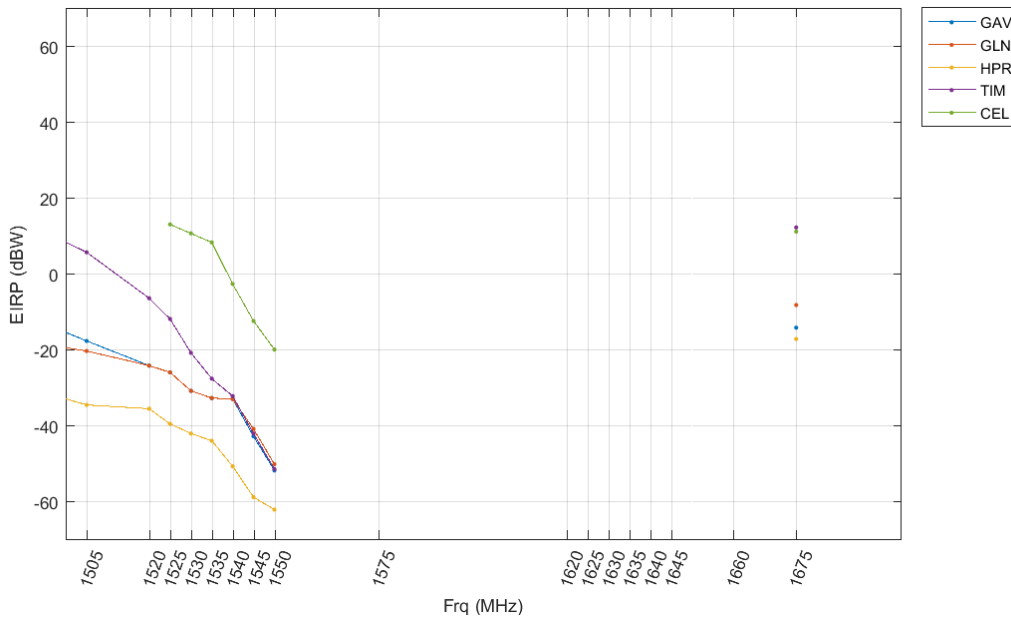


**Figure J-15: GPS L1 C/A, Macro Urban, Bounding EIRP Mask: FSPL,  $d_{\text{Standoff}} = 10$  m**

### J.1.2.1.2 2-Ray Path loss model

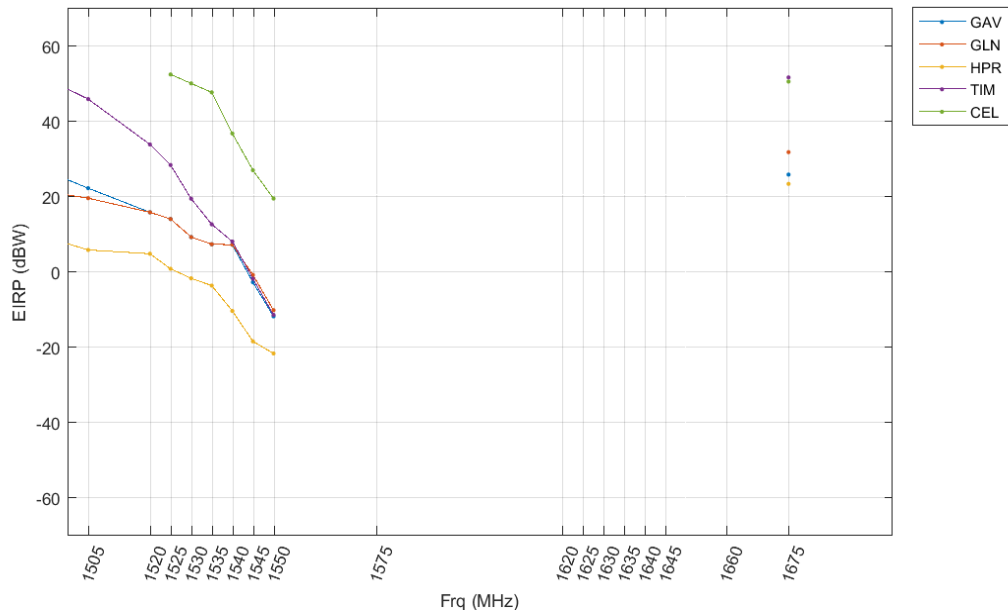


**Figure J-16: GPS L1 C/A, Macro Urban, Bounding EIRP Mask: 2-Ray,  $d_{\text{Standoff}} = 1000 \text{ m}$**

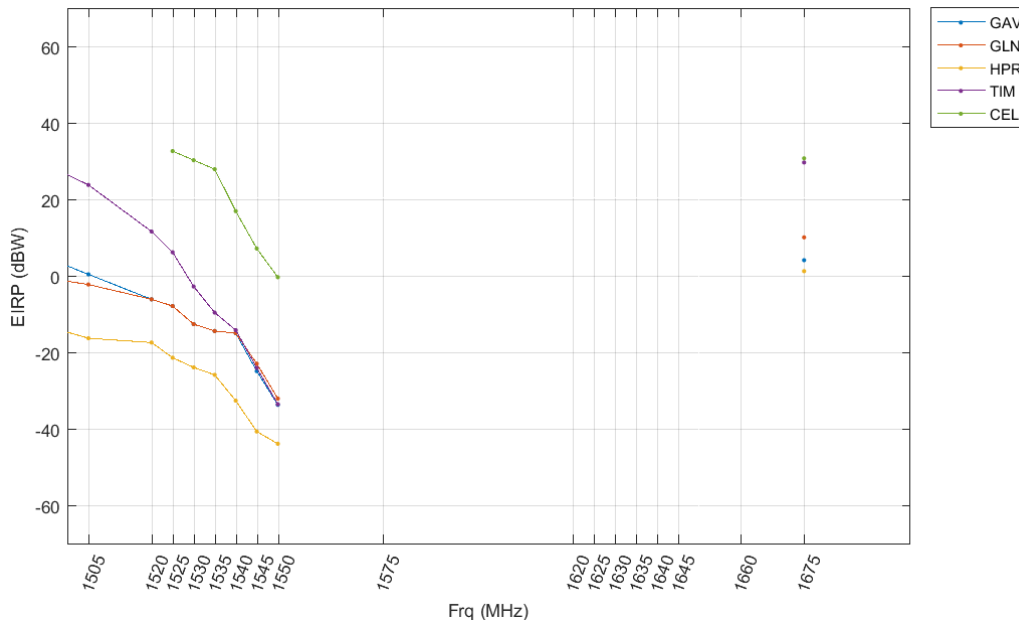


**Figure J-17: GPS L1 C/A, Macro Urban, Bounding EIRP Mask: 2-Ray,  $d_{\text{Standoff}} = 100 \text{ m}$**

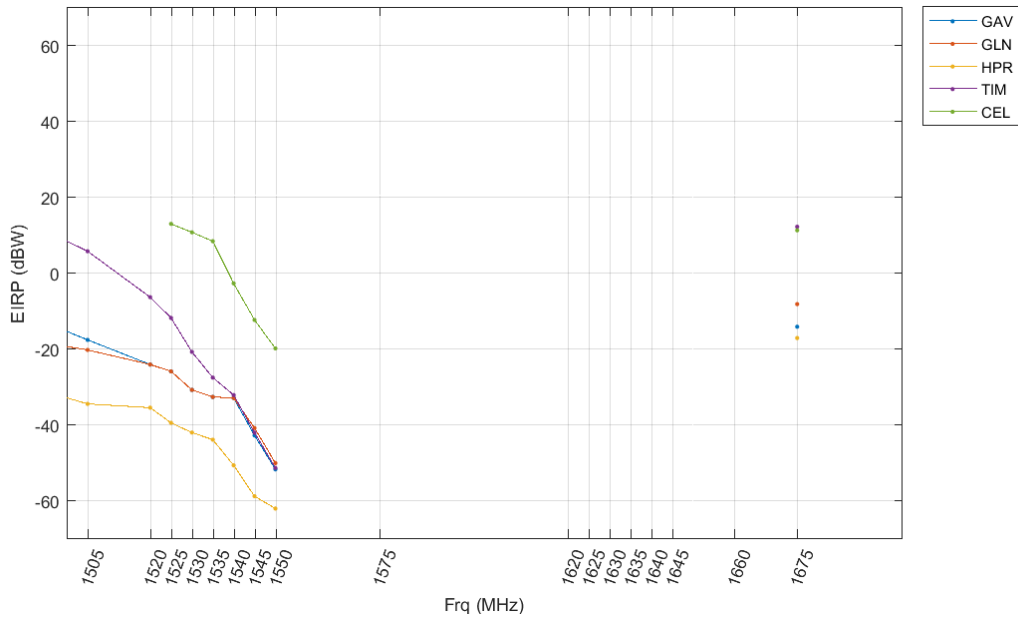


**Figure J-18: GPS L1 C/A, Macro Urban, Bounding EIRP Mask: 2-Ray,  $d_{\text{Standoff}} = 10 \text{ m}$**

### J.1.2.2 Median ETMs

#### J.1.2.2.1 FSPL Propagation Model

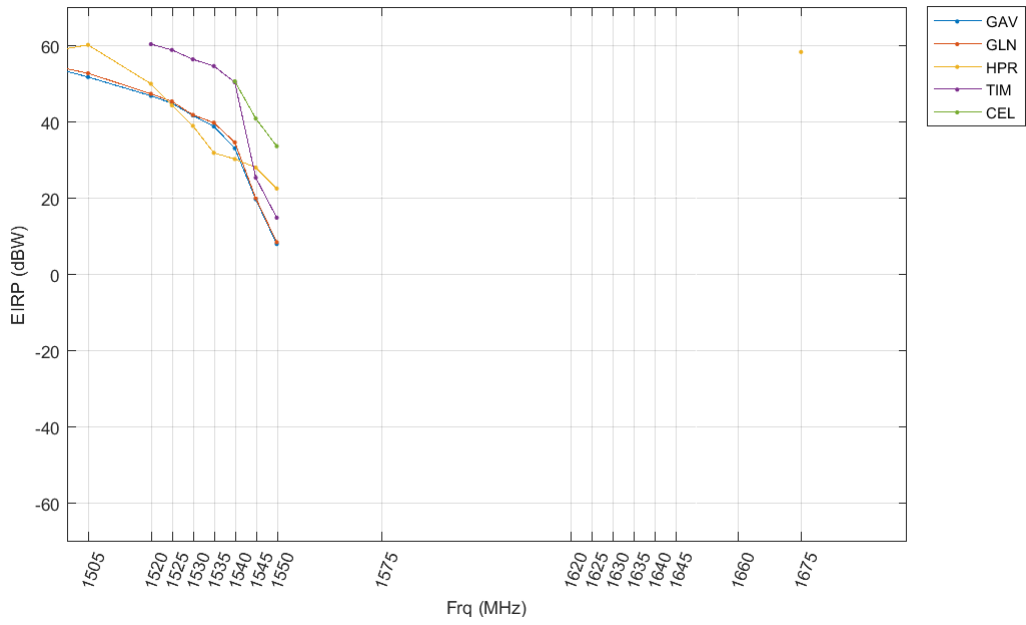


**Figure J-19: GPS L1 C/A, Macro Urban, Median EIRP Mask: FSPL,  $d_{\text{Standoff}} = 1000 \text{ m}$**

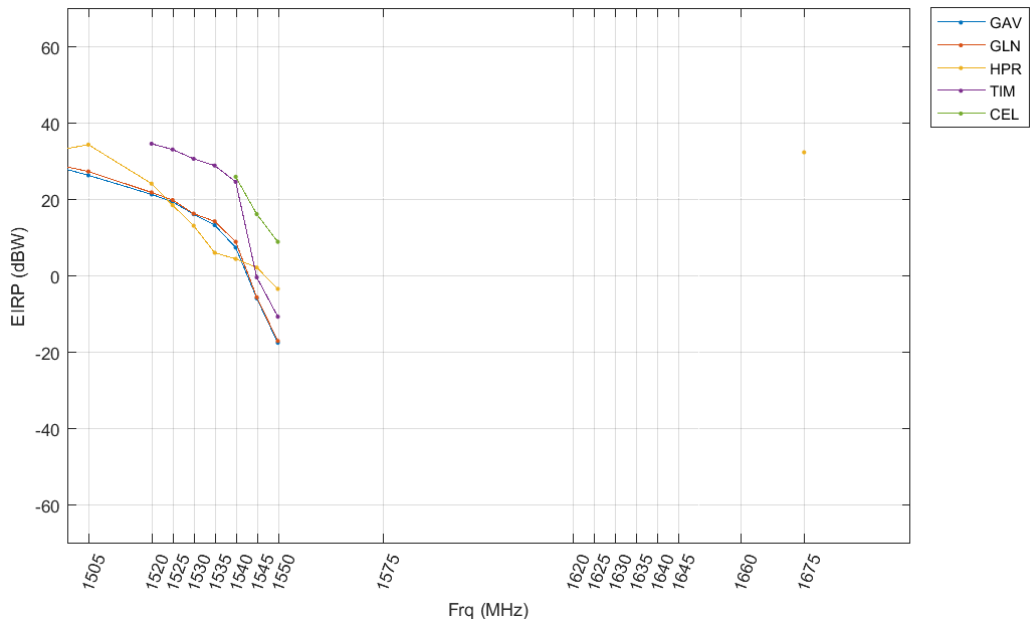


**Figure J-20: GPS L1 C/A, Macro Urban, Median EIRP Mask: FSPL,  $d_{\text{Standoff}} = 100 \text{ m}$**

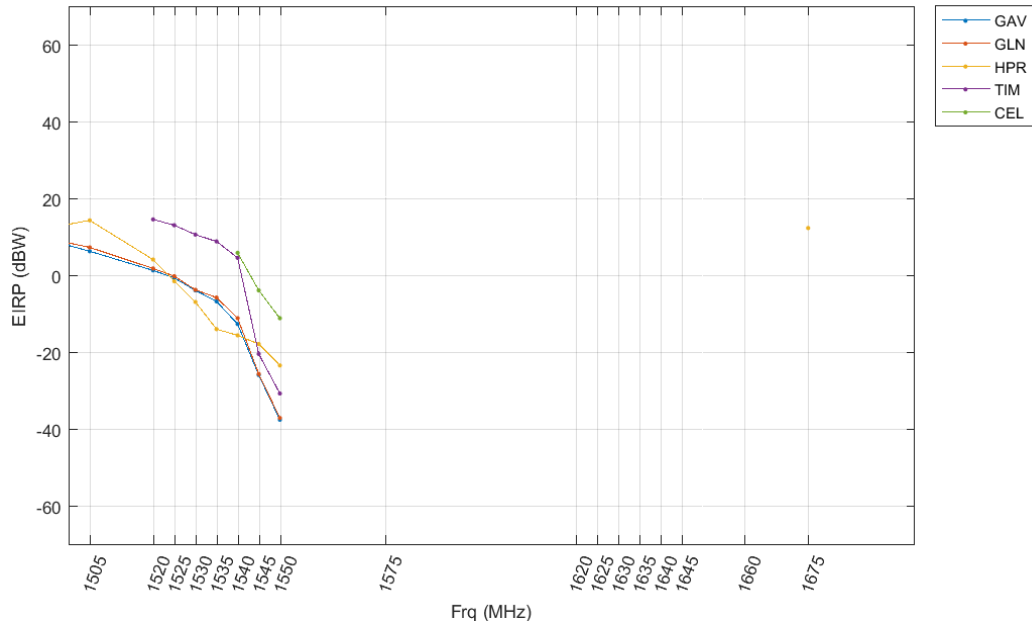


**Figure J-21: GPS L1 C/A, Macro Urban, Median EIRP Mask: FSPL,  $d_{\text{Standoff}} = 10 \text{ m}$**

#### J.1.2.2.2 2-Ray Path loss model



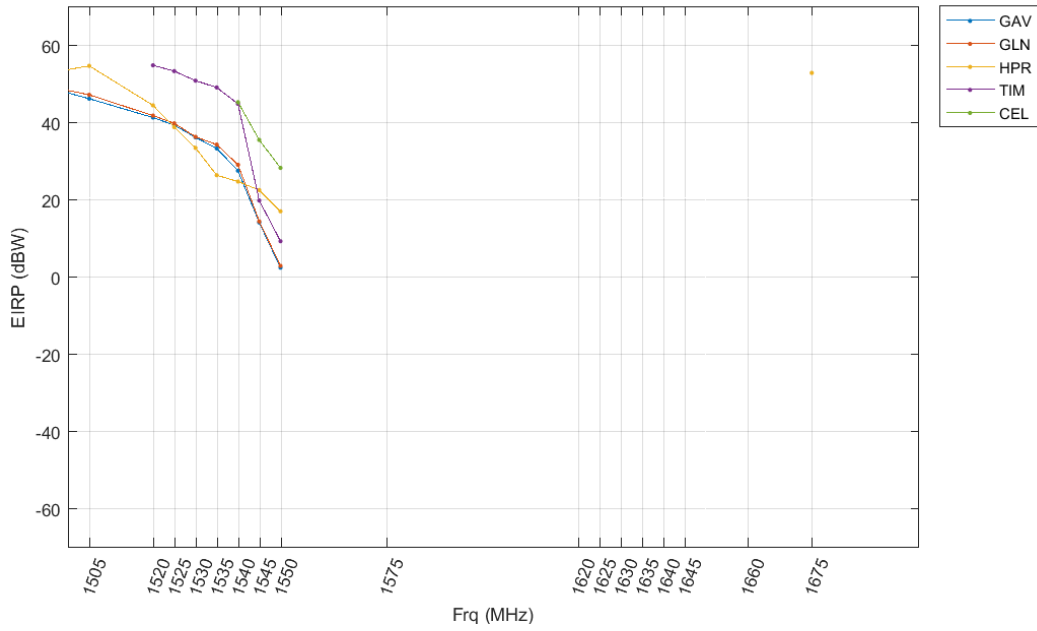


**Figure J-22: GPS L1 C/A, Macro Urban, Median EIRP Mask: 2-Ray,  $d_{\text{Standoff}} = 1000$  m**

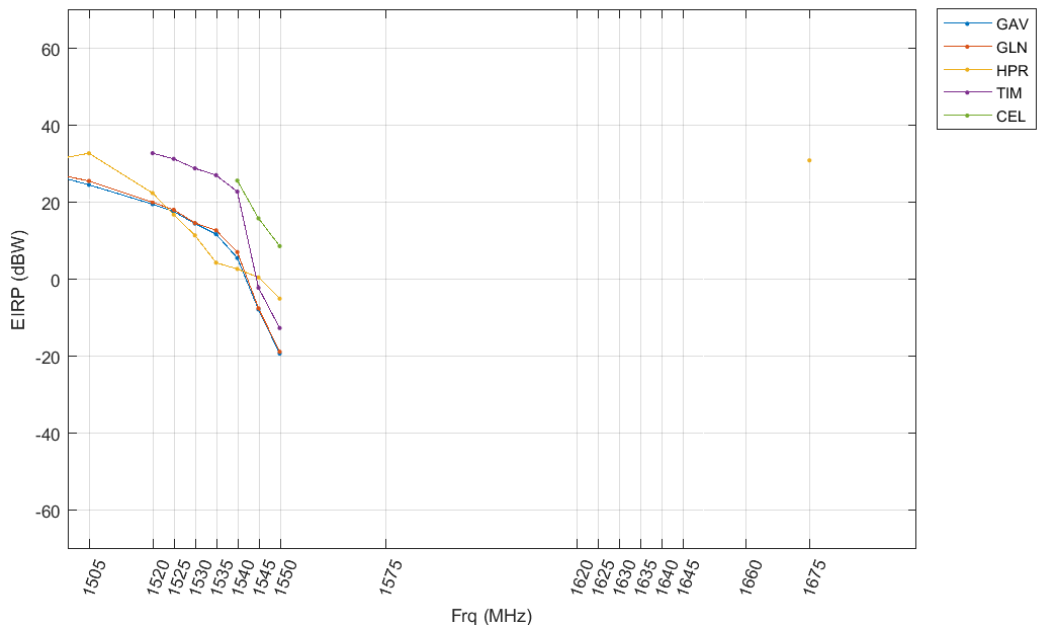


**Figure J-23: GPS L1 C/A, Macro Urban, Median EIRP Mask: 2-Ray,  $d_{\text{Standoff}} = 100$  m**

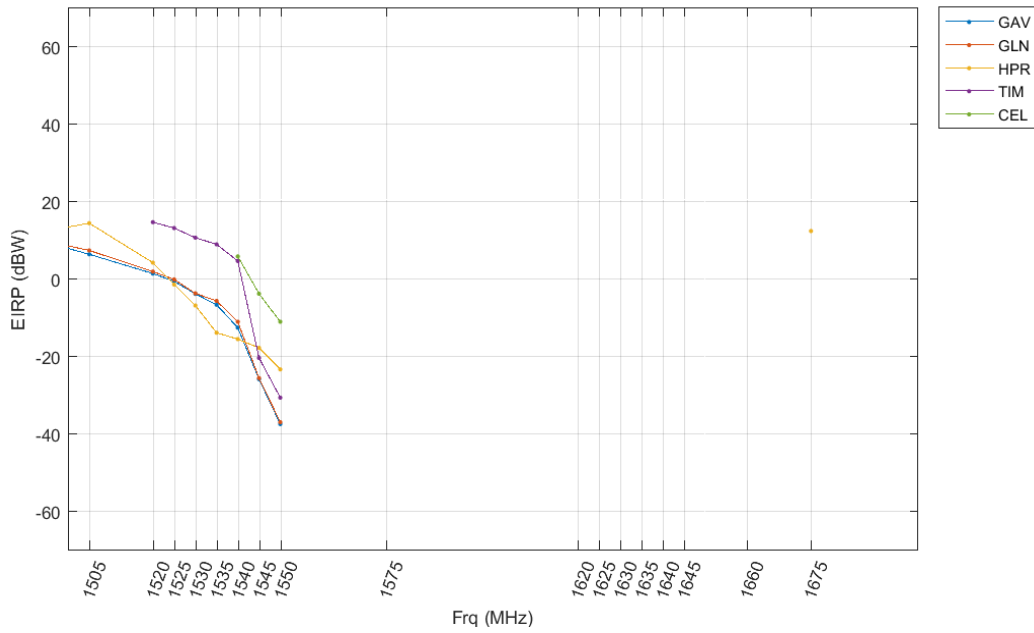


**Figure J-24: GPS L1 C/A, Macro Urban, Median EIRP Mask: 2-Ray,  $d_{\text{Standoff}} = 10 \text{ m}$**

## J.2 All GNSS services

### J.2.1 Micro Urban Deployment

#### J.2.1.1 Bounding ETMs

##### J.2.1.1.1 FSPL Propagation Model

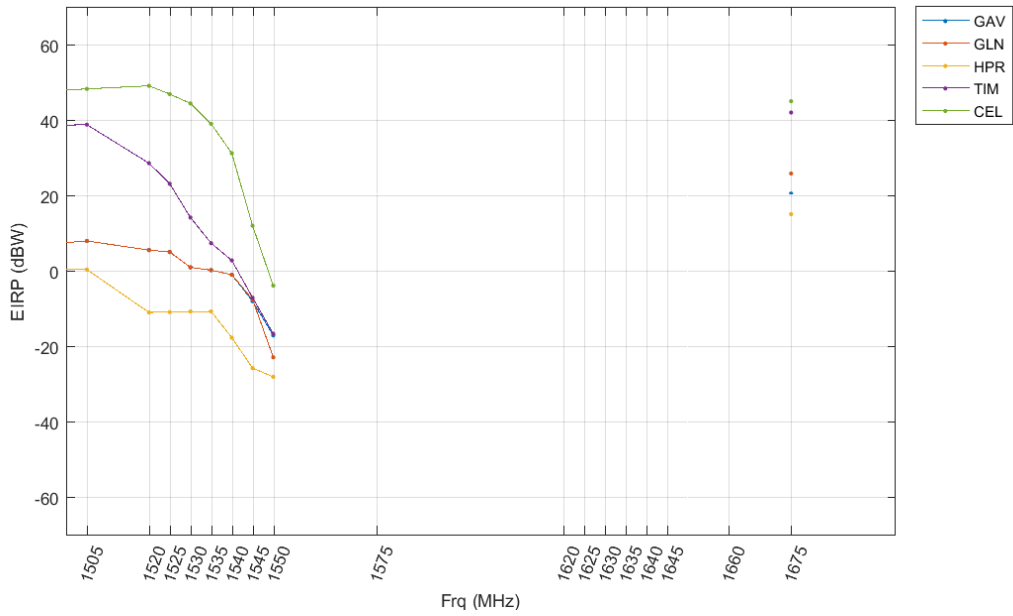


**Figure J-25: All GNSS, Micro Urban, Bounding EIRP Mask: FSPL,  $d_{\text{Standoff}} = 500$  m**

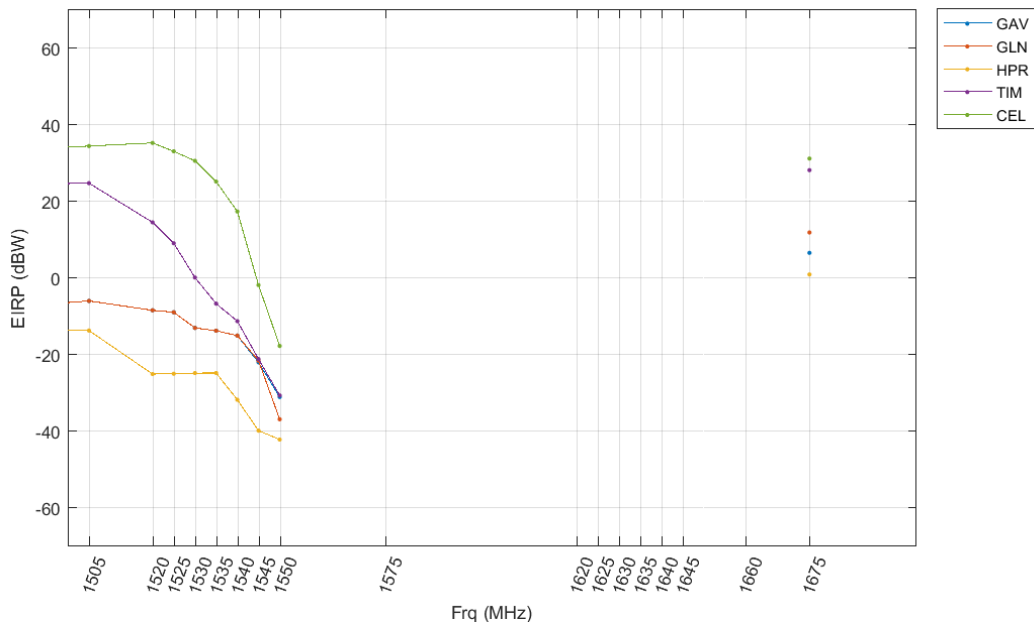


**Figure J-26: All GNSS, Micro Urban, Bounding EIRP Mask: FSPL,  $d_{\text{Standoff}} = 100$  m**

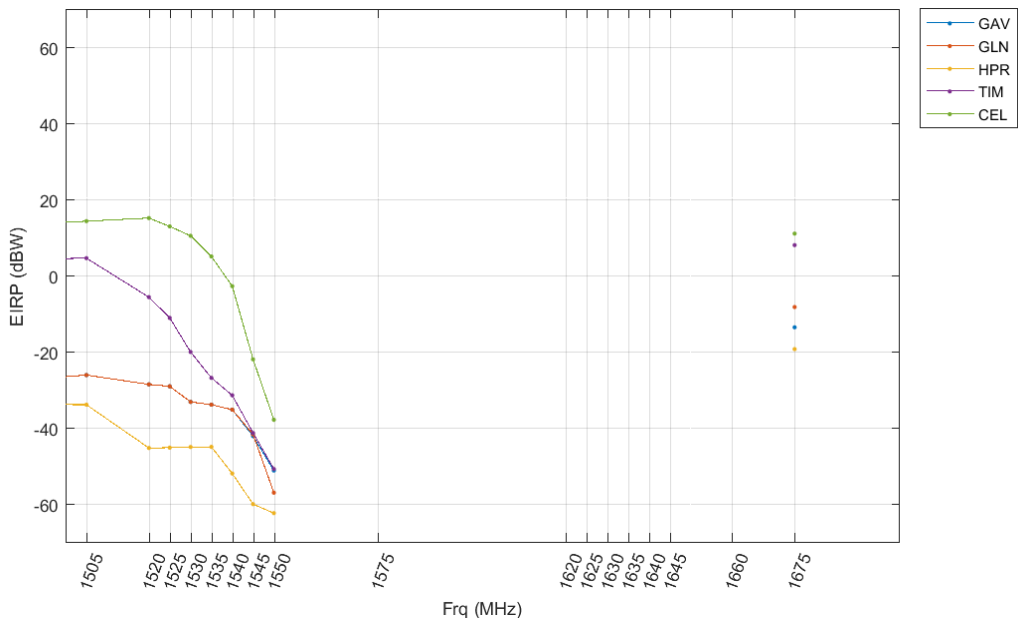


**Figure J-27: All GNSS, Micro Urban, Bounding EIRP Mask: FSPL,  $d_{\text{Standoff}} = 10 \text{ m}$**

**J.2.1.1.2 2-Ray Path loss model**

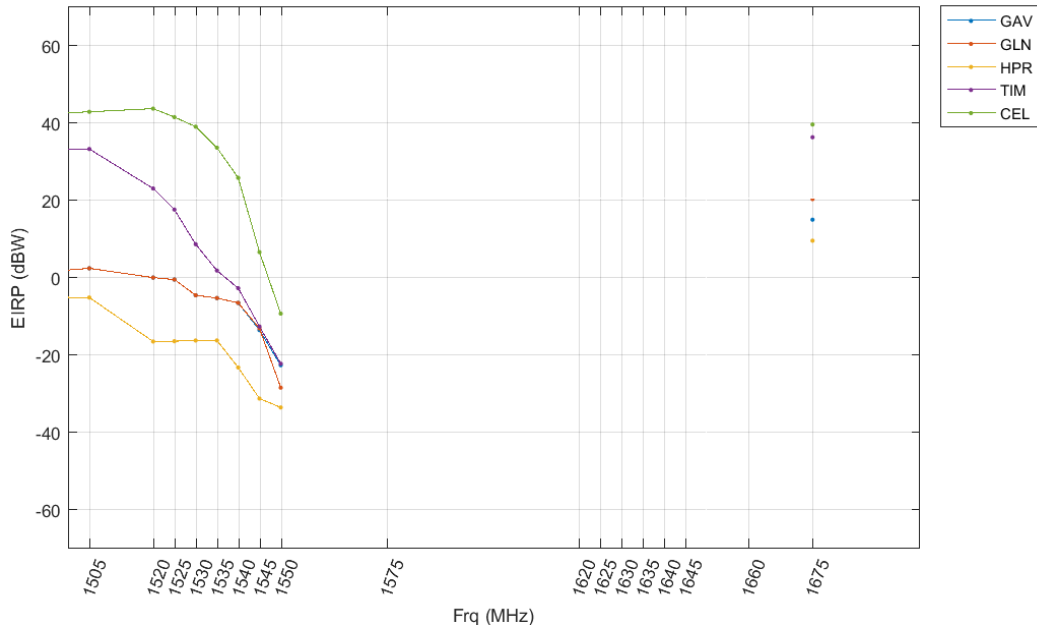


**Figure J-28: All GNSS, Micro Urban, Bounding EIRP Mask: 2-Ray,  $d_{\text{Standoff}} = 500$  m**

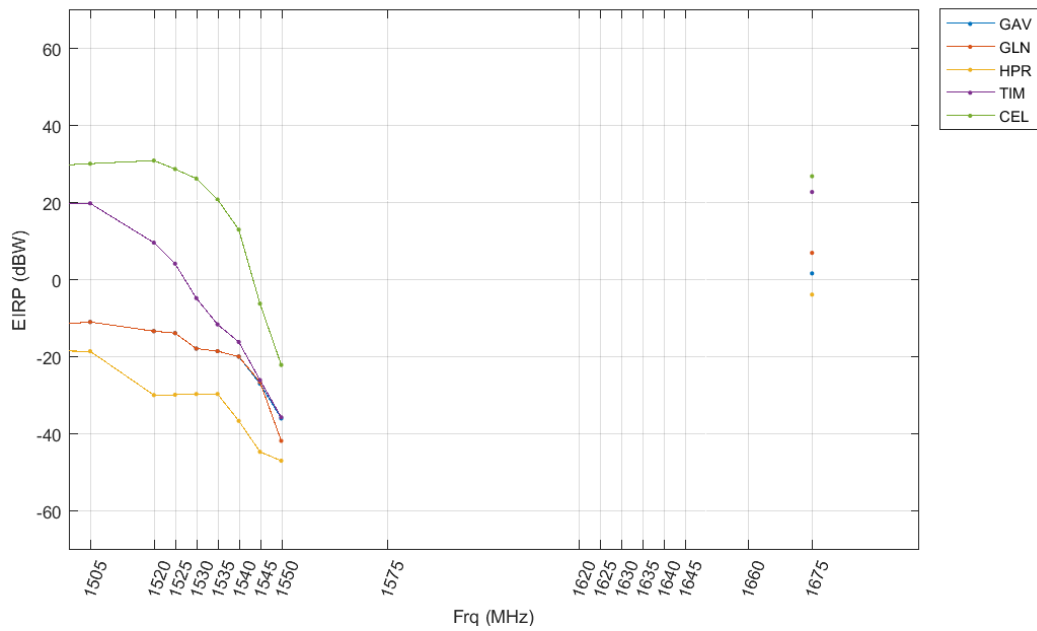


**Figure J-29: All GNSS, Micro Urban, Bounding EIRP Mask: 2-Ray,  $d_{\text{Standoff}} = 100$  m**

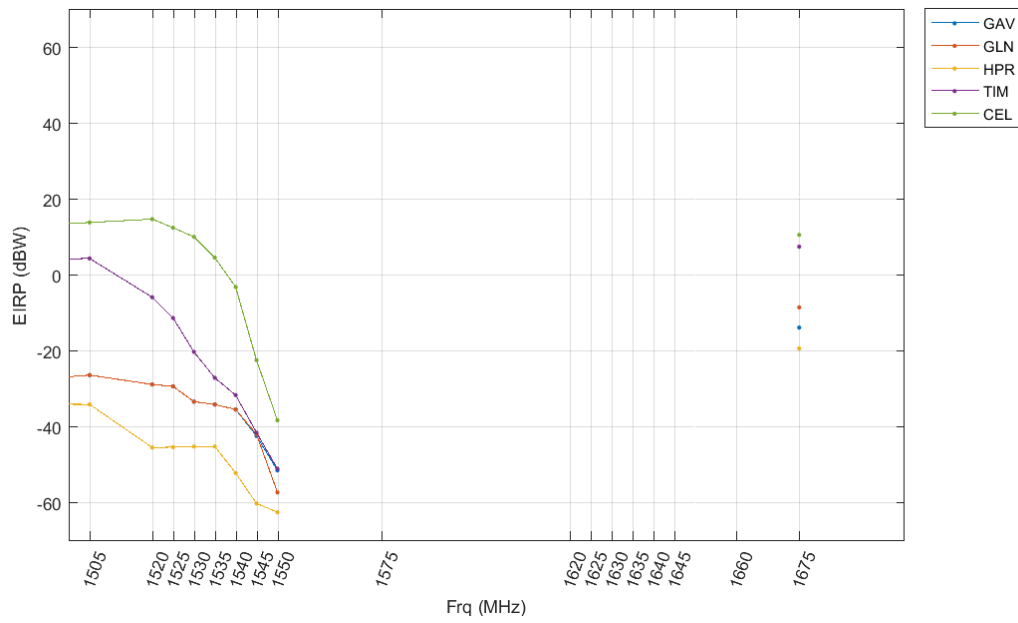


**Figure J-30: All GNSS, Micro Urban, Bounding EIRP Mask: 2-Ray,  $d_{\text{Standoff}} = 10 \text{ m}$**

### J.2.1.2 Median ETMs

#### J.2.1.2.1 FSPL Propagation Model

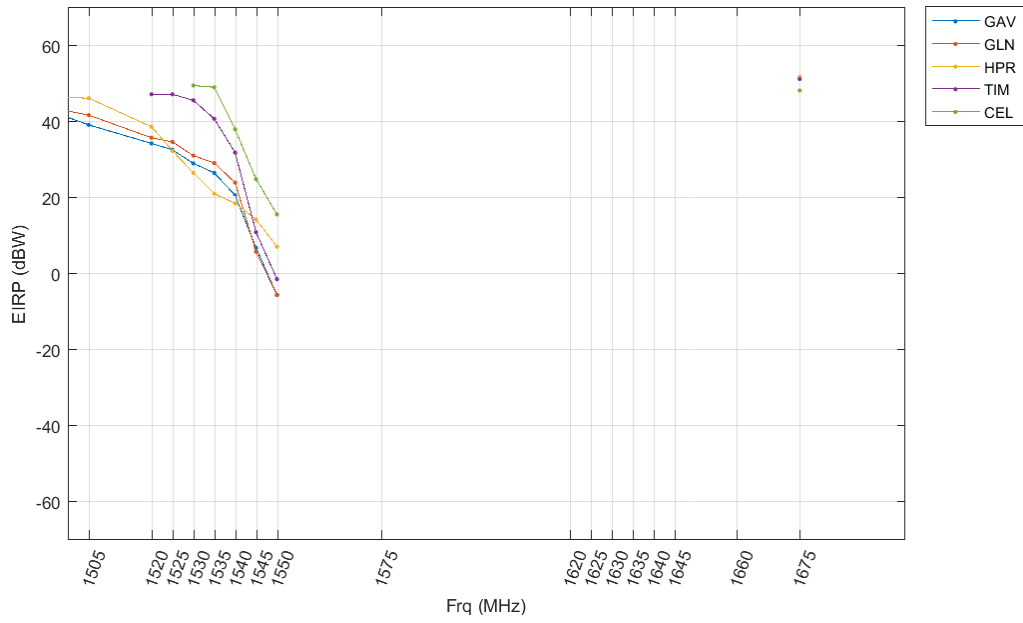


**Figure J-31: All GNSS, Micro Urban, Median EIRP Mask: FSPL,  $d_{\text{Standoff}} = 500$  m**

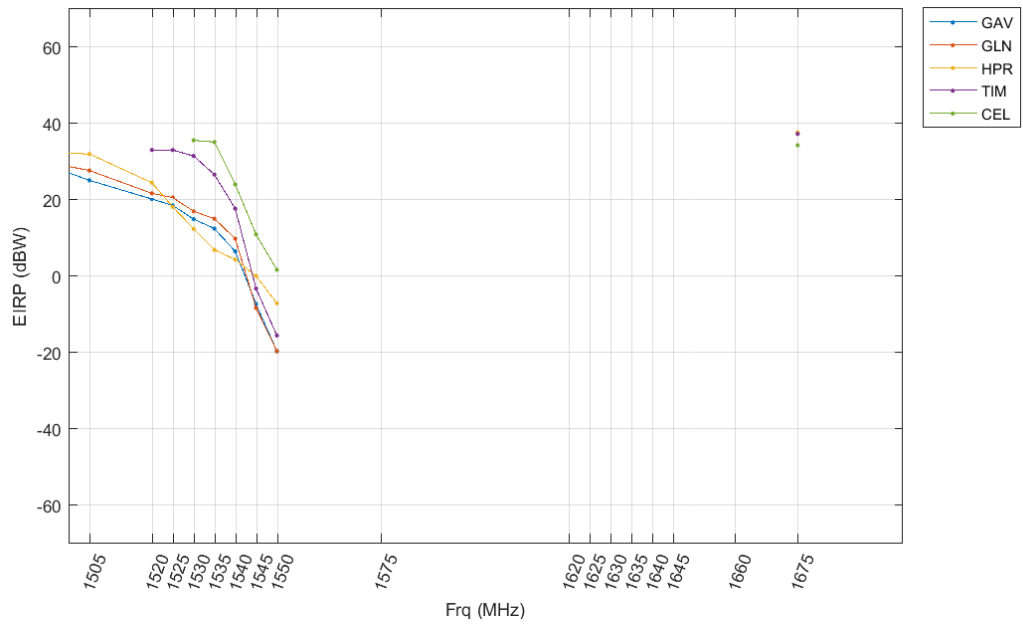


**Figure J-32: All GNSS, Micro Urban, Median EIRP Mask: FSPL,  $d_{\text{Standoff}} = 100$  m**

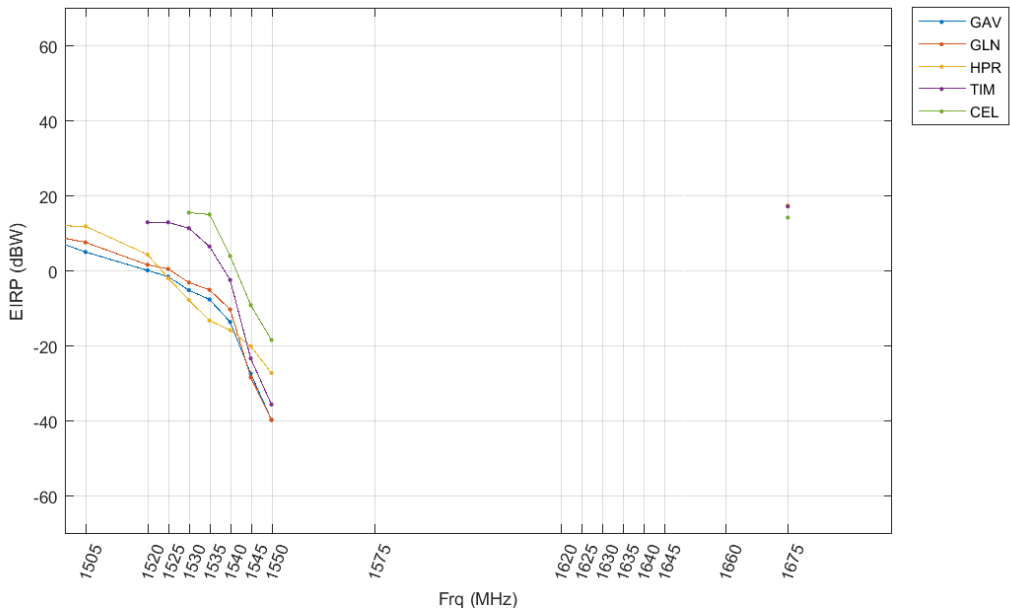


**Figure J-33: All GNSS, Micro Urban, Median EIRP Mask: FSPL,  $d_{\text{Standoff}} = 10 \text{ m}$**

**J.2.1.2.2 2-Ray Path loss model**

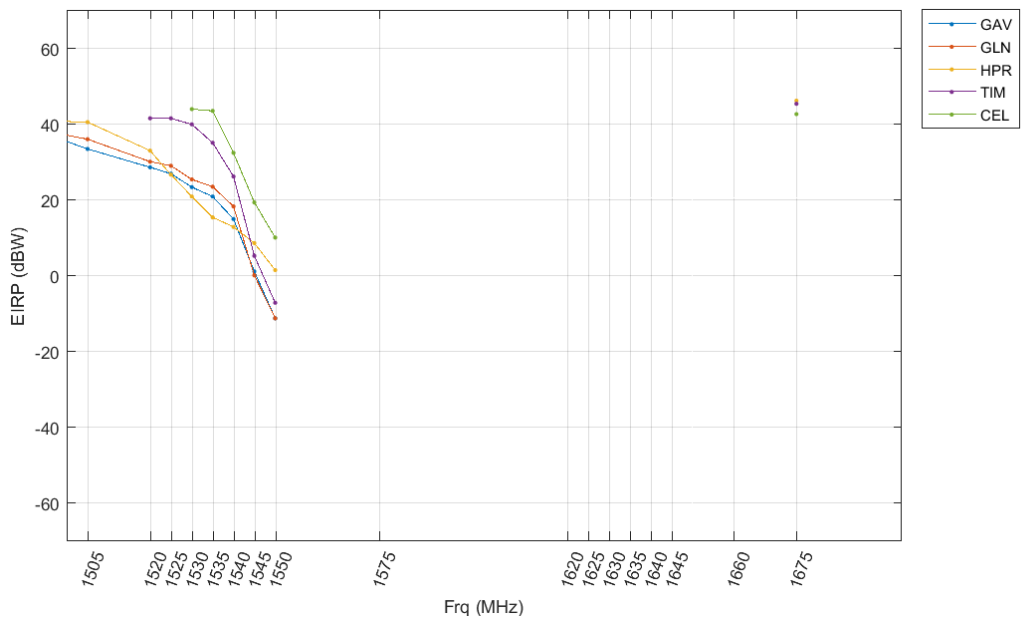


**Figure J-34: All GNSS, Micro Urban, Median EIRP Mask: 2-Ray,  $d_{\text{Standoff}} = 500 \text{ m}$**



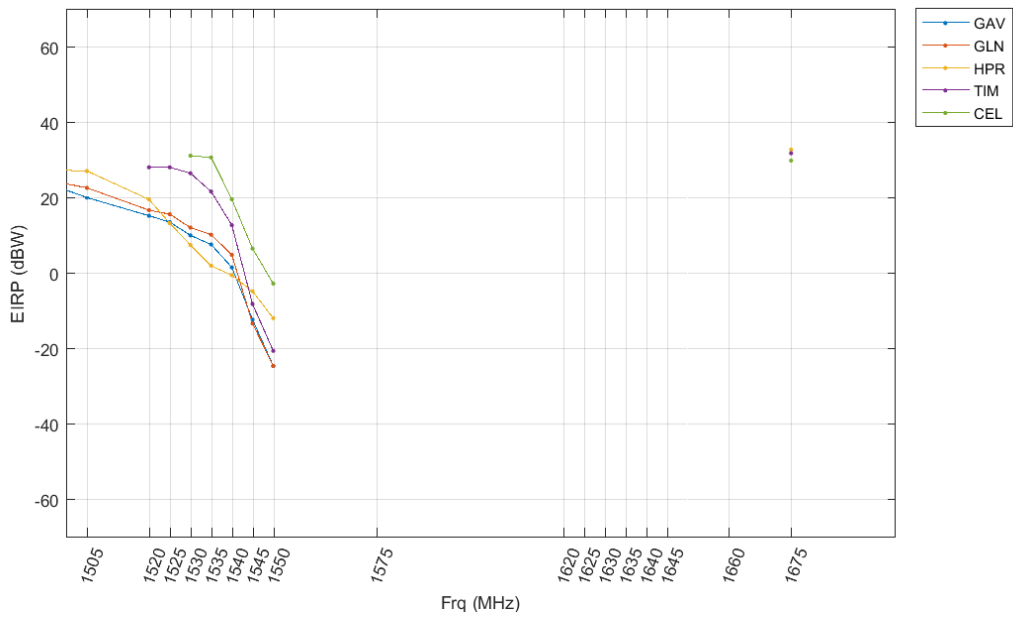


**Figure J-35: All GNSS, Micro Urban, Median EIRP Mask: 2-Ray,  $d_{\text{Standoff}} = 100$  m**

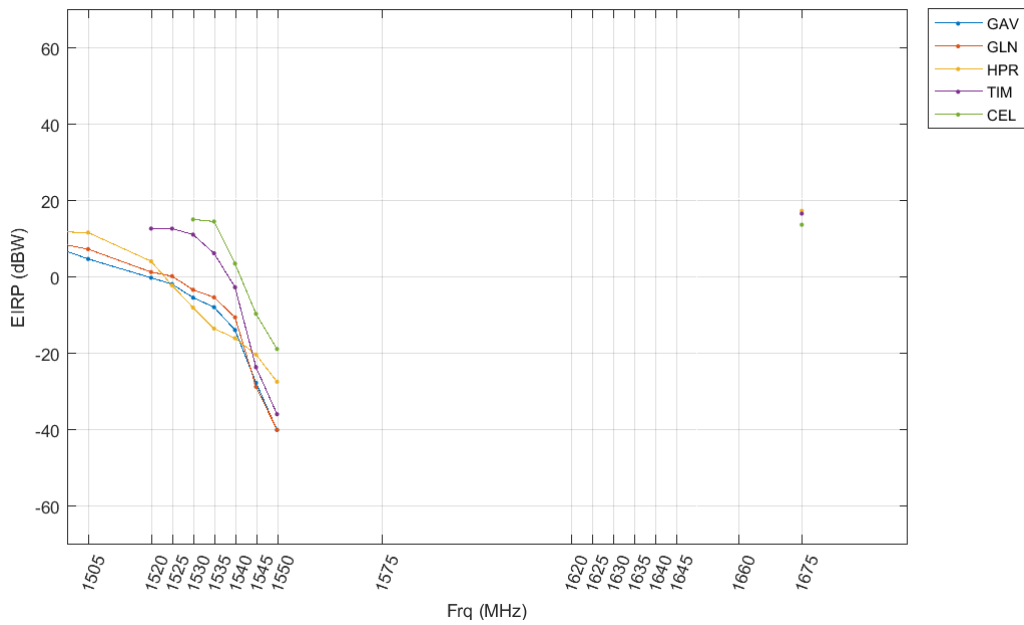


**Figure J-36: All GNSS, Micro Urban, Median EIRP Mask: 2-Ray,  $d_{\text{Standoff}} = 10$  m**

## J.2.2 Macro Urban Deployment

## J.2.2.1 Bounding ETMs

### J.2.2.1.1 FSPL Propagation Model

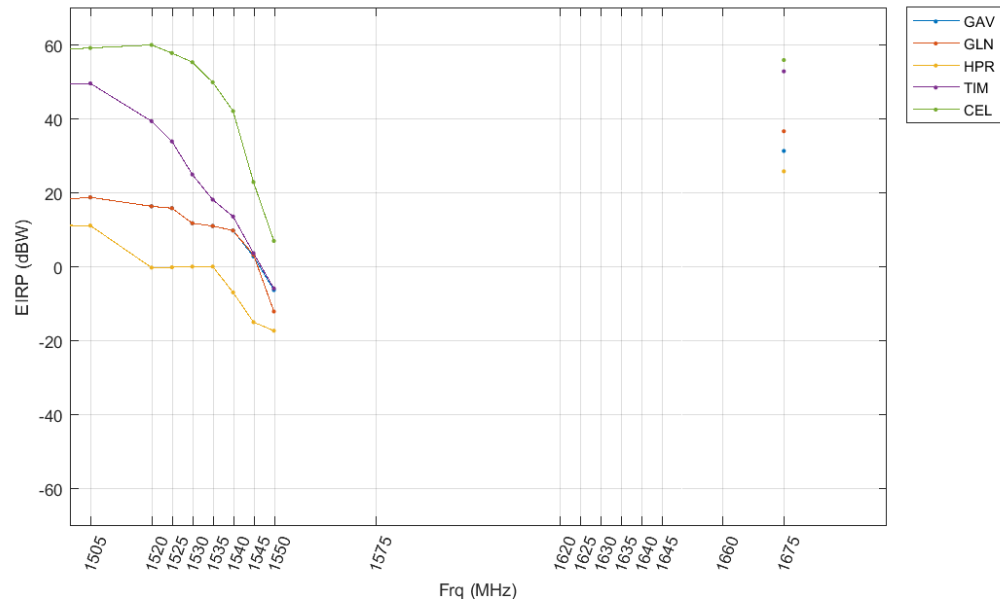


**Figure J-37: All GNSS, Macro Urban, Bounding EIRP Mask: FSPL,  $d_{\text{Standoff}} = 1000$  m**

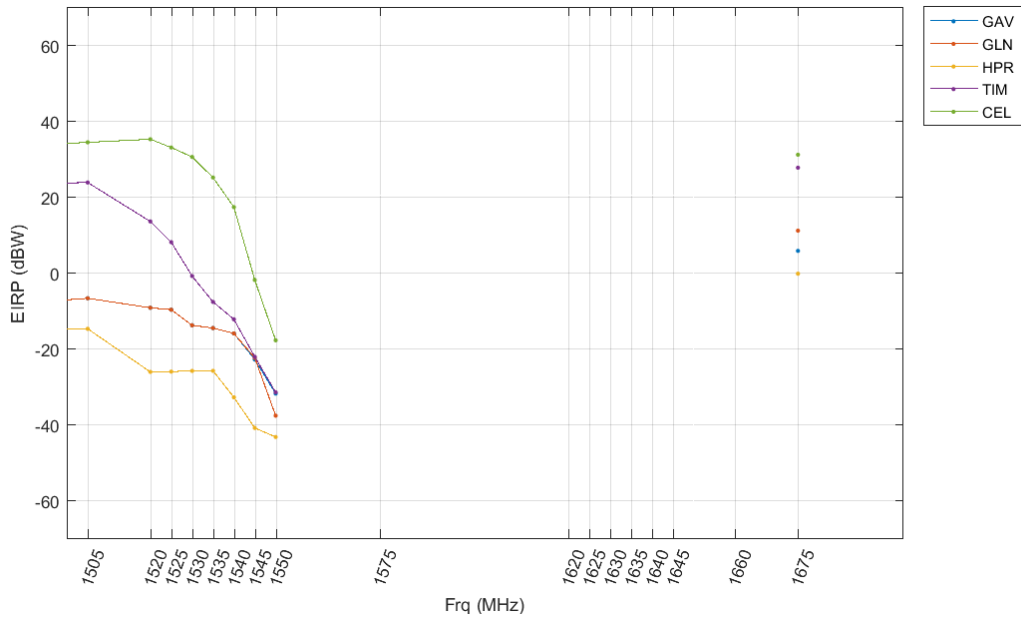


**Figure J-38: All GNSS, Macro Urban, Bounding EIRP Mask: FSPL,  $d_{\text{Standoff}} = 100 \text{ m}$**

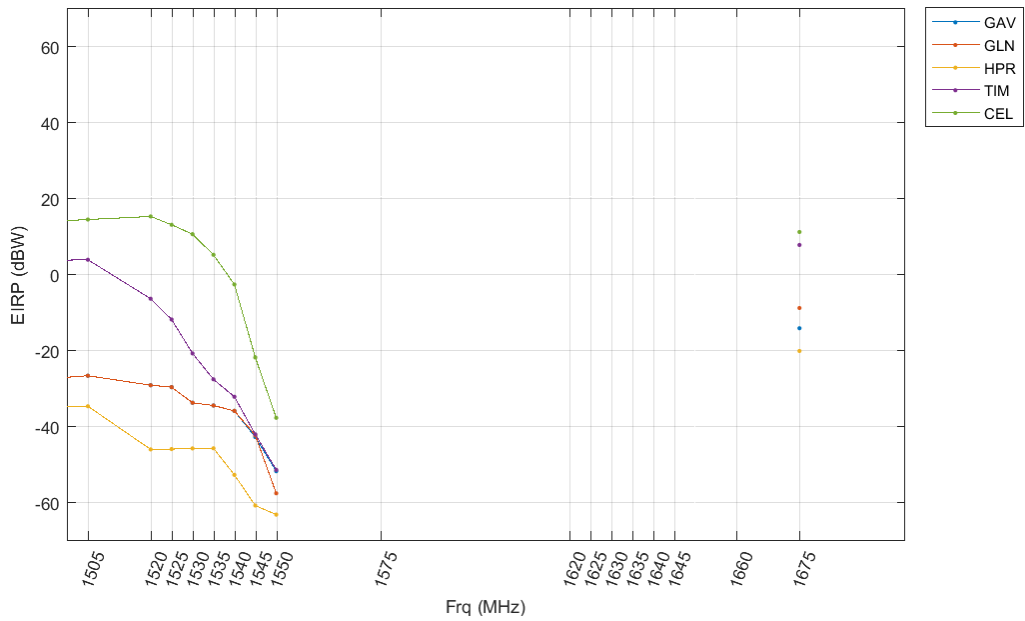


**Figure J-39: All GNSS, Macro Urban, Bounding EIRP Mask: FSPL,  $d_{\text{Standoff}} = 10 \text{ m}$**

### J.2.2.1.2 2-Ray Path loss model

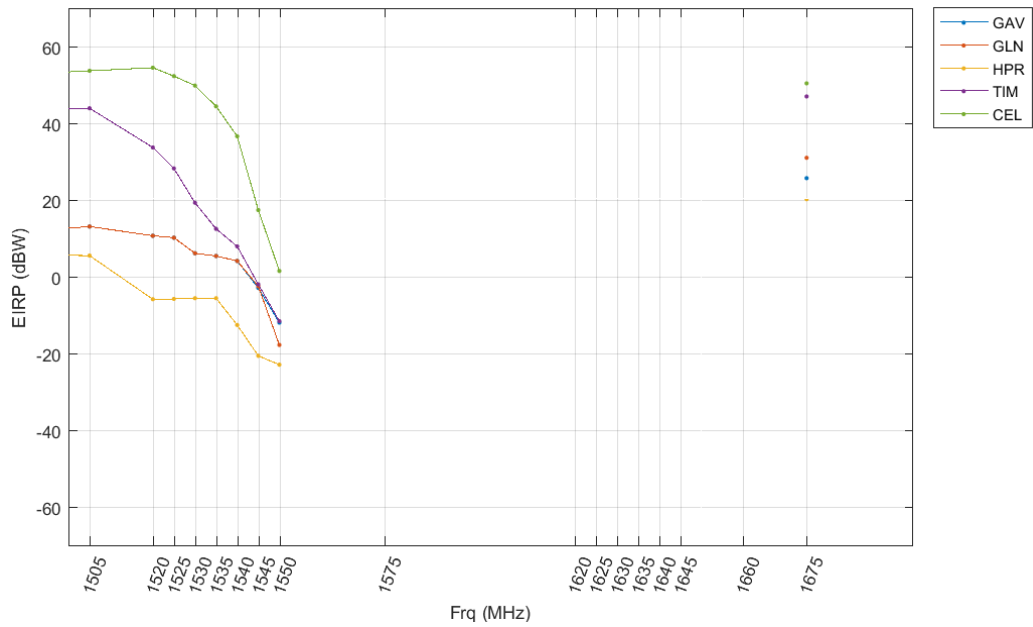


**Figure J-40: All GNSS, Macro Urban, Bounding EIRP Mask: 2-Ray,  $d_{\text{standoff}} = 1000$  m**

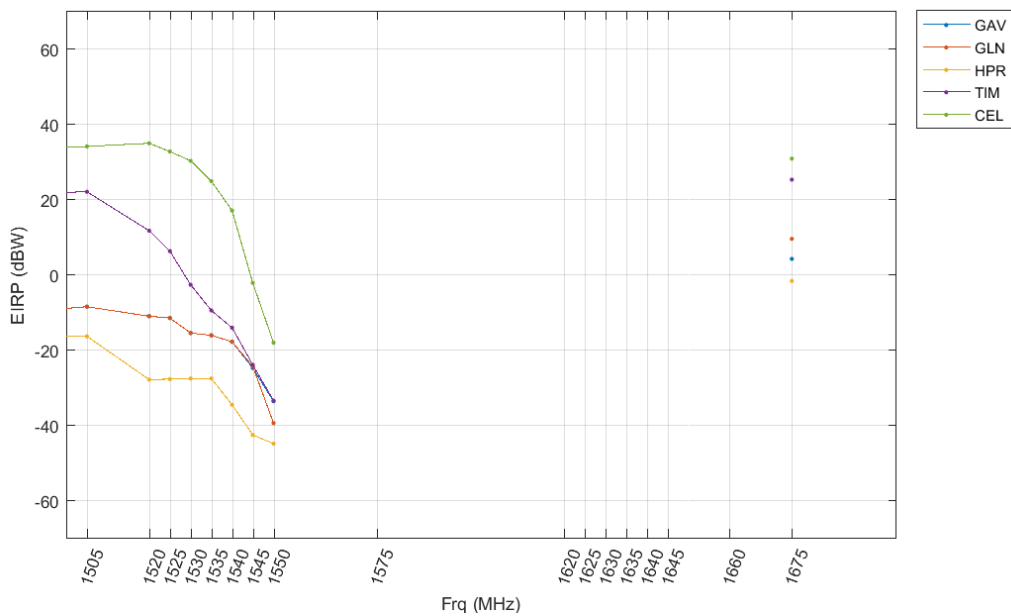


**Figure J-41: All GNSS, Macro Urban, Bounding EIRP Mask: 2-Ray,  $d_{\text{standoff}} = 100$  m**

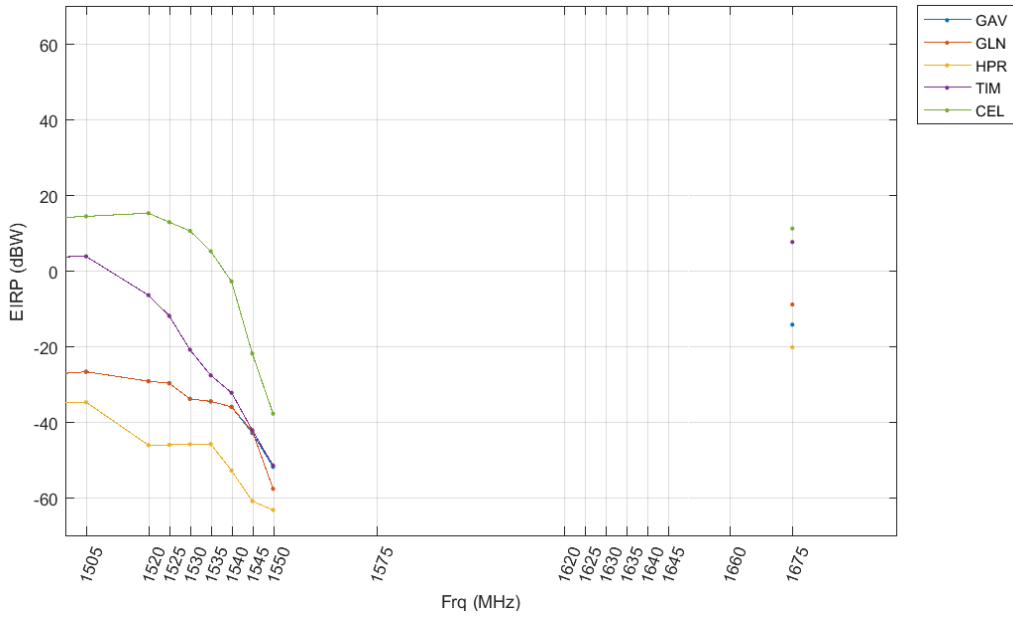


**Figure J-42: All GNSS, Macro Urban, Bounding EIRP Mask: 2-Ray,  $d_{\text{Standoff}} = 10 \text{ m}$**

### J.2.2.2 Median ETMs

#### J.2.2.2.1 FSPL Propagation Model

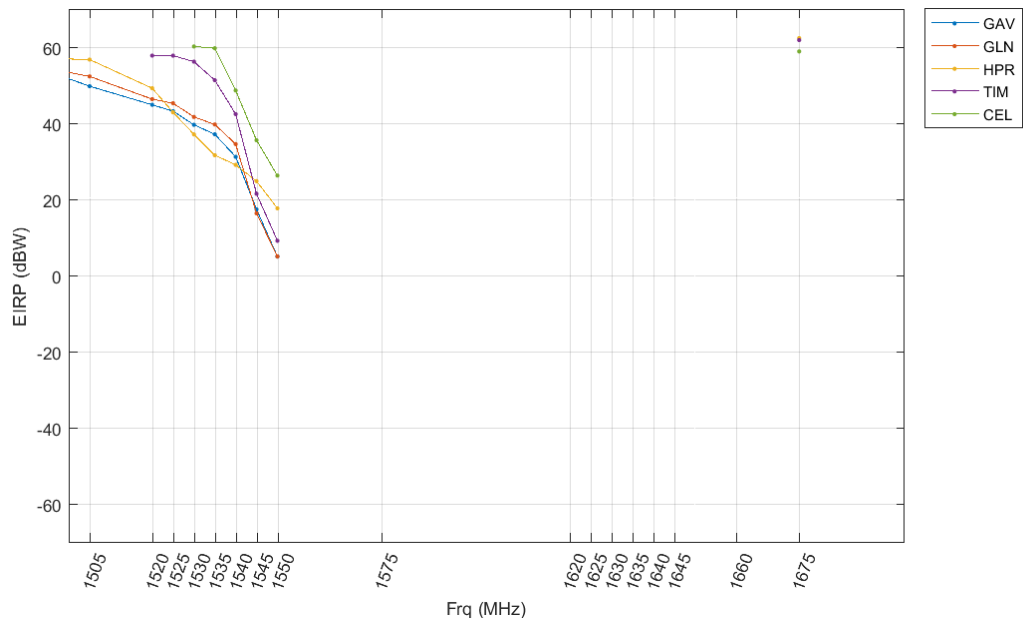


**Figure J-43: All GNSS, Macro Urban, Median EIRP Mask: FSPL, d<sub>Standoff</sub> = 1000 m**

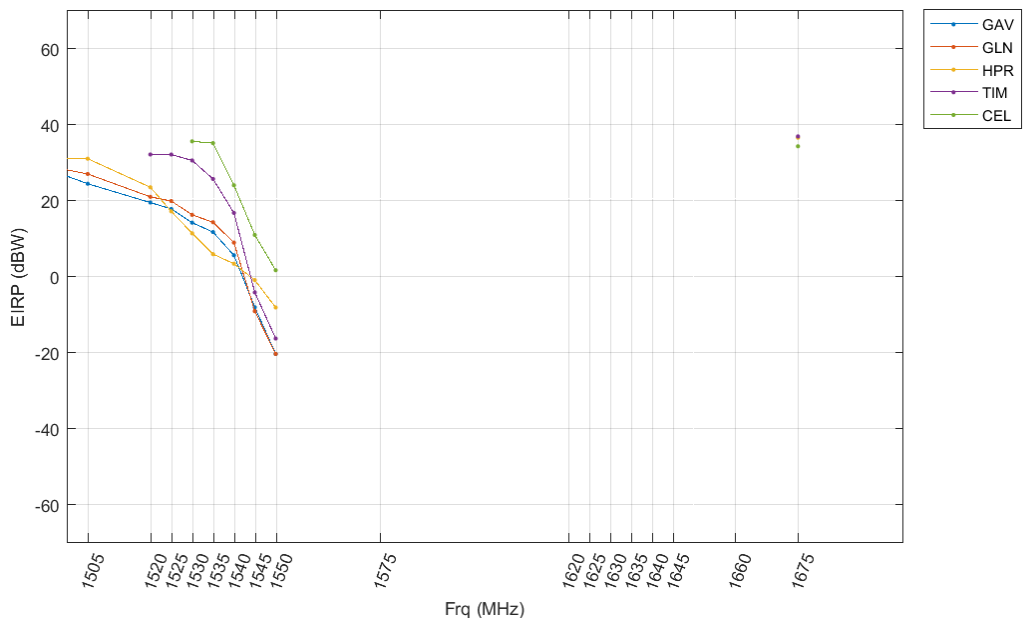


**Figure J-44: All GNSS, Macro Urban, Median EIRP Mask: FSPL, d<sub>Standoff</sub> = 100 m**

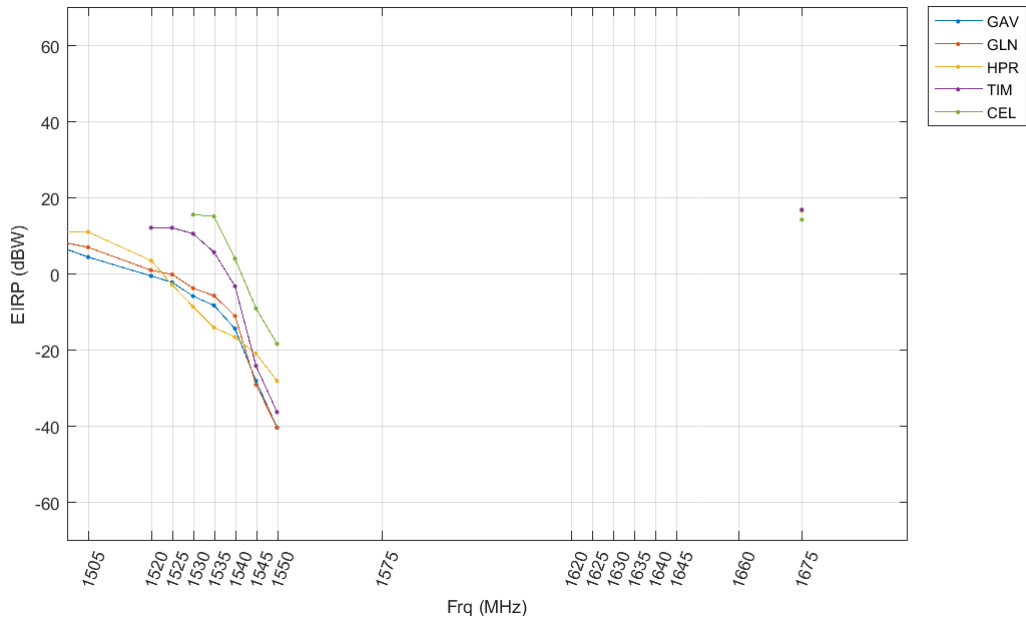


**Figure J-45: All GNSS, Macro Urban, Median EIRP Mask: FSPL,  $d_{\text{standoff}} = 10$  m**

#### J.2.2.2.2 2-Ray Path loss model

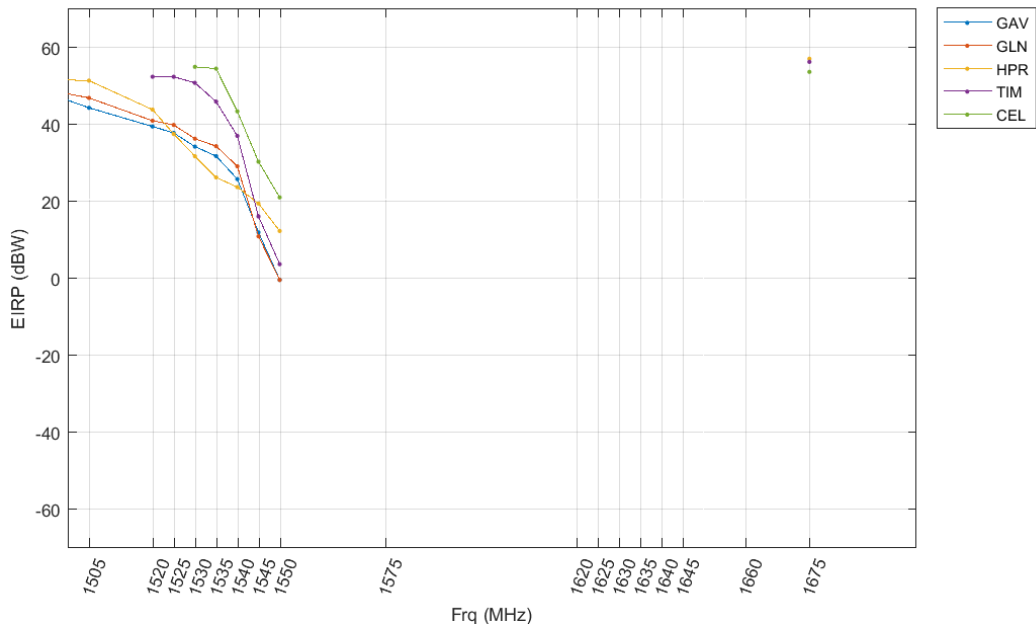


**Figure J-46: All GNSS, Macro Urban, Median EIRP Mask: 2-Ray, d<sub>Standoff</sub> = 1000 m**

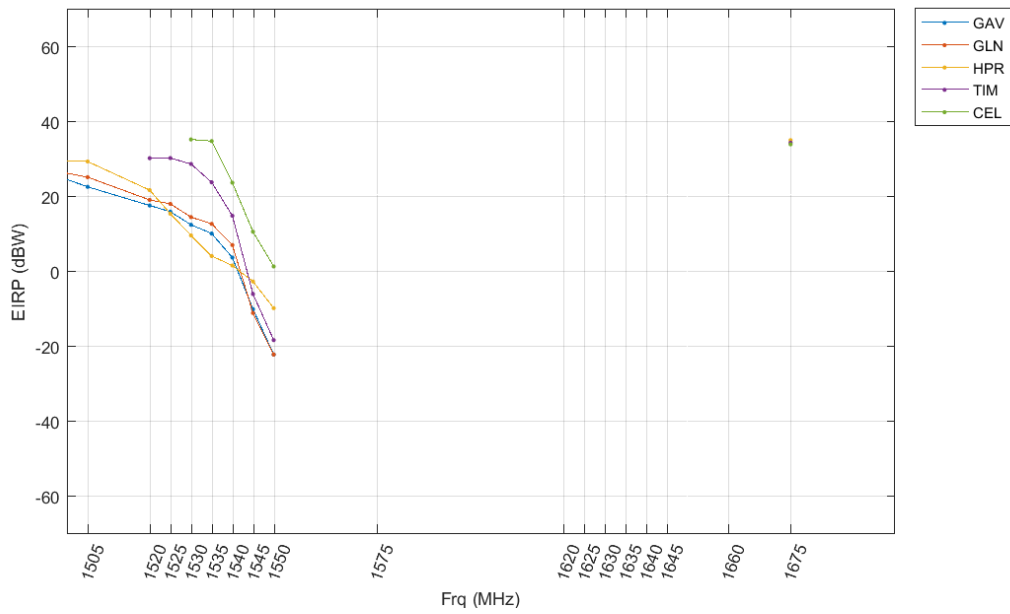


**Figure J-47: All GNSS, Macro Urban, Median EIRP Mask: 2-Ray, d<sub>Standoff</sub> = 100 m**



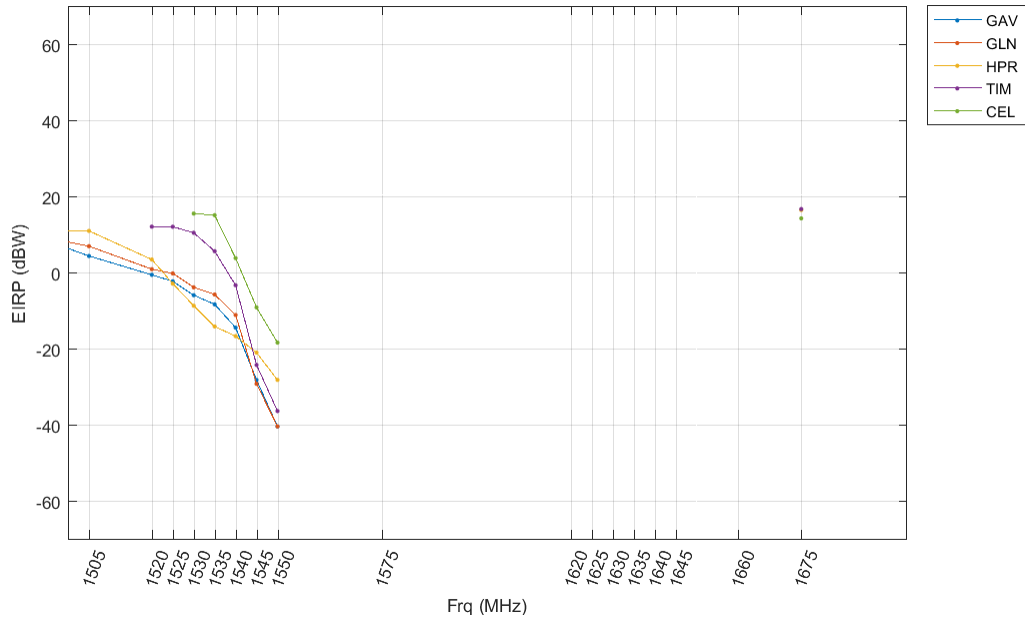


**Figure J-48: All GNSS, Macro Urban, Median EIRP Mask: 2-Ray,  $d_{\text{Standoff}} = 10 \text{ m}$**

# **APPENDIX K**

## **SPACEBORNE AND SCIENCE GNSS APPLICATIONS**

## **SPACEBORNE AND SCIENCE-APPLICATIONS**

### **Overview**

This section of the report describes the analysis and evaluation of a proposed LTE base station network's interference to space-based receivers. A comprehensive assessment on GNSS receivers, used in various applications, supporting NASA's portfolio of missions is also addressed. However, the emphasis of this section is on the assessment to GNSS receivers used for science applications.

The following evaluation assesses the impact to space-based GNSS receivers performing radio occultation ("RO") measurements (a scientific application of GNSS) of the ionosphere, stratosphere, and the troposphere. RO measurements, coupled with traditional methodologies for weather prediction, provide weather and science data observations from ocean areas, the atmosphere, and other natural phenomena, which have improved accuracy and predictability of weather forecasts by as much as two days.

Specifically, NASA's assessment focuses on the most recent developed RO receiver, called the TriG, developed by the NASA/Jet Propulsion Laboratory (JPL). The TriG is the newest RO receiver of the BlackJack class of GNSS receivers. The increase in performance by these receivers is partially due to the TriG's ability to receive all GNSS signals: GPS, Galileo, GLONASS, Compass, as well as other future navigation signals (QZSS, DORIS, etc.).

Radio Frequency Interference (RFI) is an utmost problem when GNSS signals are being used for science applications. When RFI occurs at low ray heights, the GNSS signal is defocused by tens of dB, and the signal-to-noise ratio (SNR) is already being measured in a marginal zone. In fact, in this already marginal zone, tracking loops cannot be closed and the captured data is running open loop. The spatially correlated noise can bias the captured data and affect the climate record, in addition to reducing weather forecast accuracy over the USA where the LTE base stations would be deployed.

This assessment demonstrates the effect of RFI generated by the ground-based LTE network. Several iterations of the modeling and simulation (M&S) runs were performed to more accurately model the presumed network deployment of the interfering network. The M&S scenarios estimate the receive interference levels to the TriG, utilizing specific mission parameters, and comparing them against interference limits/thresholds obtained through anechoic chamber testing described under Section 3.

### **Background**

#### **Radio Occultation (GNSS-RO)**

GNSS-RO is the measurement of GNSS signals as they are refracted by the atmosphere. RO is a relatively new method for the indirect measurement of temperature, pressure and water vapor in the stratosphere and the troposphere, and of charged particles in the ionosphere. These measurements are made from specifically designed GNSS receivers on-board a Low-Earth-Orbit

(LEO) satellite. The techniques utilize the unique radio signals continuously transmitted by the GNSS satellites (GPS, GLONASS, Galileo, etc.) orbiting the Earth at an approximate altitude of 20,000 km above the surface. The GNSS radio signals are influenced both by the electron density in the ionosphere and by the variations of temperature, pressure and water vapor in the atmosphere which are used in meteorology and climate science. RO measurements are also used to derive various ionospheric parameters (Total Electron Content (TEC), Electron Density Profiles (EDP), L-band scintillation, etc.) for understanding earth and space weather dynamics.

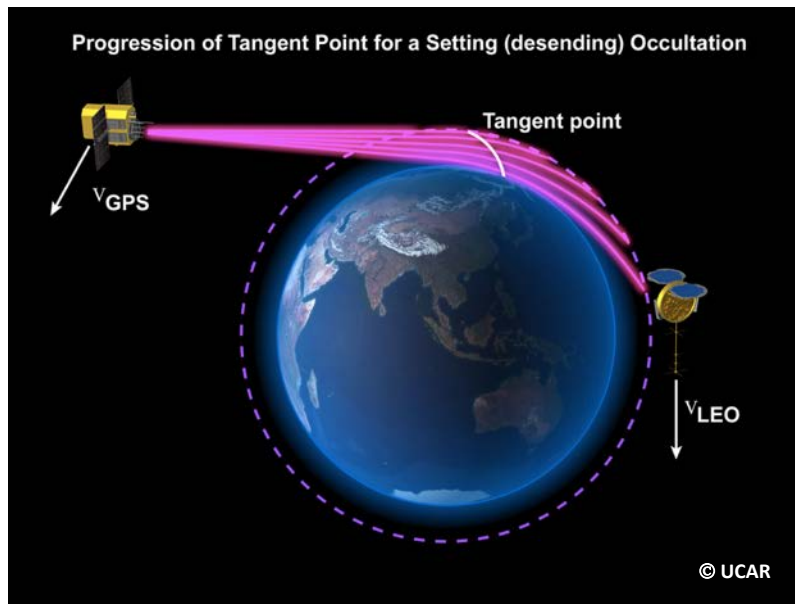


**Figure K-1: Progression of Tangent Point for a Setting (Descending) Occultation**

From the point of view of a LEO satellite (at an altitude of 700-800 km), the GNSS satellites continually rise above, or set behind, the horizon of the Earth. During these so-called "radio occultations", where the GNSS and the LEO satellite are just able to "see" each other through the atmosphere, the GNSS signals will be slightly delayed and their ray path slightly bent (refracted) on the way through the layers of the atmosphere (see **Figure K-1**). The excess range increases as the ray propagates through denser mediums and water vapor at lower altitudes. This delay is a function of density ( $n/V$ ), which is related to temperature by the ideal gas law (Equation K-1),

$$P \cdot V = n \cdot R \cdot T$$

**Equation K-1: Equation Used to Translate Refractivity to Atmospheric Temperature**

A typical occultation sounding will last one (1) to two (2) minutes, and during this time the LEO satellite will receive signals where the ray paths have different minimum distances to the surface of the Earth, from zero up to approximately 100 km. The GNSS satellites transmit on multiple frequencies, and with a receiver rate of 50 Hz this will yield around 6000 rays, making up a profile of excess phases (actual path minus straight-line path) through the lowest 100 km of the atmosphere.

The residual positioning error and determination of time delays (see **Figure K-2**), derived from the measurements taken during a RO event, are key parameters in the obtaining the temperature, pressure, and water vapor characteristics of the atmosphere at different heights. Given sub-mm measurement precision, RO can determine atmospheric temperature profiles to 0.1 – 0.5 Kelvin (K) accuracy from 8 - 25 km height levels. These are unprecedented levels of accuracy for global measurements.

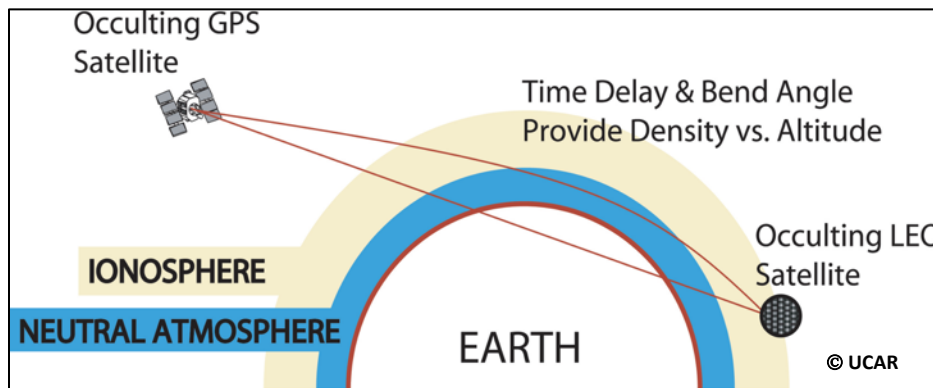


**Figure K-2: Straight Line versus Actual Path of GNSS Signal**

NASA has several radio occultation receivers in its portfolio, including the Integrated GPS Occultation Receiver (IGOR), the IGOR+, and a more recently developed receiver called the TriG receiver.

### **NASA/JPL TriG Receiver Overview**

The NASA/JPL developed TriG receiver functions as a multi-function GNSS receiver. This single receiver has multiple antenna inputs and can be configured to operate in a navigation capacity, as well as, simultaneously, in a scientific measurement role.

In its traditional function, coupled with choke ring antenna (see Figure K-3), the TriG serves as a device for space vehicle navigation and precise orbit determination (POD). The receiver provides accurate information to space vehicle operators on position, velocity, and time.



**Figure K-3: Typical Choke Ring Antenna**

Configured in a scientific measurement mode, the TriG, coupled with a series of specially designed antenna arrays, performs RO measurements of GNSS signals. TriG receiver hardware is able to receive all GNSS signals: GPS, Galileo, GLONASS, Compass, as well as other navigation signals (QZSS, DORIS, etc.). This capability increases the number of RO measurements that can be made during any given orbit.

Additional information on TriG can be found in a document titled, “TriG - A GNSS Precise Orbit and Radio Occultation Space Receiver”, written by the Jet Propulsion Laboratory and California Institute of Technology<sup>1</sup>.

### **TriG Pre-Select Filter**

Much akin to high-precision (HP) GPS receivers, the TriG has been designed with a wide front-end receiver filter. This wider pre-select filter can be derived from the ITMs developed by the DOT (see Section 3). Although the DOT developed ITMs for each of the six (6) categories of GPS receivers using bounding results, NASA specifically tested two (2) spaced-based receivers during the anechoic chamber tests.

The pre-select filter contains two 150 MHz-wide pass bands. The first covers the L5 and L1 bands. The second pass band covers only L1 but was designed with the same bandwidth to equalize filter delay changes with temperature. This is important for the ionospheric measurements, a prime product of the COSMIC-2BB mission. The TriG also has 2<sup>nd</sup> stage narrow band filters that are centered around the GPS L1 and L2 bands.

Receivers are purposely designed to have a wider bandwidth for both HP and the TriG receivers. The wider bandwidth front-end filter takes advantage of:

- The ability to track all current and future GNSS L-band signals:
  - GPS
  - Galileo (Europe)
  - GLONASS (Russia)
  - Compass/BeiDou (China)
  - QZSS (Japan)
  - NaVIC (formerly, IRNSS) (India)
  - DORIS (France)
  - GPS augmentation systems operating on mobile satellite service (MSS) frequency allocations, and
  - Other future GNSS constellations.
  
- Avoiding the disadvantages that narrow filters with sharp cutoffs produce, such as:
  - Distorted ranging code transitions
  - Introduction of inter-signal biases which vary with temperature and Doppler
  - Increased insertion loss that degrade SNR, and
  - Phase and delay distortion across signal band.

---

<sup>1</sup>[http://authors.library.caltech.edu/21729/1/Esterhuizen2009p12347Proceedings\\_of\\_The\\_22Nd\\_International\\_Technical\\_Meeting\\_of\\_The\\_Satellite\\_Division\\_of\\_The\\_Institute\\_of\\_Navigation\\_\(Ion\\_Gnss\\_2009\).pdf](http://authors.library.caltech.edu/21729/1/Esterhuizen2009p12347Proceedings_of_The_22Nd_International_Technical_Meeting_of_The_Satellite_Division_of_The_Institute_of_Navigation_(Ion_Gnss_2009).pdf)

In addition to the typical advantages afforded to HP receivers that are designed with wider front-end bandwidth filters, the TriG gains additional benefits for employing wide bandwidth filters by:

- Avoiding extensive development cost and time,
- Avoiding the additional cost for pre-flight testing,
- Avoiding the additional costs associated with size and mass restrictions of flight instrument, and
- Leveraging on advanced techniques such as:
  - Oversampling the GNSS signal and use of narrow-lag correlators for better precision, and
  - On-receiver multipath mitigation techniques.

### Upcoming TriG Missions

TriG receivers will be flown on the next generation radio occultation capable satellites as part of the COSMIC-2B<sup>2</sup> mission, which is sponsored by several U.S. federal agencies and NASA international partners. The COSMIC-2 mission is broken down into two (2) sub-missions, which will deploy six (6) satellites each. Table K-1 displays the upcoming missions where the TriG receiver will be deployed.

*Note:* The list of missions in Table K-1 depicts the known missions, as of the writing of this report. As NASA continues to develop partnerships with other International Space Agencies and other U.S. Federal partners, coupled with the success of integrating RO measurements into the weather prediction models, it should be noted that this list may change in the future.

Mission	Launch Date	TriG Function
Deep Space Atomic Clock (DSAC)	Jul-18	Precise clock validation
		Timing
		POD
Constellation Observing System for Meteorology, Ionosphere and Climate (COSMIC)-2 (A) - 6 satellites	Jul-18	RO
		SWO
Gravity Recovery and Climate Experiment (GRACE) Follow-On	Feb-18	Micron ranging
		POD
		RO
COSMIC-2B (B) - 6 satellites		RO

<sup>2</sup> Reference, <http://www.cosmic.ucar.edu/cosmic2/>

	2020 (pending funding) *	SWO
Sentinel-6A and B (2 launches)	2020 and 2025*	RO
		POD
Surface Water and Ocean Topography (SWOT)	2021*	POD
NASA-ISRO Synthetic Aperture Radar (NISAR)	2021*	POD

**Table K-1: TriG Mission List (as of Oct-2017)**

Table Legend:

POD – Precision Orbit Determination

RO – Radio Occultation

SWO – Space Weather Observation

\* Tentative mission launch year

**Other Scientific Applications of GNSS**

GNSS technology has become an essential tool to monitor and improve our understanding of earth systems, including weather monitoring and solid earth hazards such as earthquakes and volcanic activity. This knowledge of our environment and its changes is also used for resource management and protection, and environmental impact mitigation. Some examples of the use of GNSS to improve our knowledge of the Earth are determining the atmosphere’s water content, improving the accuracy of weather forecasts, enabling ocean topography measurements to determine currents and secular changes in sea height. Ground based GNSS networks are also playing an increasingly prominent role to monitor ground movement to identify potential conditions that may precede Earthquakes and volcanic activity. In addition, some insurance companies use GNSS-based maps of accumulated tectonic strain to predict risk. The same data are used by other government agencies beyond NASA. GNSS technology assists NASA scientists in understanding the physical characteristics of the earth and its atmosphere, and changes over time. NASA scientists use GPS science receivers, in combination with other measurement techniques such as laser ranging and radar altimeters, to monitor the changes in Earth’s surface, sea level height, and atmospheric measurements and provide precise knowledge of Earth’s shape and rotation.

As the scientific community continues to embrace leveraging on GNSS, additional techniques have been developed to measure and monitor earth and space weather phenomena. These techniques take advantage of:

- Existing development and deployment of satellite constellations, thereby, saving money in developing and deploying a separate constellation for science signals;



- Existing satellite constellations providing signals known and consistent position determinations all around the Earth; and
- GNSS signals transmit precise time and positioning information continuously in all weather conditions.

### **Ground-based GNSS Receivers Used for Integrated Precipitable Water Measurements**

This recently developed technique in performing atmospheric observations utilizes ground-based GNSS receivers that employ zenith (away from earth) pointing antennas to measure GNSS signals. As the GNSS satellite comes into view of the antenna overhead, the amount of measured delay of the signal due to water vapor in the atmosphere can be measured and attributed to specific weather conditions. As a meteorological application, ground-based GNSS receiver data is used to derive the Integrated Precipitable Water which is fed into the Numerical Weather Prediction model. This data is complementary to the space-based data (RO), and together, they provide valuable ionospheric information for space weather specification and forecasting.

In this system, commercially available HP GPS/GNSS receivers are typically utilized and the data is fed into post-processing algorithms to determine the precipitable water vapor content of the atmosphere.

Although NASA utilizes such systems to correlate the water vapor data with RO measurements to more accurately predict weather phenomena, NASA did not perform any specific assessments to these systems under the DOT ABC Assessment. Since NASA leverages on commercial HP GPS/GNSS receivers to perform these measurements, any such protection criteria and separation distances afforded to the HP category of receivers under Section 3 will be applicable to locations where ground-based GPS/GNSS receivers are used for metrology.

### **Reflectometry (GNSS-R)**

In addition to radio occultation and ground-based GNSS measurements, measuring the characteristics of Earth and bodies of water through a technique called “reflectometry” (GNSS-R) is also valuable application for science and weather.

For example, NASA’s Cyclone Global Navigation Satellite System (CYGNSS) mission, consisting of eight (8) small satellite observatories, which was launched in 2016, will make frequent and accurate measurements of ocean surface winds throughout the life cycle of tropical storms and hurricanes. In addition to using GNSS signals for satellite navigation, each satellite observatory can measure four (4) separate GNSS signals at the specular reflection points on the ocean to obtain information about ocean surface roughness. Ocean surface roughness is correlated to surface wind speed. The CYGNSS data will enable scientists to probe key air-sea interaction processes that take place near the core of storms, which are rapidly changing and play a critical role in the genesis and intensification of hurricanes.

Spacecraft equipped with GNSS-R systems receive a direct GNSS signal, as well as a “reflected” GNSS signal from the Earth’s surface. The direct signal is transmitted from a GNSS satellite and received by a zenith pointing antenna onboard the spacecraft, while the reflected signal is received by the two (2) nadir (towards the earth) pointing antennas. If the surface is perfectly

smooth, the specular reflection point is the location on the surface where all of the scattering originates. In comparison, if the surface is roughened (e.g., due to over the surface wind speed), the scattering of the GNSS signal originates from a diffuse region called the glistening zone around the specular point. Figure K-4 demonstrates a pictorial of GNSS-R concept of operations.

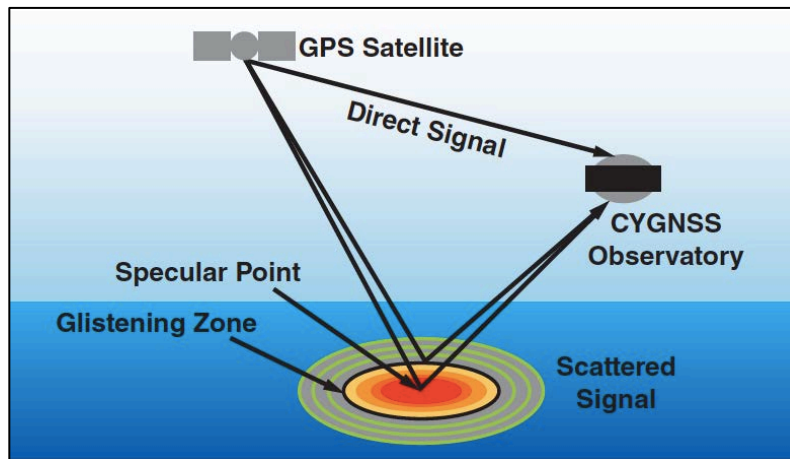


**Figure K-4: GNSS-R Concept of Operations (Image Credit – University of Michigan)**

Algorithms measure the amplitude of the reflected signal versus delay and Doppler shift. If the surface is smooth, nearly all power originates at the specular reflection point. If the surface is rough, there are reflections from facets separated from the specular points. Those reflections have more delay, and a spread of Doppler shifts. An example of Delay Doppler Maps for 2, 7, and 10 meter per second (m/s) wind speeds [top to bottom] is shown in Figure K-5.

[Illustration Note: The images show how progressively stronger wind speeds, and therefore progressively rougher sea surfaces, produce a weaker maximum signal (at the top of the “arch”) and a scattered signal along the arch that is closer in strength to the maximum. A perfectly smooth surface would produce a single red spot at the top of the arch.<sup>3</sup> Image credit: University of Michigan.]

In addition to weather forecasting (e.g., cyclonic and hurricane activity), GNSS-R has shown promises to predict other Earth surface phenomena relating to

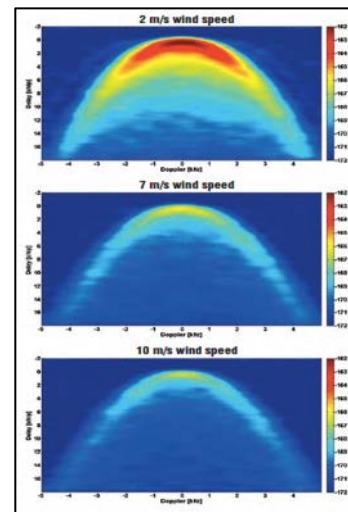


**Figure K-5: Example Delay Doppler Maps**

<sup>3</sup> Additional information on CYGNSS can be found at the following weblink to the NASA CYGNSS Mission site: <https://www.nasa.gov/cygnss/overview>.

bodies of water. NASA scientists are exploring the capability of GNSS-R receivers to monitor and anticipate:

- Coastal tidal surges,
- River and lake overflows,
- Flood plains,
- Water surges beneath foliage canopies (e.g., swamps and mangroves),
- Potential dyke, reservoir, and dam exceedances, and
- Many more areas that may be impacted due to watershed anomalies.

Since GNSS-R is a relatively new technique used as a scientific application of GNSS, NASA was unable to obtain a GNSS-R receiver to be tested during the testing phases (anechoic chamber or conducted) of the DOT ABC Assessment. Therefore, the effects of adjacent band LTE operations to GNSS-R are currently unknown.

### **Geodesy/Geodetics**

Geodesy or geodetics is the science of accurately measuring and obtaining data to understand the properties of the Earth. In this scientific discipline, observations are performed to obtain information on the Earth's geometric shape, orientation (relative to Earth's axis and the sun), crustal motion, oceanic tides, and Earth's gravitational field. Since these Earth properties are continuously changing, measurements are taken with respect to time. To ensure stability and consistency in these measurements, scientists leverage on a known and constant signal source, like GPS and other GNSS signals, where accurate three-dimensional positioning attributes and timing can be obtained.

In order to accurately measure these Earth properties, commercially available HP GPS/GNSS receivers are typically utilized at fixed locations on the Earth's surface. Scientifically measured data is fed into post-processing algorithms to determine the three-dimensional positioning (in some cases such as for earthquake monitoring, accuracy levels must be down to millimeters). The variations of the receiver positions with time are compared with physical models to determine inter-earthquake strain accumulation, earth orientation parameters, etc.

Since NASA leverages on commercial HP GPS/GNSS receivers to perform these scientific measurements, any such protection criteria and separation distances afforded to the HP category of receivers under Section 3 will be applicable to locations where ground-based GPS/GNSS receivers are used for geodesy/geodetic science.

### **Real-time Response to Natural Hazards**

The U.S. Geological Survey (USGS) mandate includes monitoring and responding to natural hazards due to earthquake faults, volcanoes, landslides, and tsunamis. Many of these applications depend critically upon GNSS data and require the broadest available spectrum of GNSS signals, including side bands, to achieve the highest station position accuracy and precision possible in real-time. In particular, the USGS Earthquake Hazards Program, in collaboration with universities and other governmental and private agencies, is developing an earthquake early warning (EEW) system, called ShakeAlert (USGS OFR # 2014-1097).

ShakeAlert will issue life-critical alerts of impending strong ground motion for public safety and emergency response in the event of a major earthquake.

Seismometers often go off-scale when recording seismic waves during large and great earthquakes, and magnitudes calculated from the earliest portion of a seismogram can be significantly underestimated. In an EEW system this leads, in turn, to underpredicted ground shaking. GNSS data have the unique capability to measure large displacements reliably at the centimeter level without going off-scale, thus augmenting seismic data to enable accurate magnitude estimates for M7+ earthquakes.

In order to do this, the GNSS component of ShakeAlert requires real-time, uninterrupted GNSS signals without interference at all times from a broadly distributed network with stations near the earthquake faults. Even brief outages due to RFI can significantly affect the precision of the GNSS observations and degrade the performance of the system. In addition to data from GNSS stations in the earthquake source region themselves, calculating their absolute positions in real-time also requires the continuous availability of data from GNSS stations outside the affected region in order to generate real-time clock correction streams. It can take up to 15 minutes for a receiver to recover from its own loss of lock and/or loss of the correction streams and resume production of the position streams. During this recovery time, a receiver cannot contribute to EEW because it will not output reliable positions, which are needed for rapid earthquake and ground motion characterization. Since early warnings must be sent within seconds of the onset of an earthquake to be useful, such delays would compromise the EEW system. The growing USGS volcano alert system could be similarly affected by RFI-related outages.

In addition to the use of GNSS-derived positions for earthquake response, the USGS seismic networks rely on the GNSS constellation L1 signal in order to mitigate seismometer clock drift. To implement this, seismic instruments typical of those used by USGS networks include a GPS chipset centered at 1550 MHz. The accuracy of time tags assigned to seismic data recorded in the field is critical for determining accurate earthquake locations, but GPS loss of lock leads to clock drift. This is particularly detrimental for EEW, in which the correct location of an earthquake must be determined within seconds in order to maximize the warning time that can be given to affected populations.

### **Other NASA Applications of GNSS Receivers**

Statistically, nearly 60% of projected worldwide space missions present-2027 will operate in LEO. Additionally, 35% of space missions that will operate at higher altitudes will remain at or below Geostationary-Earth-Orbit (GEO). Therefore, approximately 95% of projected worldwide space missions over the next 20 years will operate within the GNSS service envelope and will rely on GNSS for space activities associated with navigation, POD, science, and other applications.

The following sections describe the uses of GNSS receivers that support various NASA missions.

Note: Although the following applications, coupled with the science applications of GNSS (in above sections) provide for a comprehensive list of NASAs' uses of GNSS, it should be noted that this does not provide a full complement of NASA's uses of GNSS receivers. Other uses for day-to-day operations, NASA security, fire and rescue, etc., typically utilize GLN receivers, which are addressed in Section 3. Therefore, any constraints to LTE operations required to protect GLN devices will be applicable to these NASA functions.



**Figure K-6: NASA Security Vehicle**

### Aviation Systems

NASA's Aeronautical Research Mission Directorate operates NASA owned, maintained, and operated aircraft, which are certified by the FAA to operate in the National Airspace System. If such NASA aircraft are equipped with GPS receivers, they are required to be compliant with FAA Certification Regulations and are equipped with FAA certified GPS receivers.



**Figure K-7: Example of NASA Aircraft Fleet**

Moreover, NASA also possesses and operates several Unmanned Aerial Systems (UAS) that are equipped with GPS receivers. Some of the UAS are designed and developed by NASA Program Offices, while other UAS are operated under a leasing contract with the UAS developer. UAS



**Figure K-8: Example of NASA UAS**

are used by NASA in various manners, from developing UAS Traffic Management policies and procedures - to performing airborne science measurements - to performing research and development of new aircraft materials and aircraft designs. Regardless what mission or function the UAS is supporting, if required and necessary for flight in the National Airspace System, UAS will be equipped with certified aviation receivers or with general aviation (GAV) receivers.

## Spacecraft

Spacecraft, as defined by the International Telecommunication Union (ITU)<sup>4</sup>, is a man-made vehicle which is intended to go beyond the major portion of the Earth's atmosphere. NASA's spacecraft portfolio consists of, but not limited to:

- Space vehicles,
- Space stations,
- Space platforms, and
- Satellites.

The orbital mechanics and flight operation of spacecraft, including navigation, POD, metrics tracking, timing, velocity, and attitude, rely on GNSS signals for accuracy. During development, spacecraft are typically fitted with either commercially available HP GPS/GNSS receivers or NASA developed GNSS receivers.

Throughout the years, NASA has developed and continues to develop GNSS receivers that meet specific mission requirements and designed with the robustness to withstand the harsh elements of space. Some of these devices are the:

- TurboRogue,
- BlackJack, IGOR, and IGOR+,
- Navigator, and
- TriG.

Employed to perform orbital mechanics and flight operations, GNSS receivers (commercial or NASA-developed) are unlikely to be significantly affected by the ground-based LTE broadband operations in adjacent bands. NASA has previously studied the IGOR, TriG<sup>5</sup>, and Navigator<sup>6,7</sup> in this mode of operation. This is due to the configuration and placement of the antenna. Since most spacecraft operate within GNSS constellation orbits, antennas are located in the zenith (away from earth) position of the spacecraft.

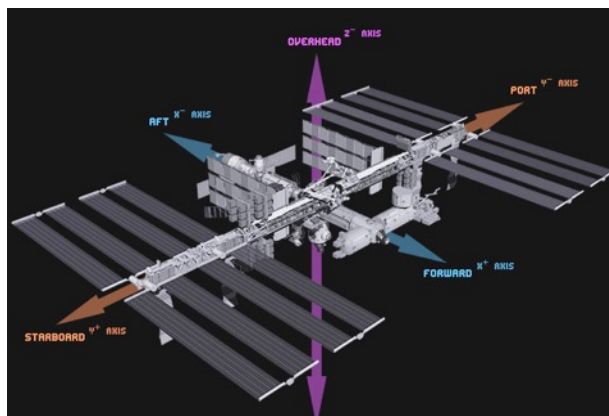


**Figure K-9: Orientation Designations of Spacecraft**

## Launch Vehicles

Launch vehicles are rockets used to propel a payload from the Earth's surface to outer space. In some cases (e.g., sounding rockets), the rockets are designed to carry a scientific measuring

<sup>4</sup> International Telecommunication Union, Radiocommunication Sector, (ITU-R), Radio Regulations, Edition 2016, Volume 1, Chapter I – Terminology and technical characteristics. (<http://www.itu.int/pub/R-REG-RR-2016>)

<sup>5</sup> 2011 National Space-Based Positioning, Timing, and Navigation Systems Engineering Forum Report, Subtask 6, NASA Simulations.

<sup>6</sup> GPS Navigator (Nav) Near-band and In-band RFI Susceptibility Report (461-NAV-ANYS-0256), NASA Goddard Space Flight Center.

<sup>7</sup> Limited distribution due to proprietary system information contained within the document.

device into sub-orbital altitudes; while some rockets are designed with enough inertia and thrust to enable its payload to entirely escape Earth orbit.

Through the past two decades, the design and development of launch vehicles include the equipping of GNSS receivers. The use of these receivers facilitates ground control operators by providing key metric tracking of launch vehicles. Integrated metric tracking units provide accurate and stable positioning on high dynamic platforms.

More recently, NASA has implemented an Autonomous Flight Safety System (AFSS)<sup>8</sup>, which is a real-time safety system comprised of the ground software used to write mission rules and convert the mission rules into a mission data load. Coupled with the ground system, the AFSS includes on-board hardware and software. Specifically, the launch vehicle is equipped with an Automated Flight Termination Unit (AFTU) used for the Automated Flight Termination System (AFTS) of the AFSS.



**Figure K-10: Antares Rocket Launch, Wallops Island, Oct-2016  
(Photo Credit: NASA/Joel Kowsky)**

The AFTS augments or replaces the functions of the traditional human-in-the-loop (HITL) process and procedures. Redundant AFTS processors evaluate data from onboard AFTUs, which include GNSS receivers and other navigation sensors, and are used to make flight termination decisions. The mission rules are developed by the local Range Safety Authorities using the inventory of rule types taken from current HITL operational flight safety practices<sup>9</sup>. HP GNSS receivers are typically configured in the AFTUs to achieve the high-level of accuracy necessary to track the position of the launch vehicle within the projected launch path safety boundary.

---

<sup>8</sup> [An Autonomous Flight Safety System](https://ntrs.nasa.gov/archive/nasa/casi.ntrs.nasa.gov/20080044860.pdf), James B. Bull and Raymond J. Lanzi, NASA Goddard Space Flight Center and NASA Wallops Flight Facility. <https://ntrs.nasa.gov/archive/nasa/casi.ntrs.nasa.gov/20080044860.pdf>

<sup>9</sup> Reference: Autonomous Flight Termination System Reference Design Hardware, Lisa Valencia, Robert Morrison, and Roger Zoerner, NASA Kennedy Space Center, FL. <http://www.techbriefs.com/component/content/article/ntb/tech-briefs/machinery-and-automation/24084>

NASA employs commercial HP GNSS as a part of the AFTU and any such protection criteria and separation distances afforded to the HP category of receivers under Section 3 will be applicable to locations where these receivers are used on launch vehicles as part of the AFSS.

### **Spaceborne Receiver Assessment for Science-Based Applications**

NASA has performed an assessment of the potential impacts caused by a proposed terrestrial LTE network operating in the adjacent band to GPS L1. Two (2) future science missions, COSMIC-2B and Sentinel-6 (formerly, Jason Continuity of Service (Jason-CS)), were used as the basis for these assessments. NASA's assessment is to the TriG receiver performing a science application using the RO technique.

To determine the impact to the TriG receiver, the aggregate interference power at the output of the TriG receiver antenna was calculated using MATLAB to model the interference scenario, as well as the TriG receiver system, and simulate the interference effects to the satellites in orbit. Satellites operating in LEO gain a much broader view of the earth (dependent upon antenna characterizations and operating parameters), which must be accounted for in performing the analysis.

Unlike the assessments performed in Section 3, in-orbit satellites will see a greater number of potential interference sources (e.g., increased number of terrestrial base stations) and the aggregate of those interference sources will be the major contributing factor in the assessment, see **Figure K-11**.



**Figure K-11: Example Satellite View of the U.S. Cities**



This section describes the modeling and simulation (M&S) for a variety of terrestrial LTE base station deployment scenarios. Further, this section will also describe, where applicable, assumptions made in the M&S, population density of the LTE network, and other dependent parameters or characteristics. Finally, this section will also provide the results and NASA’s assessment on impacts/effects on TriG mission performance.

**Assumptions**

**Interference Protection Threshold (TriG)**

NASA participated during the DOT ABC Testing of various GPS/GNSS receivers at the ARL facility in WSMR, NM. One (1) of the various systems NASA tested was the TriG receiver (see Section 3). The results of the testing produced an interference protection threshold of -73 dBm. This protection threshold value is based upon the IPC of -1 dB C/N<sub>0</sub> for LTE signals being present in 1526 – 1536 MHz.

Furthermore, the testing produced a loss-of-lock threshold down to -59 dBm.

**Table K-1: TriG Interference Protection Threshold**

<u>Parameter</u>	<u>Threshold</u>	<u>Effect on TriG</u>
-1 dB C/N <sub>0</sub>	-73 dBm	Degraded performance, inaccurate measurements
Loss-of-Lock	-59 to -35 dBm	Saturated/jammed (no longer able to receive signals)

**Impacted Receiver Satellite Orbit Specifications**

The impacted receiver, in the context herein, is referred to at the receiver system that will be impacted by interference from the interfering source (e.g., terrestrial LTE broadband network).

Typical TriG receiver specifications have been previously described in this Appendix. The following provides the satellite-specific parameters for each of the assessed Missions.

**Table K-2: Simulation Parameters - Satellite Orbit Parameters**

<b>Orbit Characteristic</b>	<b>COSMIC-2B</b>	<b>Sentinel-6</b>
Altitude	800 km	1330 km
Inclination Angle	72°	66°

**TriG Receiver Antenna**

The TriG receiver system can be configured to use a variety of NASA/JPL developed antennas to meet its mission needs. The following provides a description of the antenna configurations used to support COSMIC-2B and Sentinel-6.

## Antenna Configuration for COSMIC-2B Mission

The antenna configuration to support COSMIC-2B utilizes a set of two (2) proprietary beam forming array antennas. Each antenna is a 12-element array comprising 3 subarrays of 4 vertically stacked elements with a peak gain at 1530 MHz of +13.4 dBic. Each array uses a 60 cm tall x 40 cm wide backplane mounted on the spacecraft so that the plate is vertical and the outward normal to the plate is parallel to the spacecraft's velocity vector (assuming circular orbit). The first antenna is mounted in the forward direction of a satellite (to receive rising GNSS satellite signals) and the second antenna is mounted in the aft direction (to receive setting GNSS satellite signals). The TriG receiver has eight (8) independent antenna inputs (three (3) inputs from each of the two (2) subarrays and two (2) inputs from the antennas performing POD and space weather data acquisition functions.) Three (3) subarrays (performing the RO technique) are combined for the fore and aft antennas, increasing the gains by approximately 4.8 dB to a total main beam gain of +18.2 dBic. Note that the gain and beam shape used for the simulation is from the 4-element subarray. Since each subarray has its own filter/LNA chain, the effects of RFI apply at the subarray level.

Based on the satellite altitude (for COSMIC-2B altitude = 800 km), the receiver main-beam is directed towards the earth limb (approximately  $26.2^\circ$  below the satellite velocity vector). **Figure K-12** demonstrates an example of an in-orbit satellite with the forward antenna subarray with its down-tilt. [Note: For graphical simplicity, the aft subarray is not pictured.] Consequently, the potential interfering signals from terrestrial LTE BS will be in view of the receive antenna array main-beams.

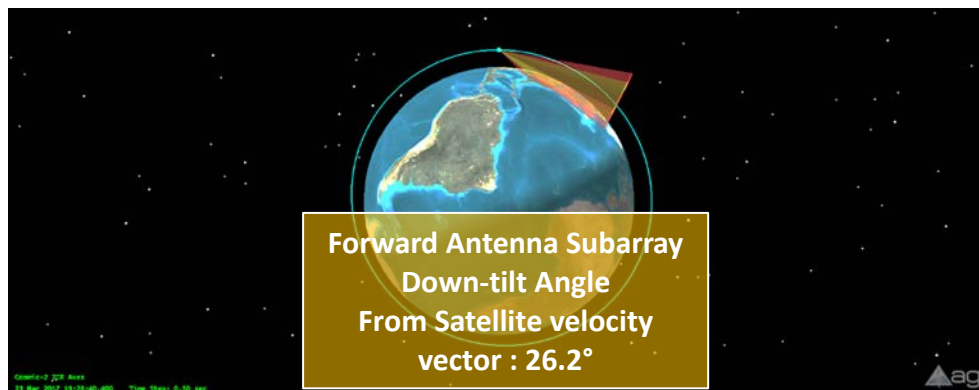


**Figure K-12: TriG RO Antenna Array Main-Beam Down-tilt ( $26.2^\circ$ )**

The antenna subarrays are designed to receive right-hand circular polarized signals from the GNSS satellites. For the analysis, an antenna coupling mismatch (cross-polarization loss) of -3 dB is used (assuming a typical vertically polarized LTE signal).

**Figure K-13** and **Figure K-14** show the gain pattern for the forward antenna with the main-beam directed  $26.2^\circ$  below the satellite velocity vector towards earth limb.

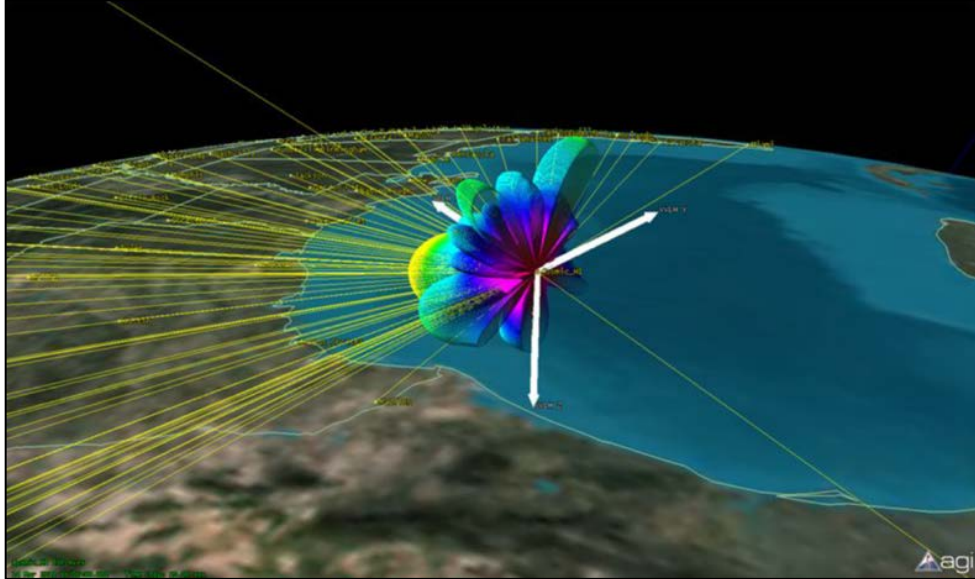


**Figure K-13: Forward Direction Antenna Array (12-Element, 13.4 dBic @ 1530 MHz, main-beam pointed towards Earth limb)**

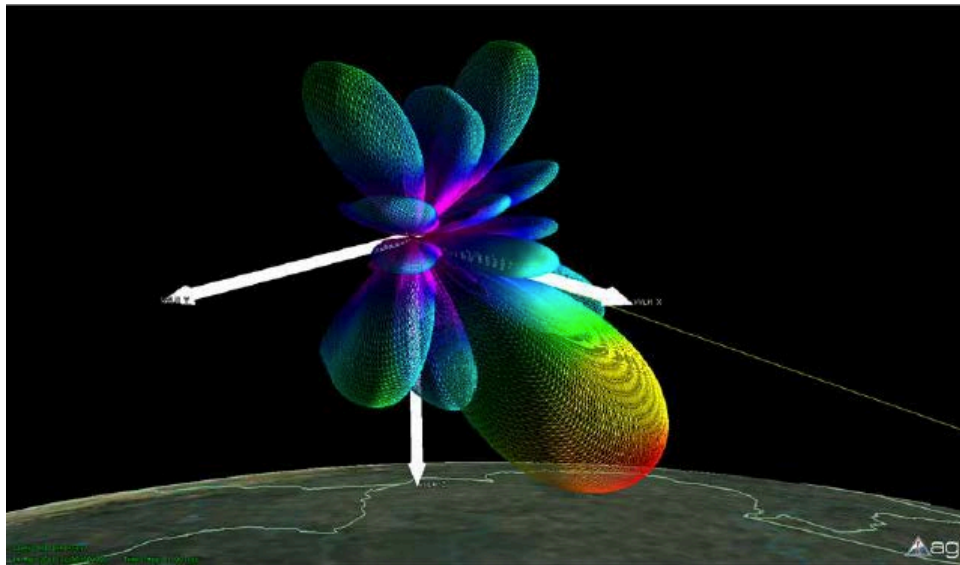


**Figure K-14: Aft Direction Antenna Array (12-Element, 13.4 dBic @ 1530 MHz, main-beam pointed towards Earth limb)**

Based upon the antenna array specifications and operational parameters, above, the 3 dB antenna beam width coverage footprint from COSMIC-2B is approximately 1.6 million square miles. The yellow shaded area over the U.S. in **Figure K-15** displays the footprint for the forward antenna array. [*Note:* It should be noted that a similar area of coverage (mirror-image in the horizontal plane) would also be succeeding the satellite.]

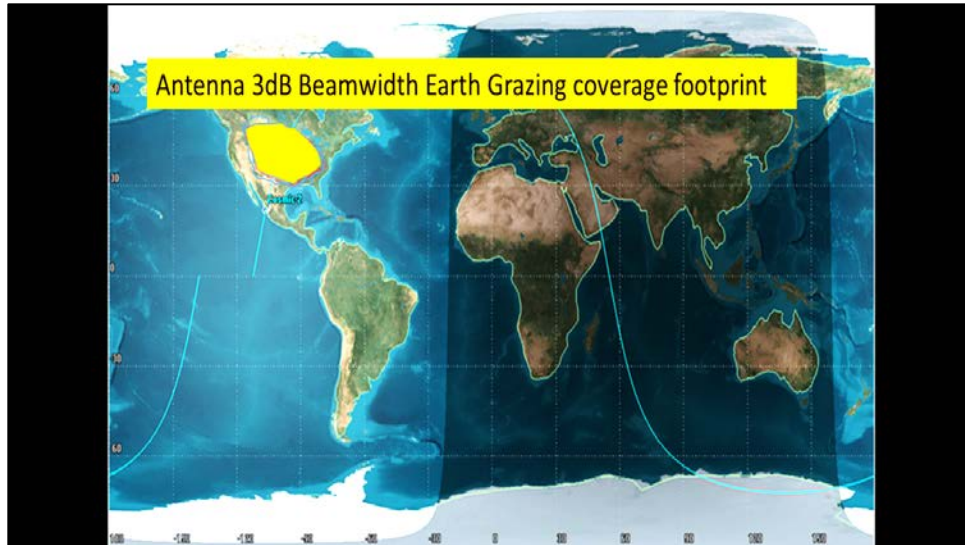


**Figure K-15: COSMIC-2B Antenna 3 dB Beam width Coverage Footprint**

### **COSMIC-2B Antenna Configuration Used for M&S Analysis**

Although the COSMIC-2B antenna has 2 beamforming arrays the M&S was configured to model only the forward antenna since the aft antenna should show near-identical RFI statistics when averaged over ten days.

The effects of this modification are discussed in the results section for COSMIC-2B.

### **Antenna Configuration for Sentinel-6 Mission**

Similar to the COSMIC-2B antenna configuration, the antenna configuration to support Sentinel-6 utilizes a set of two (2) proprietary beam forming array antennas. However, the mission requirements for Sentinel-6 call for a different array configuration, as well as a difference of subarrays on the forward and aft directions of the spacecraft.

The forward antenna array is comprised of a six (6) element array in a 2 x 3 configuration. This array will nominally produce a main beam gain of approximately +15.5 dBic at 1530 MHz. Based on the orbit altitude of Sentinel-6 (1330 km), the forward antenna is mechanically down-tilted so that the main-beam is 34.2° below the satellite velocity vector towards earth limb.

The aft antenna array is comprised of a 12-element array in a 4 x 3 configuration. This array will nominally produce a main beam gain of approximately +17.5 dBic at 1530 MHz. Based on the orbit altitude of Sentinel-6 (1330 km), the aft antenna is electrically phased down (down-tilted) by 22°, as well as mechanically down-tilted an additional 12.0° below the satellite velocity vector towards earth limb.

### Sentinel-6 Antenna Configuration Used for M&S Analysis

The Sentinel-6 antenna will digitally combine the outputs of each of the three subarrays on the fore and aft antennas. Because each RF front end is separate for each subarray, the effect on a single subarray was analyzed for degradation and saturation. For the forward subarray, a 2-element array (2 x 1 configuration) with a peak main beam gain of +10.5 dBic at 1530 MHz was modeled for the simulation. In the aft subarray, a 4-element array (4 x 1 configuration) with a peak main beam gain of +12.5 dBic at 1530 MHz was modeled for the simulation.

The effects of this modification are discussed in the results section for Sentinel-6.

### Summary of TriG Receiver System Characteristics Used for Analyses

**Table K-3** summarizes the satellite TriG receiver system characteristics for the analyses performed on COSMIC-2B and Sentinel-6. The interference threshold in this table is the RFI power at the output of the flight RO antenna which causes a -1 dB C/No degradation in the TriG receiver as used in the COSMIC2 mission. It was derived from the power density observed by the 0 dBiL standard gain horn used in during the DOT ABC test at a RFI power level causing a 1 dB C/No degradation. Since the TriG choke ring antenna was located at a different spot, it actually received about 3.2 dB more RFI power per meter squared (m<sup>2</sup>). In addition, the choke ring antenna had about +3.7 dBi linear gain toward the RFI source, adding 3.7 dB to the threshold power. After these corrections, the LTE power at 1530 MHz that causes a 1 dB C/No degradation is  $-78.2 \text{ dBm} + 3.2 \text{ dB} + 3.7 \text{ dB} = -71.3 \text{ dBm}$ , defined at the output of the receive antenna.

Another adjustment that was made to estimate the effect on the flight receiver is the difference in noise floors due to the extra antenna temperature from black body radiation coming from the ceiling and walls of the WSMR anechoic chamber. During the test, the noise floor is estimated to be 349 Kelvin (K). This is based on preamplifier (Preamp) noise of 51 K, antenna temp of 300 K, and filter loss of 0.8 dB. The noise floor in flight is estimated to be 224 K based on Preamp noise of 51 K, antenna temp of 150 K, and filter loss of 0.8 dB. This difference shows an adjustment to lower the 1 dB threshold by 1.9 dB. Therefore, the normalized in-flight RFI power of is calculated to be approximately  $-73 \text{ dBm}$  ( $-71.3 \text{ dBm} - 1.9 \text{ dB} = -73.2 \text{ dBm}$ ) from the antenna corresponding to a -1 dB degradation of C/No.

**Table K-3: Summary Table of Satellite TriG Receiver Characteristics Used for M&S**

Receiver Characteristic	COSMIC-2B	Sentinel-6
Satellite Orbit Altitude	800 km	1330 km
Satellite Orbit Inclination Angle	72°	66°
TriG Forward Receive Antenna Type	12-Element Array	6-Element Array
TriG Forward Receive Antenna Downtilt (relative to satellite velocity vector)	26.2°	34.2°

TriG Forward Receiver Antenna Subarray Gain @ 1530 MHz	+ 13.4 dBic	+ 10.5 dBic
TriG Aft Receive Antenna Type	Not modeled	12-Element Array
TriG Aft Receive Antenna Downtilt (relative to satellite velocity vector)	Not modeled	34.0°
TriG Aft Receiver Antenna Subarray Gain @ 1530 MHz	Not modeled	+ 12.5 dBic
Interference Threshold (-1 db C/N <sub>0</sub> )	- 73 dBm	- 73 dBm
Loss-of-Lock ( <i>Note</i> : The LOL value ranged from a low of -59 dBm for Test 04 at 1525 MHz to a high of -35 dBm for Test 04 at 1530 MHz, all corrected for antenna location and gain.)	- 59 to -35 dBm	- 59 to -35 dBm
Antenna Coupling Mismatch (Cross-Polarization Loss)	- 3 dB	- 3 dB

### Terrestrial LTE Deployment Scenarios

The aggregate interference is dependent upon several factors. A few of those factors are the satellite related, to include, orbital parameters and receiver system characteristics. The other determining factor comes from the interference sources. Most importantly, the transmitter characteristics and the total number of sources (e.g., LTE BS). Since TriG receiver systems (performing the RO technique) operate in LEO, they have a direct line-of-sight to a broad area of the U.S., and the aggregate interference is dependent upon the long-term deployment scenario of the LTE operator.

The following describes the LTE parameters and the developed scenarios used during M&S.

### Base Stations used for LTE Deployment

To model the terrestrial LTE base station deployment, the analyses used base station (BS) macro and microcell parameters, which are primarily derived from ITU-R M.2292.

For this analysis, the following BS macro and microcell antenna bore-sites with respect to True North were assumed:

- Macrocell Sector-1 bore-site: 0°
- Macrocell Sector-2 bore-site: 120°
- Macrocell Sector-3 bore-site: 240°
- Microcell Sector bore-site: Randomly selected from (0°, 120°, 240°)

NASA used two (2) different methodologies to determine the total number of BS that could be deployed to support the LTE network. The assumptions used for each of the methodologies are described below and resulted in a different number of cell sites.

### City Zone Model

The City Zone model was used to determine the physical area around a city center location that the simulated LTE network would be deployed over. The baseline City Zone model was chosen to conform to the only available accepted model given in ITU Report ITU-R SA.2325-0<sup>10</sup> (International Mobile Telecommunication (IMT) sharing at 2GHz) for an BS deployment based on three (3) zones (e.g., urban, suburban, and rural) with given radial distances from a city center latitude/longitude location. Figure K-16 demonstrates an example of the City Zone model with the typical macro cellular hexagonal grid layout deployed about a city center.

Because the LTE services to be provided by the proposed and analyzed network may not be as widespread in terms of city area as the conventional LTE deployment described in SA.2325-0 a second City Zone model with a smaller Suburban and Rural zone size was analyzed. Parameters for both the City Zone models are listed in Table K-4.

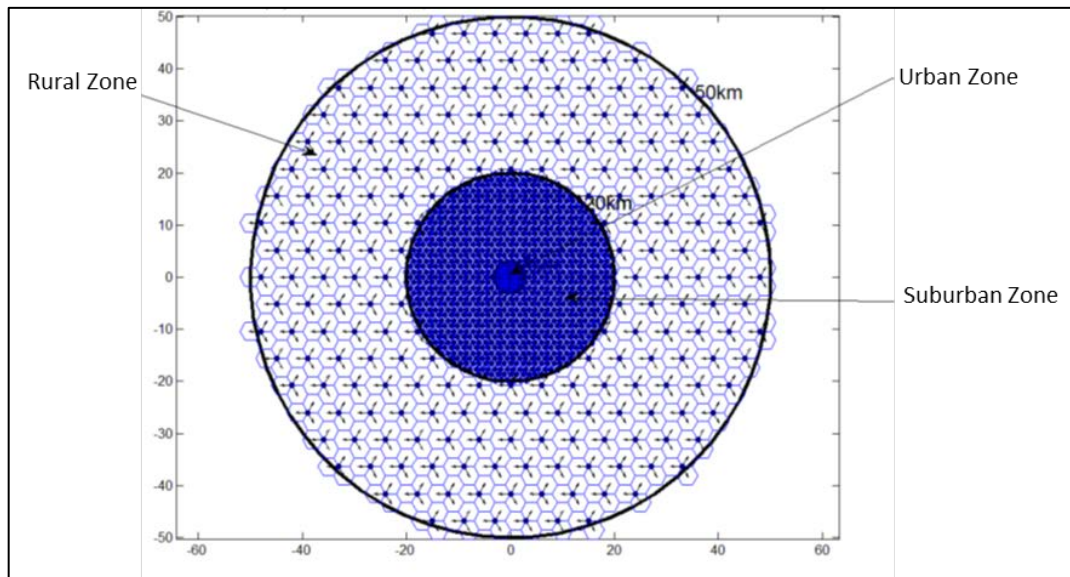


**Figure K-16: Base Station Deployment Zone Model (Report ITU-R SA. 2325-0)**

<sup>10</sup> Reference, [https://www.itu.int/dms\\_pub/itu-r/opb/rep/R-REP-SA.2325-2014-PDF-E.pdf](https://www.itu.int/dms_pub/itu-r/opb/rep/R-REP-SA.2325-2014-PDF-E.pdf)

**Table K-4: Zone Model - BS Zone-specific Radial Distance from City Center**

Zone Model	Urban Zone (km)	Suburban Zone (km)	Rural Zone (km)
1	0 – 3	3 – 20	20 – 50
2	0 – 3	3 – 10	10 – 30

### City Population Size / Base Station Cell Radius

In addition to a City Zone model it was necessary to define the BS cell radius (CR) parameter in order to determine the BS grid layout within each City Zone. The typical ITU-R M.2292 zone values listed in Table K-6 were used as the baseline cell radius (CR) in the simulation.

**Table K-5: Typical Cell Radius (CR) - ITU-R M.2292**

Zone type	City Population	CR (km)
Urban	All	0.5
Suburban	All	1.0
Rural	All	5.0

In consideration to the where the proposed LTE network is to be deployed, the size of the city population was an additional parameter that was included in the simulations. If a U.S. city had a population of greater than 125,000, but less than 250,000, it was included in the analyses for half of the simulations. Cities with populations of over 250,000 were included in all simulations. Accordingly, the number of assumed cities included in each simulation was chosen from:

- City Population > 125K: 225 cities or
- City Population > 250K: 82 cities

Additionally, since a smaller population city could have a smaller amount of Base Stations with a larger Cell Radius (CR), then the typical M.2292 CR values where scaled by the city population and included in the set of simulation runs. Table K-7 shows the addition inclusion of the largest M.2292 CR Table values.



**Table K-7: Cell Radius Scaled by City Population Density (ITU-R M.2292)**

Zone type	City Population (in 1000s)	CR (km)
Urban	> 125 > POP < 250	1.0
	> 250 > POP < 500	0.75
	POP > 500	0.5 (Typical)
Suburban	> 125 > POP < 250	2.0
	> 250 > POP < 500	1.5
	POP > 500	1.0 (Typical)
Rural	> 125 > POP < 250	10.0
	> 250 > POP < 500	10.0
	POP > 500	5.0 (Typical)

**Total Number of Base Stations in Simulations**

Using the set of Zone Model, City Population and Cell Radius parameters, NASA calculated the total number of BS required for deployment for each simulation run. Table K-8 depicts the number of base stations for the set of three parameters for a LTE network deployment consisting of only macrocells. Table K-9 accounts for microcells to be included in the LTE network deployment.

**Table K-8: Total # of BS (Macrocell Deployment Only)**

Zone Model	City Population (in 1000s)	Cell Radius	Number of BS			
			Urban	Suburban	Rural	Total
1	> 125	Table K.6	11,700	143,100	29,700	184,500
1	> 250	Table K.6	4,264	52,152	10,824	67,240
1	> 125	Table K.7	5,330	58,962	10,320	74,612
1	> 250	Table K.7	3,024	35,796	6030	44,868
2	> 125	Table K.6	11,700	33,750	12,150	57,600
2	> 250	Table K.6	4,264	12,300	4,428	20,992
2	> 125	Table K.7	5,330	13,500	5,310	24,140
2	> 250	Table K.7	3,042	8352	2,736	14,130

**Table K-9: Total # of BS (Macro + Microcells)**

Zone Model	City Population (in 1000s)	Cell Radius	Number of BS		
			Macrocells	Microcells	Total
1	> 125	Table K.6	184,500	97,686	282,186
1	> 250	Table K.6	67,240	35,601	102,841
1	> 125	Table K.7	74,612	41,014	115,626
1	> 250	Table K.7	44,868	24,609	69,477
2	> 125	Table K.6	57,600	36,450	94,050
2	> 250	Table K.6	20,992	13,284	34,276
2	> 125	Table K.7	24,140	15,555	39,695
2	> 250	Table K.7	14,130	9,240	23,370

**Additional LTE Network Deployment Assumptions for Analysis**

In addition to the parameters described above, the following simulation parameters were considered and chosen by NASA for the analysis performed.

- Since specific latitude and longitude locations for the BS in each city were not available, BS are placed at respective city center latitude/longitude and BS power aggregated for urban, suburban and rural BS transmitters to get single equivalent urban, suburban, rural and microcell BS.

*Rationale 1:* The angular separation between two (2) BS separated by 10 km is only 0.7°, assuming a TriG receiver at 800 km altitude. This angular separation is relatively small with respect to the transmitter and receiver antenna gain patterns.

*Rational 2:* The time and resources required to model separate BS locations for each city would be exhaustive. Further, the computational time to run the simulations and amount of processing power would be extensive.

- BS antenna side-lobe pattern:
  - ITU-R F.1336-4 Recommends 3.1. (Macro)
  - ITU-R F.1336-4 Recommends 3.2. (Micro)
- Per M.2292, 30% of the macrocell BS are below rooftop and the simulation considered half of the 30% blocked from contributing interference and have already been excluded in the total BS calculations in Table K-8.

- Per M.2292, microcell BS antennas are below rooftop with 50% of the microcells in the urban zone and 30% of the microcells in the suburban zone considered blocked. These BS have already been excluded in the total BS calculations in Table K-9.
- Elevation Mask:  
Consideration given to blockage from terrain, vegetation, and addition man-made structures. This was simulated by providing a 5° transmitter elevation mask in the vertical plane of the transmitter, 360° around the BS in the horizontal plane.  
Two (2) BS mask angles are utilized for the analysis:
  - A 0° elevation mask on the BS so that all BS which see the satellite above 0° elevation angle are included in the aggregate interference calculation, and
  - A 5° mask angle so that only BS which see the satellite above 5° elevation angle contribute to the aggregate interference.
- One (1) 10 MHz LTE channel per sector.
- Propagation Loss: Free-space
- BS Activity Factor (AF):  
An AF of 3 dB, corresponding to 50% of the base stations transmitting simultaneously, is used throughout the analysis.

*Note:* If 100% of the base stations are transmitting simultaneously, the peak interference levels in the results will be 3 dB higher. This will also hold true for other resultant statistics, as well.

- BS Transmitter Power (EIRP):  
Table K-10 depicts the nominal transmit power used for some of the simulations (as per ITU-R M.2292). Considerations were also given to the maximum transmit powers of +10 dBW<sup>11</sup> and +32 dBW<sup>12</sup> EIRP per channel per sector.

---

<sup>11</sup> Proposed maximum transmit power per channel per sector through negotiations with the FAA.

<sup>12</sup> Maximum transmit power per channel per sector as authorized in the current FCC license.

**Table K-10: Assumed Maximum Transmitter Levels per Sector  
(Typical per ITU-R M.2292)**

BS Type	Typical Max. Transmit Power/Channel/Sector (EIRP)
Macrocell - Urban	26 dBW
Macrocell - Suburban	26 dBW
Macrocell - Rural	28 dBW
Microcell (any zone)	7 dBW

### TriG Receiver Analysis

Two (2) NASA missions (COSMIC-2B and Sentinel-6) that include the TriG receiver, as a science-based function (e.g., RO technique) were utilized for analysis. A MATLAB simulation program was developed to model the receiver on-board a satellite, using mission-specific parameters, and interference statistics were calculated for an LTE network deployment of BS distributed in U.S. cities.

### MATLAB Simulation

For the spaceborne receiver analysis the aggregate interference power at the output of the GPS receiver antenna is calculated at ten (10) second time steps in the satellite orbit from BS distributed among U.S. cities. The MATLAB program was setup to model a 10-day orbit of the satellite. **Figure K-17** provides an example of the COSMIC-2B satellite simulation of a 10-day orbit.

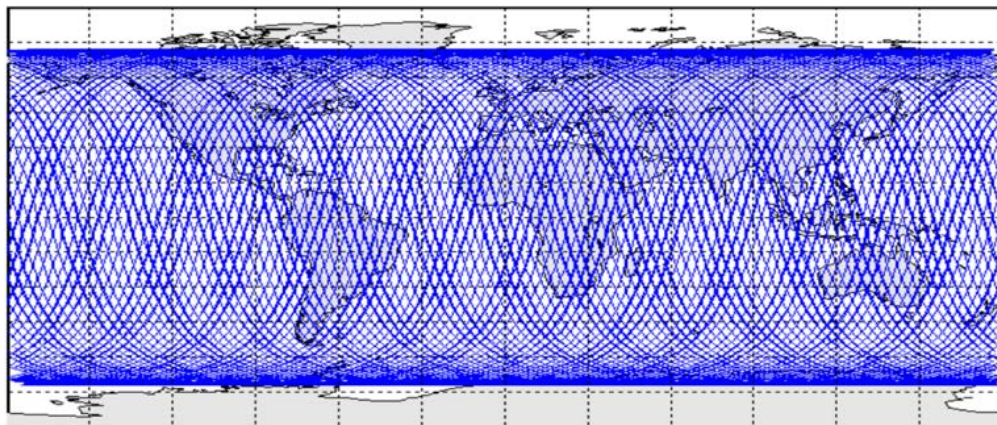


**Figure K-17: Ground Track of COSMIC-2B Orbital Path (10-Day Simulation at 10-Second Time Steps)**

A similar program written in Python was implemented for the Sentinel-6 simulation.

## Aggregate Interference Calculation

The analysis calculates the  $I_o/N_o$  value and is not dependent upon the carrier (C) signal. Thresholds for determining the saturation (-1 dB C/ $N_o$ ) and jammed (loss-of-lock) values of the TriG are discussed in this report.

The aggregate interference to the receiver antenna output is calculated using a summation of the interference from each source. A simple link budget formula is used to calculate the interference received by a single source, LTE BS. The total aggregate interference is determined through the summation of interference from the individual sources, see Equation K-2.

$$\text{Rx Int Pwr}_{\text{agg}} = \sum(\text{Int sources}) \text{ Tx Pwr (EIRP)}_{\text{off-boresite}} - \text{FSPL} - \text{Pol Loss} + \text{Rx Ant Gain}_{\text{off-boresite}}$$

### Equation K-2: Formula in Determining Received Aggregate Interference at the TriG Antenna Output

Where,

$\text{Rx Int Pwr}_{\text{agg}}$  = Aggregate interference power level (dBm)

$\text{Tx Pwr (EIRP)}_{\text{off-boresite}}$  = Tx power output including antenna off-boresite calculations (dBm) (See below)

FSPL = Free Space Path Loss (dB)

Pol Loss = Loss of dissimilar polarizations (Linear to RCHP Polarization = - 3 dB)

$\text{Rx Ant Gain}_{\text{off-boresite}}$  = Rx antenna gain including antenna off-boresite calculations (dBic)

The BS sector antenna gain towards the satellite is calculated by first determining the appropriate azimuth (AZ) (horizontal plane) and elevation (EL) (vertical plane) angles based on the BS and satellite geometry. The antenna off-boresite gain is calculated by, first, summing the AZ plane discrimination with the EL plane discrimination and, secondly, subtracting this total discrimination from the maximum sector gain<sup>13</sup> to get the net sector gain towards the satellite.

*Note:* The maximum interference from an BS will occur when it sees the satellite at low elevation angles.

## Simulation Runs

A total of 96 simulation runs were performed for COSMIC-2B, while a lesser number, but still representative, number of runs (16 runs) were performed for Sentinel-6. Each of the simulation runs varied one or more LTE BS deployment parameters.

While it is unknown for how the LTE operator will be performing their network deployment, the variations in simulation runs should be demonstrative. Further, the variations in runs may be representative of an LTE network through its various phases of deployment (initial deployment through full deployment). **Table K-6** summarizes the various simulation runs.

---

<sup>13</sup> As defined in ITU-R M.2292 and ITU-R F.1336-4.

**Table K-6: Summary of Simulation Runs**

Run	Sim No.	Run Designator	COSMIC-2B	Sentinel-6	BS Tx Power	Zone Model	City Population	Cell Radius	Elevation Mask	Macrocell Only	Macro + Microcell	Total # of Base Stations
1	1	a	X		M.2292 levels	1	> 125K	Typical	0°	X		184,500
2	1	b	X	X	M.2292 levels	1	> 125K	Typical	5°	X		184,500
3	1	c	X		32 dBW	1	> 125K	Typical	0°	X		184,500
4	1	d	X		32 dBW	1	> 125K	Typical	5°	X		184,500
5	1	e	X		10 dBW	1	> 125K	Typical	0°	X		184,500
6	1	f	X	X	10 dBW	1	> 125K	Typical	5°	X		184,500
7	2	a	X		M.2292 levels	1	> 250K	Typical	0°	X		67,240
8	2	b	X	X	M.2292 levels	1	> 250K	Typical	5°	X		67,240
9	2	c	X		32 dBW	1	> 250K	Typical	0°	X		67,240
10	2	d	X		32 dBW	1	> 250K	Typical	5°	X		67,240
11	2	e	X		10 dBW	1	> 250K	Typical	0°	X		67,240
12	2	f	X	X	10 dBW	1	> 250K	Typical	5°	X		67,240
13	3	a	X	X	M.2292 levels	1	> 125K	Scaled	0°	X		74,612
14	3	b	X	X	M.2292 levels	1	> 125K	Scaled	5°	X		74,612
15	3	c	X	X	32 dBW	1	> 125K	Scaled	0°	X		74,612
16	3	d	X	X	32 dBW	1	> 125K	Scaled	5°	X		74,612
17	3	e	X	X	10 dBW	1	> 125K	Scaled	0°	X		74,612
18	3	f	X	X	10 dBW	1	> 125K	Scaled	5°	X		74,612

19	4	a	X	X	M.2292 levels	1	> 250K	Scaled	0°	X		44,850
20	4	b	X	X	M.2292 levels	1	> 250K	Scaled	5°	X		44,850
21	4	c	X	X	32 dBW	1	> 250K	Scaled	0°	X		44,850
22	4	d	X	X	32 dBW	1	> 250K	Scaled	5°	X		44,850
23	4	e	X	X	10 dBW	1	> 250K	Scaled	0°	X		44,850
24	4	f	X	X	10 dBW	1	> 250K	Scaled	5°	X		44,850
25	5	a	X		M.2292 levels	2	> 125K	Typical	0°	X		57,600
26	5	b	X		M.2292 levels	2	> 125K	Typical	5°	X		57,600
27	5	c	X		32 dBW	2	> 125K	Typical	0°	X		57,600
28	5	d	X		32 dBW	2	> 125K	Typical	5°	X		57,600
29	5	e	X		10 dBW	2	> 125K	Typical	0°	X		57,600
30	5	f	X		10 dBW	2	> 125K	Typical	5°	X		57,600
31	6	a	X		M.2292 levels	2	> 250K	Typical	0°	X		20,992
32	6	b	X		M.2292 levels	2	> 250K	Typical	5°	X		20,992
33	6	c	X		32 dBW	2	> 250K	Typical	0°	X		20,992
34	6	d	X		32 dBW	2	> 250K	Typical	5°	X		20,992
35	6	e	X		10 dBW	2	> 250K	Typical	0°	X		20,992
36	6	f	X		10 dBW	2	> 250K	Typical	5°	X		20,992
37	7	a	X		M.2292 levels	2	> 125K	Scaled	0°	X		24,140
38	7	b	X		M.2292 levels	2	> 125K	Scaled	5°	X		24,140

39	7	c	X		32 dBW	2	> 125K	Scaled	0°	X		24,140
40	7	d	X		32 dBW	2	> 125K	Scaled	5°	X		24,140
41	7	e	X		10 dBW	2	> 125K	Scaled	0°	X		24,140
42	7	f	X		10 dBW	2	> 125K	Scaled	5°	X		24,140
43	8	a	X		M.2292 levels	2	> 250K	Scaled	0°	X		14,130
44	8	b	X		M.2292 levels	2	> 250K	Scaled	5°	X		14,130
45	8	c	X		32 dBW	2	> 250K	Scaled	0°	X		14,130
46	8	d	X		32 dBW	2	> 250K	Scaled	5°	X		14,130
47	8	e	X		10 dBW	2	> 250K	Scaled	0°	X		14,130
48	8	f	X		10 dBW	2	> 250K	Scaled	5°	X		14,130
49	9	a	X		M.2292 levels	1	> 125K	Typical	0°		X	282,186
50	9	b	X		M.2292 levels	1	> 125K	Typical	5°		X	282,186
51	9	c	X		32 dBW	1	> 125K	Typical	0°		X	282,186
52	9	d	X		32 dBW	1	> 125K	Typical	5°		X	282,186
53	9	e	X		10 dBW	1	> 125K	Typical	0°		X	282,186
54	9	f	X		10 dBW	1	> 125K	Typical	5°		X	282,186
55	10	a	X		M.2292 levels	1	> 250K	Typical	0°		X	102,841
56	10	b	X		M.2292 levels	1	> 250K	Typical	5°		X	102,841
57	10	c	X		32 dBW	1	> 250K	Typical	0°		X	102,841
58	10	d	X		32 dBW	1	> 250K	Typical	5°		X	102,841



59	10	e	X		10 dBW	1	> 250K	Typical	0°		X	102,841
60	10	f	X		10 dBW	1	> 250K	Typical	5°		X	102,841
61	11	a	X		M.2292 levels	1	> 125K	Scaled	0°		X	115,626
62	11	b	X		M.2292 levels	1	> 125K	Scaled	5°		X	115,626
63	11	c	X		32 dBW	1	> 125K	Scaled	0°		X	115,626
64	11	d	X		32 dBW	1	> 125K	Scaled	5°		X	115,626
65	11	e	X		10 dBW	1	> 125K	Scaled	0°		X	115,626
66	11	f	X		10 dBW	1	> 125K	Scaled	5°		X	115,626
67	12	a	X		M.2292 levels	1	> 250K	Scaled	0°		X	69,477
68	12	b	X		M.2292 levels	1	> 250K	Scaled	5°		X	69,477
69	12	c	X		32 dBW	1	> 250K	Scaled	0°		X	69,477
70	12	d	X		32 dBW	1	> 250K	Scaled	5°		X	69,477
71	12	e	X		10 dBW	1	> 250K	Scaled	0°		X	69,477
72	12	f	X		10 dBW	1	> 250K	Scaled	5°		X	69,477
73	13	a	X		M.2292 levels	2	> 125K	Typical	0°		X	94,050
74	13	b	X		M.2292 levels	2	> 125K	Typical	5°		X	94,050
75	13	c	X		32 dBW	2	> 125K	Typical	0°		X	94,050
76	13	d	X		32 dBW	2	> 125K	Typical	5°		X	94,050
77	13	e	X		10 dBW	2	> 125K	Typical	0°		X	94,050
78	13	f	X		10 dBW	2	> 125K	Typical	5°		X	94,050

79	14	a	X		M.2292 levels	2	> 250K	Typical	0°		X	34,276
80	14	b	X		M.2292 levels	2	> 250K	Typical	5°		X	34,276
81	14	c	X		32 dBW	2	> 250K	Typical	0°		X	34,276
82	14	d	X		32 dBW	2	> 250K	Typical	5°		X	34,276
83	14	e	X		10 dBW	2	> 250K	Typical	0°		X	34,276
84	14	f	X		10 dBW	2	> 250K	Typical	5°		X	34,276
85	15	a	X		M.2292 levels	2	> 125K	Scaled	0°		X	39,695
86	15	b	X		M.2292 levels	2	> 125K	Scaled	5°		X	39,695
87	15	c	X		32 dBW	2	> 125K	Scaled	0°		X	39,695
88	15	d	X		32 dBW	2	> 125K	Scaled	5°		X	39,695
89	15	e	X		10 dBW	2	> 125K	Scaled	0°		X	39,695
90	15	f	X		10 dBW	2	> 125K	Scaled	5°		X	39,695
91	16	a	X		M.2292 levels	2	> 250K	Scaled	0°		X	23,370
92	16	b	X		M.2292 levels	2	> 250K	Scaled	5°		X	23,370
93	16	c	X		32 dBW	2	> 250K	Scaled	0°		X	23,370
94	16	d	X		32 dBW	2	> 250K	Scaled	5°		X	23,370
95	16	e	X		10 dBW	2	> 250K	Scaled	0°		X	23,370
96	16	f	X		10 dBW	2	> 250K	Scaled	5°		X	23,370

## Results

The aggregate interference results for the TriG receiver, functioning as a science measurement instrument, are presented in the following sections.

The received aggregate interference levels calculated during the simulations range from -90 dBm to -40 dBm.

The following tables use an aggregate interference threshold of -73 dBm (1526 – 1536 MHz) which corresponds to a -1 dB degradation of receiver C/No.

It should be noted that the loss-of-lock threshold for the TriG receiver occurs between -59 to -35 dBm aggregate interference power in the 1526-1536 MHz band. Loss-of-Lock at -59 dBm was seen in Test 04 with RFI at 1525 MHz and LOL at -35 dBm was seen in Test 04 at 1530 MHz.

The entries in the results tables are interpreted as follows:

- Column 3: Max Int. Level (dBm)

Indicates the maximum aggregate interference level calculated at the receiver antenna output.

*Note:* Any value  $\geq$  -66 dBm in this column indicates that there is sufficient aggregate interference received from the terrestrial LTE network for the TriG receiver to lose lock.

- Column 4: % Time > Threshold

Indicates the percent time, over the 10-day simulation period, where the aggregate interference at the TriG receiver antenna output exceeds the threshold level (-73 dBm).

As an example, if the value is about 10% of the time, the TriG receiver will have C/No degraded by at least 1 dB for a cumulative of 24 hours. This is calculated by, as an example:

10 days (total period of simulation run) = 240 hours

% Time > Threshold = 10%

10% of 10 days (240 hours) =  $0.10 \times 240 = \underline{24 \text{ hours}}$

*Note:* The value reported represents the % Time > Threshold for the entire 10-days of the simulation, to include the time and instances where the continental U.S. is not within the field-of-view of the satellite. Consideration must be taken based on this. If the master time schedule only included the instances where the continental U.S. (and surrounding bodies of water) were in the field-of-view of the satellite, these values would increase.

- Column 5: # of Int Events

Indicates that over the 10-day period, the total number of interference events which exceed the -73 dBm threshold.

*Note:* The interference time intervals for each interference occurrence may be short or long depending on how many interfering BS the satellite sees on the particular orbit pass over the U.S. The sum duration of all of the interference events (provided in this column) is the reported in column 4 (% Time > Threshold). Furthermore, it should be noted that there can be multiple interference events for a single satellite pass, as different BS pass through the field-of-view of the TriG receiver antenna.

- Column 6: Avg Dur Int Event (min)

Indicates the mean average duration (in minutes) of an interference event for the entire 10-day period.

*Note:* As discussed in Section 5.3.1, the duration of an atmospheric occultation (as the signal path moves from skimming the Earth's surface to an altitude of about 100 km) is one to two minutes.

- Column 7: Max Int Event (min)

Indicates the maximum duration (in minutes) that was recorded for a single interference event over the 10-day period.

- Column 8: Max Allow EIRP Level (dBW)

Indicates a reverse-engineered maximum BS transmitter power level (in dBW) distributed across a 10 MHz bandwidth per channel per sector. The calculated level is based on the maximum interference level received during the 10-day period.

*Note 1:* The reverse-engineered value calculated in this column would bring the interference level below the -73 dBm threshold value. However, it should be also noted that interference to the TriG receiver occurs well before the -73 dBm threshold value occurs, which causes degradation in scientific measurements (e.g., interference occurs at interference levels -90 dBm to -73 dBm (threshold)).

*Note 2:* Where applicable (i.e., simulations that utilized variable maximum transmitter power levels), the maximum allowable EIRP level is linearly calculated for each zonal category of BS sector.

As an example, if the maximum interference level (column 3) indicates -70 dBm, the BS transmitter power needs to be reduced by 3.1 dBm in order for the received interference to be below the -73 dBm threshold. The 3.1 dBm reduction in power is linearly attributed to each of the maximum transmitter power for the urban/suburban (+26 dBW), rural (+28

dBW), and microcells (+7 dBW). The resulting maximum allowable transmitter power is calculated for the urban/suburban zone as +22.9 dBW, rural zone as +24.9 dBW, and microcells as +3.9 dBW.

## **Results Caveats**

### *Caveat 1:*

The results are only for the LTE deployment scenarios derived from parameters outlined. Deviation of such LTE system characteristics from ITU-R M.2292 may adversely impact the interference received at the satellite. This is especially true if the typical BS antennas vary in the vertical plane from what was defined in ITU-R F.1336-4, or if the nominal down-tilt angles, as defined in ITU-R M.2292, are deployed at 0 deg or with an up-tilt (e.g., more LTE BS signal energy pointing directly over the horizon or into the atmosphere).

### *Caveat 2:*

The results presented in the following sections are intended to draw no conclusions or make any recommendations as to what level of interference may be tolerated by the other missions employing the TriG receiver for science applications. Aggregate interference received by the TriG receiver system in-orbit is dependent upon the satellite orbit parameters and receive antenna configurations.

### *Caveat 3:*

The results are for the simulated operational use of the TriG receiver while in-orbit. It should be noted that the TriG receivers are currently researched, developed and tested (RD&T) in facilities that are not electromagnetically shielded from the existing RF environment. As such, the TriG receivers may be impacted by LTE BS sites located within close proximity. The effects to the RD&T facilities have not been studied and additional analyses would be required to further understand the impacts to the TriG receivers at the RD&T facilities.

## **Results for COSMIC-2B**

Tables **Table K-7** through

**Table K-12** provides a results summary of the analyses performed for the TriG receiver simulated aboard a single COSMIC-2B satellite, and for all simulation parameters shown in **Table K-6**. (The COSMIC-2B mission is comprised of six (6) total satellites.)

[*Note:* Only the forward antenna array was used in the M&S. In reality, COSMIC-2B will utilize a set of 3 subarrays on the forward and aft ends of the satellite. These three (3) subarrays (each having +13.4 dBc gain at 1530 MHz) will be digitally combined in the TriG receiver to achieve a total of +16.7 dBc antenna gain at 1530 MHz in both the fore and aft antennas.]

The results below show results for the fore antenna. The viewing geometries will be similar for the aft antenna, and the calculated values for the tables below would be expected to have similar values from the aft antenna. There will be slight variations due to the fact the individual Base Stations are viewed from azimuths which differ by about 180 degrees (in the BS reference frame).

**Table K-7: COSMIC-2B Interference Results  
(Macro BS Only, Urban/Suburban: Tx Power +26 dBW,  
Rural Tx Power: +28 dBW)**

Sim No.	Run Designator	Max int. Level (dBm)	% Time > Thresh	# of Int Events	Avg Dur Int. Event (min)	Max Int Event (min)	Max Allow EIRP Level (dBW)	
							Urban/Suburban BS	Rural BS
1	a	-57	3.3	83	5.5	11.0	10	12
1	b	-62	2.1	61	4.8	8.8	15	17
2	a	-62	1.8	59	4.1	9.0	15	17
2	b	-67	1.1	43	3.4	6.3	20	22
3	a	-62	1.9	62	4.3	9.0	15	17
3	b	-66	1.2	40	4.0	7.0	19	21
4	a	-64	1.3	44	3.9	7.7	17	19
4	b	-68	0.6	31	2.8	4.8	21	23
5	a	-63	1.6	52	4.2	8.5	16	18
5	b	-67	0.9	32	3.7	6.7	20	22
6	a	-68	0.7	43	2.2	5.5	21	23
6	b	-72	0.1	10	1.9	2.7	25	27
7	a	-67	0.8	32	3.4	6.0	20	22
7	b	-71	0.2	19	1.4	3.0	24	26
8	a	-69	0.4	31	1.6	4.2	22	24

8	b	-74	0.0	0	0.0	0.0	27	29
---	---	-----	-----	---	-----	-----	----	----

**Table K-8: COSMIC-2B Interference Results  
(Macro BS Only, All BS Tx Power +32 dBW)**

Sim No.	Run Designator	Max int. Level (dBm)	% Time > Thresh	# of Int Events	Avg Dur Int. Event (min)	Max Int Event (min)	Max Allow EIRP Level (dBW)
1	c	-52	5.4	137	5.5	13.2	11
1	d	-56	3.7	84	6.2	10.7	15
2	c	-57	3.7	115	4.5	10.7	16
2	d	-61	2.3	67	4.9	9.3	20
3	c	-57	3.9	93	5.8	11.5	16
3	d	-61	2.5	70	5.1	9.5	20
4	c	-58	3.1	87	5.0	10.5	17
4	d	-63	2.0	57	4.8	8.0	22
5	c	-57	3.4	83	5.7	11.2	16
5	d	-61	2.2	57	5.4	8.8	20
6	c	-62	1.9	62	4.2	9.2	21
6	d	-66	1.2	47	3.5	6.5	25
7	c	-62	2.1	66	4.4	9.2	21
7	d	-66	1.3	47	3.9	7.3	25
8	c	-64	1.4	44	4.3	7.8	23
8	d	-68	0.7	32	3.2	5.3	27

**Table K-9: COSMIC-2B Interference Results  
(Macro BS Only, All BS Tx Power +10 dBW)**

Sim No.	Run Designator	Max int. Level (dBm)	% Time > Thresh	# of Int Events	Avg Dur Int. Event (min)	Max Int Event (min)	Max Allow EIRP Level (dBW) <sup>14</sup>
1	e	-74	0.0	0	0.0	0.0	10
1	f	-78	0.0	0	0.0	0.0	10
2	e	-79	0.0	0	0.0	0.0	10
2	f	-83	0.0	0	0.0	0.0	10
3	e	-79	0.0	0	0.0	0.0	10

<sup>14</sup> Based on the assumption that the maximum transmitter power level is limited to +10 dBW.



3	f	-83	0.0	0	0.0	0.0	10
4	e	-80	0.0	0	0.0	0.0	10
4	f	-85	0.0	0	0.0	0.0	10
5	e	-79	0.0	0	0.0	0.0	10
5	f	-83	0.0	0	0.0	0.0	10
6	e	-84	0.0	0	0.0	0.0	10
6	f	-88	0.0	0	0.0	0.0	10
7	e	-84	0.0	0	0.0	0.0	10
7	f	-88	0.0	0	0.0	0.0	10
8	e	-86	0.0	0	0.0	0.0	10
8	f	-90	0.0	0	0.0	0.0	10

**Table K-10: COSMIC-2B Interference Results  
(Macro + Microcells, Urban/Suburban: Tx Power +26 dBW,  
Rural Tx Power: +28 dBW, Microcell Tx Power +7 dBW)**

Sim No.	Run Designator	Max int. Level (dBm)	% Time > Thresh	# of Int Events	Avg Dur Int. Event (min)	Max Int Event (min)	Max Allow EIRP Level (dBW)		
							Urban/Suburban BS	Rural BS	Microcell
9	a	-57	3.3	81	5.8	11.2	10	12	-9
9	b	-62	2.1	60	5.0	8.8	15	17	-4
10	a	-62	1.8	59	4.3	9.0	15	17	-4
10	b	-66	1.1	42	3.8	6.3	19	21	0
11	a	-62	2.0	62	4.5	9.0	15	17	-4
11	b	-66	1.2	43	3.9	7.0	19	21	0
12	a	-64	1.3	44	4.1	7.8	17	19	-2
12	b	-68	0.7	30	3.1	5.0	21	23	2
13	a	-63	1.7	52	4.5	8.7	16	18	-3
13	b	-67	1.0	43	3.1	6.8	20	22	1
14	a	-68	0.7	40	2.5	5.5	21	23	2
14	b	-71	0.2	15	1.4	2.8	24	26	5
15	a	-67	0.8	33	3.4	6.2	20	22	1

15	b	-71	0.2	18	1.8	3.0	24	26	5
16	a	-69	0.4	35	1.5	4.3	22	24	3
16	b	-73	0.0	4	0.1	0.2	26	28	7

**Table K-11: COSMIC-2B Interference Results  
(Macro + Microcells, All S Tx Power +32 dBW/10MHz)**

Sim No.	Run Designator	Max int. Level (dBm)	% Time > Thresh	# of Int Events	Avg Dur Int. Event (min)	Max Int Event (min)	Max Allow EIRP Level (dBW)
9	c	-49	8.5	160	7.5	15.5	8
9	d	-50	6.3	136	6.5	13.5	9
10	c	-53	7.0	147	6.7	13.5	12
10	d	-54	5.2	128	5.6	11.5	13
11	c	-53	6.9	137	7.0	14.3	12
11	d	-54	5.1	111	6.5	11.8	13
12	c	-55	6.4	135	6.7	13.2	14
12	d	-56	4.6	132	4.9	11.2	15
13	c	-53	6.5	128	7.2	13.8	12
13	d	-54	4.9	111	6.2	11.7	13
14	c	-58	4.9	119	5.7	11.8	17
14	d	-59	3.5	97	5.0	10.2	18
15	c	-57	4.8	95	7.1	12.3	16
15	d	-58	3.5	86	5.7	10.5	17
16	c	-59	3.8	91	5.9	11.0	18
16	d	-61	2.7	71	5.3	9.5	20

**Table K-12: COSMIC-2B Interference Results  
(Macro + Microcells, All BS Tx Power +10 dBW)**

Sim No.	Run Designator	Max int. Level (dBm)	% Time > Thresh	# of Int Events	Avg Dur Int. Event (min)	Max Int Event (min)	Max Allow EIRP Level (dBW) <sup>15</sup>
9	e	-71	0.5	32	1.9	3.8	7
9	f	-72	0.1	12	1.0	2.2	8
10	e	-75	0.0	0	0.0	0.0	10
10	f	-76	0.0	0	0.0	0.0	10
11	e	-75	0.0	0	0.0	0.0	10
11	f	-76	0.0	0	0.0	0.0	10
12	e	-77	0.0	0	0.0	0.0	10
12	f	-78	0.0	0	0.0	0.0	10
13	e	-75	0.0	0	0.0	0.0	10
13	f	-76	0.0	0	0.0	0.0	10
14	e	-80	0.0	0	0.0	0.0	10
14	f	-81	0.0	0	0.0	0.0	10
15	e	-79	0.0	0	0.0	0.0	10
15	f	-80	0.0	0	0.0	0.0	10
16	e	-81	0.0	0	0.0	0.0	10
16	f	-83	0.0	0	0.0	0.0	10

**Results for Sentinel-6**

Tables **Table K-13** through **Table K-15** report the results of the analyses performed for the TriG receiver simulated aboard the Sentinel-6 satellite.

[*Note:* A 2-element subarray (2 x 1 configuration) with a gain of +10.5 dBic at 1530 MHz was modeled for the forward subarray, and a 4-element subarray (4 x 1 configuration) with a peak gain of +12.5 dBic at 1530 MHz was modeled for the aft subarray. Results represent the total interference in both antennas. When the full array output is combined, the 6-element forward array consisting of three 2x1 subarrays will have a main beam gain of +15.5 dBic at 1530 MHz, and the 12-element aft array consisting of three 4x1 subarrays will have a main beam gain of +17.5 dBic at 1530 MHz.]

---

<sup>15</sup> Based on the assumption that the maximum transmitter power level is limited to +10 dBW.

**Table K-13: Sentinel-6 Interference Results  
(Macro BS Only, Urban/Suburban: Tx Power +26 dBW,  
Rural Tx Power: +28 dBW)**

Sim No.	Run Designator	Max int. Level (dBm)	% Time > Thresh	Max Allow EIRP Level (dBW)	
				Urban/Suburban BS	Rural BS
1	b	-66	3.7	19	21
2	b	-70	1.9	23	25
3	b	-72	0.6	25	27
4	b	-76	0	29	31
3	a	-70	2.1	23	25
4	a	-74	0.2	27	29

**Table K-14: Sentinel-6 Interference Results  
(Macro BS Only, All BS Tx Power +32 dBW)**

Sim No.	Run Designator	Max int. Level (dBm)	% Time > Thresh	Max Allow EIRP Level (dBW)
3	c	-64	5.8	23
3	d	-66	3.7	25
4	c	-68	3.4	27
4	d	-70	1.9	29

**Table K-15: Sentinel-6 Interference Results  
(Macro BS Only, All BS Tx Power +10 dBW)**

Sim No.	Run Designator	Max int. Level (dBm)	% Time > Thresh	Max Allow EIRP Level (dBW) <sup>16</sup>
1	f	-76	0	10
2	f	-76	0	10
3	f	-78	0	10
4	f	-82	0	10
3	e	-76	0	10
4	e	-80	0	10

**Results Summary**

The results tables represent a myriad of LTE BS deployment scenarios and reports the maximum allowable EIRP levels for the terrestrial LTE BS sectors per channel.

In the case of COSMIC-2B, for the simple scenario of macro cell BS at 32 dBW EIRP, as the number of stations decreases from simulation 1 to 2 for the zone-1 model, and from simulation 5 to 6 for the zone-2 model, there is about 5 dB less interference in zone-2 compared to zone-1, which is expected because the zone-2 model uses about 3 times less stations. There is about 4 dB less interference in models using transmitter elevation mask of 5° (run d) compared to the 0° mask (run c), indicating that less than half of the available stations affect the satellite in the 5° mask case.

For the most challenging model (1c), using 184,500 macro cell stations, the tolerable EIRP is 11 dBW(i.e., 12.6 Watts). For a deployment of macro and microcells, utilizing the same transmitter power, the maximum tolerable EIRP is approximately 8 dBW(i.e., 6.3 Watts).

In the case of the Sentinel-6, for the simple scenario of macro cell BS at 32 dBW EIRP, as the number of stations decreases from simulation 3 to 4 for the zone-1 model, there is about 2 dB less interference in models using transmitter elevation mask of 5° (run d) compared to the 0° mask (run c). For the most challenging model (3c), using 74,612 macro cell stations, the tolerable EIRP is 23 dBW.

It should be noted that simulations 3 and 4 use the aforementioned variation of the cell model, referred to as ‘scaled’ model, in which the cell radius increases up to double its typical value, as the city population decreases; this results in fewer stations, and less interference, compared to the simulations 1 and 2.

---

<sup>16</sup> Based on the assumption that the maximum transmitter power level is limited to +10 dBW.

These tolerances only predict the impact to two (2) NASA Missions (COSMIC-2B and Sentinel-6), and the results from these simulations cannot be used to deduce the impacts of other missions where the TriG receiver will be employed for science applications. Specific orbit and antenna configuration for other TriG missions will need to be considered in order to make a holistic determination of the maximum tolerance values (e.g., maximum transmitter power and total number of LTE BS) for the terrestrial LTE network.

As an example of this, while the maximum antenna gain for Sentinel-6 is lower than the antenna configuration used for COSMIC-2B, the percent time above the threshold (-73 dBm) is greater. This is due to the higher orbit altitude of the Sentinel-6 providing a much larger field-of-view of the U.S. resulting in a larger total number of LTE BS in view. This results in a lower peak interference power due to greater space loss, but greater average power.

Also, consideration needs to be given to the reported results on TIME, when assessing the overall impact of the scientific measurements. The typical duration for an atmospheric sounding using RO is only one (1) to two (2) minutes. In certain modeled LTE BS deployment scenarios, the average duration of an interference event may be well above the one (1) or two (2) minutes needed to perform an occultation measurement. Loss of any data during a given RO event will generally result in loss of the entire RO profile.

Further, in conjunction with the TIME aspect, the time associated when a satellite in-orbit has the continental U.S. (and adjacent areas in surrounding bodies of water – Atlantic Ocean, Pacific Ocean, and Gulf of Mexico) within its field-of-view needs to be considered. As the reported results under the % Time > Threshold are referenced to a timeframe that is representative of a satellite orbiting the entire Earth, the deduced interference time to occultations performed over the continental U.S. will be significant. The results tables indicate that the TriG receiver will effectively be degraded (> threshold) up to 9.6% of the time during a 10-day orbit. Since the continental U.S. (and surrounding bodies of water) represent approximately 2.5% of the surface of the earth, this represents a significant degradation to the ability for the TriG receiver in providing valuable scientific data.

Finally, it is important to note that the results generated here use a 50% utilization factor. In a time of weather crisis such as a hurricane, the utilization may increase substantially in response to emergency responder and population communication needs. This increase in utilization would increase the interference by 3dB at a time when the occultation measurements would be useful in predicting a storm's intensity and direction.

### **Impact Plots**

It is important to provide a visual representation of the areas affected by the aggregate interference received by the terrestrial LTE BS network. **Figure K-18** through **Figure K-20** depict the areas where the TriG receiver will be impacted for COSMIC-2B and Sentinel-6, respectively. These figures are provided as a sample - additional impact plots for all of the simulations run for COSMIC-2B, and for a majority of the simulations for Sentinel-6, are available.

## COSMIC-2B Impact Plots

**Figure K-18** demonstrates the locations of where the TriG receiver will receive various levels of interference. In the COSMIC-2B plots, below, the colored levels are defined as:

**Table K-16: COSMIC-2B Impact Plot Threshold Levels**

Received Interference Level (dBm)	Color	Comment
$< -90$	None	Below simulation parameters. No interference recorded.
$\leq -90 < -73$	YELLOW	Interference received, but below -73 dBm (-1 dB C/No) threshold
$\leq -73 < -59$	ORANGE	Interference received above -73 dBm (-1 dB C/No) threshold, but below -66 dBm (loss-of-lock ) threshold
$\geq -59$	RED	Interference received causes TriG to lose lock

Although the impact plots provide a representation of the areas where degraded performance of the TriG receiver will occur, it must be noted that the position of the degradation signifies the location of the LEO satellite and not where the occultation measurement is taking place, which is about 3,200 km (COSMIC-2BB) or 4,200 km (Sentinel-6) before and behind the satellite.

The plots demonstrate the received interference levels based on the simulation parameters. Therefore, the plots for COSMIC-2B depict simulations with the forward antenna subarray. RO measurements from the forward array will slightly skew the overlaid interference plots toward the equator, while the satellite is traversing in the southwest to northeast direction. In converse, the RO measurements from the forward array while traversing over the U.S. in a northwest to southeast direction will skew the overlaid interference plots toward the north pole.

Additional consideration must be given to the aft antenna array for COSMIC-2B, in combination with these plots.

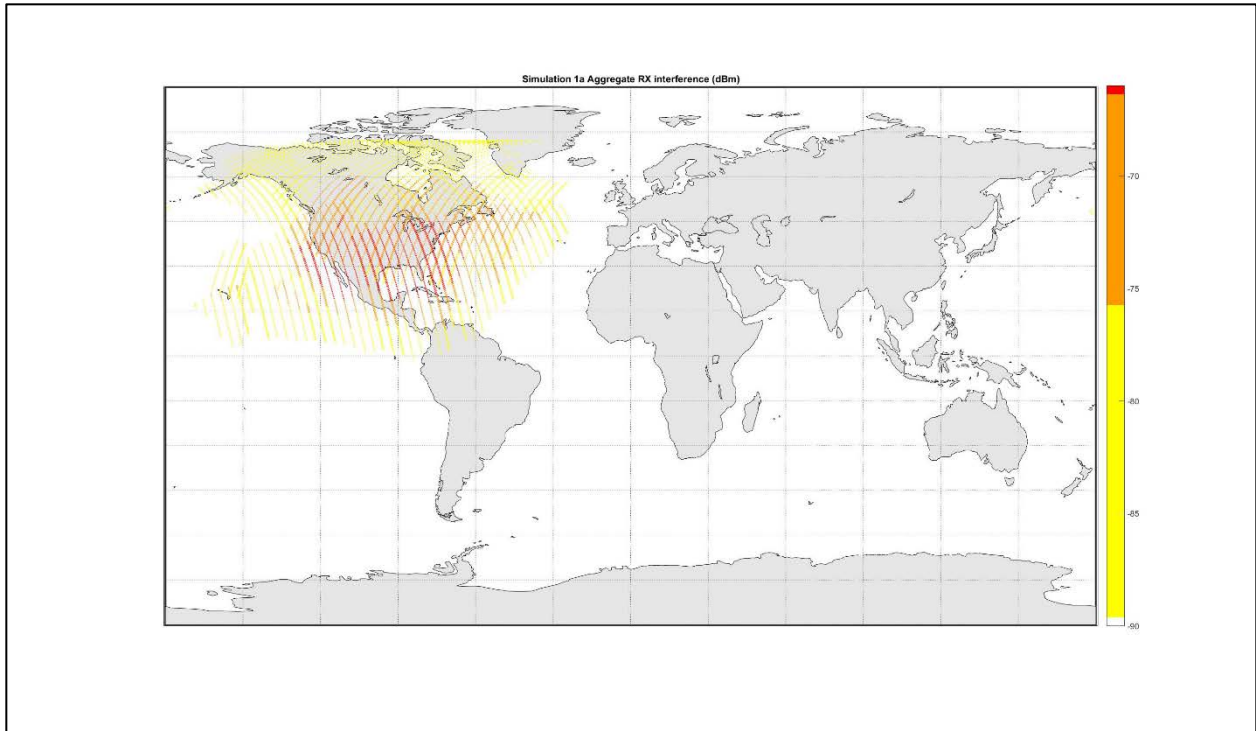
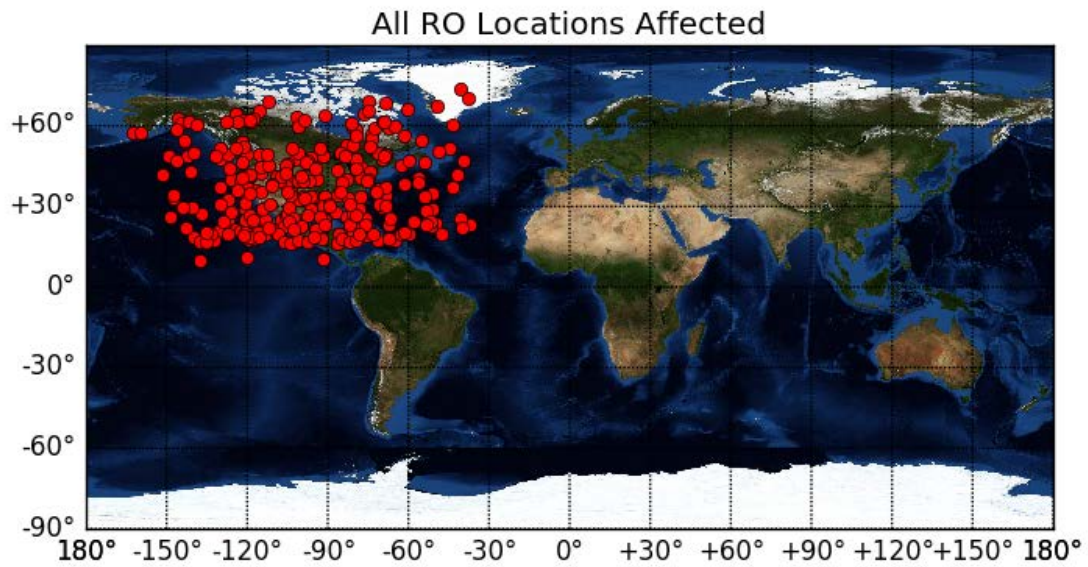


**Figure K-18: COSMIC-2B Interference Impact Plot for Simulation 1a (Sample Plot)**

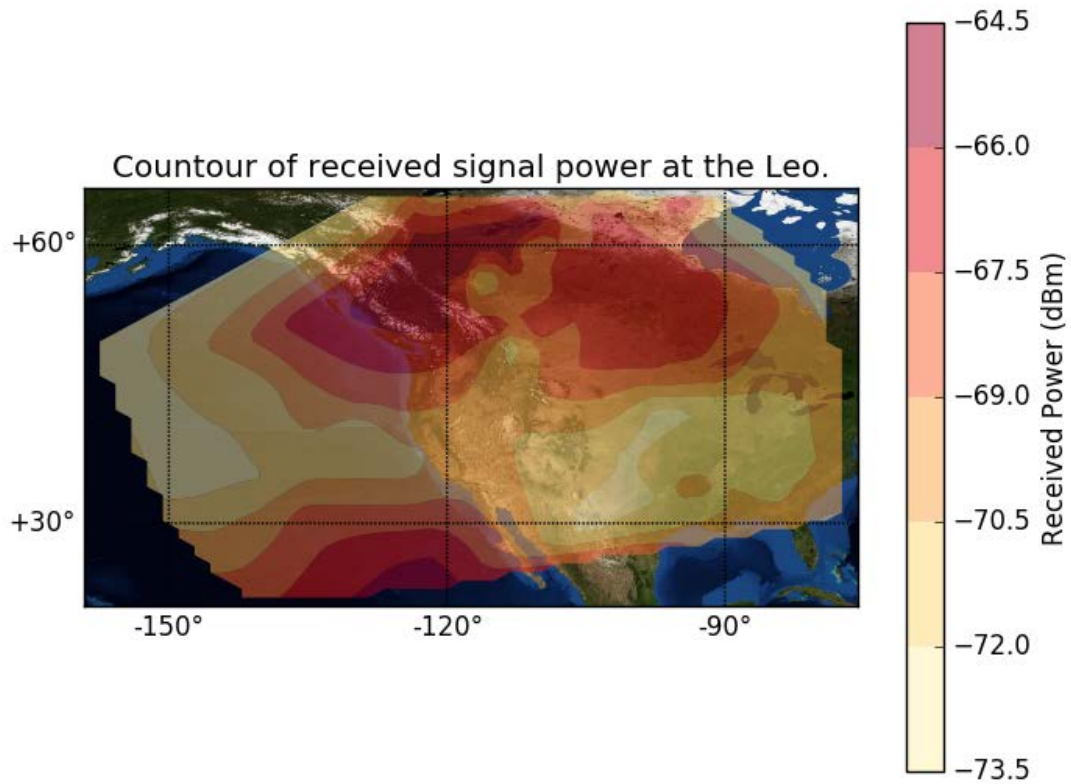
### **Sentinel-6 Impact Plots**

Figure K-19 and Figure K-20 demonstrate the interference impacts to Sentinel-6. Figure K-19 depicts the positions where the RO measurements are located when the interference power is greater than 73 dBm. Coupled with Figure K-19, Figure K-20 depicts the level of received interference from the LTE BS network as experienced at the satellite as it passes over the Continental United States. These two (2) plots have been generated for each of the Sentinel-6 simulation runs performed with simulation 3c depicted.





**Figure K-19: Sentinel-6 Plot of RO Locations for Simulation 3c (Sample Plot): Occultation measurement locations affected when interference power is greater than 73 dBm**



**Figure K-20: Sentinel-6 Interference Impact Plot of Simulation 3c (Sample Plot)** This plot shows the level of interference in dBm experienced when the satellite passes over the Continental United States.